

VALIDATION OF A COMPUTER MODEL
OF A PARACHUTE

by

John A. Eaton

Copyright © by John A. Eaton, 1982.
All rights reserved.

A thesis submitted to the University of Leicester
for the degree of Doctor of Philosophy

MARCH 1982

TO MY MOTHER

VALIDATION OF A COMPUTER MODEL OF A PARACHUTE

John A. Eaton

ABSTRACT

Although many sophisticated stability models of parachutes have appeared, advances are concentrated in the simulation of dynamics of the solid body components of multibody systems. For the complex canopy aerodynamics it is routine to quote several standard simplifying assumptions, few of which can be factually justified since none of the models has convincingly demonstrated its validity by detailed comparison with experimental data. Such demonstrations are essential for confident prediction.

This study investigates a fundamental three-dimensional parachute model. Fluid accelerative reactions are represented by an idealised added mass tensor, and it is shown that the equations of motion in previous treatments are either inadequately or incorrectly derived and/or implemented. Nonlinear solutions of the six degree-of-freedom equations for a rigid axisymmetric system are obtained, and a parameter sensitivity analysis for dynamic stability of a typical personnel parachute indicates that the most important aerodynamic parameters are the added mass components and the pitch damping derivative, not one of which has been adequately estimated.

A systematic validation method is outlined. The kinematics of four free-falling parachute scale models, with canopy flight diameters from 1.4 m to 5.8 m, have been acquired from a strapdown inertial measurement system. Spectral analysis of the transducer signals reveals sharply defined frequencies of oscillation. Comparisons of simulation and experiment demonstrate that satisfactory agreement in frequencies and mean amplitudes of oscillation can be extracted. However, no inherent influence is evident in the model to enable the observed, apparently random amplitude modulation to be reproduced. Sources of the random motion are discussed, one significant and hitherto ignored source being self-excited unsteadiness of the separated flow around the canopy. Measurements of unsteady aerodynamic forces on parachute canopies are needed, also improved estimates of fluid accelerative reactions and aerodynamic damping.

"Iṛ mór aṅ nī aṅ neart!" aṛraṅ
Dreóilín nuair a tarrainṅ
rḗ aṅ riart ar aṅ ríoc.

Seandocal 3ae1ac

ACKNOWLEDGEMENTS

I am especially grateful to my supervisor, Dr. D.J. Cockrell for being a constant source of wisdom, guidance, encouragement and assistance, and to Professor G.D.S. MacLellan, Head of the Department of Engineering, for his continual support and interest. For their considerable skills and patience, I thank Messrs. C.Harris, S.Brown, D.Dryden, G.Burdett, T.Shearer, D.Pratt, D.Jorgensen, C.Morrison and J. Pearson. Drs. A.C.Tory, K.W. Brodlie, H.Bez and Messrs. A.Corbett and G. Tolton and many others provided helpful discussions and advice. The award of a travelling grant by the University Research Board is gratefully acknowledged.

I wish to thank Drs. W.G.S.Lester, J.S.Lingard, Messrs. D.Dennis, A.Arnold and T.Hayden of E.P. Department, RAE Farnborough, for their enthusiasm and technical assistance. Sgts. Thurston and Carse of the PTU Unit, RAE Cardington supervised the running of the drop tests. This study was supported in part by the Procurement Executive, Ministry of Defence, under Research Agreement AT/2026/017AE.

Mr. J.K. Edgley of Edgley Aircraft Ltd. made possible the speedy construction of the drop test body. Mr. T. Andrews and his staff in RAD-NAV Department, RAE Farnborough gave every assistance in calibration of the gyros, and Mr. N. Capaldi, of Smiths Aerospace Industries Ltd., kindly calibrated the accelerometers. Mr. S.B. Jackson of Irvin (GB) Ltd. carried out the porosity measurements. I thank Professor L.F. Crabtree and Dr. R. Barrett, of the Department of Aeronautical Engineering, University of Bristol, for making available the large wind tunnel.

I am particularly grateful to my mother, Mrs. K. Eaton, for her support and encouragement throughout, and whose apt advice I ought to have taken sooner. My thanks to the typists, Mrs. L. Friel, Ms. M. Wims, and, above all, Mrs. H. Townsend for their excellent and expeditious work.

CONTENTS

	Page
Abstract	
Acknowledgements	
Contents	vi
List of Tables	x
List of Figures	xi
Nomenclature	xvii
1. INTRODUCTION	1
1.1 General	1
1.2 The Present Study	2
1.3 Review of Previous Work	3
1.3.1 Single-Body Models	6
1.3.2 Multi-Body Models	12
1.3.3 Comparisons with Flight Tests	14
1.4 Aims of the Present Study	17
2. THE COMPUTER MODEL	18
2.1 Historical Note	18
2.2 The Equations of Motion	19
2.2.1 Discussion of the Equations of Motion	20
2.2.2 The Added Mass/Included Mass Dichotomy	24
2.3 The Current Simulation Model	25
2.3.1 Dynamics	25
2.3.2 Aerodynamics	26
2.3.2.1 Canopy	26
2.3.2.2 Store	28
2.3.3 Mass-Geometric Quantities	29
2.3.4 Kinematics	30
2.3.5 Solution	33

2.3.6	Inputs	33
2.3.7	Outputs	34
2.4	Parameter Sensitivity Analysis	34
2.4.1	Reduction of Results	35
2.4.2	Baseline	36
2.4.3	Mass-Geometric Parameters	37
2.4.4	Aerodynamic Parameters	38
2.4.4.1	Force/Moment Coefficient Curves	38
2.4.4.2	Damping Moment Derivative	44
2.4.4.3	Added Mass Components	45
2.4.4.4	Store	48
2.4.5	Fluid Density	49
2.4.6	Summary of Results	50
2.5	Conclusions	50
3.	FREE-FLIGHT EXPERIMENTS	52
3.1	Introduction	52
3.1.1	Defining an Optimal Flight Test Programme	52
3.1.2	Implementation of the Physical Model	54
3.2	Instrumentation	55
3.3	Kinematic Analysis	56
3.4	Experimental Apparatus	57
3.4.1	Instrumented Flight Test Body	58
3.4.2	Large Flight Test Body	60
3.4.3	The Data Acquisition System	60
3.4.4	Support Equipment	64
3.5	Calibration	65
3.6	Experimental Technique	65
3.7	Summary and Results of Experiments	67
3.7.1	Summary of Experiments	67

	Page
3.7.2 Observations	67
3.8 Reduction of Data	69
3.8.1 Transducer Signals	69
3.8.2 Fourier Analysis	70
3.8.3 Angular Rate Derivatives	72
3.8.4 Pitot-Static Signals	72
3.8.5 Integration and Synthesis	74
3.8.6 Error Propagation due to Noise	75
3.8.7 Bias Corrections	76
3.8.8. Results	77
3.9 Discussion of Results	78
3.10 Conclusions	82
4. COMPARISON OF EXPERIMENTS WITH CURRENT SIMULATION MODEL	83
4.1 Method	83
4.2 Input Parameters	84
4.3 Results	85
4.4 Discussion	86
4.4.1 Drop Distance	86
4.4.2 Drag Accounting	87
4.4.3 Descent Mode	88
4.4.4 Euler Angles	88
4.4.5 Speeds and Aerodynamic Angles	89
4.5 Remarks	90
4.5.1 Atmospheric Effects	90
4.5.2 Self-Excited Unsteady Flow	90
4.6 Conclusions	92
CONCLUSIONS	93

APPENDIX B1	Derivation of the Equations of Motion	96
APPENDIX C1	Development of the Rigging Line Arrangement to Produce a Rigid Body System	103
APPENDIX C2	Kinematic Analysis of the IMU Signals	105
APPENDIX C3	The MPU Data Acquisition Programme	110
APPENDIX C4	Calibration	112
APPENDIX C5	Estimation of the Bias Corrections	122
Tables		127
References		148
Figures		154

LIST OF TABLES

<u>No.</u>	<u>Title</u>	<u>Page</u>
1.1	Conceptual dynamic stability models of parachutes: single-body models	127
1.2	Conceptual dynamic stability models of parachutes: multi-body models	128
2.1	C_N, C_T curve coordinates from Heinrich and Haak	129
2.2	C_N, C_T curve coordinates from Ayres	131
3.1	Basic parachute stability and performance parameters	53
3.2	Drop test procedures	132
3.3	Production drop tests from balloon rig	136
3.4	Ratios of mean descent speeds to peak mean wind speeds	138
4.1	Comparison of calculated distances fallen with release altitude	86
4.2	Sources and estimates of errors (%) in $C_D(\alpha = 0)$	87
4.3	Estimated mass ratios for canopy/store configurations tested	90
C4.1	x-direction gyro, pre-trial calibration	139
C4.2	y-direction gyro, pre-trial calibration	140
C4.3	z-direction gyro, pre-trial calibration	141
C4.4	x-direction gyro, post-trial calibration	142
C4.5	y-direction gyro, post-trial calibration	143
C4.6	z-direction gyro, post-trial calibration	144
C4.7	Accelerometer pre-trial calibrations	145
C4.8	Accelerometer post-trial calibrations	146
C4.9	Data acquisition system calibration	147

LIST OF FIGURES

<u>No.</u>	<u>Title</u>
1.1	Coordinate systems
1.2	System geometry and coordinate frames
2.1	Input parameters for baseline case
2.2	Results of baseline run
2.3	Results of baseline run
2.4	Effect of variation in the line length on stability
2.5	Effect of variation in the store mass on stability
2.6	Effect of variation in the canopy diameter on stability
2.7	Force components measured by Heinrich and Haak
2.8	Comparison of C_N, C_T curves for zero-porosity flexible and rigid circular flat canopy models
2.9	Comparison of C_N, C_T curves for $\lambda_e = 0.3\%$ (flexible), $\lambda_G = 0$ (rigid)
2.10	Comparison of C_N, C_T curves for $\lambda_e = 1\%$ (flexible), $\lambda_G = 2\%$ (rigid)
2.11	Comparison of C_N, C_T curves for $\lambda_e = 4.2\%$ (flexible), $\lambda_G = 4\%$ (rigid)
2.12	Comparison of measured and assumed steady-state moments about the origin for baseline: $K_{11} = 0.25$, $K_{33} = 0.40$
2.13	Results of applying experimental C_{M_0} to baseline configuration
2.14	Effects of Heinrich and Haaks' and Ayres' C_N, C_T curve pairs on stability
2.15	Results for Heinrich and Haaks' $\lambda = 0$ (flexible) data
2.16	Results for Heinrich and Haaks' $\lambda = 0$ (flexible) data
2.17	Results for Heinrich and Haaks' $\lambda_e = 0.3\%$ (flexible) data
2.18	Results for Heinrich and Haaks' $\lambda_e = 0.3\%$ (flexible) data
2.19	Results for Heinrich and Haaks' $\lambda_e = 1.0\%$ (flexible) data
2.20	Results for Heinrich and Haaks' $\lambda_e = 1.0\%$ (flexible) data
2.21	Effect of scaling of C_N, C_T curves on stability
2.22	Effect of variation in damping moment derivative on stability

LIST OF FIGURES (continued)

- 2.23 Effect of variation of lateral added mass component A_{11} on stability
- 2.24 Effect of variation of longitudinal added mass component A_{33} on stability
- 2.25 Results for added mass coefficient $K_{11} = 2.5$
- 2.26 Results for added mass coefficient $K_{11} = 2.5$
- 2.27 Effect of large variation in A_{33} on stability
- 2.28 Results for added mass coefficient $K_{33} = 5.0$
- 2.29 Results for added mass coefficient $K_{33} = 5.0$
- 2.30 Effect of variation in A_{11} on stability using experimental C_{M_0}
- 2.31 Effect of variation in A_{33} on stability using experimental C_{M_0}
- 2.32 Effect of variation in added moment of inertia A_{55} on stability
- 2.33 Effect of scaling of added mass on damping and on amplitude
- 2.34 Effect of scaling of added mass on frequency
- 2.35 Results for $|[A]| = 0$
- 2.36 Results for $|[A]| = 0$
- 2.37 Results for $|[A]|/|[A]|^0 = 0.5$
- 2.38 Results for $|[A]|/|[A]|^0 = 0.5$
- 2.39 Effect of variation in fluid density σ on stability ($\sigma = 0.05 - 10.$)
- 2.40 Effect of variation in fluid density σ on stability ($\sigma = 0.05 - 1.$)
- 3.1 Layout drawing of the instrumented body
- 3.2 The instrumented drop test body
- 3.3 Instrumented body and impact attenuator development model
- 3.4 SB, dummy and BB drop test bodies
- 3.5 Sectional sketch of large test body
- 3.6 Schematic of the microprocessor-controlled data acquisition system
- 3.7 Outline sketches of the four canopy/store configurations used
- 3.8 BB24 configuration

LIST OF FIGURES (continued)

- 3.9 BB12 configuration
- 3.10-12 SB06 configuration: impact attenuators stowed/deployed
- 3.13 SB12 configuration
- 3.14 SB12 configuration: canopy edge luffing
- 3.15 Rigging arrangement (SB12 configuration; impact attenuators not fitted)
- 3.16 High-level flow diagram of programme CSPT
- 3.17-38 Unconditioned transducer signals for Drops 00-32
- 3.39 High-level flow diagram of programme PROS
- 3.40 Amplitude spectra of inertial transducer signals for BB24-configuration drops
- 3.41-42 Amplitude spectra of inertial transducer signals for BB12-configuration drops
- 3.43-44 Amplitude spectra of inertial transducer signals for SB06-configuration drops
- 3.45 Amplitude spectra of inertial transducer signals for SB12-configuration drops
- 3.46-49 Time derivatives of processed transducer signals; amplitude spectra of Pitot-static sensor signal for the four configurations
- 3.50 Calibration curve interpolation for Pitot-static sensor of BB
- 3.51 Position-error correction curves
- 3.52 Implementation of the position-error correction factor
- 3.53 High-level flow diagram of programme KIN
- 3.54 Noise input signals from trial UF06
- 3.55 Noise input signals from trial CH01
- 3.56 Time derivatives of noise input signals from trial UF06
- 3.57 Euler angle and attitude errors: trial UF06

LIST OF FIGURES (continued)

- 3.58 Euler angle and attitude errors: trial CH01
- 3.59 Position and speed errors: trial UF06
- 3.60 Position and speed errors: trial CH01
- 3.61 Euler angle plots: trial UF06 with $\phi_o = \theta_o = 30$ deg.
- 3.62 Calculated time histories of angles for Drop 2 (BB24)
- 3.63 Calculated trajectory and speeds for Drop 2 (BB24)
- 3.64 Calculated time histories of angles for Drop 10 (BB12)
- 3.65 Calculated trajectory and speeds for Drop 10 (BB12)
- 3.66 Axonometric view of trajectory for Drop 10 (BB12)
- 3.67 Calculated time histories of angles for Drop 25 (SB06)
- 3.68 Calculated trajectory and speeds for Drop 25 (SB06)
- 3.69 Calculated time histories of angles for Drop 29 (SB12)
- 3.70 Calculated trajectory and speeds for Drop 29 (SB12)
- 3.71 Power spectra for record partitions of Drop 2 (BB24)
- 4.1-2 Calculated and simulated results for Drop 2 (BB24)
- 4.3-5 Calculated and simulated results for Drop 29 (SB12)
- 4.6-8 Calculated and simulated results for Drop 10 (BB12)
- 4.9-10 Calculated and simulated results for Drop 25 (SB06)
- B1.1 Plane-symmetric body: location of body coordinate frame to
minimize the number of added mass components
- B1.2 Two-fold-symmetric body: location of the body coordinate frame
to minimize the number of added mass components
- C1.1 Conventional rigging, twin riser-pairs
- C1.2 Peripheral, frustum rigging arrangement
- C1.3 Drop test dummy body on hoisting rig in the airship hangar
- C1.4 View of the catchnet arrangement
- C1.5 Final ('geodetic') rigging arrangement
- C2.1 Coordinate frames for kinematic analysis

LIST OF FIGURES (continued)

- C2.2 Assumed initial velocity conditions
- C3.1 Memory map for the MPU data acquisition programme
- C3.2 Flow diagram of the MPU data acquisition programme
- C3.3 Flow diagram of the sampling routine
- C3.4 Read macros for packing 12-bit data into 8-bit memory bytes
- C4.1 x-direction gyro, pre-trial calibration
- C4.2 y-direction gyro, pre-trial calibration
- C4.3 z-direction gyro, pre-trial calibration
- C4.4 x-direction gyro, post-trial calibration
- C4.5 y-direction gyro, post-trial calibration
- C4.6 z-direction gyro, post-trial calibration
- C4.7 x-direction accelerometer, pre-trial calibration
- C4.8 y-direction accelerometer, pre-trial calibration
- C4.9 z-direction accelerometer, pre-trial calibration
- C4.10 x-direction accelerometer, post-trial calibration
- C4.11 y-direction accelerometer, post-trial calibration
- C4.12 z-direction accelerometer, post-trial calibration
- C4.13 Calibrations of the 0.02 psid pressure transducer used in
SB Pitot-static wind-tunnel tests and in drop trials
- C4.14 Calibrations of the 0.2 psid pressure transducer used in
BB Pitot-static wind-tunnel tests
- C4.15 Calibrations of the 0.02 psid pressure transducer for
different excitation voltages
- C4.16 SB Pitot-static sensor test rig in the Leicester University
2.5 m x 1.8 m wind-tunnel
- C4.17 SB Pitot-static sensor calibration test rig in the Bristol
University 7ft x 5ft wind-tunnel
- C4.18 Calibration curves for the SB Pitot-static sensor

LIST OF FIGURES (continued)

- C4.19 Velocity distribution in the return section of the Bristol University 7ft x 5ft wind tunnel
- C4.20 BB Pitot-static calibration in the return section of the Bristol University 7ft x 5ft wind-tunnel
- C4.21 Calibration curves for the BB Pitot-static sensor
- C5.1 Measured bias, p-gyro
- C5.2 Measured bias, q-gyro
- C5.3 Measured bias, r-gyro
- C5.4 Measured bias, x-direction accelerometer
- C5.5 Measured bias, y-direction accelerometer
- C5.6 Measured bias, z-direction accelerometer

NOMENCLATURE

[A]	added mass tensor
A_{ij}	components of [A], $i, j = 1, \dots, 6$ Eqn.(1.2))
A'_{ij}	components of added moments of volume tensor (Eqn.(1.4))
A_k, B_k	Fourier coefficients for frequency f_k
A_0	zero-frequency Fourier coefficient
a	distance along axis of symmetry from centre of added mass to origin
[B]	quadratic form of rigid body inertia tensor [36]
B_{ij}	components of [B] wrt Oxyz, $i, j = 1, \dots, 6$; $B_{ij} = B_{ji}$; $B_{ij} = m\delta_{ij}$; $B_{i,j+3} = m\epsilon_{ijk} x_k^*$; $B_{i+3,j+3} = I_{ij}$
B'_{ij}	components of rigid body moments of volume tensor (Eqn.(1.4))
C_D, C_L	drag, lift force coefficients: $C_D = D/qS_p, C_L = L/qS_p$
C_N, C_T	normal, tangential force coefficients: $C_N = N/qS_p, C_T = T/qS_p$
C_M	pitching moment coefficient: $= M/qS_p D_p$
D	drag force
D_0	open (flat) diameter of canopy
D_p	projected (inflight) diameter of canopy
d_s	store diameter
$F(X,Y,Z)$ or (F_1, F_2, F_3)	total external force
F_k	frequency spectral amplitude modulus $= (A_k^2 + B_k^2)^{1/2}$
F_Z	force along Oz axis, Wolf and Spahr's notation [56]
f_k	spectral frequency: $= f_s k/T, k = 0, 1, \dots, (T/f_s) - 1$
f_s	sampling frequency
\underline{g}	gravitational acceleration vector
g_n	magnitude of \underline{g}
$\underline{H}(H_1, H_2, H_3)$	angular momentum of system wrt Oxyz
h_c	canopy projected height (base plane to apex)
I_{ij}	components of rigid body moment of inertia tensor wrt Oxyz

$I_{ij\alpha}$	components of rigid body moment of inertia tensors wrt respective mass centres
K_{ij}	nondimensional added mass coefficients: $i, j = 1, \dots, 6$ (Eqn. (2.14))
K_1	1st moment of inertia about $Ox, Oy = \sum_{i=1}^n m_i z_i^2$
K_x, K_y, K'	"apparent mass" coefficients, Tory-Ayres notation [4]
$\underline{k}, \underline{k}'$	unit vectors along Oz, IZ axes
$[L_{IO}]$	direction-cosine matrix (Eqn. (2.23))
L	lift force; moment about Ox axis
L_p	$= \partial L / \partial p$
l_L	separation distance between store and canopy base planes
l_p	nondimensional derivative of pitch damping moment (Eqn. (2.13))
l_s	length of store
$M(L, M, N)$ or (M_1, M_2, M_3)	total external moment wrt $Oxyz$
M_q	$= \partial M / \partial q$
M_x, M_y	moments about origin, Wolf and Spahr's notation [56]
M_∞	Mach number
m	total solid body mass $= \sum_{i=1}^n m_i$
m_c	mass of canopy
m_E	"included mass" (Appendix B1)
m_L	mass of rigging lines
m_q	nondimensional derivative of damping moment about Oy axis (see l_p)
m_s	mass of store
N	normal force; moment about Oz axis
N_1, N_2	normal force components, Heinrich and Haak's notation [31]
\underline{P} (P_1, P_2, P_3)	momentum of system
p	angular speed about Ox axis; pressure
Δp	pressure difference

q	dynamic pressure = $\frac{1}{2}\rho w^2$ or $\frac{1}{2}\rho V_{rcp}^2$; angular speed about Oy axis
Re	Reynolds number
\underline{r} (x,y,z)	position vector wrt Oxyz
r	angular speed about Oz axis
S_o	reference area = $\pi D_o^2/4$
S_p	reference projected area = $\pi D_p^2/4$
T	kinetic energy; sampling time interval
T_{ij}	components of KE; $i,j = 1, \dots, 6$
t	time
U	airspeed; average speed across cloth (Eqn.(2.34))
$\underline{u}(u_1, \dots, u_6)$	generalised velocity wrt I
u_i	= \dot{x}_i
u_i^o	= u_i (0,0,0), $i = 1, \dots, 6$: generalised velocity of 0 wrt I
\underline{V} (u,v,w) or \underline{V} (V_1, V_2, V_3)	translational velocity of 0 wrt I
V_B	characteristic body volume
V_r	resultant speed = $(u^2 + w^2)^{1/2}$
V_{rcp}	resultant speed at centre of pressure = $(u_{cp}^2 + v_{cp}^2 + w_{cp}^2)^{1/2}$
w	inertial velocity component along axis of symmetry Oz
w_N	corrected Pitot-static derived airspeed
X, Y, Z	external forces; displacement vector components in IXYZ
\underline{x} (x_1, \dots, x_6)	generalised position coordinates in I
\underline{x}^* (x_1^*, x_2^*, x_3^*)	position coordinates of rigid body mass centre wrt 0
Z	altitude; external force along Oz
z_a	$\equiv a$; Wolf and Spahr's notation [56]
z_s	distance from 0 to store mass centre
z_o	distance from IMU origin to initial point of suspension
α	angle of attack (Eqn.(2.10))
α_g	statically-stable glide angle of attack
$\alpha_{V_{rcp}}$	angle of attack at centre of pressure of canopy

β	sideslip angle (Eqn.(2.11))
γ	phase angle of projection of Oz from IX in IXY plane (Eqn.(2.29))
δ	phase angle of projection of $\omega_{V_{XY}}$ from IX in IXY plane (Eqn.(2.33))
ζ	damping ratio = $\text{Ln}(\theta_i/\theta_{i+1})/2\pi$ (cf.[41])
θ	Euler angle (about Oy axis, for planar motion in IXZ)
λ_e	effective porosity of canopy cloth (Eqn.(2.34))
λ_G	geometric porosity
μ_{ij}	inertia or mass ratio (Eqn.(1.4))
ρ	density
σ	density ratio of fluid = ρ/ρ_0
τ	period of oscillation
ϕ	Euler angle
ψ	Euler angle
ω (p,q,r) or ($\omega_1, \omega_2, \omega_3$)	angular velocity of O wrt I
$\omega_{V_{XY}}$	resultant angular velocity of O in IXY plane (Eqn.(2.31))
ω_V	$\equiv \omega^I$ (Eqn.(2.30))
ω_n	frequency of oscillation in Hz

Subscripts

A	about apex
a_x, a_y, a_z	x- (y-,z-) direction accelerometers
B	body
c	canopy
cp	at centre of pressure of canopy
D	drag
E	"included mass"
e	effective
F	fluid

G	geometric
g	glide
i	indicated value
L	rigging lines; lift
M	measured value; moment
N	at store nose; normal force
O	open
o	initial value
P	arbitrary point in parachute; reference point for output of trajectory and velocity
p	projected; p-direction gyro
q,r	q- (r-) direction gyros
S	store
T	tangential force
v	apex vent
∞	at infinity; freestream value

Superscripts

c	centralised values (for A_{ij} components)
I	wrt IXYZ frame
O	wrt Oxyz frame
o	baseline value(s)
*	derived from added mass components

Operators

δ_{ij}	Kronecker delta; = 1, $i = j$; = 0, $i \neq j$
ϵ_{ijk}	permutation symbol; = 0, $i = j$, $j = k$ or $k = i$ = +1, i, j, k cyclic; = -1, i, j, k acyclic
	modulus
O()	of order

$\dot{(\)}$	derivative wrt t
$\bar{(\)}$	mean value
$\hat{(\)}$	peak value

Reference Frames

IXYZ	inertial reference frame
Oxyz	body-fixed frame

Abbreviations

ADC	analogue to digital converter
AGL	above ground level
ASL	above sea level
BB	large drop test body
BB12	BB/12 ft. D_0 circular flat canopy configuration
BB24	BB/24 ft. D_0 circular flat canopy configuration
DCO	data counter register
EMI	electromagnetic interference
FFT	Fast Fourier Transform
FSO	full-scale output
FSR	full-scale range
GPSU	ground-power supply unit
H_____	hexadecimal format
I24	circular flat canopy type
IMU	inertial measurement unit
ISA	International Standard Atmosphere
LSB	least-significant bit
MPU	microprocessor unit
MUX	multiplexer
PCB	printed circuit board
PSU	power supply unit
QL	quantization level
RAM	random-access memory

Rx	receiver
SB	instrumented test body
SB06	SB/6ft D _o circular flat canopy configuration
SB12	SB/12ft D _o circular flat canopy configuration
SRB	Solid Rocket Booster
Tx	transmitter

SECTION 1

INTRODUCTION

1.1 General

From humble beginnings as a device for 18th century exhibitionists, the parachute now enjoys unchallenged employment in a variety of demanding roles. The widespread use of the parachute is by virtue of its unequalled capacity as a reliable aerodynamic decelerator which can be stored in a minimal volume prior to rapid deployment. Application categories [1] for parachutes currently include: Emergency Recovery - bailout, ejection seats and capsules, etc.; Vehicle Recovery - such as spacecraft, drones and sounding rockets; Airdrop of material and personnel - e.g. paratroops; Ordnance Stabilization and Delivery - bombs, torpedoes, etc.; Aircraft Deceleration and Stall/Spin Recovery; and many other special uses such as in air-to-air retrieval systems and in skyjumping. A considerable amount of development [1] has been necessary to bring parachute technology to its present state.

Next to reliability, stability is one of the main criteria used in the selection of parachutes for many applications. A typical, unconstrained personnel parachute might exhibit any or all of three principal descent modes: a pendulum oscillation, a glide - vertical or oblique - or a spiral (coning) motion. Several other modes, both continuous and transient, are also possible depending on the stability of the particular configuration and the degree of external disturbances.

Parachute stability, or rather the lack of it, has been of concern from the very beginning. Indeed, the first types oscillated so violently that they caused the parachutists to be sick [2]. In many applications use of a particular descent mode is specified, and it may be essential that

the system retain a sufficient margin of stability in this mode under all likely operating conditions. A system designed to follow a ballistic trajectory, for example, would be useless if a sudden gust could send it into an off-course glide. The state of motion at landing is often critical: many types of store, including spacecraft and the paratrooper, are not stressed to cope with landings far off the vertical, so that an oscillating descent must be avoided; likewise, torpedoes are designed to enter the water at a precisely controlled attitude.

Because of the considerable costs, difficulties and risks that can be involved in full-scale testing it is desirable that these be reduced where possible, hence the need for the development of reliable mathematical methods for optimum design and performance prediction.

1.2 The Present Study

This work forms part of a research programme which was initiated in 1972 with the aim of developing a design package for parachute systems operating at subsonic speeds. The programme, conducted by the Parachute Group at the University of Leicester under the supervision of Dr. D.J. Cockrell, is concentrated on the dynamics of systems in the post full-inflation phase of operation; a complete package would also cater for the deployment phase. The design procedure requires the ability to confidently predict the stability and dynamic characteristics of parachute configurations, and to this end work at Leicester produced a lumped-parameter digital computer model [3,4] which simulated the descent behaviour in three-dimensional space of a single, rigid-body parachute.

The current study deals with analytical and experimental steps taken to assess the validity of the Leicester computer model in its predictions of the dynamic behaviour of parachutes.

The predictions will depend on how adequately the complete physical system has been analysed and reproduced in conceptual form. Several fundamental aspects of parachute modelling, the canopy aerodynamics in particular, are considered here. Under present conditions, where our understanding and

knowledge of the physical system is limited, the validity of the model predictions can only be judged by comparison with the behaviour of the real system. The acquisition of data suitable for this purpose is also treated.

1.3 Review of Previous Work

With a few exceptions, principally of UK origin, scientific investigation of the parachute, as opposed to the empirical cut-and-try approach, dates from the exigencies of World War 2. More recent impetus to parachute research has been provided by the various space projects, where the highest reliability and weight-effectiveness are demanded.

A conservative survey of conceptual dynamic models of parachute systems will reveal about 40 versions published to date in the open literature. About half of these supply numerical solutions to the equations of motion, and of this set two-thirds provide solutions in 3D space for systems with a variety of degrees of sophistication - ranging from single 5 DoF bodies to multiply-connected nonlinear viscoelastic systems with stochastic wind inputs. Some of the more significant contributions are mentioned here along with the sources of input data on which they rely.

Definition of Added Fluid Mass

One fluiddynamic concept which frequently appears in the treatment of parachute dynamics is that of added fluid mass. This is now briefly defined and assessed for significance.

Consider the general motion of a solid body B in an infinite fluid region R (Fig.1.1). The fluid is assumed to be at rest at infinity, with respect to an inertial co-ordinate system I , and we specify a Cartesian mean body co-ordinate system $Oxyz$. Describing by the co-ordinates x_1, \dots, x_6 the six degrees of freedom of motion in I , the kinetic energy of the fluid T_F may then be conveniently written in terms of the body origin velocities u_i^0 in the form

$$T_F(t) = \sum_{i,j=1}^6 T_{Fij}(\underline{u}, \rho) = \frac{1}{2} \sum_{i,j=1}^6 A_{ij}(\underline{u}, \rho) u_i^0(t) u_j^0(t) \quad (1.1)$$

where $A_{ij}(\underline{u}, \rho) =$

$$= (1/u_i^0(t) u_j^0(t)) \iiint \rho(x_1, x_2, x_3, t) u_i(x_1, x_2, x_3, t) u_j(x_1, x_2, x_3, t) dR \quad (1.2)$$

The A_{ij} , having the dimensions of mass, first and second moments and products of inertia in Eqn. (1.1), are called the components of the added mass tensor [A].

In accelerating the body via external forces and moments the fluid kinetic energy also changes, e.g. take $A_{ij} = \text{const.} \neq 0$ in Eqn. (1.1). To achieve a particular change in velocity \underline{u}^0 of the body the external forces and moments may therefore be divided into two sets, those required to accelerate the body and those needed to accelerate the A_{ij} . We may thus state that in general, rigid body motion the added mass will be of dynamical significance when any combination of the ratio

$$T_{Fij} / T_{Bij} \geq 0(1); \quad i, j = 1, \dots, 6 \quad (1.3)$$

where

$$T_{Bij} = \frac{1}{2} B_{ij} u_i^0 u_j^0 \text{ is significant, } B_{ij} \text{ being components of the}$$

rigid body inertia tensor.

Define a mean fluid density $\bar{\rho}$ ($\bar{\rho} = \rho_\alpha(Z)$, say), a mean solid body density $\rho_B = m/V_B^\dagger$, and using Eqn. (1.3) we find that any A_{ij} will be significant when its inertia or mass ratio

$$\mu_{ij} = A_{ij}/B_{ij} = (\bar{\rho}/\rho_B) (A'_{ij}/B'_{ij}) > 0(1) \quad (1.4)$$

where

$$A'_{ij} = A_{ij}/\bar{\rho}, \quad B'_{ij} = B_{ij}/\rho_B.$$

† For a parachute canopy the solid body volume may be very small; in this case V_B is taken as the projected volume enclosed by the canopy.

As a rough guide, for a sphere in ideal flow [5], $A'_{11}/B'_{11} = 0.5$, suggesting that added mass will be important when the mean fluid and body densities are comparable. This statement must be treated as a very first order approximation; in particular, the added mass A_{33} (Fig.1.2) of parachute canopies has been shown to decrease rapidly with increasing geometric porosity [6]. Exprn. (1.4) holds for parachute systems with low terminal descent speeds and/or low porosity canopies, as typified by the personnel parachute.

For a given body shape, each of the 36 components of $[A]$ will depend at any instant t on a large number of parameters;

$$A_{ij}(t) = f(u_1, \dots, u_6, \dot{u}_1, \dots, \dot{u}_6, \rho_\infty, M_\infty, Re) \quad (1.5)$$

Experiments in real fluids [7,8], mostly in the range $Re = 10^3$ to 10^5 , confirm the considerable extent of the problem; even for such a regular shape as a sphere, results indicate that variations of about two orders of magnitude in the non-dimensionalised added mass component A'_{ii}/B'_{ii} ($i = 1,2,3$) are possible [9,10].

Full analytical evaluation of the A_{ij} (see Eqn. (1.2)) amounts to solution of the parachute canopy flowfield problem, and is beyond the current state of the art of computational fluid mechanics: the general flow may be classified as compressible, turbulent, separated, three dimensional, and most significantly, unsteady [11]; the typical canopy is porous, has holes and is a flexible, tensile structure *par excellence*.

Comprehensive flowfield modelling would in any case seem to be premature, at least until minimal real flow data are available for validation. At present, experimental data of one form or another offer the best prospect for progress in estimating the A_{ij} .

1.3.1 Single-Body Models (Table 1.1)

In 1918 Brodetsky [12] of Bristol treated the stability of a parachute descending vertically at terminal velocity. He assumed the parachute to be axisymmetric and rigid ("the passenger ... being supposed to hold on tight so that he has no independent oscillation"), and using the Euler angle notation [13] to specify the orientation in space of a body-fixed axis set located at the centre of gravity, he obtained the six equations of motion. Following the linear aerodynamic force and moment velocity-derivative assumption due to Bryan [13], Brodetsky considered the effects of small perturbations on the motion. His solutions were necessarily limited by lack of information on the aerodynamic derivatives, but he found in general that longitudinal motion (along and about the axis of symmetry) was stable. He pointed out that because of (axi)symmetry the general theory of the lateral stability of the parachute is only a two-dimensional problem. Using the Routh criteria, he arrived at conditions on the disposition of the masses ("umbrella" and "passenger") to ensure lateral stability.

Nayler *et al.* [14] in 1919 considered the rigid 6 DoF parachute as a particular case of a system comprising a rigid canopy attached with elastic lines to a point-mass store. To solve the linearised equations for lateral motion they calculated the necessary aerodynamic derivatives from static forces and moments measured on model canopies in a wind-tunnel [15]. Lacking experimental data for aerodynamic damping of the pitching motion, they suggested how this could be measured using the free oscillation technique. They also described, though did not implement, how acceleration effects could be represented by introducing an added mass and an added moment of inertia.

Jones [16] reported in 1943 on a comprehensive series of investigations undertaken to study the effect of porosity on the stability of a parachute. He conducted experiments to obtain data which could be applied in the

equations of motion: rigid canopy models were perforated to simulate porosity, and three-component balance measurements were made on a variety of complete parachute models consisting of a forebody (store), rigging lines and canopy. Jones also carried out experiments to measure the pitch damping and the added mass, and calculated that a reasonable value for the added mass would be 1.4 times the mass of air "contained" in the canopy. Jones was the first to implement added mass in the parachute equations of motion. Using the linearised planar form of Nayler's equations, he treated it as a single point mass located at the canopy centroid. His solutions to the linearised equations, for a variety of canopy-store combinations with $\mu_{11}(=\mu_{22} = \mu_{33})$ from 0.7 to 6.0, showed that the inclusion of added mass greatly increased the period of oscillation and reduced the damping to zero.

Henn [17] in 1944 was the second to take added mass into account in a planar, 3 DoF study of parachute stability. To obtain input values for the added mass components Henn and others turned to classical hydrodynamic theory [18,19], where it has been shown that by idealizing the body-fluid system it is analytically possible to reduce the number of different added mass components needed, and also to calculate their values, which are constants for a given shape. For the basic stability modelling of a parachute with a fully deployed canopy conventional practice has hence been to assume the fluid to be inviscid, irrotational and incompressible, and the canopy to be rigid and axisymmetric [20-24]. Further reductions in the added mass terms may be obtained by additionally confining the canopy shape to have an extra plane of symmetry, as with an ellipsoid [17,4] or, most simply, a sphere [25-28]. Assuming the canopy to be replaced with an ellipsoidal, air-filled body, Henn's added mass components comprised contributions from the fluid regions interior (these he called "included mass" and "included moments of inertia") and exterior ("additional apparent" masses and moment of inertia) to the body. In the present notation (see Eqn. (1.1) and Fig.1.2) his added mass components were A_{11} , A_{33} and

A₅₅. By analytical solution of the 3 linearised equations of motion, Henn demonstrated strong influences on the damping and frequency of lateral oscillations (of a mass-geometrically typical personnel parachute) due to individual variations of A₁₁ and A₃₃ withing the ranges $\mu_{11} = 0.0$ to 0.6, $\mu_{33} = 0.0$ to 1.0, around baseline values $\mu_{11} = \mu_{33} = 0.5$.

Henn's rather arbitrary rationale in choosing the baseline added mass values is exemplary: the canopy was replaced by an ellipsoid of axis ratio 0.43, for which analysis [19] gave $\mu_{11} = 0.545$, $\mu_{33} = 1.000$; because the canopy underside is in reality open, he then chose $\mu_{33} = \mu_{11} = 0.545$. Henn's equations were widely used until 1962, when Lester [20] showed that they were erroneous; in uncritically applying to the added mass components the rigid-dynamical equations, rather than the fundamental Kirchhoff equations [18], Henn had violated the concept of added mass. Following Kirchhoff, Lester carefully derived the planar motion equations for an axisymmetric parachute, showing that, in general, four added mass components (A₁₁, A₃₃, A₅₅ and A₁₅ in the present notation) should be considered. The author [24] has found that Lester's *implementation* of added mass is fundamentally inconsistent, and that the same errors appear in other works [21,22,23,29] (Section 2). Lester did not solve the linearised equations of motion because of lack of reliable values for both the aerodynamic force and moment coefficients and for the added mass components. He pointed out the known limitations [8] of applying ideal flow analysis to real flow phenomena, and the need for experimental investigation of the added mass concept in relation to the parachute.

Ludwig and Heins [25], again for planar 3 DoF motion, confined their added mass implementation to Henn's two isotropic "included" terms, but solved the nonlinear equations of motion using both analogue and digital techniques. They treated large-amplitude lateral oscillations of the personnel guide surface parachute, obtaining input data from aerodynamic

force coefficient measurements[†] by Heinrich and Haak 1962 [30].

Using values of μ_{11} ($= \mu_{33}$) in the range 0.6 to 1.4, they concluded that the added mass mainly affected oscillation amplitude and damping, had a minor effect on frequency, and overall was not very important.

Both Jones and Henn found that typical parachutes could not fall vertically because of the shape of the normal (sideforce) coefficient curves at zero angle of attack. A small deflection in α gives a normal force away from the axis of symmetry, so that the system is statically unstable. Their small-disturbance results indicated that one possible descent mode was an unsteady oblique glide with the parachute axis oscillating about the vertical. Their analyses were limited to consideration of angles of attack up to about 30° - Henn's because of a lack of confidence in the input data and Jones by a belief that equilibrium conditions could only be satisfied at $\alpha = 0$. Heinrich [32] later pointed out that equilibrium does not necessarily require $\alpha = 0$: the conditions are met at an $\alpha = \alpha_g$ for which both (i) the normal force is zero and (ii) the tangential (axial) force balances the weight. For static stability around α_g it is also necessary that any perturbation to α be resisted by a restoring moment. Heinrich called α_g the stable glide point, since at this angle the parachute will glide with its axis vertical. Note that although the conditions described are *necessary* for both static and dynamic stability, they may not be *sufficient* for dynamic stability. The value of α_g varies widely from one canopy shape to another; measurements by Heinrich and Haak [31] and others [33] indicate that it may be 45° or more.

Wolf [26] and White and Wolf [34] dealt with the in-plane and out-of-plane dynamic stability of a steady gliding motion in a 3 dimensional, 5 DoF computer model of a single rigid body parachute. The obtained solutions to both the linearised and nonlinearised equations of motion, and

[†] These were later found to be incorrect [31], so Ludwig and Heins' results must be treated with reserve, also other results [34] which rely on the same data.

presented a criterion for glide stability. Employing the same scalar added mass components as Ludwig and Heins, they referred for input data to experimental and theoretical investigations of added mass by Ibrahim [35,36], also to the (incorrect) measurements of Heinrich and Haak. For a system which satisfied their criterion for dynamic stability ("glide-stable") at the glide point, they found that small in-plane disturbances were damped and that neutral stability was shown for small out-of-plane perturbations. A system which was glide-unstable was found to diverge to a large angle pitching oscillation for an in-plane disturbance and to a vertical, large angle coning motion for an out-of-plane disturbance.

One exception to the trend of reducing the representations of added mass was the 6 DoF model introduced in 1972 by Tory and Ayres [3,4,37], where, on the basis of the dubious assumption of a real (physical) distinction between "included" and "apparent" mass [38,39] they reverted to Henn's original collection of components. Three-component data were obtained from measurements on rigid canopy models [33,39]. As part of the overall model validation [40] the author carried out a sensitivity analysis [41] for a typical personnel parachute system. This indicated that A_{33} and A_{55} were not important as regards lateral dynamic stability, but that the magnitude of A_{11} and its location had a significant effect on damping. Damping increased with increasing store mass, as found by White and Wolf, but was unaffected by A_{33} . Baseline mass ratio values used were $\mu_{11} (= \mu_{22}) = 0.5$, $\mu_{33} = 0.9$, and the ranges covered were $\mu_{11} = 0.0$ to 6.7 and $\mu_{33} = 0.0$ to 6.5.

Byushgens and Shilov [22], in a purely theoretical 3 DoF study, pointed out inadequacies of added mass modelling in previous models [25,42,43,27]. Linearising their equations, and carrying out a root locus analysis for the particular case of single DoF angular motion about the store, they showed strong effects of A_{11} and A_{44} on the stability.

They suggested dynamic wind tunnel tests using a frequency response technique to find the added mass components. Using the same planar 3 DoF equations of motion, Shilov also investigated the stability boundary for lateral oscillation [21] and the damping of the same motion [23]. In the latter study [23] he suggests that his damping model be used in parameter identification analysis from flight test experiments. These equations implement added mass in a manner similar to that of Lester, whose work they appear to be unaware of, and, as will be seen, are similarly inconsistent.

Discovery of Refs.[21, 22, 23] in early 1980 prompted the author to check the added mass terms in Tory and Ayres' model; their equations of motion were found to be erroneous, having suffered, to a greater degree than Henn's, from application of the rigid dynamical equations. Following the added mass expressions of Kirchhoff, Lester and Ibrahim [36], the author was the first both to derive the full 6 DoF equations from fundamentals, and to obtain nonlinear solutions [44-46, 24]. In all known previous treatments of parachute stability, the full significance of added mass has yet to be appreciated due to inadequate or incorrect derivation and/or implementation of the added mass tensor. It is shown here (Section 2) that added mass effects are more significant than hitherto predicted.

Schulz and Hamel [27] used harmonic describing functions to model the normal force coefficient in a simple planar 3 DoF model, and hence obtained approximate nonlinear analytical solutions for limit-cycle type lateral oscillations. Comparison of their nonlinear analytical solutions with "exact" solutions by numerical integration gave good agreement in estimates for amplitude and frequency. Churkin and Kosarchuk [47] modelled a similar system using the same techniques, and also demonstrated good agreement with a numerical solution.

Goodrick [48,49] has been developing a three-dimensional model of a

gliding parachute. In this case the canopy is plane-symmetric (rather than axisymmetric), so that the aerodynamic force and moment coefficient inputs are more complex. Although Goodrick models the steady-state aerodynamic forces in a three-dimensional form, he treats the added mass as a rigid-body "included" mass (cf. Henn). It is shown in Section 2 that for the motion of a plane-symmetric rigid body in an *ideal* fluid there are at least 12 unique non-zero added mass components.

1.3.2 Multi-Body Models (Table 1.2)

As early as 1919 Nayler *et al.* [14] studied the dynamics of a two-body system consisting of a point mass connected via elastic lines to a rigid canopy. They concluded that for longitudinal (axisymmetric) motion the system was stable under all conditions.

Many of the more recent works on multi-body (or "non-rigid" [43]) models have been concerned with dynamic stability investigations of particular major projects, for which steady-state aerodynamic input data are usually individually determined. Thus Neustadt *et al.* [42] considered the planar dynamics of a model applicable to the Apollo crew module. Vaughn and Matejka [50] analysed the structural failure of a very high altitude (100-225,000 ft) nuclear debris sampler as being due to dynamic instability of the parachute-load system. Talay *et al.* [51], following a mathematical model developed by Gamble [52], modelled the Viking parachute system which was to be used for soft-landing on Mars. Doyle and Burbrick [29] and Ibrahim and Engdahl [53] both analysed the proposed recovery system for the Space Shuttle Solid Rocket Booster (SRB). Bolton [54] and Schatzle and Curry [55] both simulated lifting parachute systems for laydown delivery of the B-77 nuclear bomb [1].

Wolf [43] was one of the first to study the three-dimensional motion of a nonrigid parachute and payload system. Both the parachute and payload were assumed to be rigid bodies, each with 5 DoF (no roll (spin)

about the axis of symmetry), and were coupled together with a fixed-length riser (connecting tieline). Orientations of the 3 body axes systems were described by three sets of Euler angle sequences: the rigid-body equations were obtained for the parachute and payload individually, and then the velocity constraint (coupling) equations for the riser. This gave a total of 21 first-order ordinary differential equations, which were then solved numerically. The steady aerodynamic forces acting on the canopy and on the store were assumed to be functions only of the instantaneous angle of attack, and aerodynamic damping was not considered. Wolf and Spahr [56,57] extended the analysis to cover a 6 DoF forebody coupled via viscoelastic risers to a cluster of rigid 5 DoF canopies. This analysis assumed the canopy added mass components normal to and along the parachute axis to be different (A_{11} , A_{33} , A_{55} in the present notation), as opposed to the spherical "included mass" type components in Wolf's previous analyses [34, 43]: the present work finds Wolf and Spahr's added mass derivations to be inconsistent (Section 2). Wolf's models do not contain aerodynamic angular damping coefficient terms.

Doyle and Burbrick [29] modelled a 6 DoF forebody connected by viscoelastic tether to a 5 DoF (no spin) parachute. Treating added mass components A_{11} , A_{33} , A_{55} (present notation), they used the Hamilton-Lagrange equation to derive the equations of motion. In implementing their equations of motion, they incorporate inconsistencies similar to those of Lester and Shilov.

Ibrahim and Engdahl's SRB recovery system model permits 6 DoF to both the SRB and the parachute, and includes viscoelastic representation for the rigging lines and riser. Although they claimed a "more general representation of apparent mass effects", inspection of their equations of motion for the parachute (Ref. [53], Eqns. 4c and 5c) reveals that they treated added mass in effectively the same manner as Tory and Ayres

(see Section 1.3.1 above and Section 2), i.e. more or less as a rigid body. Ibrahim and Engdahl's model is advanced in other respects, however: a numerical technique allows the system's equations of motion to be linearized at selected points of the descent trajectory and the calculation of the eigenvalues describing the principal motions, hence root locus plots giving the variation in stability characteristics as a function of time can be obtained. An input option allowing the system to be subjected to specified wind and gust profiles, in order to assess their effects on the stability of the recovery system, was also used. Other models have also catered for a wind input [4, 24, 28, 48, 49] .

The recent models of Bolton and of Schatzle and Curry used a hybrid (analogue/digital) computer technique, for a quick turnaround between consecutive simulation runs, during design studies of a lifting non-rigid parachute system. Six-component aerodynamic coefficient data were obtained for input [54] , and these were represented by polynomial curve fits for speed of computation. Both models appear to omit added mass effects altogether, seemingly because of the high-porosity canopies under consideration.

1.3.3 Comparisons with Flight Tests

It is remarkable how very few of the conceptual models have been tested against any experimental results whatsoever. Neustadt *et al.*, Bolton and Schatzle and Curry compare time histories of quantities such as total velocity, descent speed, dynamic pressure, axial deceleration and riser tension and obtain excellent agreement (only one experimental flight was considered in each case). However, as pointed out in Ref. 55, this is to be expected since these quantities depend primarily on the inflation characteristics of the parachute system, and representative inflation histories were supplied as inputs in each case. In effect, these quantities show only that the drag has realistically been accounted for.

For their planar non-rigid model, Neustadt *et al.* also obtained good agreement for the period and peak angles of oscillation of the store, and the store angular velocity was close to the estimated bounds. White and Wolf found good agreement in coning rate for two cases of coning motion; in a third case their calculated coning rate was about half the observed rate.

Talay *et al.* also supplied an inflation history as an input to their 2 x 6 DoF model. Although their model (from [52]) caters for a large number of aerodynamic coefficients due to angular rate inputs, none of these was known, so all but three were set equal to zero. Values for the pitch/yaw moment angular rate damping coefficients of the parachute (equal by axisymmetry) and the roll (spin) moment angular rate damping coefficient of the vehicle were found from iterative matching of simulation with a single flight test. Other input parameters which were also obtained by iterative simulations were the initial angular rates of the parachute (i.e. *initial conditions*), and the suspension line elasticity and damping (the line damping was assumed to be a function of strain only, and not of strain rate). They presented the pitch, yaw and roll-rate results of the vehicle to illustrate the agreement between simulation and experiment, and it can be seen that the envelope of the oscillation amplitude agrees reasonably well for yaw-rate (over an interval of 50s), but the simulated pitch rate is too large. The simulated roll rate curve matches the flight test data well in average value, but it must be remembered that the vehicle roll-rate damping coefficient was chosen to give a good fit. Likewise, the overall pitch and yaw-rate histories match well initially because both the initial angular rates and the damping of the parachute were specified to give good fits to the low-frequency modulation of the vehicle angular rate histories. The simulated and flight test derived aerodynamic angles at the vehicle do not agree very well, but the flight-derived data were subject to Euler angle errors of about $\pm 10^\circ$, and to wind data errors. It

may be noted that the "terminal" descent speed of the system considered by Telay *et al.* was about $170 \pm 20 \text{ ms}^{-1}$ (Mach 0.5); observed winds at the deployment altitude of 45,000 m (147,000 ft) were about 50 ms^{-1} (160 ft s^{-1}) throughout the test.

Telay *et al.* observe that the simulation programme "appears to give similar general trends and magnitudes in the simulation of the vehicle attitude rates but has difficulty in matching flight-test results point-for-point". They conclude that "significant voids in the knowledge of decelerator technology, particularly with regard to parachute aerodynamic characteristics and suspension-system physical properties, appear to be a major obstacle to obtaining very accurate simulations and to the use of the analytical model in a predictive mode".

Before it can be hoped that the detailed dynamic behaviour of a complex, multi-body parachute system can be accurately simulated, it is reasonable to expect that the ability to simulate the motion of the simplest, single-body form of parachute will have been demonstrated to a corresponding degree. Previous works have not achieved this, primarily because of lack [26, 4] of *suitable* flight test data. A major difficulty with flight tests is the unknown extent of atmospheric air movements. Thus, although Tory and Ayres [4] compare simulated trajectories with experimental trajectories that have been "corrected" [58] for a steady wind, the unknown influences of the accompanying turbulence and gusts are not accounted for, so that large uncertainties exist both in the experimental data and in the simulations. Still-air conditions are ideal for testing, for obvious reasons; Stimler and Ross [59] carried out hundreds of drop tests in an airship hanger, but they used non-rigid parachute models, where the parachute had at least 2 angular degrees of freedom about the store, so that their data are of limited value for validating rigid-body models.

1.4 Aim of the Present Study

The ability to formulate and to solve the equations of motion of quite sophisticated parachute systems appears to have been demonstrated. Because of the complexity of the canopy aerodynamics, the majority of models incorporate a number of similar simplifications regarding these components - the fluid acceleration effects in particular. These simplifications are difficult to justify in the absence of experimental verification, so that uncertainties to an unknown degree exist in both the input data and in the simulations.

The present study has the primary aim of assessing the simulation ability of a fundamental, three-dimensional model of a parachute, with particular respect to the detailed oscillatory motion.

Subordinate objectives are as follows:

1. To critically review the computer model [4] and its input data.

The assumptions regarding fluid inertia effects are frequently used uncritically, and the implementation of the effects varies widely from one model to another. As outlined in Section 1.3 above, the effects are likely to be significant in many cases, and hence are worthy of closer investigation (Section 2).

2. To identify the important parameters in the present computer model [24]. In this way resources will not be wasted in overspecifying unimportant parameters, and the need for improved measurements can be judged (Section 2).
3. To obtain a variety of experimental flight test data suitable for simulation comparisons of the oscillatory motion (Section 3).
4. To compare the simulations of the present computer model with the flight test data, and hence to assess its capabilities and limitations (Section 4).

SECTION 2

THE COMPUTER MODEL

2.1. Historical Note

The original Leicester computer model was written by Dr. A.C. Tory and issued as an internal report in 1972 [3]. Although a number of parachute simulation models were already in existence (Section 1.3) the only one referred to by Tory was the White and Wolf model [34]. The objective appears to have been to improve on some of the apparent shortcomings of White and Wolf's model - the restriction to 5 DoF and the confusing non-dimensionalised notation. Another useful feature was the introduction of a wind input option, which allowed simulation of the system response to a steady or turbulent wind. It was assumed that the "hydrodynamic" mass (Wolf's terminology [26]) and moment of inertia could be approximated by single scalar values (cf. also [26]); other simplifying assumptions were the same as currently prevailed for single, rigid-body models - axisymmetric canopy, quasistatic aerodynamic force/moment coefficient curves and a flat Earth for trajectory calculation.

The model was intended to reproduce as simply as possible the full three-dimensional behaviour of a parachute. The sixth (roll/spin) degree of freedom permitted the simulation of a "steerable" system. The computer programme was written in FORTRAN and arranged in a subroutine form which allowed easy modification of specific operations. Parallel work at Leicester was aimed at supplying the aerodynamic inputs to the programme [33]. Modelling added mass as a sphere in ideal flow, it was found that the stability of the system was extremely sensitive to small variations in the slope $\partial C_N / \partial \alpha$ of the normal force coefficient [3]. The three principal descent modes - glide, pendulum oscillation, coning - were observed; a lateral (out of plane) perturbation to a steady glide produced

either a lateral oscillation or coning, depending on the size of the disturbance, as found by White and Wolf [34].

One of the modifications to the programme was to replace the isotropic added mass with an anisotropic system, modelled on the values for a prolate spheroid in ideal flow [38,33,39]. This idea was proposed by Henn [17] in 1944, and Henn's "included" fluid components were also adopted. After investigation of this form of the model, the authors concluded that added mass was not very important [4,33,39]. Subsequently, however, a more detailed parameter sensitivity analysis [41] by the present author disagreed with this, finding that the A_{11} component had a strong effect on damping.

Later analysis by the author [24] has shown that the equations of motion derived by Tory and Ayres [4] were incorrect in respect of their derivation of the added mass terms. The correct (for the adopted assumptions) form of the equations was implemented in the computer model, and was found to significantly alter the response to inputs. The author and others also carried out pilot experiments to assess the degree of pitch damping due to angular rates [60,61]; these were found to be important, and were therefore incorporated in the model.

2.2. The Equations of Motion

The detailed derivations of the equations of motion for an axisymmetric parachute are presented in Appendix B1. The equivalent external forces and moments due to the fluid inertia terms are also given for bodies with planar and two-fold symmetries, which may be useful when these configurations are being considered.

2.2.1. Discussion of the Equations of Motion

In deriving the equations of motion (Appendix B1, Eqns.(B1.22), (B1.23)) the assumptions were:

1. The fluid is incompressible, inviscid and irrotational.
2. The fluid region is infinite.
3. The solid components of the parachute form a single rigid body.
4. The body external shape has rotational symmetry.
5. The canopy is imporous.
6. Body axes are chosen specifically so that the only non-vanishing components of the added mass tensor are
 A_{11} , A_{22} ($=A_{11}$), A_{33} , A_{44} , A_{55} ($=A_{44}$), A_{15} , A_{24} ($= -A_{15}$).
7. Body axes are chosen to be parallel to the principal solid body axes.

To implement these equations we must consider the external forces and moments which give rise to the motion: for an unconstrained parachute these will comprise components due to gravity, aerodynamic lift and drag forces, etc. First, let us consider what the added mass expressions in Eqns. (B1.22) and (B1.23) represent: the added mass components have been grouped together with the solid body inertia components on the RHS of the equations, as is conventional. Superficially, this might suggest that the added mass tensor can be regarded (and treated) as simply providing additional, passive inertia quantities which form a composite body with generalised inertia components ($B_{ij} + A_{ij}$); this viewpoint is inadequate, because it masks important properties of the added mass.

Arising from motion of the solid body, the fluid inertia effects (as generally expressed in Eqns.(B1.9) and (B1.10)) are manifest as a pressure distribution on the surface of the solid body, and ought properly to be regarded as fluid reactions, and therefore placed on the LHS (with

the appropriate change of sign) in Eqns.(B1.22) and (B1.23).

The motion of the body need not be unsteady to give rise to fluid inertia effects. Note the couple terms $(A_{33}-A_{11})vw$ and $-(A_{33}-A_{11})uw$ in Eqns.(B1.23); these are non-zero for any *steady* translational motion ($\underline{V} = \text{const.}, \underline{\omega} = 0$) which is not directed along the principal axes [18] of added mass, since in general A_{33} will be different from A_{11} . The corresponding steady moment for two-dimensional ideal flow is discussed by Sedov [62], who uses it to demonstrate, inter alia, the classical aerofoil theory result of the quarter-chord location of the aerodynamic centre. Moments may also arise due to steady rotation ($\underline{\omega} = \text{const.}$) about the body axes, cf. the fluid moment equations for the plane- and two-fold-symmetric shapes (Eqns.(B1.12) and (B1.14)).

In the present computer model aerodynamic forces and moments on the canopy are obtained from the instantaneous angle of attack, the necessary quasi-static functions - e.g. lift, drag and moment - being derived from wind-tunnel measurements. The steady-state added mass couples (henceforth: "[A] couples") will also be contained in the pitch and yaw moments measured in the wind-tunnel.[†] In all previous implementations of the parachute equations of motion this fact appears to have gone unnoticed, either because the terms did not arise at all (due to inadequate $(A_{33}=A_{11})$ or incorrect (Henn, Tory and Ayres) derivations of the equations of motion), or because their physical significance was overlooked, e.g. Lester, Shilov, Doyle and Burbrick. To avoid duplication of the steady-state moments, the following approaches are suggested for their implementation:

- (i) Specify the steady-state forces and moments fully from 3- or 6-component measurements, and omit the [A] couples.

[†]*Sequel:* If, for bodies with two-fold- or axisymmetry, one of A_{11}, A_{22}, A_{33} is known (e.g. A_{33} from [6]), the other two can easily be estimated from *static* 3-component measurements.

(ii) Take the body axes origin (0) to be the aerodynamic centre: the steady-state moments then disappear, by definition.

(iii) Assume 0 is not the aerodynamic centre, and use the [A] couples only.

The first approach is to be preferred, since it is realistic. The second requires nearly the same amount of effort: Doherr [63] has estimated the axial location of the aerodynamic centre for some flexible canopy models from 3-component measurements, and Ayres [33] has estimated its planar location from the surface pressure distributions on small rigid canopy models; in both cases the centres, averaged over $\alpha = \pm 30^\circ$ or so, were calculated to lie within about $\pm 0.2 D_p$ of the canopy base.

The [A] couples are easily expressed in non-dimensional (coefficient) form: in the usual notation for moment coefficient about 0 we have

$$C_{M_0}(\alpha) = M_0(\alpha) / (\rho V_r^2 \pi D_p^3 / 8) \quad (2.1)$$

$$\text{with } V_r^2 = u^2 + w^2, \quad \alpha = \tan^{-1}(u/w) \quad (2.2)$$

The [A] reaction couple for the Oxz (pitching) plane is (Eqn.B1.23)

$$M_0^* = (A_{33} - A_{11})uw \quad (2.3)$$

The added mass coefficients K_{ij} are defined to scale on appropriate inertia components of a reference sphere of fluid: thus

$$K_{ii} = A_{ii} / \rho \left(\frac{1}{6} \pi D_p^3 \right), \quad \text{for } i = 1, 2, 3 \quad (2.4)$$

Hence, from Eqns.(2.1) to (2.4)

$$C_{M_0}^*(\alpha) = \frac{2}{3} (K_{33} - K_{11}) \sin 2\alpha \quad (2.5)$$

Note that $C_{M_0}^*$ is stabilizing ($\partial C_{M_0}^* / \partial \alpha > 0$) around 0 at $\alpha = 0$ only

if $K_{33} > K_{11}$; also the stiffness of the pitching moment coefficient ($|\partial C_{M_0}^* / \partial \alpha|$) is proportional to the difference ($K_{33} - K_{11}$).

The values of the A_{ij} depend on the location of O , so that a shift of origin along the axis of symmetry will change the values (constants) of A_{55} and A_{15} (axisymmetric case) [18]; A_{11} ($=A_{22}$) and A_{33} are invariant under this transformation. If the location of the centre of added mass is known, the values of A_{11}^c , A_{33}^c , and A_{55}^c can be used [18,21-23,62] to derive the equations of motion referred to any other body origin on the axis of symmetry, thus retaining only 3 different components. Wolf and Spahr [56] adopted this approach for the 5 DoF (no spin) equations of motion for the canopies in their multibody model. They assumed that the canopy centre of pressure (taken to lie on the axis of symmetry) for the unsteady (acceleration) forces coincided with that for the quasi-steady forces, which permits the [A] couples to be dropped. Examination of their equations of motion ([56], p.3, Eqns.(4)) indicates however that added mass terms are missing from their expressions for F_z , M_x and M_y . The missing terms are (in Wolf and Spahr's notation): $-m_{ax} z_a (P^2 + Q^2)$ from F_z ; $m_{ax} z_a PW$ from M_x ; and $m_{ax} z_a QW$ from M_y . This may be confirmed by transforming the added mass components in Eqns.(B1.15), (B1.16) as follows (e.g. Ref.22, Eqns.(2)), with $r = 0$:

$$\begin{aligned} A_{11} &= A_{11}^c \\ A_{33} &= A_{33}^c \\ A_{55} &= A_{55}^c + A_{11}^c a^2 \\ A_{15} &= A_{11}^c a \end{aligned} \tag{2.6}$$

where the c superscript refers to centralized values of A_{ij} , and $a \equiv z_a$ is the distance between the centre of added mass and the origin. Wolf and Spahr's equations are therefore incorrect for the assumptions adopted.

2.2.2. The Added Mass/Included Mass Dichotomy

The concept of added mass, as a means of accounting for acceleration forces and moments, has been misrepresented and misunderstood since its first associations with parachute stability studies. Much of the problem may be founded in a general attitude, brought about by the predicament of being forced, through lack of data, to conjecture real fluid effects with unreal assumptions; e.g. "pending experimental evidence, one guess is as good as another".

It is asserted from Section 2.1.1. above that misrepresentation, even on the remote basis of ideal flow assumptions (in effect, constant A_{ij} values), follows when A_{33} is taken to be the same as A_{11} ($= A_{22}$). It is suggested that part of the misunderstanding lies in semantics: what was defined in Section 1.3 as added mass has been variously, and simultaneously, referred to in other parachute studies as apparent mass, apparent additional (or vice versa) mass, co-accelerated mass, hydrodynamic mass, hydraulic inertia, induced mass, virtual mass; to be readily confused with "included mass".

"Included mass" was introduced in 1944 by Henn [17]. The idea was to simulate the mass of air which was believed to be "contained at rest" within the canopy. Henn assumed this mass to take the rigid shape of an ellipsoid, with which he then associated the added mass components appropriate to ideal flow [19]. The dichotomy arises when the "included mass" is then treated as a (weightless) *rigid* body, with isotropic mass qualities ($A_{11} = A_{22} = A_{33}$), and lumped with the solid body B_{ij} components; the idealized added mass tensor, which is anisotropic, in general, ought to be treated as in Appendix B1.

The "included mass" idea has been perpetuated by Heinrich [6], the various editions of the authoritative Parachute Handbook [64,1], and, not least, by members of the Parachute Group at Leicester [38,39,33].

Inconsistency and confusion arise when both added and included mass are treated as interchangeable. For example, despite Ibrahim's excellent doctoral thesis on added mass [36], in his stability model [53] he claims a "more general representation of apparent mass effects", yet ultimately implements included mass. Similarly, the Parachute Group at Leicester protested a physical distinction between the two concepts, yet treated both in the same, rigid-body manner. Since it is the more general case, it is suggested here that the added mass approach be adopted as standard, at least until better data are available.

2.3. The Current Simulation Model

The current simulation model retains the subroutine structure of Tory's original version. A number of inconsistencies have been amended, and the input/output routines have been rewritten to improve communication and to provide more information. Major changes were made to the equations of motion, as described above, and in providing pitch/yaw rate damping moments. The model has been converted to SI units, and a routine added to calculate the instantaneous and mean frequencies and damping ratios of selected variables from their time histories. The output point in the system, used in tracking the trajectory and velocity, may be specified; Tory and Ayres referred to the trajectory of the body origin only. Graphical routines were written by the author to display the outputs along with the input parameters, so that an easily assimilable hardcopy of the results can be obtained.

2.3.1. Dynamics

The centralized form of the equations of motion (B1.22), (B1.23) are solved here, that is, the body origin is transformed to the point on

the axis of symmetry at which A_{15} disappears. As discussed above (Section 2.2.1) all the A_{ij} terms ought in principle to be placed on the left-hand-side of the equations, since they are in fact external (reaction) force and moment quantities. This remark is academic at this stage because the equations have to be rearranged to solve for \dot{u} , \dot{v} , \dot{w} , \dot{p} , \dot{q} and \dot{r} in any case. The external gravitational forces and moments are straightforward, the one point to note is that the equations of motion refer to body axes, so the gravity vector must be transformed to the same co-ordinate frame (see Section 2.3.4).

2.3.2. Aerodynamics

2.3.2.1. Canopy

Stiffness Terms

For the axisymmetric parachute the aerodynamic force and moment coefficients are assumed to be functions of the resultant angle of attack only. As discussed above (Section 2.2.1) the point of action of the forces needs to be considered carefully if the [A] couples are used; this aspect is dealt with in more detail in Section 2.4.4.

Two different angles of attack are used in the programme. The first, $\alpha_{V_{rcp}}$, is only used internally to obtain the angle of attack at the canopy centre of pressure in the plane containing Oz and the resultant airspeed, V_{rcp} :

$$V_{rcp} = (u_{cp}^2 + v_{cp}^2 + w_{cp}^2)^{1/2} \quad (2.7)$$

$$\alpha_{V_{rcp}} = \tan^{-1} ((u_{cp}^2 + v_{cp}^2)^{1/2} / V_{rcp}) \quad (2.8)$$

and hence to determine the usual quasistatic aerodynamic stiffness terms

$$\begin{aligned}
 N(\alpha_{V_{rcp}}) &= C_N(\alpha_{V_{rcp}}) \left(\frac{1}{2} \rho V_{rcp}^2 \right) \left(\frac{\pi D_p^2}{4} \right) \\
 T(\alpha_{V_{rcp}}) &= C_T(\alpha_{V_{rcp}}) \left(\frac{1}{2} \rho V_{rcp}^2 \right) \left(\frac{\pi D_p^2}{4} \right) \\
 M(\alpha_{V_{rcp}}) &= C_M(\alpha_{V_{rcp}}) \left(\frac{1}{2} \rho V_{rcp}^2 \right) \left(\frac{\pi D_p^3}{4} \right)
 \end{aligned} \tag{2.9}$$

N and M are then appropriately resolved along the body x and y axes. The second angle of attack, and a sideslip angle β , are defined in the conventional aeroplane notation to give the aerodynamic angles in the Oxz, Oxy planes, viz. for a fixed point P on the axis of symmetry:

$$\alpha_p = \tan^{-1} (u_p/w_p) \tag{2.10}$$

$$\beta_p = \tan^{-1} (v_p/u_p) \tag{2.11}$$

and these quantities are used for output.

The aerodynamic stiffness functions are input in discrete form and interpolated to obtain intermediate values.

Damping Moment Terms

The simple form of the damping moment implementation is dictated by lack of data, so that all damping sources are lumped into a single linearised term. The body co-ordinate origin is taken to be arbitrarily close to the canopy centre of pressure so that pitch/yaw damping due to aerodynamic angle rate may be assumed negligible [61]. Thus only purely rotational pitch damping due to linear velocity variation over the canopy is considered: this is defined by the moment derivatives $L_p = \partial L / \partial p$ (= M_q from symmetry) so that in the usual linearised form

$$L = \frac{\partial L}{\partial p} p, \quad M = \frac{\partial M}{\partial q} q \tag{2.12}$$

The derivatives are input in the nondimensionalised form:

$$l_p = L_p / (\rho V_{rcp} \pi D_p^4 / 4) \quad (2.13)$$

Roll damping moment is defined in a similar manner, but is assumed zero here.

Mass Terms

The added mass components are assumed to be constants, determined only by the canopy shape and size and by the fluid density, as in ideal flow. Input values of the added mass components are defined in coefficient form, and scale on the inertia components of a reference sphere of fluid of diameter D_p as follows:

$$\begin{aligned} K_{ii} &= A_{ii} / (\pi \rho D_p^3 / 6) & i &= 1, 2, 3 \\ &= A_{ii} / (\pi \rho D_p^5 / 60) & i &= 4, 5, 6 \\ K_{ij} &= A_{ij} / (\pi \rho D_p^4 / 6) & i &\neq j \end{aligned} \quad (2.14)$$

2.3.2.2. Store

In the present study the store aerodynamics are of secondary importance compared to those of the canopy. It is assumed that the store size is small, both so that the interference effect of its wake on the canopy is negligible, and so that aerodynamic forces and moments on the store are small.

A simple representation is used, which is only approximate: the tangential and normal forces (T_s, N_s) on the store are estimated from the axial (w_s) and cross flow (u_s, v_s) velocity components at the store mass centre S , and are also assumed to act at S :

$$\begin{aligned} T_s &= - C_{T_s} (\pi \rho d_s^2 / 8) w_s^2 = Z_s \\ N_s &= - C_{N_s} (\rho d_s l_s / 2) (u_s^2 + v_s^2) \end{aligned} \quad (2.15)$$

N_s is resolved to give the normal force components X_s, Y_s .

$$\begin{aligned} X_s &= N_s \cos \beta_s \\ Y_s &= N_s \sin \beta_s \end{aligned} \quad (2.16)$$

where

$$\beta_s = \tan^{-1} (-v_s / -u_s) ,$$

and to give moment components about 0 :

$$\begin{aligned} L_s &= -z_s Y_s \\ M_s &= z_s X_s \end{aligned} \quad (2.17)$$

2.3.3. Mass-Geometric Quantities

The solid body inertia components are derived by modelling the parachute as a rigid body of idealised shape and mass distribution. It should be noted that for present applications of the model (Section 3) by far the largest of the solid body components of I_{xx}, I_{yy} about the chosen body origin are the $m_s z_s^2$ terms (typically about 98% or more of the total), so that mass-geometric modelling of the other components is not critical.

The system is considered in three parts - canopy, rigging lines and store.

Canopy

The canopy is approximated by a homogeneous hemispherical shell of mass m_c , diameter D_p . Its mass centre C is assumed to lie at $0.2 D_p$ from the base. Thus

$$\begin{aligned} I_{xx_c} &= I_{yy_c} \approx 0.02 m_c D_p^2 \\ I_{zz_c} &= m_c D_p^2 / 12 \end{aligned} \quad (2.18)$$

Rigging Lines

These are assumed to form a conical frustum shell, of length ℓ_L , mass m_L at L and constant mass/unit length:

$$\begin{aligned} I_{xx_L} &= I_{yy_L} = m_L \ell_L^2 / 12 \\ I_{zz_L} &= m_L (D_p^2 + 4 D_p d_s - 2d_s^2) / 12 \end{aligned} \quad (2.19)$$

Store

This is taken to comprise a homogeneous circular cylinder, mass m_s at S , diameter d_s , length ℓ_s :

$$\begin{aligned} I_{xx_s} &= I_{yy_s} = m_s \ell_s^2 / 12 \\ I_{zz_s} &= m_s d_s^2 / 8 \end{aligned} \quad (2.20)$$

2.3.4. Kinematics

The kinematics of the current model are the same as those of Tory, with the exception that the input and output kinematic states are referred to an arbitrary point P on the axis of symmetry, not necessarily the origin, as used by Tory, which was restrictive.

The orientation of the parachute with respect to an inertial reference frame is described by the conventional Euler angle method. The body frame to inertial frame (Fig.1.2) transformation consists of a non-commutative sequence of three rotations: ϕ about the body Ox axis, θ about the subsequent body Oy axis, then ψ about the body Oz axis. Details of the derivations of these transformations may be found in any standard text on flight mechanics, e.g. Etkin [65].

The Euler angle rates are obtained from the body axis angular rate by the transformation:

$$\begin{pmatrix} \dot{\phi} \\ \dot{\theta} \\ \dot{\psi} \end{pmatrix} = \begin{bmatrix} 1 & \sin\phi\tan\theta & \cos\phi\tan\theta \\ 0 & \cos\phi & -\sin\phi \\ 0 & \sin\phi\sec\theta & \cos\phi\sec\theta \end{bmatrix} \begin{pmatrix} p \\ q \\ r \end{pmatrix} \quad (2.21)$$

and the Euler angles are found by integrating $\dot{\phi}$, $\dot{\theta}$, $\dot{\psi}$; the values of p, q, r are found by rearranging the equations of motion (B1.22), (B1.23) to give $\dot{p}, \dot{q}, \dot{r}$, and then integrating (see Section 2.3.5).

An arbitrary vector \underline{r} , defined in $Oxyz$ as \underline{r}^0 , is transformed into \underline{r}^I in $Ixyz$ by the transformation $[L_{IO}]$;

$$\underline{r}^I = [L_{IO}]\underline{r}^0 \quad (2.22)$$

where

$$[L_{IO}] = \begin{bmatrix} \cos\theta\cos\psi & \sin\phi\sin\theta\cos\psi & \cos\phi\sin\theta\cos\psi \\ & -\cos\phi\sin\psi & +\sin\phi\sin\psi \\ \cos\theta\sin\psi & \sin\phi\sin\theta\sin\psi & \cos\phi\sin\theta\sin\psi \\ & +\cos\phi\cos\psi & -\sin\phi\cos\psi \\ -\sin\theta & \sin\phi\cos\theta & \cos\phi\cos\theta \end{bmatrix} \quad (2.23)$$

From the orthogonality conditions on direction cosine matrices (DCMs), the inverse transformation $\underline{r}^0 = [L_{OI}]\underline{r}^I$ is easily obtained, since

$$[L_{IO}]^{-1} = [L_{IO}]^T = [L_{OI}] \quad (2.24)$$

Consider a point P in the parachute, position vector \underline{r}_{PO} with respect to O , and \underline{r}_{PI} wrt I . Then

$$\underline{r}_{PI} = \underline{r}_{PO} + \underline{r}_{OI} \quad (2.25)$$

$$\underline{v}_{PI} = \underline{v}_{OI} + \dot{\underline{r}}_{PO} + \underline{\omega} \times \underline{r}_{PO} \quad (2.26)$$

and if P is fixed wrt O , $\dot{\underline{r}}_{PO} = 0$ and

$$\underline{v}_{PI} = \underline{v}_{OI} + \underline{\omega} \times \underline{r}_{PO} \quad (2.27)$$

Now the body axis components of $\dot{\underline{V}}_{-OI} = (\dot{u}, \dot{v}, \dot{w})$ are obtained from the equations of motion (B1.22), (B1.23); integration of $\dot{\underline{V}}_{-OI}$ gives \underline{V}_{-OI} , and application of Eqn.(2.27) gives \underline{V}_{-PI} . The space trajectory of P is found by transforming \underline{V}_{-PI} to inertial frame components using Eqn.(2.23), and then integrating to give \underline{r}_{-PI} .

The parachute attitude is defined as the angle between the parachute axis of symmetry and the space-fixed vertical IZ :

$$\begin{aligned} |\text{attitude}| &= \cos^{-1}(\underline{k}^0 \cdot \underline{k}^I) = \cos^{-1}(L_{IO})_{33} \\ &= \cos^{-1}(\cos\phi\cos\theta) \end{aligned} \quad (2.28)$$

The direction of the parachute axis in the IXY plane is here defined by the clockwise orientation angle γ from IX :

$$\gamma = \tan^{-1}(-\sin\phi\cot\theta) \quad (2.29)$$

The angular velocity of the parachute in inertial frame components is

$$\underline{\omega}_{-V} = \begin{pmatrix} \omega_{VX} \\ \omega_{VY} \\ \omega_{VZ} \end{pmatrix} = [L_{IO}] \begin{pmatrix} p \\ q \\ r \end{pmatrix} \quad (2.30)$$

The angular velocity resultant in the IXY frame may be of interest:

$$\underline{\omega}_{-V_{XY}} = \begin{pmatrix} \omega_{VX} \\ \omega_{VY} \end{pmatrix}, \quad (2.31)$$

the magnitude of which is

$$|\underline{\omega}_{-V_{XY}}| = (\omega_{VX}^2 + \omega_{VY}^2)^{1/2}, \quad (2.32)$$

and the angle between the resultant and the IX axis is

$$\delta = \tan^{-1}(\omega_{VY}/\omega_{VX}) \quad (2.33)$$

The phase angle between $\underline{\omega}_{-V_{XY}}$ and the attitude is $(\gamma-\delta)$.

2.3.5. Solution

Given the initial conditions $\phi, \theta, \psi, u_p, v_p, w_p, p, q, r, X_p, Y_p, Z_p$ the 12 linear ODEs for the variables $\dot{\phi}, \dot{\theta}, \dot{\psi}, \dot{u}, \dot{v}, \dot{w}, \dot{p}, \dot{q}, \dot{r}, u, v, w$ are integrated numerically by means of the same implementation of the Adams-Bashforth algorithm employed by Tory. This implementation allows error control to be specified on either a single variable or a sum of all the variables. The error is obtained from the difference between forward and backward difference expressions, and is controlled by adjusting the integration step length. In the present implementation the error control is applied to the sum of errors over all the variables and is set to give 4 figure accuracy at the end of a flight of 40 s. There is little point in tightening the error beyond this, since it greatly increases the execution time. Execution time also depends strongly on the input parameter mix: for the baseline case (Section 2.4.2) execution takes about 30 s on the University of Leicester's CDC CYBER 73, though for other configurations more than 120 s was possible.

The time interval for output may also be specified, and was set at 0.1 s for all runs. This allows good definition for straight-line plotting between output points.

2.3.6. Inputs

Inputs quantities required are (MKS units unless specified):

- (i) Mass/geometric parameters of the canopy, lines and store.
- (ii) Added mass coefficients K_{11}, K_{33}, K_{55}
- (iii) Aerodynamics force / (moment) function coefficients $C_N(\alpha), C_T(\alpha), C_M(\alpha)$
- (iv) Damping moment coefficient λ_p
- (v) Initial (body-axis) velocity components of P : u_p, v_p, w_p
- (vi) Initial (Earth-axis) position components of P : X_p, Y_p, Z_p

- (vii) Initial Euler angles (deg.)
- (viii) Initial angular rates (rad s^{-1})
- (ix) Ambient constants (gravity, fluid density)
- (x) Start time, printout interval, stop time.
- (xi) Integration routine error control constants.
- (xii) Identifiers (Run No., A/D coefficient curves etc.).

2.3.7. Outputs

The output file is copied onto magnetic disc, from where it may be printed or selectively plotted as required. As a check, the printout first lists all the input parameters exactly as read, and then tabulates them more descriptively and completely. The predicted time histories of a limited number of selected variables are then listed.

If estimates of frequency and damping are requested for a particular variable an additional routine is used to detect and record the occurrence of peak values in the time history. The damping between successive peaks of similar sign is calculated by the logarithmic decrement method ([41], p.15), and output along with the corresponding period. Average values are also supplied. To reduce the effect of any initial asymmetry the second peak following initiation is counted as the starting point.

2.4. Parameter Sensitivity Analysis

The present conceptual model of a parachute is only an approximation to the real, physical system, and must be appreciated as such. Further, its predictions depend on input data which are themselves subject to uncertainty. Since a large number of parameters are used in the modelling, it is desirable to use some systematic method to maximise the rate of progress towards a reliable model. It is valuable to know

the sensitivity of the model behaviour to variations in the input parameters: if it is insensitive to variation in a certain parameter, then there is little point in either measuring or specifying the parameter to a high degree of accuracy, indeed it may be acceptable to omit it altogether from the model. Equally, if a particular parameter is critical, but an accurate measure is not available, then confidence in the model predictions must be reduced accordingly.

Clearly, one is working on the premise that what is important in the model will also be important in reality, which is not necessarily true, since the model may not be adequately representative. It is also possible that factors which are important in the physical system have been misrepresented or overlooked completely - this cannot be detected by sensitivity analysis. It is important to appreciate that the sensitivity analysis can only indicate what is significant *in the present implementation of the model*. A shift in the baseline state may alter priorities by uncovering new sensitivities and masking others.

Once (if) all the input data can be accurately specified, and yet model predictions do not adequately match behaviour of the physical system, the fault may lie in the model itself - in the modelling assumptions, in the way they have been implemented, or because of oversight or lack of understanding of the physical system.

2.4.1. Reduction of Results

The function of the present sensitivity analysis is to identify, as much qualitatively as quantitatively, the effect of variation in particular parameters on the stability characteristics.

The stability characteristics are assessed by measuring the response of the model to a fixed initial perturbation. The model is constrained to planar motion in the IXZ plane, so that angular oscillation

with respect to Earth axes is uniquely specified by the Euler angle θ : for $\theta = 0$ the parachute axis is vertical. The equations of planar motion are solved exactly, i.e. in full nonlinear form, for a flight time of 40 s. In a previous study [41] it was found that the pendulum-type oscillation in θ of the parachute bore a close resemblance to a simple second-order system. Soon after the initial perturbation the period and damping ratio remain relatively steady with $\pm 5\%$ and $\pm 10\%$ variation, respectively, about mean values $\bar{\omega}_N, \bar{\zeta}$.

Use of the mean period and mean damping ratio gives a good reconstruction of the response, but ought to be treated critically. When the damping ratio is large ($\zeta > 0.3$) few data points will be available for calculating a mean damping, so the reconstruction of the response using time-averaged values may differ considerably in detail from the predicted nonlinear response. When the system enters a limit cycle mode, where the frequency is constant and damping is zero, the time-averaged frequency and damping will differ slightly from the long term (limit cycle) values. As a check on behaviour, for most of the results to be presented here graphical outputs have also been obtained and inspected.

2.4.2. Baseline Case

The baseline case was chosen to be representative of a 28 ft. D_0 circular flat personnel parachute with a store mass of 100 kg (Figure 2.1). The same initial conditions were used for each run:

$$\begin{aligned}\theta &= 30 \text{ deg.} \\ q &= 0 \\ u_p &= - 3.0 \text{ ms}^{-1} \\ w_p &= 5.0 \text{ ms}^{-1}\end{aligned}$$

The baseline values for the various aerodynamic parameters are discussed below under the appropriate headings. Figures 2.2 and 2.3 show the results for the baseline run. The oscillation is symmetric, lightly damped and appears to approach a limit cycle amplitude of about 19 deg. with a mean frequency of 0.184 Hz.

2.4.3. Mass-Geometric Parameters

It is useful to be able to predict the likely effect of changes in configuration on stability. Unlike many of the aerodynamic parameters, the values of the important mass-geometric parameters (rigging line length, store mass, canopy diameter) can readily be measured or calculated to an acceptable degree of accuracy.

Origin to Store Length z_s

Figure 2.4 shows that both $\bar{\zeta}$ and $\bar{\omega}_n$ decrease with increasing z_s . $\bar{\zeta}$ effectively falls to zero, while the limit cycle amplitude increases rapidly to a plateau of about ± 38 deg. before decreasing again for $z_s/z_s^0 > 3$. The damping increases rapidly with decreasing z_s ; for $z_s/z_s^0 < 0.4$, the $\bar{\zeta}$ curve should be treated as qualitative. The curve for $\bar{\omega}_n$ peaks at about $z_s/z_s^0 = 0.3$.

Store Mass m_s

In varying the store mass it has been assumed that only the density changes, and the moments of inertia have been scaled accordingly. Figure 2.5 shows that $\bar{\omega}_n$ increases monotonically with m_s , while the limit cycle mode is retained. The damping increases with decreasing m_s , and the trajectory plots show a tendency to glide, which accords qualitatively with observation for this type of canopy [59].

Canopy Projected Diameter D_p

Figure 2.6 shows that, as the canopy loading is reduced, damping increases and frequency decreases. As D_p is reduced the limit cycle amplitude increases. The frequency appears to peak at about $D_p/D_p^0 = 0.75$.

2.4.4. Aerodynamic Parameters

2.4.4.1. Force/Moment Coefficient Curves $C_N(\alpha), C_T(\alpha), C_M(\alpha)$

Attention has here been confined to data for circular flat canopies in the very low porosity [32] range $\lambda_e = 0 - 4.2\%$. Only two sources of data [30-31,33] were found, both of which are unsatisfactory in several respects.

Heinrich and Haak [30] used the 38" x 54" wind tunnel at the University of Minnesota to obtain measurements of the normal and tangential forces acting on a large number of rigid and flexible, porous and imporous model canopies of different shapes, including the circular flat. The canopy diameters were a nominal 12 in. Most of the tests were run at a tunnel speed of about 31 ms^{-1} , though "strong model vibrations" forced some (including the $\lambda_e = 1\%$ circular flat) to be run at 20 ms^{-1} . Although their apparatus was set up to measure three force components, only two components were actually used in deriving and presenting the data.

Figure 2.7 is reproduced from Figure 1 of their report: the tangent force

T at the apex, and the normal forces N_2 at the apex and N_1 at the store were measured. However measurement "over a wide range" of angle of attack (α) indicated that N_1 was much smaller than N_2 , so N_1 was neglected and the force system was assumed to be that of Figure 2.7b, with

T and N_2 acting at the canopy apex. Thus the moment coefficient curves that Heinrich and Haak present are redundant, since they have simply been calculated from N_2 and an arbitrary reference length.

Subsequent to publication of their original (1961) report, it was discovered that their reference dynamic pressure q (used to reduce each measurement) was in error, so that all of the original results were suspect. In presenting the revised data [31] (submitted for publication in 1968) it is not at all clear whether *all* of the measurements have been repeated (45 models, $30 + \alpha$ values, 2 readings; 4 runs apiece), or if some form of correction factor(s) has been found from spot checks, and then applied globally.

The data of Ref.31 refer to canopies with different "effective" porosity (λ_e), a nondimensional term introduced by Heinrich [32] to express the permeability of the cloth under different flow conditions. The effective porosity is calculated from the average flow speed U through the cloth, the differential pressure Δp across the material and the fluid density ρ :

$$\lambda_e = U / (2\Delta p / \rho)^{1/2} \quad (2.34)$$

Geometric porosity (λ_G) is simply the ratio (area of holes)/(total surface area). For the very low Mach numbers, dynamic pressures and porosities encountered throughout the present study the effective and geometric porosities will be treated as interchangeable [33].

Heinrich and Haak found, as did most other workers in the same field [15,16,63], a considerable aerodynamic interference due to the wake from the model mounting support system. To minimize the interference they used a wire suspension system, and tried a number of different configurations. They noted that the final arrangement was less than optimal in its effect on the normal force, but the effects on the tangential force were barely detectable. The mounting constraint at the apex also causes flexible canopies to distort gradually with increasing α , and ultimately leads to collapse. It is not known to what extent the distortion and its effects on the quasistatic forces differ from those experienced under

flight conditions. Heinrich and Haak's measurements were repeatable to $\pm 2\%$.

The diameter of the rigging lines (0.096 in.) used on their flexible models was about 16 times the scale diameter (0.006 in.); comparing tests with 0.096 in. and 0.020 in. lines, they found that the tangent force coefficient was increased by about 2% with the thicker lines. This contrasts with observations by Jones [16], whose work consistently shows that the addition of 0.020 in. lines to an otherwise broadly comparable base canopy *reduces* the drag coefficient by about 5% (Ref.16, p.12, Table II, Case II).

It would appear that the circular flat models used in Ref.31 did not possess apex vents, as used on full size parachutes. If measurements made by Ayres [33] (on a rigid model of a hemispherical canopy) are to be accepted (see below), the addition of an apex vent, of diameter $D_v = 0.085 D_p$ ($S_v/S_p \approx 0.007$), reduces the drag coefficient C_{D_p} at $\alpha = 0$ from 1.7 to 1.5 ([33], Fig.4.11), i.e. by about 12% on this shape, so a similar reduction might be expected for the circular flat canopy. It may be noted that the canopies in Ref.31 had 28 gores (and rigging lines) compared to the 24 gores on Ayres' and the drop test models (Section 3).

The results of Ref.31 (given in graphical form only) were non-dimensionalised with respect to the reference area S_o - the flat (opened) cloth area: in reducing their measurements, Heinrich and Haak calculated the force coefficients $C_{T_o} = T/qS_o$, $C_{N_o} = N_2/qS$. Before implementing these data in the present computer model they were tabulated and non-dimensionalised with respect to the projected (flight) area S_p , denoted here by coefficients C_T, C_N , using the values of S_o, S_p supplied in Ref.31. Most of their results are for angles of attack of not more than 40 deg., because their flexible canopies collapsed at about this angle. For input to the computer model the data are used in discrete

form at 5 deg. intervals up to 90 deg. (Table 2.1(a)-(d)), so the data of Ref.31 were extrapolated and interpolated graphically as required. The extrapolations at large α were faired to match the curves produced by Ayres, which was the only other source (Figures 2.8 - 2.11). As will be seen from the simulation results, this extrapolation is not as drastic a solution as might seem, since in all cases the greatest instantaneous α predicted lies within the range of measurement.

Ayres [33] carried out his measurements in the University of Leicester's 30 in.diameter, open working section wind tunnel on small (6 in. D_p) rigid canopy models. Ayres' experiments are poorly documented, and again the results are presented in graphical form only. He makes no mention of mounting interference corrections, which could have been significant judging from the substantial support structure used ([33], Fig.4.7) which was very close to the canopy. He does not specify if rigging lines were fitted, though an axial support sting extends well forward from the canopy apex; aerodynamic forces on the sting will have contributed to the lift, drag and moment (all three were measured at the apex) and will also have caused interference. It is not clear whether these forces have been accounted for in the tare corrections. Ayres' circular flat models did not have apex vents; he did however investigate the effect of increasing vent diameter on a hemispherical canopy model of similar size ([33], Fig.4.11), but must have used a different support arrangement to that shown in Fig.4.7 [33], where the canopy is supported at the apex. In all his experiments the freestream speed was about 21.0 ms^{-1} , giving a test Reynolds Number of about 2.5×10^5 , which is approximately $1/10$ that of a full scale personnel parachute.

Ayres simulated geometric porosity in the same way as Jones [16], i.e. by drilling a large number of uniformly distributed holes in the canopy surface. Porosity was increased simply by enlarging the holes.

The tabulated data used as inputs to the simulation model were scaled from Fig.4.13 of Ref.33 ; λ_G values of 0, 2, and 4% were considered (Figures 2.8 - 2.11, Table 2.2(a)-(c)).

In implementing the aerodynamic stiffness coefficient data the following methods were tested:

(i) The baseline data were chosen as Ayres' $\lambda_G = 0$ curves, with C_T and C_N both considered to act at the origin 0, which was taken to lie at a point one quarter of the distance between the canopy base and apex. The only steady-state aerodynamic moments allowed were those of the [A] couples. The centre of pressure was assumed to lie arbitrarily close to, but not coincident with (cf. Section 2.2.1), the origin. Figure 2.2 shows the results of the baseline run.

Figure 2.12 compares the effective steady-state moments about 0, as obtained both experimentally - by transforming Ayres' ($\lambda_G = 0$) C_{M_A}, C_N data from the apex to 0 - and analytically, from the [A] couple (Eqn. (2.5)): both curves agree well up to $\alpha \approx 30$ deg. The results of running the experimental C_M (Figure 2.13) are nearly identical ($\bar{\omega}_n = 0.180$ Hz, $|\hat{\theta}| \approx 20$ deg.) to the baseline results.

All of Heinrich and Haak's and Ayres' data were then run using only the [A] couples. The effects of using the different sets of C_N, C_T curves can thus be compared directly, since the moment curve was the same in each case. The results are shown in Figure 2.14. Ayres' curves for $\lambda_G = 8\%$ ([33], Fig.4.13) were also run to see if any trend developed, which proved to be the case. For Ayres' data the frequency decreases with increasing porosity; the damping decreases up to $\lambda_G \approx 4\%$, accompanied by an increase in limit cycle amplitude to 26 deg., and then begins to increase again. The results for Heinrich and Haak's data are less consistent; for the two zero porosity cases (near identical results) the motion converges within 2 or 3 cycles to a glide mode with $\theta_g \approx -3$ deg. (Figures 2.15,2.16).

For $\lambda_e = 0.3\%$ the tendency to glide remains, but convergence is slower (Figures 2.17,2.18), while for $\lambda_e = 1\%$ and 4.2% the mode is symmetric; the $\lambda_e = 1\%$ case appears to approach a $|\hat{\theta}|$ of about 21 deg. (Figure 2.19,2.20), and the $\lambda_e = 4.2\%$ case a $|\hat{\theta}|$ of about 12 deg. The estimated $\bar{\zeta}$ (Figure 2.14) for Heinrich and Haak's $\lambda_e = 0, 0.3\%$ cases should be treated only as qualitative.

Note that in implementing these data the added mass quantities were left unchanged (though it has been found that the A_{ij} depend strongly on porosity [6,35]). This was done to isolate the individual effect of the aerodynamic stiffness curves from those of the A_{ij} . Overall and individual scaling of the A_{ij} are treated separately later.

(ii) For the baseline case the effect of individually scaling the C_N, C_T curves throughout the range $\alpha = [0,90]$ deg. was tested. This simulates errors in the derivation of the curves, such as those incurred by neglecting blockage corrections to the reference dynamic pressure. Results are shown in Figure 2.21: even for large changes ($\pm 30\%$) the effects of scaling errors in C_N , and to a lesser extent in C_T , are negligible. In the earlier sensitivity analysis [41] of the Tory-Ayres model similar tests were carried out on the C_L, C_D curves (which may be obtained by applying a rotation of $(-\alpha)$ to the C_N, C_T data pairs) and indicated that changes of $\pm 5\%$ strongly affected the damping ([41], Fig.10). It must be remembered that in the present case the scaling does not affect the steady-state moment, which depends only on A_{11}, A_{33} and α .

(iii) As a measure of the error introduced by using *both* experimentally derived and analytically assumed (from [A] couples) steady-state moment terms - as perpetrated by Lester, Byushgens and Shilov, Doyle and Burbrick - the baseline case was run with both sets implemented simultaneously.

The effect was small, but noticeable: the mean damping increased from 0.008 to 0.016, the mode changed from limit cycle to convergent, and $\bar{\omega}_n$ increased from 0.184 Hz to 0.195 Hz ($\bar{\tau}$ reduced from 5.4 s to 5.1 s). The magnitude of the error clearly depends on the relative stiffness ($\partial C_{M_0} / \partial \alpha$) of the two moment terms; in the present case both moments are quite weak, as evidenced by the small incremental effect.

2.4.4.2. Damping Moment Derivative ℓ_p

The author and others carried out experiments [60,61] using both free- and forced-oscillation techniques to determine the magnitude of the pitch/yaw damping moment derivative ℓ_p for a model canopy of aeroconical shape. The results must be treated as approximate on account of the erratic behaviour of the model: Jones [16] reported similar behaviour in "not very successful" experiments in attempting to find the damping moment derivatives for the NPL canopy shape. In Ref.61 the value of ℓ_p was estimated at -0.08, with an experimental uncertainty of 20%, which compares reasonably with an analytical estimate of -0.13, based on the assumption of a uniform pressure distribution over the canopy.

As a first approximation it was assumed that the damping coefficient for the circular flat shape is the same as that for the aeroconical, so a baseline value of $\ell_p = -0.08$ was used. Figure 2.22 shows the effect of variation of ℓ_p between 0 and -0.15. Note that the assumption of a constant ℓ_p (nondimensional) implies a damping moment proportional to the descent speed (cf. Section 2.3.2.1.).

2.4.4.3. Added Mass Components

Since the centralised form of $[A]$ is used, we deal only with the components A_{11} , A_{33} and A_{55} , and seek representative baseline values for a circular flat canopy.

Jones [16] carried out experiments on 10 in. D_p porous and imporous models of the NPL shape ([15], p.20), for which $h_c/D_p = 0.47$. Jones' experiments were done by swinging canopy models as a simple pendulum in air and water, on the assumption that the added mass in air would be small in relation to the mass of the model, whereas in water the two would be comparable. He does not make it clear which way the canopies were orientated, though since he is treating the lateral equations of motion, and also refers to "the plane of the periphery" being "finished smooth in each case" (solid canopy models), it seems likely to be A_{11} . His results show that A_{11} reduces with porosity, and found $K_{11} = 0.74$ (zero porosity), $K_{11} = 0.56$ ($\lambda_G = 18\%$). In conclusion he suggested that an added mass of about 1.4 times the mass of air "contained" in the canopy, with a corresponding additional moment of inertia. Ibrahim [35] measured $K_{11} = 0.31$ for a hemispherical model canopy ($h_c/D_p = 0.50$).

Deceleration experiments to measure A_{33} were carried out on parachutes following a suggestion by Von Kármán [66]. The results of these experiments, the only ones of this type known to the author, were sketchily described by Heinrich [6]. The technique employed was to measure the instantaneous deceleration of a parachute after release of a known weight. The tests were carried out using different canopy shapes with effective porosities of 0,5 and 11%, from which Heinrich produced two curves, one for results obtained from steady, non-oscillatory descents, the other from oscillatory descents. The curve for oscillatory tests is of questionable value because Heinrich appears to have constructed a hyperbola through two points. No mention is made of the test conditions, nor

the parachute sizes, parachute construction, store masses or descent speeds, nor is it stated how repeatable the results were.

The most obvious conclusion from Heinrich's curves is that A_{33} falls off very rapidly with increasing porosity; at $\lambda_e = 5\%$, A_{33} is only about $1/10$ its value of $\lambda = 0$ (non-oscillatory curve). Here a baseline A_{33} value appropriate to a circular flat canopy of $\lambda_e \approx 3\%$ will be employed, since this is the porosity used in the free-flight models (Section 3). From Heinrich's oscillatory curve ([6], Fig.4) we find for $\lambda_e = 0.02, 0.04$ that the quantity "apparent mass/enclosed mass" = 1.0, 0.5. Reducing these values to a convenient form is vexing since Heinrich based the enclosed mass on a reference volume in the shape of a hemisphere of diameter = $(2/3)D_o$. The current experiments (Section 3) yielded $D_p = (0.80 \pm 0.02)D_o$ for a wide range of circular flat canopy sizes. Standardizing the reference volume as a sphere of diameter D_p , K_{33} is estimated at 0.2 - 0.4. This may be compared with Ibrahim's analytical value [36] of $K_{33} = 1.07$ for potential flow about an imporous hemispherical cup.

The only experimental estimates of K_{11} and K_{55} for the circular flat canopy are those of Ibrahim [35]. These were derived from the difference in frequencies of oscillation of rigid canopies in air and water. A torsional pendulum was used at very small amplitudes (± 2 deg.), and hence very low mean Reynolds Numbers (about 140 in air, 1600 in water), by which Ibrahim justified the assumption that the results were equivalent to potential flow data. These experiments confirmed that K_{11} and K_{55} fall off rapidly with increasing porosity. For the imporous canopy Ibrahim gives $K_{11} = 0.252$, $K_{55} = 0.223$ (about an axis $0.165 D_p$ from the base plane).

The chosen baseline K_{ij} values were $K_{11} = 0.25$, $K_{33} = 0.40$, $K_{55} = 0.22$. Note that the values of A_{ij} are very sensitive to D_p : $A_{11}, A_{33} = f(D_p^3)$ and $A_{55} = f(D_p^5)$. The added mass components were then tested as follows:

(i) For the baseline case (i.e. using [A] couples) both A_{11} and A_{33} were varied individually. The results are given in Figures 2.23, 2.24, with both expressed in mass ratio form. All of the stability parameters - $\bar{\omega}_n$, $\bar{\zeta}$ and $|\hat{\theta}|$ - depend strongly on A_{11} and A_{33} . When $A_{11} > A_{33}$, the sign of $\partial C_{M_0} / \partial \alpha$ (Eqn. 2.5) at $\alpha = 0$ changes from stabilizing ($\partial C_{M_0} / \partial \alpha > 0$) to destabilizing: this effect is reflected in both plots for $\bar{\zeta}$.

The inclination (θ_g) in the glide mode appears to be a function of the difference ($A_{33} - A_{11}$), and hence of the steady-state moment: for $K_{11} = 2.5$ ($\mu_{11} = 4.2$) we find $\theta_g = 45$ deg. (Figures 2.25, 2.26). As K_{33} is increased the frequency rises monotonically, and the limit cycle amplitude decreases (Figure 2.27); Figures 2.28, 2.29 show the output plots for $K_{33} = 8.0$ ($\mu_{33} = 8.3$).

(ii) In this series of runs only the experimentally-derived moment was implemented, and A_{11} , A_{33} were again varied (Figures 2.30, 2.31). The effect of variation in A_{11} is now stronger on damping, but weaker on $\bar{\omega}_n$. The frequency is also less affected by A_{33} . Note that θ_g is now independent of ($A_{11} - A_{33}$), and that $|\hat{\theta}|$ grows monotonically with A_{33} . For $K_{33} = 1.0$, $|\hat{\theta}| = 87$ deg., and for $K_{33} = 1.2$, θ is divergent.

In the first series of runs ((i) above) the pitching moment stiffness $|\partial C_{M_0} / \partial \alpha|$ was a function of ($K_{33} - K_{11}$), hence the strong effect on frequency. In this series it is the same for each run. In general, variations in the added mass components will in practice be accompanied by variations in the steady-state forces and moments.

(iii) The baseline magnitude of $\mu_{55} = A_{55} / B_{55} = (K_{55} \pi \rho D_p^5 / 60) / \sum (I_{yy_i} + m_i z_i^2)$ ≈ 0.026 is small. Figure 2.32 indicates that even at this value its effect is detectable, principally on the frequency. For larger μ_{55} all

of the stability parameters are affected: $\bar{\omega}_n$ decreases monotonically, along with $\bar{\zeta}$, and $|\hat{\theta}|$ grows monotonically.

(iv) The result of scaling all of the baseline A_{ij} components simultaneously is shown in Figures 2.33, 2.34. Such a scaling might simulate the effect of porosity. Note again that the pitching moment stiffness is proportional to the scale $|A_{ij}|/|A_{ij}|^0$. The limit cycle mode is retained up to about $|A_{ij}|/|A_{ij}|^0 = 4$, above which the mode appears to be divergent. Note that $\bar{\omega}_n$ changes little between $|A_{ij}|/|A_{ij}|^0 = 2$ and 5, indicating that the increase in the inertia components is balanced by the stiffness. If the pitching moment stiffness were decoupled from [A], we might expect the frequency to decrease in this region, and $|\hat{\theta}|$ to increase more rapidly.

Since the baseline values of the A_{ij} were chosen to be representative of a very low porosity canopy ($\lambda_G \approx 3\%$), the region $|A_{ij}|/|A_{ij}|^0 = 0$ to 1 may be considered as indicative of the (added mass) effects of reducing porosity from 100% to zero. The discontinuity in $\bar{\omega}_n$ and $\bar{\zeta}$ around $|A_{ij}|/|A_{ij}|^0 = 0.5$ accompany a change in sign of the preferred θ_g . Qualitatively, damping increases with increasing porosity, and frequency decreases. Figures 2.35, 2.36 show results for $|A_{ij}| = 0$, and Figures 2.37, 2.38 for $|A_{ij}|/|A_{ij}|^0 = 0.5$.

2.4.4.4. Store C_{N_s}, C_{T_s}

For a hemisphere-cylinder body of length/diameter = 2.0, the axial and normal drag coefficients (based on the respective projected areas) are estimated at 0.36 and 0.86, respectively ([67], pp.312,317). These values were rounded to 0.4, 0.9 to give baseline values for C_{T_s}, C_{N_s} .

The results of varying C_{T_s} between 0 and 2.0 indicated that the influence of this component is negligible over this range. Likewise, C_{N_s} has little effect; doubling the baseline value brought a very slight decrease in $\bar{\omega}_n$ (0.002 Hz) and in $|\hat{\theta}|$ (-1.5 deg.). The approximate representation of the aerodynamic forces on the store (Section 2.3.2.2.) is reasonable in the light of these results.

2.4.5. Fluid Density

Parachutes are used to recover payloads at very high altitudes, e.g. 250 - 300,000 ft. (cf. AIAA *Astro. and Aero.*, April 1981, p.51), where the fluid density ratio $\sigma = \rho/\rho_0$ may be very small. The baseline magnitude for ρ_0 was taken as 1.225 Kg m^{-3} , which is the sea level ISA value. The effects of variation in σ between 0.05 (~75,000 ft. ASL, ISA) and 10.0 are shown in Figures. 2.39, 2.40. With σ reducing from 1.0, both $|\hat{\theta}|$ and $\bar{\omega}_n$ increase; $|\hat{\theta}|$ appears to peak at $\sigma \approx 0.2$ (45,000 ft. ASL). Stability increases with σ .

Since the magnitude of the A_{ij} are proportional to σ , the qualitative effect of variation of σ may be explained in terms of the shift in location, with increasing altitude, of the mass centre towards the store. To a first approximation, the magnitude of the steady-state aerodynamic forces and moments will be unchanged, since the dynamic pressure $q = \frac{1}{2} \rho w^2$ will be maintained constant by an adjustment in descent speed. If the store is regarded as performing a simple pendulum motion about the mass centre, the frequency will increase as the mass centre is moved towards the store. The damping couple due to ℓ_p , which scales with ρw , will be reduced, though, to a lesser extent, this will be offset by the increase in frequency.

2.4.6. Summary of Results

For the baseline case tested here, i.e. a typical personnel parachute, the most sensitive parameters as regards stability are the two added mass components A_{11} , A_{33} and the damping moment derivative ℓ_p . Unfortunately, these are also the most difficult parameters to specify. The fact that the magnitude of A_{11} will not, in general, be the same as that of A_{33} is significant; this applies whether the steady-state pitching moment is specified experimentally or accounted for by the [A] couples. In contrast with results of a previous study [41], scaling of the C_N, C_T curves does not have much effect. The reason is most likely because in the present baseline implementation neither force component exerted a moment about the origin, the (weak) moment being supplied by the [A] couple. With Heinrich and Haak's data for the low porosity flexible canopies, where the $C_N - \alpha$ curves differ considerably from those obtained by Ayres from rigid canopy tests, the computer model tends to glide; with Ayres' data the oscillations remain symmetric. Neither Heinrich and Haak's nor Ayres' data are of sufficient quality or completeness to allow them to be used with confidence.

2.5. Conclusions

The concept of added mass and its significance have been discussed. Its representation in parachute stability studies has been reviewed, and in this respect it has been shown that the equations of motion used in all known previous treatments have been either inadequate or incorrect in their derivation, or else incorrectly implemented. A general method for expressing the fluid reactions due to the idealized added mass tensor was given, and illustrated by application to rigid bodies with planar and two-fold symmetries. The correct form of the added mass tensor for a rigid

axisymmetric parachute in ideal flow has been implemented in a six degree-of-freedom computer model. The model has been described, and by a parameter sensitivity analysis it has been shown that added mass effects are more significant than hitherto predicted. In particular, the component of added mass along the axis of symmetry has a strong influence on stability. The most important aerodynamic parameters are the added mass components and the aerodynamic damping moment derivative, and these quantities are also the least well evaluated.

SECTION 3

FREE-FLIGHT EXPERIMENTS

3.1. Introduction3.1.1. Defining an Optimal Flight Test Programme

The present research programme is concerned with all aspects of parachute stability and performance in the fully-developed subsonic phase of flight. The principal aim of the experiments described here is to provide well-defined, quantitative kinematic data for validating conceptual models of parachutes. A secondary goal, treatment of which is outside the scope of the current study, is to gain understanding of scaling effects in physical models of parachutes.

A great number of, in the main, isolated drop test experiments has been carried out by different groups of workers (e.g. [1,64,68]), using measurement and assessment techniques of varying degrees of sophistication, but almost invariably on an *ad hoc* basis in support of particular projects. The results of these trials are equally particular and fragmentary, and no evident attempt has been made to consolidate them into a general unified form from which any underlying laws or order might be traced and benefited from. For example, the identification of scaling laws - geometric, mass, stiffness, speed - on stability behaviour would be of great value as a design tool; little useful information is available to date on Reynolds number, flexibility and porosity scaling of canopies.

In contrast with wind tunnel work, drop tests allow fully unconstrained dynamic behaviour and the achievement of higher working Reynolds numbers. Extra complicating factors may enter however, the principal problem for open-air tests, in the low subsonic regime especially, is that the system inputs - mean wind speed, direction and turbulence - are generally unknown. These inputs are functions of space and time, and their

measurement poses a considerable difficulty. Even if they can be measured, such complex stochastic functions serve only to amplify the already formidable primary task of analysing the parachute system. A typical parachute has a large number of degrees of freedom, and full instrumentation to measure the behaviour of such a system, in response to even the most basic input functions, would be involved, expensive and time consuming; data processing and reduction into assimilable form would also require much work, and because of the number of parameters, nonlinearities and interactions within the system it is unlikely that our understanding of it would be much improved.

Quicker and more genuine progress can be made, it is suggested, by carrying out an experimental programme in a more systematic, scientific manner under still-air conditions. What is required is a rigorous series of tests designed to isolate, and to *quantify*, the influences of individual parameters on the dynamic behaviour of a *fundamental physical model*. This will allow scaling laws to be developed, and the performance of numerical models of the same basic system to then be assessed and appropriate adjustments incorporated. Once the fundamental configuration has been analysed, the next stage is to progressively relax the isolating constraints to permit possible interactions to develop and be measured, thus building up a solid conceptual framework of the system. A set of identifiable parameters which need to be isolated is shown in Table (3.1).

Geometric/mass	Shape	Structural	Fluid Dynamic
Canopy size Line length Store mass Store size	Canopy shape Store shape Line number Line thickness	Canopy stiffness Line end fixity Line stiffness Line damping	Fluid density Reynolds number

Table (3.1) Basic parachute stability and performance parameters

3.1.2. Implementation of the Physical Model Concept

It was decided therefore to initiate such a programme, using free flight models for the tests. To provide a starting point for a scaling law investigation it seemed advisable to decide upon a particular canopy shape - the canopy shape parameter is taken here to include porosity, cut-outs, asymmetries as well as profile and is thus potentially the most variable of the above set. Canopy shape has a dominant influence on the external forces and on the mass distribution, in both steady and unsteady states, so it is more practical, for a first approximation, to detail influences directly from continuous-running wind-tunnel experiments rather than infer them stochastically from multi-degree-of-freedom flight trials.

The ubiquitous circular flat canopy was chosen as the baseline shape. This is arguably the simplest practical axisymmetric shape for a canopy, and it can also be constructed imporously. It is known to exhibit a broad range of stability characteristics [59], which makes it of particular interest, and a number of wind-tunnel tests have been carried out on it by various workers, thus providing sources of aerodynamic data as needed for simulation work.

Since the results of the proposed drop test experiments were to be compared with the existing computer model, it was decided to begin by reproducing as far as possible the current constraints of the conceptual model in physical form. These constraints reduce essentially to the single, six-degree-of-freedom body and negligible wake interference assumptions.

The first (rigid body) constraint demands that the store should not move out of alignment with the canopy as the parachute oscillates. This is easy to arrange with a rigid canopy and flexurally stiff rigging lines, but the solution for a flexible, tensile canopy and lines was not so obvious and required an amount of preliminary experimentation. A number of proving trials were carried out in one of the airship hangers at

Cardington, Beds., with ultimate success. This development work is described in Appendix C1. Satisfactory rigid body behaviour was achieved within 3 to 10 s, depending on the scale of the parachute, from a static release. The nett cost was that two sets of rigging lines were required, making 48 lines in all.

The second constraint requires the wake from the store to have a negligible effect on the aerodynamics of the canopy, and, for a given canopy-store separation distance, is approximated by minimizing the store size. For the experiments under consideration, minimum store volume is dictated by the measurement technique and choice of instrumentation. A self-contained measurement system was used, and was fixed inside the store. The instrumented store was of hemisphere-cylindrical form, of diameter $d_s = 0.240$ m, and length $l_s = 0.480$ m ($C_D = 0.36$ at $\alpha = 0$ [67]), and a dummy store of twice this size was also used. For the worst case canopy/store configuration reported here the ratio $D_p/d_s = 5.9$ and the ratio (base separation distance/ d_s) = 4.4; empirical data indicate ([1], p.280) that this causes a reduction in canopy drag coefficient of less than 5% at $\alpha = 0$.

3.2. Instrumentation

Since it was anticipated that opportunities for carrying out the proposed drop tests could be limited by weather and schedule constraints, it was desirable to obtain as much information as possible from each experiment. Much consideration was given to the choice of suitable instrumentation, and the drop-test environment and required end-product data influenced thinking on this to a large extent. To enable simulation comparisons it was essential, whatever the end-product data, that the full kinematic state (i.e. initial conditions) at some point in the parachute be known at some instant during the rigid-body phase of flight. The drop-tests were

to take place either from tethered balloons under dead-calm weather conditions, or within the Cardington airship hangars.

A strapdown inertial measurement unit (IMU) located in the store was finally opted for, since this would give, either by direct measurement or by calculation, the angular velocity and Euler angles, the acceleration, linear velocity and trajectory of any point in the store: once rigid-body motion was established, the local incident airspeeds and aerodynamic angles at any other point - the canopy centre of pressure, for example - could also be estimated. In addition to the IMU, a specially developed Pitot-static type sensor [11,69] was used to provide a back-up measurement of the airspeed. A solid-state, microprocessor-controlled digital data acquisition unit [69-73] was also designed and developed for onboard recording, thus making the complete measurement system self-contained and suitable for use either outdoors or in the hangar.

3.3. Kinematic Analysis

The IMU supplies continuous signals from six inertial sensors: a mutually orthogonal triad of angular rate sensors, and a similar mutually orthogonal triad of linear accelerometers. The sensitive axes of the sensor triads are parallel, but not coincident. Given the initial orientation of the store with respect to an inertial reference frame, as specified by the Euler angle method, say, along with the outputs from the angular rate sensors, the orientation of the store at any subsequent instant can be calculated. This information allows vectors to be transformed from the body frame to the inertial frame, and vice-versa. Thus, knowing the orientation of the local gravity field, the gravity field components can be eliminated from the accelerometer readings, after which the accelerometer signals can be successively integrated to provide the velocity and displacement vectors.

The kinematic analysis for performing these operations has been arranged to allow direct comparison of drop-test and simulation results, and is presented in Appendix C2. The principal assumption is that Earth-fixed and inertial space-fixed reference frames are identical, which implies that the Earth's angular rate ($7.3 \times 10^{-5} \text{ rad s}^{-1}$) is negligible: for the short flight time ($< 50 \text{ s}$) and very low velocity ($< 15 \text{ ms}^{-1}$) data considered here the errors incurred are insignificant [74]. Note that the same assumption (the "flat Earth" approximation) has been used in the simulation model.

Numerical solution of the equations developed in the analysis is outlined in Section 3.8.5.

3.4. Experimental Apparatus

The experimental apparatus comprised the model parachutes, the data acquisition and storage system, also ancillary support equipment needed for power supply, hoisting, control and recovery. Most of the apparatus had to be purpose-designed and developed. Details of the considerable amount of development work have been reported elsewhere [69]; to preserve continuity only outline information is presented here.

The parachutes consisted of specially commissioned scale fabric models of the circular flat canopy, with nominal flat diameters of 6ft. (quarter-scale), 12ft. (half-scale) along with a 24ft. full-scale version. The canopy fabric material was nominally the same in each case, but the rigging line diameters were scaled.

Two identically shaped flight test bodies were used. The first, smaller body carried the full instrumentation and could be nested in the second, which was a twice-scale container. Initial drop testing, which successfully proved the feasibility of the experimental technique and of the instrumentation/data acquisition system, was performed in the airship

hangar, and demonstrated that little useful data could be obtained therein because of the short drop duration. To enable outdoor testing of a sufficient duration, much of the apparatus had to be modified and redeveloped, both to allow an increase in the data storage capacity and to withstand ground impact (a large catchnet had been used indoors).

3.4.1. Instrumented Body

A layout drawing of the instrumented test body (SB) is shown in Figure 3.1, and a photograph in Figure 3.2. The main components to be accommodated in the test body were the instrument block, a static inverter for the gyros, and batteries.

To enable the best range of store mass ratios it was desirable that the store be as light as possible in its basic form. Using initial mass estimates, preliminary calculations indicated that the inertial gyro torque reactions could have a noticeable effect on the motion of the store. The task of rendering the gyro-induced angular acceleration negligible suggested using a body of elongated shape to increase the moments of inertia - this would also be convenient for maintaining a narrow wake.

The instrument block and inverter were arranged to be mounted inside a rigid rectangular spine, and a cylindrical skin was fitted around the spine. A hemispherical nose was selected for simplicity of construction, also so that aerodynamic data for the complete store could easily be obtained if required. Care was taken at all stages with the disposition of mass in the stores; components were located so that the mass centre lay on the axis of symmetry, and also in such a way that the distribution of mass along the axis was as near symmetrical as possible. The latter is necessary to avoid whirling of the store due to dynamic imbalance [50].

With the transducers located in the central spine, the various circuit boards associated with voltage regulation, data acquisition, control and storage were fitted in the compartments between the spine and the skin, thus providing mutual protection from electromagnetic and thermal interference. The rechargeable battery packs were contained in a rigid plastic foam in the nose cone, and interchangeable packs were made up to save recharging during a trials session.

Landing impact attenuators had to be provided to prevent damage to the SB and its instrumentation. Where the SB comprised the full payload, a set of three legs was used for this purpose. The legs protruded beyond the store nose on landing and absorbed the kinetic energy by plastic, flexural deformation at a number of predetermined "hinge" points, thus reducing the shock loading to about 45 g for the highest descent speed tested. During flight the legs were folded back to avoid interfering with the Pitot-static system, and were deployed by telecommand at an altitude of almost 30 m AGL. Figures 3.3, 3.4 show the SB along with a dummy substitute body used for test purposes. The detachable support frame and legs used on the SB are seen in the foreground of Figure 3.4. The functioning of the impact attenuators was an ever-present worry, since failure to deploy correctly would have meant the end of the programme. Also, there was always the risk that the parachute would land at too oblique an attitude for the attenuators to be effective, with equally disastrous possibilities. A commercial radio-control system, as used with model aircraft, was used to release the shock absorbing legs. The system operated in the interference-prone 27 MHz waveband, but no alternative set was available at the time. Onboard units consisted of an integral receiver/decoder and an electro-mechanical servo, along with an independent battery pack. Checks were made for evidence of any mutual interference between the radio set and measurement system, but nothing detectable was found, even at maximum range.

3.4.2. Large Flight Test Body

A sectional sketch of the large test body (BB) is shown in Figure 3.5. The SB was centrally located in an aluminium guide tube which was lined with Tufnol rails to give a sliding fit. At the top the SB was pretensioned to a rigid frame with a bungee cord system, and this together with the guide tube prevented relative motion in flight.

Upon impact, the bungees extended to absorb kinetic energy from the SB; once an appointed tension was reached (corresponding to a pre-determined reduction in SB energy) the bungee and SB were separated via shear pins, and the remainder of the SB energy was dissipated by a foam rubber compression block and sliding friction. Foam plastic pads were fitted to the frame to avoid rebound damage. Lateral shocks due to inclined landings, and toppling over after landing, were cushioned by inflated rubber tubes surrounding the guide tube. The nosecone contained the shrouded Pitot and static tapings, and was connected to the pressure transducer in the instrumented body with 3 mm bore PVC tubing.

3.4.3. The Data Acquisition System

A self-contained microprocessor-controlled data acquisition system using semiconductor memory as a data storage medium was specially designed and developed for inflight recording of the parachute kinematics [69-73]; a schematic of the system is shown in Figure 3.6. The microprocessor unit (MPU), operating in accordance with preprogrammed instructions, controls the selection of the analogue sensor signals, their digitization and their storage in random-access memory (RAM). A major advantage of this type of system is its flexibility in dealing with changes in input configurations: the number of input channels can easily be expanded and different sampling rates accommodated by software modifications, with minimal changes in hardware.

With each of eight input channels being sampled at 10 Hz, the memory capacity of the prototype system (about 4900 8-bit bytes) provided for a run of 40.5 s (at 12-bit precision), which was estimated to be sufficient to cover about 8 oscillations of the largest parachute to be tested. This was reckoned to be more than sufficient for simulation matching purposes, and the 5.0 Hz Nyquist frequency gave a reasonable factor over the first few harmonics of the expected 0.2 Hz fundamental mode. The smallest parachute to be tested was estimated to have a fundamental mode at less than 1.0 Hz, thus even allowing for quadrupling of the sampling rate to maintain the aliasing margin, 5 K of memory provided adequate coverage to give a kinematic record similar to that of the largest parachute.

The 'data acquisition and conversion' block in Figure 3.6 consists of a single integrated package. A 14-bit analogue to digital converter (ADC) would have brought the quantization level down to the nominal quiescent noise level of the sensors, but would not have been convenient to implement. The integrated 12-bit ADC was chosen because it allowed easy packing of the data without an excessive demand on programming space and execution time. The integrated data acquisition system, a Burr-Brown SDM853 unit, incorporates a low drift, high speed instrumentation amplifier and is used at unity gain; the transducer outputs are arranged to give ± 2.5 V full-scale output (FSO). The analogue input multiplexer is a sixteen channel device, and the input signals were set up so that the signals, in filtered and unfiltered form, could be selected as required (Figure 3.6). This was necessary because it became apparent that it would not be possible to realise the individual low-pass filters for cost reasons (an individual filter is required on each line to avoid filter settling time delays due to the high-speed channel switching). An alternative, though not completely satisfactory solution, is to use numerical

filtering instead of electronic conditioning; strictly speaking, this can only be applied to frequencies up to the Nyquist frequency, so to minimize aliasing errors the Nyquist frequency must encompass as much as possible of the energy spectrum of the signal. In the event the bank of active low-pass filters was not used in the drop tests. Provision had been made in the programming to sample at 10 or 20 Hz/channel, but an opportunity did not arise to try the higher rate. It will be seen from the results, however, that the 10 Hz rate appears to have given an adequate aliasing margin for all the drop test configurations tried.

The programme controlling the MPU is loaded from digital magnetic cassette tape into RAM via a Texas Instruments Silent 700ASR communications terminal, and an external interrupt command to the MPU will then initiate the data sampling. Once sampling has finished the data are dumped onto magnetic tape, again via the terminal, from where they are transferred to a mainframe computer for processing.

The choice of MPU was not critical since it was used simply as a control device, rather than as a processor per se. A Fairchild F8 MPU system was used in the current application. This has a set of about 70 different instructions, the majority of which can be executed in 2 μ s. A useful feature is the large number, 32 in all, of bidirectional input/output (I/O) lines which are arranged as four I/O "ports", each 8 bits wide. A quartz crystal reference clock was added to the basic F8 system to ensure precise timing, and the memory was expanded from 1K to 5K 8-bit bytes.

All programming on the F8 had to be carried out at the most fundamental level, using machine code. The data acquisition programme was arranged to scan, at fixed time-intervals, a sequence of 8 input channels as quickly as possible; only 7 of the channels were actually used, and these were scanned in 528 μ s. Thus, if the 4th channel is taken as a reference, say, the other channels are sampled with a lead/lag of not more than 265 μ s, which, for current computational purposes, is assumed to be

negligible in the context of 100,000 μs time steps. The first reading of channel 4 occurs in the time interval (320,330) μs , and again, for practical purposes, is taken as instantaneous. The MPU data acquisition programme and its actuation are described in Appendix C3.

For the power supplies (Figure 3.6) several different DC voltage levels were necessary: 26 V for the gyros and demodulators, ± 15 V for the multiplexer, amplifier and ADC, 12 V for the MPU, 6 V for the accelerometers, 5 V for the memory and TTL logic circuitry, an independent 26 V for the speed sensor, and the majority of these also required voltage regulation. To make the complete system self-contained in flight, all power was provided by rechargeable nickel-cadmium battery packs. For weight reasons it was not feasible to size the packs for the recommended 10 hr. discharge rate, so it was decided to run them at the limiting safe discharge rate and to accept a reduced battery life. The most critical packs were the two supplying the rate gyros and the RAM, each of which gave a running time of about 5 minutes from a full charge.

To improve the 7.5 W heat dissipation of the 5 V regulator it was fixed directly on to the outer skin of the test body, which made a good heatsink. Dissipation from the four main bays - transducers, regulators, data acquisition and MPU/memory - was assisted by cooling vents in the nose, side and base of the test body. The bays had purposely been separated from one another to minimize thermal and electromagnetic interference (EMI).

Apart from the 5 V regulator and the 4 K memory board, both of which were fitted close to the skin, the other main heat sources were the solid-state inverter and the gyros. These were located close together within the central spine, along with the other transducers and demodulators. Under typical (static) field conditions it took about 10 minutes for the gyros to reach the calibration temperature of 25°C, so as a rule ground running times for the gyros were limited in order to give an in-flight

temperature of about this level. The temperature in the filter/data acquisition bay stabilized within a few minutes of powering up, so prolonged ground running of this and the MPU/memory was acceptable.

3.4.4. Support Equipment

For the outdoor experiments the parachutes were attached to a bomb-bar which was suspended under a barrage balloon. The balloon was allowed to rise to the desired altitude by means of a mobile winch. A telecommand link to the bomb-release mechanism allowed the parachute to fall. All of the drop tests were recorded on high-speed movie film, and to enable synchronization of the movie records and sensor signals a powerful flash bulb, which was fixed to the bomb-bar, was fired at the instant of receipt of the 'release' command. Upon landing, the parachute was recovered as quickly as possible by a Land Rover or similar vehicle, and returned to a mobile caravan for extraction of the data on to magnetic tape. Since all of the activity took place in the field, a mobile mains voltage generator was also supplied.

To preserve the batteries during ground running an external mains driven power supply unit (GPSU) was designed and constructed. This contained constant current voltage regulator circuits, which were trimmed to simultaneously power the test vehicle systems and to trickle-charge the batteries. For both utility and safety accurate and stable outputs from the GPSU were essential: the memory/logic supply line, for example, required 1410 mA at 10.80 V with tolerances of (+ 0, - 10) mA.

Since it was not practicable to fix this mains driven GPSU to the winched bomb-release rig, an alternative self-contained power supply system was also needed to maintain the batteries while the test body was on the winch and away from ground support. For this system power was provided by a pair of 24 V aircraft batteries, regulated by Zener diode and

transistor switching, but supplying only the two most heavily loaded lines - those for the gyros and the memory/logic circuits.

3.5. Calibration

Full details of the calibration techniques and results may be found in Appendix C4.

3.6. Experimental Technique

All of the drop tests were carried out near the airship hangars at the Royal Aircraft Establishment, Cardington. The parachutes were dropped from tethered barrage balloons from altitudes of up 1400 feet, and each drop was subject to stringent weather constraints.

Most of the test bodies, parachutes, measurement, communications and ancillary apparatus had to be transported from Leicester to Cardington on each occasion, and to make the most of potential periods of suitable weather conditions a start had to be made early in the day. Short and medium term meteorological forecasts for the Cardington area were therefore obtained at 7 a.m. on each prospective (dry, low wind) day: a maximum predicted steady wind speed of less than 2.5 ms^{-1} (5 kt) at 150 m (500 ft.) AGL was the (travel/no travel) criterion for experimental purposes, but official clearance to deploy a balloon also depended on the lightning risk being acceptable. It is remarkable how frequently low-wind conditions are accompanied by a high lightning risk.

Once in site; every effort was made to ensure that drops took place in intervals of relative calm. The release altitude was selected to give about 40 s of flight time, and varied between nominal values of 180 m (600 ft.) and 430 m (1400 ft.) depending on the store/canopy combination. At release altitude, the store and canopy were scrutinized through binoculars, and release was not initiated until both wind conditions on the

ground and as evidenced at the parachute were observed as having been minimal for a period of 20 s or so. A note was made of the time of release (to nearest minute) to enable the windspeed to be checked from anemometer recordings at the on-site meteorological station. The anemometer was located on top of a 40 m mast, about 200 m distant from the drop zone; this instrument needed a gust of 2.5 ms^{-1} (5 kt) to overcome static friction in the bearings, and then gave horizontal wind readings down to $0.5 - 1.0 \text{ ms}^{-1}$. The wind quantities noted in the following results are the worst case values recorded from the anemometer in the $\pm 60 \text{ s}$ around release time, and may therefore be regarded as upper bounds on the influence of horizontal atmospheric air movements (at 40 m AGL) on the tests.

Assistance during the experiments was provided by a number of R.A.F. and R.A.E. personnel, and an R.A.F. cameraman gave movie coverage to each drop. A base for loading and unloading the MPU system was set up in the caravan; this was located close to the balloon and winch so that the SB could be continuously maintained on external power. The drop test procedures followed for each canopy/store configuration are listed in detail in Tables 3.2(a) - (d).

Although rigid canopy models had been prepared, for time reasons it was not possible to carry out drop tests on these configurations. This is unfortunate, however as will be appreciated the necessary experimental techniques, the technology, the data processing, etc., have been developed and demonstrated for the most difficult extreme of the proposed programme for single body type, free-flight experiments. Little technical risk or physical effort will now be needed to fill in the primary and intermediate stages.

3.7. Summary and Results of Experiments

3.7.1. Summary of Experiments

A total of 32 production drops was conducted using four different canopy/store configurations: the SB on quarter-scale (SB06) and half-scale (SB12), and the BB on half-scale (BB12) and full-scale (BB24) canopies. These are sketched to scale in Figure 3.7, and inflight photographs are shown in Figures 3.8 - 3.14. Outline details of the production drop tests are given in Table 3.3.

3.7.2. Observations

The primary constraint on all operations, apart from the weather, was the fact that internal battery supplies to the MPU were only good for about five minutes running time. The RAM/TTL and gyro lines drew currents of 1400 mA and 960 mA, respectively, as opposed to the 60 mA (10 hr.) discharge rate recommended for their NiCd battery packs. It was anticipated that two or three drops could be obtained from each battery pack before recharging, but to ensure results it proved necessary to charge the RAM/TTL pack after each flight.

The battery difficulty also meant that the test body had to be recovered as quickly as possible after landing, before the data stored in the memory was lost, so a Landrover was commissioned for this task. The Landrover usually arrived at the touchdown point at the same time as the parachute, whereupon the test body and canopy were bundled into the back of the vehicle, resting on a shock-absorbing mattress during the speedy return to base. This method was not without its difficulties - on one occasion (Drop 3) the 12 ft. parachute inflated suddenly en route and extracted the large store from the Landrover, resulting in loss of the data because of the delay.

Sequencing of the tests was arranged to minimize the risk of catastrophic damage to the instrumentation. Fortunately, the impact attenuators functioned as required in that the equipment survived to the end, though the landing after Drop 12 was heavy, and caused a couple of the printed circuit boards to damage their mountings. While the radio-controlled legs had functioned faultlessly for the preliminary test-drops with the dummy store, during the production trials they were released prematurely on several occasions owing to radio-interference. This at least was fail-safe, and the source of the interference was suspected as other operators on the range using the same frequency, also noise from the diesel generator, since the problem disappeared when both of these factors were eliminated. On one occasion it was failed to actuate the legs in time, so that the store hit the ground with the legs still in the folded position; this was on Drop 29 (SB12 combination), and, since no damage had been done, the legs were dispensed with for further drops of the same configuration (Figure 3.15).

As anticipated, the circular flat parachutes exhibited a broad range of flight behaviour. Steady modes observed included non-oscillatory vertical and glide descents; near-planar oscillation, both vertical and glide; coning motion; and breathing (canopy inflation/deflation). On some drops (e.g. BB24 configuration) a particular mode predominated; on others (e.g. SB06) many or all of the above modes were observed. The durations of the modes appeared to be random, particularly for the BB12 and SB06 configurations, where the descent speeds were about 2-3 times those of the BB24 and SB12 configurations. When the amplitude of oscillation was large, luffing (partial collapse) of the canopy edge was occasionally observed; this can be seen in Figure 3.14.

Not all of the drops were successful in yielding data, the major culprit being run-down batteries: although there were programme options in the MPU for selecting filtered data and/or a sampling rate per channel

of 20 Hz, for time reasons neither of these options were exercised. All measurements were of unconditioned signals sampled at 10 Hz.

For the drops which were successful the ratios of mean descent speeds to peak mean wind speeds are shown in Table 3.4.

3.8. Reduction of Data

The raw data from the drop tests were recorded in two forms - in hexadecimal-coded binary on magnetic cassette tape and on 24 frames s^{-1} movie film. The binary data from the transducers were comprehensively analysed and processed on a mainframe computer, and then obtained in numerical listing and graphical forms. Both movie and still analyses of the films were carried out. The stills were analysed with the aid of a film digitizer to provide both the initial conditions for the computations and the inflight geometries of the parachutes, while the movies, by means of the 0.01 s film timing marks, were used to correlate transient events, such as canopy edge luffing, with the inertial sensor signals.

Processing of the transducer signal data was carried out in progressive stages by a suite of FORTRAN programmes, a graphical output and/or numerical listing being obtained after each stage as a check for sensible results.

3.8.1. Transducer Signals

The first stage was to reconstruct the seven transducer signals, in MKS units, from the raw coded data. This process is shown in flow diagram form in Figure 3.16. Following the heavy landing of Drop 12, a sporadic fault appeared in all subsequent drops, but was confined to the r , a_x and a_z data stored in the memory area H0800-H0A00. The exact source of the fault was not traced, but its effect, which was to add a binary 000010000000 (256 bits) to the afflicted locations, was easily remedied by applying a

binary filter with a threshold of 160 bits.

To convert the data from voltage form to kinematic units the full calibration hysteresis curves were interpolated. The data point in question was tested against the previous point in the same time series to detect if it was increasing or decreasing, and the appropriate calibration curve was then selected. This technique was used for the rate gyro and accelerometer signals, though in the case of the accelerometer data the advantage was probably marginal, because of the mutual proximity of the calibration curves. Error propagation is considered in Section 3.8.6. For the airspeed sensor the zero offset, as determined individually for each drop, was first subtracted from each reading; a simple scale factor (linear least-squares fit) was applied to convert the voltage to mm of water gauge.

The interpolation routine (TRPLV) used a cubic polynomial, and employed a slope averaging subroutine (TRPLS) to obviate the inclusion of extraneous maxima. Before interpolation, each data point was tested to ensure that it was valid: the calibration curve arrays were tested for monotonicity, and the data point was tested to see if it was within the calibration range; a warning flag was output if any of the tests failed. Plots of the reconstructed signals are presented in Figures 3.17 - 3.38; the plots are drawn with straight line segments connecting the discrete data points.

3.8.2. Fourier Analysis

The second stage was to Fourier-analyse the discrete signal time histories, both to determine the frequency power density spectra and for numerical filtering purposes. The frequency density spectra were obtained primarily as a check on the adequacy of the 10 Hz sampling rate, with the secondary objective of identifying any predominant modes of oscillation of the body. Numerical lowpass filtering was particularly required for the

Pitot-static signal on low descent speed drops, since here the individual or combined effects of high angles of attack and atmospheric turbulence occasionally gave a negative (pressure difference) signal (cf. Figure 3.18), which could not be converted into an air speed. Time derivatives of the rate gyro signals were also needed (Appendix C2), and since these were to be obtained numerically, optional lowpass filtering was made available in case the extra order of unsteadiness proved either excessive or intractable for computational purposes.

Amplitude and Power Spectra

A program was written around a NAG Library Fast Fourier Transform (FFT) ([82], CO6ADF); the data flow diagram is outlined in Figure 3.39. For each signal time history a record partition is defined, within which the data points are uniformly weighted. These data are then Fourier transformed, and the real (A_k) and imaginary (B_k) Fourier components are calculated. In Figures 3.40 - 3.45 the spectral amplitude components $F_k = (A_k^2 + B_k^2)^{1/2}$ for the inertial sensors are plotted as a function of frequency; to emphasise the peaks, the maximum (non-zero frequency) F_k value has been used as a normalizing factor on each plot (the power spectral density is proportional to F_k^2). The mean value of the signal is obtained from the zero-frequency component (A_0), and can be used to detect any bias (see below). Note that in Figures 3.40 - 3.45 for each individual drop the record length analysed consists of the full interval ($t = 0$, $t = \text{touch-down}$), and hence also includes the initial transients.

Digital Filtering [83]

Where lowpass filtering is needed the series of Fourier components (A_k, B_k) is truncated (rectangular window) to remove any frequency content at and above the specified cut-off frequency. The truncated series is

then inverse-FFT transformed to reconstitute the filtered signal. Only the record within the window is filtered.

Bias Estimation

The signal bias can be estimated, within a specified (time) window, by means of the FFT. For bias compensation, however, a constant correction is applied to all data points within the full time record. Programme options exist which allow either a fixed value to be applied, or for the measured bias to be adjusted to a preferred value (e.g. zero).

3.8.3. Angular Rate Derivatives

After preconditioning by numerical filtering, if applied, the time derivatives of the angular rate signals p , q and r are estimated at the sampling points by means of the routine TRPLS. This calculates the backward and forward slopes at the data point: if the slopes are monotonic the mean value is taken; if not monotonic, the slope (derivative) is set at zero. The same technique is used in estimating the time derivative of the airspeed w_N .

Figures 3.46 - 3.49 show the calculated time derivatives of p , q and r for four drops representative of the configurations tested. The signals have been lowpass filtered at 5.00 Hz throughout the record. Also shown is the time derivative of the airspeed, \dot{w}_N , compared with the filtered z -accelerometer signal.

3.8.4. Pitot-Static Signal

As noted above, and as evident from the unconditioned signal plots (cf. Drops 2-7, 28-32), the output from the Pitot-static sensor is occasionally negative. The likely causes are excessive angles of attack

at the store nose (cf. Figures C4.18, C4.21) and atmospheric turbulence. For analysis purposes, all of the Pitot-static records were lowpass filtered at 2.50 Hz, and this removed the negative values in all cases. Figures 3.46 - 3.49 show the frequency amplitude spectra of the Pitot-static signal for the different drops.

Using outside air temperature and barometric pressure measurements obtained from the on-site meteorological station, a value for the air density at field elevation was calculated for each drop. This value was taken as the constant effective air density during the flight, and was also used for simulation purposes.

In converting the indicated Pitot-static reading to airspeed units two scale correction factors were applied. The first factor was derived from the calibration curves for the sensor, and was applied as a constant throughout the flight. For the SB, where U_i/U_∞ is effectively independent of Reynolds Number (Figure C4.18), a single value of $U_\infty/U_i = 0.949$ was estimated; this was obtained from a linear least squares fit (s.d. = 0.9%) for all points in the range $\alpha = \pm 15$ deg. For the BB, this scale factor was obtained from a plot of U_i/U_∞ ($\alpha = 0$) vs U_∞ (Figure 3.50); the value was estimated as $U_\infty/U_i = 1.11 \pm 0.01$ for the BB24 configuration, and 1.00 ± 0.01 for the BB12 configuration.

The second factor was applied to compensate for the error introduced by the presence of the canopy, which causes the airspeed to be underestimated. Two different ideal flow models were used for calculating the effect; I am grateful to Dr. J.S. Lingard of the RAE for suggesting both of these models, also for supplying a numerical solution to the first. In the first, the canopy was treated as a hemispherical cup in uniform axisymmetric potential flow: in the second, the canopy was modelled as a ring vortex in uniform flow with a boundary condition of zero axial velocity at the centre ([84], p.93). The solutions are plotted on Figure 3.51 in the form of the velocity ratio along the axis of symmetry as a function of distance from

the canopy mouth plane; in both cases the presence of the store has been ignored. The hemispherical cup solution is treated as exact for present purposes, with x (Figure 3.51) taken to be the distance from the canopy mouth plane to the tip of the store nose, as estimated from photographs. The values used for the second factor were:

<u>Configuration</u>	<u>U_{∞}/U_N</u>
BB24	1.022
SB12	1.046
BB12	1.031
SB06	1.036

The second factor was implemented as a unity-ramp-constant gain function (see Figure 3.52).

3.8.5. Integration and Synthesis

Final integration and synthesis of the processed data were executed by programme KIN, a high-level flow diagram of which is shown in Figure 3.53. Integration of $\dot{\phi}$, $\dot{\theta}$, $\dot{\psi}$, \dot{u}_{OI} , \dot{v}_{OI} , \dot{w}_{OI} , u_{PI} , v_{PI} and w_{PI} (see Appendix C2) is carried out by the same predictor-corrector routine, based on the Adams-Bashforth algorithm, as used in the simulation model. Geometric constants and initial Euler angles, as determined from photographs, are read by INTKIN and used to specify the initial conditions and initial transformation matrices. Data values for instants between sampling points are interpolated by the subroutines TRPLV and TRPLS. An output time step of 0.1 s was used for all runs. OUTKIN calculates instantaneous resultant velocities, aerodynamic angles, etc. The results can be presented as a listing or in a variety of plot formats. Output is terminated 0.2 s before the final input data point.

The initial Euler angles were obtained by using an angular digitizer on a film analyser rig. The movie camera was distantly located from the drop zone so that a good side-view of the parachute was obtained from

release to touchdown. Using the built-in bubble level, the camera was accurately levelled before each series of trials, and a suitable telescopic lens was fitted so that the picture frame was filled by the parachute. Since only one camera view was available it was necessary to assume that the misalignment in the orthogonal plane was zero; for the majority of drops analysed the initial deviation from the vertical was less than 1 deg., so this assumption is reasonable. Using the chequered markings for identification, the initial orientation and the projections of the vertical deviation angle were then employed to give ϕ_0 and θ_0 . The angle ψ_0 , which is arbitrary for the axisymmetric parachute, was set to zero in each case.

3.8.6. Error Propagation due to Noise

Several tests were carried out as an overall check on error propagation due to signal noise, the sources of which might be real (EMI) or induced during the data decalibration process (Section 3.8.1). The noise source data were obtained by performing two 'dummy' trials (CH01 and CH02) in which the SB was placed upright, as judged by eye, on a table and the sensor outputs were recorded by the onboard data acquisition system. The trials were performed in a warm office, after a warm-up run of 30 min.; the GPSU and the TI700 terminal, both mains powered, were plugged into the SB. Under these conditions the effects of thermal and EMI-generated noise may be regarded as extreme compared to the effects encountered under flight conditions. Similar data, though unsolicited, were obtained from a run under field conditions; these data were logged during a test trial ('Drop' 6) in the caravan, and for this case it may also be assumed that background shocks and vibration were also picked up.

The power spectra from trials UF06 and CH01 are shown in Figures 3.54, 3.55; no windowing has been applied, i.e. the full record lengths

have been used. Also plotted are the unfiltered source signals, with their bias errors removed (the preferred bias values and the measured bias errors are listed in the right-hand column, viz. for a_z the preferred value is $-9.8/25 \text{ ms}^{-2}$, and the measured error is -0.1674 ms^{-2}). The sources of the spectral peaks at around 1.5 Hz and 4.3 Hz have not been identified, but since no well-defined peaks at these frequencies appear in the actual flight data (Figures 3.40 - 3.45), they may be associated with mains interference.

The unfiltered, but bias-corrected signals, along with the associated angular rate derivatives (e.g. Figure 3.56), were then run in programme KIN to check the overall effect of background noise: Figures 3.57, 3.58 show the results for the Euler angles and attitude errors. Figures 3.59, 3.60 show the effects on the velocities and space trajectories of the virtual origin of the IMU; a_z was corrected to zero bias before entering KIN, hence the peculiar trajectory plots. In the above runs, all initial values of the integration variables were zero. Figure 3.61 shows a run for UF06 data with $\phi_0 = \theta_0 = 30 \text{ deg}$.

Bearing in mind that these are extreme, coloured-noise trials the results are taken to represent upper-bound error values for signal noise in the raw data. It is reasonable to assume that the Euler angles will not be affected by more than about $\pm 1 \text{ deg}$.

3.8.7. Bias Corrections

Initial results of KIN runs were disappointing. Using unfiltered data from Drop 2 the calculated Euler angles at $t = 37.0 \text{ s}$ were $(\phi, \theta, \psi) = (-186.0, -5.59, -0.75) \text{ deg}$. The angles ϕ and θ give the inclinations of the parachute axis of symmetry from the vertical, and for the present experiments did not exceed 60 deg. Inspection of the plot of ϕ revealed it to be oscillating about a monotonically increasing mean value, the cause

of which is a bias in the rate signal. The most likely source of this bias is thermal drift in the gyro and/or measurement chain. The angle ϕ is derived primarily from the p-gyro signal (Eqns.2.21), which has a quantization level (QL) of $3.6 \times 10^{-3} \text{ rad s}^{-1}$. The estimated signal bias on p is about $-7.0 \times 10^{-2} \text{ rad s}^{-1}$, or nearly 20 times the QL. Similar, though smaller, biases exist on the other signals.

The measurement of and compensation for errors in inertial measurement systems is a comprehensive science in itself, and this study must of necessity be limited to a first order treatment. This is also justified on the grounds that the measurement interval was very short - so that ambient conditions and drift levels may be assumed to change little over this interval - and because it gives sufficient accuracy.

Determination of the bias corrections is described in Appendix C5. The corrections for p, q, r and a_z gave excellent results when implemented. Those for a_x and a_y did not; residual biases in a_z and a_y are detected directly as divergences in u_p , v_p and V_{rcp} , and indirectly as an oscillatory divergence in w_p . Fortunately, using the Pitot-static derived speed w_N as a guide, the bias corrections in a_x and a_y can be finely adjusted by trial and error to give a good fit of w_p with w_N . The integrity of w_p is checked against the distance fallen, for which the release altitude is an upper bound (since the nominal release altitude was taken as the length of balloon cable paid out).

3.8.8. Results

It was found that the optimum bias adjustments were uniquely identifiable for each of the several drops analysed (with the exception of Drop 25; see below) - only one combination of a_x and a_y corrections would both give a good fit of w_p with w_N , and remove the monotonic divergences from the time histories of u_p , v_p and V_{rcp} - and were well defined, i.e.

to within $\pm 0.01 \text{ ms}^{-2}$. The trial and error process, though effective, was time consuming because the adjustments required were best judged graphically. For this reason only one fully-synthesized set of results for each canopy/store configuration is presented here; these are for Drops 2, 10, 25 and 29 (Figures 3.62 - 3.70). In these cases the bias corrections used were:

Drop No.	Bias correction for a_x (ms^{-2})	Bias correction for a_y (ms^{-2})
2	-0.76	-0.86
10	-1.16	0.04
25	-0.41	-0.31
29	-0.88	-1.01

For Drop 25 the estimated corrections (Appendix C5) were used since the spin made it difficult to identify the optimum values.

It has been confirmed that all of the remaining drops give acceptable Euler angle results; however these will be held over pending identification of the optimum accelerometer corrections. The results given here may be regarded as representative of the range of configurations tested.

In Figures 3.62 - 3.70, values of ψ and β_{cp} which exceed ± 180 deg. have been wrapped around to limit the plot space used. Note also that the point P is the virtual origin of the IMU and lies in the store: mass/geometric parameters of the parachutes are treated in Section 4.2.

3.9. Discussion of Results

Figure 3.17 shows the transducer signals for Drop 0, which was a development trial. Note in particular the torsional oscillation about the axis of symmetry (r signal) and its effects on the x- and y- gyros; also the clipping of the r-waveform due to topping/bottoming out of the gyro. Following this trial the rigging configuration was altered (Appendix C1) and the gyro exchanged for one with a larger range. The

new rigging configuration was successful in quickly damping out the initial torsional perturbation, as can be confirmed from the p and q gyro plots (Figure 3.18).

From inspection of the frequency amplitude spectra the 5 Hz aliasing frequency appears to have been more than sufficient for the majority of trials. Drops 19-27 (SB06 configuration) show distinct peaks at about 3.9 Hz in several instances (cf. Figure 3.44, Drop 25, p and a_y), but there is little energy content above this, least of all in the gyro signals. The only way of substantiating the sufficiency, or otherwise, of the 10 Hz sampling rate used would be to sample at a much higher rate and then check the power spectra. The z -accelerometer signal would have benefited from a higher sampling rate during the first 5 s after release, where large initial transients need to be defined. Fortunately the information required was available from the Pitot-static signal (Appendix C2).

The transducer signals - especially the p and q rate gyro signals (Figures 3.18 - 3.38) - corroborate visual observations of the different types of oscillatory motion (Section 3.7.2). Drops with the BB24 configuration (Figures 3.18 - 3.20) behave fairly regularly after the initial perturbations, with apparently little change in oscillation frequency or amplitude. Few of the other drops show any lasting sign of steadiness; Drops 8-18 (BB12; Figures 3.21 - 3.27) display intervals of calm punctuated by bursts of strong oscillation. These are particularly clear in Drop 13 (Figure 3.24): note the amplitude correlation between the p and q signals. Similar random oscillations are seen in Drops 19-27 (SB06, Figures 3.28 - 3.34); they are quite distinct in Drops 26 and 27. In contrast, the SB12 configuration performs swings around alternate x and y body axes, so that large swings around one axis tend to be accompanied by little motion in the orthogonal plane (cf. Drops 28 and 32, Figures 3.35, 3.38). Note that in these, and in many of the other drops, the time dependence of the signals appears to comprise amplitude

modulation of a single, predominant background frequency.

Comparison of the amplitude spectra for groups of trials of the one configuration confirms the existence of predominant frequencies of oscillation. These are quite distinct, particularly in the p - and q -gyro spectra for the BB24, BB12 and SB12 configurations. As a test for stationarity, also of efficacy of the rigging method, the signal records for Drop 2 were partitioned and Fourier analysed. Attention was concentrated on the interval after $t = 10$ s, since prior to this effects of the initial transients are noticeable. The power spectra for overlapping partition lengths of 12.5 s (125 sample points) are shown in Figures 3.7(a)-(c) along with their peak values: they are practically identical in shape and in peak magnitudes. Note that there is negligible energy content in r at the torsional frequency seen in Figure 3.40(a) (Drop 0). Note also that the a_y signal, though apparently much noisier than the other accelerometer signals, is in fact plotted to a scale an order of magnitude smaller.

All of the SB06 drops show a spin bias in the same direction, with a constant clockwise spin rate of about 3 rpm. Because of the small size of this parachute, and also the low spin rate, the spin was not detected until after completion of the tests, when the movies were developed and analysed. The source of the spin is not known, but is probably due to z -axis asymmetry of the parachute: possible causes are a canopy rigging asymmetry or a torque induced by the impact attenuator legs. The latter seems unlikely since the spin exists whether the legs are up (Figure 3.27) or down (Figure 3.32). The computer model can cope with an initial spin rate, so simulation is not a problem. In this context also, the fact that the impact attenuator legs deployed prematurely on some flights does not render these drops unusable; on the contrary, since the different mass distributions can easily be simulated, as step functions, say, the perturbation might well prove useful in determining the system

transfer function characteristics. The effects of the wakes from the deployed impact attenuator legs on the Pitot-static system are not significant; they show up as a sudden dropout in the signal (e.g. Figures 3.17 - 3.29), but after filtering the signal content is more than sufficient for completing the integration and synthesis.

In all of the final results presented (Figures 3.62 - 3.70) the inertial transducer signals are unfiltered since any lowpass filtering was found to attenuate the integral values. Thus the full information content of the signals (other than the transducer bias) has been retained. Features of the results are discussed in Section 4 in conjunction with simulation matching.

In considering the uncertainty in the final results, the primary source is seen as that due to transducer bias. Note that the frequency content of the results, which are important for simulation matching, are unaffected by bias errors. The three rate gyro and the a_z bias corrections have been satisfactorily estimated by elementary analysis of flight trial and stationary trial data, which gave agreement in mean values to within an order of the individual quantization levels (Appendix C5). On the basis of the differences in mean bias values ($\Delta p = 0.0026 \text{ rad s}^{-1}$, $\Delta q = 0.0047 \text{ rad s}^{-1}$, $\Delta r = 0.0038 \text{ rad s}^{-1}$), the final direct deviations (i.e. ignoring the mutual interactions, which are small for small angles, Eqns. 3.21) in Euler angles after a 40 s flight would be $(\Delta\phi, \Delta\theta, \Delta\psi) = (6.0, 10.8, 8.7)\text{deg}$. Even these seem rather large, but the deviations are linear in time so that for t between 5 s and 10 s, where initial conditions for simulation are obtained, the uncertainties are correspondingly smaller. The attitude adopted to the final results is that, with the simple bias correction estimates used, they are sufficiently well defined at $t = 40 \text{ s}$ for the bias uncertainties in the Euler angles, for simulation starting at $t = 8 \text{ s}$, to be about $\pm 2.5 \text{ deg}$; the bias uncertainty (at $t = 8 \text{ s}$) for the speed w_p (using w_N ($\pm 3\%$ overall uncertainty

(@ $|\alpha_N| < 15$ deg), say) and $\Delta a_z = \pm 0.015 \text{ ms}^{-2}$ for a Δt of 5 s) $\approx \pm 0.5 \text{ ms}^{-1}$; and for $u_p, v_p \approx \pm 0.8 \text{ ms}^{-1}$ (from w_p ($\pm 0.5 \text{ ms}^{-1}$) and $\Delta a_x, \Delta a_y = \pm 0.01 \text{ ms}^{-2}$ for 8 s). There ought to be scope for improving the bias corrections by applying a more sophisticated statistical analysis technique to the individual trials. This would also give proper confidence interval estimates. For present purposes, i.e. as a first step in the direction of acquiring data suitable for validation, and particularly in view of the constraints of the equipment and measurement system used - 12 bit accuracy on a strapdown IMU, in conjunction with a 10 Hz sampling rate - the current results are felt to be more than acceptable. In Section 4 these data are discussed further in respect of their use and usefulness for validation.

3.10. Conclusions

A systematic method for validating conceptual models of parachutes has been outlined. An experimental technique has been developed which causes a parachute system comprising a flexible canopy attached to a store to oscillate as a single rigid body, thus enabling its simulation by a fundamental six degree-of-freedom computer model. Experimental apparatus, structured around a strapdown inertial measurement unit, has been developed to acquire the kinematic behaviour of free-falling parachutes. The kinematics of four parachutes of different scales, with canopy flight diameters from 1.4 m to 5.8 m, have been recorded in 21 drop tests under optimal atmospheric conditions. The experiments demonstrated a considerable degree of random flight behaviour, but spectral analysis of the transducer signals revealed sharply defined frequencies of oscillation for each physical configuration. The drop test results have been comprehensively analysed and synthesised to provide data both for initiating simulation and for subsequent comparison purposes.

SECTION 4

COMPARISON OF EXPERIMENTS WITH THE CURRENT SIMULATION MODEL

4.1. Method

The full unconstrained, three-dimensional descent behaviour of four different canopy/store configurations has been simulated using the current computer model. Since the computer model assumes rigid body motion, the simulations were initiated as soon as this condition was judged to hold, which for most trials was between 3 s and 10 s after the release (the calculated aerodynamic angles at the canopy provide a good measure of steadiness because fluctuations in the body angular rates are amplified in these quantities).

Since a large number of input parameters are used to specify the computer model, and because the experimental results exhibit much apparently random behaviour, the tactic adopted was to hold all parameters other than the most sensitive (Section 2.4.6) fixed while attempting to improve overall agreement, as assessed by visually matching output plots from simulation and experiment. The alternative approach would be to apply multivariate optimal estimation techniques [86], but in the light of the tentative (though conventional) assumptions used in the model - regarding the added mass tensor, for example - this would seem to be premature, at least until better (i.e. order of magnitude) measures of the added mass components and of their variability are available for the canopy.

The Euler angles and body-axis speeds are presented here for comparison purposes. It might appear easier to use the computer model to simulate the rate gyro and accelerometer signals, but this would then require (visually) matching time histories with an additional degree of unsteadiness, which was felt to be impractical. Also, the Euler angles and speeds must in any case be calculated from the experimental data to provide initial

conditions for simulation.

4.2. Input Parameters

The inflight parachute dimensions were obtained by measurement using the movie film digitiser. Where canopy breathing (axisymmetric inflation-contraction mode of oscillation) was occurring care was taken that measurements were only recorded midway between breathing extremes. The derived displacements were scaled on the known store dimensions and were then averaged. Variations around the average were in all cases within $\pm 5\%$ in projected diameter and in store/canopy separation distance. The store masses were measured to within ± 0.01 Kg, and the store centre of gravity locations to within ± 0.002 m. The solid body moments of inertia were calculated as described in Section 2.3.3.

To determine the appropriate aerodynamic input parameters the canopy porosities were tested on a U.K. standard porosity measurement rig [87]; this gave volumetric flow rate values of 9.0, 8.7 and 10.6 ft³/ft² sec, at a pressure difference of 10 in water pressure, for the 24 ft., 12 ft. and 6 ft. canopy materials respectively, with a variation of less than ± 1.0 ft³/ft² sec in each case. Heinrich and Haak's force coefficient data [31] refer to porosity values measured to the U.S. standard, which uses a pressure difference of 0.5 in water pressure. For the necessary conversion from the U.K. standard to the U.S. standard, it was assumed that the material behaves similarly to one tested by Lingard [88]: this then gives effective porosity [32] estimates of $\lambda_e = 2.6, 2.5$ and 3.0% for the three canopies (using the pressure differences to provide a straight velocity ratio of $(10.0/0.5)^{1/2}$ gives upper bound [89] estimates of $\lambda_e = 4.3, 4.2$ and 5.1%). As a starting point for simulation purposes, the force coefficient curves presented by Heinrich and Haak for a flexible, circular flat canopy with $\lambda_e = 1\%$ were used. Since Heinrich and Haak did

not measure the pitching moment, this was implemented in the added mass couple terms only, with the body coordinate origin taken to lie at $0.25 h_c$ (Section 2.4.4.1). Baseline added mass coefficient values were the same as derived in Section 2, viz. $K_{11} = 0.25$, $K_{33} = 0.40$, $K_{55} = 0.27$, $K_{15} = 0$, and the damping moment derivative coefficient ℓ_p was taken as -0.08 .

Initial conditions were taken directly from the output listing of programme KIN (Section 3.8.5).

4.3. Results

Drop 2 (BB24 configuration) was arbitrarily chosen as the test case. The first run, using the baseline added mass values, indicated that the frequency of oscillation was underestimated. The ratio K_{33}/K_{11} was increased to raise the frequency, and ℓ_p was also increased slowly to contain the amplitudes, as seen in the attitude angle. A combination of $K_{33}/K_{11} = 2$, with $K_{11} = 0.3$ and $\ell_p = -0.1$ was found to give good agreement: the results of this run are shown in Figures 4.1 and 4.2.

The speeds along the axis of symmetry agree well, and this is confirmed by the vertical distance fallen (Z): for Drop 2 the release altitude was a nominal 183 m (600 ft.) above ground level, and experimental results give a distance fallen of 179.3 m at 0.2s before impact; simulation predicts 177.4 m for the same instant, which is remarkably close.

The same added mass and damping moment coefficient values were therefore applied to Drops 10, 25 and 29. The frequency and amplitude results for Drop 29 (SB12) (Figures 4.3, 4.4, 4.5) were acceptable, but Drop 10 (BB12) (Figures 4.6, 4.7, 4.8) and Drop 25 (SB06) (Figures 4.9, 4.10) needed increases in damping moment coefficient of about 50% to limit the attitude.

It is beyond the scope and means of the present study to take the simulation matching any further. Clearly, there are areas which need to

treated - the effects of different initial conditions need to be examined, for example. This has been looked at briefly, simply by choosing different start times from the output listing of programme KIN: the indications are that the detailed oscillatory response does depend to a large extent on initial conditions, but that the global behaviour - viz. frequency and attitude peaks - does not.

4.4. Discussion

4.4.1. Drop Distance

As an overall check on performance the estimated distances fallen at impact were compared with the nominal release altitude (Table 4.1). Recall that the release altitude is assumed to be the same as the balloon cable length, which is therefore an overestimate if anything. The cable is light and under tension, and hence, to a first approximation, may be considered a straight line; under these conditions, for a (large) cable slant angle of 10° the slant length is only 1.5% greater than the vertical distance.

Drop No.	Nominal Release		Calculated Distance Fallen			
	Altitude Z (m)	Experiment		Simulation		
		(m)	$\Delta Z\%$	(m)	$\Delta Z\%$	
2	183	180	-2	178	-3	
29	213	225	+6	211	-1	
10	335	381	+14	326	-3	
25	427	458	+7	377	-12	

Table 4.1 Comparison of calculated distances fallen with release altitude

It is not clear why the experimental results overestimate to such an extent. Since the Pitot-static derived speed w_N was used as a guide for w_p , one reason may be the over-simplification of the calibration curves for the Pitot-static sensor: an iterative interpolation procedure would be more appropriate where incidence at the store nose exceeds 15° or

so. This was not investigated for time reasons. For Drop 25, which was subject to a spin, the Pitot-static speed was used throughout integration of the experimental data because the inertially-derived speed w_p was found to be unstable.

If the percentage differences for simulation are based on the comparison interval, rather than total distance, the values are slightly greater, by 10% (of 12%) for Drop 25 to 26% for Drop 2. However, the simulations of Drops 2, 29 and 10 provide excellent estimates of Drop distance.

4.4.2. Drag Accounting

In each case the simulations underestimate the distance, and hence overestimate the drag. Aerodynamic force coefficient curves of Ref.31 for $\lambda_e = 1\%$ were used, compared with an estimated $\lambda_e = 3\%$. Use of the $\lambda_e = 4.2\%$ curves may be expected to increase the drop distance by less than 2% (Section 2.4.4.1) - linear interpolation suggests only 1.3% at most. Now descent distance/speed is inversely proportional to $(C_D)^{1/2}$, so fairly large errors in drag coefficient are implied: estimates for possible sources of the shortfall are tabulated below as percentages of C_D ($\alpha = 0$) (Table 4.2):

Drop	Estimated Drag Shortfall	Porosity Error [31]	Extra Rigging Lines [16]	Apex Vent	Forebody Wake Interference [1]	Legs Interference
2	7	2	3	?	<<5	NA
29	2	2	3	?	<<5	NA
10	9	2.5	3	?	<5	NA
25	27	2	4	?	<5	?

Table 4.2 Sources and estimates of errors (%) in C_D ($\alpha = 0$)

On this basis, the results for Drops 2, 29 and 10 can be accounted for. It seems improbable that the impact attenuator legs would reduce

the overall drag by as much as 20%: since only three measurements were used to average the canopy diameter for the SB06 configuration, an inaccuracy in D_p is more likely.

4.4.3. Descent Mode

Whereas the physical models display glide motion, especially the lightly loaded BB24 and SB12 configurations, all of the simulation results show a vertical descent. As implemented here, the aerodynamic pitch stiffness stabilises (for $K_{33} > K_{11}$) the system around $\alpha_{cp} = 0$ by a moment which is proportional to $(K_{33} - K_{11})$ (although K_{33} was arbitrarily increased to raise the frequency, an alternative and no less valid move would be to reduce K_{11} to give the same effect). The sensitivity analysis showed that $(K_{33} - K_{11}) = (0.40 - 0.25) = 0.15$ is a reasonable approximation to the rough experimental data; here a value of $(K_{33} - K_{11}) = (0.60 - 0.30) = 0.30$ is used, which is too large by a factor of 2. Better data are needed for progress: either the $(A_{33} - A_{11})$ moment terms ought to be replaced with good steady-state measurements, or the aerodynamic centre of the canopy should be determined to allow these moments to be eliminated altogether.

4.4.4. Euler Angles

The experimental results for ϕ and θ show an apparently random amplitude modulation which is not matched at all by the simulations. The effect can clearly be seen by comparing the attitude angle, which oscillates as a limit cycle in each of the simulations. In Drop 25 (Figure 4.9) there is amplitude modulation of ϕ and θ , but this is periodic and due to the z-axis spin. For the last few seconds of the Drop 10 simulation (Figure 4.6) a motion combining a steady spin with coning is incipient.

The spin observed during Drop 25 (Figure 4.9) is simulated very accurately up to deployment of the impact attenuator legs. No attempt has been made to simulate the deployment. Note the reversal of spin rate at deployment, and the resumption of the original rate once deployment is complete at $t = 36.2$ s.

The cause of the reversals in Euler angle ψ (Figures 4.3, 4.6) in the simulations may be puzzling at first sight since the model generates no external forces about the body z-axis. The source must lie in the derivation of the Euler angles from the body rates: in Eqns.2.21 it can be seen that

$$\dot{\psi} = (q \sin \phi + r \cos \phi) \sec \theta,$$

hence ψ is a function of ϕ , θ , q and r . Some angular rate damping about the body z-axis would help curb the divergence in ψ seen in the simulation for Drop 2 (Figure 4.1), but here again experimental data are needed.

4.4.5. Speeds and Aerodynamic Angles

There is little to be drawn from detailed comparison of the u , v body-axis speeds at P , both because of the bias uncertainty in the acceleration quantities from which they are derived and because the Euler angles do not match sufficiently closely in detail. It may be noted, however, that the peak u , v values at P compare satisfactorily between experiment and simulation (cf. Figures 4.2, 4.4, 4.7). The same may be said about the angle of attack at the canopy centre of pressure (cf. Figures 4.1, 4.3, 4.6).

In the light of these comparisons of speeds at opposite ends of the parachute, it is instructive to consider the mass distribution used in the simulations ($K_{11} = 0.3$, $K_{33} = 0.6$):

Drop No.	Configuration	D_p (m)	Σm_i (Kg)	A_{11} (Kg)	A_{33} (Kg)	μ_{11}	μ_{33}
2	BB24	5.82	40.78	37.9	75.87	0.93	1.86
29	SB12	2.92	9.4	4.79	9.58	0.51	1.02
10	BB12	2.84	36.28	4.41	8.82	0.12	0.24
25	SB06	1.41	11.13	0.54	1.08	0.05	0.10

Table 4.3 Estimated mass ratios for canopy/store configurations tested

Thus a mass ratio range of about 20 to 1 has been covered, with reasonable agreement in speeds demonstrated over a mass ratio of about 8 to 1.

4.5. Remarks

The computer model does not reproduce the apparently random oscillation amplitude modulation seen in the experiments. Two possible sources of this effect are atmospheric disturbances and self-excited unsteady flow over the canopy. For time reasons neither has been tested.

4.5.1. Atmospheric Effects

There is provision in the model for input of a wind as a function of space and time; this could be implemented in various ways, to simulate either a uniform isotropic turbulence or a turbulent atmospheric boundary layer profile, for example. The former is suggested as a start.

4.5.2. Self-Excited Unsteady Flow

Several original and fundamental aspects of the three-dimensional self-excited unsteady flow over the canopy were first conjectured by the author [11,90], and verified initially by a literature survey and subsequently by experiment [91].

While it has long been known that two-dimensional flow over bluff body shapes can give rise to significant unsteady and periodic forces, the

likelihood of analogous effects in the three-dimensional flow over parachute canopies has been overlooked, despite all the evidence of their existence. We find in virtually every report on wind-tunnel tests of parachute canopies that the model "vibrated violently" at or above certain wind-speeds [15,16, 31,63]. The possible cause is either ignored completely [31] or else vaguely mooted as support interference [63] or lack of support rigidity of some sort; the cure is invariably to reduce the wind-speed until the vibrations disappear [31], or to filter the force signals [63]. The author postulated the source as a three-dimensional vortex shedding type effect on the canopy, using the two-dimensional periodic flow over the circular cylinder as an analogue. The emergence, for example, from coherence in the 3D flow structure of a Strouhal number could also explain other parachute phenomena [11] such as breathing [92] and the marked change of canopy stability behaviour within a small range of canopy loading values [59].

A literature survey, e.g. [93-103] revealed much evidence of the existence of periodic wake phenomena and wake similarity laws for three dimensional bluff shapes such as circular discs [93-99], square plates [94], cones [99] and even spheres [96,97,100-103]. Indeed, in 1726 Isaac Newton [100] remarked on the fluttering motion and random trajectories of spheres (moulded from inflated hogs' bladders) which were dropped from the 272 ft. high cupola of St. Paul's Cathedral. The observed erratic motion of ascending meteorological balloons in clear air is a similar manifestation of the unsteady wake effect.

For purposes of determining the magnitudes and frequency content of unsteady forces it is essential that the measurement systems have a good dynamic response, so that the high-inertia weighbeam type of balance is unsuitable. The author, therefore, proposed carrying out a spectral analysis [90] of Doherr's strain gauge balance signals from measurements on flexible model canopies [63], but this proved impossible because the

signals had been lowpass filtered at source. Doherr subsequently repeated some of the experiments [91] and, analysing the results as suggested, tested the effect of the measured unsteady normal force on a constrained two-body model (4 DoF, rotary motion only). He concluded that the unsteady forces were of considerable significance in determining the detailed dynamic behaviour.

It is suggested therefore that the present computer model be tested for sensitivity to time-dependent aerodynamic forces and moments. If these prove to be important, the unsteady forces and moments ought to be measured for the circular flat canopy. In reducing the results, and in implementing them in the model, care must be taken with the time-scaling. Tests should also be made to detect any physical similarity laws, such as Reynolds number effects [11].

4.6. Conclusions

Good agreement can be obtained between the mean frequency and mean peak amplitude of oscillation for a wide range of parachute configurations using the current simulation model. Uncertainties and voids in the input parameters do not yet allow the detailed behaviour to be predicted with confidence. Input data which need to be improved or supplied are the steady-state and time-dependent aerodynamic forces and moments, the added mass components (or acceleration-dependent aerodynamic forces and moments) and the aerodynamic damping.

CONCLUSIONS

1. Under the usual ideal flow assumption, the derivations and/or implementations of the added mass tensor $[A]$ (Section 1.3), used to represent the fluid reactions to solid body accelerations, are, in all known previous treatments, either incorrect or inadequate to demonstrate the effects of the individual A_{ij} components on the dynamic stability of parachutes (Section 2.2).
2. Using the added mass concept, the equations of motion for the fluid components of some typical parachute canopy shapes - plane-symmetric, bilaterally-symmetric, axisymmetric - have been presented (Appendix B1).
3. The general equations of motion for the axisymmetric parachute contain *steady-state* ($\underline{\omega} = 0, \underline{V} = \text{const.} \neq 0$) couples when the added mass components $A_{11}(=A_{22}) \neq A_{33}$; the stiffness and the sign of the pitching moment coefficient around $\alpha = 0$ depend directly on the difference $(K_{33}-K_{11})$. These couple terms will also be contained in the static moment measurements carried out in a wind tunnel so care must be taken to avoid their duplication (Section 2.2.1.).
4. A parameter sensitivity analysis for dynamic stability of a fundamental three-dimensional 6 DoF, rigid-body computer model has been carried out around a baseline configuration representative of a circular-flat, personnel type parachute (Section 2.4). The results indicate that of the aerodynamic input parameters the most important are the added mass components and the angular rate damping derivative (Section 2.4.4). These quantities are also

subject to the greatest experimental uncertainty. The fact that the components of added mass along (A_{33}) and normal to (A_{11}, A_{22}) the axis of symmetry, are, in general, different, is significant as regards dynamic stability (Section 2.4.4.3).

5. A systematic method for validating conceptual models against experimental data has been suggested (Section 3.1.1). As part of a proposed programme of free-flight experiments, a technique has been developed which enables a parachute system with a flexible canopy and lines to behave as a single rigid body (Section 3.1.2).
6. Experimental apparatus, based on a strapdown inertial measurement system, has been developed to sense and store the kinematic behaviour of free-falling parachutes (Section 3.4). The kinematics of four parachutes of different scales, with canopy flight diameters from 1.4 m to 5.8 m, have been recorded in 21 drop tests under optimal atmospheric conditions (Section 3.7).
7. Spectral analysis of the inertial transducer signals reveals sharply defined frequencies of oscillation for the four individual configurations (Section 3.9), despite the considerable degree of random flight behaviour. The drop test results have been comprehensively analysed and synthesised to provide data suitable both for initiating simulation and for subsequent comparison of the three-dimensional oscillatory motion (Section 3.8).
8. Using the current simulation model, good agreement with experiment can be extracted for the mean frequency and mean amplitude of oscillation for a wide range of parachute configurations (Section 4.3).

Uncertainties and voids in the input parameters do not yet allow the detailed oscillatory motion to be matched.

9. One source of the observed, apparently random flight behaviour may be self-excited unsteadiness of the flow around the canopy (Section 4.5.2.). Measurements of unsteady aerodynamic forces on parachute canopies are needed, also improved estimates of fluid acceleration reactions and aerodynamic damping.

Appendix B1 : Derivation of the Equations of Motion

B1.1. The General Equations of Motion

Using Hamilton's principle, Kirchhoff [18] showed in detail how, for motion of a rigid body in an ideal fluid, the external forces and moments on the body due to the fluid inertia may be derived from the added mass tensor and the generalised velocities of the body co-ordinate origin. He also considers the effect of body shape and deduces how, with appropriate choice of body axes, the number of different added mass components can be greatly reduced when there are planes of geometric symmetry. Analogous to the solid body inertia tensor [B], principal axes and mass centre, there exist an added inertia tensor [A], principal axes and a centre of added mass. Ibrahim [36] has also given the added mass tensors for a large variety of body shapes.

Consider a dynamic system consisting of an arbitrary body moving in an arbitrary (real or ideal) fluid. Choose an orthogonal Cartesian body axis set $Oxyz$, and let P_i , H_i ($i = 1, 2, 3$) be the component linear momenta and the component angular momenta of the system referred to $Oxyz$. The origin inertial velocity and angular velocity components are V_i and ω_i , and the external forces and moments acting on the system are F_i and M_i . The general form of the Euler equations of motion for the complete system may then be written as

$$\underline{F} = \frac{\partial \underline{P}}{\partial t} + \underline{\omega} \times \underline{P} \quad (\text{B1.1})$$

$$\underline{M} = \frac{\partial \underline{H}}{\partial t} + \underline{\omega} \times \underline{H} + \underline{V} \times \underline{P} \quad (\text{B1.2})$$

Or, in more convenient tensor notation (Ibrahim [36], Eqns. (3.38))

$$F_i = \dot{P}_i + \epsilon_{ijk} \omega_j P_k \quad (\text{B1.3})$$

$$M_i = \dot{H}_i + \epsilon_{ijk} V_j P_k + \epsilon_{ijk} \omega_j H_k \quad (\text{B1.4})$$

If the fluid motion is irrotational and inviscid, P_i and H_i can be determined from the total kinetic energy T from the relations:

$$P_i = \frac{\partial T}{\partial V_i} \quad ; \quad H_i = \frac{\partial T}{\partial \omega_i} \quad (B1.5)$$

Substituting (B1.5) into (B1.4) and (B1.3) we obtain Kirchhoff's equations:

$$F_i = \frac{d}{dt} \frac{\partial T}{\partial V_i} + \epsilon_{ijk} \omega_j \frac{\partial T}{\partial V_k} \quad (B1.6)$$

$$M_i = \frac{d}{dt} \frac{\partial T}{\partial \omega_i} + \epsilon_{ijk} V_j \frac{\partial T}{\partial V_k} + \epsilon_{ijk} \omega_j \frac{\partial T}{\partial \omega_k} \quad (B1.7)$$

Again following Ibrahim, we separate T into its two components, T_B and T_F , and isolate the forces and moments due to the fluid. Expressing Eqn.(1.1) in the present notation

$$2T_F = A_{ij} V_i V_j + 2A_{i,j+3} V_i \omega_j + A_{i+3,j+3} \omega_i \omega_j \quad (B1.8)$$

by substituting from (B1.8) into (B1.7), we find that the equivalent external forces and moments exerted on the fluid are

$$F_{F_i} = A_{i\alpha} \dot{V}_\alpha + \epsilon_{ijk} \omega_j A_{k\alpha} V_\alpha \quad (B1.9)$$

$$M_{F_i} = A_{i+3,\alpha} \dot{V}_\alpha + \epsilon_{ijk} V_j A_{k\alpha} V_\alpha + \epsilon_{ijk} \omega_j A_{k+3,\alpha} V_\alpha \quad (B1.10)$$

where

$$A_{i\alpha} \dot{V}_\alpha = A_{ij} \dot{V}_j + A_{i,j+3} \dot{\omega}_j, \quad (\alpha = 1, \dots, 6; i, j=1, 2, 3)$$

$$A_{k\alpha} V_\alpha = A_{kn} V_n + A_{k,n+3} \omega_n, \quad (k, n = 1, 2, 3)$$

B1.3. Twofold-Symmetric Body

Where the body has two planes of symmetry, e.g. rectangular, square or cruciform canopies, by taking Oxyz to coincide with the planes and their lines of intersection (Figure B1.2) only 8 unique added mass components remain: A_{11} , A_{22} , A_{33} , A_{44} , A_{55} , A_{66} , A_{15} ($=A_{51}$) and A_{24} ($=A_{42}$). The resulting force and moment equations are

$$\underline{F}_F = \begin{bmatrix} A_{11} \dot{u} - A_{22} vr + A_{33} wq + A_{15} \dot{q} - A_{24} pr \\ A_{11} ur + A_{22} \dot{v} - A_{33} wp + A_{15} qr + A_{24} \dot{p} \\ -A_{11} uq + A_{22} vp + A_{33} \dot{w} - A_{15} q^2 + A_{24} p^2 \end{bmatrix} \quad (\text{B1.13})$$

$$\underline{M}_F = \begin{bmatrix} (A_{33} - A_{22}) vw + A_{44} \dot{p} + (A_{66} - A_{55}) qr - A_{15} ur + A_{24} (\dot{v} - wp) \\ (A_{11} - A_{33}) uw - (A_{66} - A_{44}) pr + A_{55} \dot{q} + A_{15} (\dot{u} + wq) + A_{24} vr \\ (A_{22} - A_{11}) uv + (A_{55} - A_{44}) pq + A_{66} \dot{r} + (A_{15} + A_{24}) (up - vq) \end{bmatrix} \quad (\text{B1.14})$$

B1.4. Axisymmetric Body

The majority of canopy types are of axisymmetric shape. In this case, with the body origin 0 located at some point on the axis of symmetry, only four different added mass components are obtained (Fig.1.2). These are A_{11} , A_{33} , A_{55} and A_{15} , since from symmetry $A_{22} = A_{11}$, $A_{44} = A_{55}$, $A_{51} = A_{15}$, $A_{42} = A_{24}$, $A_{24} = -A_{15}$; also, by shifting the body origin along Oz by a distance $a = -A_{15}/A_{11}$, the components $A_{15} = -A_{24} = 0$, and only three unique components remain (Ref. 18, p.251).

Using these, from Eqns. (B1.9) and (B1.10) we find:

$$\underline{F}_F = \begin{bmatrix} A_{11} (\dot{u} - vr) + A_{33} wq + A_{15} (\dot{q} + rp) \\ A_{11} (\dot{v} + ur) - A_{33} wp - A_{15} (\dot{p} - qr) \\ A_{33} \dot{w} - A_{11} (uq - vp) - A_{15} (p^2 + q^2) \end{bmatrix} \quad (\text{B1.15})$$

$$\underline{M}_F = \begin{pmatrix} A_{55} \dot{p} - A_{15} (\dot{v} - wp + ur) - A_{55} qr + (A_{33} - A_{11}) vw \\ A_{55} \dot{q} + A_{15} (\dot{u} + wq - vr) + A_{55} pr - (A_{33} - A_{11}) uw \\ 0 \end{pmatrix} \quad (\text{B1.16})$$

and if the body origin is centralised on [A], at A, say:

$$\underline{F}_F = \begin{pmatrix} A_{11} (\dot{u} - vr) + A_{33} wq \\ A_{11} (\dot{v} + ur) - A_{33} wp \\ A_{33} \dot{w} - A_{11} (uq - vp) \end{pmatrix} \quad (\text{B1.17})$$

$$\underline{M}_F = \begin{pmatrix} A_{55} (\dot{p} - qr) + (A_{33} - A_{11}) vw \\ A_{55} (\dot{q} + pr) - (A_{33} - A_{11}) uw \\ 0 \end{pmatrix} \quad (\text{B1.18})$$

We now treat the remainder of the particular case of a rigid parachute of axisymmetric shape. Body axes are chosen so that Ox is on the axis of symmetry and Ox, Oy are parallel to the two other principal body axes. The body mass m comprises the canopy, rigging lines and store masses (m_i) with mass centres located at C, L and S (z_i), respectively. For the solid body components, e.g. the store, we have

$$\underline{P}_{s_i} = m_{s_i} \underline{v}_{s_i} = \begin{pmatrix} m_s (u + qz_s) \\ m_s (v - pz_s) \\ m_s w \end{pmatrix}; \text{ thus } \underline{P}_B = \begin{pmatrix} P_1 \\ P_2 \\ P_3 \end{pmatrix}_B = \begin{pmatrix} mu + K_1 q \\ mv - K_1 p \\ mw \end{pmatrix}$$

and from Eqn. (B1.3)

$$\underline{F}_B = \begin{pmatrix} \dot{P}_1 + P_3 q - P_2 r \\ \dot{P}_2 - P_3 p + P_1 r \\ \dot{P}_3 - P_2 p - P_1 q \end{pmatrix} = \begin{pmatrix} m (\dot{u} - vr + wq) + K_1 (\dot{q} + rp) \\ m (\dot{v} - wp + ur) - K_1 (\dot{p} - qr) \\ m (\dot{w} - uq + vp) - K_1 (p^2 + q^2) \end{pmatrix} \quad (\text{B1.19})$$

Similarly, for the store angular momentum,

$$H_{s_i} = \epsilon_{ijk} r_{s_j} m_{s_k} v_{s_k} = \begin{pmatrix} m_s z_s^2 p - m_s z_s v + I_{xx_s} p \\ m_s z_s^2 q + m_s z_s u + I_{yy_s} q \\ I_{zz_s} r \end{pmatrix}$$

Thus

$$\underline{H}_B = \begin{pmatrix} I_{xx} p - K_1 v \\ I_{yy} q + K_1 u \\ I_{zz} r \end{pmatrix}, \text{ where } I_{xx} = \sum_{i=1}^3 (I_{xx_i} + m_i z_i^2), \text{ etc.} \quad (\text{B1.20})$$

Applying Eqn. (B1.4) to Eqn. (B1.20) we find

$$\underline{M}_B = \begin{pmatrix} I_{xx} \dot{p} - K_1 (\dot{v} - wp + ur) - (I_{yy} - I_{zz}) qr \\ I_{yy} \dot{q} + K_1 (\dot{u} + wq - vr) + (I_{xx} - I_{zz}) pr \\ I_{zz} \dot{r} + (I_{yy} - I_{xx}) pq \end{pmatrix} \quad (\text{B1.21})$$

(note that F_{B_i} could also have been found from Eqn. (B1.9) by substituting B_{ij} 's for A_{ij} 's ; likewise M_{B_i} from Eqn. (B1.10) : the calculations involved are the same.)

Combining Eqns. (B1.19) and (B1.15), (B1.21) and (B1.16), the full equations of motion for the axisymmetric system are

$$\underline{F} = \begin{pmatrix} (m + A_{11}) (\dot{u} - vr) + (m + A_{33}) wq + (K_1 + A_{15}) (\dot{q} + rp) \\ (m + A_{11}) (\dot{v} + ur) - (m + A_{33}) wp - (K_1 + A_{15}) (\dot{p} - qr) \\ (m + A_{33}) \dot{w} - (m + A_{11}) (uq - vp) - (K_1 + A_{15}) (p^2 + q^2) \end{pmatrix} \quad (\text{B1.22})$$

$$\underline{M} = \begin{pmatrix} (I_{xx} + A_{55}) \dot{p} - (K_1 + A_{15}) (\dot{v} - wp + ur) - (I_{yy} + A_{55} - I_{zz}) qr + (A_{33} - A_{11}) vw \\ (I_{yy} + A_{55}) \dot{q} + (K_1 + A_{15}) (\dot{u} + wq - vr) + (I_{xx} + A_{55} - I_{zz}) pr - (A_{33} - A_{11}) uw \\ I_{xx} \dot{r} + (I_{yy} - I_{xx}) pq \end{pmatrix} \quad (\text{B1.23})$$

Tory and Ayres assumed the added mass to be made up of an "included" air mass in the shape of an ellipsoid along with an "apparent mass" and

"apparent moment of inertia" external to the ellipsoid. The mass of the ellipsoid was m_E , with moments of inertia $I_{xx_E} = I_{yy_E}$, I_{zz_E} ; the apparent masses were $K_x m_E$ along x and y , $K_z m_E$ along z ; the apparent moments of inertia were $K' I_{xx_E}$ about x and y . For an ellipsoid in an ideal fluid $A_{15} = A_{24} = 0$.

Thus, they had in effect:

$$\begin{aligned} A_{11} &= (1 + K_x) m_E = A_{22} \\ A_{33} &= (1 + K_z) m_E \\ A_{55} &= (1 + K') I_{xx_E} = A_{44} \\ A_{66} &= I_{zz_E} \end{aligned}$$

from which they derived:

$$\underline{F}_F = \begin{pmatrix} A_{11} (\dot{u} - vr + wq) \\ A_{11} (\dot{v} - wp + ur) \\ A_{33} (\dot{w} - uq + vp) \end{pmatrix} \quad (\text{B1.24})$$

$$\underline{M}_F = \begin{pmatrix} A_{55} (\dot{p} - qr) + A_{66} qr \\ A_{55} (\dot{q} + pr) - A_{66} pr \\ A_{66} \dot{r} \end{pmatrix} \quad (\text{B1.25})$$

Comparing Eqns. (B1.17) and (B1.24) it is clear that the Tory-Ayres force equations do not contain A_{33} in F_1 or F_2 , nor A_{11} in F_3 . Note also the *steady-state* couples $(A_{33} - A_{11})vw$ and $-(A_{33} - A_{11})uw$ in Eqns. (B1.18): in the full Tory-Ayres equations for \underline{M} , as in other treatments, these two terms are concealed (though unwittingly) in the LHS expression, i.e. along with the "other" external moments. They must not be duplicated, as occurs in the implementations of Lester and Byushgens and Shilov.

Appendix C1 : Development of the Rigging Line Arrangement to produce a Rigid Body System

The usual practice is for the rigging lines to be divided into sets, each of which ends in a confluence point which in turn is fixed to the store with one or more straps (risers) (Figure C1.1). Personnel parachutes usually have two pairs of risers, so the man is free to swing with respect to the canopy in the plane perpendicular to the line containing the two confluence points. Any tendency for relative rotation in the plane containing the confluence points causes the lines and risers to slacken on one side, and the resulting gravitational moment of the store about the other side acts in the sense of restoring the line tension. Thus the tensile structure can be capable of resisting flexure if appropriately connected. This suggested connecting the rigging lines in a ring around the periphery of the body to provide a uniform "stiffness" in all directions (Figure C1.2). The wider the ring the better the stiffness, but there is evidence to suggest that the aerodynamic characteristics of the canopy are significantly influenced by the shape of the leading edge [64], which in turn is affected by the confluence angle of the rigging lines.

To prove the feasibility of this rigging method some proving trials were carried out in one of the Cardington airship hangars. A simple store was quickly prepared: it consisted of a strong aluminium canister which could be ballasted with lead shot or sand; the 24 rigging lines were tied to a circular ring which was bolted to the canister. To reduce the canopy opening time it was held with clips in a spread position to a large tubular ring (Figure C1.3). The store was supported by a tie which ran to a remotely actuated bomb release mechanism, and the entire assembly was mounted on a beam which could be raised to the roof by means of a balloon winch. Provision was made for dropping both quarter and half-scale canopies; the half scale canopy is seen in Figure C1.3, and the rig for the smaller canopy is also visible.

To prevent landing damage to the instrumented body a large net (30 m x 30 m) had been constructed which was suspended 5 m from the concrete floor (Figure C1.4). The net was connected to a block and tackle system in the roof, and could be raised and lowered quickly by a second winch. Since the mesh size was about the same as the store diameter, the net was covered in old parachute fabric to stop the store from falling through. The net worked well in practice, but for the lower descent speeds the parachutes tended to glide a considerable distance laterally and land outside it.

Ballast was added to give nominal descent speeds of 5 and 10 ms^{-1} , and several trials were performed for each configuration. The drops were recorded on high speed film. Inspection of the films showed that, following the initial transients, the store remained aligned with the canopy. With the half scale canopy falling at 5 ms^{-1} there was evidence of breathing and of luffing of the lower edges of the canopy when at peak swing. Continuous breathing also occurred on some drops with the same canopy, whereas the quarter-scale canopy exhibited only sporadic breathing and random glide excursions. Though the smaller canopy also oscillated vigorously at the higher descent speeds, even so it was not possible to discern any compound pendulum type motion.

Although the rigging method appeared on film to be completely successful in overcoming the relative pitch/yaw motion, fully instrumented drops with the full-scale canopy later revealed the same configuration to be prone to torsional oscillations about the axis of symmetry. With the rigging lines forming the generators of a narrow-angled conical frustum, torsional stiffness is vanishingly small for small torsional deflections. The solution was to arrange a pair of opposed symmetric "pre-torques" to the store by means of two sets of rigging lines (Figure C1.5). The first set was connected as before, the store then rotated by 90° relative to the canopy, and the second set next tied in to give a relative twist of 90° in the opposite direction. This arrangement was flight tested, and, proving to be satisfactory, was therefore adopted as standard for the programme. Although this solution was discovered independently, it was later found that a similar rigging technique had previously been used to stabilize heavy weapons.

Appendix C2 : Kinematic Analysis of the IMU Signals

C2.1. Co-ordinate Systems

The same inertial reference frame is used in the analysis of the experimental data as in the computer model, but the body-fixed frame differs in that it is located in the store.

A Cartesian body-fixed axis system $Oxyz$ is chosen so that Oz points downwards along the axis of symmetry (Figure C2.1), and Oxy are aligned with the sensitive axes of the sensors. An inertial co-ordinate system $WXYZ$ is specified with W coincident with O at time $t = 0$, and WZ pointing downwards along the local vertical. For short flight-time (< 50 s) and low velocity tests ($< 15 \text{ ms}^{-1}$) the assumption that Earth-fixed and space-fixed reference frames are the same will give rise to negligible errors [65,74].

C2.2. Angular Rate Sensor Signals

Body-Inertial System Transformations

An Euler angle sequence identical to that employed in the simulation model is specified.

Thus the transformation of a vector from body to inertial co-ordinates is given by Eqn.(2.22) (the superscript on vector quantities is used here to denote the co-ordinate frame (if any) to which the vector is referred).

Similarly, the Euler angle rates are found from the body axis rates by the transformation of Eqn.(2.21). The variables p, q, r are measured directly by the body-fixed angular rate sensors, which in the present case are single DoF rate gyroscopes. To allow integration of Eqns.(2.21), the only further information required are the initial values of (ϕ, θ, ψ) ; these

are obtained from the movie film records. . Once the Euler angles are known, the attitude angle (Eqn.(2.28)) and phase angles γ, δ (Eqns.(2.29), (2.33)) can be calculated, likewise the resultant angular velocity vector $\underline{\omega}_{xy}$ (Eqn.(2.31)).

C2.3. Accelerometer Signals

An accelerometer, which consists essentially of a seismic mass on a spring, measures the specific force at a point and cannot distinguish between kinematic accelerations and gravity. To reduce the outputs of the triad of accelerometers to give the true kinematic acceleration vector at a point in the store, O say, we must therefore make corrections for the individual displacements of the accelerometers from the point in question, and also remove the gravity field components.

Consider a point P in the parachute, position vector \underline{r}_{pO} with respect to O , and \underline{r}_{pI} wrt I (Figure C2.1). Then, from textbook [75] mechanics

$$\underline{r}_{pI} = \underline{r}_{pO} + \underline{r}_{OI} \quad (C2.1)$$

$$\underline{v}_{pI} = \underline{v}_{OI} + \dot{\underline{r}}_{pO} + \underline{\omega} \times \underline{r}_{pO} \quad (C2.2)$$

$$\underline{a}_{pI} = \underline{a}_{OI} + \ddot{\underline{r}}_{pO} + \dot{\underline{\omega}} \times \underline{r}_{pO} + 2\underline{\omega} \times \dot{\underline{r}}_{pO} + \underline{\omega} \times (\underline{\omega} \times \underline{r}_{pO}) \quad (C2.3)$$

Now, if P corresponds to the location of an accelerometer centre in the store, $\dot{\underline{r}}_{pO} = 0$, and the accelerometer will sense a quantity \underline{a}_{MI} , where

$$\underline{a}_{MI} = \underline{a}_{OI} + \dot{\underline{\omega}} \times \underline{r}_{pO} + \underline{\omega} \times (\underline{\omega} \times \underline{r}_{pO}) + \underline{g} \quad (C2.4)$$

and \underline{g} is the gravity vector, here assumed constant. Since

$$\underline{a}_{OI} = \dot{\underline{v}}_{OI} + \underline{\omega} \times \underline{v}_{OI},$$

we find

$$\dot{\underline{V}}_{OI} = \underline{a}_{MI} - \dot{\underline{\omega}} \times \underline{r}_{pO} - \underline{\omega} \times (\underline{\omega} \times \underline{r}_{pO}) - \underline{g} - \underline{\omega} \times \underline{V}_{OI} \quad (C2.5)$$

We assume the accelerometers are located at $\Delta r_{ax}, \Delta r_{ay}, \Delta r_{az}$ wrt 0. The point 0 is taken to lie on the axis of symmetry, and the Oxy plane through 0 contains the centre of the z-direction accelerometer. Hence 0 will be referred to as the virtual origin of the IMU.

To expand Eqn.(C2.5) in the body-axis system we first need

$$\underline{g}^o = [L_{OI}] \begin{pmatrix} 0 \\ 0 \\ -g \end{pmatrix} = \begin{pmatrix} g \sin\theta \\ -g \sin\phi \cos\theta \\ -g \cos\phi \cos\theta \end{pmatrix} \quad (C2.6)$$

Thus, the body-axis components of the kinematic acceleration of point 0 are

$$\left. \begin{aligned} \dot{u}_{OI} &= a_{MIx} + \Delta x_{ax} (q^2 + r^2) - \Delta y_{ax} (pq - \dot{r}) - \Delta z_{ax} (rp + \dot{q}) - g \sin\theta - (qw_{OI} - rv_{OI}) \\ \dot{v}_{OI} &= a_{MIy} + \Delta y_{ay} (r^2 + p^2) - \Delta z_{ay} (qr - \dot{p}) - \Delta x_{ay} (pq + \dot{r}) + g \sin\phi \cos\theta + (pw_{OI} - ru_{OI}) \\ \dot{w}_{OI} &= a_{MIz} + \Delta z_{az} (p^2 + q^2) - \Delta x_{az} (rp - \dot{q}) - \Delta y_{az} (qr + \dot{p}) + g \cos\phi \cos\theta - (pv_{OI} - qu_{OI}) \end{aligned} \right\} \quad (C2.7)$$

Integration of Eqns.(C2.7), to find the body-axis ^{velocity} components of point 0 wrt the inertial frame, requires that the initial value $\underline{V}_{OI} = (u, v, w)_{OI}$ be known. This was obtained by assuming that the store was swinging as a simple pendulum about a stationary suspension point (Figure C2.2). Thus

$$\underline{V}_{pO} = \underline{\omega} \times \underline{r} = (p, q, r) \times \begin{pmatrix} 0 \\ 0 \\ -z_o \end{pmatrix} \quad (C2.8)$$

Also needed are the angular accelerations $(\dot{p}, \dot{q}, \dot{r})$, which in the present case were obtained by differentiating the rate sensor signals. Note that the angular acceleration terms in Eqns.(C2.7) disappear if the accelerometers lie along the co-ordinate axes; equally, the complete accelerometer size terms can be neglected if the displacements of the

accelerometers from 0 are small. For the current system it was found that the differences in final (after 40 s) velocity and displacement components caused by omission of all of these terms were less than 0.4%. In all results presented here, however, the accelerometer size terms and angular acceleration terms have been retained.

Once \underline{V}_{OI} is known the velocity of any other point in the system can be found using the rigid-body assumption. Thus, for any point P fixed in the parachute wrt O ,

$$\underline{V}_{PI} = \underline{V}_{OI} + \underline{\omega} \times \underline{r}_{PO} \quad (C2.9)$$

The aerodynamic angles α_{cp} , β_{cp} at the canopy centre of pressure then follow as in Eqns.(2.10), (2.11), likewise the resultant angle of attack at the store nose, as in Eqns.(2.7), (2.8).

Integration of Eqn.(C2.9) gives the position vector of P wrt the initial position of Oxyz , i.e. the body-axis components. Transformation of these components into inertial components would then give the spatial trajectory of P , but this method is unsatisfactory as regards error accumulation: the magnitudes of the displacement components increase with time, thus small errors in the Euler angles will give rise to increasingly larger errors in the space trajectory components. In practice, it is preferable to first transform, viz.

$$\underline{V}_{PI}^I = [L_{IO}] \underline{V}_{PI}^O \quad (C2.10)$$

and then to integrate \underline{V}_{PI}^I to obtain \underline{r}_{PI}^I .

C2.4 Airspeed Sensor

The airspeed sensor measured the relative airspeed along the axis of symmetry at the store nose (w_N) , and was used as a check on the value of w_{OI} as obtained from integration of Eqns.(C2.7). It was found that the integration of \dot{w}_{OI} underestimated w_{OI} for the first few seconds after

release, due to the combination of a rapidly changing signal (free-fall/opening shock) and a low (10 Hz) sampling rate, therefore w_N was used to replace w_{OI} in Eqns.(C2.7) and elsewhere during this interval.

Appendix C3 : The MPU Data Acquisition Programme

Because of the peculiar way memory was allocated in the Fairchild F8 MPU evaluation system, specific regions of memory were reserved for "housekeeping" data, and provision had to be made for avoiding these locations during programming and data logging. A block diagram of the data acquisition programme is shown in Figures C3.1 - C3.4. After initiation of the programme it enters into an idle looping mode, from which it may be interrupted at any instant by an externally supplied signal (see below). The interrupt is serviced within 10 μ s, and data sampling begins 55 μ s later. Analogue to digital conversion takes about 35 μ s, and the 12-bit reading is fed into MPU I/O ports 0 and 1. The memory destination address for the readings are held in the Data Counter (DCO), and a buffer counter keeps a check that the destination address is a valid region. Transfer of the 12-bit readings from the I/O ports to memory is accomplished by a choice of two subprogrammes (Figures C3.3, C3.4), depending on whether the reading is to be the first or second to be packed into two contiguous memory bytes. Channel selection is kept track of by a multiplexer address counter; the eight channels are read sequentially as quickly as possible (616 μ s), and this is followed by a pause before the procedure is repeated. The sampling rate is determined by the duration of this pause, and may be adjusted simply by changing the contents of four memory locations; similarly, the choice of filtered or unfiltered data is determined by the numbers in three memory locations. Although these changes could easily be made in the field, to preclude any possibility of error under such conditions a copy of each programme configuration was held on tape, to be input as required.

Actuation of the external interrupt, used to initiate data sampling, was by telecommand. One of the spare timer outputs on the balloon bomb-bar was adjusted to give a "high" output upon receipt of the "release"

signal from a VHF transmitter on the ground. The same timer output triggered a high-intensity flash bulb which was used to synchronize movie film observations with the data records. To connect the floating level (24 V supply) output from the timer to the TTL-compatible MPU input, a current-switched optical coupler/isolater buffer circuit was made up. Connection to the interrupt was made via the external power supplies' umbilical lead; this plugged into a DIN socket on top of the SB, and disconnection was arranged to occur under gravity after release of the store. It was found that the interrupt might be tripped upon connection of the external lead, so an arm/disarm switch was incorporated. A ground test switch was also fitted to the interrupt to facilitate preliminary check runs.

Appendix C4 : Calibration

C4.1 Alignment

C4.1.1. Test body and IMU block alignment

The single degree of freedom rate gyros and accelerometers were mounted on a single machined aluminium block. Mounting hole alignment and surface orthogonality tolerances were within 20 minutes of arc, and the sensitive axes of the individual gyros were easily set to within 20 seconds of arc by using a dial gauge on the mounting flanges. The gyro block was fixed to a 12 g L72 aluminium plate which in turn was bolted to the test body. Alignment of the mounting plate with respect to the datum base of the SB was measured using a dial gauge in conjunction with a surface table; the plate was found to be very slightly twisted about a diagonal axis, with angular deflections of $\Delta\phi = 0.122$ deg. and $\Delta\theta = + 0.072$ deg. about the body x and y axes, respectively. Since the gyro block is significantly stiffer than the mounting plate, it is to be expected that it will not have been deflected to the same extent under pull-down by the mounting bolts, so these angles may be taken as upper bounds on misalignment of the IMU with respect to the SB.

C4.1.2. Alignment of the Instrumented Body within the Large Body

The parallelism of the SB within the BB was determined by laying the BB on a horizontal table (without the SB inside), and measuring the angular deviation of the guide tube using a sensitive machine level. The measurements were taken at different points around the circumference, and were accurate to within ± 0.05 deg; for a number of different readings the repeatable mean angular deviation was 0.30 ± 0.15 deg.

C4.2 Rate Gyros

The rate gyros were on loan from EP Department at RAE Farnborough, and, because of the shared usage, needed to be calibrated on a number of occasions during the project. It was not possible to fit the complete drop test body on to any of the variety of different rate tables employed at RAE, so dismantling of the transducer block was necessary each time a calibration was undertaken. The most convenient facility was found to be that kindly provided by the Radio and Navigation Department, RAE, where an automated system for determining the rate transfer characteristics had been assembled. This was the system used for both pre-test and post-test calibration of the "production" drop tests, and hence will be the only system referred to here.

In principle, because of the severe shock environment which the sensors underwent during the trials, it would have been advisable to re-calibrate before each trial. This was not possible because of funding and time constraints: it took about a day to disassemble, reassemble and test the system; calibration further involved travelling from Leicester to Farnborough, taking a full day, and also it was usually necessary to wait for a free space on one of the calibration rigs.

Details of the automated rate sensor test facility and techniques are given in [76] and [77]. The gyro is mounted on a rate table which can be rotated in either direction at accurately defined angular rates as pre-determined by a programme punched on paper tape. An environmental chamber surrounds the table, but for the current application tests were run under (measured) ambient conditions. Rates are applied in the form of a hysteresis loop in set increments, beginning at zero. The input sequence follows the pattern of one increment negative increasing up to maximum positive, plus one beyond, reducing to maximum negative, one increment beyond, and back to zero. In estimating the linear least-square fit to this data, the first

negative increment is ignored, also those values in excess of the maximum positive and negative rates. Positive input rate follows the right hand screw convention.

The gyros used were Smiths 400 Series sub-miniature type, with integral thermistor temperature compensation. Electrical supplies were 26 V 400 Hz 3 phase, 3.9 W being required for each motor and inductive pickoff. The additional demodulator unit gave a bipolar DC signal which was a linear function of the input rate. Experience showed that the full scale output from a particular gyro-demodulator combination could vary between 2 V and 7.5 V, even when using the same power supply, zero attenuation, and measured under similar conditions across a high impedance (10 M Ω) load. This is a generous manufacturing tolerance by any standard, and underlined the need to calibrate as a unit as much of the sensor system as possible.

The manufacturer's tolerance for orthogonality of the sensitive axis of the gyro with respect to the mounting face is a nominal ± 15 minutes of arc, with a typical value of ± 3 minutes of arc. Alignment of the gyro on the calibration rate table was achieved by adjusting its attitude to give a null output, then rotating it on the kinematic mounts by 90 deg: this gave an angular tolerance of better than 0.050 deg.

The sensor output was transferred from the rate table via slip-rings and fed into a voltage to current amplifier, and ran from there into a digital integrating milliammeter; an integrating time of 6 s was used for all tests. During the tests the gyro rotor power, ambient temperature, rate table tachogenerator output and time were also measured, and all of the outputs were digitized, serialised and punched on paper tape. The tapes were analysed [76] on an off-line minicomputer and the results were presented in printed and graphical form. The automated form of the test facility allowed the entire process to be repeated with minimal human intervention. Once set up, a measurement run took about 10 minutes to complete.

Pre-trial and post-trial calibration results for the three rate gyros are presented in Tables C4.1-6, Figures C4.1-6. Two or more consecutive calibration runs were carried out for each sensor on each occasion; repeatability between runs was good, typically $\pm 0.07\%$ in the scale factor. A systematic difference of about 2.5% in scale factor, between tests carried out pre- and post-trials was observed, however, although the error plots matched closely. This discrepancy was suspected, and subsequently confirmed, as having been due to loading of the gyro outputs by the voltage to current amplifier during the earlier session. The post-trial calibration curves were therefore taken as representative for analysis purposes, and selection from the various runs was made by choosing the smoothest error curves.

Equivalent full scale outputs for the gyros work out at 430, 350, and 700 deg s^{-1} for the x, y and z axes, respectively, with corresponding quantization levels of 0.21, 0.17 and 0.34 deg s^{-1} .

C4.3 Accelerometers

The linear accelerometers used were the miniature Smiths 503 ADA sensors. These consist of a spring-restrained seismic mass with inductive displacement pickoffs, and supply a linear DC signal which is proportional to the excitation voltage. The accelerometers had been comprehensively calibrated [78] at the factory with an excitation of 6.00 V, and had not been used previous to the present trials. For the trials a nominal regulated excitation of 5 V (5.044 V actual) was being supplied, so to derive pre-trial calibration curves the factory values were scaled accordingly. The plots of the output deviations of the accelerometers from their reference (ideal) values are shown in Figures C4.7 to C4.9, and the derived calibration data are tabulated in Table C4.7.

Following the trials session Smiths Aerospace Industries Ltd. kindly offered to recalibrate the accelerometers, using both 5 V and 6 V excitation values. The output deviation curves (6 V input) are shown in Figures C4.10 to C4.12, and the derived calibration data for the actual excitation are given in Table C4.8. Comparing Figures C4.7 and C4.10, it can be seen that within the ± 1 g range

of interest there has been a negligible change in calibration in the x-direction accelerometer. The y- and z-direction accelerometers show zero shifts of 18 mV and 12 mV, respectively, with corresponding acceleration shifts of 0.212 m s^{-2} and 0.283 m s^{-2} . Digitization levels for the accelerometers are 0.014 m/s^2 for the x- and y-directions, and 0.029 m s^{-2} for the z-direction.

C4.4 Pressure Transducers

The pressure transducer used for velocity measurement was a differential type Setra Model 239E with an unidirectional full scale range of 0 to 0.02 psi. A similar transducer with an FSR of 0.2 psi was employed in the calibration of the large test body. Both transducers were calibrated against a standard vernier micromanometer with a resolution of $\pm 0.02 \text{ mm}$ water-gauge; and the DC output voltage readings were read to within $\pm 0.005 \text{ V}$.

One of the transducers was found to have a scale factor very different from that supplied by the manufacturer, so a number of calibrations was made to check for repeatability of results. It was proposed to run the flight transducer straight off a pack of three small NiCd batteries, without intermediate regulation, therefore additional calibrations were carried out over the expected range of input excitation to verify operation of the manufacturer's claimed internal regulation circuit.

Results of the different calibration tests are plotted in Figures C4.13 to C4.15. It was found that the zero-shift on warm-up could be as much as 50 mV, so a five to ten minute warm-up time was always allowed, during both calibration and drop trials; before and after readings of the zero value were also taken to check for any interim drift. Figure C4.15 shows the excellent insensitivity to excitation voltage, but it should be noted that all of these runs were carried out over a short period; the evidence of Figure C4.13 suggests that the long-term calibration of this

transducer is time-dependent and ought to be checked at regular intervals.

C4.5 Pitot-Static Sensors

Note that both Pitot-static sensors were calibrated in the absence of a parachute. In practice, the finite dimensions of the canopy distorts the flowfield and subjects the airspeed measurement to an error which depends on the location of the sensor with respect to the canopy. This position error correction is considered in the main text (Section 3.8.4).

C4.5.1. Small Test Body

Initial development and calibration runs of the special Pitot-static type sensor for the instrumented body (SB) were carried out in the large wind-tunnel at the University of Leicester (Figure C4.16). The tunnel flow was non-uniform and unsteady however, due to unsatisfactory inlet conditions, and the final calibration trials took place in the 7 x 5 ft. wind tunnel at the University of Bristol (Figure C4.17).

A full scale model of the SB was employed for the calibration. This was supported by a stiff sting made up of 50 mm gun barrel tubing, and the complete assembly was held to the floor of the working section by two 50 lb weights. Variation in angle of attack was achieved by pivoting the assembly about the nose of the SB; in this way the tip of the Pitot-static sensor remained at the same point throughout the calibration, i.e. in the centre of the working section. The yaw-angle could be selected by clamping the SB at different roll settings on the horizontal sting. Tunnel speed was set with a Betz manometer, and the Pitot-static output was measured by using the actual pressure transducer assigned for flight trials in conjunction with a DVM.

It was found that the DVM output fluctuated continuously during the calibration, but this appeared to be caused by electrical noise rather than

flow unsteadiness. By using the integration facility on the DVM all of the readings were repeatable to ± 50 mV. Since the tunnel had to be stopped before the model incidence could be changed, the adopted test procedure was to set the incidence and then take readings at different speeds. An incidence range of $\pm 45^\circ$ was covered.

The results are plotted in Figure C4.18. A constant area blockage correction has been applied in calculating the derived speed ratio. This correction was based on the projected model/support area at zero incidence, which gives an area blockage ratio of 1.6%; at 45° incidence the area blockage ratio is about 4.8%, but the direct application of such a factor would be difficult to justify. Strictly, what is needed is a solid blockage factor which corrects for the perturbation to the local flow about the nose of the SB: the effect of a boundary constraint will be to displace streamlines far away from the model more than those on the centre line. In the absence of this information, the calibration is assumed to be as in Figure C4.18. At the lowest tunnel speed used (3.0 ms^{-1}) the plot for incidences greater than 15° deviates from those obtained for higher speeds. There is little apparent Reynolds number dependence other than in this region of the calibration. Values for yaw angles of $\pm 45^\circ$ coincide with the curves shown, confirming operation of the true-mean reading static system.

For the drop trials the nose of the tunnel model was transferred to the instrumented body. The interference effect of the stowed impact attenuator legs was not measured.

C4.5.2. Large Test Body

It was not possible to find a date to calibrate the large test body (BB) until after the drop trials were completed, with the result that the BB was tunnel tested in a somewhat battered state. Care had been taken during the drop tests that any dents or cracks in the nose of

the BB were repaired and made good with Plasticene, but small roughnesses were simply scraped smooth. The cylindrical and base sections of the BB also suffered from dents, and these were knocked out where accessible. For the tunnel measurements the nose of the BB was tested in both rough and smooth surface states and the remainder of the body was left as it was.

Calibration of the BB was carried out in the 18 x 8 ft. return section of the 7 x 5 ft. wind tunnel at the University of Bristol. There is a degree of non-uniformity in the mean velocity distribution in this section [79], but as can be seen from Figure C4.19 the BB and the monitoring Pitot-static probe were set up in the centre of a constant velocity contour. The BB was supported on a frame of steel tubing; it was arranged to pivot about a point directly under the nose, and provision was made for setting the incidence from outside the working section. A photograph of the BB in the wind tunnel is shown in Figure C4.20.

Tunnel speed and Pitot-static pressure difference were measured in the same way as the SB calibration, but a maximum tunnel speed of only 9.5 ms^{-1} was available. An incidence range of $\pm 50^\circ$ was covered in most runs, with some spot measurements at higher incidences. Yaw angle could be adjusted in a similar manner to that used in the SB tests, and the body was aligned with the tunnel floor by using a bubble level.

The results are plotted in Figure C4.21. It can be seen that the useful working range of this sensor is for an incidence cone of half-angle of about 35° . There is evidence of a Reynolds Number dependence around the lowest speeds tests (2.7 ms^{-1}), and also of some asymmetry. There is also a difference in plots for the rough and smooth noses (plots 4 and 5) but these had been run at slightly different speeds. Comparing plots 2 and 10, for example, suggests that this asymmetry may be due to a model deviation rather than to a flow or rigging asymmetry; the most likely source of the discrepancy is a partly blocked static tapping or pinched connection tube, which would have been difficult to detect without

disassembling the complete system. It is not known where or when the asymmetry arose, since all pre-flight checks had included tests for blockage and leakage of the system.

Some further development work would have been desirable, both to ascertain the source of asymmetry and to remove the Reynolds Number dependence, but because of other demands this was not feasible. The fall-off in output with incidence is due to flow separation on the leeward side of the nose [80], and the location of the separation line has been shown to move downstream at a Reynolds Number of about 1.7×10^5 . Conventional aerodynamic "fixes" should cure this problem, but for the purposes of the drop tests the integral Pitot-static sensors fulfil their designed function.

C4.6 Data Acquisition System

The specifications of the Burr-Brown SDM 853 data acquisition system are detailed in the manufacturer's user manual [81]. The overall root-sum-square accuracy, at 30 kHz throughout, gain =1 and at 25°C is quoted as $\pm 0.025\%$ FSR; system linearity and quantizing error, under the same conditions, are $\pm 1/2$ LSB (least significant bit). With an FSR of ± 2.5000 V the LSB value for the present application was 1.22 mV. Static calibration of the system was straightforward; a calibration voltage was applied to each multiplexer input in turn, and the corresponding instrumentation amplifier and ADC input values were measured, and the ADC digital output was recorded. For channels 0 to 7 calibration voltages were applied to the active filter inputs; channels 6 and 14 used a potential divider to attenuate the 5V FSO of the pressure transducer, and here again the complete channels were dealt with. From these measurements the individual and overall zero offsets and scale factors for the 16 channels were determined, and these are presented in Table C4.9. The pre- and post-trial values were the same in each case.

Noise levels within the system were very low. The complete data acquisition system was contained in an EMI-shielded package, and all the supplies were decoupled on the board to minimize ripple. With the test transducers on-line, input signal noise levels to the ADC were 3 mV peak to peak for the gyros and accelerometers, and 9 mV peak to peak for the pressure transducer; the difference in noise level between filtered and unfiltered channels was negligible.

Dynamic checks of the data acquisition system were carried out by applying constant \pm FSR voltages to adjacent channels and then sequentially scanning the channels to determine the minimum overall delay time required for the MPU programme. The specified settling time for the multiplexer/amplifier (unity gain)/sample-hold (aperture = 30 ns) chain is 9 μ s, and the ADC conversion time is quoted as 24 μ s, all for 12-bit resolution at 30 kHz throughput; the system was found to be well within specification. To make sure of full resolution readings, the actual settling time allowed in the programme was 53 μ s.

Appendix C5: Estimation of the Bias Corrections

C5.1 Sources of the Biases

Hardware sources of bias could be supply current drop or drift, transducer offset drift and/or ADC offset drift. Supply current errors may be discounted, since there was always more than sufficient power for the gyros: gyro supply voltage was measured before and after each drop, and in any case the motor, pickoff and demodulator use AC excitation, and are stabilized to be independent of supply voltage over a wide input range. It is conceivable, though unlikely, that supply energy indirectly affected the gyro offsets, because of the variation in thermal dissipation from the PSU with the slow decrease in supply voltage. This would have tended to reduce the rate of any thermal drift.

Transducer offset drift is the most likely source. The gyros were calibrated in every instance at IMU block temperatures of 24-25 deg.C, hence their temperature characteristics are not known from these tests. They were not enclosed during calibration, so that cooling was by free convection and by conduction via the IMU block to a massive metal baseplate. As determined by their overall performance specifications [85], these gyros are by no means of inertial navigation quality [70]: from the manufacturer's introductory literature [85] a scale factor shift, for temperature compensated models, of $\pm 5\%$ is quoted for the range -45 deg.C to +85 deg.C (re 20 deg.C, presumably). For present purposes, let us assume that the transducers have reached an equilibrium temperature before the drop, and that this temperature changes negligibly during the 40 s flight. Ignoring the scale factor variation with temperature, let us assume that the magnitude of the zero offset drift rate is comparable to that of the scale factor, which gives a drift rate of about 0.083% FSO per deg.C. With a calibration temperature of 25 deg.C, and an inflight temperature of 35 deg.C, say, this gives an estimated offset drift of 0.83% FSO; measured drift is about 0.95% FSO, which is

of the right order.

By comparison with the estimated transducer drift the data acquisition system offset drift is negligible. For the SDM853 the worst case drift error occurs at FSO, and is specified as ± 30 ppm/deg.C. [81] re 25 deg.C; assuming an operating temperature in the SDM853 bay of not more than 30 deg.C. above ambient (ambient range encountered: 2 deg.C. to 15 deg.C.), this gives a very worst case (i.e. at FSO) bias error of 1.5 mV, or about 1 LSB, whereas the observed bias is around 25 mV.

Software sources of bias could be due to a numerical error in the calibration data, so these were carefully checked to obviate this possibility. Note that the zero values of the data acquisition system are specified to $\pm \frac{1}{2}$ LSB, which sets a lower bound on all bias errors.

C5.2. Estimation of the Corrections

Corrections must be made to compensate for the bias, whatever the source. All of the drop test data, other than those from Drops 20, 21 and 23, which were not to hand, were therefore analysed to measure the observed bias. Four processing runs were made for each drop - using pre- and post-trial calibration curves applied to unwindowed ($t = [0.0, t_{\max}]$ s, where $t_{\max} = \min(t_{\text{land}}, 40.0)$ s) and windowed ($t = [10.0, t_{\max}]$ s) records. The results, presented as corrections (additive) to a preferred value, are shown in Figures C5.1 to C5.6; these include the results for the stationary trials UF06, CH01, CH02 (Section 3.8.6). The individual quantization levels (QL) are also indicated.

C5.2.1. Rate Gyro Biases

Only the results for the post-trial gyro data are treated here, since during the pre-trial gyro calibrations the outputs were loaded (Appendix C4). In Drops 19 to 27 the parachute rotated slowly (about

3 rpm) around the axis of symmetry; this was confirmed from movie film.

p-direction gyro

The results were grouped according to drop configuration (cf. Figure C5.1), with trials UF06, CH01 and CH02 treated separately. Average group bias corrections (wrt a preferred value of zero) were (rad s^{-1}):

Group Run Type	A	B	C	D	Mean of A,B,C,D	Mean of A,B,D	UF06
Windowed	0.0646	0.0715	0.0833	0.0676	0.0728	0.0686	0.0708
Unwindowed	0.0618	0.0652	0.0757	0.0729	0.0692	0.0668	0.0702

Results from CH01, CH02 are omitted because the ambient test conditions were extreme. The unwindowed correction for UF06 was taken as the most representative value, since this was obtained for a stationary trial under field conditions. Note that this value is within 0.7 QL

($QL_p = 0.0036 \text{ rad s}^{-1}$) of the windowed means, 0.0728 and 0.0686 rad s^{-1}

Note also that the uncertainty in the zero value of the data acquisition system ($\pm \frac{1}{2}$ LSB) is included in the above analysis.

q-direction gyro

Similar results for the q-corrections were:

Group Run Type	A	B	C	D	A,B,C,D	A,B,D	UF06	Mean of UF06,CH01, CH02
Windowed	-0.0109	-0.0202	-0.0125	-0.0198	-0.0164	-0.0180	-0.0256	-0.0261
Unwindowed	-0.0056	-0.0201	-0.0079	-0.0331	-0.0172	-0.0207	-0.0254	-0.0257

Here again, the unwindowed value for UF06 was taken as representative.

This value is within 2.6 QL ($QL_q = 0.0028 \text{ rad s}^{-1}$) of the windowed mean of groups A,B,D, and within 1.7 QL of the unwindowed mean.

r-direction gyro

For the axisymmetric parachute there is no preferred flight orientation, also the Euler angle ψ is unbounded, hence there is little to be gained by considering the flight data. Accordingly, only the stationary bias measurements are considered. The unwindowed values give a better estimate, since the records are longer:

Trial	UFO6	CHO1	CHO2
Unwindowed	0.0254	0.0216	0.0266
Bias measurement			

The mean of these three values is $0.0254 \text{ rad s}^{-1}$, which is the same as the UFO6 value (the deviation from the mean is less than 0.5 QL) and this was taken as representative.

C5.2.2. Accelerometer Biases

The flight data are of little use for determining the accelerometer biases since the measured values are affected to an unknown extent by the orientation of the body to the vertical. For the stationary trials the body was aligned to within 5 deg. of the vertical, hence the gravity component error along a_z was less than $0.004 g_n$ (0.04 ms^{-2}), and less than $0.087 g_n$ (0.854 ms^{-2}) along a_x and a_y . These values may be compared to the QLs : 0.029 ms^{-2} for z , and 0.014 ms^{-2} for x and y ; hence the estimate of the a_z bias (due to thermal drift) from the stationary trials should be good to within about 1 QL - this was therefore taken from the unwindowed mean of trials UFO6, CHO1 and CHO2, and estimated as a correction of $-0.169 \pm 0.002 \text{ ms}^{-2}$ (pre-trial calibration curve).

To estimate the a_x and a_y biases the SB was accurately ($\pm 0.1 \text{ deg.}$) set up on a horizontal ($\pm 0.04 \text{ deg.}$) surface table; x- and y-accelerometer readings were measured for a sequence of 16 mutually orthogonal body-axis orientations, thus averaging out any alignment errors. After

allowing for offset in the data acquisition chain, the estimated bias corrections were 0.41 ms^{-2} for a_x , 0.31 ms^{-2} for a_y (both $\pm 0.02 \text{ ms}^{-2}$, pre-trial calibration curves). Note that for most instances these fall short of those shown in Figures C4.5, C5.5. As illustrated above, the x- and y-accelerometers are much more sensitive than the z-accelerometer to misalignment with the vertical, which may be the cause of shortfall, if such is the case; it is remarkable, however, that in all of the trials the measured corrections are of the same sign, which would not be the case for (random) misalignment.

Author(s)	Year	2D/ 3D	No. of DoF	Nonlinear solution?	No. of [A] components	Angular Damping Terms	Model Type +	Remarks
BRODETZSKY [12]	1918	3D	6	NO	NONE	YES	At	Linear derivative notation
NAYLER <i>et al.</i> [14]	1919	3D	6	NO	NONE	YES	At	Linear derivative notation
JONES [16]	1943	2D	3	NO	2	YES	At	Linear derivative notation
HENN [17]	1944	2D	3	NO	3	YES	At	
LESTER [20]	1962	2D	3	NO	3	NO	At	Corrects previous treatments
LUDWIG, HEINS [25]	1963	2D	3	YES	2	NO	At, D	First nonlinear solutions
WOLF [26]	1965	3D	5	YES	2	NO	D	First 3D nonlinear solutions
SCHULZ, HAMEL [27]	1970	2D	3	YES	2	NO	At, D	Harmonic linearization of aerodynamic force fns.
SHILOV [21]	1971	2D	3	NO	4	YES	At	
BYUSHGENS, SHILOV [22]	1972	2D	3	NO	4	YES	At	
TORY, AYRES [4]	1972	3D	6	YES	3	NO	D	Wind input option
HUME [28]	1973	2D	3	YES	1	NO	D	Wind input
SHILOV [23]	1973	2D	3	NO	4	YES	At	
GOODRICK [48]	1975	2D	3	YES	NONE	NO	D	Gliding system. Wind input
CHURKIN, KOSARCHUK [47]	1978	2D	3	YES	3	NO	At, D	Harmonic linearization
GOODRICK [49]	1979	3D	6	YES	2	YES	D	Gliding system. Wind input. Distributed aerodynamic forces
EATON [24]	1981	3D	6	YES	4	YES	D	Corrects previous treatments

† At = analytical. A1 = analogue. D = digital.

Table 1.1. Conceptual Dynamic Stability Models of Parachutes : Single-Body Models

Author(s)	Year	2D/ 3D	No. of DoF	Nonlinear solution?	No. of [A] components	Angular Damping Terms	Model Type †	Remarks
NAYLER <i>et al.</i> [14]	1919	3D	9	NO	NONE	YES	At	Elastic lines. Linear derivative notation
NEUSTADT <i>et al.</i> [42]	1964	2D	7	YES	2	YES	D	Elastic tether and lines. Deployment & descent simulation
VAUGHN, MATEJKA [50]	1965	2D	6	NO	NONE	YES	At	
GAMBLE [52]	1968	3D	12	YES	1	YES	D	Elastic lines. Gliding system
WOLF [43]	1971	3D	9	YES	2	NO	D	
TALAY <i>et al.</i> [51]	1974	3D	12	YES	3	YES	D	Viscoelastic lines. Deployment & descent
DOYLE, BUBRICK [29]	1974	3D	12	YES	3	YES	D	Viscoelastic tether. Multistage simulation
IBRAHIM, ENGD AHL [53]	1974	3D	13	YES	4	NO	D	Elastic Canopy, lines & tether. Turbulent wind input option
WOLF, SPAHR [56]	1975	3D	6 + 6n	YES	3	NO	D	Viscoelastic tether. Cluster of n canopies
BOLTON [54]	1979	3D	9	YES	NONE	YES	H	6-component aerodynamic input data
SCHATZLE, CURRY [55]	1979	3D	9	YES	NONE	YES	H	Elastic lines. Deployment & multistage simulation

† At = analytical. A1 = analogue. D = digital. H = hybrid (analogue/digital).

Table 1.2. Conceptual Dynamic Stability Models of Parachutes : Multi-Body Models

ALPHA	CN	CT	CN	CT
0.0000	0.0000	1.1111	0.0000	1.1111
0.0000	0.0042	1.1111	0.0056	1.1111
0.0000	0.0053	1.1111	0.0067	1.1111
0.0000	0.0082	1.1111	0.0077	1.1111
0.0000	0.0077	1.1111	0.0088	1.1111
0.0000	0.0076	1.1111	0.0099	1.1111
0.0000	0.0107	1.1111	0.0111	1.1111
0.0000	0.0105	1.1111	0.0122	1.1111
0.0000	0.0120	1.1111	0.0133	1.1111
0.0000	0.0119	1.1111	0.0144	1.1111
0.0000	0.0150	1.1111	0.0155	1.1111
0.0000	0.0144	1.1111	0.0166	1.1111
0.0000	0.0155	1.1111	0.0177	1.1111
0.0000	0.0151	1.1111	0.0188	1.1111
0.0000	0.0173	1.1111	0.0199	1.1111
0.0000	0.0166	1.1111	0.0210	1.1111
0.0000	0.0177	1.1111	0.0221	1.1111
0.0000	0.0173	1.1111	0.0232	1.1111
0.0000	0.0199	1.1111	0.0243	1.1111
0.0000	0.0190	1.1111	0.0254	1.1111
0.0000	0.0200	1.1111	0.0265	1.1111
0.0000	0.0194	1.1111	0.0276	1.1111
0.0000	0.0211	1.1111	0.0287	1.1111
0.0000	0.0200	1.1111	0.0298	1.1111
0.0000	0.0222	1.1111	0.0309	1.1111
0.0000	0.0211	1.1111	0.0320	1.1111
0.0000	0.0233	1.1111	0.0331	1.1111
0.0000	0.0222	1.1111	0.0342	1.1111
0.0000	0.0244	1.1111	0.0353	1.1111
0.0000	0.0233	1.1111	0.0364	1.1111
0.0000	0.0255	1.1111	0.0375	1.1111
0.0000	0.0244	1.1111	0.0386	1.1111
0.0000	0.0266	1.1111	0.0397	1.1111
0.0000	0.0255	1.1111	0.0408	1.1111
0.0000	0.0277	1.1111	0.0419	1.1111
0.0000	0.0266	1.1111	0.0430	1.1111
0.0000	0.0288	1.1111	0.0441	1.1111
0.0000	0.0277	1.1111	0.0452	1.1111
0.0000	0.0300	1.1111	0.0463	1.1111
0.0000	0.0288	1.1111	0.0474	1.1111
0.0000	0.0311	1.1111	0.0485	1.1111
0.0000	0.0300	1.1111	0.0496	1.1111
0.0000	0.0322	1.1111	0.0507	1.1111
0.0000	0.0311	1.1111	0.0518	1.1111
0.0000	0.0333	1.1111	0.0529	1.1111
0.0000	0.0322	1.1111	0.0540	1.1111
0.0000	0.0344	1.1111	0.0551	1.1111
0.0000	0.0333	1.1111	0.0562	1.1111
0.0000	0.0355	1.1111	0.0573	1.1111
0.0000	0.0344	1.1111	0.0584	1.1111
0.0000	0.0366	1.1111	0.0595	1.1111
0.0000	0.0355	1.1111	0.0606	1.1111
0.0000	0.0377	1.1111	0.0617	1.1111
0.0000	0.0366	1.1111	0.0628	1.1111
0.0000	0.0388	1.1111	0.0639	1.1111
0.0000	0.0377	1.1111	0.0650	1.1111
0.0000	0.0400	1.1111	0.0661	1.1111
0.0000	0.0388	1.1111	0.0672	1.1111
0.0000	0.0411	1.1111	0.0683	1.1111
0.0000	0.0400	1.1111	0.0694	1.1111
0.0000	0.0422	1.1111	0.0705	1.1111
0.0000	0.0411	1.1111	0.0716	1.1111
0.0000	0.0433	1.1111	0.0727	1.1111
0.0000	0.0422	1.1111	0.0738	1.1111
0.0000	0.0444	1.1111	0.0749	1.1111
0.0000	0.0433	1.1111	0.0760	1.1111
0.0000	0.0455	1.1111	0.0771	1.1111
0.0000	0.0444	1.1111	0.0782	1.1111
0.0000	0.0466	1.1111	0.0793	1.1111
0.0000	0.0455	1.1111	0.0804	1.1111
0.0000	0.0477	1.1111	0.0815	1.1111
0.0000	0.0466	1.1111	0.0826	1.1111
0.0000	0.0488	1.1111	0.0837	1.1111
0.0000	0.0477	1.1111	0.0848	1.1111
0.0000	0.0500	1.1111	0.0859	1.1111
0.0000	0.0488	1.1111	0.0870	1.1111
0.0000	0.0511	1.1111	0.0881	1.1111
0.0000	0.0500	1.1111	0.0892	1.1111
0.0000	0.0522	1.1111	0.0903	1.1111
0.0000	0.0511	1.1111	0.0914	1.1111
0.0000	0.0533	1.1111	0.0925	1.1111
0.0000	0.0522	1.1111	0.0936	1.1111
0.0000	0.0544	1.1111	0.0947	1.1111
0.0000	0.0533	1.1111	0.0958	1.1111
0.0000	0.0555	1.1111	0.0969	1.1111
0.0000	0.0544	1.1111	0.0980	1.1111
0.0000	0.0566	1.1111	0.0991	1.1111
0.0000	0.0555	1.1111	0.1002	1.1111
0.0000	0.0577	1.1111	0.1013	1.1111
0.0000	0.0566	1.1111	0.1024	1.1111
0.0000	0.0588	1.1111	0.1035	1.1111
0.0000	0.0577	1.1111	0.1046	1.1111
0.0000	0.0600	1.1111	0.1057	1.1111
0.0000	0.0588	1.1111	0.1068	1.1111
0.0000	0.0611	1.1111	0.1079	1.1111
0.0000	0.0600	1.1111	0.1090	1.1111
0.0000	0.0622	1.1111	0.1101	1.1111
0.0000	0.0611	1.1111	0.1112	1.1111
0.0000	0.0633	1.1111	0.1123	1.1111
0.0000	0.0622	1.1111	0.1134	1.1111
0.0000	0.0644	1.1111	0.1145	1.1111
0.0000	0.0633	1.1111	0.1156	1.1111
0.0000	0.0655	1.1111	0.1167	1.1111
0.0000	0.0644	1.1111	0.1178	1.1111
0.0000	0.0666	1.1111	0.1189	1.1111
0.0000	0.0655	1.1111	0.1200	1.1111
0.0000	0.0677	1.1111	0.1211	1.1111
0.0000	0.0666	1.1111	0.1222	1.1111
0.0000	0.0688	1.1111	0.1233	1.1111
0.0000	0.0677	1.1111	0.1244	1.1111
0.0000	0.0700	1.1111	0.1255	1.1111
0.0000	0.0688	1.1111	0.1266	1.1111
0.0000	0.0711	1.1111	0.1277	1.1111
0.0000	0.0700	1.1111	0.1288	1.1111
0.0000	0.0722	1.1111	0.1299	1.1111
0.0000	0.0711	1.1111	0.1310	1.1111
0.0000	0.0733	1.1111	0.1321	1.1111
0.0000	0.0722	1.1111	0.1332	1.1111
0.0000	0.0744	1.1111	0.1343	1.1111
0.0000	0.0733	1.1111	0.1354	1.1111
0.0000	0.0755	1.1111	0.1365	1.1111
0.0000	0.0744	1.1111	0.1376	1.1111
0.0000	0.0766	1.1111	0.1387	1.1111
0.0000	0.0755	1.1111	0.1398	1.1111
0.0000	0.0777	1.1111	0.1409	1.1111
0.0000	0.0766	1.1111	0.1420	1.1111
0.0000	0.0788	1.1111	0.1431	1.1111
0.0000	0.0777	1.1111	0.1442	1.1111
0.0000	0.0800	1.1111	0.1453	1.1111
0.0000	0.0788	1.1111	0.1464	1.1111
0.0000	0.0811	1.1111	0.1475	1.1111
0.0000	0.0800	1.1111	0.1486	1.1111
0.0000	0.0822	1.1111	0.1497	1.1111
0.0000	0.0811	1.1111	0.1508	1.1111
0.0000	0.0833	1.1111	0.1519	1.1111
0.0000	0.0822	1.1111	0.1530	1.1111
0.0000	0.0844	1.1111	0.1541	1.1111
0.0000	0.0833	1.1111	0.1552	1.1111
0.0000	0.0855	1.1111	0.1563	1.1111
0.0000	0.0844	1.1111	0.1574	1.1111
0.0000	0.0866	1.1111	0.1585	1.1111
0.0000	0.0855	1.1111	0.1596	1.1111
0.0000	0.0877	1.1111	0.1607	1.1111
0.0000	0.0866	1.1111	0.1618	1.1111
0.0000	0.0888	1.1111	0.1629	1.1111
0.0000	0.0877	1.1111	0.1640	1.1111
0.0000	0.0900	1.1111	0.1651	1.1111
0.0000	0.0888	1.1111	0.1662	1.1111
0.0000	0.0911	1.1111	0.1673	1.1111
0.0000	0.0900	1.1111	0.1684	1.1111
0.0000	0.0922	1.1111	0.1695	1.1111
0.0000	0.0911	1.1111	0.1706	1.1111
0.0000	0.0933	1.1111	0.1717	1.1111
0.0000	0.0922	1.1111	0.1728	1.1111
0.0000	0.0944	1.1111	0.1739	1.1111
0.0000	0.0933	1.1111	0.1750	1.1111
0.0000	0.0955	1.1111	0.1761	1.1111
0.0000	0.0944	1.1111	0.1772	1.1111
0.0000	0.0966	1.1111	0.1783	1.1111
0.0000	0.0955	1.1111	0.1794	1.1111
0.0000	0.0977	1.1111	0.1805	1.1111
0.0000	0.0966	1.1111	0.1816	1.1111
0.0000	0.0988	1.1111	0.1827	1.1111
0.0000	0.0977	1.1111	0.1838	1.1111
0.0000	0.1000	1.1111	0.1849	1.1111
0.0000	0.0988	1.1111	0.1860	1.1111
0.0000	0.1011	1.1111	0.1871	1.1111
0.0000	0.1000	1.1111	0.1882	1.1111
0.0000	0.1022	1.1111	0.1893	1.1111
0.0000	0.1011	1.1111	0.1904	1.1111
0.0000	0.1033	1.1111	0.1915	1.1111
0.0000	0.1022	1.1111	0.1926	1.1111
0.0000	0.1044	1.1111	0.1937	1.1111
0.0000	0.1033	1.1111	0.1948	1.1111
0.0000	0.1055	1.1111	0.1959	1.1111
0.0000	0.1044	1.1111	0.1970	1.1111
0.0000	0.1066	1.1111	0.1981	1.1111
0.0000	0.1055	1.1111	0.1992	1.1111
0.0000	0.1077	1.1111	0.2003	1.1111
0.0000	0.1066	1.1111	0.2014	1.1111
0.0000	0.1088	1.1111	0.2025	1.1111
0.0000	0.1077	1.1111	0.2036	1.1111
0.0000	0.1100	1.1111	0.2047	1.1111
0.0000	0.1088	1.1111	0.2058	1.1111
0.0000	0.1111	1.1111	0.2069	1.1111
0.0000	0.1100	1.1111	0.2080	1.1111
0.0000	0.1122	1.1111	0.2091	1.1111
0.0000	0.1111	1.1111	0.2102	1.1111
0.0000	0.1133	1.1111	0.2113	1.1111
0.0000	0.1122	1.1111	0.2124	1.1111
0.0000	0.1144	1.1111	0.2135	1.1111
0.0000	0.1133	1.1111	0.2146	1.1111
0.0000	0.1155	1.1111	0.2157	1.1111
0.0000	0.1144	1.1111	0.2168	1.1111
0.0000	0.1166	1.1111	0.2179	1.1111
0.0000	0.1155	1.1111	0.2190	1.1111
0.0000	0.1177	1.1111	0.2201	1.1111
0.0000	0.1166	1.1111	0.2212	1.1111
0.0000	0.1188	1.1111	0.2223	1.1111
0.0000	0.1177	1.1111	0.2234	1.1111
0.0000	0.1200	1.1111	0.2245	1.1111
0.0000	0.1188	1.1111	0.2256	1.1111
0.0000	0.1211	1.1111	0.2267	1.1111
0.0000	0.1200	1.1111	0.2278	1.1111
0.0000				

ALPHA	CN	CT
0.000	0.000	1.224
0.000	.028	1.122
0.000	.040	1.111
0.000	.064	1.111
0.000	.092	1.111
0.000	.069	1.111
0.000	.032	1.111
0.000	.000	1.111
0.000	.060	1.111
0.000	.137	1.111
0.000	.234	1.111
0.000	.295	1.111
0.000	.355	1.111
0.000	.326	1.111
0.000	.326	1.111
0.000	.305	1.111
0.000	.298	1.111
0.000	.284	1.111
0.000	.295	1.111

$\lambda=1.0\%$ (flex.)

ALPHA	CN	CT
0.000	0.000	1.224
5.000	.018	1.122
10.000	.018	1.111
15.000	.009	1.111
20.000	.000	1.111
25.000	.007	1.111
30.000	.008	1.111
35.000	.012	1.111
40.000	.024	1.111
45.000	.065	1.111
50.000	.129	1.111
55.000	.270	1.111
60.000	.336	1.111
65.000	.348	1.111
70.000	.347	1.111
75.000	.330	1.111
80.000	.297	1.111
85.000	.267	1.111
90.000	.237	1.111

$\lambda=4.2\%$ (flex.)

TABLE 2.1(b) C_N, C_T curve coordinates from Heinrich and Haak

CANOPY AERODYNAMIC COEFFS. (MEASURED AT APOX)

ALPHA	CN	CT	CM
0.000	0.000	1.453	0.000
0.500	.0026	1.461	.014
1.000	.0035	1.482	.028
1.500	.0024	1.522	.039
2.000	.021	1.569	.055
2.500	.012	1.616	.069
3.000	.012	1.661	.085
3.500	.017	1.697	.102
4.000	.033	1.743	.119
4.500	.063	1.791	.124
5.000	.131	1.789	.110
5.500	.227	1.719	.069
6.000	.324	1.522	.028
6.500	.351	1.200	.014
7.000	.330	.919	.000
7.500	.286	.652	.000
8.000	.293	.418	.000
8.500	.290	.201	.000
9.000	.295	.056	.000

$\lambda=0$ (rigid)

ALPHA	CN	CT	CM
0.000	0.000	1.403	0.000
0.500	.030	1.417	.014
1.000	.043	1.438	.022
1.500	.036	1.477	.031
2.000	.040	1.516	.043
2.500	.043	1.553	.059
3.000	.032	1.584	.072
3.500	.024	1.638	.090
4.000	.041	1.648	.099
4.500	.137	1.531	.083
5.000	.234	1.559	.040
5.500	.295	1.444	.000
6.000	.355	1.248	.000
6.500	.322	1.010	.000
7.000	.305	.770	.000
7.500	.298	.473	.000
8.000	.284	.278	.000
8.500	.295	.136	.000
9.000	.295	.056	.000

$\lambda=2.0\%$

ALPHA	CN	CT	CM
0.000	0.000	1.375	0.000
0.500	.032	1.385	.014
1.000	.048	1.408	.019
1.500	.046	1.439	.028
2.000	.053	1.480	.040
2.500	.066	1.503	.052
3.000	.053	1.548	.065
3.500	.005	1.557	.079
4.000	.070	1.573	.084
4.500	.158	1.552	.062
5.000	.253	1.411	.014
5.500	.308	1.352	.000
6.000	.341	1.199	.000
6.500	.337	.933	.000
7.000	.320	.664	.000
7.500	.311	.452	.000
8.000	.301	.255	.000
8.500	.284	.136	.000
9.000	.295	.056	.000

$\lambda=4.0\%$

TABLE 2.2 C_N, C_T curve coordinates from Ayres

0 BEFORE ALL TESTS: Check External Battery Volts ON LOAD: should be ~ 32.0V, 11.4 V

I Large Body (35 kg) on 12 foot or 24 foot I24 canopy

A) Rigging Zone Checks

1. Nose clean. Pressure holes clear. Dents filled.
2. Plastic pressure leads clear (blow through using pump).
Leak test both leads if they appear damaged.
3. Inner tube pressures all 5 p.s.i.
4. Aluminium guide tube lined up with mark and at correct depth.
Pressure leads up inside of tube.
5. Rigging lines not tangled. Attachment clips all free.
6. Bomb bar battery supplies switched on. Flash bulb renewed.
Release cables attached. Power lead secured.
7. Bring external power lead down through apex vent.
8. Suspend canopy by apex ring.
9. Hoist until just clear of ground. Check length of power lead o.k.
Wait for instrumented body.
10. Fit instrumented body. Check orientation (see I C).

B) Caravan: Instrumented Body Preparation

1. Check body and pressure leads undamaged; components, wires etc.
inside all o.k. Replace lid and mounting brackets.
2. Check battery voltages off load. Replace pack if necessary. Have
old pack put on charge immediately.
3. Attach supporting frame correct way around.
Shear pin sizes: 0.070" ali for 12 foot; 19g copper for 24 foot.
4. Mains power supply (PSU) plugged in and leads free. Outputs off.
5. Connect external power and Silent 700. Read program tape and blank
tape with leader. Use only PSU + 20V and + 10V lines.
6. Load program. ALLOW 5 minute warm-up time for pressure transducer (ΔP).
7. Power up gyros on PSU.
8. Check MO - 20 . Read EO - 100.
9. Run program using interrupt switch. Record readings EO - 100 and
13D0 - 1400 for ΔP zero value.
10. Switch off + 30 and - 20 psu. Switch off gyros and ΔP . Disable INTERRUPT.
11. Restart program using RESET.
12. Check rigging zone people ready (See I A).

C) Rigging Zone: Final Assembly

1. Bring body to rigging zone, still connected to external PSU.
2. Start gyros and ΔP .
3. Switch on mains + 30 and - 20 on PSU.
4. Check Ext. Int. switch disabled; reset indicator lights on side.
Check Rx off.
5. Attach pressure leads.

6. Change over power leads. Switch off mains on PSU. Enable INTERRUPT.
7. Fit release plug.
8. Fit instrument body to large body; check pressure leads free.
9. Screw down butterfly nuts.
10. Check rigging line attachment clips all free on large body. Check lines all o.k. again.

NOW READY FOR HOISTING

D) Release and Recovery Procedure

1. Hoist to release altitude.
2. Release control by JAE - calls:-

READY ! CAMERA ON ! EYES UP !

TWO ONE GO !

- Release pressed when body vertical. Slight swinging acceptable. Note orientation of large body.

3. On GO, stop watch times required are:

- a) GO to fully inflated
- b) GO to behaviour of system as a rigid body.
- c) GO to touchdown.
- d) GO to reconnection of PSU.

Flash bulb operates on GO. Test body emits high pitched tone while program runs.

4. Drop body recovered as quickly as possible by fast vehicle with a shock-proof carrier. Returns to caravan.
5. Butterfly nuts removed as quickly as possible (en route) to allow instrumented body to be reconnected to PSU.
6. Switch gyros and ΔP off as soon as possible. Take care not to touch any other switches.
7. Instrumented body removed from large body. Pressure leads disconnected. Place in 3 legged stand.
8. Reconnect Silent 700.
9. Check M0 - 20 ; E0 - 100 ; 13D0 - 1400 ; M3B0-420.
10. Complete leaders on recording tape. Dump MEO - 1400 onto tape: use timer to check when dumping finished.
11. Take copy dump of E0 - 1400.
12. Switch off PSU and disconnect all leads. Remove cover from instrumented body and inspect for damage.

II Instrumented Body (10 kg) on 6 foot or 12 foot I24 canopy

A) Caravan : Preparation

1. Check body and nose undamaged; components wires etc. inside all o.k. Replace lid and mounting brackets.
2. Check battery voltages off load. Replace pack if necessary. Check pressure leads free when replacing nose. Put old pack on immediate charge.
3. Replace bent legs with a straightened set.
4. Check radio control operative.
5. Store legs in retracted position. Switch off Rx, then Tx.
6. Rigging crew ensure canopy lines and mounting ring o.k. Attach mounting ring.
7. Mains power supply unit (PSU) plugged in and leads free. Outputs off.
8. Connect PSU and Silent 700 to body. Ready program tape and blank tape with leader. Use only PSU + 20V and + 10V lines.
9. Load program. Allow 5 minute warm up time for ΔP .
10. Power up gyros on PSU.
11. Check MO - 20 ; EO - 100.
12. Run program using interrupt switch. Record EO - 100 and 13DO - 1400.
13. Switch off +30 and -20 PSU lines. Switch off gyros and ΔP .
14. Restart program using RESET.
15. Check bomb bar people ready.

B) Rigging : Final Assembly

1. Bring body to bomb bar, still connected to PSU.
2. Start gyros and ΔP .
3. Switch on +30V and -20V on PSU.
4. Check Ext. Int. switch enabled ; reset indicator lights on side.
5. Bomb bar battery supplies switched on. Flash bulb renewed. Release cables attached. Power lead secured.
6. Bring power lead down through apex vent.
7. Suspend canopy by apex ring.
7. Hoist until just clear of ground. Check length of power lead o.k.
9. Change over power leads. Switch off mains on PSU.
10. Fit release plug. Attach Rx aerial to a rigging line.
11. Check all lines free and untangled.
12. Switch on Rx.

NOW READY FOR HOISTING

C) Release and Recovery

1. Hoist to release altitude (+100 ft. included).
2. Switch on legs release Tx. Handle carefully. CHECK ON.
3. Observe body with binoculars (JAE).
4. Release control by JAE - calls:-

READY !

CAMERA ON ! EYES UP !

TWO.....ONE.....GO !

- release pressure when body vertical. Slight swinging acceptable. Note orientation of body.

5. On GO, stop watch times required are:
 - a) GO to fully inflated.
 - b) GO to behaviour as a rigid body.
 - c) GO to touchdown.
 - d) GO to reconnection of PSU.
6. IMPORTANT: Legs - release to be operated when body 100 feet from ground. Legs actuated by pressing right hand lever on Tx fully forward and holding.
7. Drop body recovered as quickly as possible by fast recovery vehicle. Switch gyros off as soon as possible. Take care not to touch any other switches etc. Vehicle returns to caravan.
8. Reconnect PSU +20V and +10V as soon as possible.
Same as in I from 8 on. Canopy may be removed along with lid for disentangling.

Drop No.	Date	Time (hr.)	Canopy D ₀ (ft.)	Store	Wind @ 40m AGL (ms ⁻¹)	Temperature °C	Release Altitude (ft.)	T open (sec.) from film record	T legs (sec.) from film record	T land (sec.) from film record	Data?	Remarks
01	021079	1150	24	BB	2.0	14.0	600	4.21		41.75	NO	Data lost en route in Landrover.
02		1330			2.0	18.2		3.67		37.35	YES	
03		1430			3.0	18.5		4.66*		39.74*	NO	BB LAPESed from Landrover.
04		1533			4.0	18.6		3.82*		49.76*	NO	Data lost on re-connecting 5V supply
05	051079	1155			1.0	14.1		3.96		56.37*	YES	Lines slightly twisted.
06		1357			3.5	15.8		3.95*		43.29*	NO	Ext. power/control cable torn off on release. MPU not triggered. Dud data.
07		1533			3.0	16.1		3.67		40.96	YES	Generator failed during data extraction.
08	111079	1148	12	BB	5.5	16.1	1100	3.75		35.14*	YES	
09		1337			5.0	16.9		2.20*		36.62*	NO	Landing heavy. Data lost on reconnecting 5V.
10		1403			3.5	16.9		3.67		36.33	YES	
11		1435			5.0	17.9		3.33		39.13	YES	
12		1500			-	-	1250	2.38*		42.36*	NO	Heavy landing. Data lost on reconnecting 5V. SB dented & PCBs moved.
13	161079	1203			4.5	13.6		3.00		40.71	YES	Ext. power cable torn on release.
14		1230			-	-		3.65*		40.44*	NO	5V level too low.
15		1319			-	-		2.62*		38.04*	NO	Lines twisted. Dud data - cause unknown.
16		1350			3.0	14.3		3.21		40.75	YES	Lines slightly twisted.
17		1412			-	-		2.57*		41.61*	NO	Bomb-bar problems. Data lost en route in Landrover.
18		1437			4.0	13.8		2.60*		40.68*	YES	Bomb-bar problems. 3 attempts needed for release.

* Stop-watch measurement

Table 3.3. Production Drop Tests from Balloon Rig

continued/....

Drop No.	Date	Time (hr.)	Canopy D ₀ (ft.)	Store	Wind @ 40m AGL (ms ⁻¹)	Temperature °C	Release Altitude (ft.)	T open (sec.) from film record	T legs (sec.) from film record	T land (sec.) from film record	Data?	Remarks
19	171079	1157	6	SB	6.0	13.2	1400	2.50	0.00	40.26*	YES	Legs deployed prematurely. Nose damaged.
20		1406			5.5	15.0		1.75	11.75	39.29*	YES	Legs deployed prematurely. Nose damaged.
21		1502			6.5	14.8		2.50	21.13	38.89*	YES	Windy. Legs deployed prematurely.
22	291079	1336			-	-		1.87	-	40.54*	NO	Data lost on reconnecting 5V. Heavy landing. Internal damage.
23	021179	1111			3.5	9.5		1.75	12.92	40.48*	YES	Legs deployed prematurely.
24		1157			2.5	11.2		1.83	4.25	39.89*	YES	Legs deployed prematurely.
25		1345			3.0	12.3		1.67	36.20	40.55*	YES	Very good.
26		1432			3.0	12.0		1.63	36.46	41.76*	YES	Very good.
27		1515			2.5	9.3		1.92*	4.75	40.61*	YES	Legs deployed prematurely.
28	131179	1203	12	SB	1.0	2.6	700	2.25	-	42.29	YES	Legs failed to release - Tx switched off.
29		1343			3.5	5.3		1.83	-	44.05*	YES	Legs deployed after landing. Movie camera failed.
30		1430			4.0	4.3		1.84*	-	57.48*	YES	Legs not fitted.
31		1511			-	-	600	1.81*	-	44.43*	NO	Legs not fitted. Premature release. 5V level run down.
32		1536			3.0	2.2		2.29*	-	41.73*	YES	Bounced on landing.

* Stopwatch measurement.

Table 3.3. Production Drop Tests from Balloon Rig (Cont'd)

Drop No.	Peak mean horizontal wind speed V_{WH} at 40m AGL ($\text{ms}^{-1} \pm 0.5$)	Mean descent speed W_N (ms^{-1})	W_N/V_{WH}
2	2.0	4.0	2.0
5	1.0	4.0	4.0
7	3.0	4.0	1.3
8	5.5	10.5	1.9
10	3.5	10.5	3.0
11	5.0	10.5	2.1
13	4.5	10.0	2.2
16	3.0	10.5	3.5
18	4.0	10.5	2.6
19	6.0	11.0	1.8
20	5.5	11.0	2.0
21	6.5	11.0	1.7
23	3.5	11.0	3.1
24	1.5	11.5	7.7
25	3.0	11.5	3.8
26	3.0	11.5	3.8
27	2.5	11.0	4.4
28	1.0	4.5	4.5
29	3.5	5.0	1.4
30	4.0	5.0	1.3
32	3.0	4.5	1.5

Table 3.4. Ratios of mean descent speeds to peak mean wind speeds

RATE TRANSFER TEST NO. 2 TYPE 401 GYRO #024 11 Sept 79
 TABLE NO. 339 R.T.S.F 82.78 MV/DEG/SEC
 SWITCH ON 1255 HOURS SWITCH OFF 1317 HOURS
 RUN UP TIME 0.0 SECS RUN DOWN TIME 0.0 SECS
 MAX TEMP 24.67 DEG C MIN TEMP 24.31 DEG C

TACHO MV	TABLE RATE DEG/SEC	GYRO OUTPUT MV	GYRO ERRORS DEG/SEC	GAGE ERRORS
-7.00	-0.03	6.30	-1.4519	0.0000
2644.00	31.94	-183.30	-0.5144	-1.9236
5236.00	63.86	-373.20	0.2972	0.4655
7949.00	95.03	-561.80	0.7304	0.7607
10599.00	123.04	-749.30	1.1305	0.8830
13254.00	150.11	-934.70	1.1072	0.5915
15917.00	192.23	-1119.50	0.3835	0.4595
18556.00	224.23	-1302.00	0.4314	0.1923
21193.00	255.02	-1432.70	-0.0662	-0.0253
23864.00	288.23	-1660.00	-1.6330	-0.5838
26527.00	320.45	-1833.80	-3.8082	-1.1884
26523.00	320.40	-1835.70	-3.4315	-1.0710
23857.00	288.20	-1664.50	-0.3205	-0.2847
21205.00	255.16	-1489.40	0.9471	0.3697
18560.00	224.21	-1311.30	2.1115	0.9418
15907.00	192.16	-1129.40	2.7157	1.4133
13254.00	150.11	-947.70	3.3545	2.0951
10603.00	123.09	-764.00	3.6234	2.8238
7950.00	95.04	-577.40	3.4151	3.5560
5284.00	63.83	-390.00	3.2256	5.0532
2647.00	31.98	-201.30	2.4610	7.6962
-5.00	-0.06	-11.40	1.5702	0.0000
-2683.00	-32.47	182.40	0.5796	-1.7350
-5342.00	-64.53	372.30	-0.1870	0.2898
-7973.00	-95.38	560.30	-0.9291	0.9641
-10646.00	-123.51	749.90	-1.3884	1.0796
-13297.00	-150.63	935.30	-1.4993	0.9337
-15951.00	-192.69	1120.90	-1.4367	0.7456
-18599.00	-224.53	1303.90	-1.0831	0.4820
-21256.00	-256.78	1480.20	0.5375	-0.2093
-23913.00	-288.87	1656.80	2.1062	-0.7291
-26559.00	-320.84	1826.40	4.7521	-1.4812
-26553.00	-320.77	1827.00	4.5759	-1.4266
-23918.00	-288.93	1653.80	1.3209	-0.6302
-21268.00	-256.92	1435.10	-0.1646	0.0641
-18603.00	-224.79	1308.40	-1.7522	0.7795
-15948.00	-192.66	1127.50	-2.6312	1.3657
-13289.00	-160.53	949.30	-3.9302	2.4482
-10640.00	-128.53	766.50	-4.3305	3.3691
-8001.00	-95.65	579.30	-3.3493	3.9826
-5337.00	-64.47	383.90	-3.1170	4.8347
-2686.00	-32.45	201.20	-2.6944	8.3040
-7.00	-0.08	7.70	-1.6075	0.0000

TABLEC4.1

x-direction gyro, pre-trial calibration

RATE TRANSFER TEST NO. 1 TYPE 406 GYRO #066 11 Sept 79
 TABLE NO. 339 R.T.S.F 32.78 MV/DEG/SEC
 SWITCH ON 1140 HOURS SWITCH OFF 1150 HOURS
 RUN UP TIME 0.0 SECS RUN DOWN TIME 0.0 SECS
 MAX TEMP 24.46 DEG C MIN TEMP 24.02 DEG C

TACHO MV	TABLE RATE DEG/SEC	GYRO OUTPUT MV	GYRO ERRORS DEG/SEC	%AGE ERRORS
27.00	0.33	11.00	-0.0739	0.0000
4670.00	55.41	-453.20	4.0439	7.1681
9325.00	112.55	-903.90	5.9142	6.1379
13943.00	163.49	-1359.50	9.5097	5.6439
18536.00	224.52	-1802.70	10.9642	4.9833
23227.00	230.59	-2235.60	11.0466	3.9370
27369.00	336.66	-2656.60	9.5734	2.8436
32507.00	392.69	-3052.30	5.1542	1.5697
37150.00	443.78	-3447.50	0.0488	0.0109
41757.00	504.43	-3803.40	-8.9094	-1.7464
46402.00	560.55	-4141.30	-21.6804	-3.8577
46423.00	560.80	-4145.20	-21.4931	-3.8326
41759.00	504.46	-3814.30	-8.0684	-1.5994
37154.00	443.33	-3456.30	1.1288	0.2515
32493.00	392.52	-3072.90	7.7082	1.9533
27354.00	336.60	-2668.90	11.2291	3.3360
23226.00	230.58	-2249.50	12.3615	4.5840
18532.00	224.47	-1817.30	12.9061	5.7495
13949.00	163.51	-1375.10	11.5209	6.8371
9304.00	112.39	-924.30	9.1553	8.1546
4669.00	55.40	-468.00	5.9755	10.5944
26.00	0.31	-2.50	1.6891	0.0000
-4634.00	-55.98	465.70	-2.7421	4.3934
-9244.00	-111.67	924.40	-6.5452	5.8512
-13923.00	-163.19	1376.90	-8.7106	5.1789
-18553.00	-224.18	1820.20	-10.2143	4.5562
-23192.00	-230.16	2255.00	-10.6276	3.7934
-27903.00	-337.13	2577.70	-8.4810	2.5156
-32464.00	-392.17	3096.60	-5.4775	1.6517
-37137.00	-443.62	3477.40	-0.7129	0.1589
-41773.00	-504.69	3344.20	7.7773	-1.5411
-46333.00	-559.71	4134.70	18.6407	-3.3304
-46424.00	-560.81	4139.10	19.1593	-3.4181
-41790.00	-504.93	3352.30	6.8722	-1.3613
-37163.00	-443.94	3483.60	-1.3515	0.4124
-32523.00	-392.95	3100.30	-7.5460	1.9204
-27843.00	-336.41	2693.50	-11.2551	3.3457
-23187.00	-230.10	2270.90	-12.7502	4.5520
-18543.00	-224.00	1836.10	-12.4577	5.5614
-13393.00	-167.90	1392.10	-10.9719	6.5347
-9259.00	-111.85	940.50	-3.4521	7.5566
-4626.00	-55.83	430.70	-4.7842	3.5611
26.00	0.31	12.10	-0.2045	0.0000

TABLE C4.2 y-direction gyro, pre-trial calibration

RATE TRANSFER TEST NO. 4 TYPE 401 GYRO #025 11 Sept 79
 TABLE NO. 339 R.T.S.F 82.78 MV/DEG/SEC
 SWITCH ON 1420 HOURS SWITCH OFF 1450 HOURS
 RUN UP TIME 0.0 SECS RUN DOWN TIME 0.0 SECS
 MAX TEMP 24.72 DEG C MIN TEMP 24.50 DEG C

PACED MV	TABLE RATE DEG/SEC	GYRO OUTPUT MV	GYRO ERRORS DEG/SEC	%AGE ERRORS
-9.00	-0.11	11.20	-0.4399	0.0000
3295.00	39.82	-133.30	0.4318	1.0845
6501.00	79.74	-273.40	1.1910	1.4936
9953.00	120.23	-422.00	1.1011	0.9153
13249.00	150.05	-564.90	1.4907	0.9314
16563.00	200.08	-705.30	1.3815	0.6905
19386.00	240.23	-843.10	0.9943	0.4141
23203.00	230.30	-983.60	0.4555	0.1625
25505.00	320.19	-1127.80	-0.2684	-0.0938
29335.00	350.41	-1265.90	-1.6400	-0.4550
33113.00	400.01	-1402.10	-2.9180	-0.7295
33124.00	400.14	-1403.30	-2.7133	-0.6781
29317.00	360.20	-1267.60	-0.9443	-0.2621
25513.00	320.23	-1130.00	0.2540	0.0793
23193.00	230.18	-991.20	1.3073	0.4668
19376.00	240.11	-851.30	2.0160	0.8395
16562.00	200.07	-710.30	2.3734	1.1838
13252.00	150.21	-563.50	2.3466	1.4647
9939.00	120.07	-425.80	2.3394	1.9484
6509.00	79.84	-282.30	2.1917	2.7451
3303.00	39.90	-137.70	1.4445	3.6203
-4.00	-0.05	7.00	0.6314	0.0000
-3364.00	-40.64	153.90	-0.0606	0.1490
-6503.00	-79.33	293.50	-1.5567	1.9501
-9975.00	-120.50	442.70	-1.4543	1.2069
-13295.00	-150.51	535.80	-1.6103	1.0026
-16618.00	-200.75	727.80	-1.4206	0.7075
-19935.00	-240.32	369.00	-1.0732	0.4477
-23245.00	-230.30	1009.00	-0.4327	0.1719
-25571.00	-320.98	1143.10	0.5592	-0.1742
-29873.00	-350.93	1235.80	1.7655	-0.4892
-33192.00	-400.97	1422.30	3.3940	-0.8455
-33195.00	-401.00	1423.60	3.0645	-0.7542
-29873.00	-350.37	1238.10	1.0580	-0.2932
-25564.00	-320.90	1150.90	-0.3132	0.0976
-23243.00	-230.34	1012.20	-1.3463	0.4795
-19944.00	-240.93	372.50	-1.9542	0.8111
-16617.00	-200.74	731.70	-2.5299	1.2603
-13297.00	-160.63	589.40	-2.5990	1.6180
-9979.00	-120.55	446.40	-2.4471	2.0299
-6555.00	-30.51	302.30	-2.0779	2.5808
-3353.00	-40.50	153.20	-1.4033	3.4645
-6.00	-0.07	11.60	-0.5837	0.0000

TABLE C4.3 z-direction gyro, pre-trial calibration

A AXIS R.T. NO. 4 TYPE 401 GYRO #024 29 Jan 80
 TABLE NO. 339 R.T.S.F 82.78 MV/DEG/SEC
 SWITCH ON 1100 HOURS SWITCH OFF 1433 HOURS
 RUN UP TIME 0.0 SECS RUN DOWN TIME 0.0 SECS
 MAX TEMP 24.56 DEG C MIN TEMP 24.22 DEG C

TACHO MV	TABLE RATE DEG/SEC	GYRO OUTPUT MV	GYRO ERRORS DEG/SEC	%AGE ERRORS
52.00	0.63	6.90	-1.2940	0.0000
2704.00	32.66	-187.90	-0.5358	-1.6404
5350.00	64.63	-382.50	0.2612	0.4041
8008.00	96.74	-575.40	0.6270	0.6482
10662.00	128.80	-767.30	0.8728	0.6777
13306.00	160.74	-957.80	1.0038	0.6245
15964.00	192.85	-1147.60	0.8477	0.4396
18614.00	224.86	-1335.00	0.3843	0.1709
21262.00	256.85	-1519.70	-0.5095	-0.1984
23916.00	288.91	-1701.70	-1.9304	-0.6682
26566.00	320.92	-1880.60	-3.8248	-1.1918
26568.00	320.95	-1880.20	-3.9163	-1.2202
23916.00	288.91	-1705.80	-1.2402	-0.4293
21264.00	256.87	-1526.70	0.6448	0.2510
18612.00	224.84	-1344.90	2.0751	0.9230
15962.00	192.82	-1159.80	2.9258	1.5173
13310.00	160.79	-971.80	3.3124	2.0601
10662.00	128.80	-783.20	3.5496	2.7559
8012.00	96.79	-592.50	3.4575	3.5723
5352.00	64.65	-400.40	3.2505	5.0276
2706.00	32.69	-207.40	2.7229	8.3296
54.00	0.65	-11.90	1.8468	0.0000
-2668.00	-32.23	190.10	0.7221	-2.2404
-5314.00	-64.19	384.70	-0.0749	0.1167
-7970.00	-96.28	579.30	-0.7511	0.7802
-10624.00	-128.34	772.20	-1.1653	0.9080
-13268.00	-160.28	963.30	-1.3973	0.8718
-15926.00	-192.39	1153.00	-1.2244	0.6364
-18576.00	-224.40	1340.80	-0.8283	0.3691
-21226.00	-256.41	1525.90	0.0224	-0.0087
-23884.00	-288.52	1708.00	1.4747	-0.5111
-26532.00	-320.51	1886.10	3.4797	-1.0857
-26534.00	-320.54	1883.90	3.8742	-1.2087
-23884.00	-288.52	1708.90	1.3232	-0.4586
-21226.00	-256.41	1529.10	-0.5164	0.2014
-18576.00	-224.40	1346.70	-1.8216	0.8117
-15926.00	-192.39	1161.00	-2.5712	1.3365
-13268.00	-160.28	972.80	-2.9966	1.8696
-10624.00	-128.34	784.00	-3.1519	2.4559
-7970.00	-96.28	592.80	-3.0239	3.1407
-5312.00	-64.17	399.90	-2.6580	4.1422
-2666.00	-32.21	206.60	-2.0799	6.4581
54.00	0.65	6.00	-1.1667	0.0000

TABLE C4.4

x-direction gyro, post-trial calibration

A AXIS R.T. NO. 4 TYPE 406 GYRO #066 29 Jan 80

TABLE NO. 339

R.T.S.F 82.78 MV/DEG/SEC

SWITCH ON 1715 HOURS

SWITCH OFF 1815 HOURS

RUN UP TIME 0.0 SECS

RUN DOWN TIME 0.0 SECS

MAX TEMP 24.50 DEG C

MIN TEMP 24.16 DEG C

TACHO MV	TABLE RATE DEG/SEC	GYRO OUTPUT MV	GYRO ERRORS DEG/SEC	%AGE ERRORS
106.00	1.28	14.20	1.1541	90.1315
4754.00	57.43	-463.80	5.1082	8.8948
9384.00	113.36	-932.40	8.0978	7.1434
14028.00	169.46	-1395.90	10.2769	6.0645
18664.00	225.47	-1850.60	11.4463	5.0767
23308.00	281.57	-2294.80	11.1987	3.9773
27946.00	337.59	-2727.50	9.5776	2.8370
32590.00	393.69	-3143.40	5.7716	1.4660
37226.00	449.70	-3537.60	-0.6662	-0.1481
41862.00	505.70	-3906.50	-10.2852	-2.0338
46506.00	561.80	-4247.60	-23.4964	-4.1823
46506.00	561.80	-4252.00	-22.9432	-4.0838
41864.00	505.73	-3914.00	-9.3663	-1.8521
37228.00	449.72	-3547.30	0.5293	0.1177
32590.00	393.69	-3154.60	7.1799	1.8237
27948.00	337.62	-2740.20	11.1503	3.3026
23310.00	281.59	-2309.40	13.0103	4.6203
18668.00	225.51	-1864.20	13.1080	5.8125
14030.00	169.49	-1410.30	12.0634	7.1177
9390.00	113.43	-946.80	9.8359	8.6711
4758.00	57.48	-478.20	6.8705	11.9534
114.00	1.38	0.10	2.8304	205.5271
-4632.00	-55.96	491.30	-1.5995	2.8586
-9262.00	-111.89	963.50	-5.0418	4.5061
-13906.00	-167.99	1433.50	-8.0382	4.7850
-18542.00	-223.99	1894.20	-9.9620	4.4475
-23186.00	-280.09	2347.70	-10.8838	3.8858
-27826.00	-336.14	2787.70	-10.1564	3.0215
-32472.00	-392.27	3211.90	-7.3699	1.8788
-37110.00	-448.30	3615.30	-2.0647	0.4606
-41750.00	-504.35	3993.80	6.3955	-1.2681
-46400.00	-560.52	4343.60	18.5853	-3.3157
-46400.00	-560.52	4346.70	18.1955	-3.2462
-41750.00	-504.35	3999.10	5.7291	-1.1359
-37112.00	-448.32	3623.50	-3.0716	0.6851
-32472.00	-392.27	3221.80	-8.6147	2.1961
-27826.00	-336.14	2798.60	-11.5270	3.4292
-23186.00	-280.09	2360.00	-12.4304	4.4380
-18540.00	-223.97	1908.50	-11.7842	5.2616
-13904.00	-167.96	1447.00	-9.7599	5.8107
-9260.00	-111.86	977.60	-6.8388	6.1136
-4628.00	-55.91	504.50	-3.3076	5.9162
110.00	1.33	14.30	1.0932	82.2714

TABLE C4.5

y-direction gyro, post-trial calibration

A AXIS R.T. NO. 5 TYPE 401 GYRO #025 29 Jan 80

TABLE NO. 339

R.T.S.F 82.78 MV/DEG/SEC

SWITCH ON 1550 HOURS

SWITCH OFF 1642 HOURS

RUN UP TIME 0.0 SECS

RUN DOWN TIME 0.0 SECS

MAX TEMP 24.29 DEG C

MIN TEMP 23.99 DEG C

TACHO MV	TABLE RATE DEG/SEC	GYRO OUTPUT MV	GYRO ERRORS DEG/SEC	%AGE ERRORS
54.00	0.65	9.50	0.6634	0.0000
3368.00	40.69	-140.20	1.7051	4.1909
6682.00	80.72	-287.40	2.0608	2.5531
9998.00	120.78	-432.50	1.8162	1.5038
13308.00	160.76	-577.80	1.6990	1.0568
16622.00	200.80	-722.80	1.4511	0.7226
19938.00	240.86	-866.50	0.8223	0.3414
23254.00	280.91	-1010.00	0.1387	0.0494
26568.00	320.95	-1152.60	-0.7678	-0.2392
29878.00	360.93	-1293.60	-2.0649	-0.5721
33180.00	400.82	-1433.40	-3.5946	-0.8968
33180.00	400.82	-1434.40	-3.3203	-0.8284
29876.00	360.91	-1295.70	-1.4645	-0.4058
26570.00	320.97	-1154.90	-0.1609	-0.0501
23254.00	280.91	-1012.20	0.7423	0.2642
19940.00	240.88	-869.30	1.5664	0.6503
16624.00	200.82	-725.30	2.1129	1.0521
13310.00	160.79	-579.70	2.1961	1.3659
10000.00	120.80	-434.30	2.2860	1.8923
6684.00	80.74	-289.30	2.5580	3.1681
3370.00	40.71	-141.60	2.0651	5.0726
56.00	0.68	7.00	1.3252	0.0000
-3332.00	-40.25	158.90	0.5738	-1.4255
-6646.00	-80.29	308.30	-0.3856	0.4803
-9960.00	-120.32	455.40	-0.7139	0.5934
-13270.00	-160.30	601.60	-0.8436	0.5263
-16584.00	-200.34	747.90	-0.9524	0.4754
-19904.00	-240.44	893.50	-0.7967	0.3313
-23220.00	-280.50	1038.50	-0.5246	0.1870
-26536.00	-320.56	1182.40	0.0493	-0.0154
-29848.00	-360.57	1324.70	1.0139	-0.2812
-33152.00	-400.48	1465.40	2.3208	-0.5795
-33152.00	-400.48	1466.20	2.1013	-0.5247
-29848.00	-360.57	1326.90	0.4102	-0.1138
-26536.00	-320.56	1185.40	-0.7739	0.2414
-23218.00	-280.48	1042.40	-1.6189	0.5772
-19904.00	-240.44	898.80	-2.2509	0.9361
-16584.00	-200.34	753.80	-2.5713	1.2835
-13270.00	-160.30	608.00	-2.5997	1.6217
-9958.00	-120.29	461.80	-2.4942	2.0734
-6644.00	-80.26	314.70	-2.1659	2.6985
-3330.00	-40.23	165.30	-1.2065	2.9991
54.00	0.65	13.40	-0.4067	0.0000

TABLE C4.6

z-direction gyro, post-trial calibration

Input (Gn)	Output (Volts)		Output (Volts)	
	Increasing	Decreasing	Increasing	Decreasing
-3.00000	-2.57580	-2.57244	-2.43793	-2.43625
-2.70000	-2.32234	-2.31604	-2.18910	-2.18657
-2.40000	-2.06174	-2.05501	-1.94110	-1.93942
-2.10000	-1.80533	-1.79987	-1.69478	-1.69310
-1.80000	-1.55061	-1.54473	-1.45015	-1.44763
-1.50000	-1.29715	-1.29210	-1.20552	-1.20300
-1.20000	-1.04327	-1.03822	-.96088	-.95836
-.90000	-.79023	-.78560	-.71625	-.71373
-.60000	-.53635	-.53130	-.47077	-.46909
-.30000	-.28162	-.27868	-.22614	-.22530
0.00000	-.02606	-.02438	.01934	.01892
.30000	.22698	.23034	.26313	.26061
.60000	.48044	.48464	.50230	.50608
.90000	.73306	.73811	.74525	.74903
1.20000	.98694	.99241	.99199	.98736
1.50000	1.23998	1.24713	1.23410	1.22948
1.80000	1.49471	1.50185	1.47621	1.47201
2.10000	1.75111	1.75867	1.71874	1.71496
2.40000	2.00877	2.01760	1.96296	1.95959
2.70000	2.26896	2.27737	2.20801	2.20591
3.00000	2.53125	2.53965	2.45517	2.45517

x-direction accelerometer

y-direction accelerometer

Input (Gn)	Output (Volts)	
	Increasing	Decreasing
-6.00000	-2.56361	-2.56235
-5.40000	-2.30847	-2.30343
-4.80000	-2.05165	-2.04702
-4.20000	-1.79693	-1.79188
-3.60000	-1.54262	-1.53842
-3.00000	-1.28958	-1.28538
-2.40000	-1.03528	-1.03150
-1.80000	-.78098	-.77762
-1.20000	-.52584	-.52289
-.60000	-.26985	-.26733
0.00000	-.01009	-.00757
.60000	.24590	.24968
1.20000	.50020	.50440
1.80000	.75324	.75660
2.40000	1.00544	1.00754
3.00000	1.25680	1.25932
3.60000	1.50816	1.51152
4.20000	1.76036	1.76372
4.80000	2.01256	2.01760
5.40000	2.26602	2.27106
6.00000	2.52200	2.52620

z-direction accelerometer

TABLE C4.7 Accelerometer pre-trial calibrations

Input (Gn)	Output (Volts)		Output (Volts)	
	Increasing	Decreasing	Increasing	Decreasing
-3.00000	-2.57748	-2.57244	-2.48165	-2.47660
-2.70000	-2.31923	-2.31116	-2.22440	-2.21734
-2.40000	-2.05997	-2.05190	-1.96817	-1.96010
-2.10000	-1.80172	-1.79264	-1.71294	-1.70790
-1.80000	-1.54548	-1.53842	-1.45973	-1.45671
-1.50000	-1.29126	-1.28420	-1.20854	-1.20552
-1.20000	-1.03503	-1.02898	-.95836	-.95432
-.90000	-.78182	-.77577	-.70717	-.70515
-.60000	-.52760	-.52054	-.45699	-.45497
-.30000	-.27238	-.26733	-.20680	-.20680
0.00000	-.01513	-.01513	.04237	.04237
.30000	.23707	.24211	.28953	.28953
.60000	.49129	.49835	.53870	.53870
.90000	.74651	.75256	.78686	.78686
1.20000	1.00073	1.00678	1.03402	1.03402
1.50000	1.25495	1.26100	1.28319	1.28319
1.80000	1.51219	1.51824	1.53237	1.53539
2.10000	1.76944	1.77549	1.78255	1.78860
2.40000	2.02971	2.03576	2.03475	2.04181
2.70000	2.28695	2.29300	2.28897	2.29502
3.00000	2.55731	2.56235	2.54722	2.55126

x-direction accelerometer

y-direction accelerometer

Input (Gn)	Output (Volts)	
	Increasing	Decreasing
-6.00000	-2.52805	-2.52503
-5.40000	-2.27283	-2.26778
-4.80000	-2.01760	-2.01356
-4.20000	-1.76388	-1.76036
-3.60000	-1.51118	-1.50916
-3.00000	-1.25797	-1.25797
-2.40000	-1.00880	-1.00779
-1.80000	-.75660	-.75660
-1.20000	-.50440	-.50440
-.60000	-.25422	-.25321
0.00000	-.00202	-.00101
.60000	.25119	.25220
1.20000	.49936	.50036
1.80000	.75055	.75156
2.40000	.99972	1.00073
3.00000	1.24990	1.25091
3.60000	1.50109	1.50109
4.20000	1.75128	1.75229
4.80000	2.00247	2.00449
5.40000	2.25467	2.25769
6.00000	2.50989	2.50989

z-direction accelerometer

TABLE C4.8 Accelerometer post-trial calibrations

Channel	Zero offset LSB $\pm \frac{1}{2}$	Scale Factor mV/LSB
0	2063	1.2469
1	2060	1.2571
2	2052	1.2508
3	2070	1.2453
4	2055	1.2407
5	2069	1.2555
6	2065	2.6631
7	2064	3.2949
8	2064	1.2180
9	2064	1.2180
10	2064	1.2180
11	2064	1.2180
12	2064	1.2180
13	2064	1.2180
14	2058	2.5221
15	2065	3.2895

Table C4.9 Data acquisition system calibration

REFERENCES

1. Ewing, E.G., Bixby, H.W. and Knacke, T.W., "Recovery Systems Design Guide", USAF Flight Dynamics Laboratory, Wright-Patterson AFB, Ohio, AFFDL-TR-78-151, Dec. 1978.
2. Gibbs-Smith, C.H., *Sir George Cayley's Aeronautics 1796-1855*, HMSO, London, 1962.
3. Tory, A.C., "Computer Simulation of a Free-Falling Fully Deployed Parachute System", Univ. of Leicester Engineering Dept., Report 72-24, Oct. 1972.
4. Tory, A.C. and Ayres, R.M., "Computer Model of a Fully Deployed Parachute", *Journal of Aircraft*, Vol. 14, July 1977, pp.675-679.
5. Green, G., *Mathematical Papers*, 1833, p.315.
6. Heinrich, H.G., "Experimental Parameters in Parachute Opening Theory", *Shock and Vibration Bulletin*, No.19, Dept. of Defence, Feb. 1953.
7. Birkhoff, G., *Hydrodynamics - A Study in Logic, Fact and Similitude*, 2nd Edn., Princeton Univ. Press, 1960, pp.148-178.
8. Luneau, J.L., "Sur L'Influence de l'Acceleration sur la Resistance au Mouvement dans les Fluides", *Publ. Sci. Min. Air.*, No.363, Paris 1950.
9. Iversen, H.W. and Balent, R., "A Correlating Modulus for Fluid Resistance in Accelerated Motion", *Jour. App. Physics*, Vol.22, 1951, pp.324-328.
10. Bugliarello, G., "La Resistenza al Moto Accelerato di Sfere in Acqua", *Ricerca Scientifica*, Vol.26, 1956, pp.437-461.
11. Eaton, J.A. and Cockrell, D.J., "The Validity of the Leicester Computer Model for a Parachute with Fully-Deployed Canopy", AIAA Paper 79-0460, March 1979.
12. Brodetsky, S., "The Stability of the Parachute", *The Tohoku Mathematical Journal*, Vol.14, 1918, pp.116-123.
13. Bryan, G.H., *Stability in Aviation*, MacMillan, London, 1911.
14. Nayler, J.L., "The Stability of Parachutes in Rectilinear Motion"; also Glauert, H.B. and Gates, S.B., "The Stability of a Parachute", both in *Aero. Research Comm.*, R & M No.862, compiled by R. Jones, London, June 1923, pp.50-62.
15. Jones, R. and Williams, "Experiments on Parachute Models", Advisory Comm. for Aeron., T. Nos.1354, 1389 and 1418 (unpublished), in *Aero. Research Comm.*, R & M No.862, compiled by R. Jones, London, June 1923, pp.28-50.
16. Jones, R., "Experiments on Rigid Parachute Models", *Aero. Research Comm.*, R & M No.2520, London, Nov. 1943.
17. Henn, N., "Die Absinkseigenschaften von Fallschirmen", *ZWB - U & M No.6202*, Berlin, Oct. 1944.
18. Kirchhoff, G., "Über die Bewegung eines Rotationskörpers in einer Flüssigkeit", *Grelles Jour.*, Vol.71, 1869, pp.237-273.
19. Lamb, H., *Hydrodynamics*, 6th Edn., Cambridge Univ. Press, 1932.
20. Lester, W.G.S., "A Note on the Theory of Parachute Stability", *Aero. Research Council*, London, R & M No. 3352, 1962.

21. Shilov, A.A., "The Stability of Motion of a Parachute in the Steady-State Reduction Mode", *Uchenyye Zapiski TsAGI*, Vol.2, No.4, 1971, pp.76-83 (Translation FTD-MT-24-465-75, Jan. 1975).
22. Byushgens, A.G. and Shilov, A.A., "The Dynamic Model of a Parachute and Determination of its Characteristics", *Uchenyye Zapiski TsAGI*, Vol.3, No.4, 1972, pp.49-58 (Translation FTD-MT-24-510-75, Jan. 1975).
23. Shilov, A.A., "An Analysis of the Plane Slightly Damped Oscillations of a Parachute in Free Steady Descent", *Uchenyye Zapiski TsAGI*, Vol.4, No.1, 1973, pp.137-143 (Translation FTD-MT-24-510-75, Jan. 1975).
24. Eaton, J.A., "Added Fluid Mass and the Equations of Motion of a Parachute", to be published in the *RAeS Aero. Quarterly*.
25. Ludwig, R. and Heins, W., "Theoretische Untersuchungen zur Dynamischen Stabilität von Fallschirmen", *Jahrbuch 1962 der WGLR*, pp.224-230; also "Investigations on the Dynamic Stability of Personnel Guide Surface Parachutes, AGARD Report 444, April 1963.
26. Wolf, D.F., "An Investigation of Parachute Dynamic Stability", M.Sc. Thesis, University of Rhode Island, 1965.
27. Schulz, W. and Hamel, P., "Einige neuere Ergebnisse der Flugmechanik", *Jahrbuch 1970 der WGLR*, pp.9-29.
28. Hume, R.G., "A Two-Dimensional Mathematical Model of a Parachute in Steady Descent", *RAE Tech. Report 73040*, April 1973.
29. Doyle, G.R., and Burbrick, J.W., "Dynamics of Two Bodies Connected by an Elastic Tether - Six Degrees of Freedom Forebody and Five Degrees of Freedom Decelerator", *NASA CR-12026*, April 1974.
30. Heinrich, H.G. and Haak, E.L., "Stability and Drag of Parachutes with Varying Effective Porosity", *Wright-Patterson AFB, Ohio, ASD-TDR-62-100*, Sept. 1962.
31. Heinrich, H.G. and Haak, E.L., "Stability and Drag of Parachutes with Varying Effective Porosity", *Wright-Patterson AFB, Ohio, AFFDL-TR-71-58*, Feb. 1971.
32. Heinrich, H.G., "Drag and Stability of Parachutes", *Aero. Eng. Review*, Vol.15, June 1956, pp.73-81.
33. Ayres, R.M., "The Simulation of the Decent Characteristics of Fully Inflated Subsonic Parachutes", *University of Leicester Engineering Department Report 74-14*, July 1974.
34. White, F.M. and Wolf, D.F., "A Theory of Three-Dimensional Parachute Dynamic Stability", *Journal of Aircraft*, Vol.5, Jan-Feb. 1968, pp.86-92.
35. Ibrahim, S.K., "Experimental Determination of the Apparent Moment of Inertia of Parachutes", *Wright-Patterson AFB, Ohio, AFFDL-TDR-64-153*, April 1965.
36. Ibrahim, S.K., "Apparent Added Mass and Moment of Inertia of Cup-Shaped Bodies in Unsteady Incompressible Flow", *Ph.D. Thesis, University of Minnesota, Minneapolis*, May 1965.
37. Ayres, R.M., "The Aerodynamic Behaviour of Fully Inflated Parachutes", *Aeronautical Jour.*, Vol.82, Jan. 1978, pp.38-44.
38. Huntley, I.D., "The Distinction between Apparent Mass and Included Mass of Parachute Models", *University of Leicester Engineering Department Report 75-2*, Feb. 1975.

39. Cockrell, D.J., Huntley, I.D. and Ayres, R.M., "Aerodynamic and Inertial Forces on Model Parachute Canopies", AIAA Paper 75-1371, Nov. 1975.
40. Cockrell, D.J. and Eaton, J.A., "Aerodynamic Modelling of Fully-Deployed Parachute Canopies", Research Progress Report for Aero. Research Council Meeting, 21st May 1976.
41. Eaton, J.A., "Sensitivity Analysis of the Leicester Parachute Model", University of Leicester Engineering Department Report 76-20, Nov. 1976.
42. Neustadt, M., *et al.*, "A Parachute Recovery System Dynamic Analysis", *Journal of Aircraft*, Vol.4, March 1967, pp.321-326.
43. Wolf, D.F., "Dynamic Stability of Non-rigid Parachute and Payload System", *Journal of Aircraft*, Vol.8, August 1971, pp.603-609.
44. Eaton, J.A., Research Progress Report, University of Leicester, March 1980.
45. Eaton, J.A., private communication to D.R. Dennis, RAE Farnborough, April 1980.
46. Eaton, J.A., private communication to K.-F. Doherr. DFVLR Braunschweig, Jan. 1981.
47. Churkin, V.M. and Kosarchuk, N.A., "On Free Periodic Parachute System Oscillations in the Axial Plane", *Izv. VUZ. Av. Tekh.*, Vol.21, No.2, 1978, pp.144-146 (Translation by Allerton Press, N.Y., 1978).
48. Goodrick, T.F., "Theoretical Study of the Longitudinal Stability of High-Performance Gliding Airdrop Systems", AIAA Paper 75-1394, Nov. 1975.
49. Goodrick, T.F., "Simulation Studies of the Flight Dynamics of Gliding Parachute Systems", AIAA Paper 79-0417, March 1979.
50. Vaughn, H.R. and Matejka, D.Q., "Dynamic Analysis of the SAND Sampler", SC-RR-65-286, Vol.III, Sandia Laboratories, Albuquerque, New Mexico, Sept. 1965.
51. Talay, T.A., "Parachute-Deployment-Parameter Identification Based on an Analytical Simulation of Viking BLDT AV-4", NASA TN D-7678, April 1974; also Talay, T.A., *et al.*, "An Advanced Technique for the Prediction of Decelerator System Dynamics", AIAA Paper 73-460, May 1973.
52. Gamble, J.D., "A Mathematical Model for Calculating the Flight Dynamics of a General Parachute-Payload System", NASA TN D-4859, 1968.
53. Ibrahim, S.K. and Engdahl, R.A., "Parachute Dynamics and Stability Analysis", NASA CR-120326, 1974.
54. Bolton, W.R., "Trajectory Simulation of a Parachute System", AIAA Paper 79-0470, March 1979.
55. Schatzle, P.R. and Curry, W.H., "Flight Simulation of a Vehicle with a Two-Stage Parachute System", AIAA Paper 79-0448, March 1979.
56. Wolf, D.F. and Spahr, H.R., "A Parachute Cluster Dynamic Analysis", AIAA Paper 75-1398, Nov. 1975.
57. Wolf, D.F. and Spahr, H.R., "Parachute Cluster Dynamic Analysis", *Journal of Aircraft*, Vol.14, No.4, April 1977, pp.321-322.
58. Drake, V.N., "Comparative Ejection Trials 1972 using Aeroconical and I24 Parachutes", A & AEE Note No.3137, Dec. 1973.

59. Stimler, F.J. and Ross, R.S., "Drop Tests of 16,000 sq.in. Model Parachutes", Vol.VIII, AF-TR-5867, May 1954.
60. Cockrell, D.J. and Eaton, J.A., "Parachute Aerodynamic Inputs caused by Angular Motion", University of Leicester Engineering Department Report 77-8, May 1977.
61. Cockrell, D.J., Eaton, J.A. and Morgan, C.J., "Longitudinal Oscillation Damping for Fully-Inflated Parachute Canopies", AIAA Paper 79-0459, March 1979.
62. Sedov, L.I., *Two-Dimensional Problems in Hydrodynamics and Aerodynamics*, J. Wiley and Sons, New York, 1965, pp.14-35.
63. Doherr, K.-F., "Dreikomponentenmessungen an Fallschirmmodellen zur Ermittlung der statischen Stabilität", DLR FB 68-50, Braunschweig, March 1968.
64. Solt, G.A., "Performance and Design Criteria for Deployable Aerodynamic Decelerators", USAF Flight Dynamics Laboratory, Ohio, ASD-TR 61-579, Dec. 1963.
65. Etkin, B., *Dynamics of Flight*, J. Wiley and Sons, New York, 1959.
66. Von Kármán, T., "Note on the Analysis of the Opening Shock of Parachutes at Various Altitudes", AIT 200-814, Army Air Corps Scientific Advisory Group, August 1945.
67. Hoerner, S.F., *Fluiddynamic Drag*, published by the author, 1965.
68. Pepper, W.B. and Maydew, R.C., "Aerodynamic Decelerators - an Engineering Review", *Journal of Aircraft*, Vol.8, No.1, Jan. 1971, pp.3-19.
69. Eaton, J.A., "Validation of a Computer Model of a Parachute", University of Leicester Engineering Department Report 81-6, April 1981.
70. Eaton, J.A., "Wind-Free Parachute Drop Tests", DFVLR Parachute Symposium, Braunschweig, August 1977.
71. Eaton, J.A., "Wind-Free Parachute Trials", RAE Parachute Conference, Royal Aircraft Establishment, Farnborough, November 1977.
72. Cockrell, D.J. and Eaton, J.A., "Can Telemetry be Avoided?", Telemetry Systems Symposium, The Royal Aeronautical Society, London, January 1978.
73. Eaton, J.A., and Cockrell, D.J., "An Experimental Technique for Data Acquisition from Parachutes in Flight", AIAA Paper 79-0439, March 1979.
74. Fernandez, M. and Macomber, G.R., *Inertial Guidance Engineering*, Prentice-Hall, 1962.
75. Synge, J.L. and Griffith, B.A., *Principles of Mechanics*, 3rd Edn., McGraw-Hill, 1970.
76. Andrews, T.F., "Calibration of the Rate Transfer Characteristics of a Rate Sensor", DGON Symposium on Gyro Technology: RAE Tech. Memo RAD-NAV 31, 1976.
77. Bent, R.G., "Rate Sensor Testing and Precision Motion Systems", *Wireless World*, August 1977, pp.55-58.
78. Smiths Aerospace Industries Ltd., "Specification No.S.6027, Transducer, Acceleration, Linear Inductive Type AL-V-692", 1976.
79. Lingard, J.S., "The Aerodynamics of Parachutes during the Inflation Process", Ph.D. Thesis, University of Bristol, 1978.

80. Smith, R.A. and Evbouma, S.N., "Nose Pressure Distribution and Separation on an Inclined Axisymmetric Body", *AIAA Journal*, Vol.11, No.1, Jan. 1973, pp.125-126.
81. Burr-Brown Research Corporation, "User's Manual for the SDM 853 Data Acquisition System PDS-358", September 1976.
82. Numerical Algorithms Group, *NAG FORTRAN Library Manual*, Mark 6, Oxford, May 1977.
83. Beauchamp, K.G., *Signal Processing Using Analog and Digital Techniques*, George Allen & Unwin, London 1973.
84. Duncan, W.J., Thom, A.S., and Young, A.D., *Mechanics of Fluids*, 2nd Edn., Edward Arnold, London 1970.
85. Smiths Aerospace Industries Ltd., "Rate Gyroscopes", Publication No. SAV 254V.
86. Ross, A.J., "Application of Parameter Identification Techniques to Analysis of Flight Data", *Prog. Aero. Sci.*, Vol.18, 1979, pp.325-350.
87. Brown, W.D., *Parachutes*, Pitman & Sons Ltd., London 1951.
88. Lingard, J.S., "A Semi-Empirical Theory to Predict the Load-Time History of an Inflating Parachute", *RAE TR 79141*, Nov. 1979.
89. Payne, P.R., "The Theory of Fabric Porosity as Applied to Parachutes in Incompressible Flow", *RAeS Aero Quarterly*, Vol.29, No.3, 1978, pp.175-206.
90. Eaton, J.A., private communication to K.-F. Doherr, DFVLR Braunschweig, Jan. 1979.
91. Doherr, K.-F., "Theoretisch-experimentelle Untersuchung des dynamischen Verhaltens von Fallschirm - Last-Systemen bei Windkanalversuchen", *DFVLR 81-29*, Braunschweig, 1981.
92. Hume, R.G. and Stevens, G.W., "Observations on Breathing and Related Phenomena in some Paratroop Type Parachutes when Freely Descending", *ARC 33749*, London, 1972.
93. Stanton, T.E., and Marshall, D. "Eddy Systems behind Discs", *Aero. Research Comm.*, R & M No.1358, Jan. 1930.
94. Fail, R., Lawford, J.A. and Eyre, R.C.M., "Low-Speed Experiments on the Wake Characteristics of Flat Plates normal to an Air Stream", *Aero. Research Council No.3120*, June 1957.
95. Willmarth, W.W., Hawk, N.E. and Harvey, R.L., "Steady and Unsteady Motions and Wakes of Freely Falling Disks", *Physics of Fluids*, Vol.7, No.2, Feb. 1964.
96. Calvert, J.R., "Experiments on the Flow Past an Inclined Disk", *J. Fluid Mech.*, Vol.29, 4, 1967, pp.691-703.
97. Roos, F.W. and Willmarth, W.W. "Some Experimental Results on Sphere and Disk Drag", *AIAA Journal*, Vol.9, No.2, Feb. 1971, pp.285-291.
98. Roberts, J.B., "Coherence Measurements in an Axisymmetric Wake", *AIAA Journal*, Vol.11, No.11, Nov. 1975, pp.1569-1571.

99. Calvert, J.T. "Experiments on the Low-Speed Flow Past Cones", *J. Fluid Mech.*, Vol.27, 2, 1967, pp.273-389.
100. Newton, I., *Principia*, Book 2, Section 7, 3rd Edn., Cambridge 1726.
101. Willmarth, W.W. and Enlow, R.L., "Aerodynamic Lift and Moment Fluctuations of a Sphere", *J. Fluid Mech.*, Vol.36, 3, 1969, pp.417-432.
102. Achenbach, E., "Vortex Shedding from Spheres", *J. Fluid Mech.*, Vol.62, 2, 1974, pp.209-221.
103. Pao, H-S. and Kao, T.W. "Vortex Structure in the Wake of a Sphere", *Physics of Fluids*, Vol.20, No.2, Feb. 1977, pp.187-191.

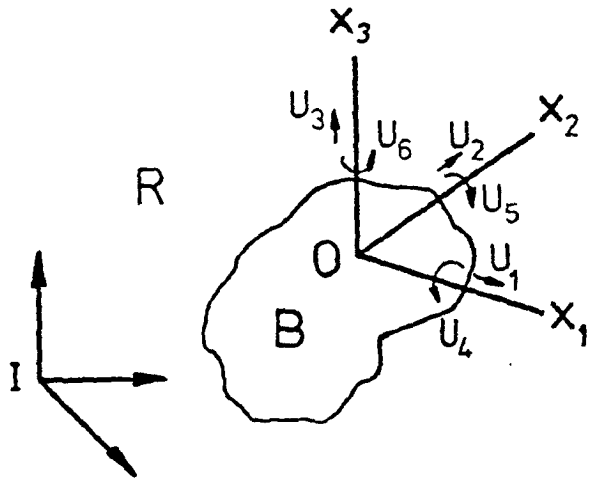


FIGURE 1.1 Coordinate systems

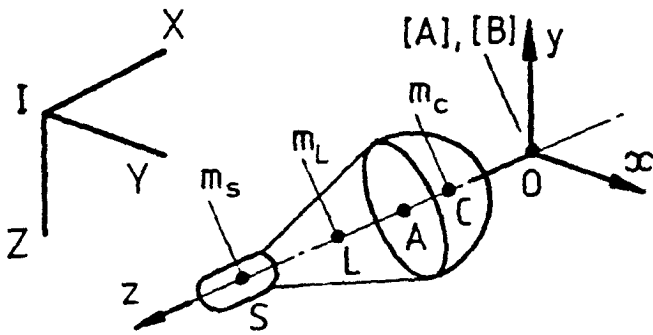
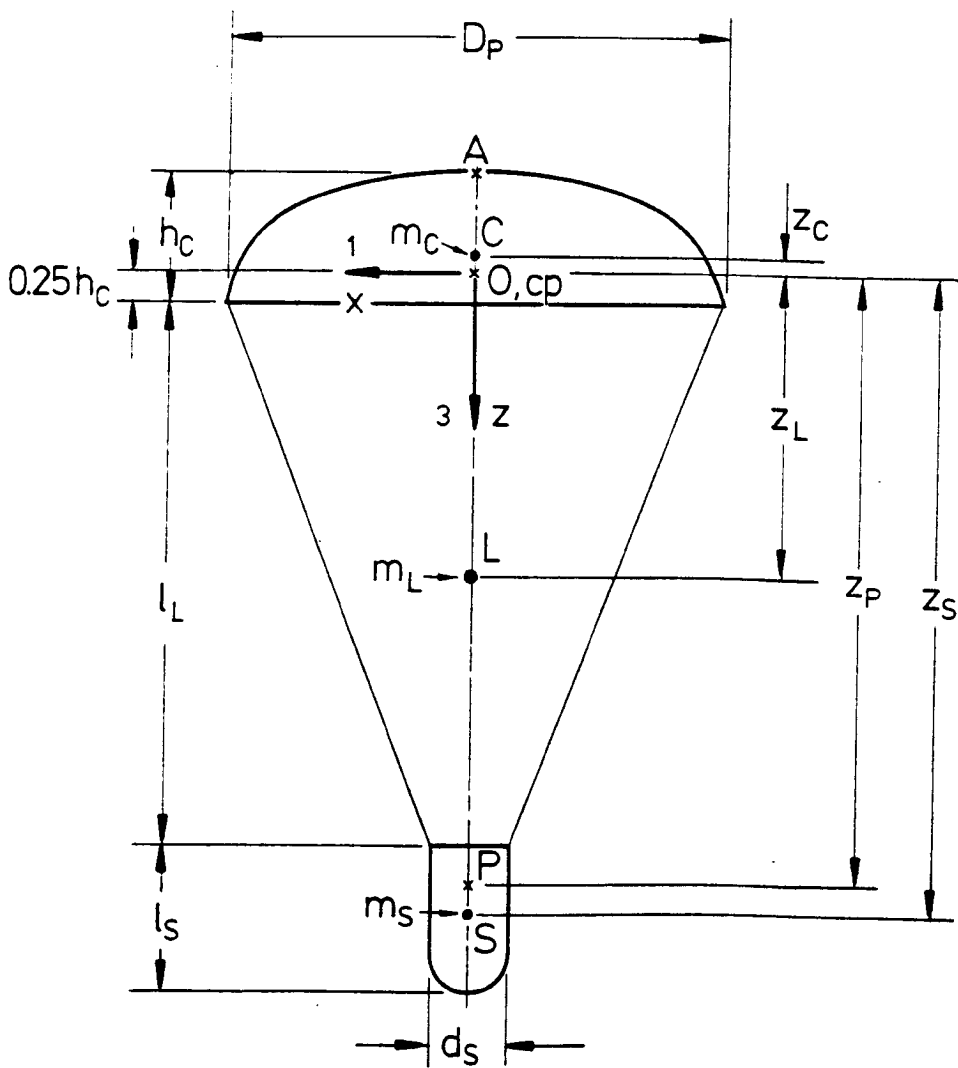
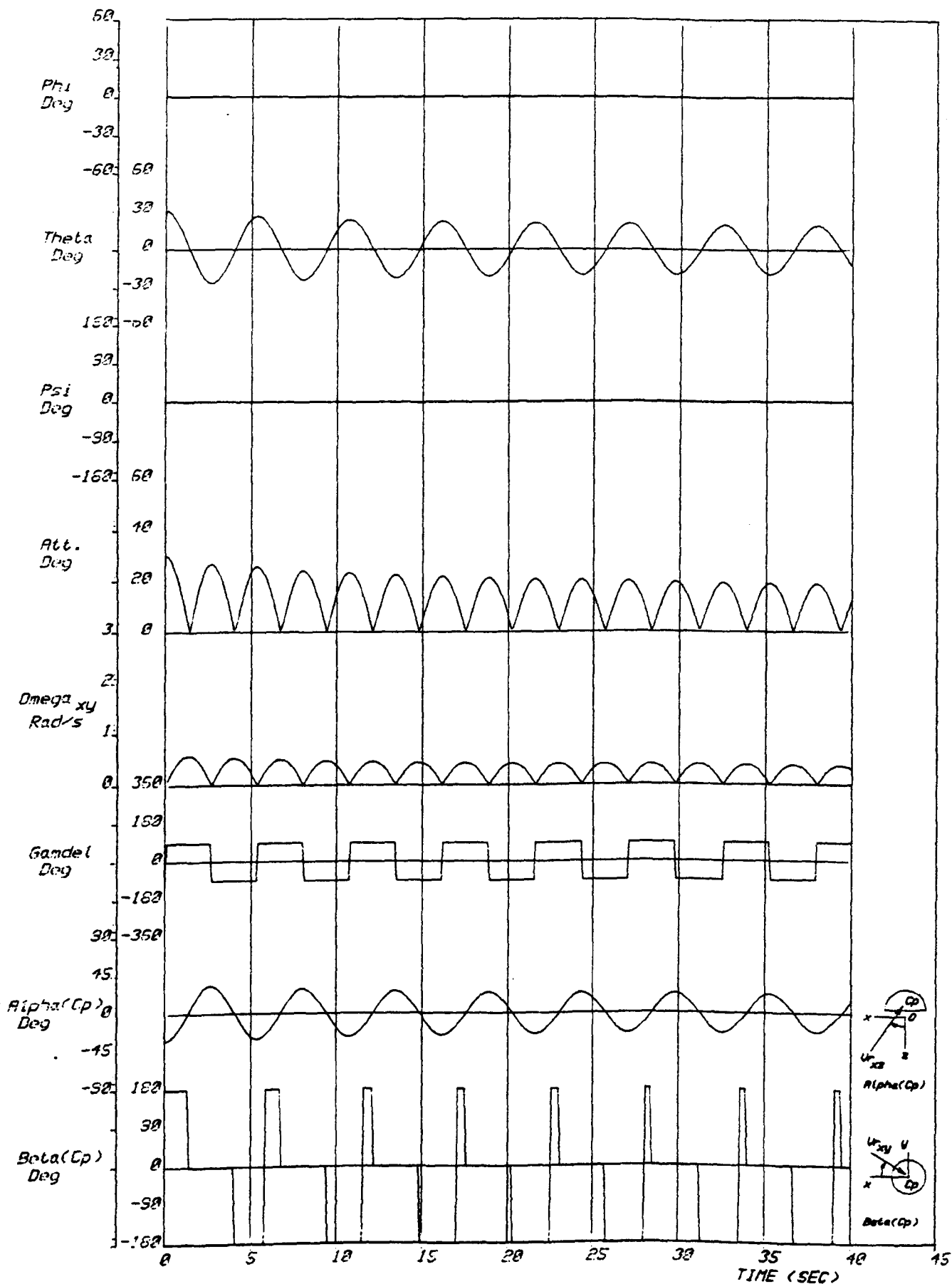


FIGURE 1.2 System geometry and coordinate frames



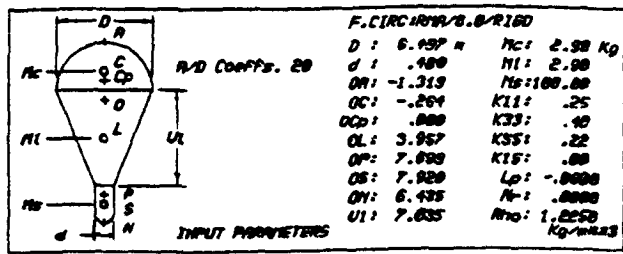
D_P	6.50	m	m_C	2.90	kg
d_s	0.48		m_L	2.90	
h_c	1.76		m_S	100.00	
l_L	7.04		e_o	1.225	kgm^{-3}
l_s	0.96		K_{11}	0.25	-
z_C	0.26		K_{33}	0.40	
z_L	3.96		K_{55}	0.22	
z_S	7.92		K_{15}	0.0	
z_P	7.70		l_p	-0.08	

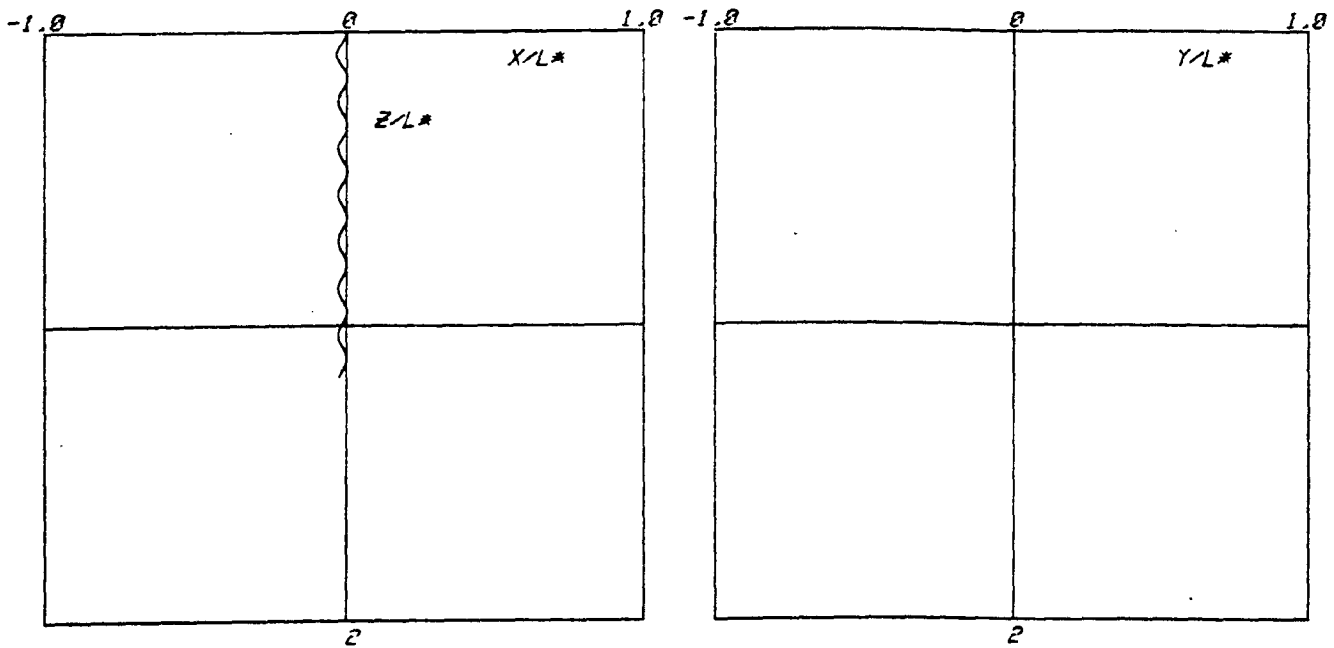
FIGURE 2.1 Input parameters for baseline case



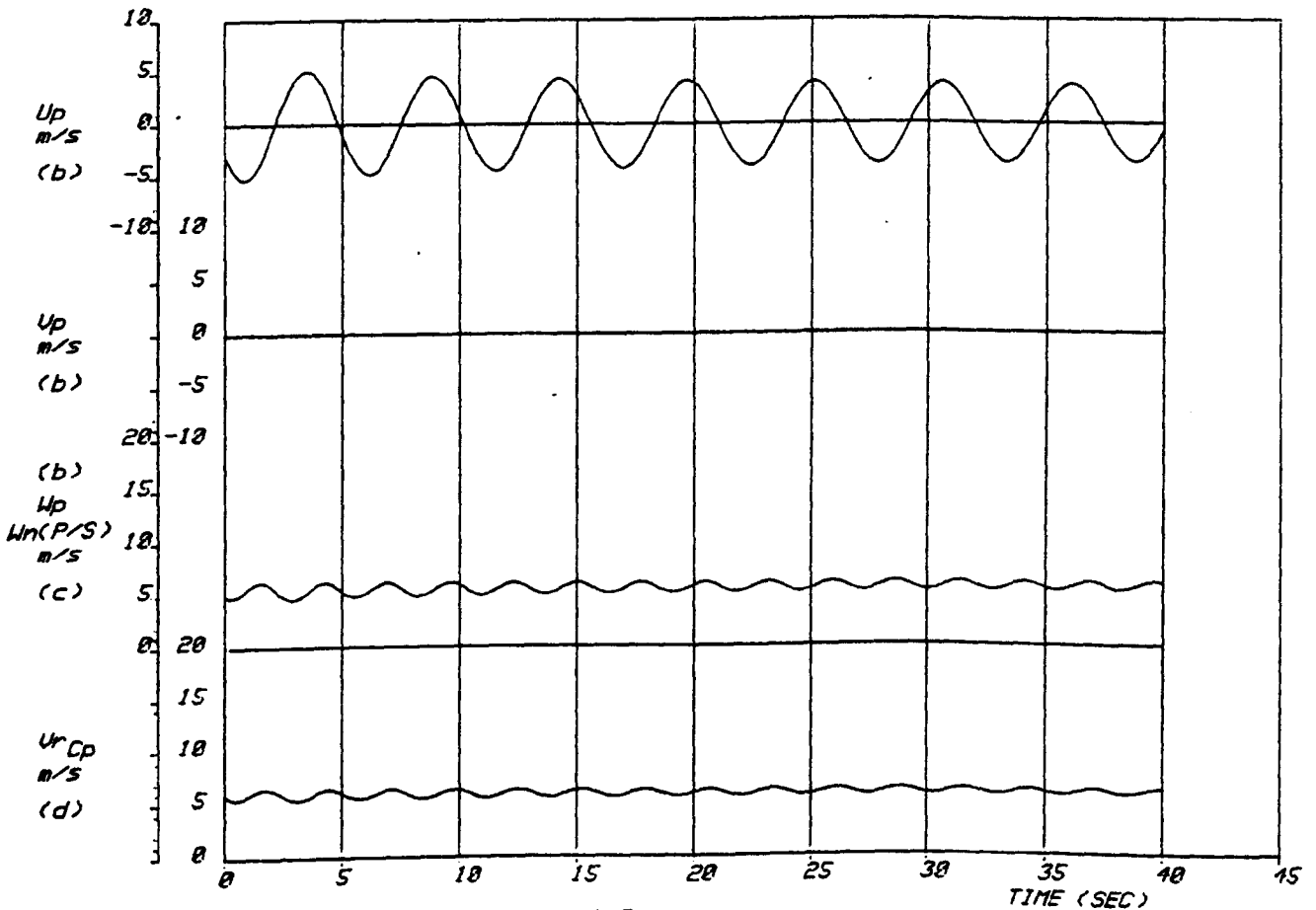
Results of baseline run

FIG. 2.2



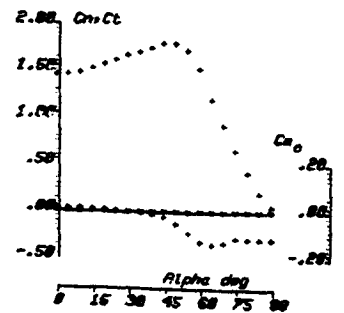


(a) Spatial trajectory of point P ($L^*=200.0m$)



(b) Velocity components along body axes at P
 (c) airspeed along z at N
 (d) resultant airspeed at canopy Cp

Results of baseline run



F.CIRC 001/0.0/RT00
 A/D Coeffs. 20 used
 For simulation

FIG.	
2.3	

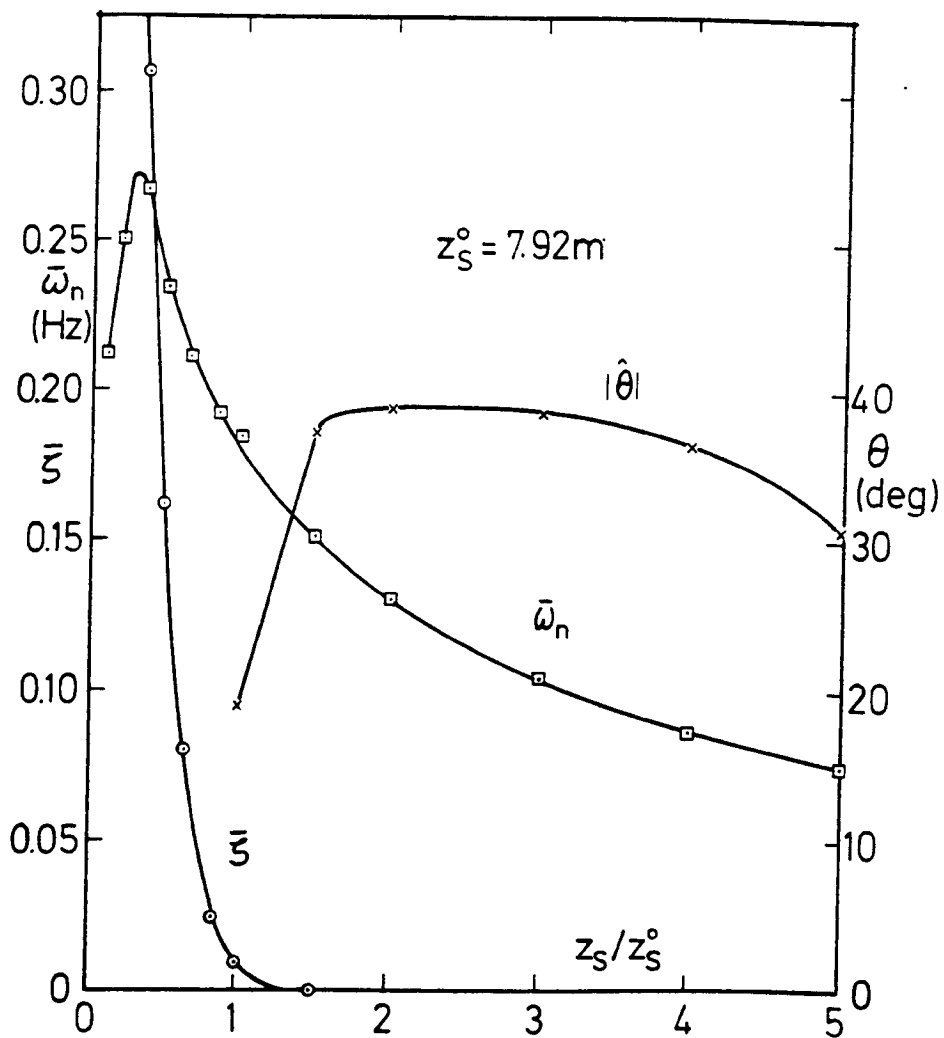


FIGURE 2.4 Effect of variation in the line length on stability

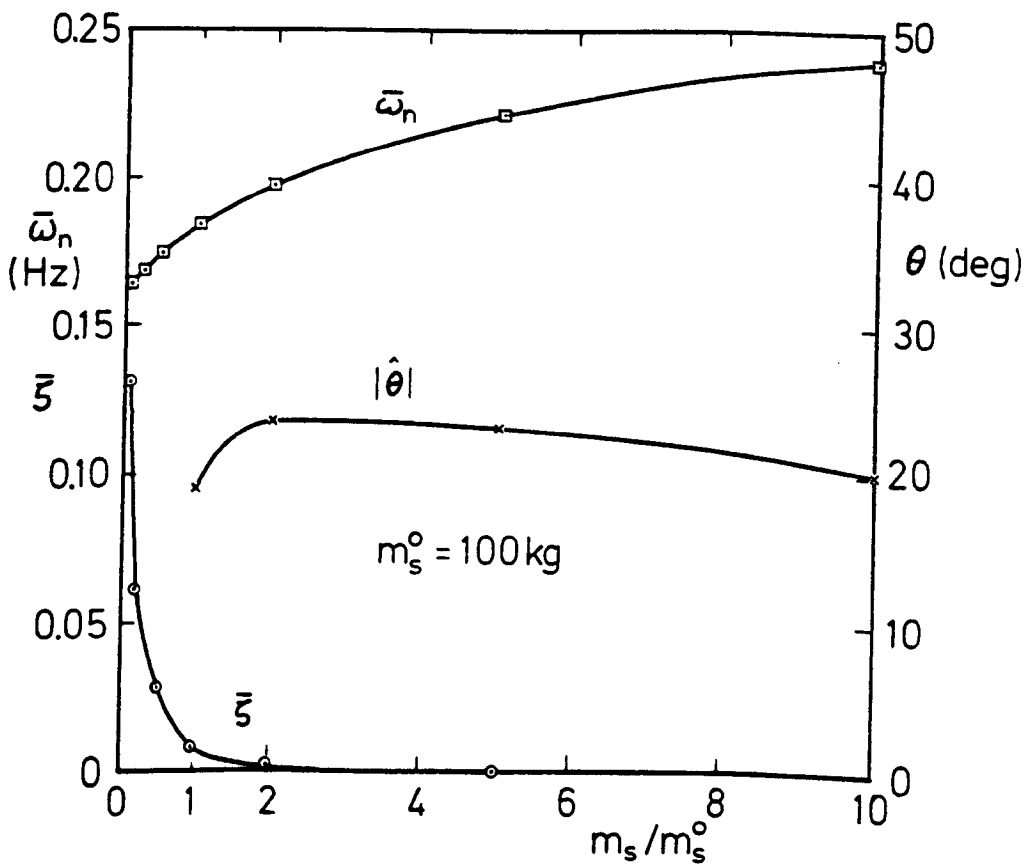


FIGURE 2.5 Effect of variation in the store mass on stability

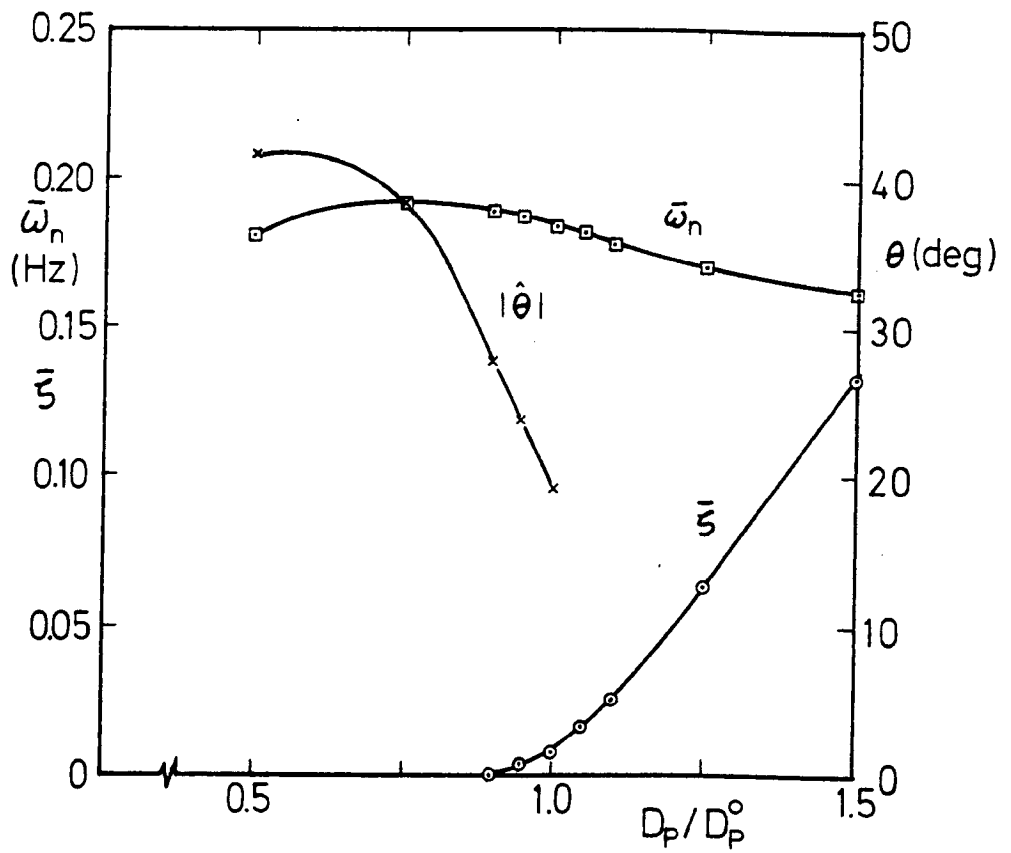


FIGURE 2.6 Effect of variation in the canopy diameter on stability

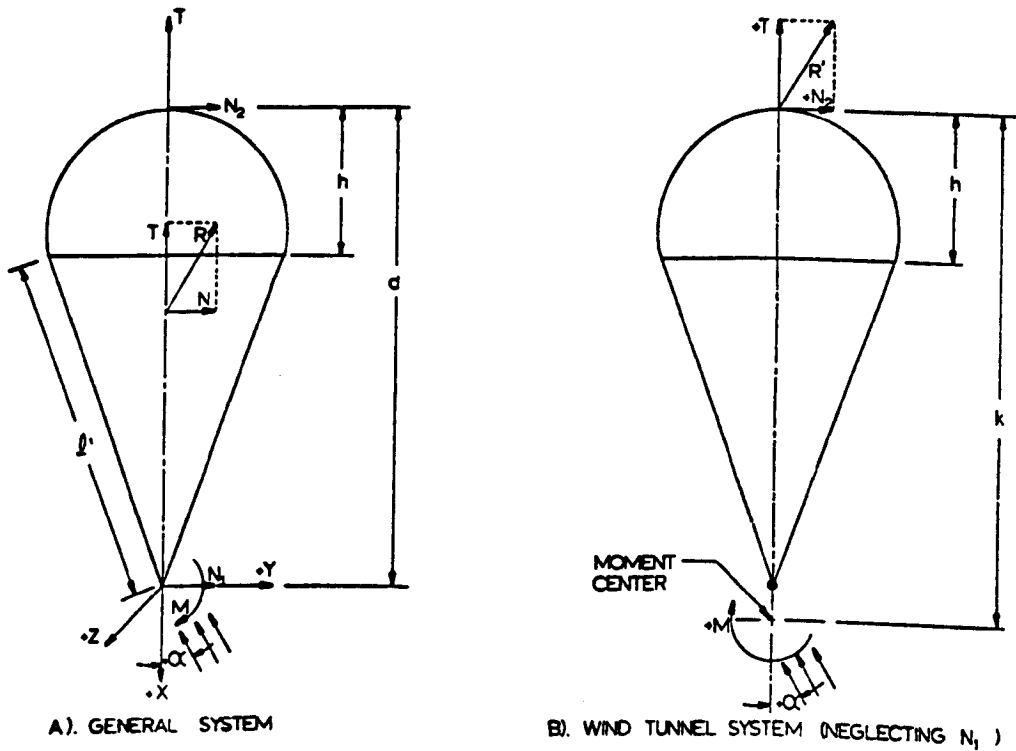


FIGURE 2.7 Force components measured by Heinrich and Haak[31]

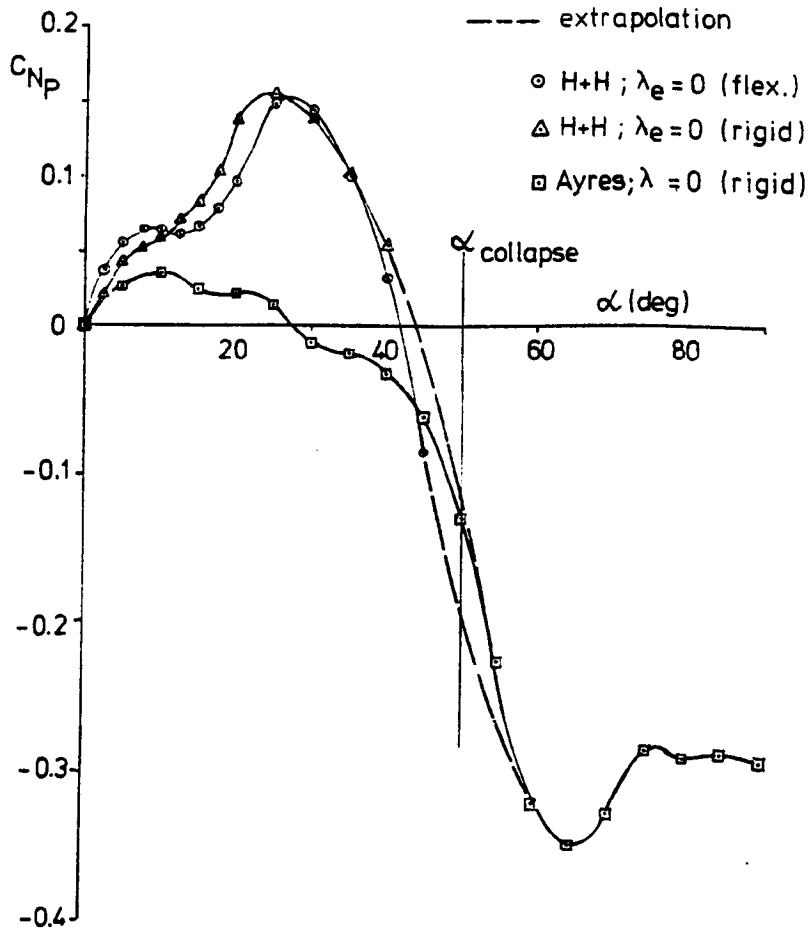
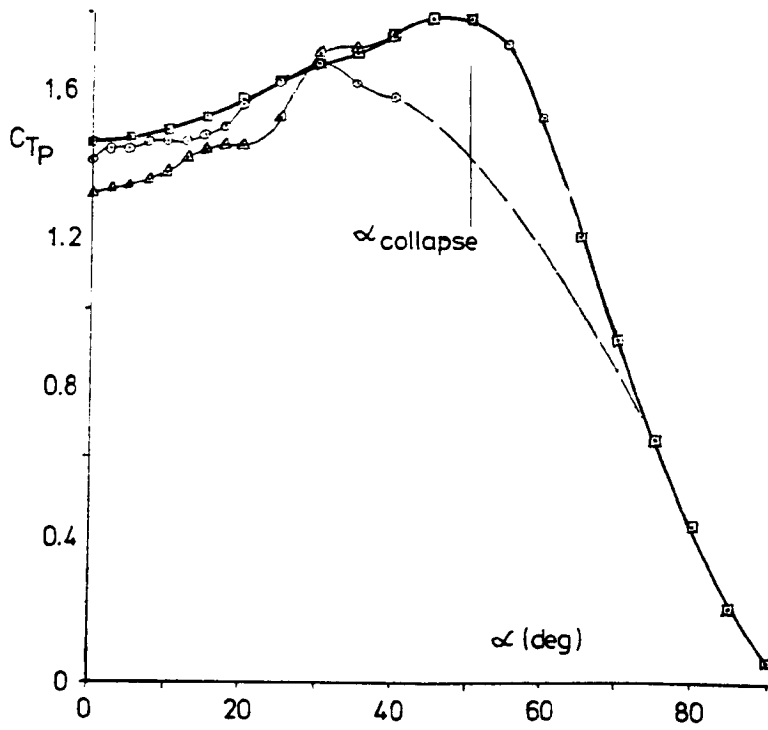


FIGURE 2.8 Comparison of C_N, C_T curves for zero-porosity flexible and rigid circular flat canopy models

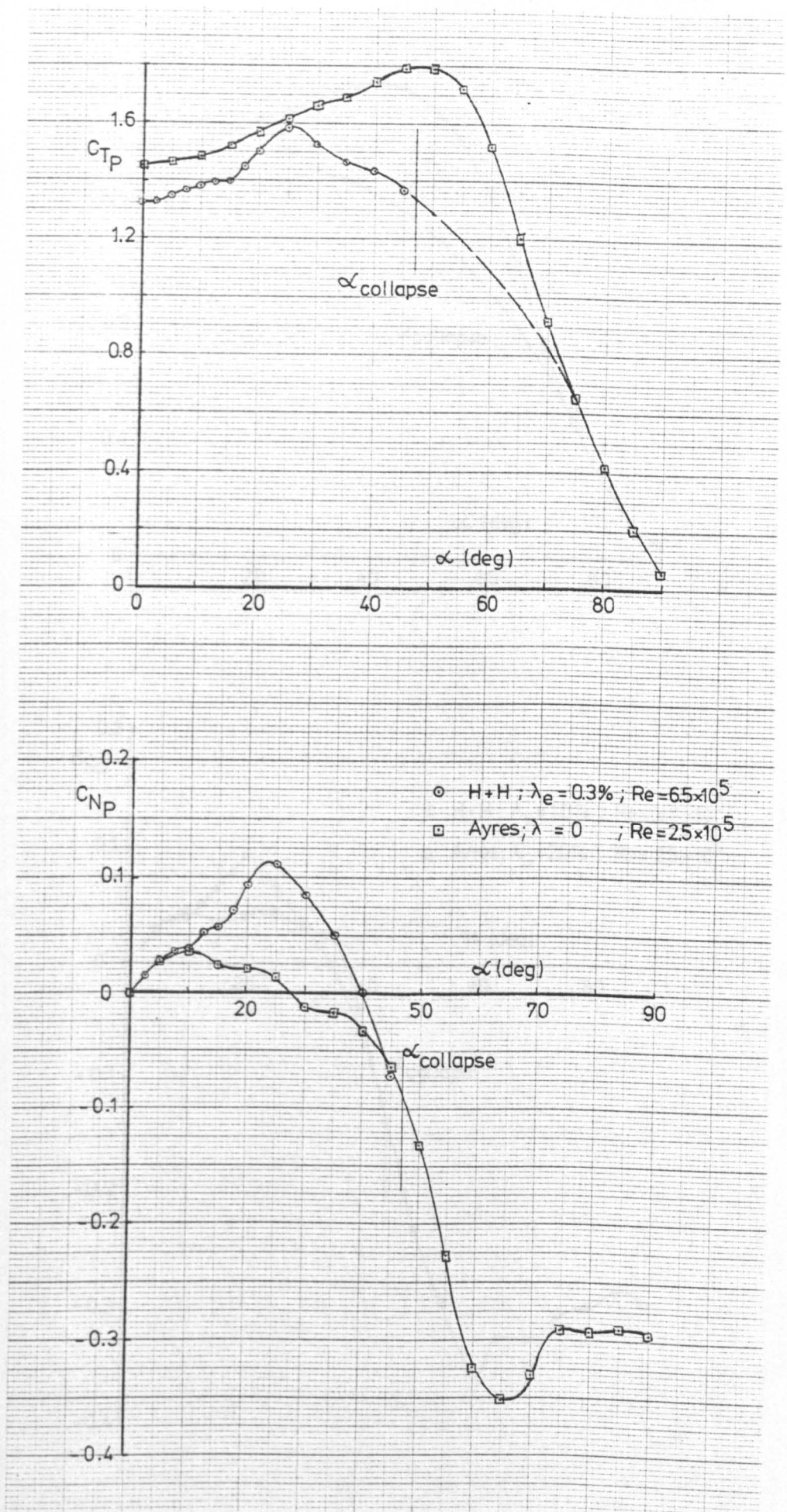


FIGURE 2.9 Comparison of C_N, C_T curves for $\lambda_e = 0.3\%$ (flexible), $\lambda_G = 0$ (rigid)

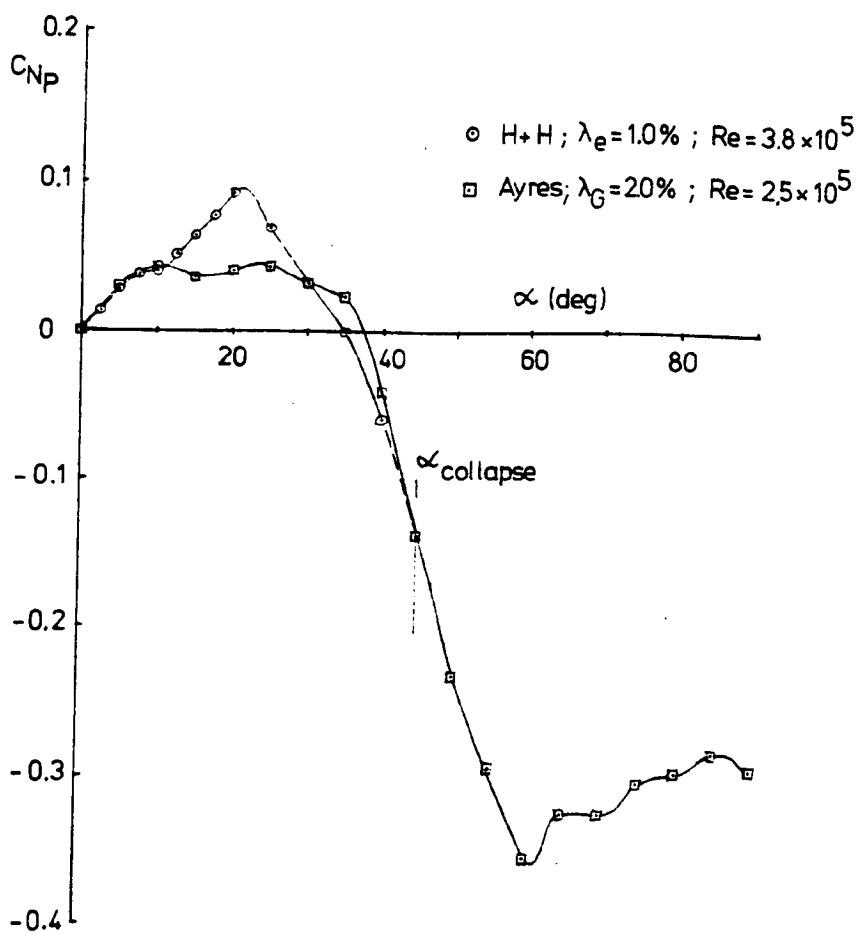
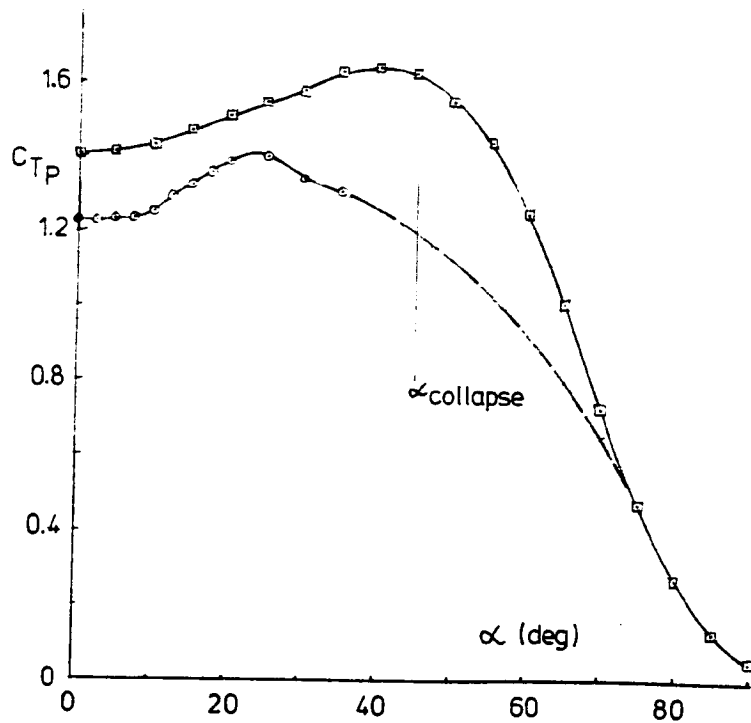


FIGURE 2.10 Comparison of C_N, C_T curves for $\lambda_e = 1\%$ (flexible), $\lambda_G = 2\%$ (rigid)

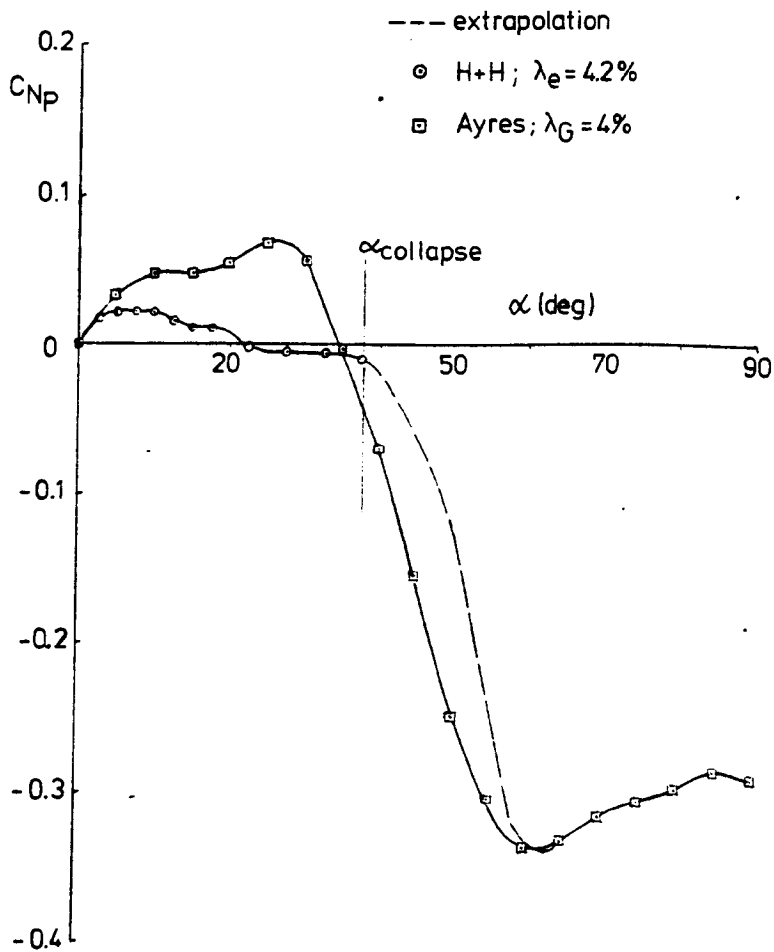
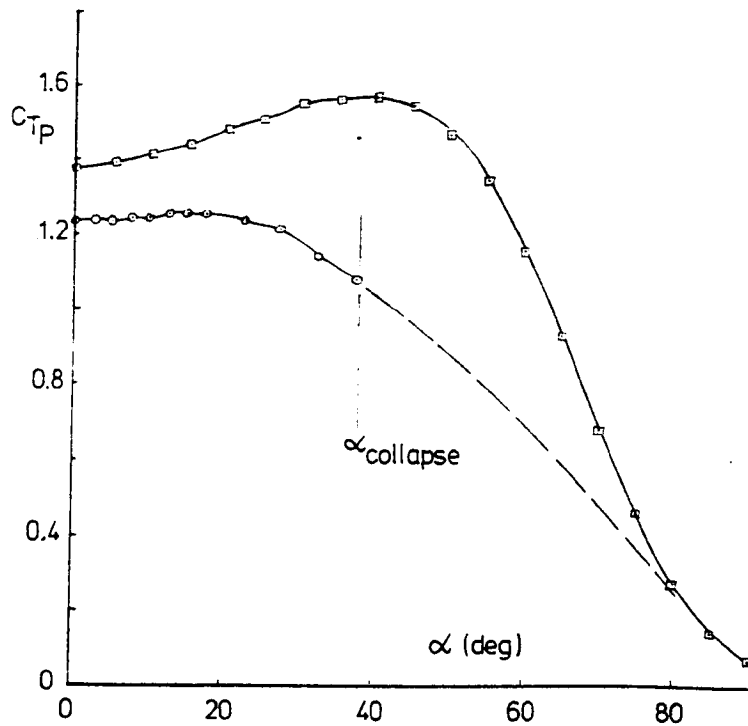


FIGURE 2.11 Comparison of C_N, C_T curves for $\lambda_e = 4.2\%$ (flexible), $\lambda_G = 4\%$ (rigid)

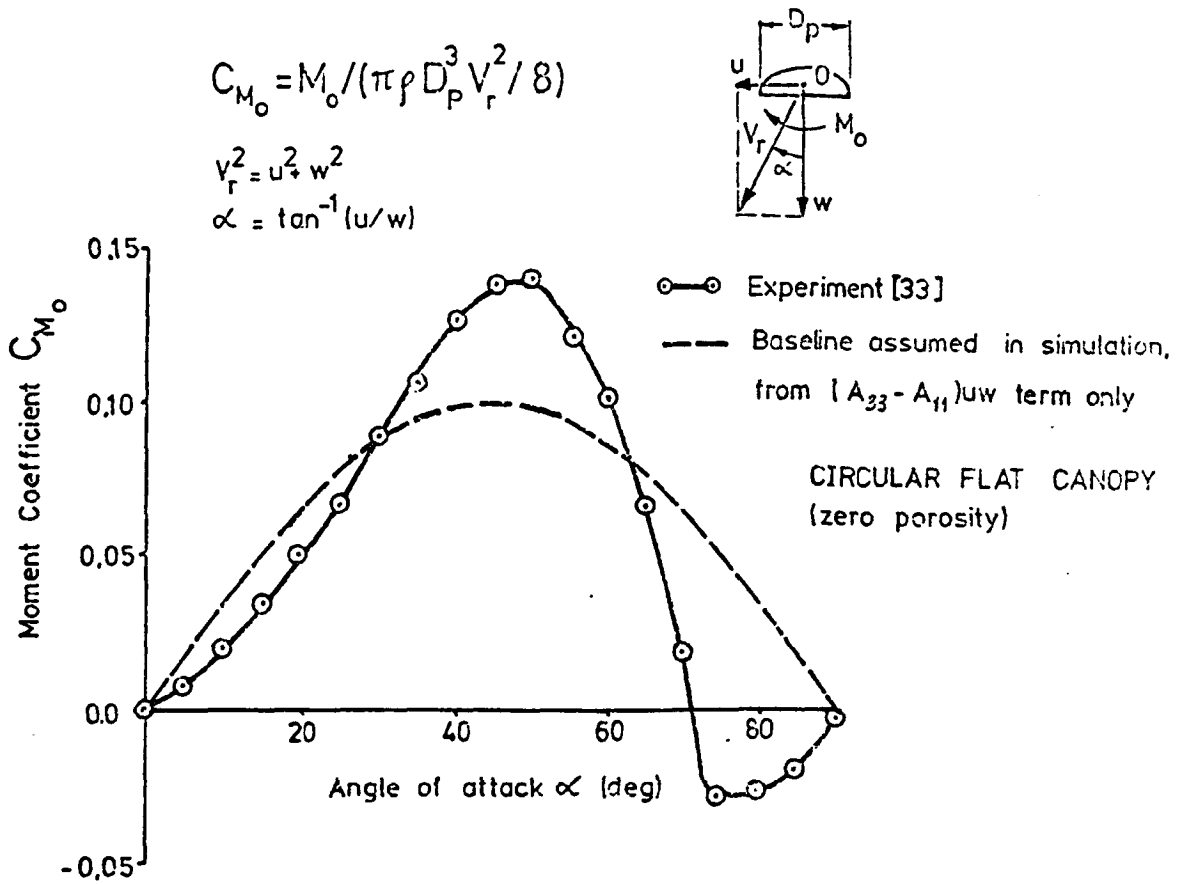


FIGURE 2.12 Comparison of measured and assumed steady-state moments about the origin for baseline: $K_{11} = 0.25$, $K_{33} = 0.40$

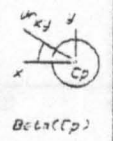
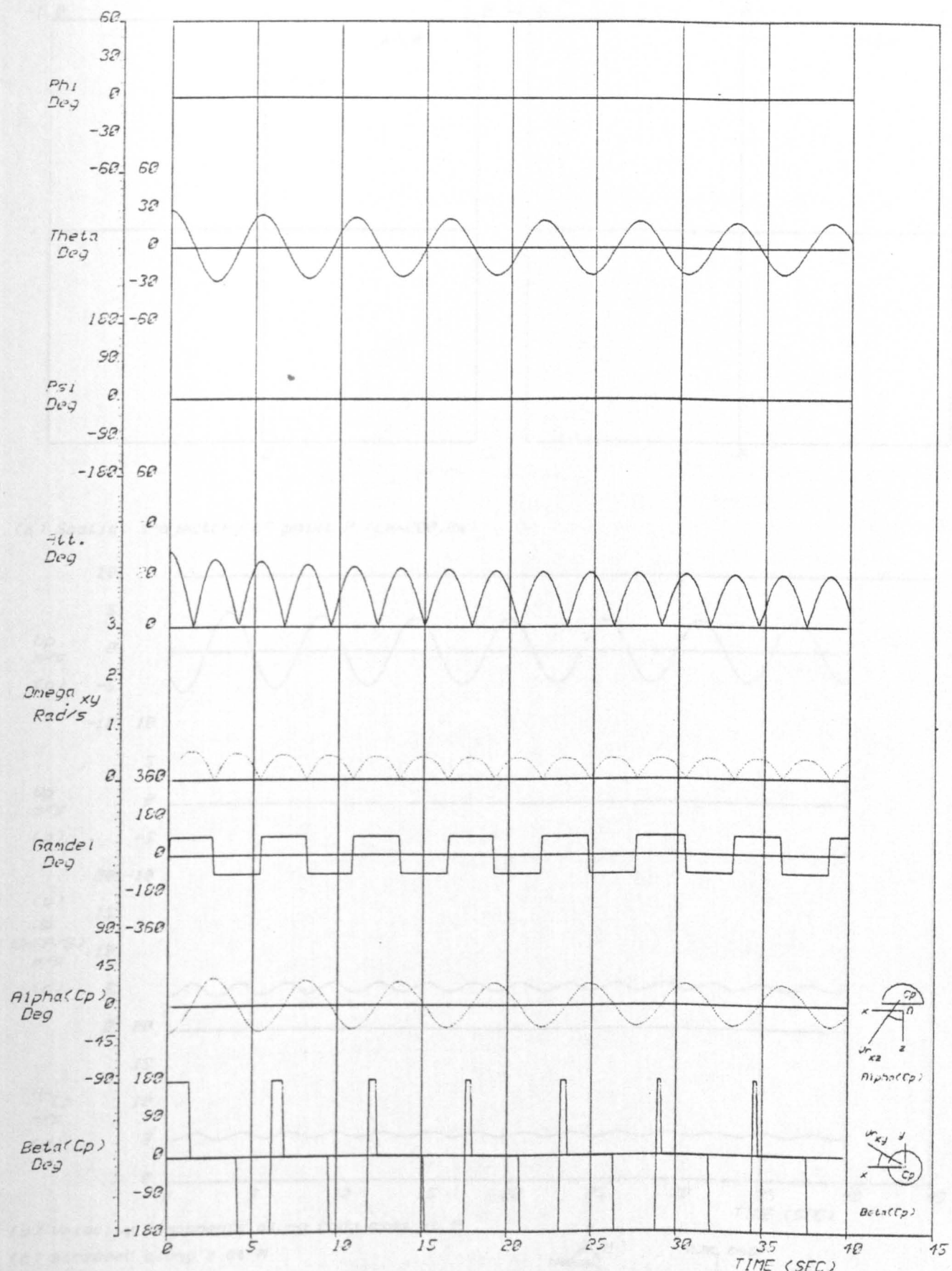
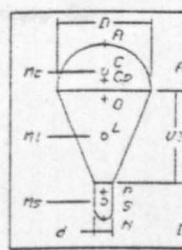


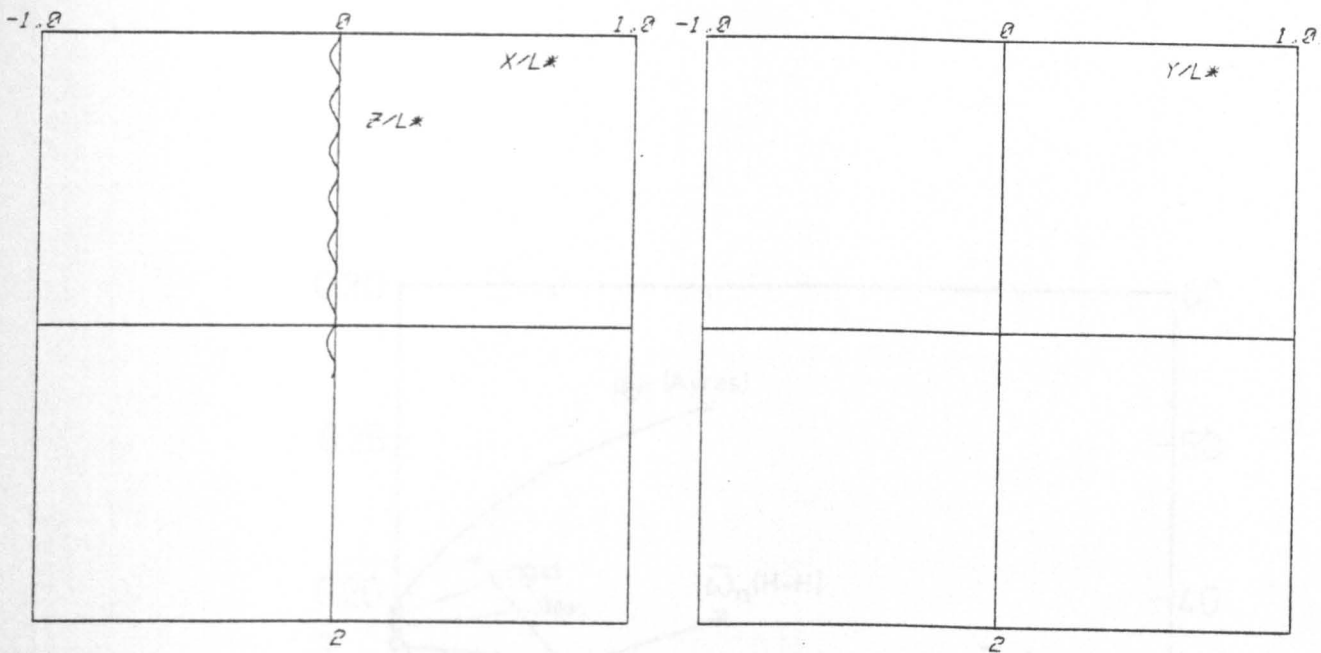
FIG. 2.13a



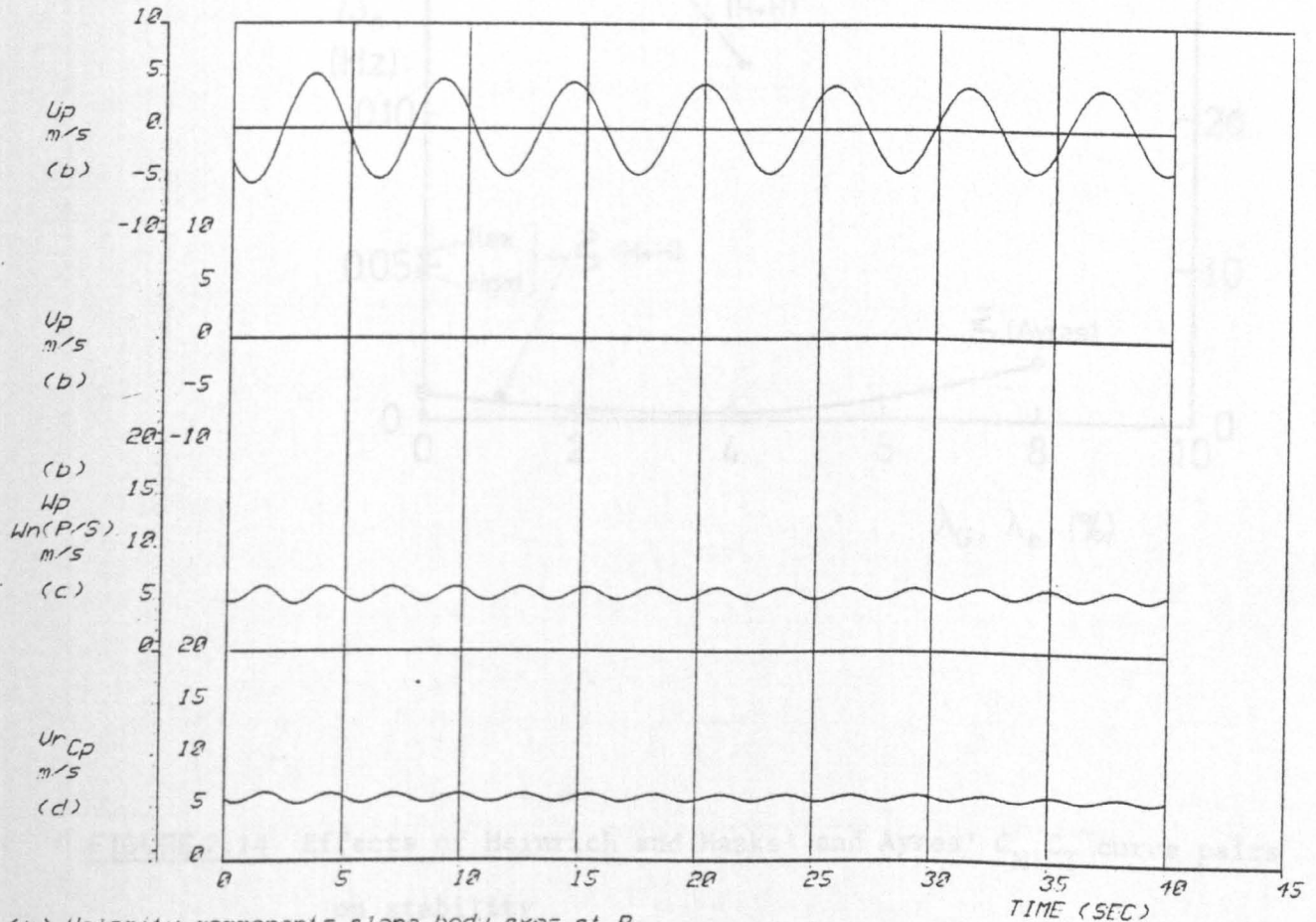
F. CIRC: RTMB. 0/RIGN

D = 0.457	M = 2.59 K3
d = .459	M1 = 2.39
DR = 1.312	M2 = 130.00
DC = -.254	K11 = .25
DCD = .000	K33 = .49
DL = 3.737	K25 = .32
DM = 2.552	L15 = .00
DS = 2.522	LP = -.0000
DT = 0.435	MP = .0000
DU = 7.077	RP = 1.2230
	Kg/m**3

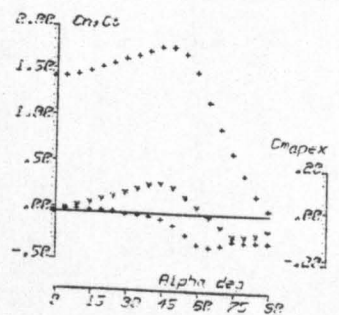
Results of applying experimental C_{M0} to baseline configuration



(a) Spatial trajectory of point P ($L^*=200.0m$)



(b) Velocity components along body axes at P
 (c) airspeed along z at N
 (d) resultant airspeed at canopy Cp



F. CIRCULAR BARRIAD
 A-D Coeffs. 10 used
 For simulation

FIG.	
213b	

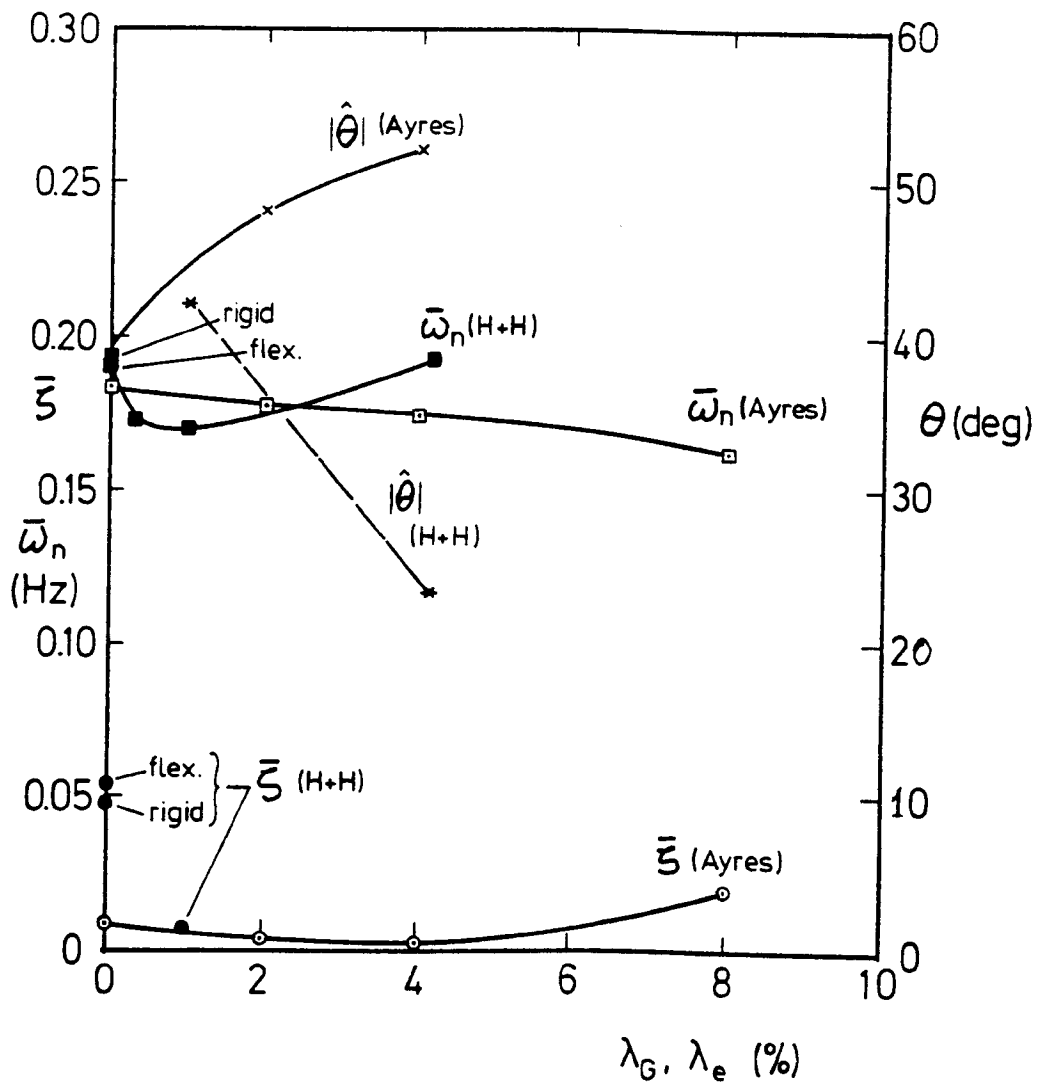


FIGURE 2.14 Effects of Heinrich and Haaks' and Ayres' C_N, C_T curve pairs on stability

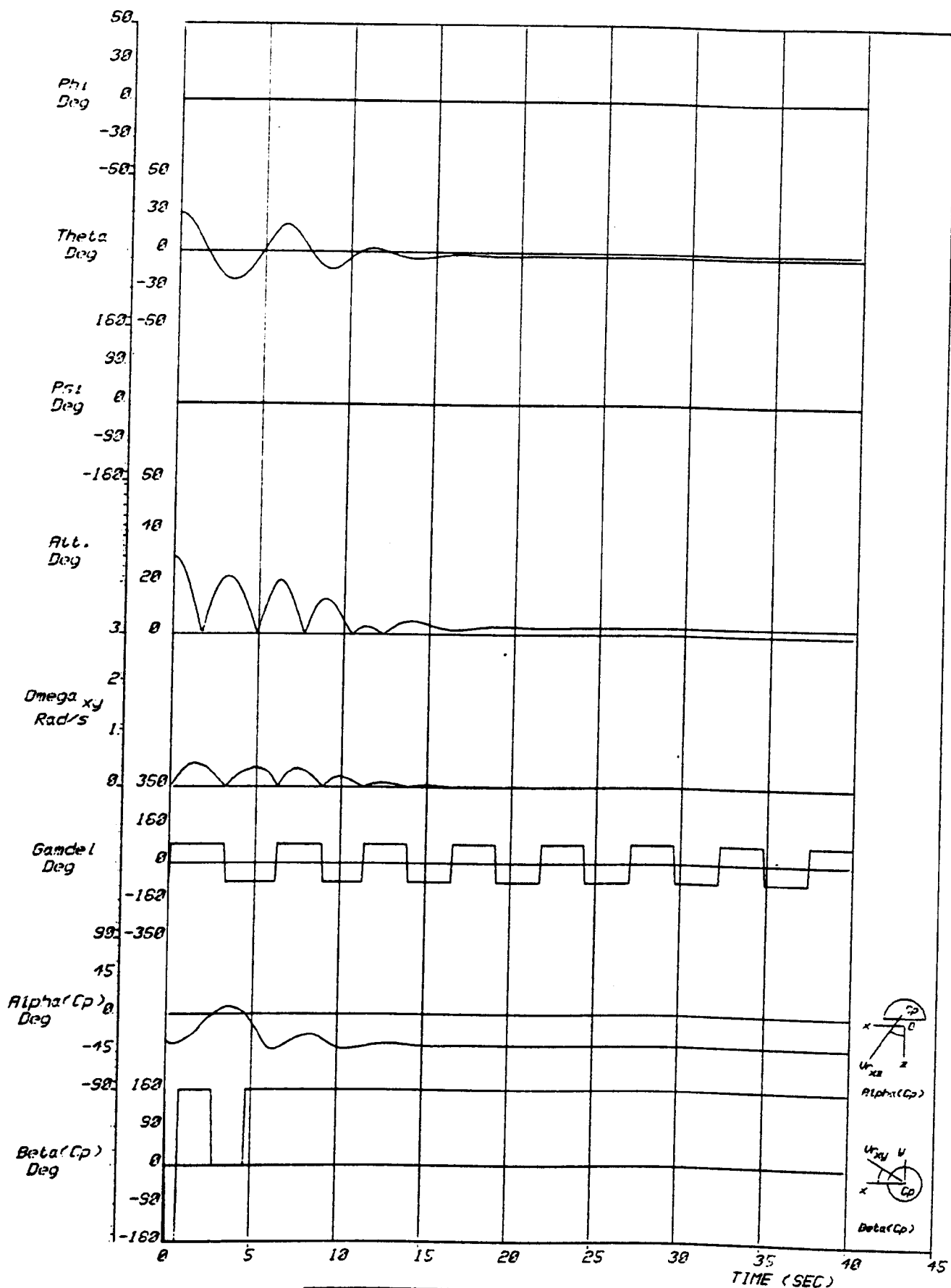
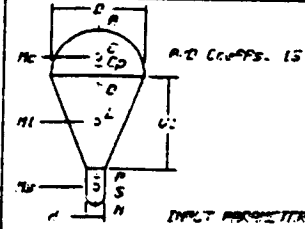


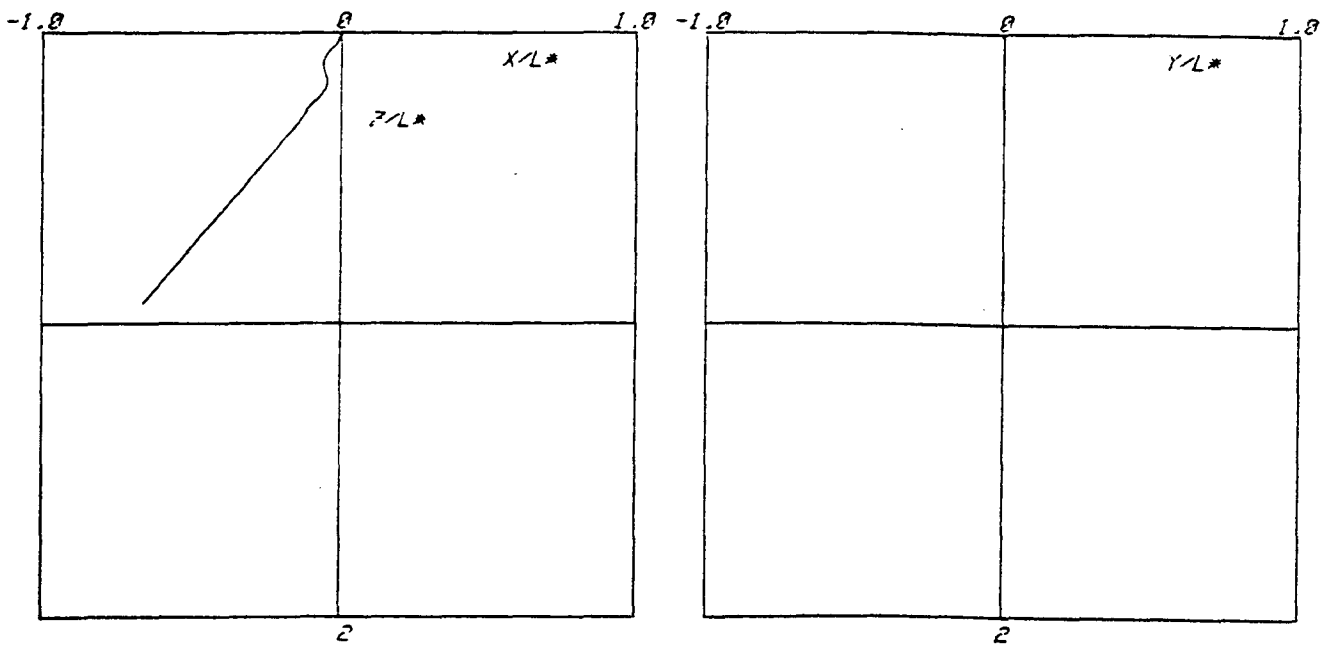
FIG. 215
 1 OF 2



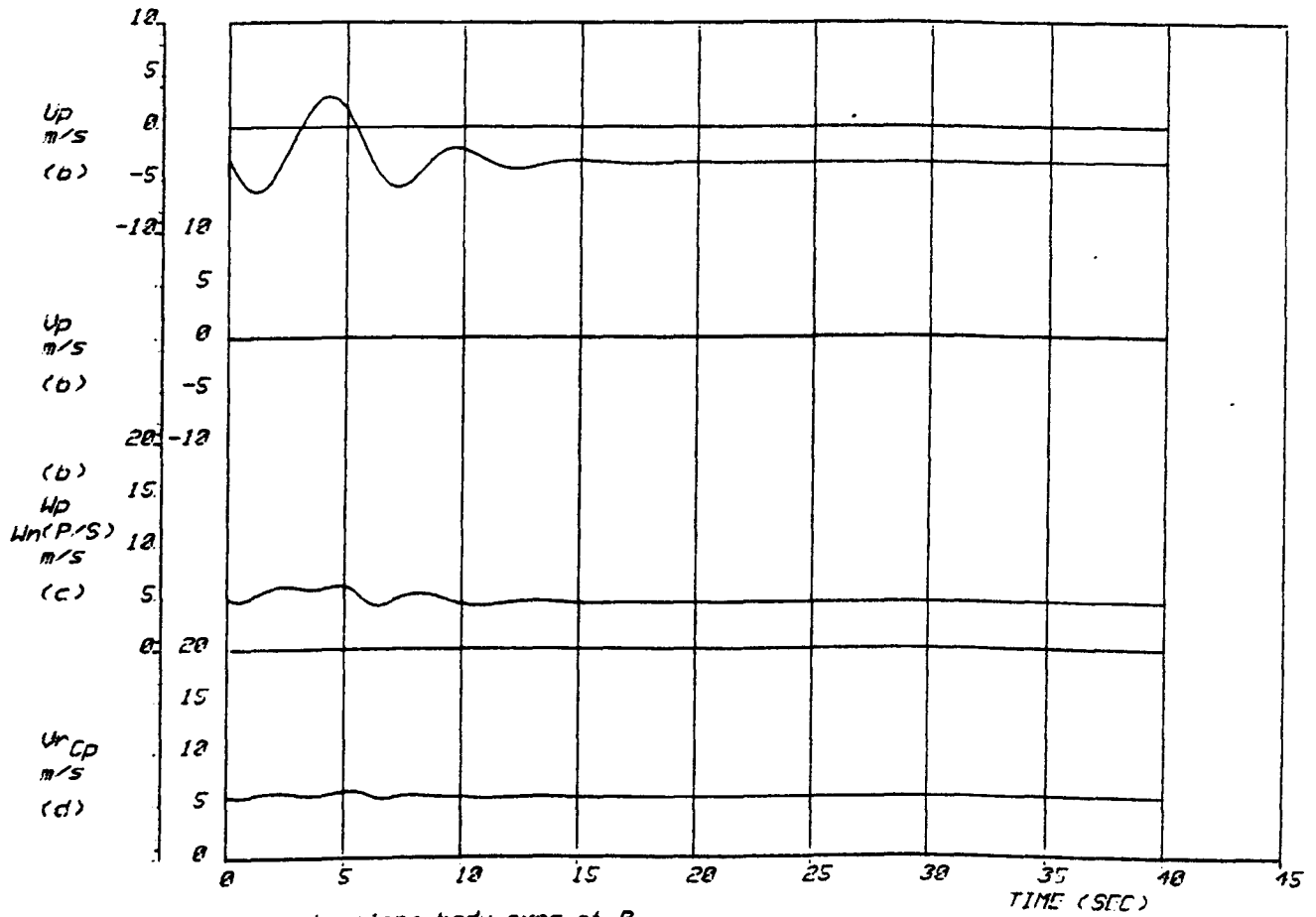
F. CIRCHINI/B.FLEX		
D = 6.45" A	M = 2.30 Kg	
c = 400	M2 = 2.30	
CR = -1.315	M3 = 100.00	
CC = .254	K11 = .25	
CCD = .000	K33 = .40	
CL = 3.557	K55 = .10	
CP = 7.555	K10 = .00	
CP = 7.555	Lp = .0500	
CP = 0.157	M = .0000	
CL = 7.557	Rho = 1.3250	
		Kg/M^3

INPUT PARAMETERS

Results for Heinrich and Haaks' $\lambda = 0$ (flexible) data



(a) Spatial trajectory of point P ($L^* = 200.0m$)



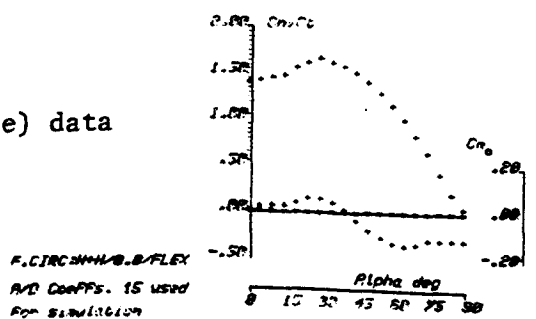
(b) Velocity components along body axes at P

(c) airspeed along z at M

(d) resultant airspeed at canopy C_p

Results for Heinrich and Haaks' $\lambda = 0$ (flexible) data

FIG.	
216	
2 OF 2	



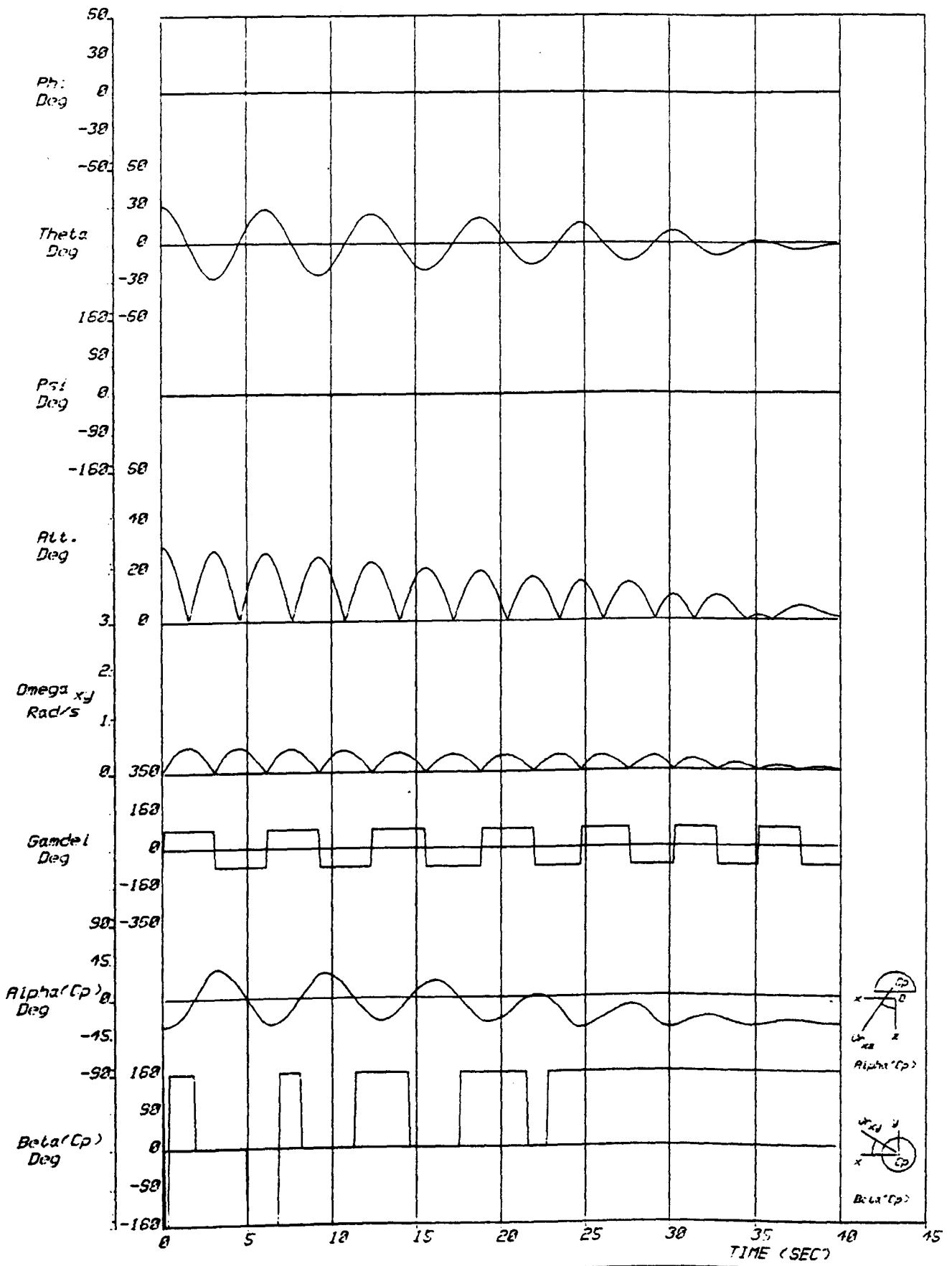
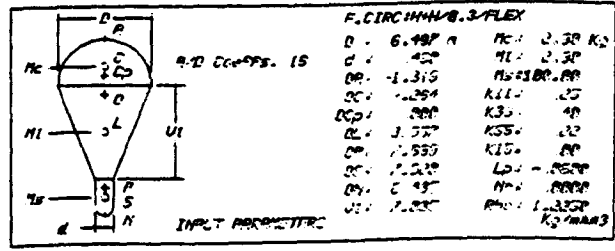
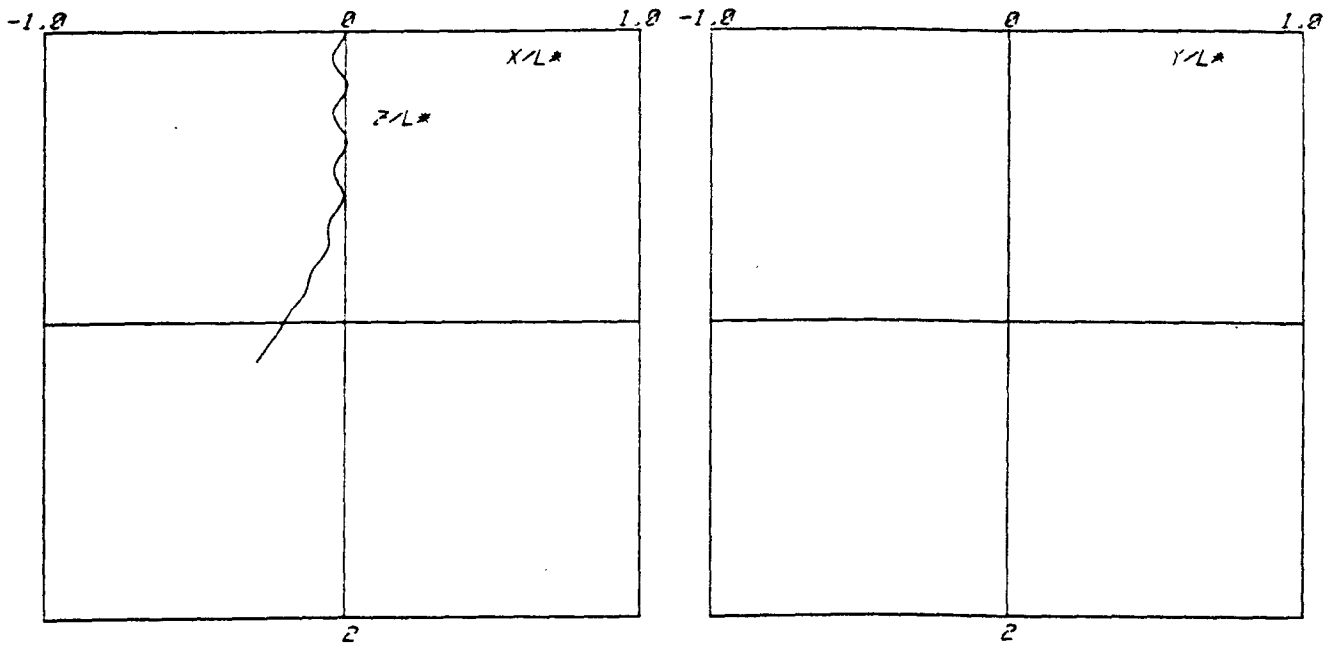


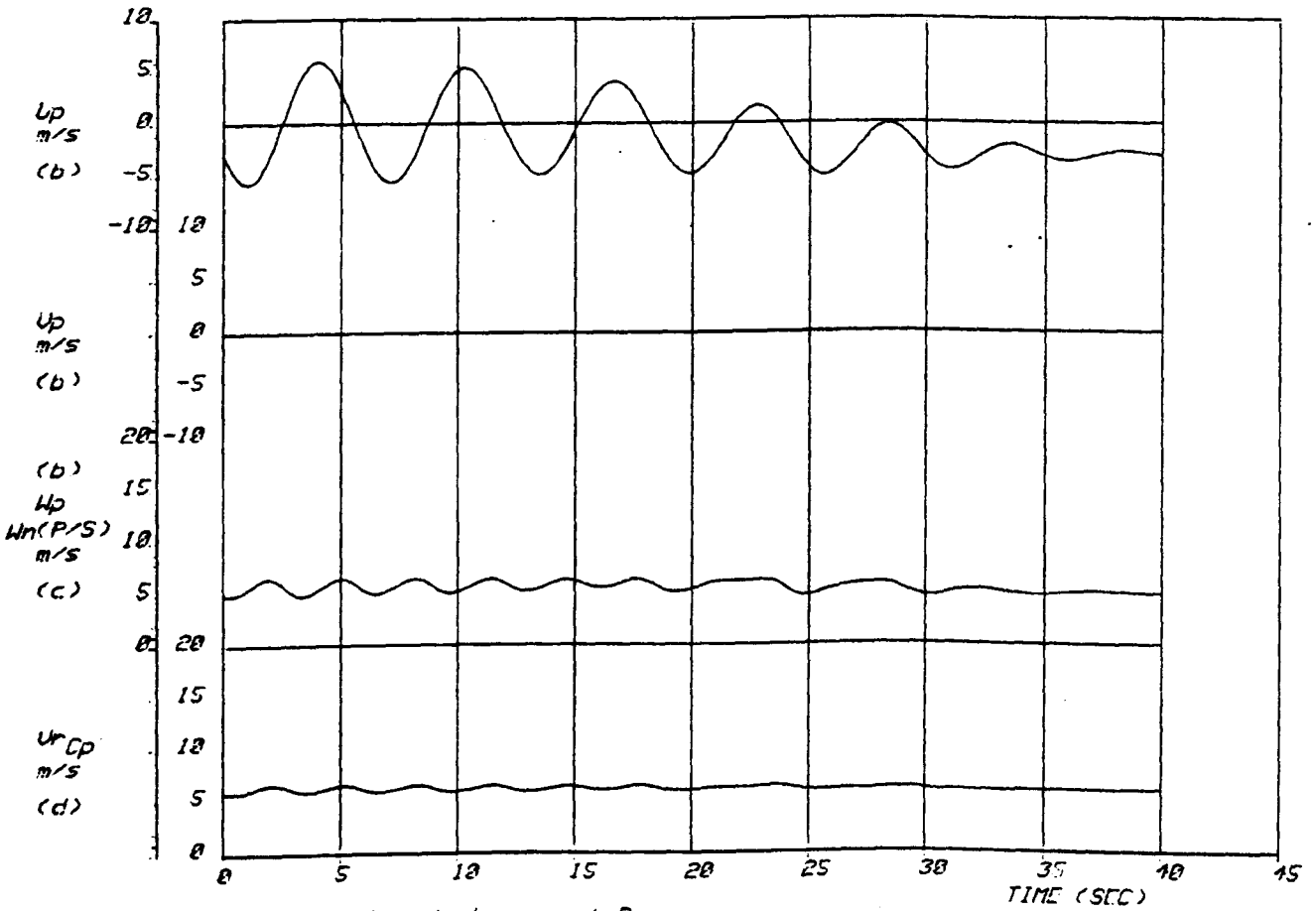
FIG. 2.17
1 OF 2



Results for Heinrich and Haaks' $\lambda_e = 0.3\%$ (flexible) data



(a) Spatial trajectory of point P ($L^* = 200.0m$)



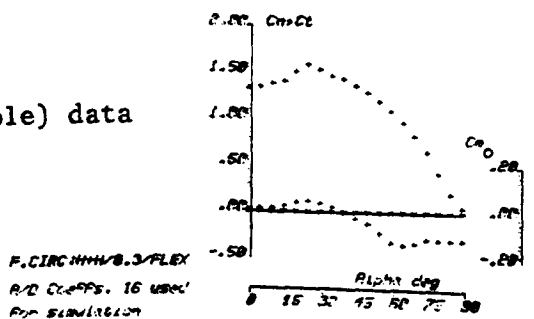
(b) Velocity components along body axes at P

(c) airspeed along z at N

(d) resultant airspeed at canopy C_p

Results for Heinrich and Haaks' $\lambda_e = 0.3\%$ (flexible) data

FIG.	
218	
2 OF 2	



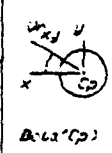
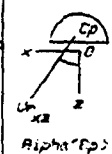
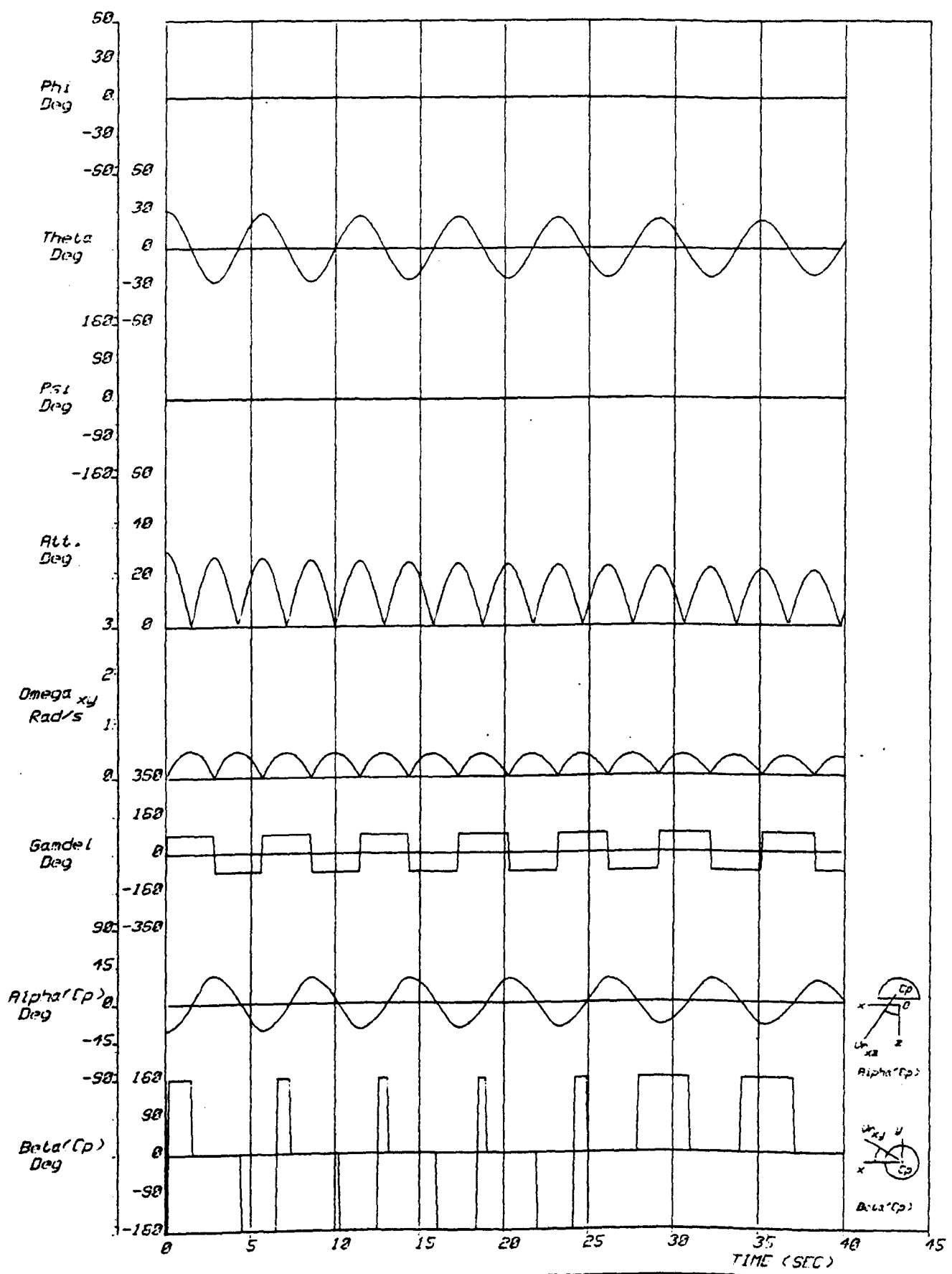
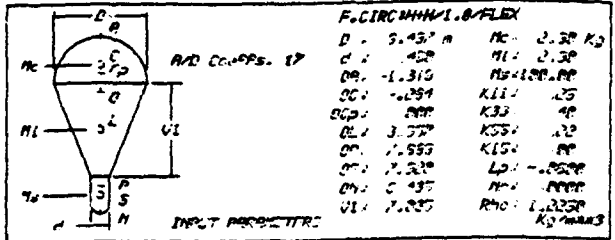
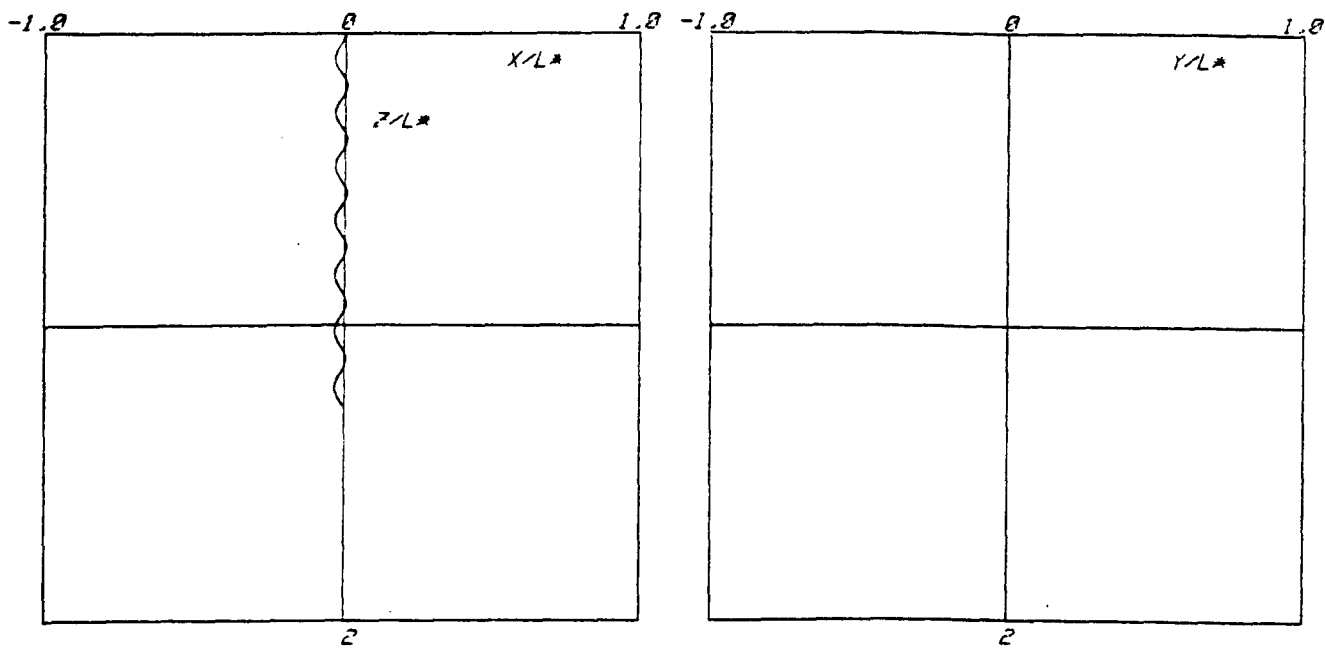


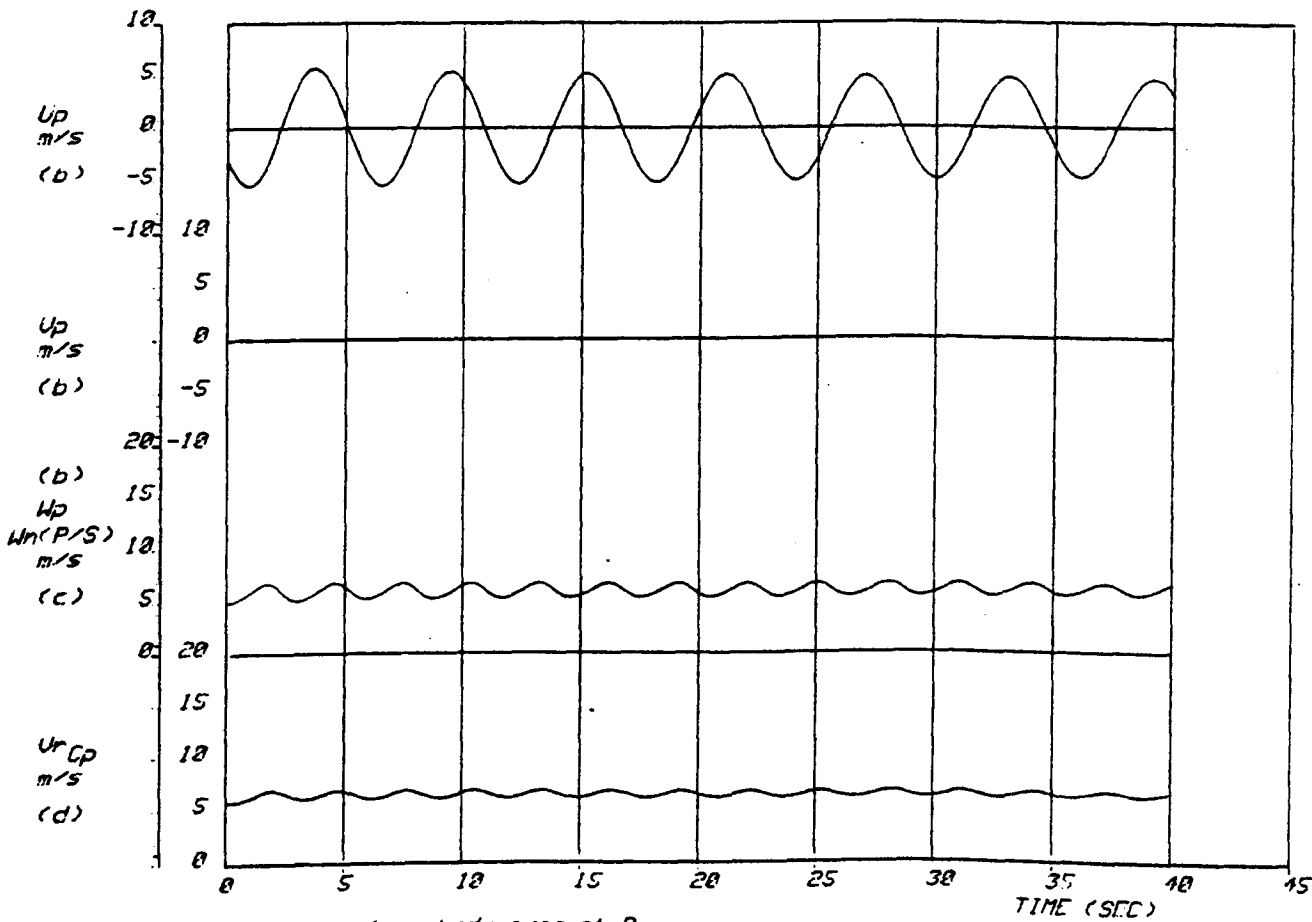
FIG. 219
1 OF 2



Results for Heinrich and Haaks' $\lambda_e = 1.0\%$ (flexible) data



(a) Spatial trajectory of point P ($L^* = 200.0m$)



(b) Velocity components along body axes at P

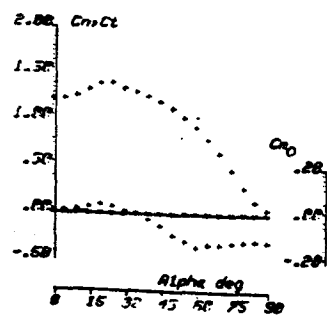
(c) airspeed along z at N

(d) resultant airspeed at canopy Cp

Results for Heinrich and Haaks' $\lambda_e = 1.0\%$ (flexible) data

FIG.	
2.20	
2 OF 2	

F. CIRCUM/1.0/FLEX
 R-D Coeffs. 17 used
 For simulation



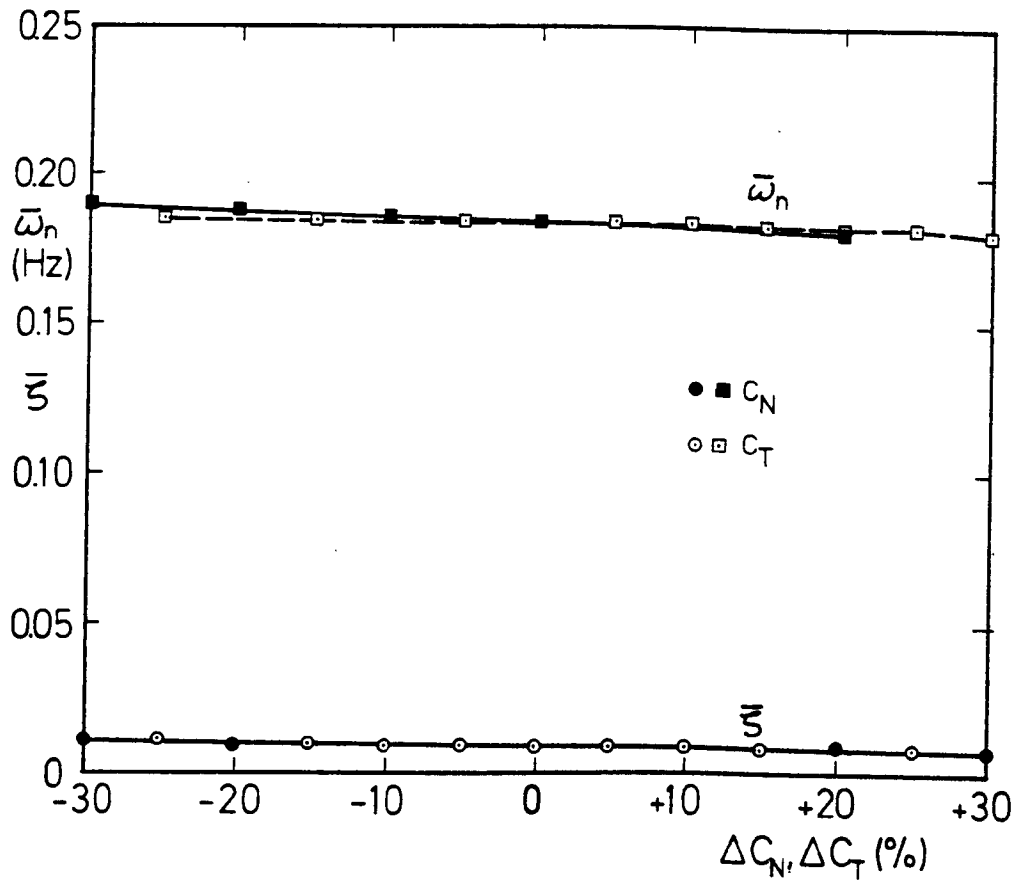


FIGURE 2.21 Effect of scaling of C_N, C_T curves on stability

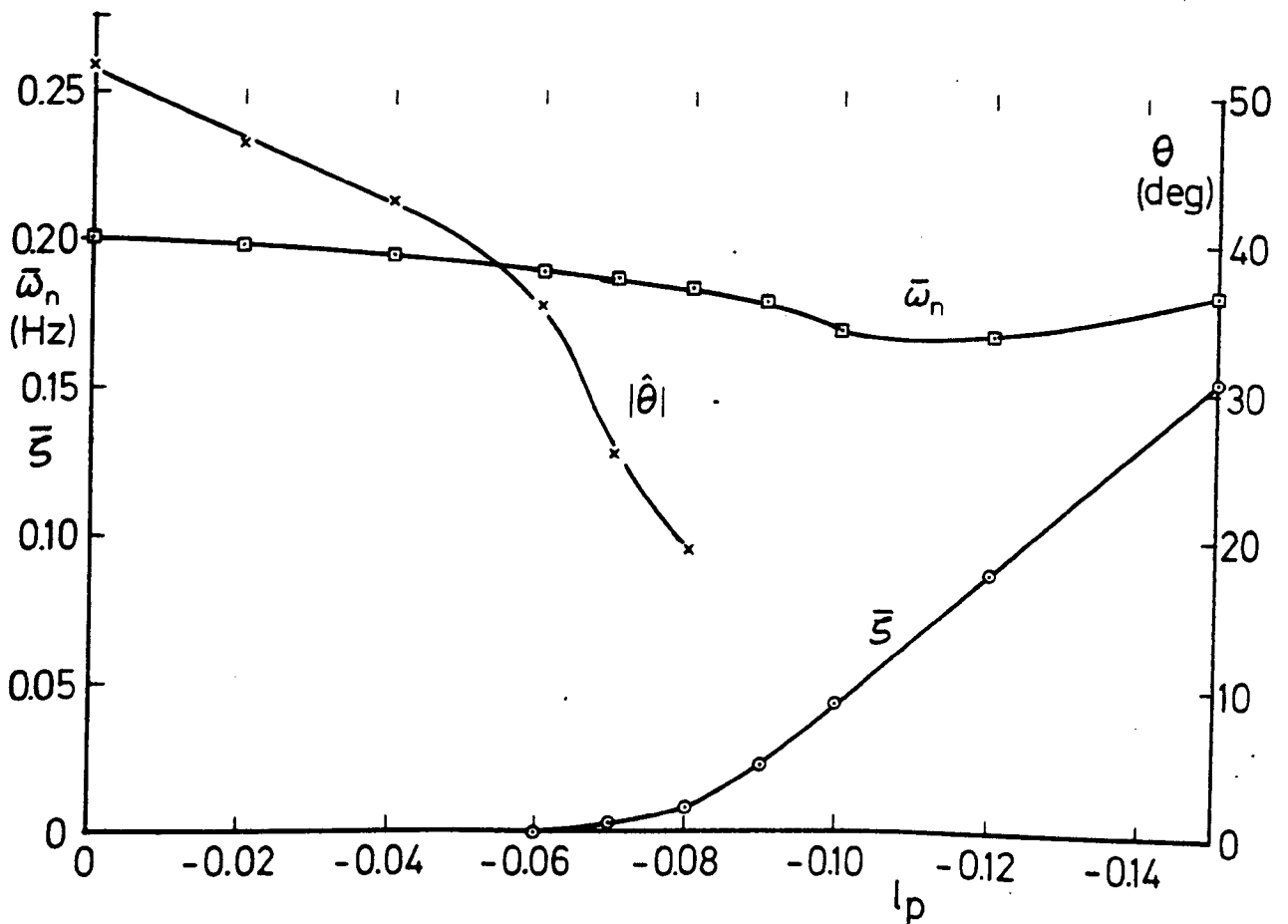


FIGURE 2.22 Effect of variation in damping moment derivative on stability

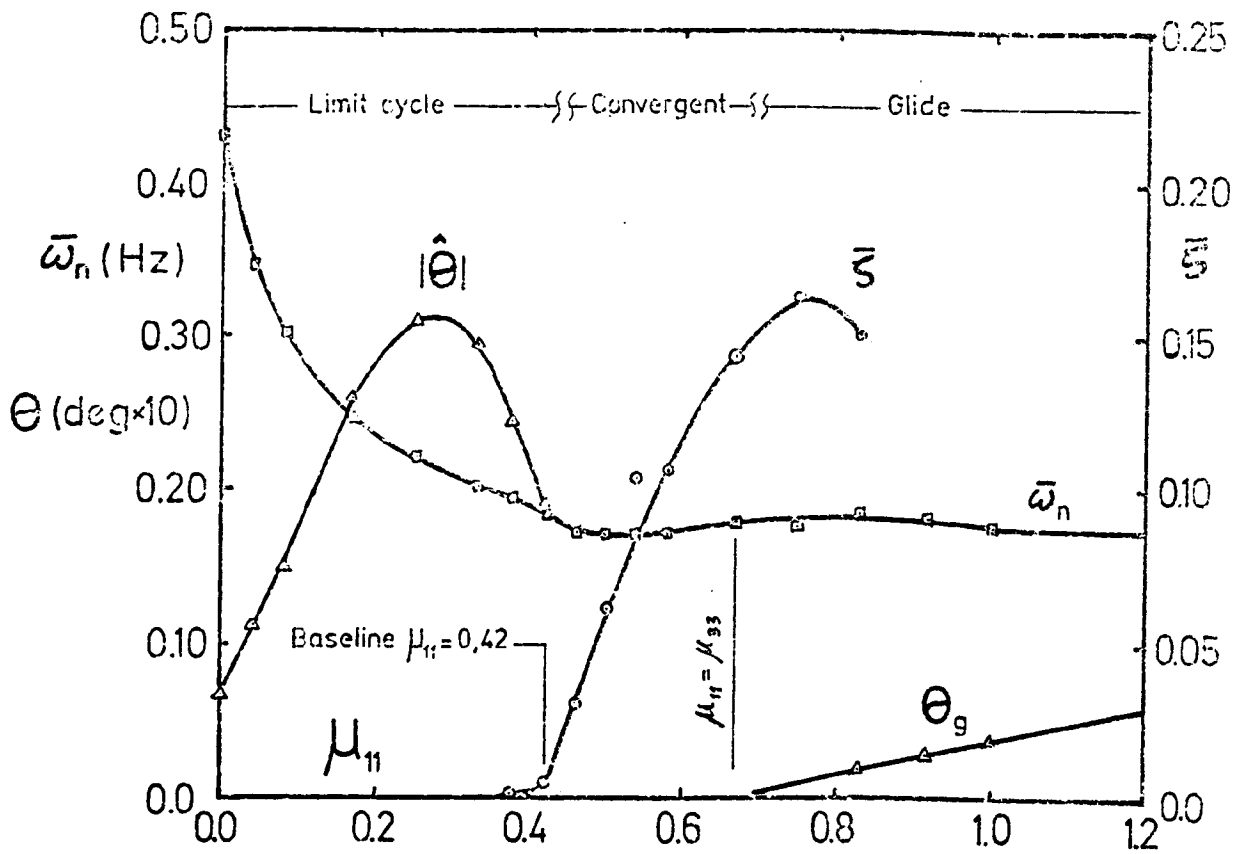


FIGURE 2.23 Effect of variation of lateral added mass component A_{11} on stability

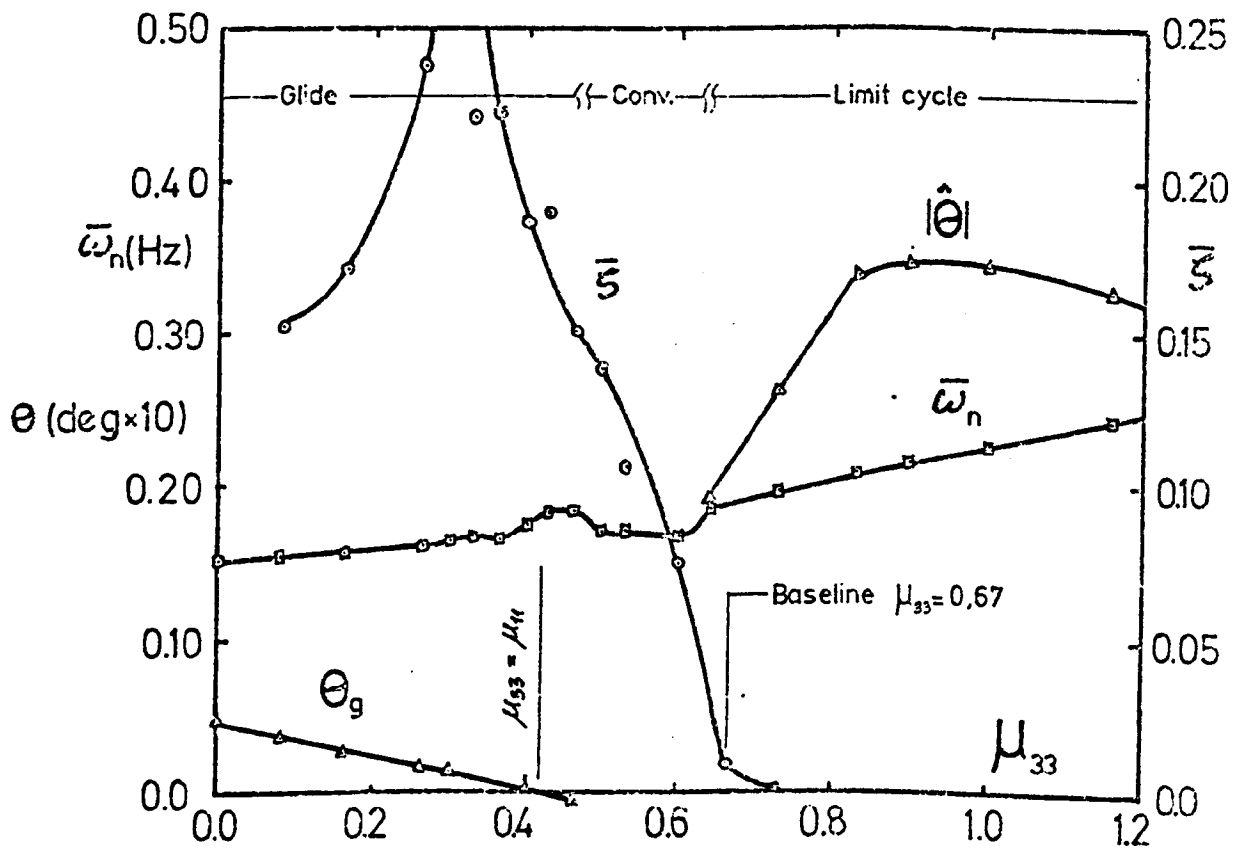


FIGURE 2.24 Effect of variation of longitudinal added mass component A_{33} on stability

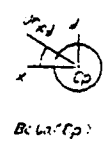
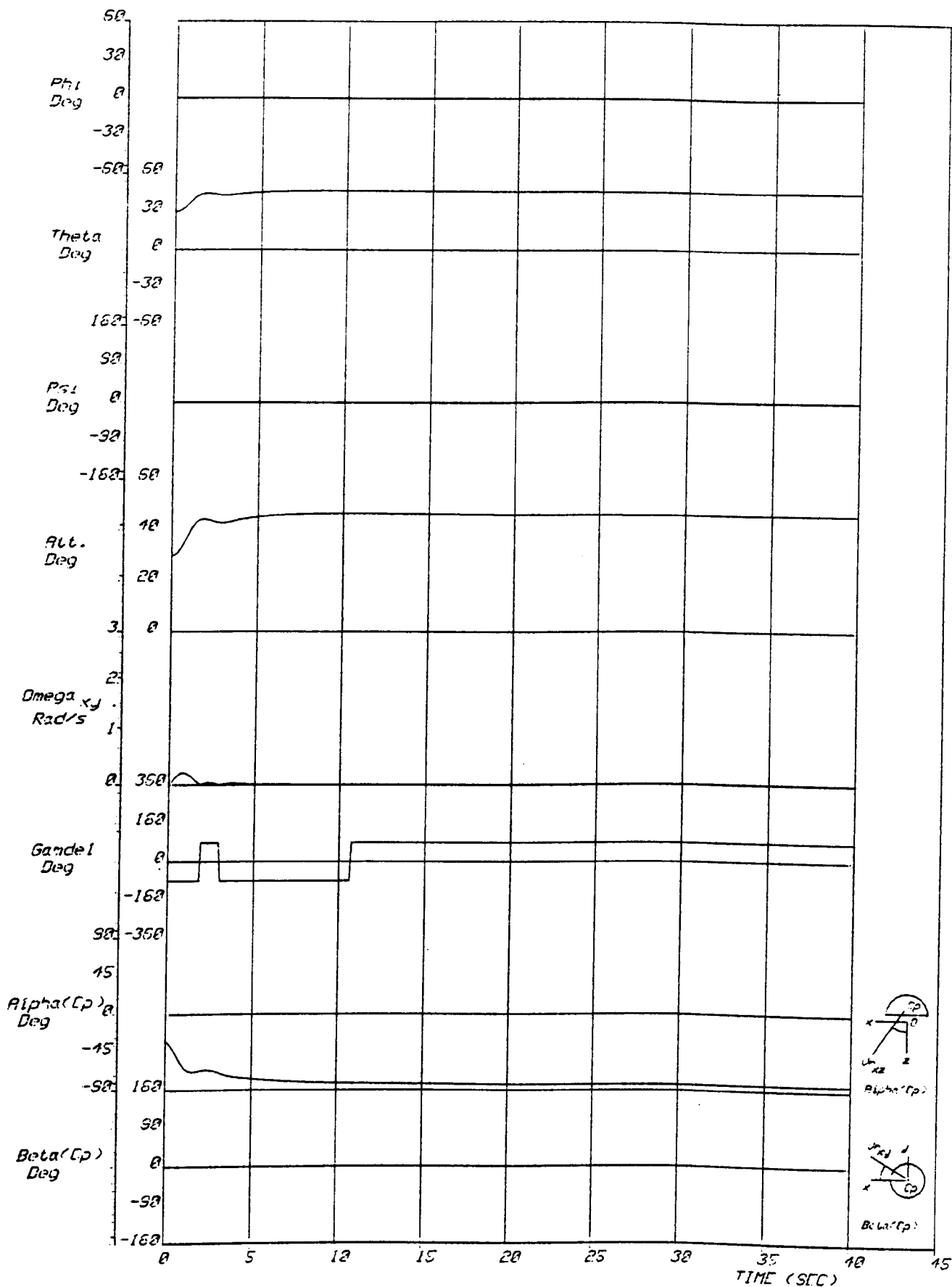
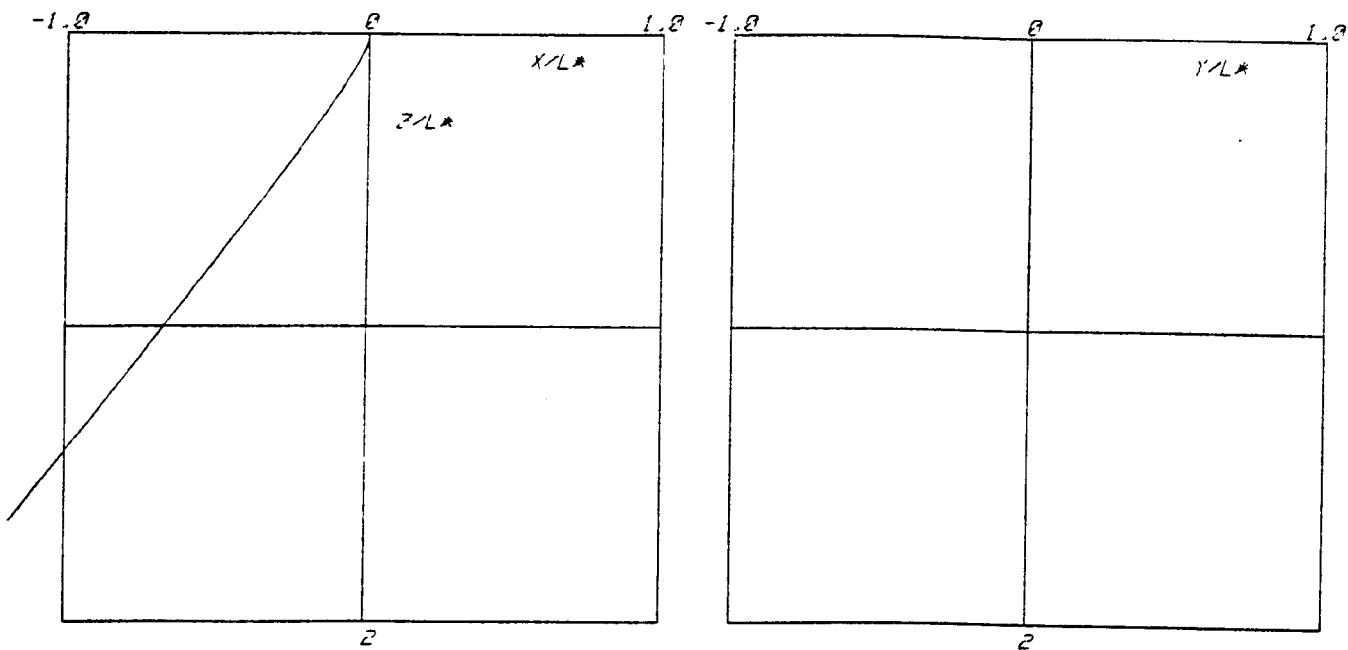


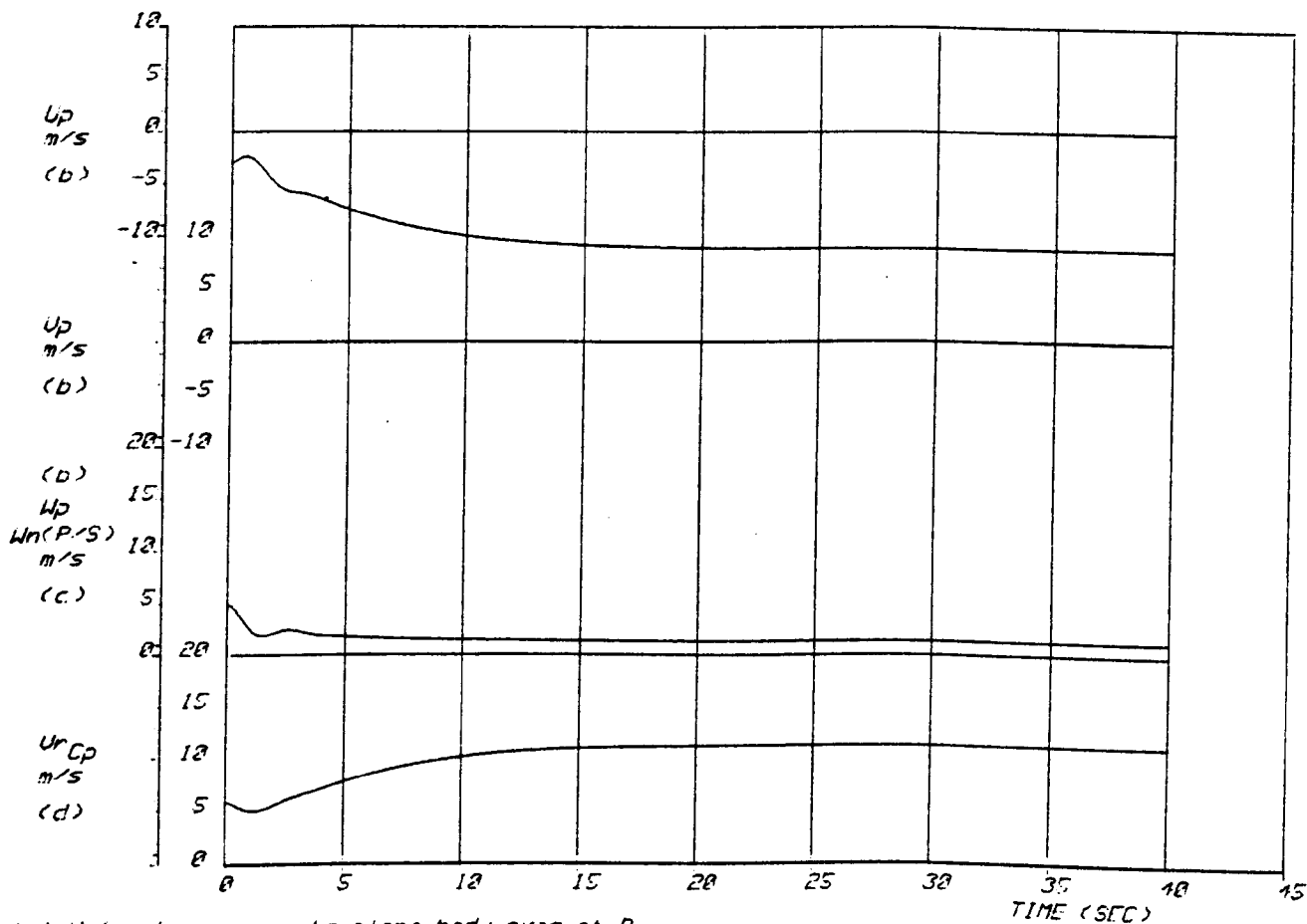
FIG. 2.25
 1 OF 2

INPUT PARAMETERS		
D	5.457 m	M_c 2.50 K2
d	.420	M_L 2.38
DR	-1.310	M_S 1.00 PP
DC	-.254	K_{11} 2.50
DCp	.000	K_{35} .48
CL	3.077	K_{05} .22
CP	7.550	K_{15} .10
CR	7.500	L_p -.0500
CRH	0.437	N_H .0000
CRV	7.000	R_{10} 1.2350
		K_{33} 1.0000

Results for added mass coefficient $K_{11} = 2.5$



(a) Spatial trajectory of point P ($L^* = 200.0m$)



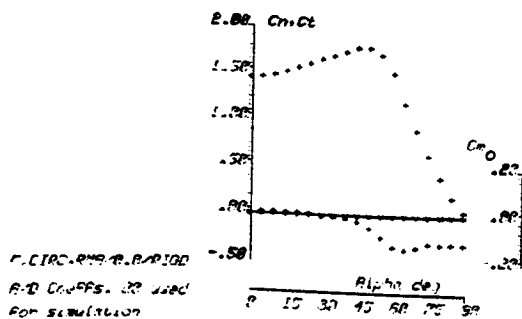
(b) Velocity components along body axes at P

(c) airspeed along z at N

(d) resultant airspeed at canopy Cp

Results for added mass coefficient $K_{11} = 2.5$

FIG.	
2.26	
2 OF 2	



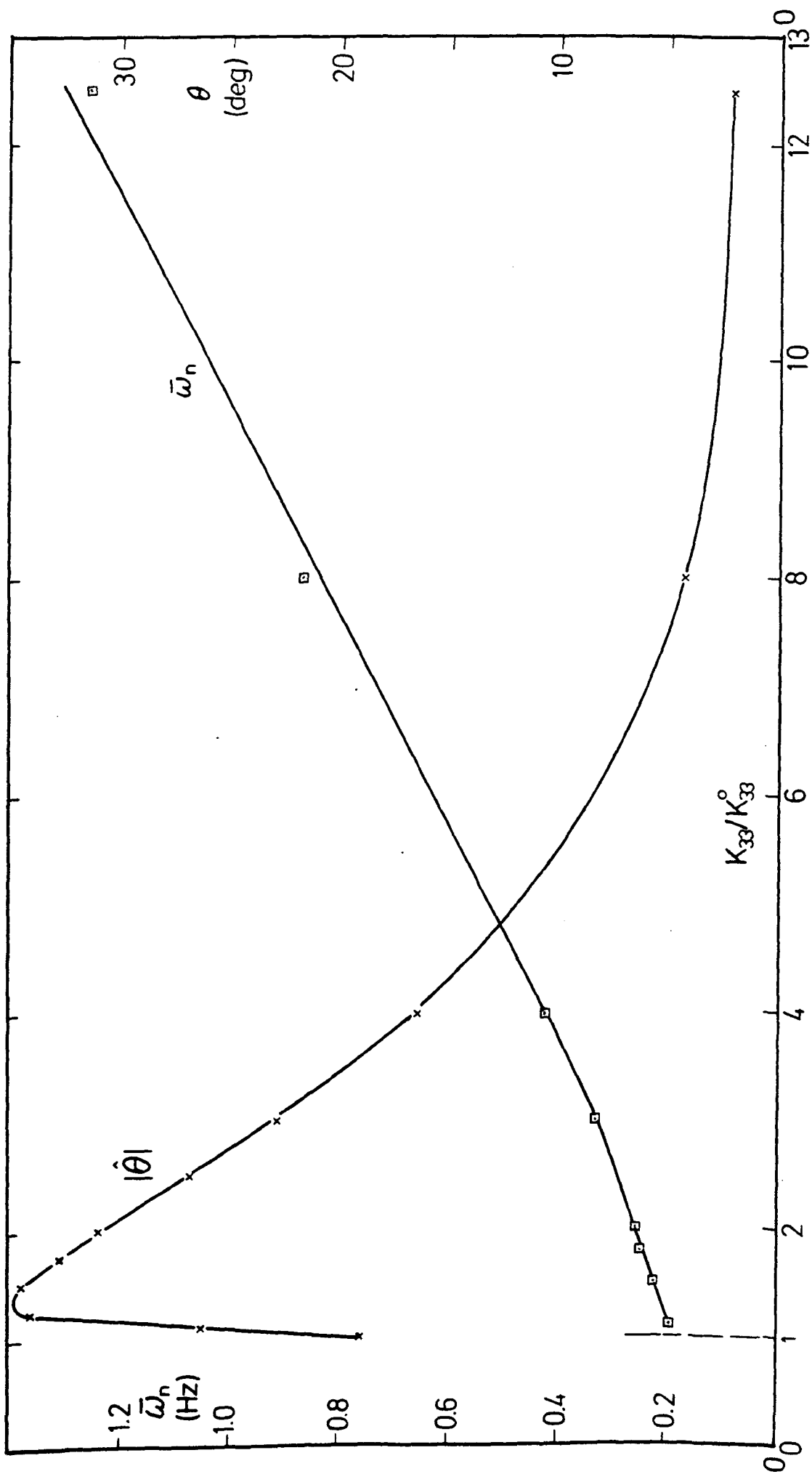


FIGURE 2.27 Effect of large variation in A_{33} on stability

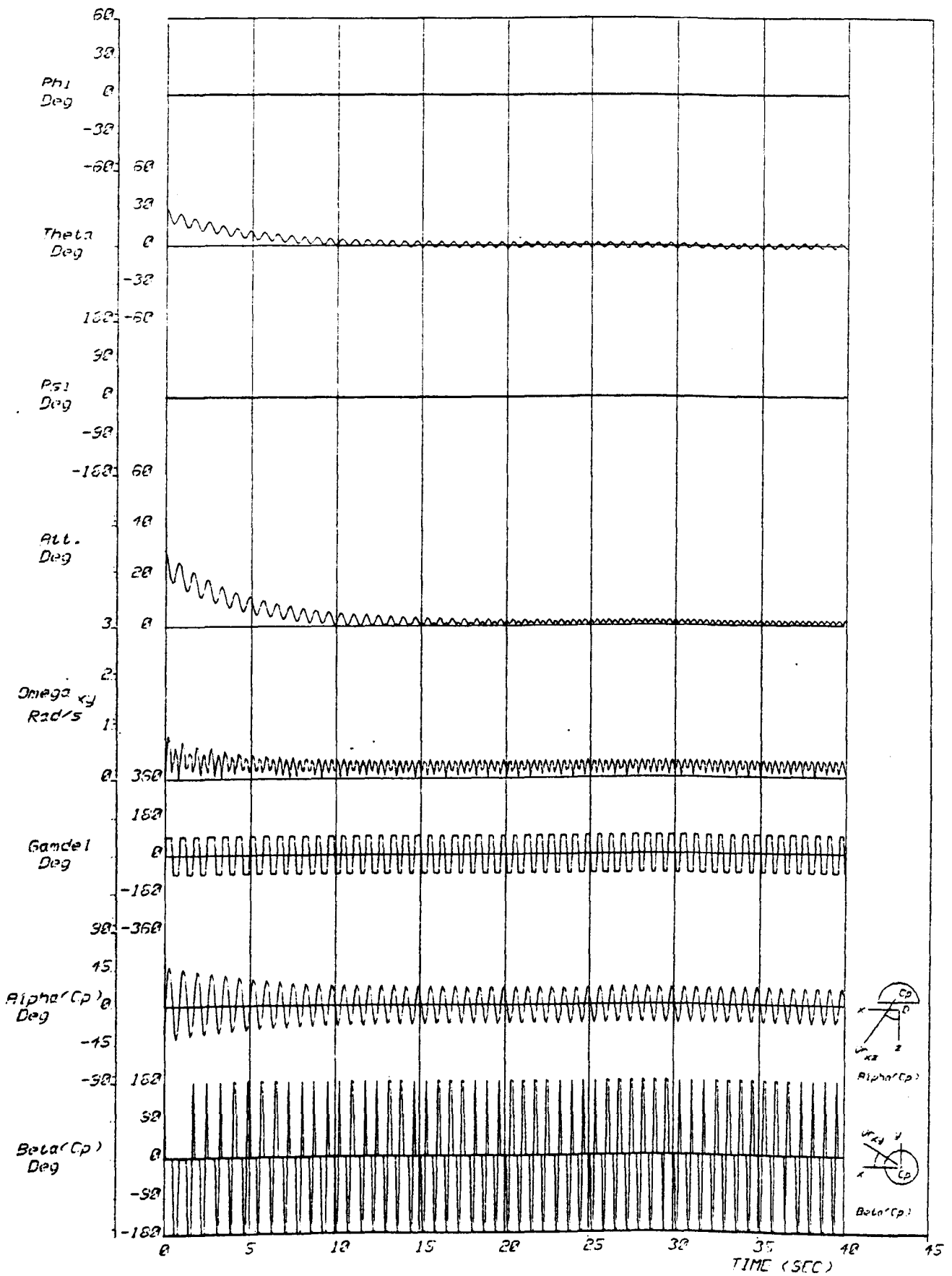
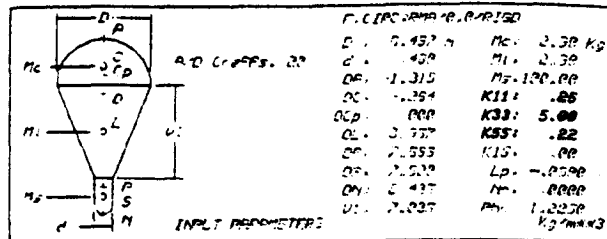
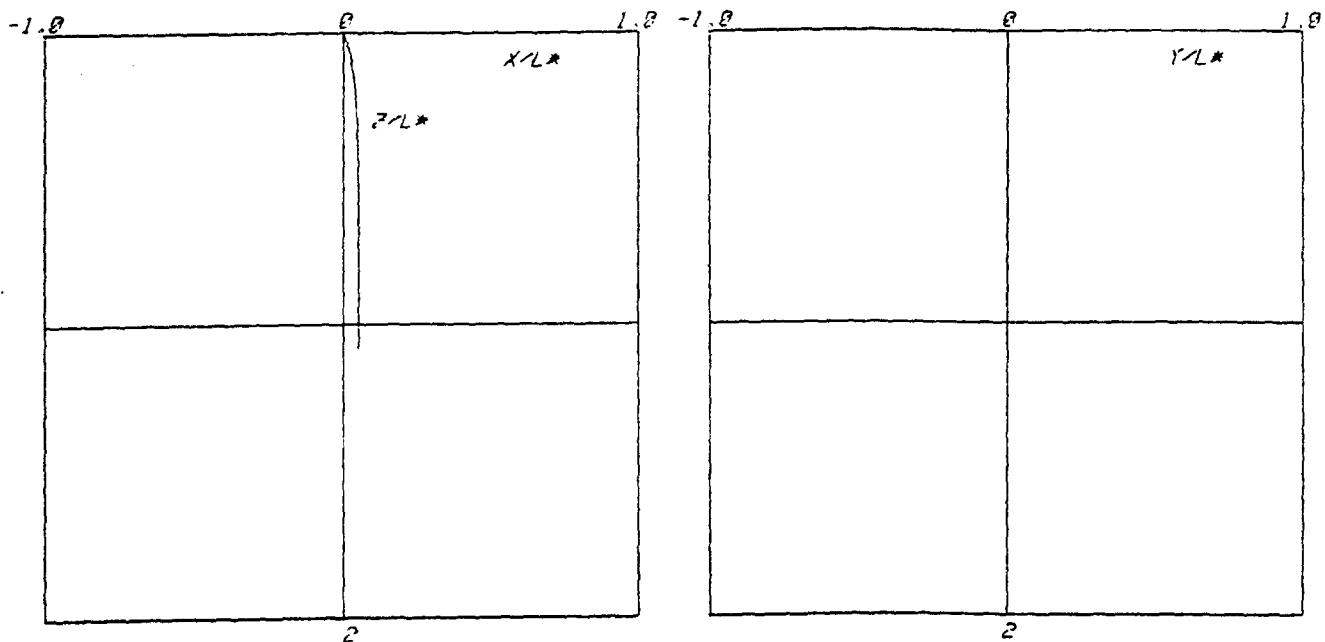


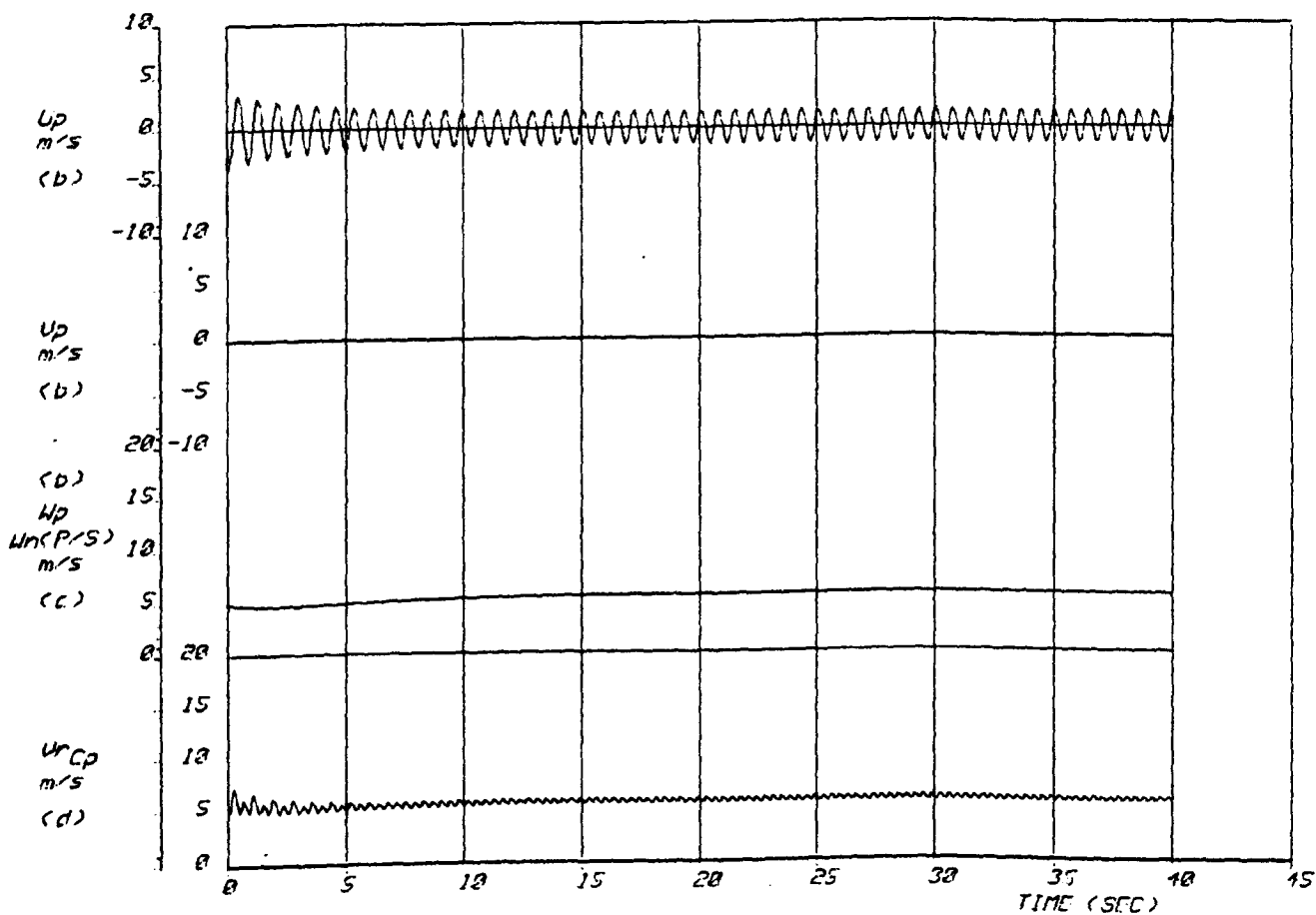
FIG. 2.28
 1 OF 2



Results for added mass coefficient $K_{33} = 5.0$



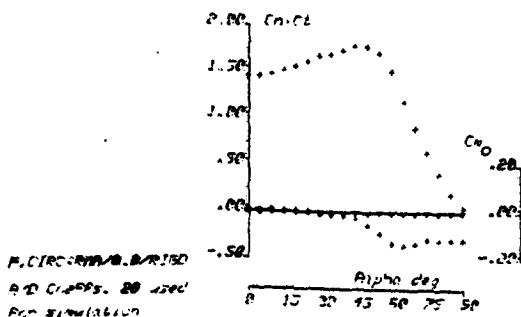
(a) Spatial trajectory of point P ($L^* = 200.0m$)



(b) Velocity components along body axes at P
 (c) airspeed along z at N
 (d) resultant airspeed at canopy Cp

Results for added mass coefficient $K_{33} = 5.0$

F16.	
2.29	
2 OF 2	



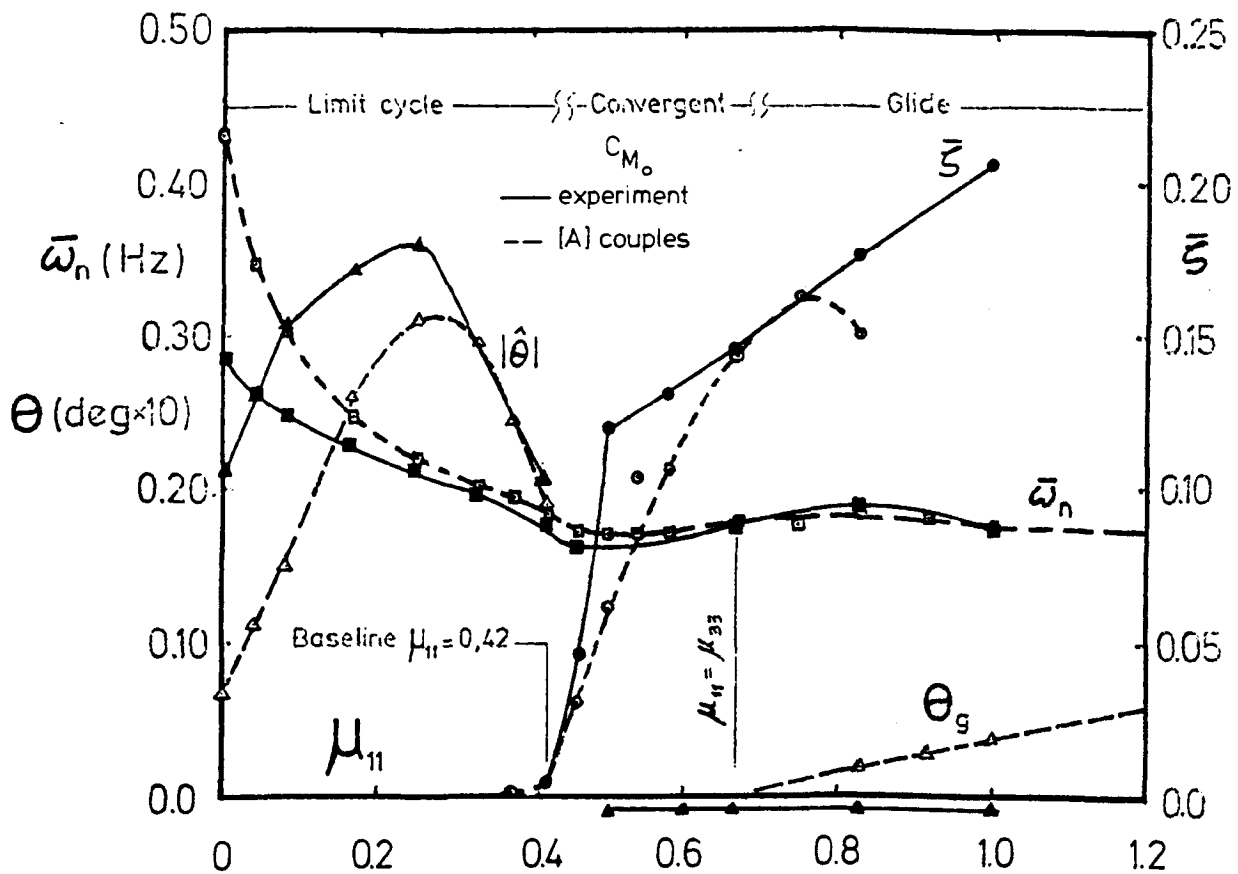


FIGURE 2.30 Effect of variation in A_{11} on stability using experimental C_{M_0}

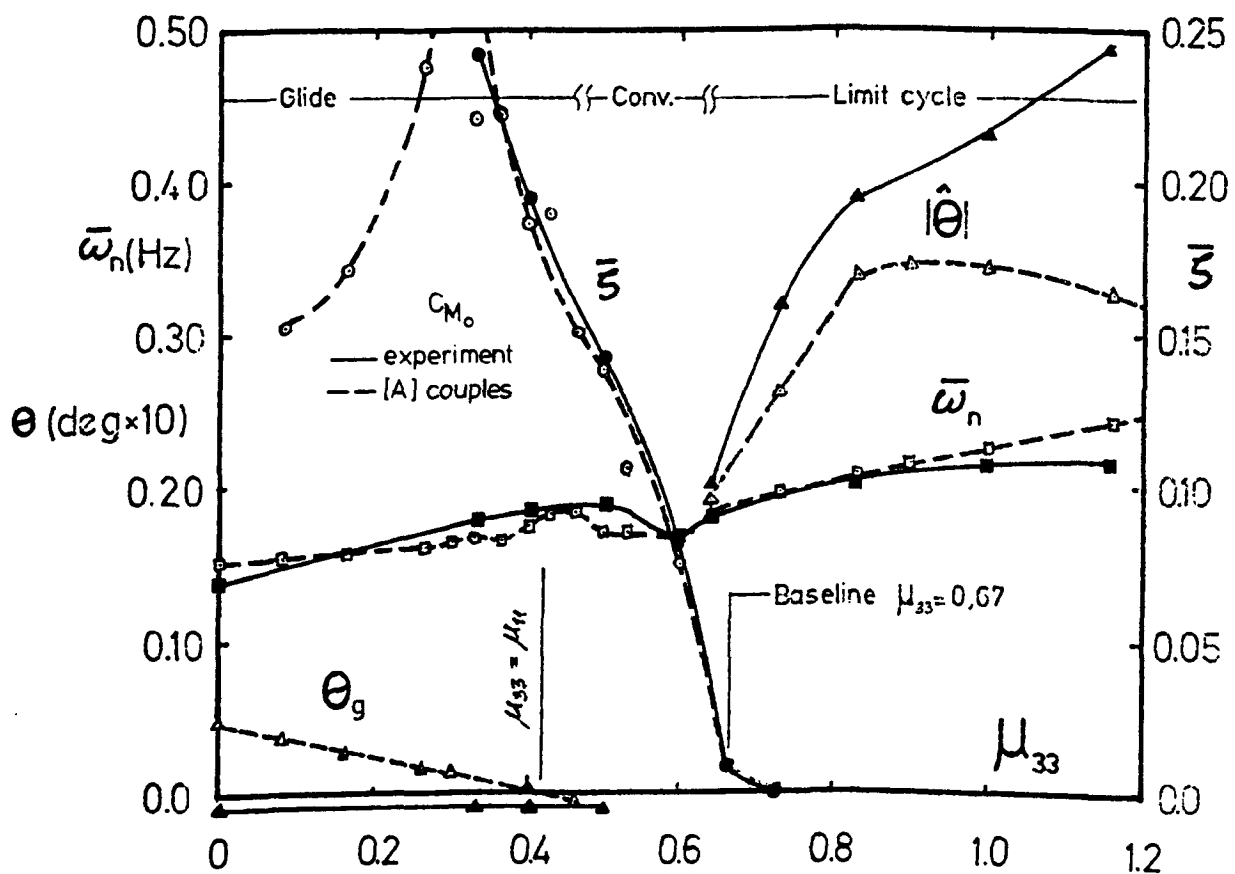


FIGURE 2.31 Effect of variation in A_{33} on stability using experimental C_{M_0}

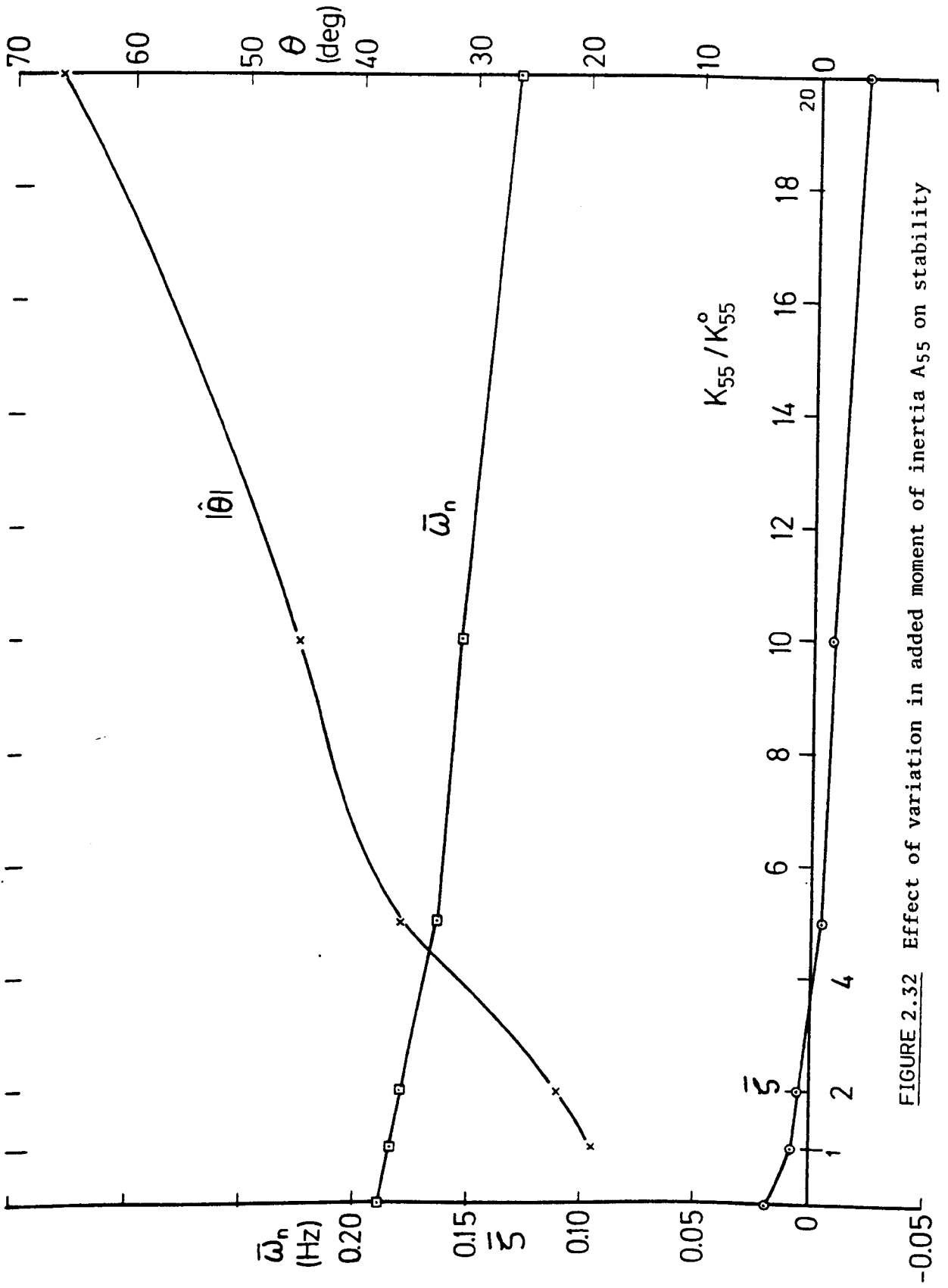


FIGURE 2.32 Effect of variation in added moment of inertia A_{55} on stability

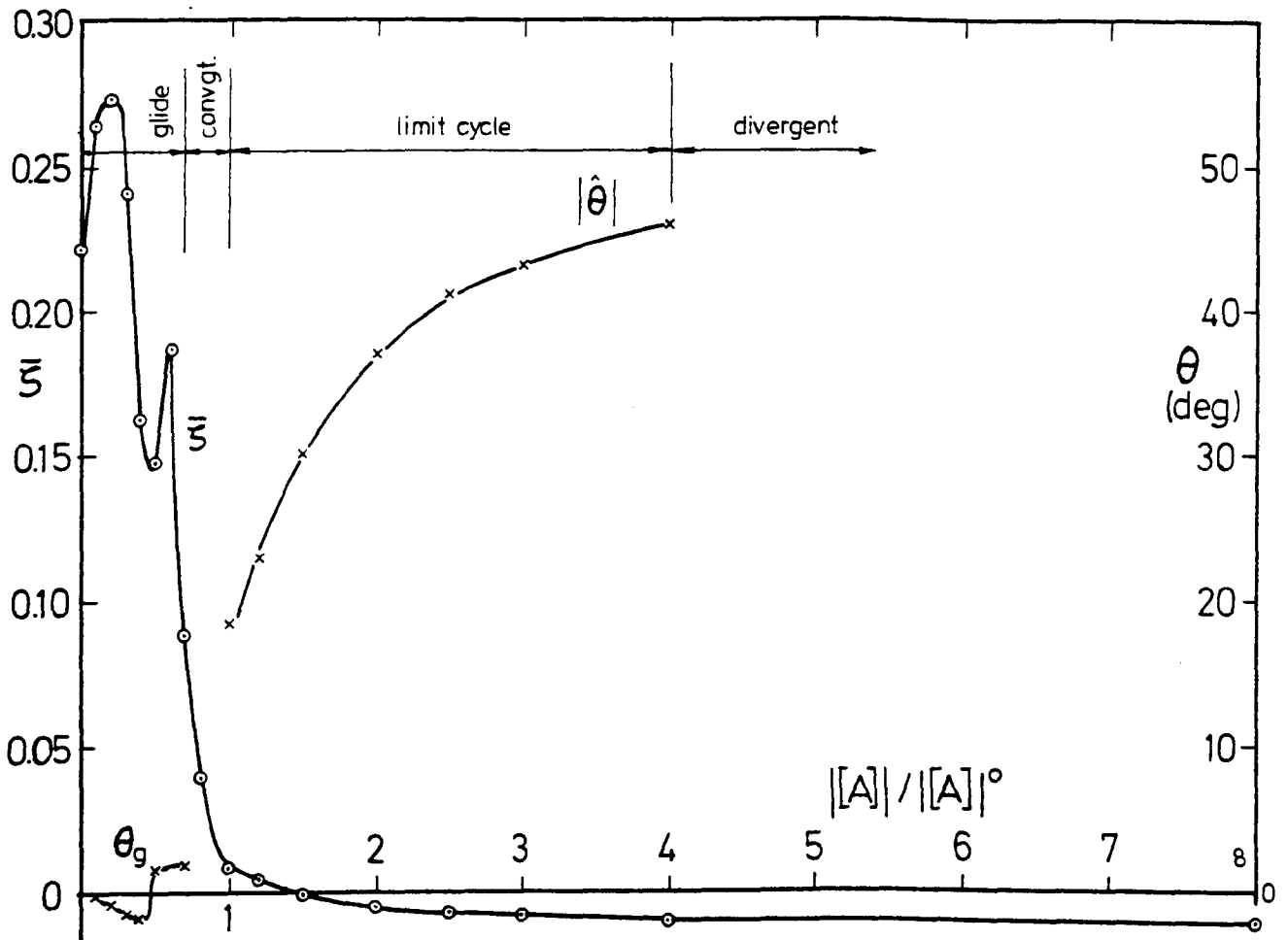


FIGURE 2.33 Effect of scaling of added mass on damping and on amplitude

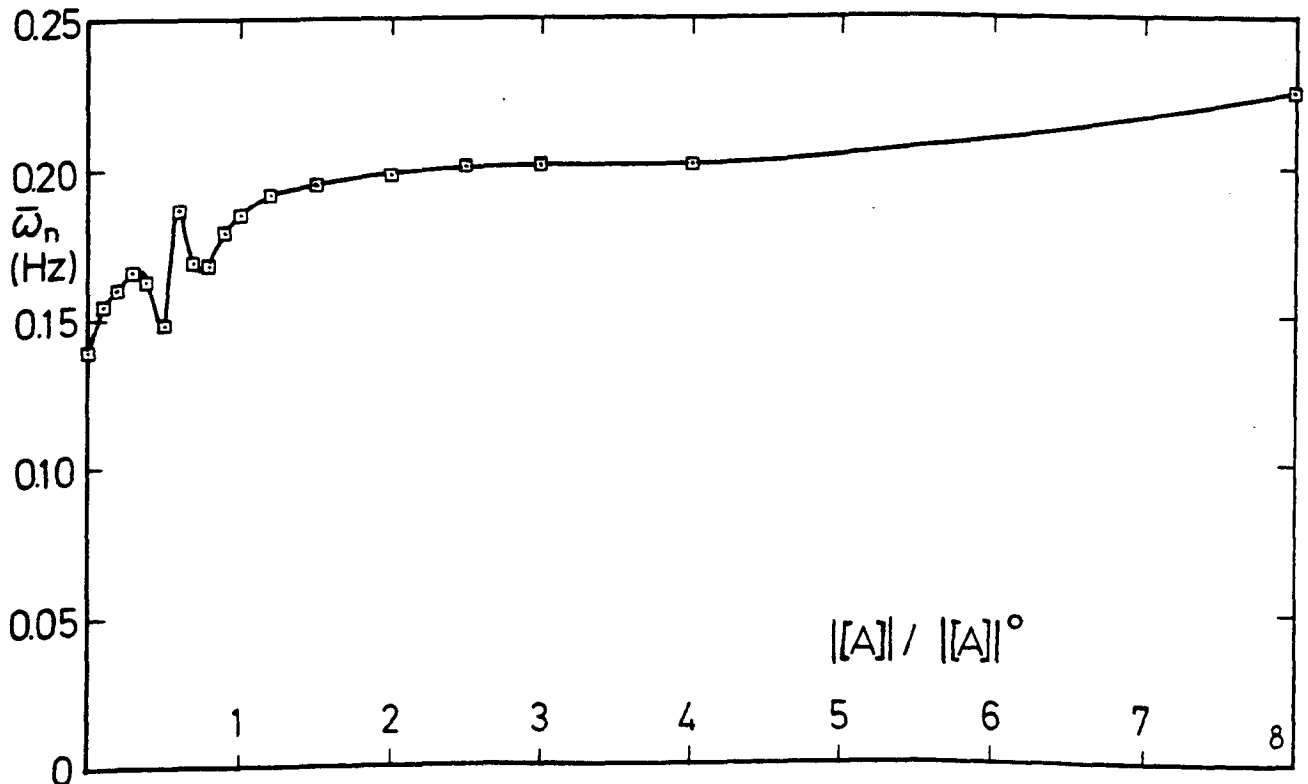
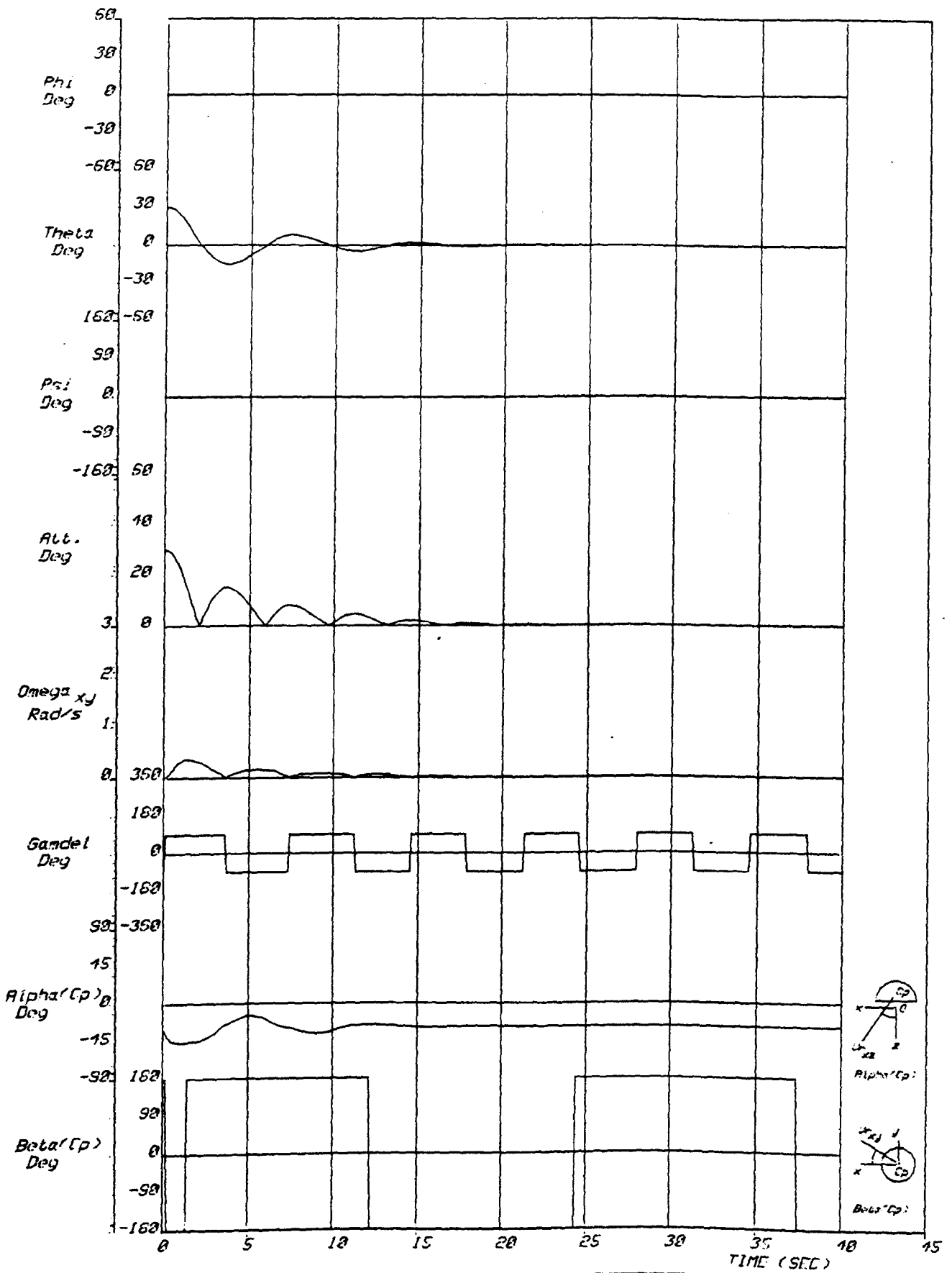
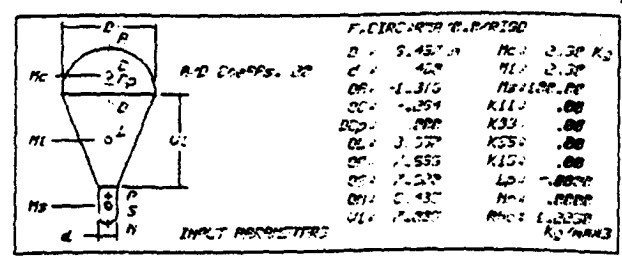


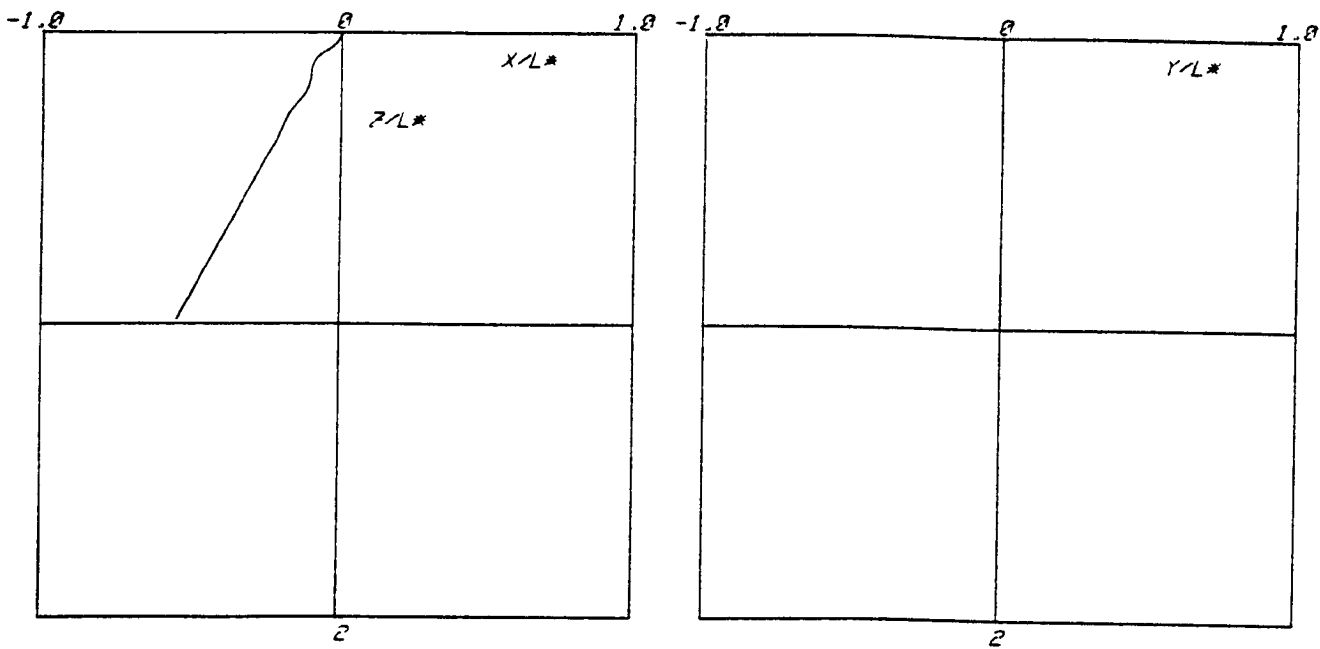
FIGURE 2.34 Effect of scaling of added mass on frequency



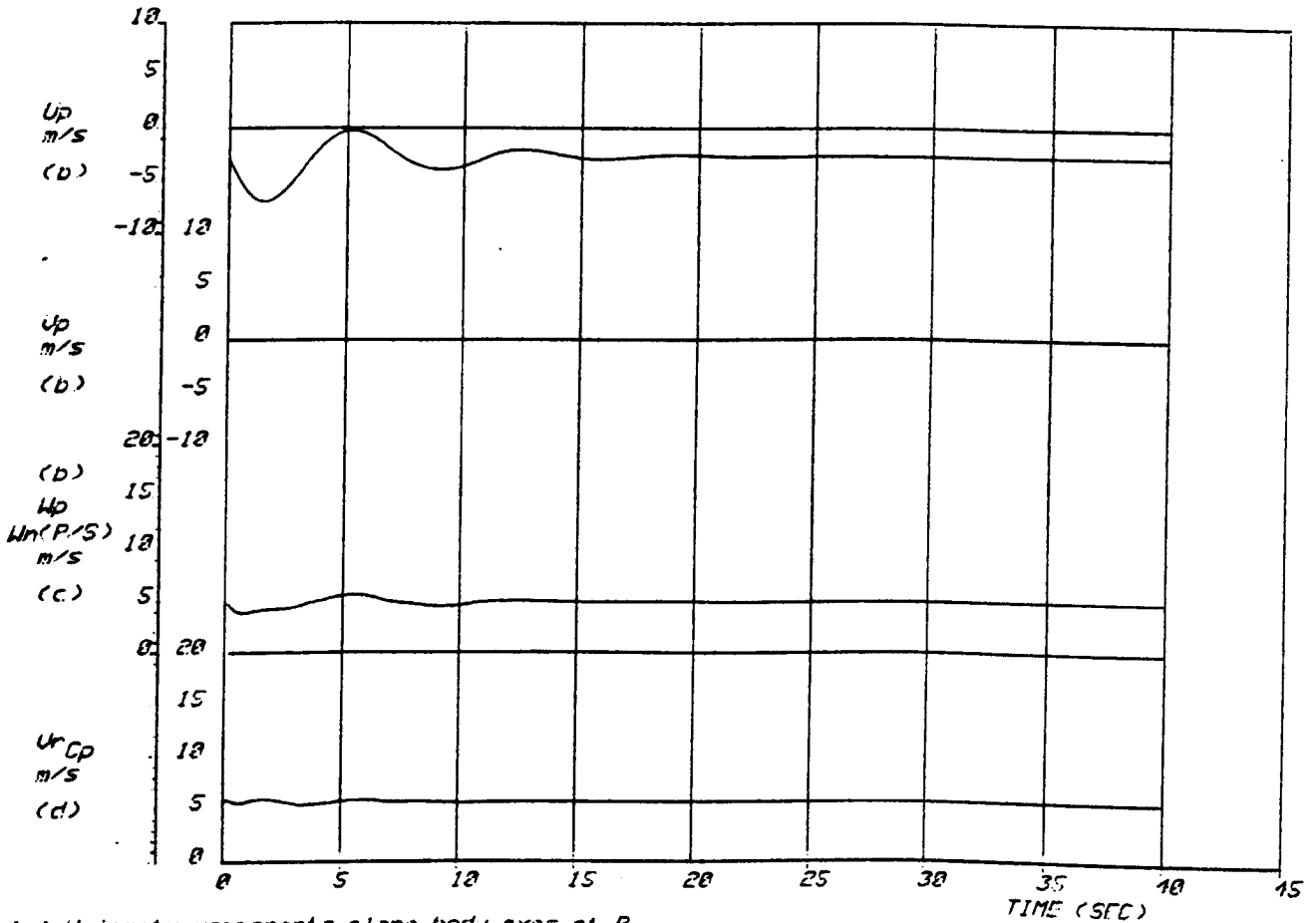
Results for $|[A]| = 0$

FIG.	
2.35	
1 OF 2	





(a) Spatial trajectory of point P ($L^* = 200.0m$)



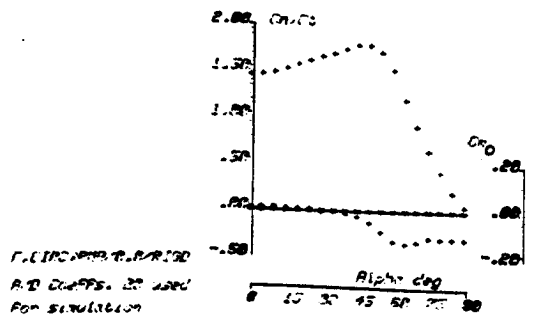
(b) Velocity components along body axes at P

(c) airspeed along z at N

(d) resultant airspeed at canopy C_p

Results for $|\alpha| = 0$

FIG.	
2.36	
2 OF 2	



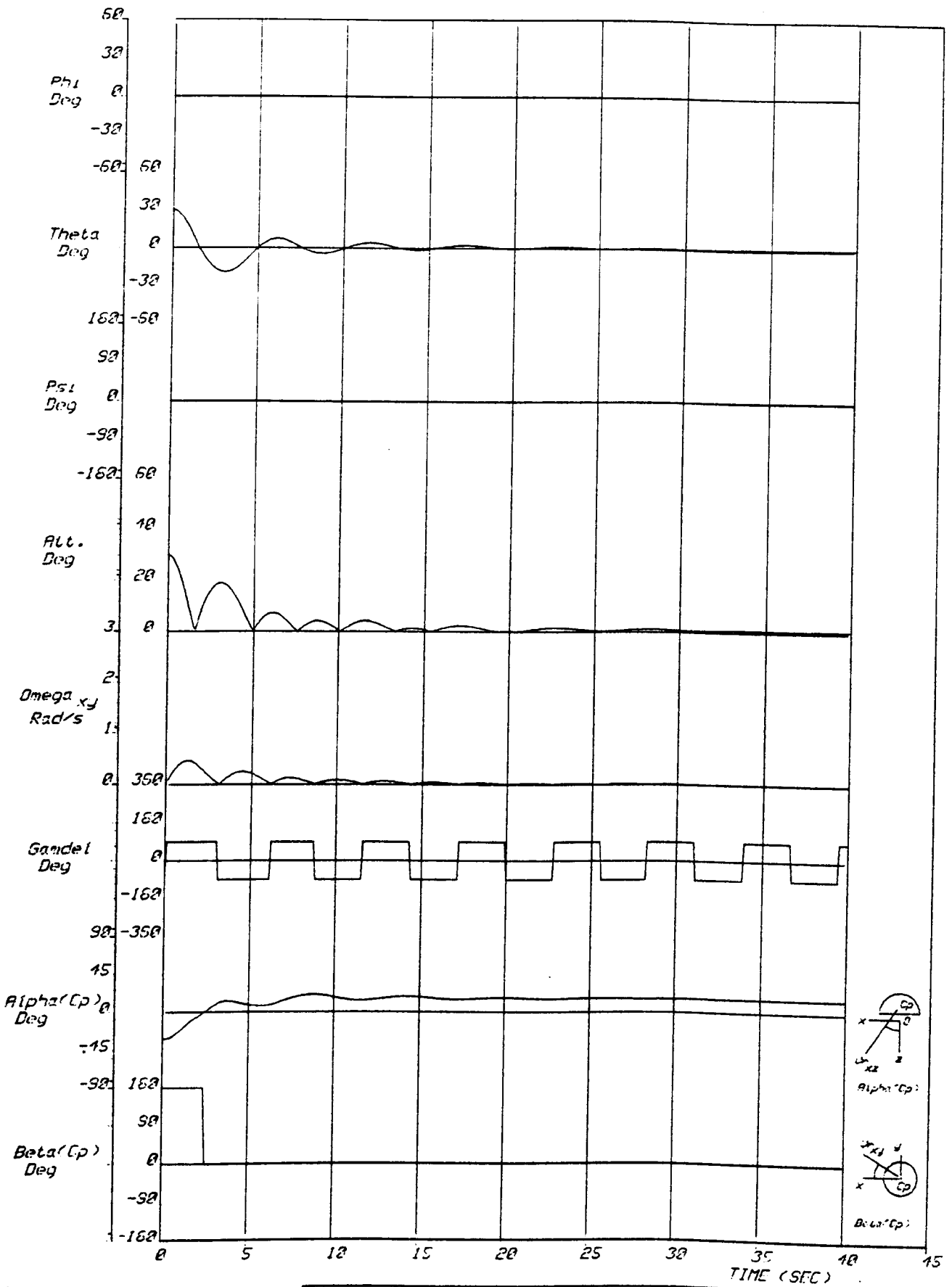
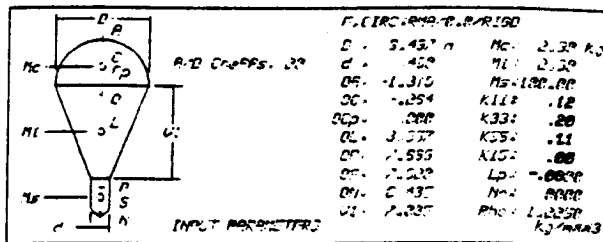
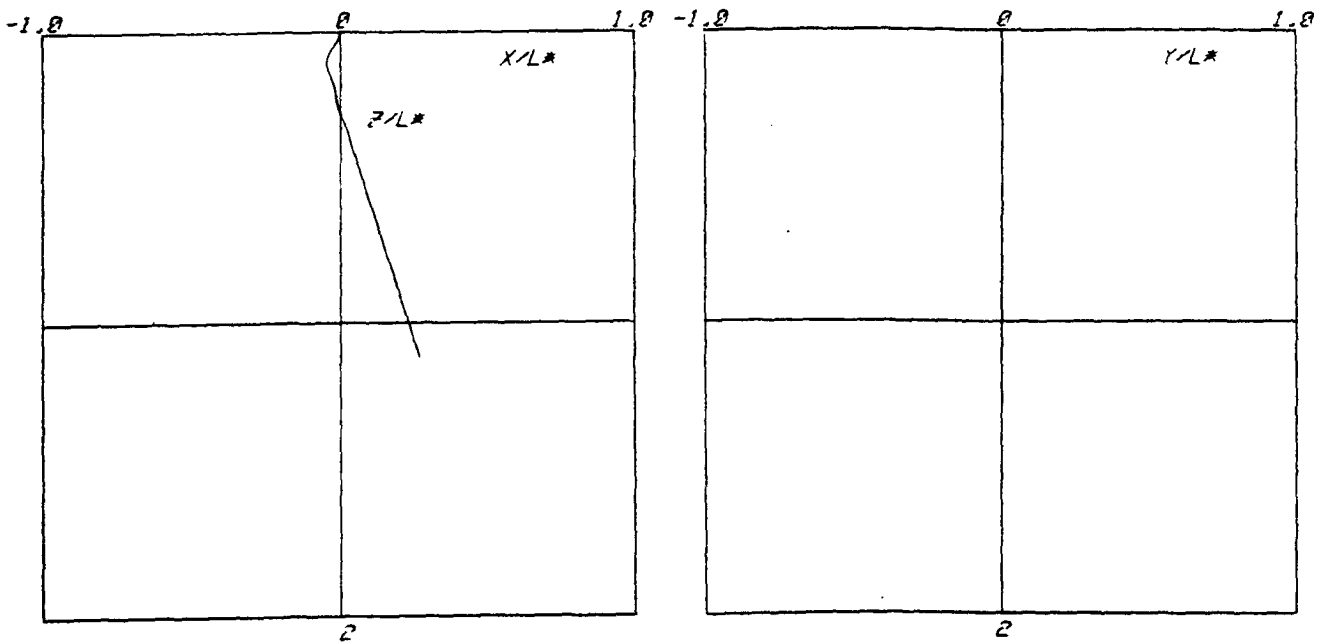


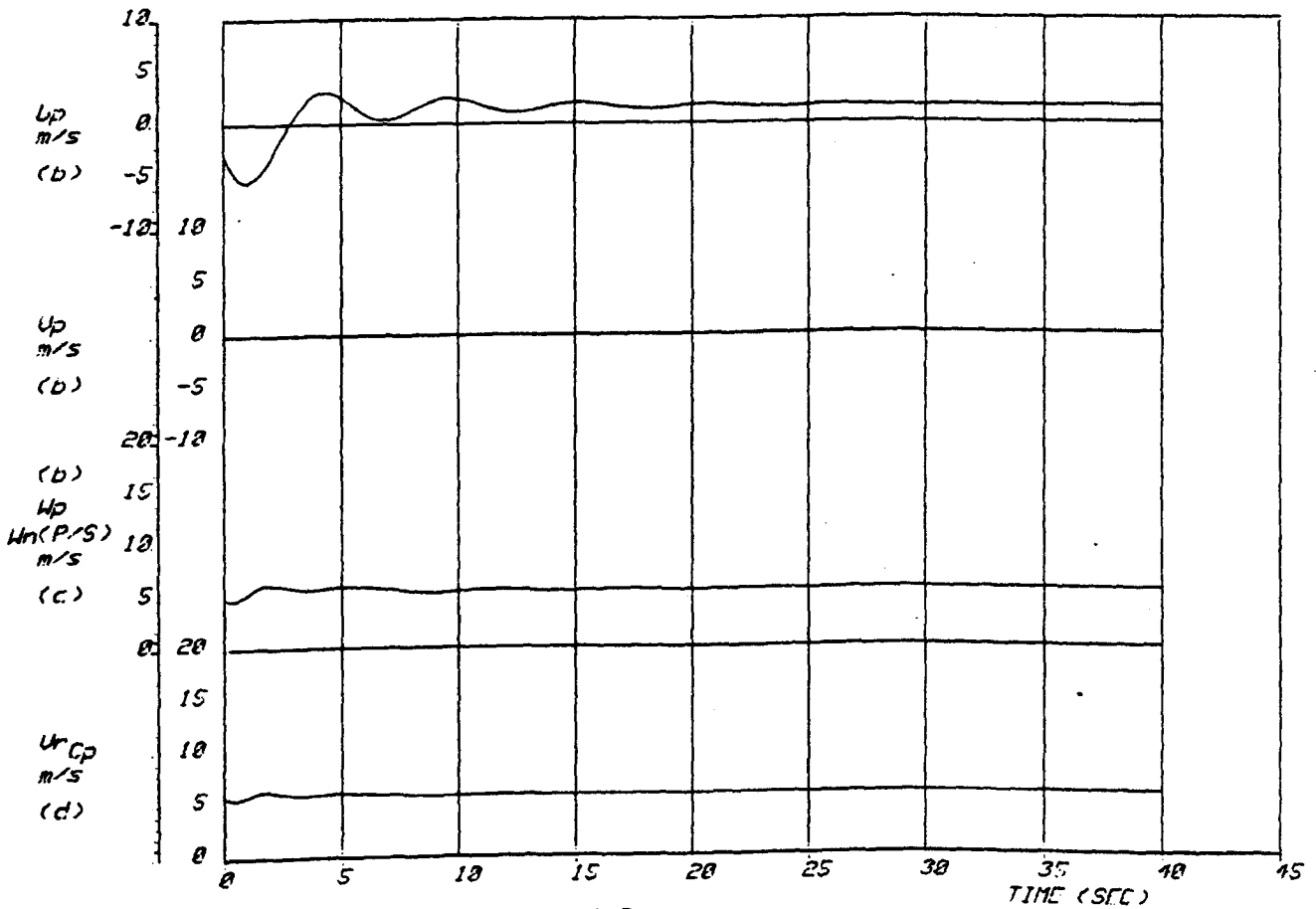
FIG.	
2.37	
1 OF 2	



Results for $||[A]||/|[A]|^0 = 0.5$



(a) Spatial trajectory of point P ($L^* = 200.0m$)



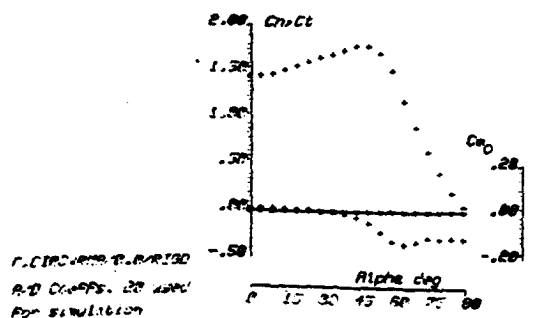
(b) Velocity components along body axes at P

(c) airspeed along z at N

(d) resultant airspeed at canopy Cp

Results for $|\frac{[A]}{[A]}|^0 = 0.5$

FIG.	
2.38	
2 OF 2	



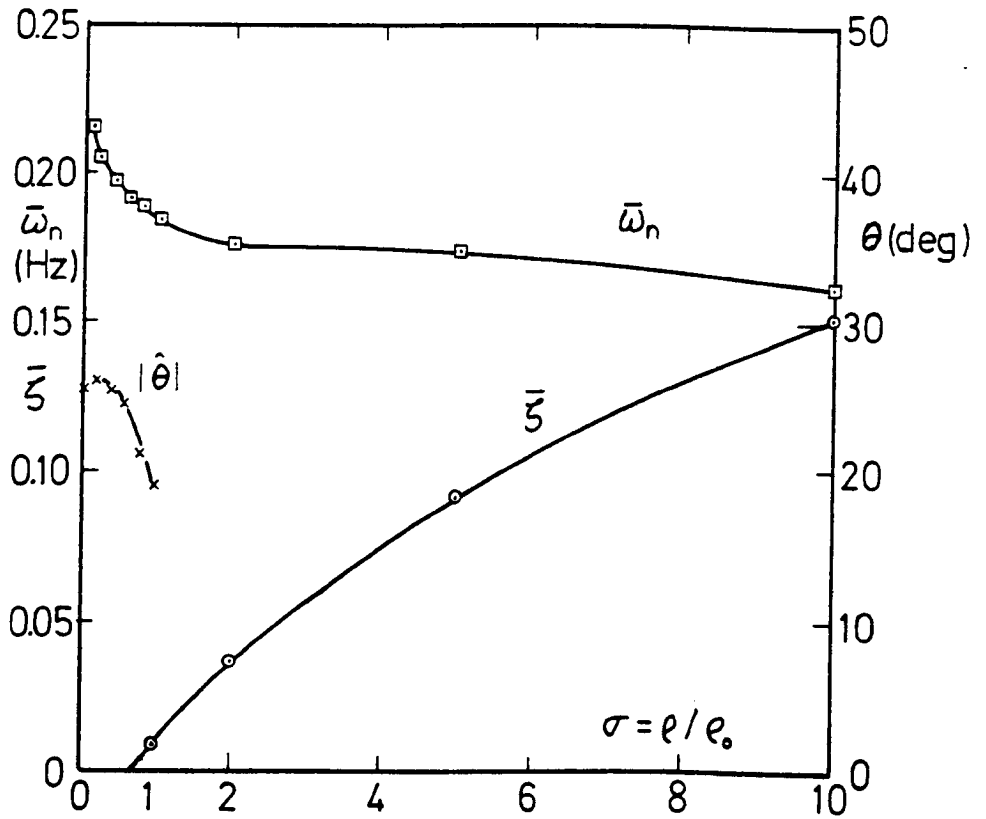


FIGURE 2.39 Effect of variation in fluid density σ on stability ($\sigma = 0.05 - 10.$)

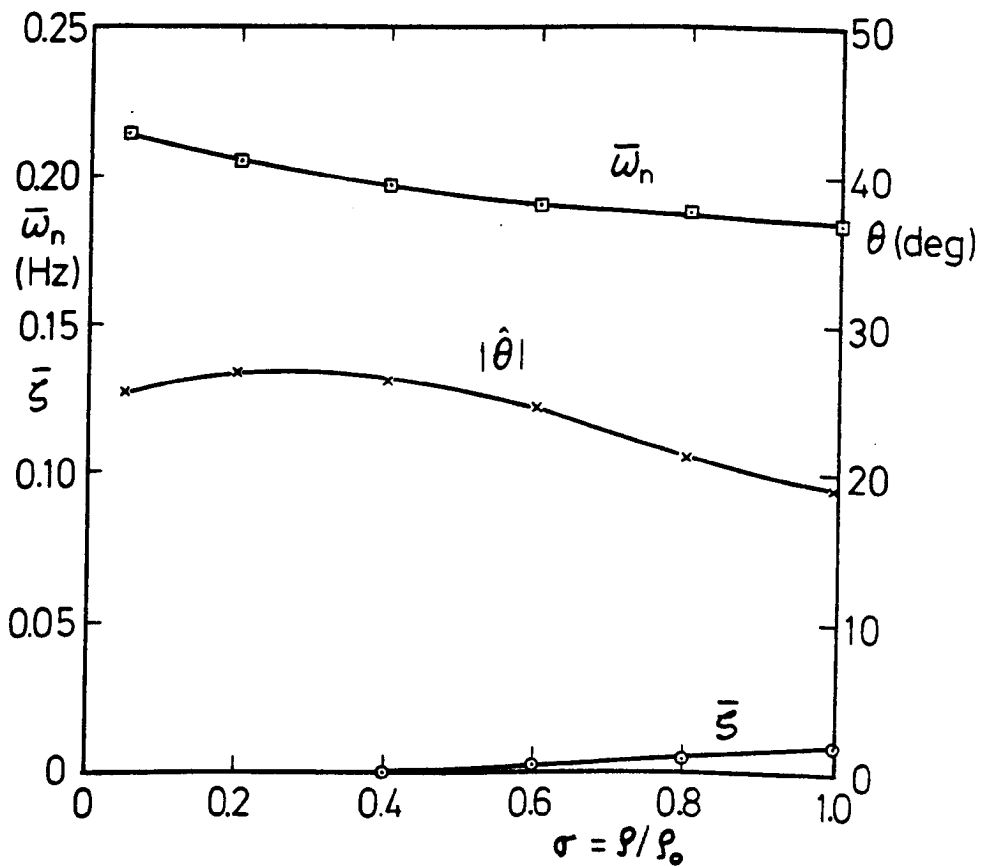
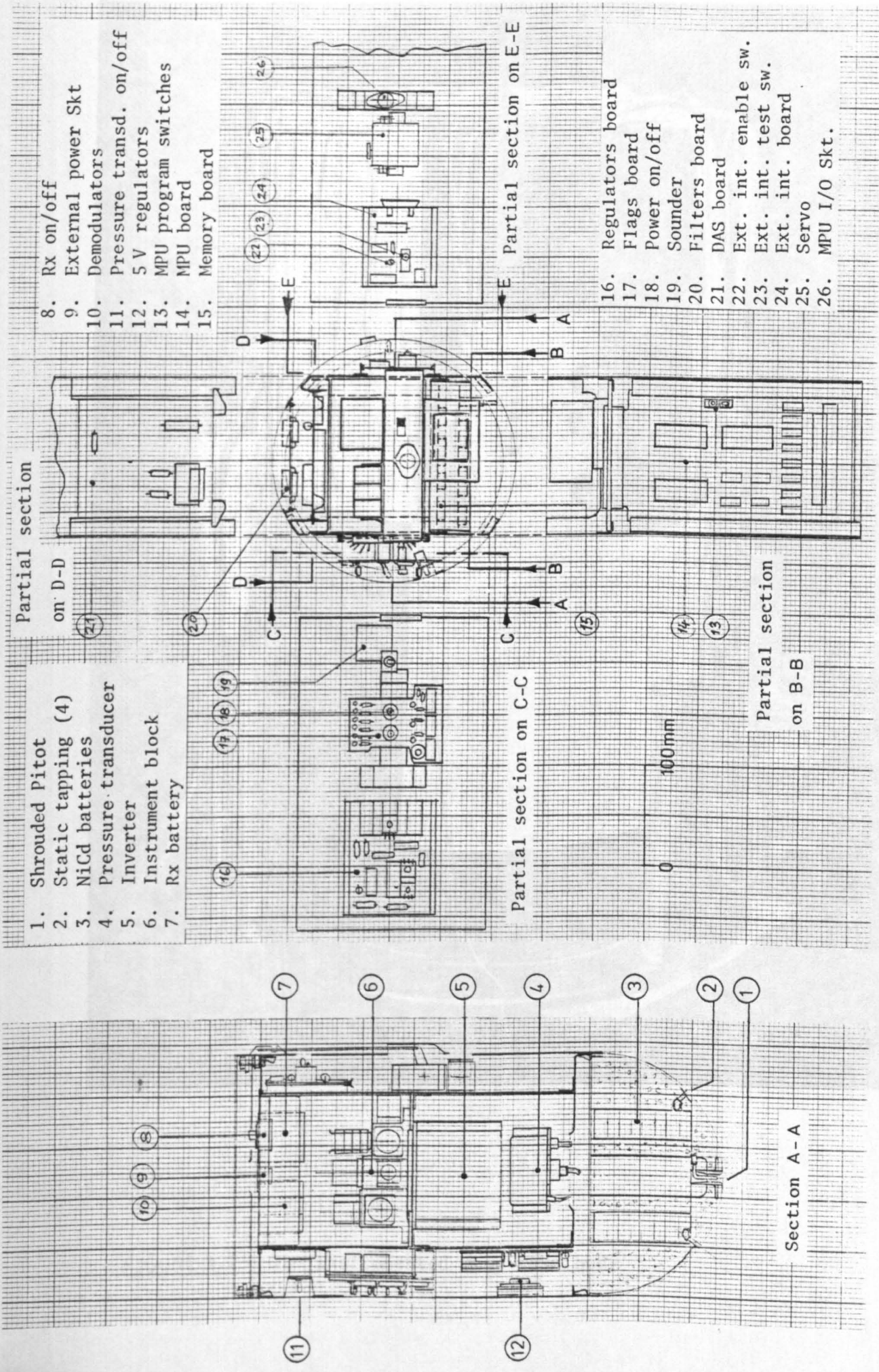


FIGURE 2.40 Effect of variation in fluid density σ on stability ($\sigma = 0.05 - 1.$)



1. Shrouded Pitot
2. Static tapping (4)
3. NiCd batteries
4. Pressure transducer
5. Inverter
6. Instrument block
7. Rx battery

8. Rx on/off
9. External power Skt
10. Demodulators
11. Pressure transd. on/off
12. 5 V regulators
13. MPU program switches
14. MPU board
15. Memory board

16. Regulators board
17. Flags board
18. Power on/off
19. Sounder
20. Filters board
21. DAS board
22. Ext. int. enable sw.
23. Ext. int. test sw.
24. Ext. int. board
25. Servo
26. MPU I/O Skt.

FIGURE 3.1 Layout drawing of the instrumented body

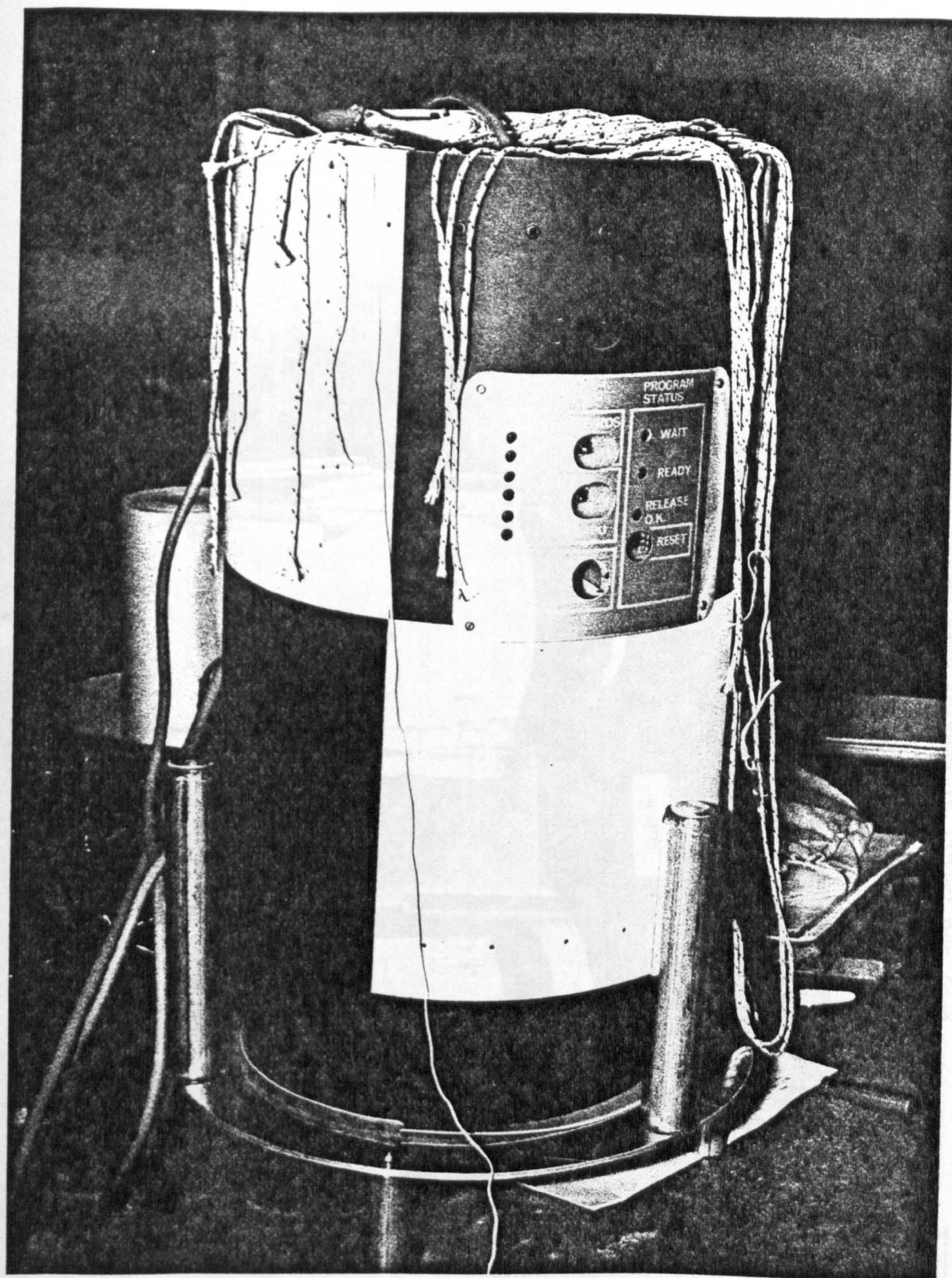


FIGURE 3.2 The instrumented drop test body

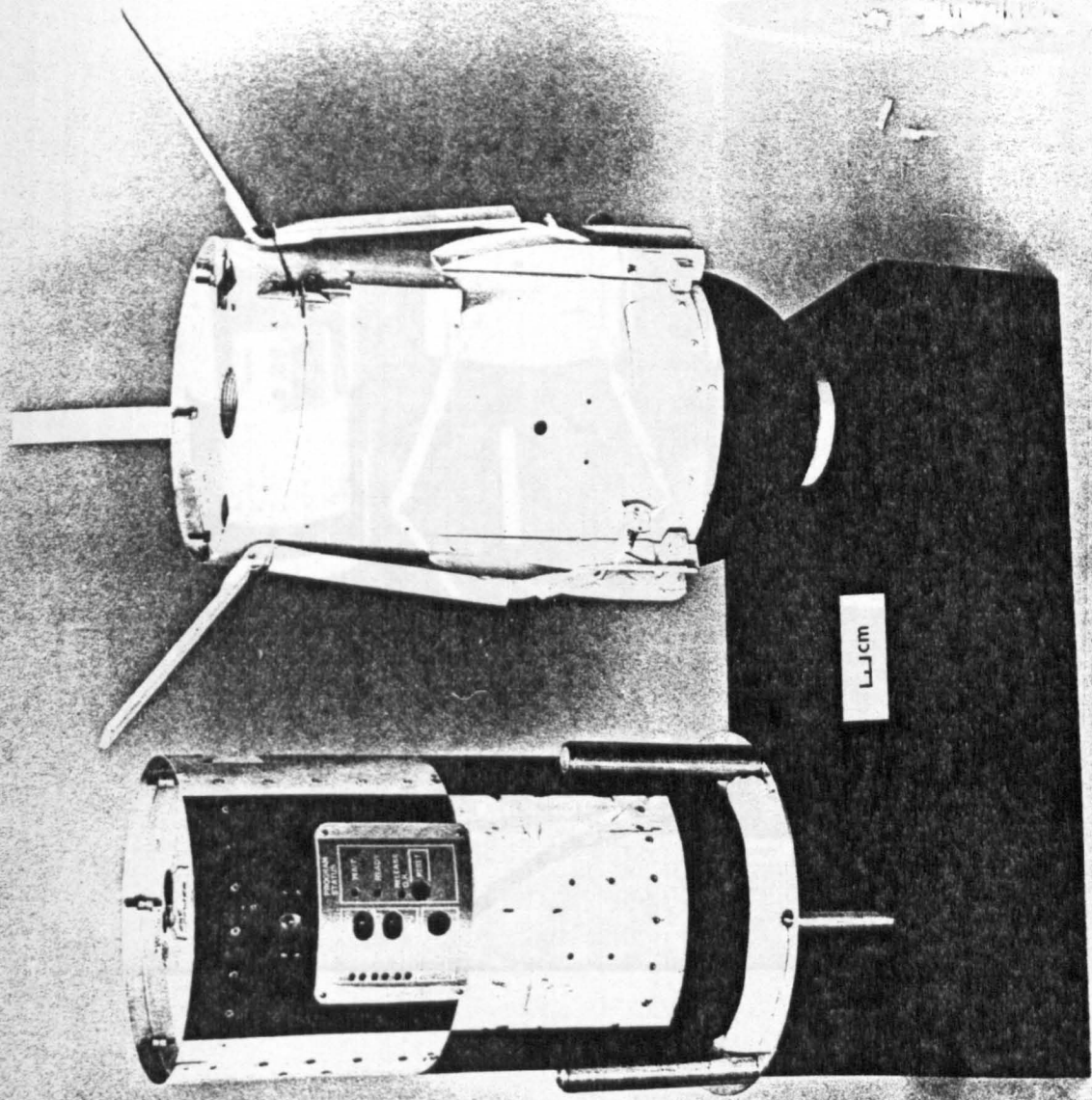


FIGURE 3.3 Instrumented body and impact attenuator development model



FIGURE 3.4 SB, dummy and BB drop test bodies

FIGURE 3.7 Sectional sketch of large test body

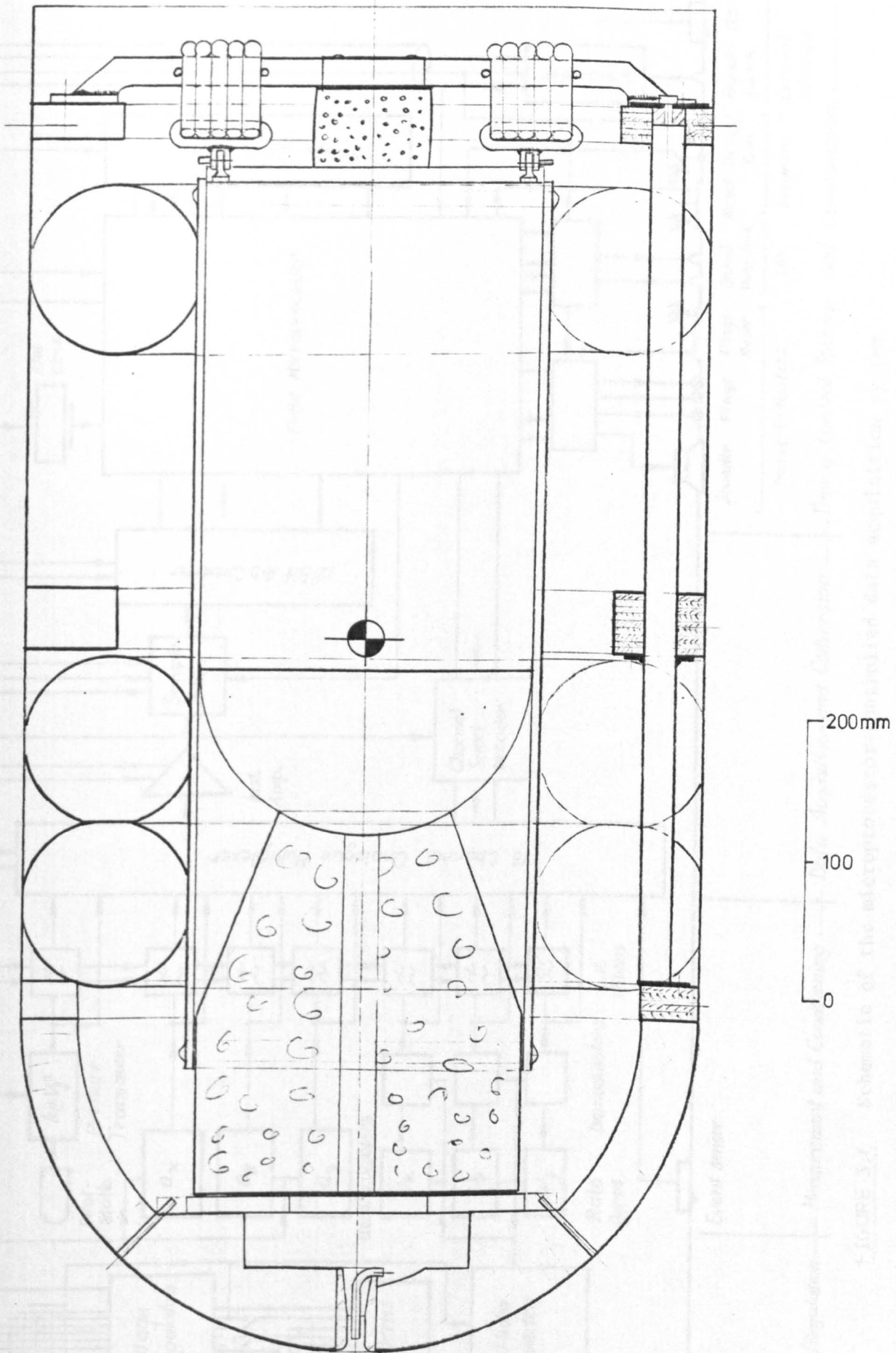


FIGURE 3.5 Sectional sketch of large test body

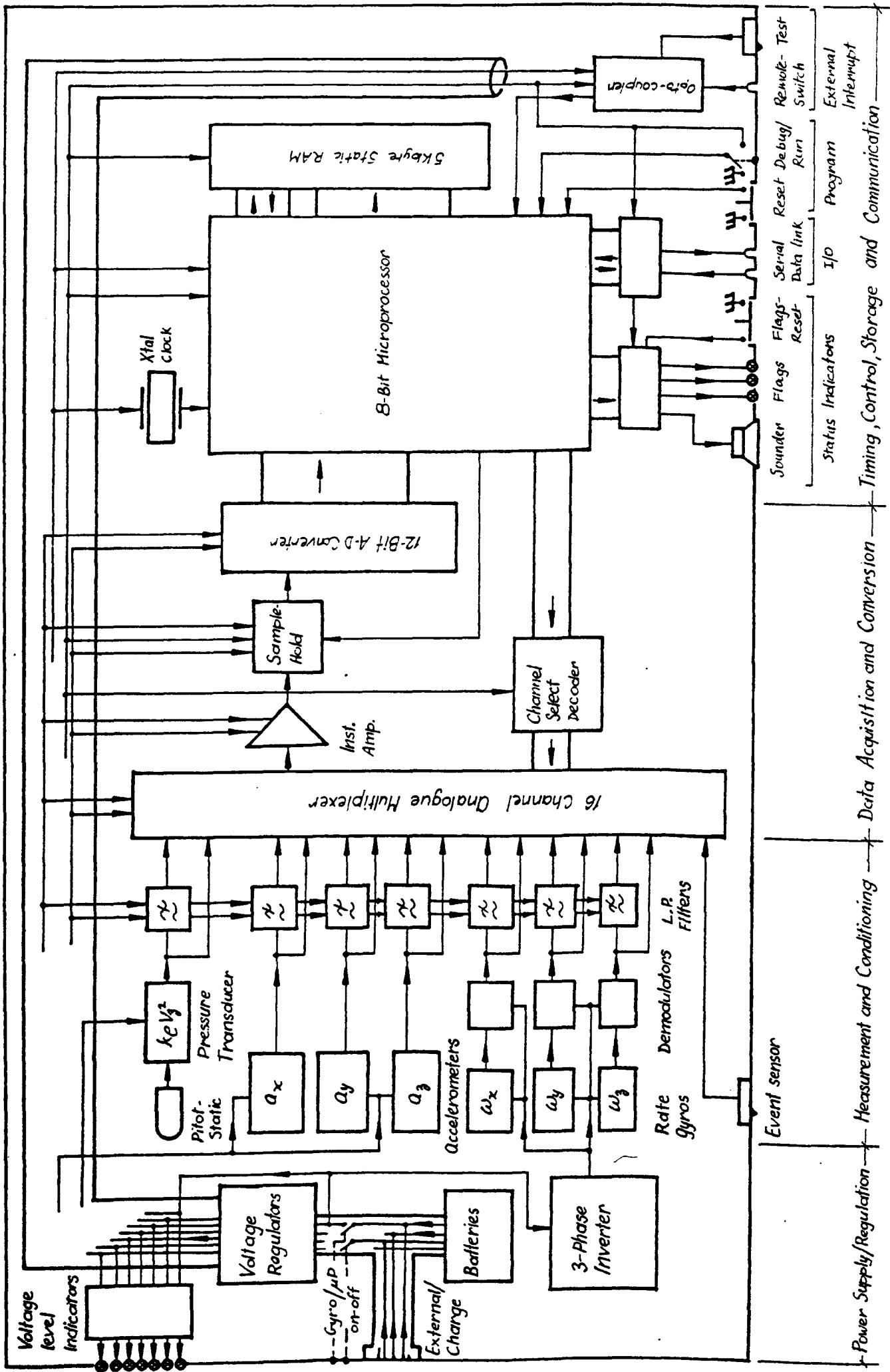
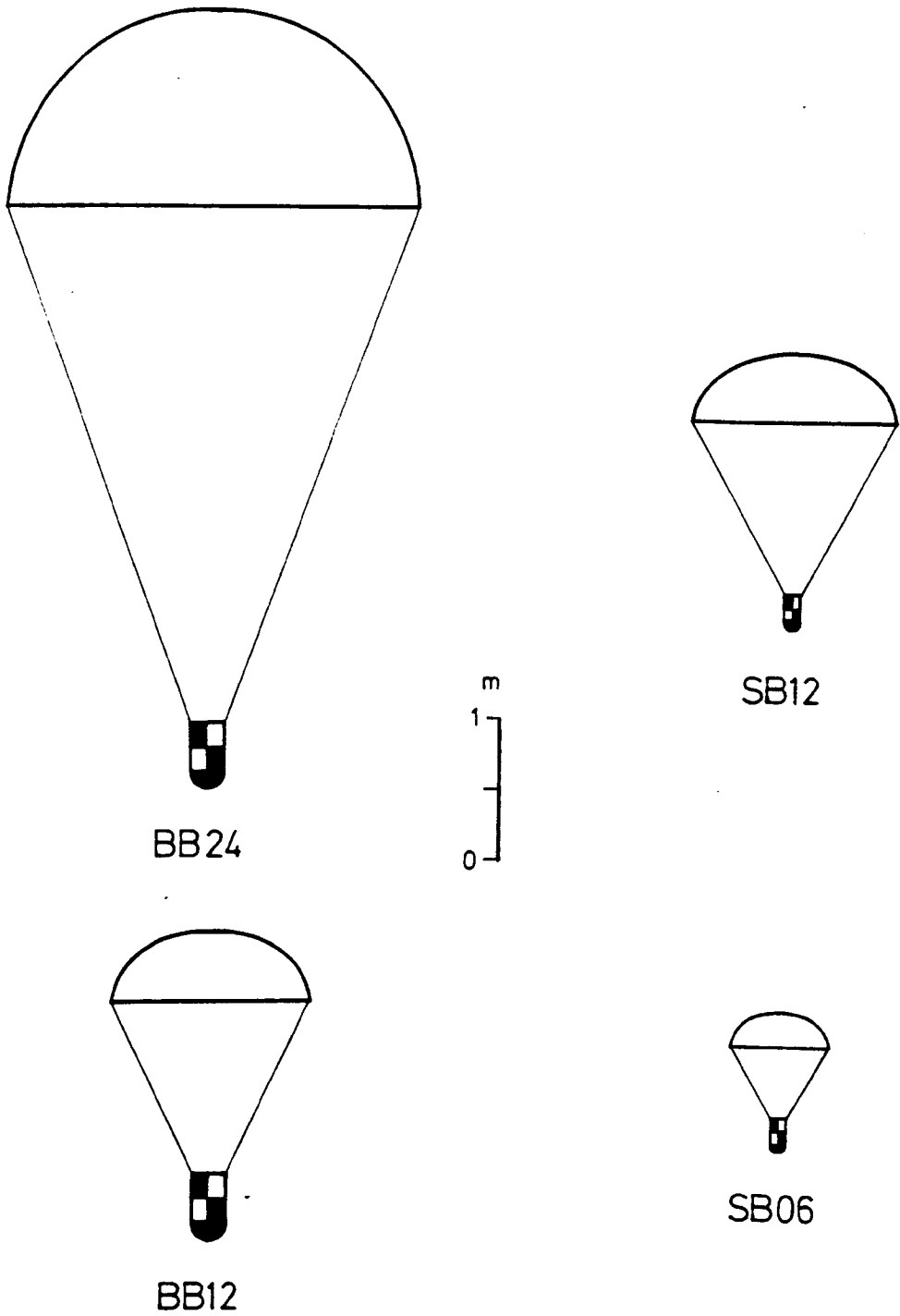


FIGURE 3.6 Schematic of the microprocessor-controlled data acquisition system



	D_p / d_s	l_L / d_s
BB24	0.082	15.1
SB12	0.082	10.0
BB12	0.169	5.0
SB06	0.170	4.4

FIGURE 3.7 Outline sketches of the four canopy/store configurations used

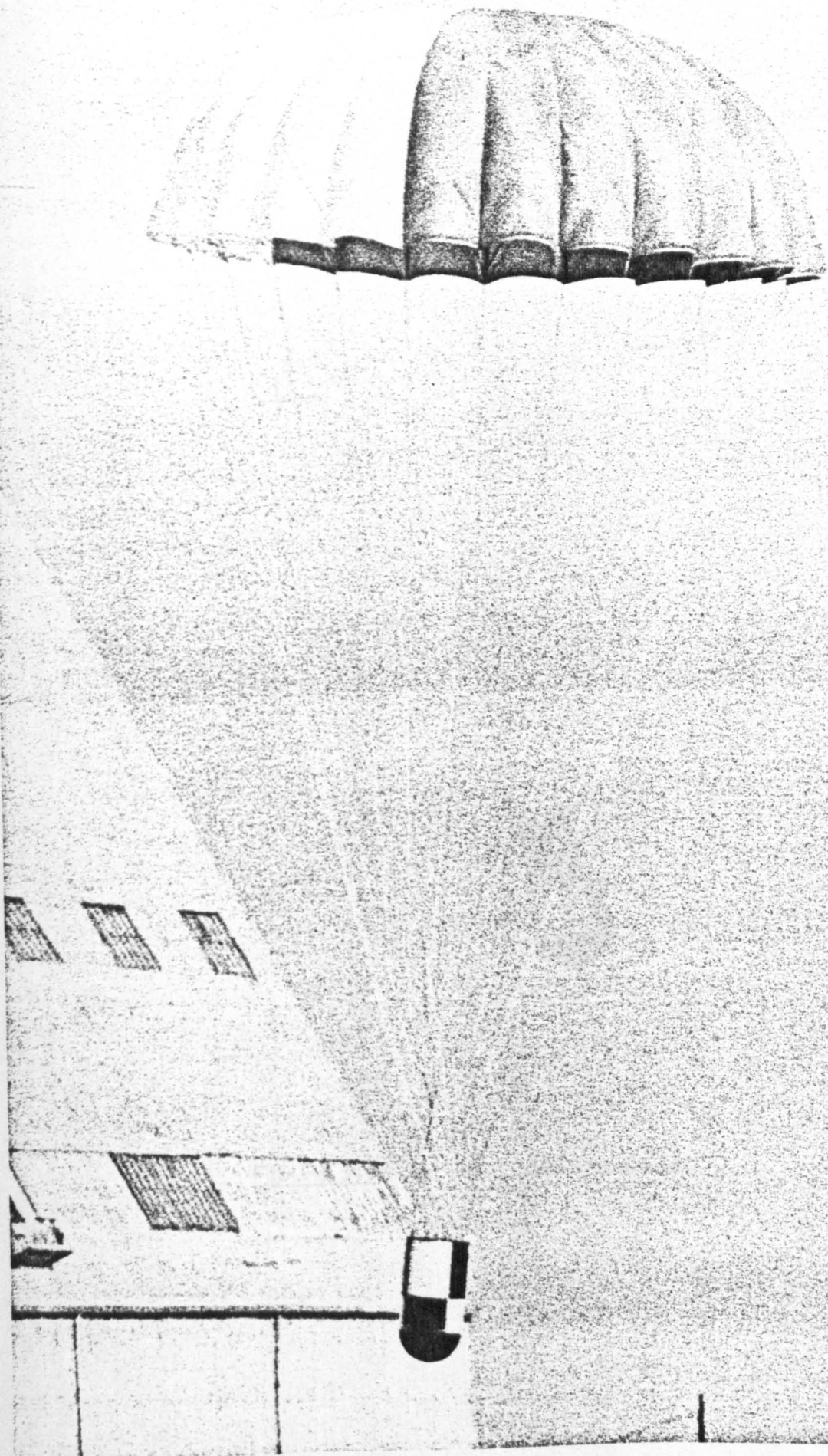


FIGURE 3.8 BB24 configuration

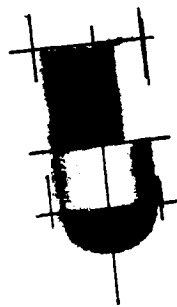
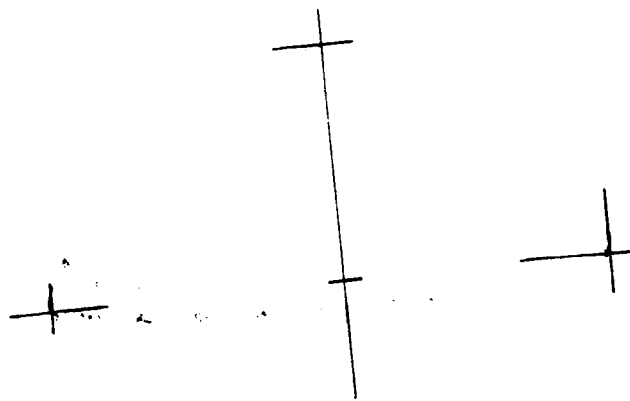
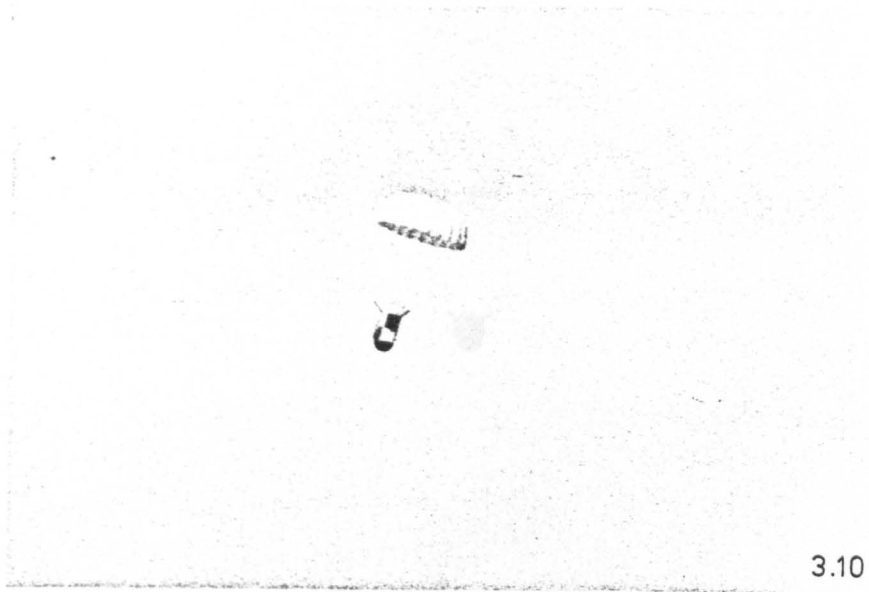


FIGURE 3.9

BB12 configuration

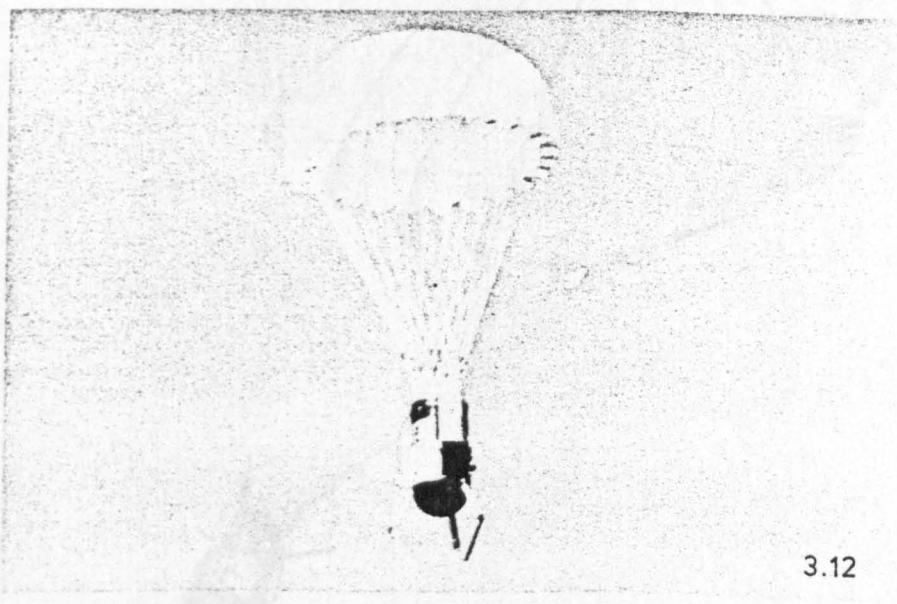


3.10

FIGURE 3.11 SB06 configuration: impact attenuator



3.11



3.12

FIGURES 3.10-12 SB06 configuration: impact attenuators stowed/deployed

FIGURE 3.13 SB06 configuration: canopy edge luffing

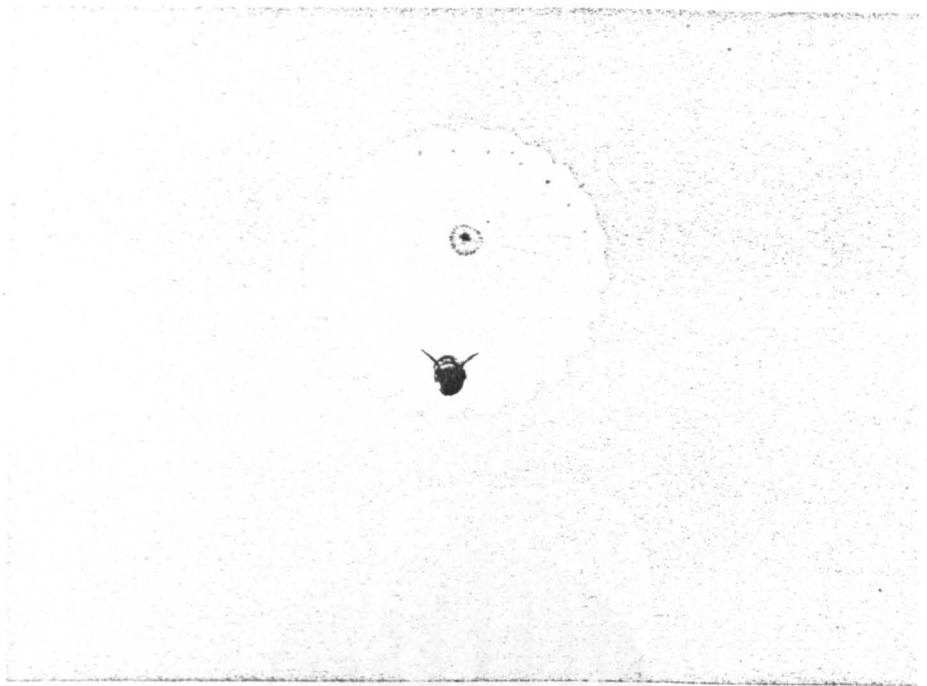


FIGURE 3.13 SB12 configuration

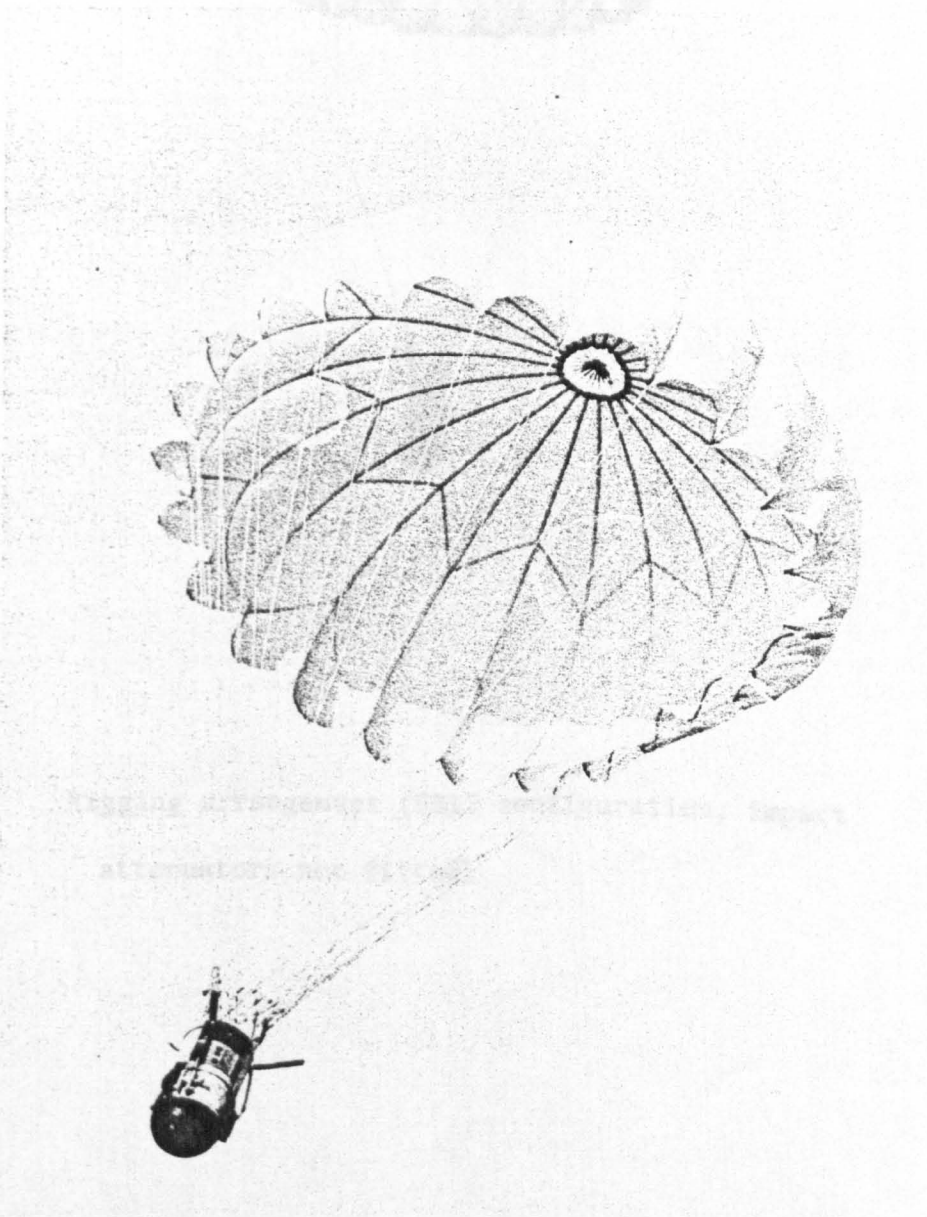


FIGURE 3.14 SB12 configuration: canopy edge luffing

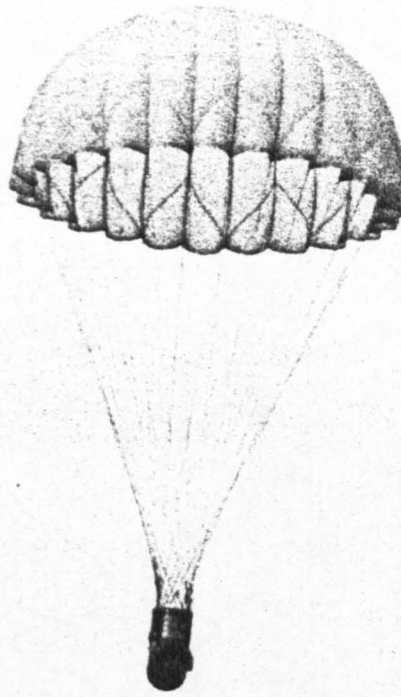


FIGURE 3.15

Rigging arrangement (SB12 configuration; impact attenuators not fitted)

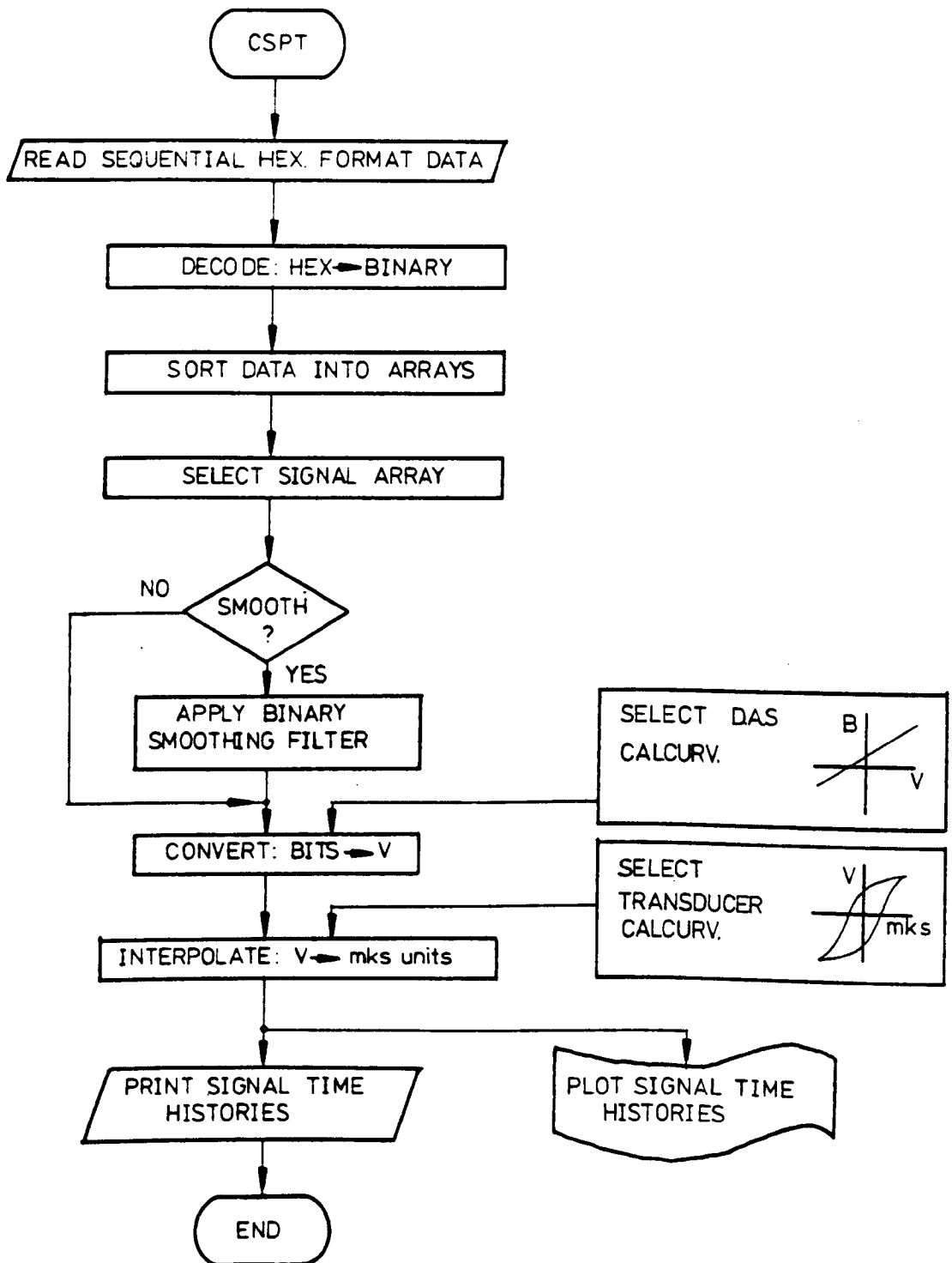


FIGURE 3.16

High-level flow diagram of programme CSPT

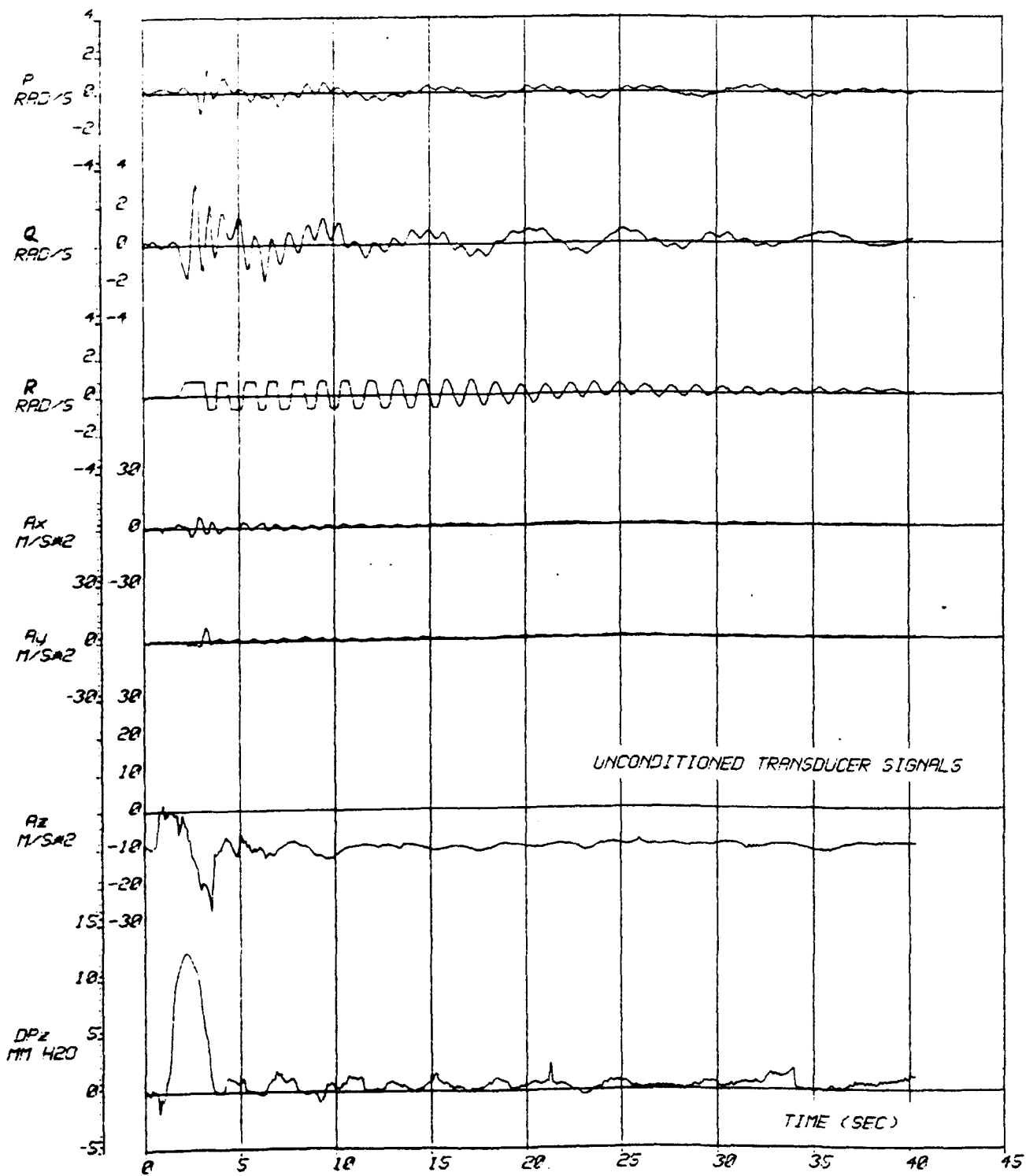


FIG. 3.17 1 OF 5	DROP NO. 24UF00	CANOPY FC1/1	SAMP. RATE/CH. 10/S	DAQPROG: JAE 310
	DATE 2005.75	DIAMETER 5.50 M.	T/OPEN 3.06 S	SOURCEFILE: JEC500
	TIME 1432	BASE SEPN. 7.04 M	T/SS: NA	
	WIND 15 KTS	STORE MASS 34.91 KG	T/FINISH 44.85 S	

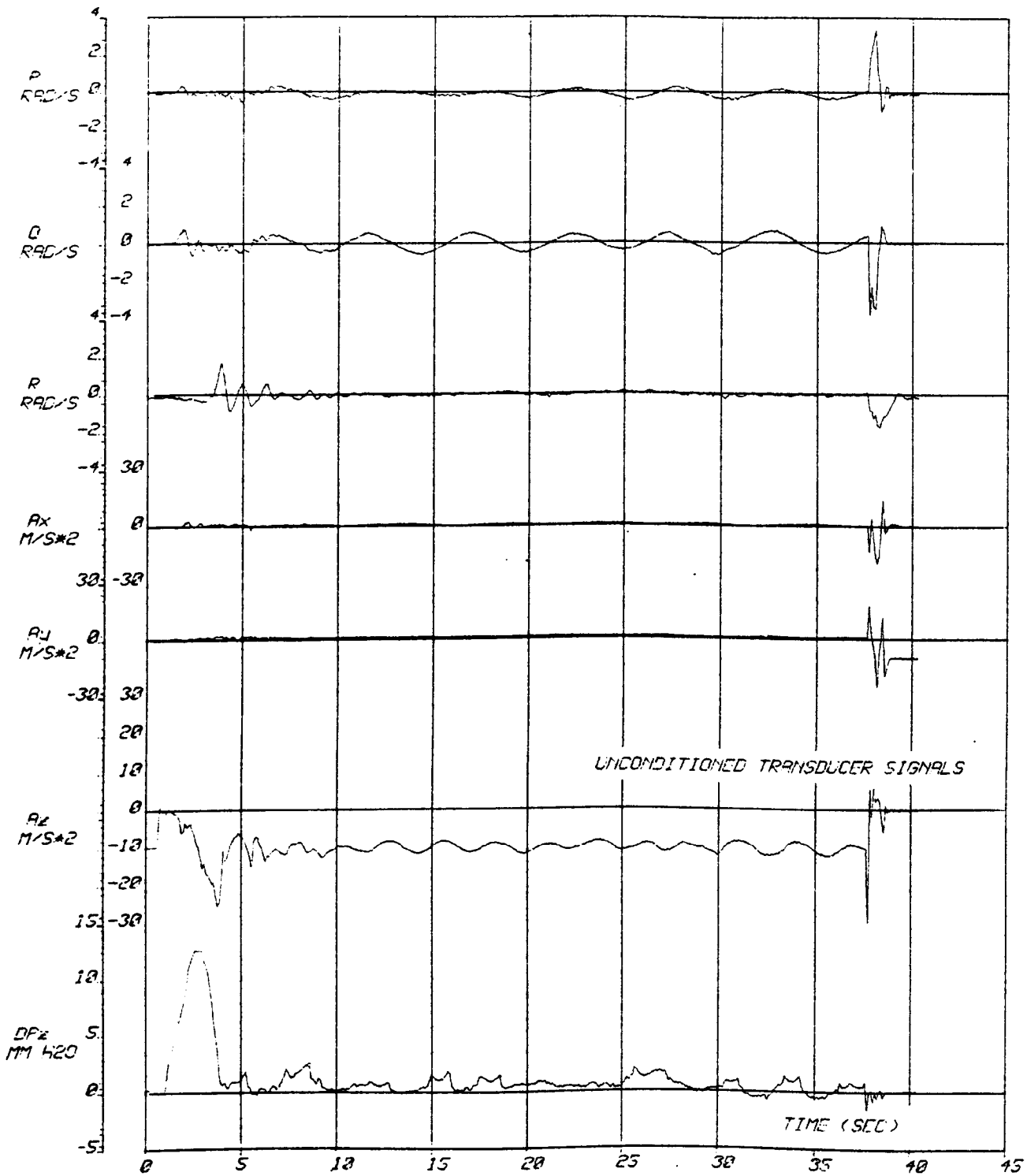


FIG. 318 1 OF 5	DRCP NO. 24UF02	CANOPY: FC1/1	SAMP. RATE/CH.: 10/S	DAQPROG: JAE 318
	DATE: 021075	DIAMETER: 5.50 M	T/OPEN: 3.77 S	SOURCEFILE: JECS02
	TIME: 1332	BASE SEPN.: 7.04 M	T/SS: 6 S	
	WIND: 6 KTS	STORE MASS: 34.95 KG	T/FINISH: 37.32 S	

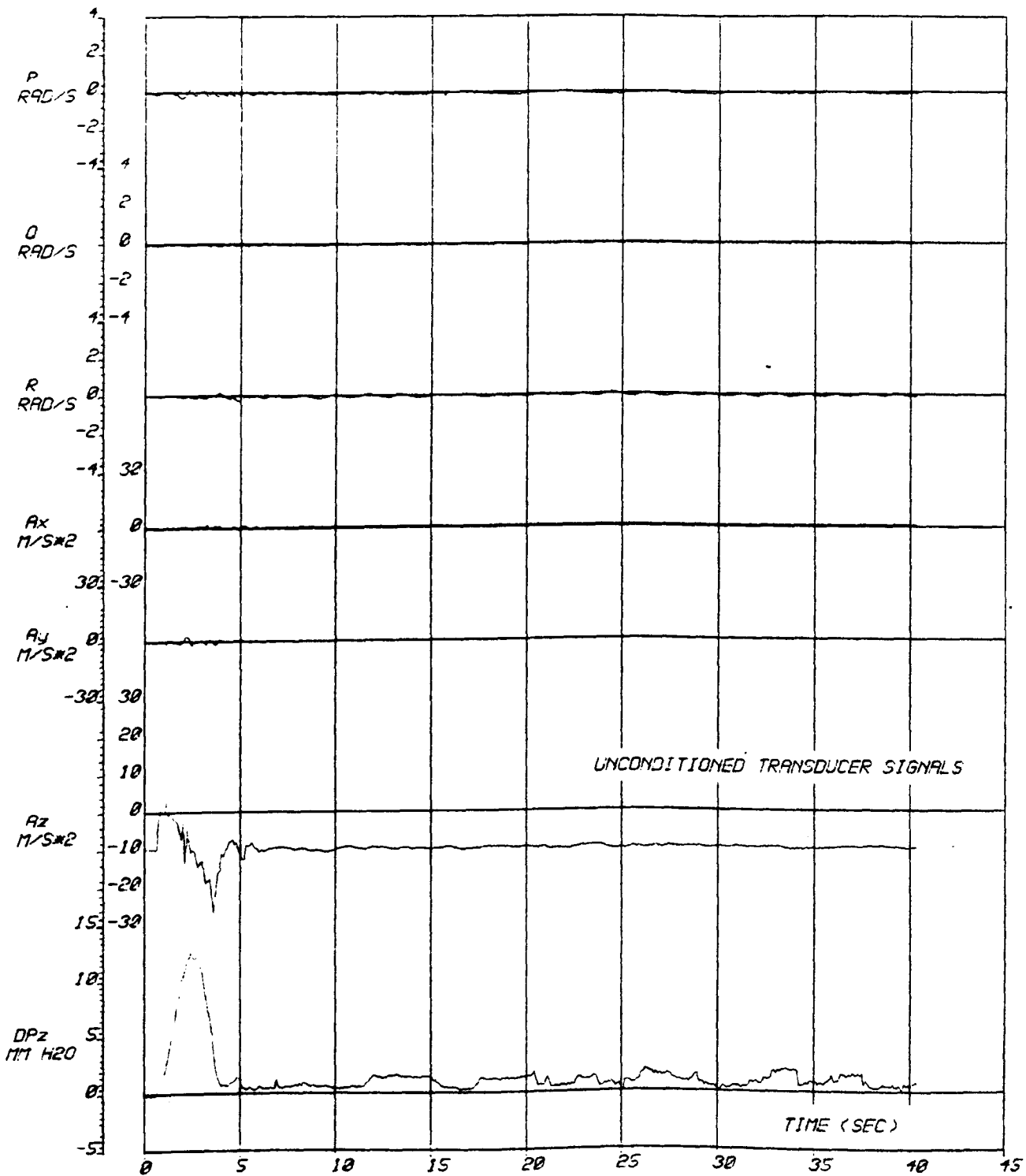


FIG. 3.19	DROP NO.: 24UF05	CANDPY: FC1/1	SAMP. RATE/CH.: 10/S	DAQPROG: JAE 310
	DATE: 051079	DIAMETER: 6.50 M	T/OPEN: 3.79 S	SOURCEFILE: JECS05
	TIME: 1155	BASE SEPN.: 7.04 M	T/SS: 5 S	
1 OF 5	#WIND#: 2 KTS	STORE MASS: 34.95 KG	T/FINISH: 56.37 S	

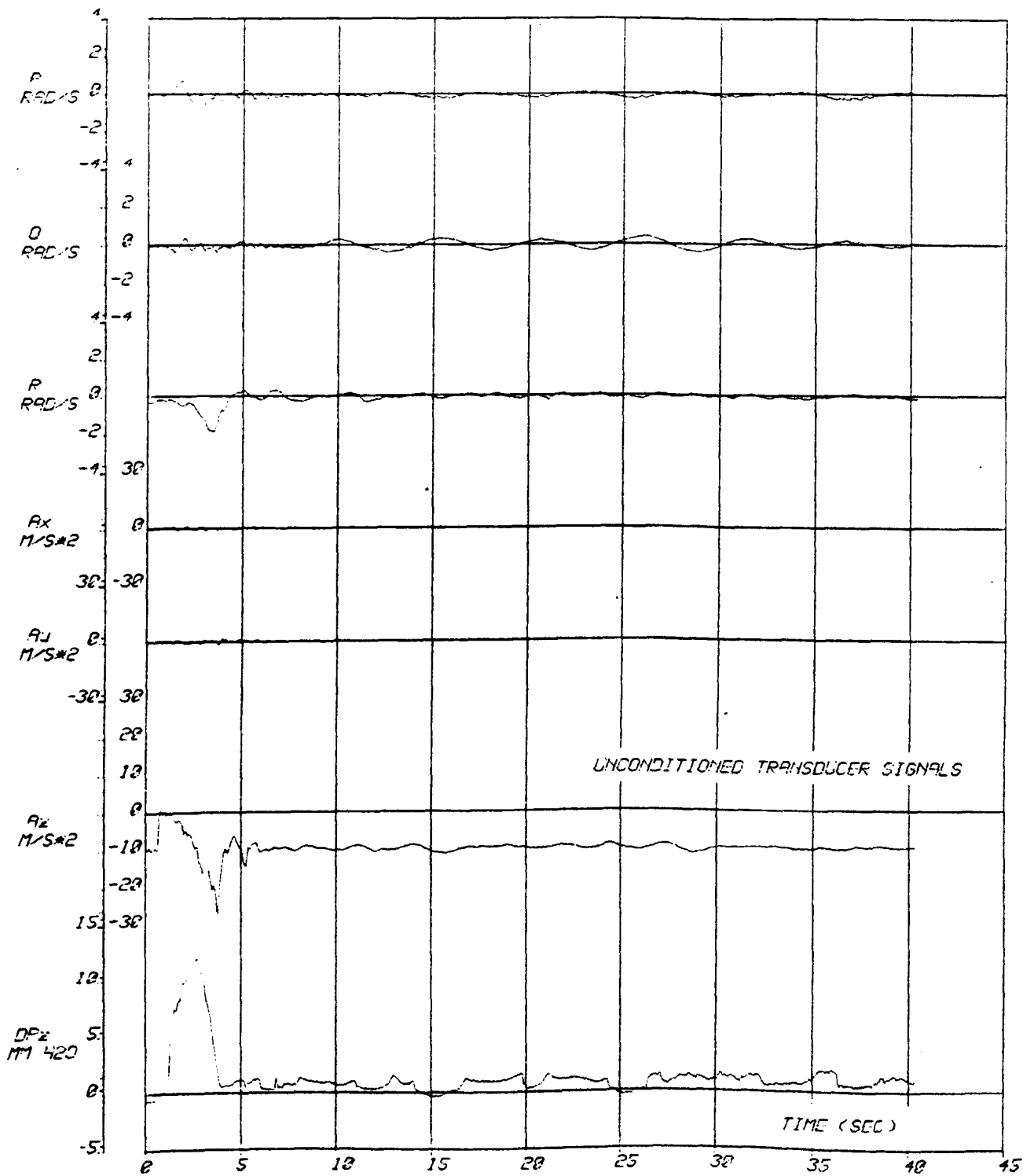


FIG. 3.20 1 OF 5	DROP NO. 24LFB7	CANDPY.FC1/1	SAMP.RATE/CH. 10/S	DAGPROG:JAE 310
	DATE:BS107S	DIAMETER:6.50 M	T/OPEN:3.04 S	SOURCEFILE:JEC007
	TIME:1533	BASE SEPN.:7.24 M	T/SS:5 S	
	WIND:5 KT	STORE MASS:34.99 KG	T/FINISH:43.02 S	

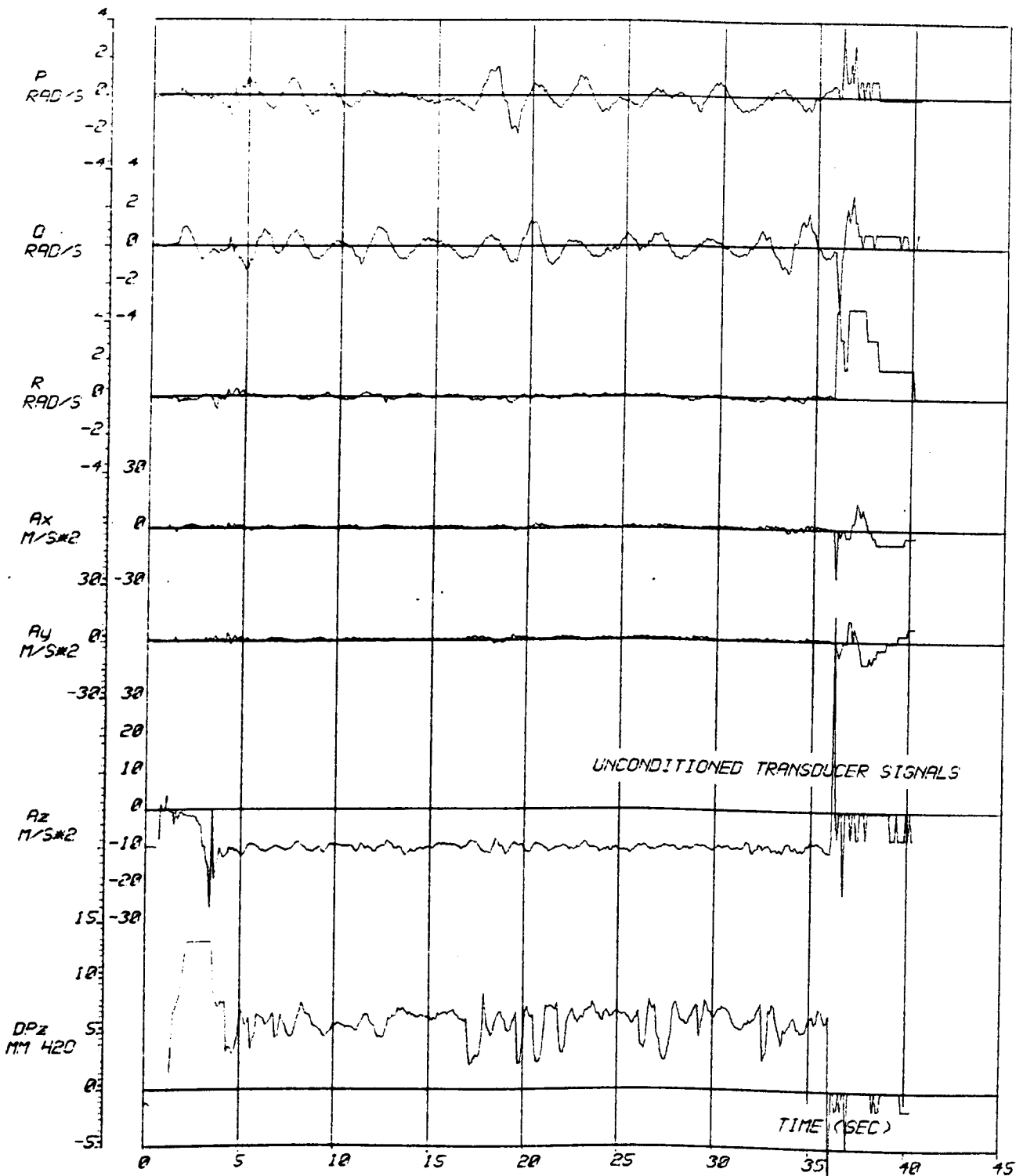


FIG. 3.21 1 OF 5	DROP NO.: 12UF05	CANOPY: FC1/2	SAMP. RATE/CH.: 10/S	DAGPROG: JAE 310
	DATE: 111875	DIAMETER: 2.95 M	T/OPEN: 2.41 S	SOURCEFILE: JEC506
	TIME: 1146	BASE SEPN.: 2.35 M	T/SS: 4.3 S	
	WIND: 11 KTS	STORE MASS: 34.95 KG	T/FINISH: 35.14 S	

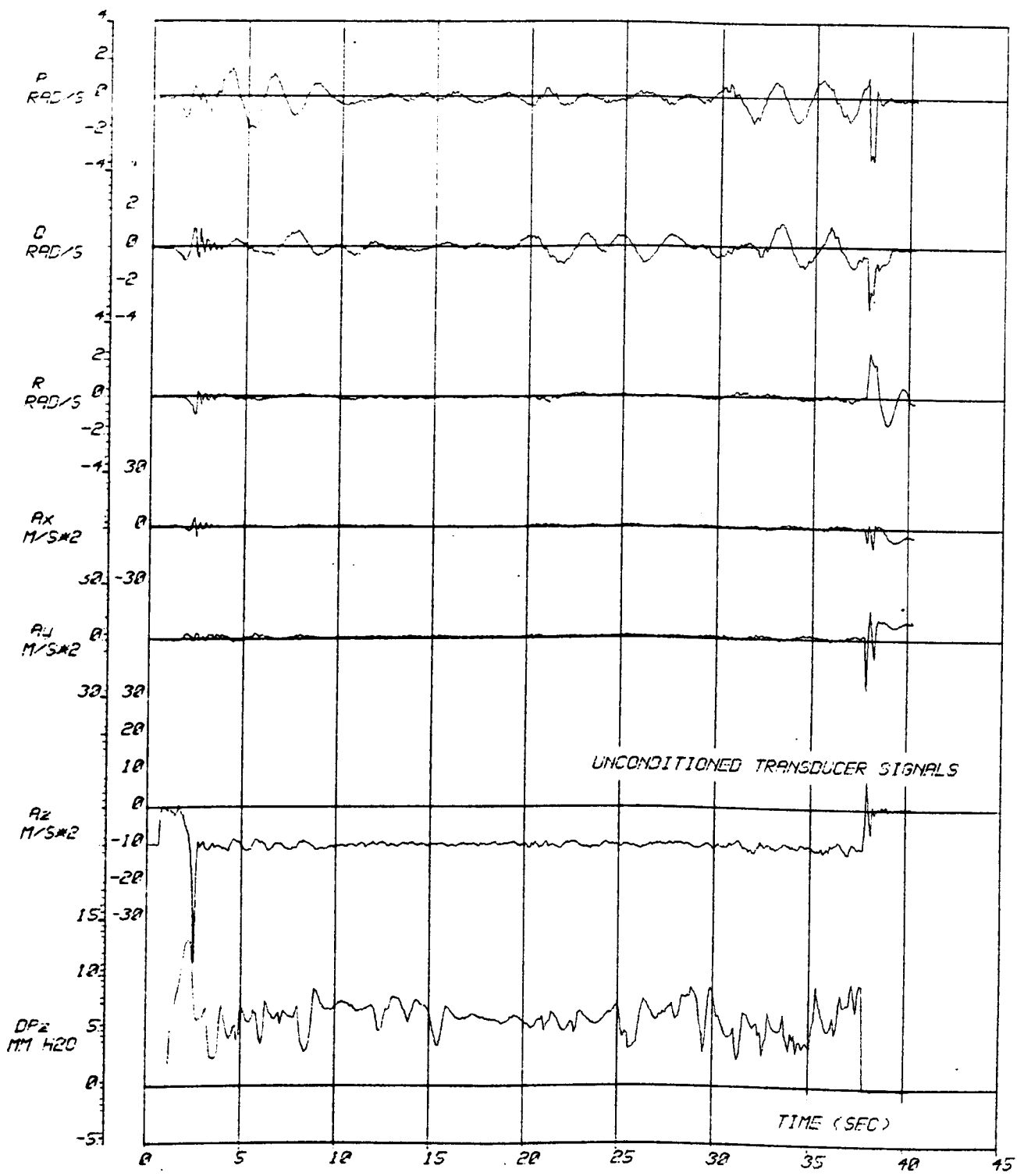


FIG. 3.22	DROP NO.: 120F10	CANOPY: FCI/2	SAMP. RATE/CH.: 10/S	DAGPROG: JAE 310
	DATE: 111075	DIAMETER: 2.35 M	T/OPEN: 2.12 S	SOURCEFILE: JECS10
	TIME: 1403	BASE SEPN.: 2.35 M	T/SS: 5.5 S	
	1 OF 5	#WIND#: 7 KTS	STORE MASS: 34.95 KG	T/FINISH: 35.60 S

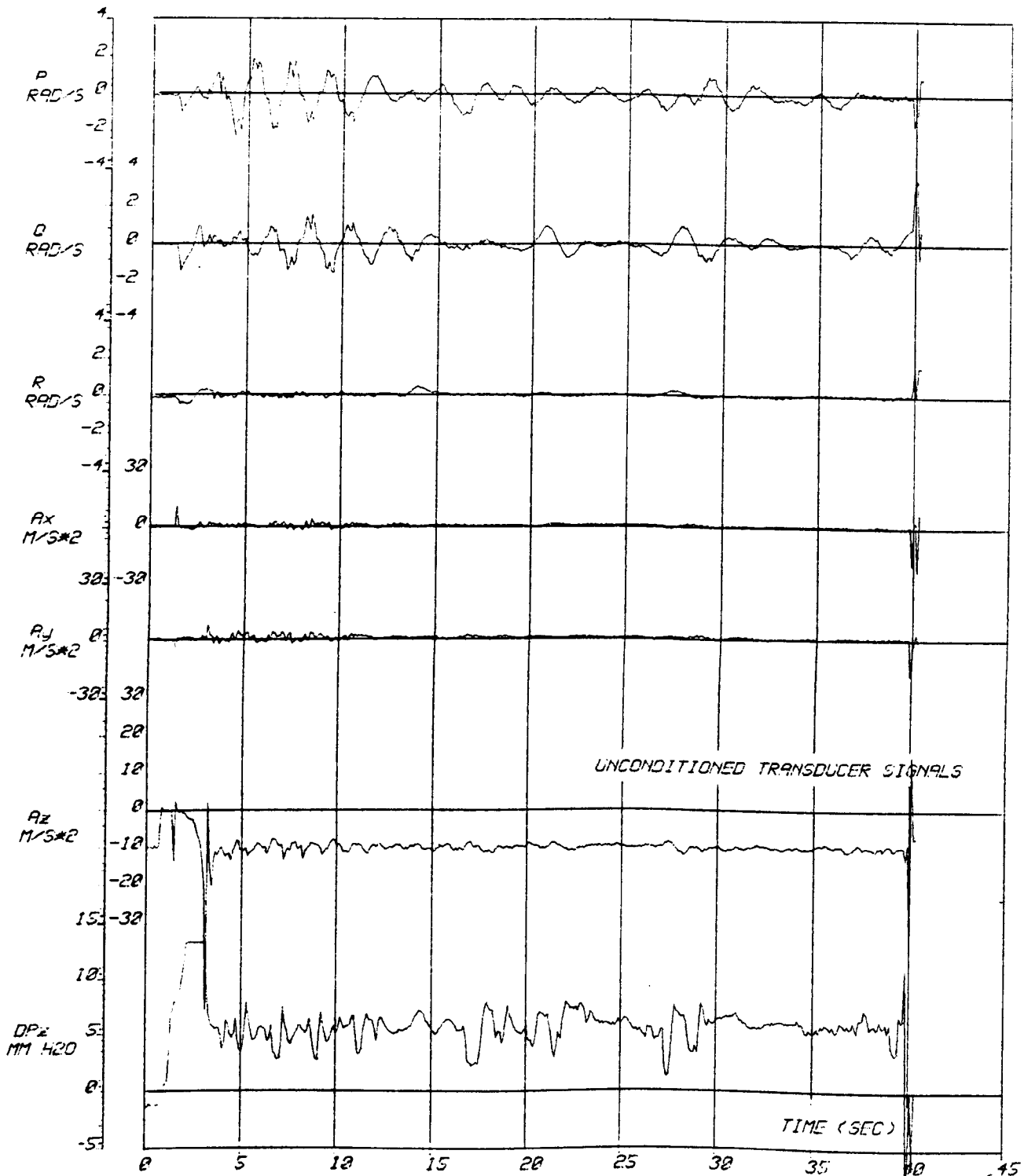


FIG. 3.23 1 OF 5	DROP NO.: 12UF11	CANOPY: FC1/2	SAMP. RATE/CH.: 112/S	DAQPROG: JAE 312
	DATE: 111873	DIAMETER: 2.95 M	T/OPEN: 2.53 S	SOURCEFILE: JECS11
	TIME: 1.435	BASE SEPN.: 2.35 M	T/SS: 5.5 S	
	WIND: 12 KTS	STORE MASS: 34.95 KG	T/FINISH: 37.25 S	

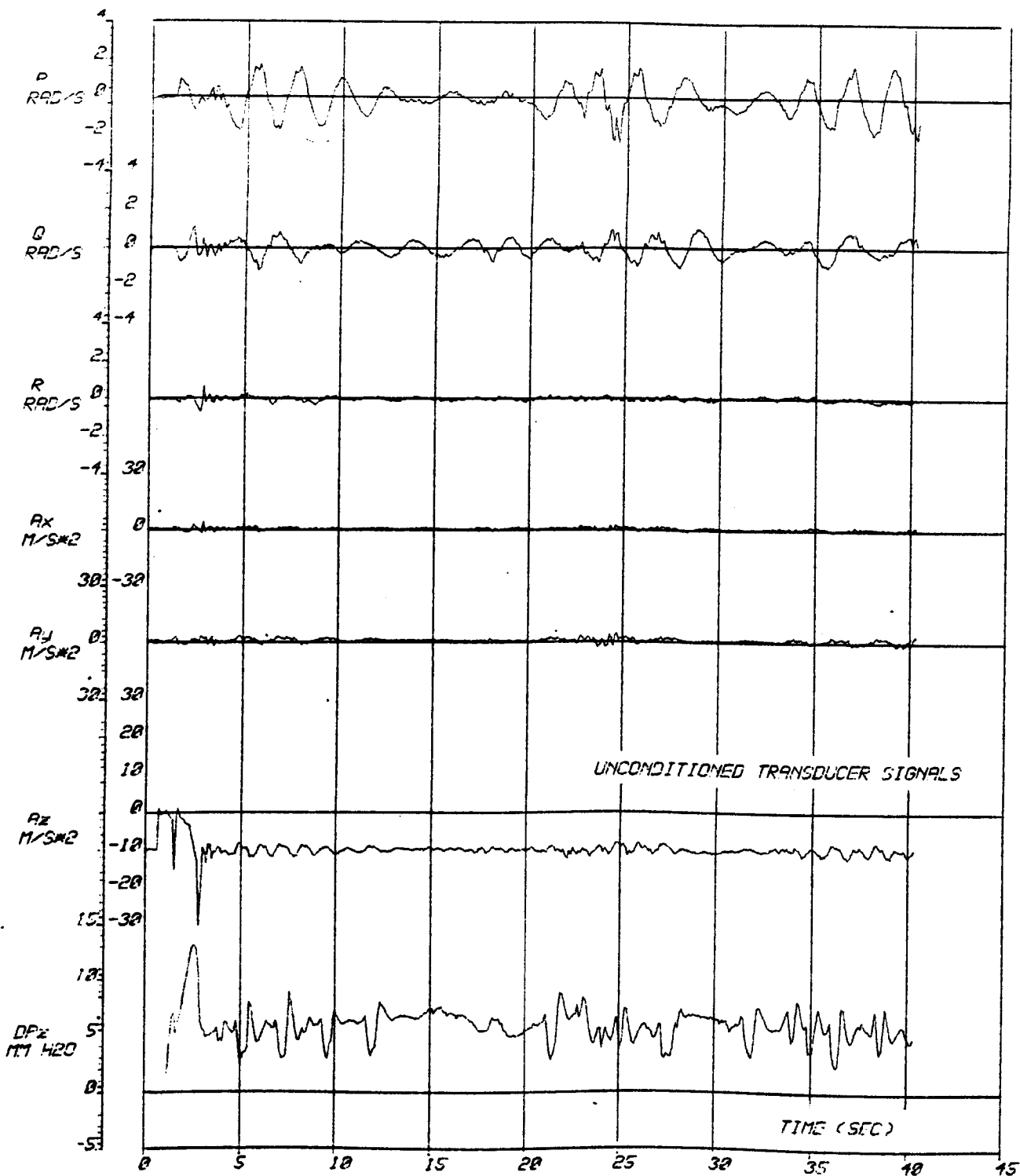


FIG. 3.24 1 OF 5	DROP NO.: 12UF13	CANOPY: FC1/2	SAMP. RATE/CH.: 10/S	DAGPROG: JAE 310
	DATE: 161273	DIAMETER: 2.38 M	T/OPEN: 2.27 S	SOURCEFILE: JECS13
	TIME: 1203	BASE SEPN.: 2.35 M	T/SS: 6 S	
	#WIND#: 5 KTS	STORE MASS: 34.96 KG	T/FINISH: 41.6 S	

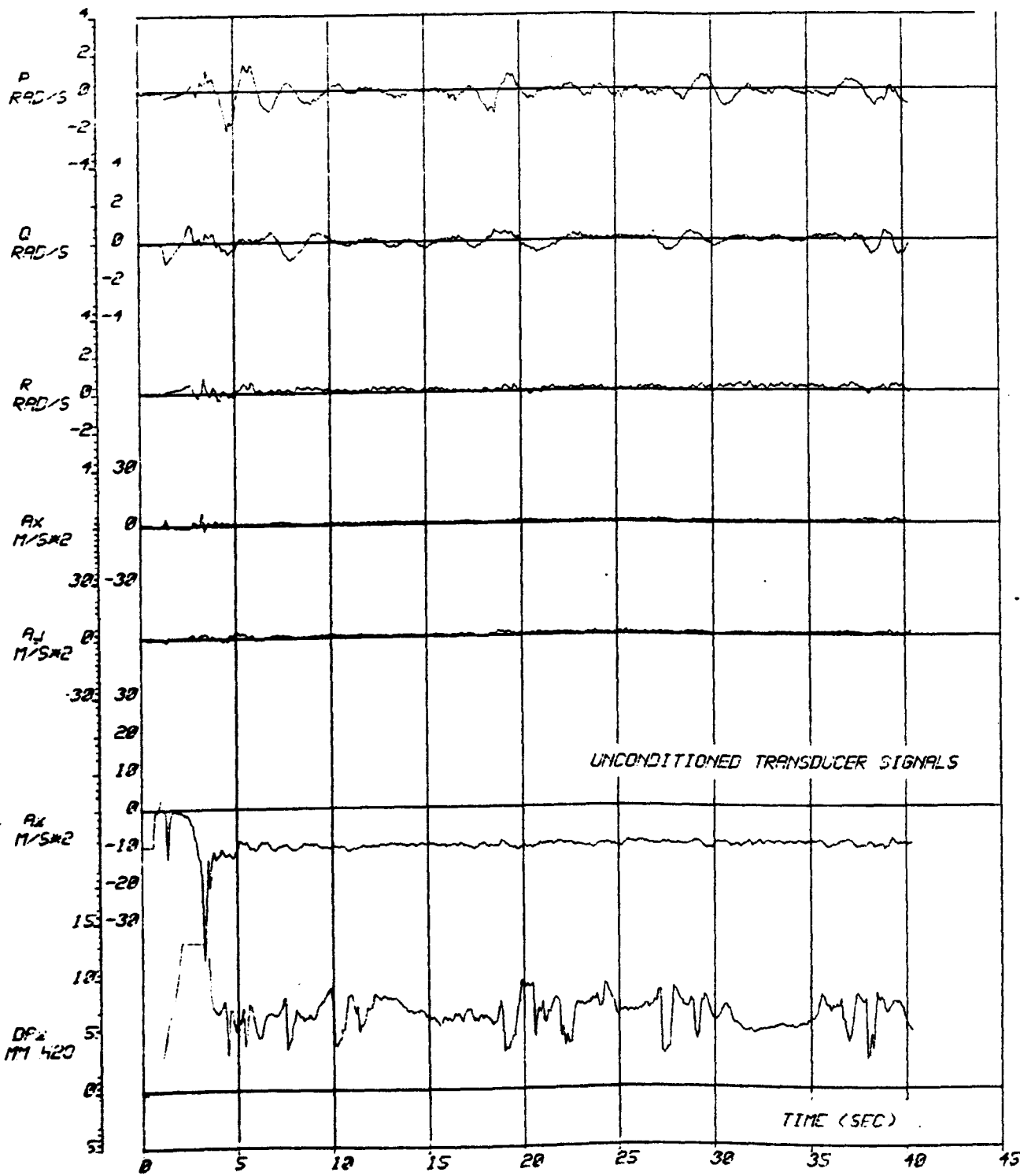


FIG. 3.25	DROP NO.: 12JF16	CANOPY: FC1/2	SAMP. RATE/CH.: 12/S	DAGPROG: JAE 310
	DATE: 161875	DIAMETER: 2.35 M	T/OPEN: NA	SOURCEFILE: JEC516
1 OF 5	TIME: 1350	BASE SEPN.: 2.35 M	T/SS: 2.3 S	
	#WIND#: 6 KTS	STORE MASS: 34.35 KG	T/FINISH: NA	

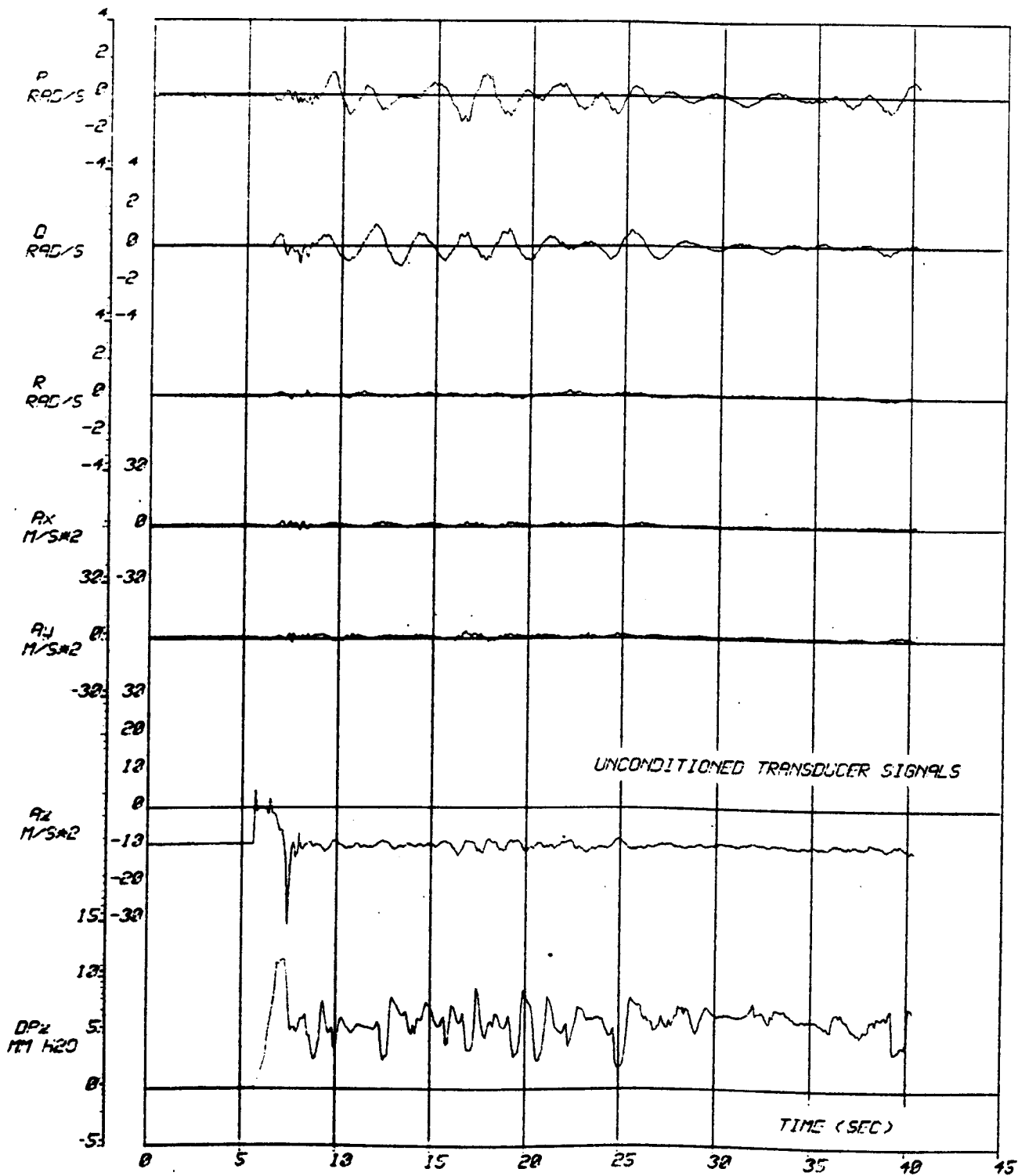


FIG. 3.26 1 OF 5	DROP NO. 12JF16	CANOPY FC1/2	SAMP. RATE/CH. 10/S	DAGPROG: JAE 310
	DATE 161875	DIAMETER 2.58 M	T/OPEN 2.6 S	SOURCEFILE: JEC518
	TIME 1437	BASE SEPN. 2.35 M	T/SS. NA	
	#WINDING KTS	STORE MASS 34.58 KG	T/FINISH 48.65 S	

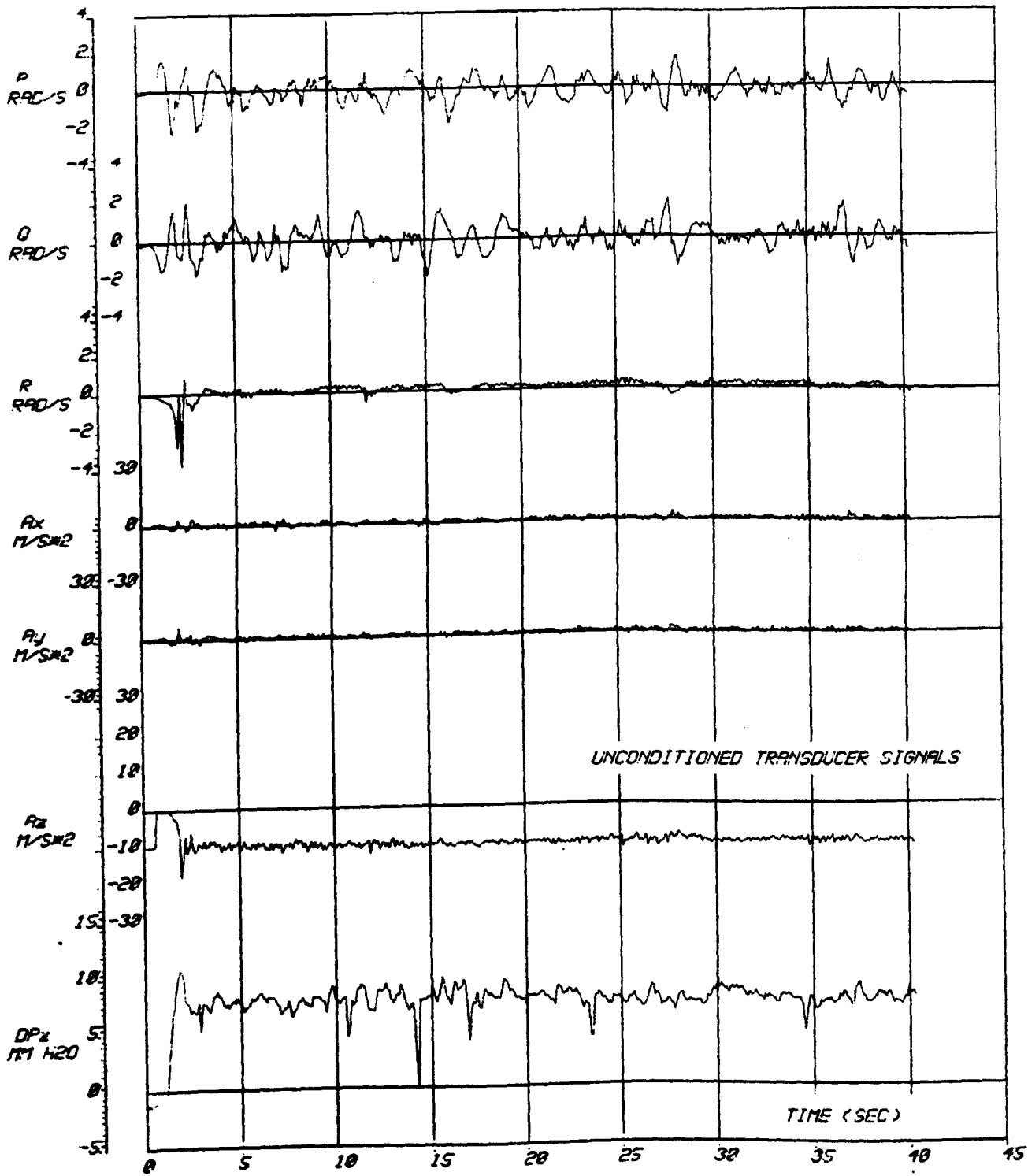


FIG. 3.27 1 OF 5	DROP NO. 86UF19	CANOPY: FC1/1	SAMP. RATE/CH.: 10/S	DAGPROG: JAE 310
	DATE: 171075	DIAMETER: 1.48 M	T/OPEN: 1.65 S	SOURCEFILE: JECS19
	TIME: 1157	BASE SEPN.: 1.03 M	T/SS: 7.5 S	
	#WIND: 12 KTS	STORE MASS: 10.92 KG	T/FINISH: 40.26 S	

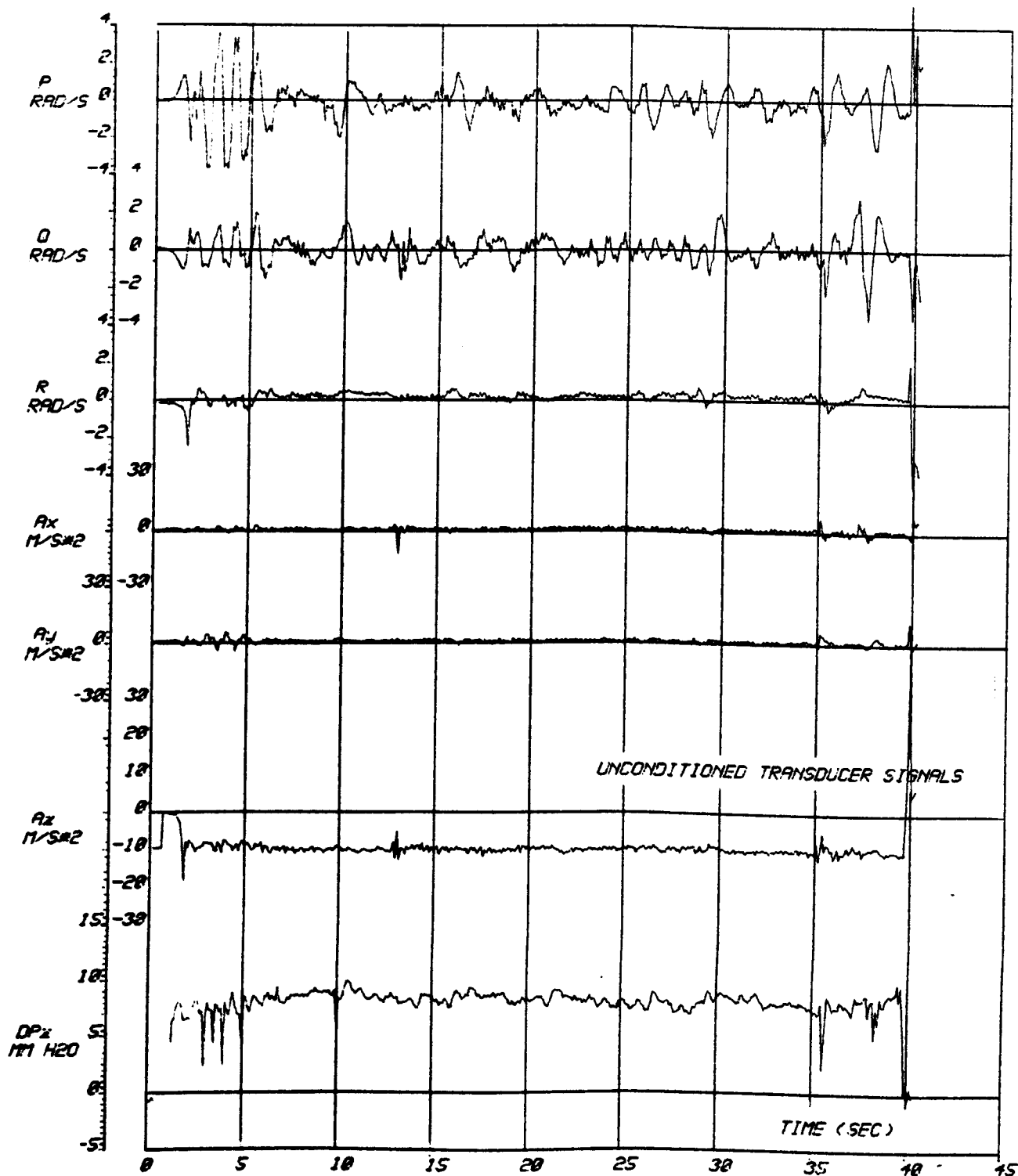


FIG. 3.28 1 OF 5	DROP NO.: 06UF20	CANOPI: FC1/1	SAMP. RATE/CH.: 10/S	DAGPROS: JAE 310
	DATE: 171075	DIAMETER: 1.46 M	T/OPEN: 2.07 S	SOURCEFILE: JEC520
	TIME: 1406	BASE SEPN.: 1.03 M	T/SS: 12.0 S	
	WIND: 11 KTS	STORE MASS: 10.92 KG	T/FINISH: 39.29 S	

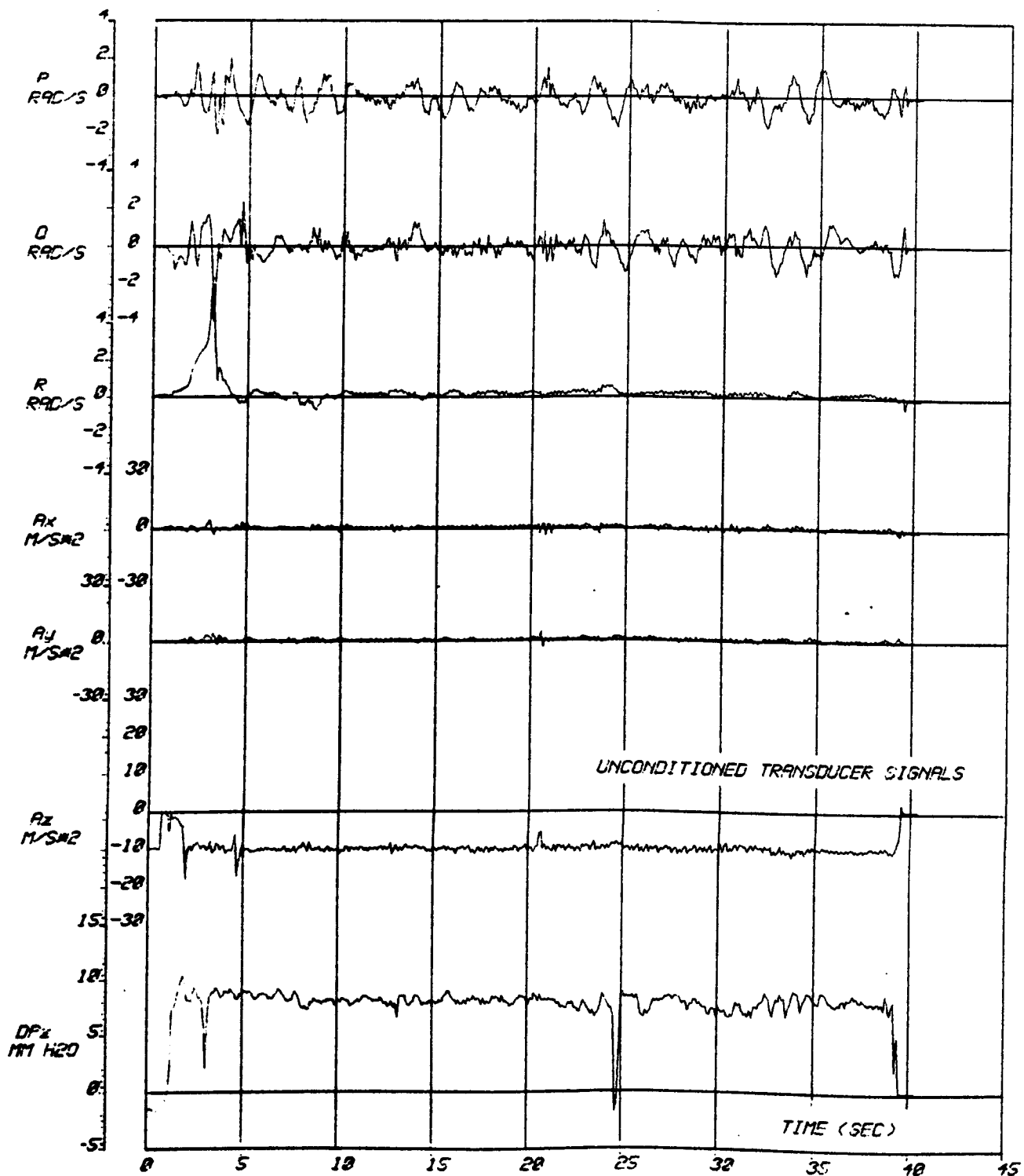


FIG. 329 1 OF 5	DROP NO.: 06UF21	CANOPI: FC1/4	SAMP. RATE/CH.: 10/S	DROPROS: JAE 310
	DATE: 17187S	DIAMETER: 1.48 M	T/OPEN: 1.37 S	SOURCEFILE: JEC521
	TIME: 1582	BASE SEPN.: 1.03 M	T/SS: 21.12 S	
	WIND: 13 KTS	STORE MASS: 10.92 KS	T/FINISH: 38.80 S	

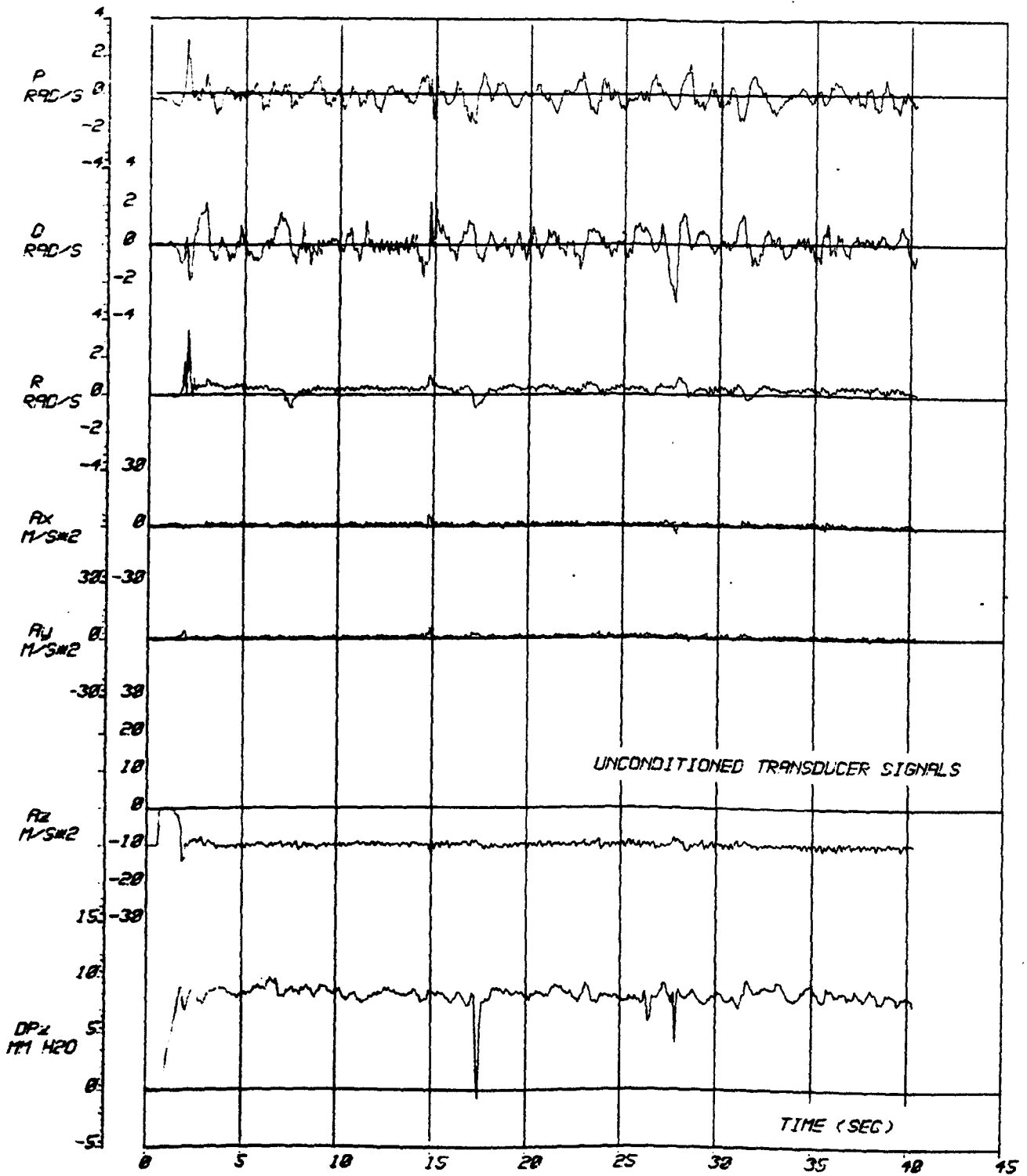


FIG. 3.30 1 OF 5	DROP NO.: 06UF23	CANOPY: FC1/4	SAMP. RATE/CH.: 10/S	DROP PROG.: JAE 310
	DATE: 021175	DIAMETER: 1.48 M	T/OPEN: 1.66 S	SOURCE FILE: JEC523
	TIME: 1111	BASE SEPN.: 1.03 M	T/SS: ?	
	WIND: 7 KTS	STORE MASS: 12.76 KG	T/FINISH: 40.46 S	

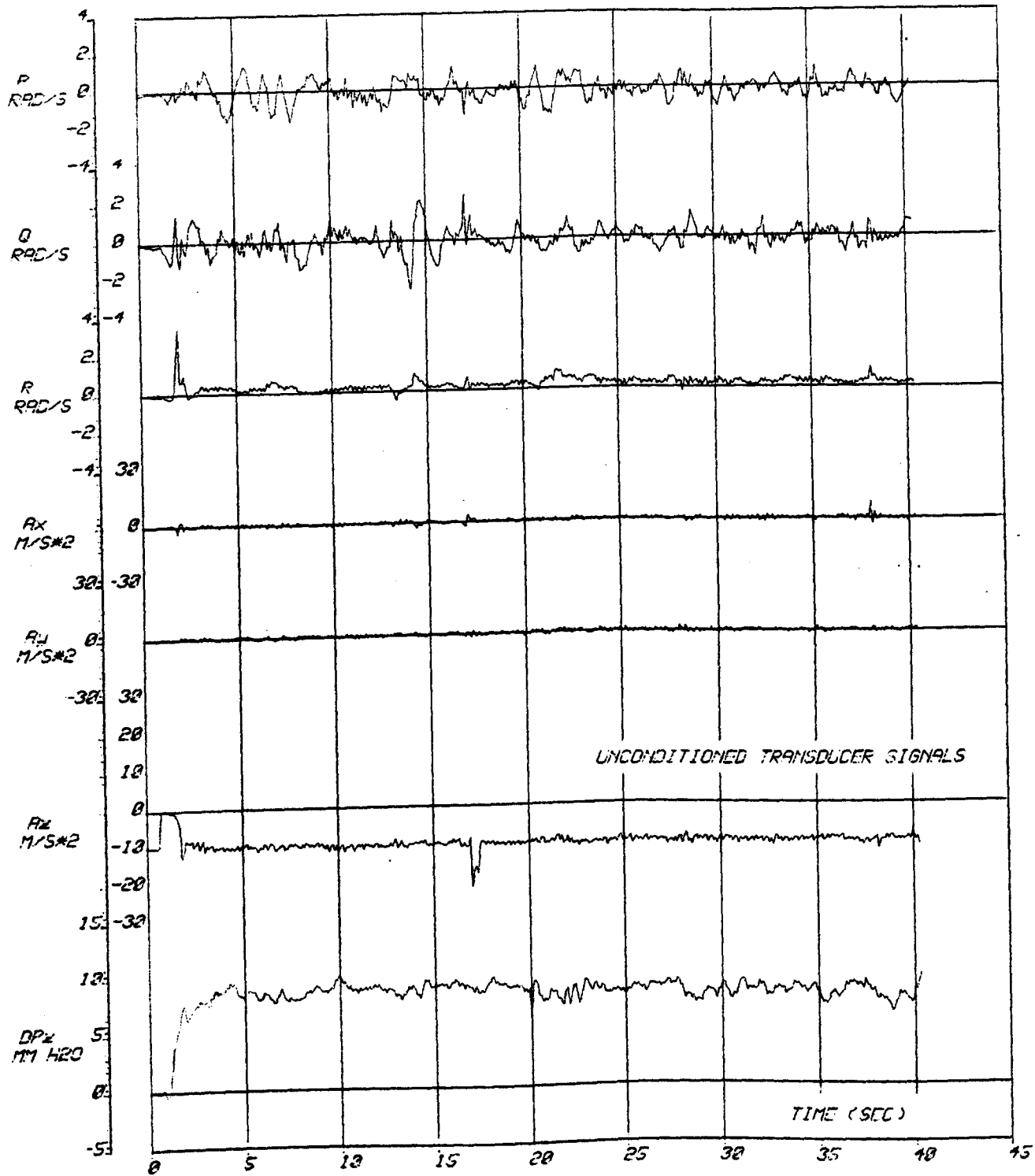


FIG. 3.31 1 OF 5	DROP NO.: 260F24	CANOPY: FC1/4	SAMP. RATE/CH.: 12/S	DAQPROG: JAE 310
	DATE: 021175	DIAMETER: 1.48 M	T/OPEN: 1.86 S	SOURCEFILE: JEC024
	TIME: 1157	BASE SEPN.: 1.83 M	T/SS: NA	
	WIND: 3 KTS	STORE MASS: 13.78 KG	T/FINISH: 39.59	

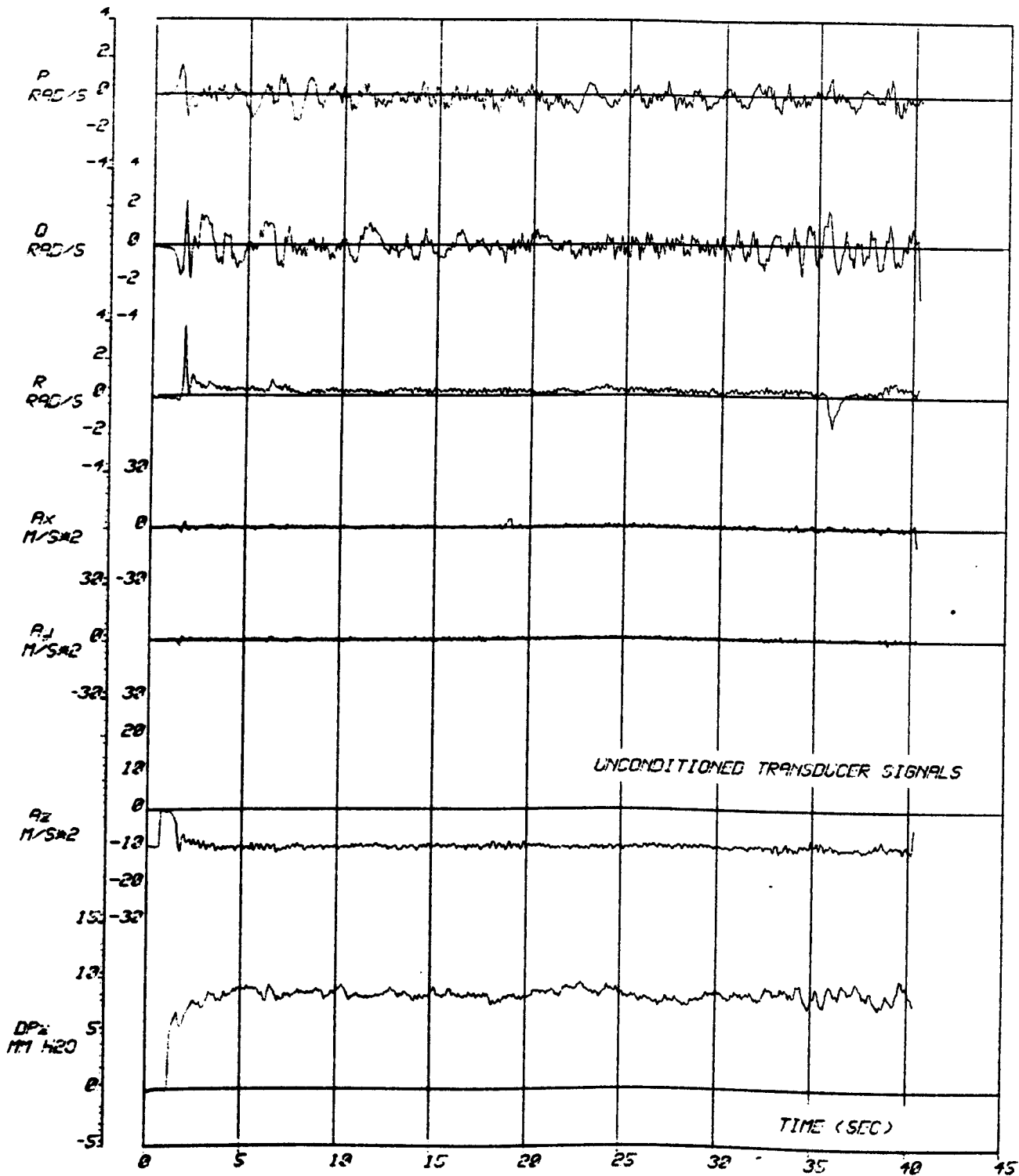


FIG. 3.32 1 OF 5	DROP NO. 06L25	CANOPY: FC1/4	SAMP. RATE/CH. 18/S	DAGPROG: JAE 312
	DATE: 021175	DIAMETER: 1.48 M	T/OPEN: 1.75 S	SOURCEFILE: JEC525
	TIME: 1347	BASE SEPN.: 1.03 M	T/SS: NA	
	WIND#: 5 KTS	STORE MASS: 12.76 KG	T/FINISH: 35.4 S	

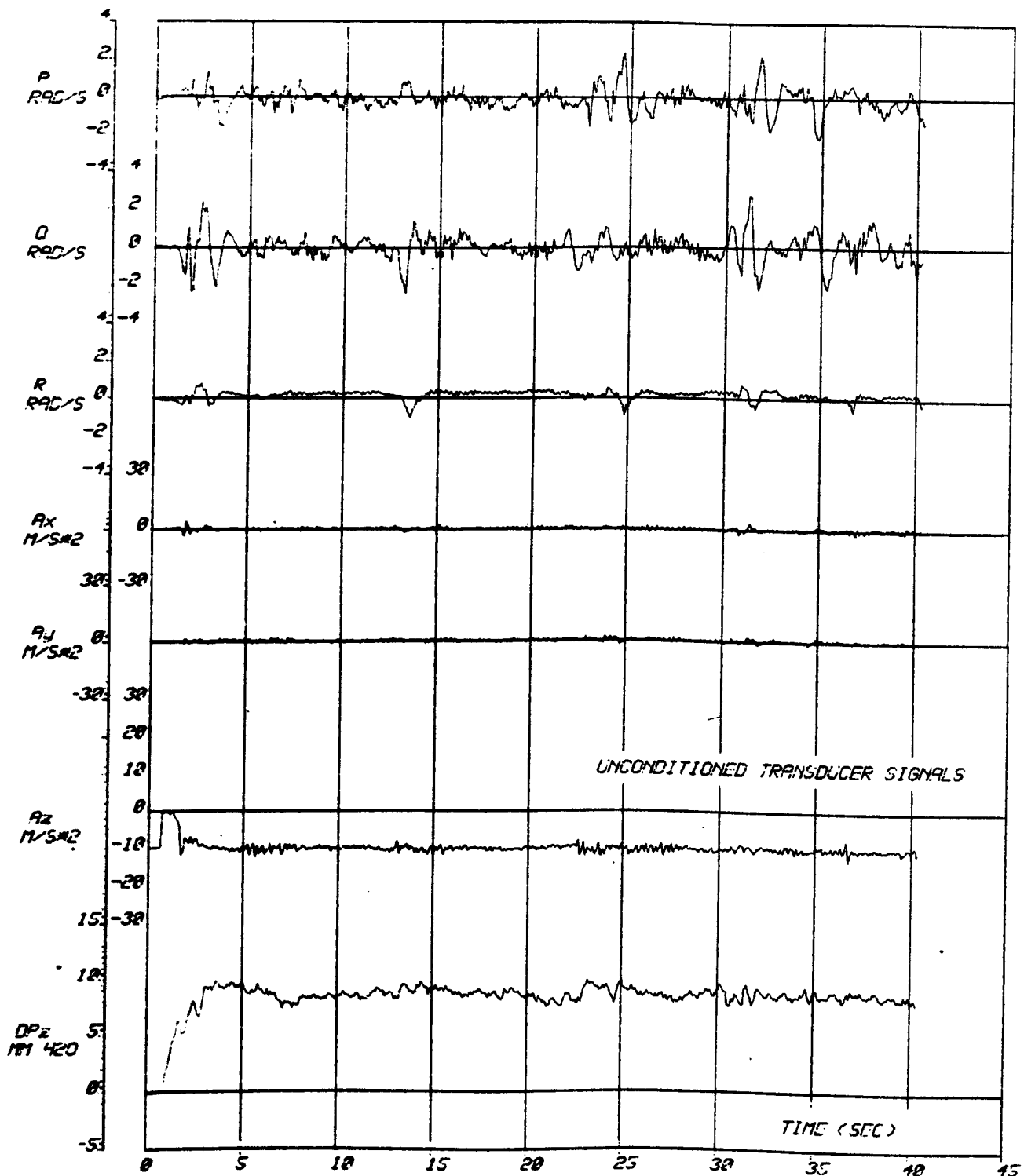


FIG. 3.33 1 OF 5	DROP NO. 06UF26	CANOPY:FC1/4	SAMP. RATE/CH.: 10/S	DAGPROS: JAE 310
	DATE: 021175	DIAMETER: 1.48 M	T/OPEN: 1.62 S	SOURCEFILE: JEC526
	TIME: 1:32	BASE SEPN.: 1.03 M	T/SS: NA	
	WIND: 5 KTS	STORE MASS: 10.76 KG	T/FINISH: 39.63 S	

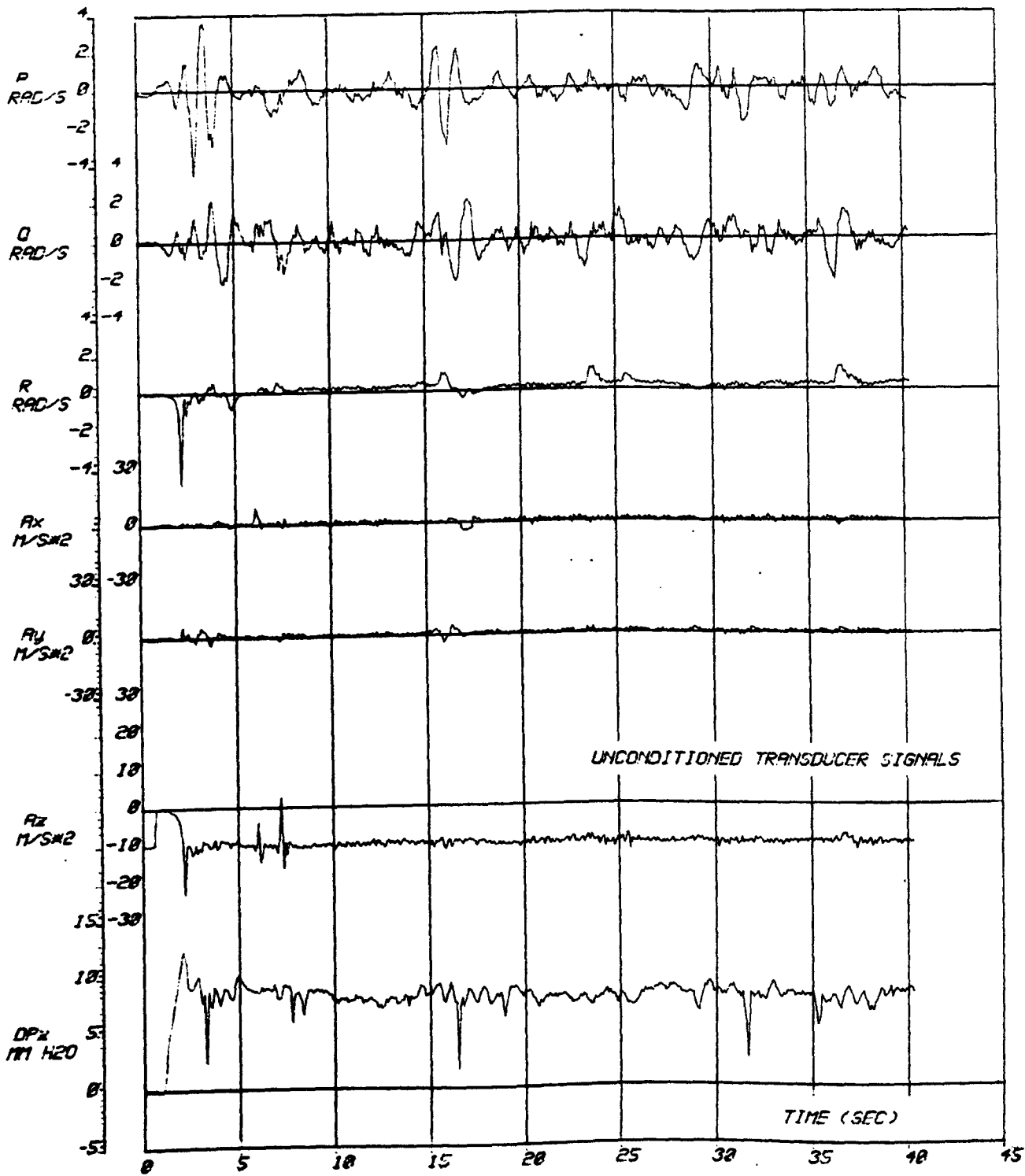


FIG. 3.34 1 OF 5	DROP NO.: 06UF27	CANOPY: FC1/4	SAMP. RATE/CH.: 10/S	DAGPROS: JAE 310
	DATE: 021175	DIAMETER: 1.40 M	T/OPEN: 1.92 S	SOURCEFILE: JECS27
	TIME: 1515	BASE SEPN.: 1.03 M	T/SS: 7.72 S	
	WIND: -5 KTS	STORE MASS: 10.76 KS	T/FINISH: 40.61 S	

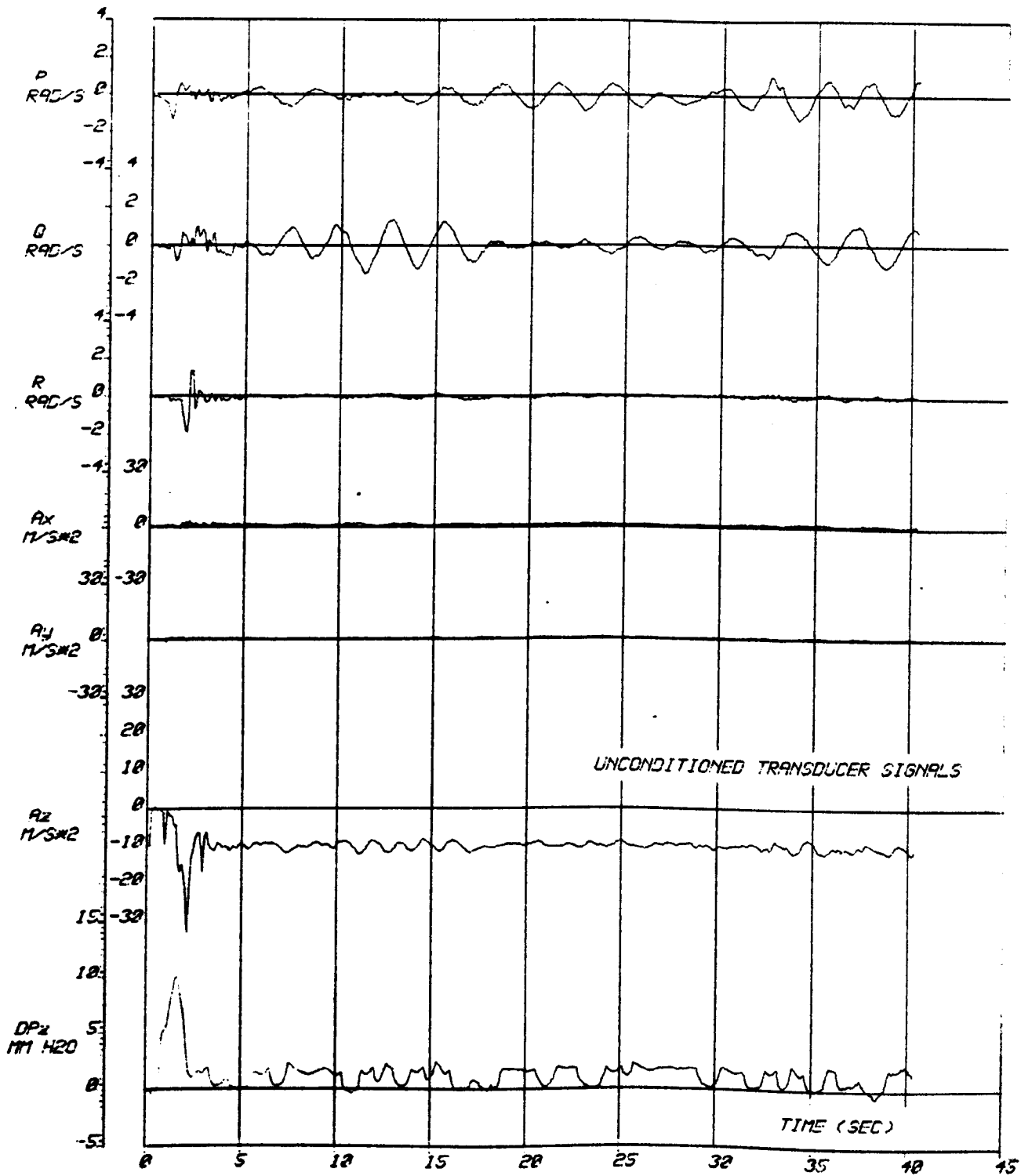


FIG. 3.35 1 OF 5	DROP NO.: 12UF26	CANOPY: FC1/2	SAMP. RATE/CH.: 10/S	DAQPROG: JAE 310
	DATE: 131175	DIAMETER: 2.57 M	T/OPEN: 1.96 S	SOURCEFILE: JEC325
	TIME: 1203	BASE SEPN.: 2.36 M	T/SS: NA	
	WINDX: 2 KTS	STORE MASS: 10.62 KG	T/FINISH: NA	

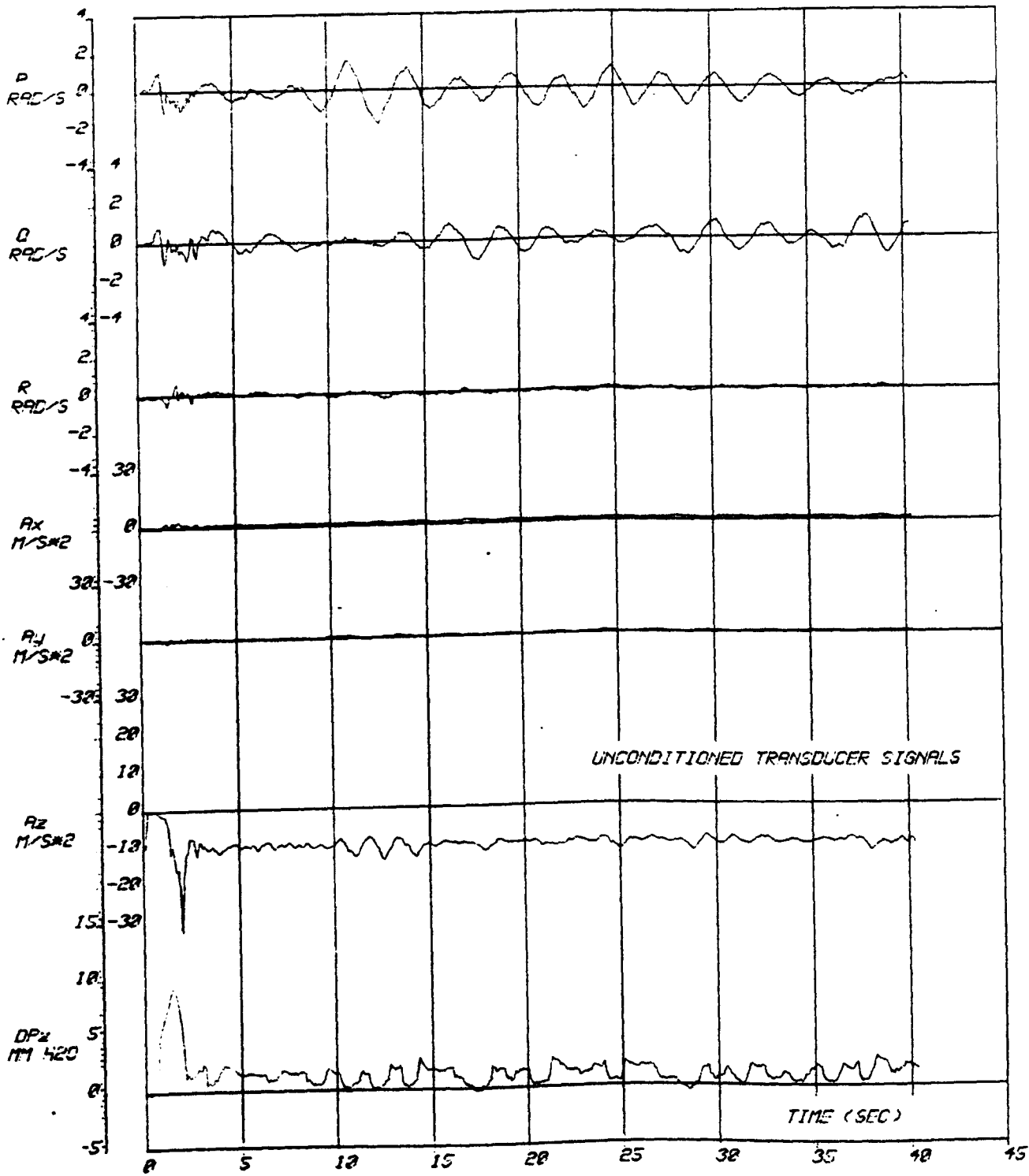


FIG. 3.36 1 OF 5	DROP NO.: 120F29	CANOPY: FC1/2	SAMP. RATE/CH.: 12/S	DROPROG: JAE 312
	DATE: 131179	DIAMETER: 2.57 M	T/OPEN: 1.80 S	SOURCE FILE: JEC329
	TIME: 1343	BASE SEPN.: 2.36 M	T/SS: NA	
	WIND#: 27 KT	STORE MASS: 12.60 KG	T/FINISH: 44.05 S	

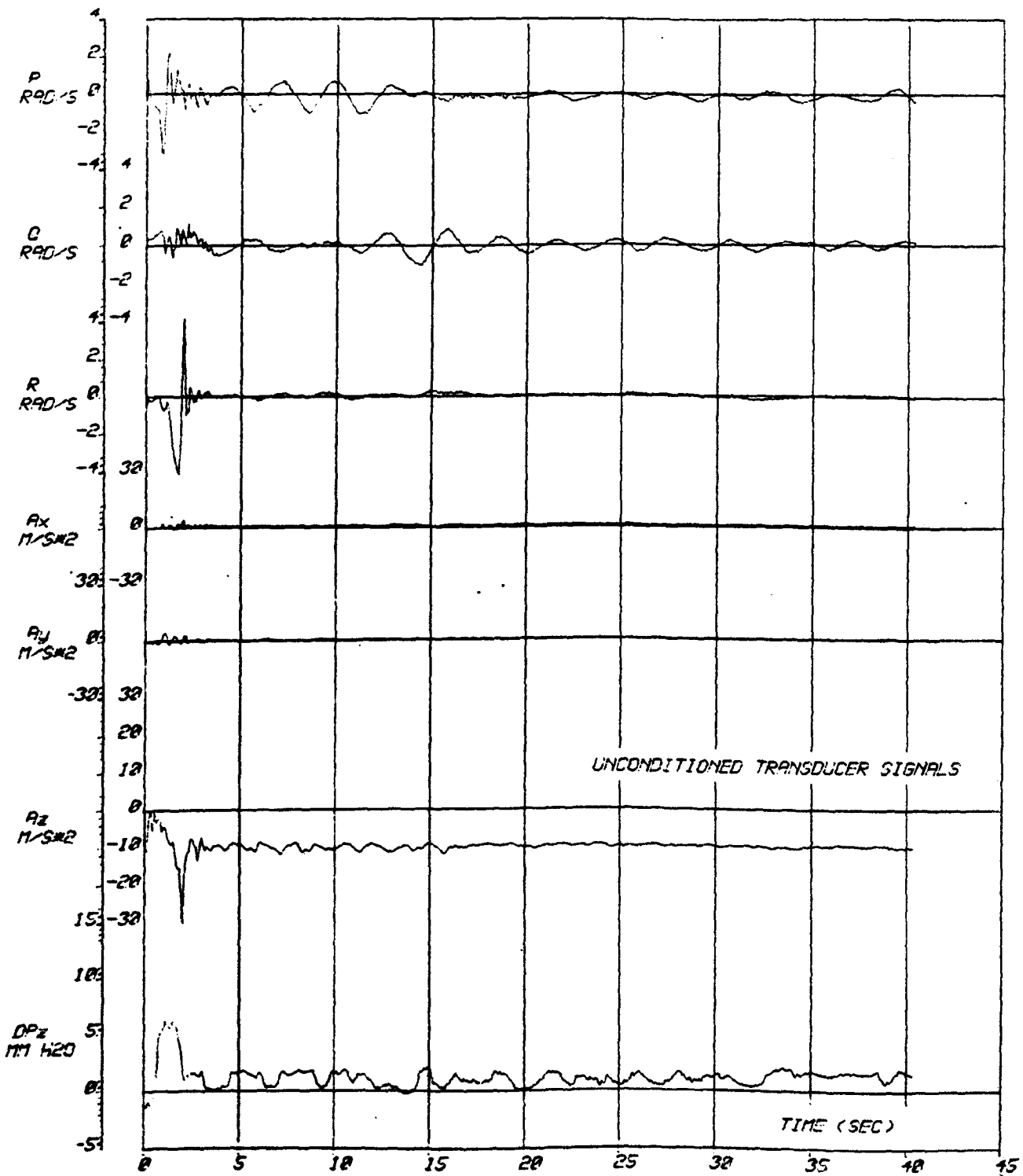


FIG. 3.37	DROP NO. 12UF30	CANOPY:FC1/2	SAMP. RATE/CH.: 10/S	DROPROS:JAE 310
	DATE:131175	DIAMETER:2.67 M	T/OPEN:1.64 S	SOURCEFILE:JEC530
	TIME:1.432	BASE SEPN.:2.36 M	T/SS:NA	
1 OF 5	#WIND#:6 KTS	STORE MASS:5.30 KG	T/FINISH:57.48 S	

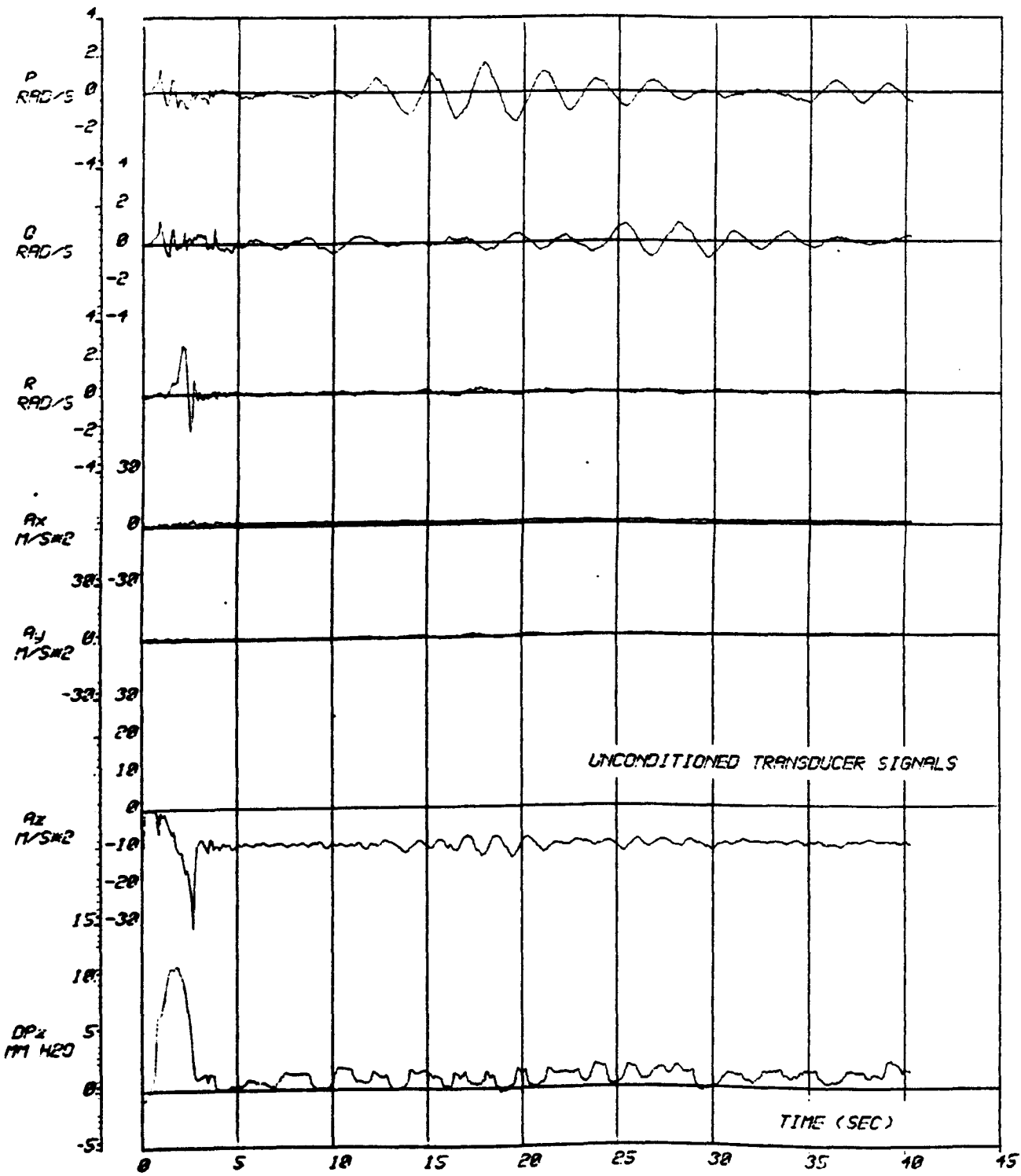


FIG. 3.38 1 OF 5	DROP NO.: 12UF32	CANOPY: FC1/2	SAMP. RATE/CH.: 112/S	DAQPROG: JAE 310
	DATE: 131179	DIA METER: 2.57 M	T/OPEN: 2.29 S	SOURCE FILE: .ECS32
	TIME: 1535	BASE SEPN.: 2.36 M	T/SS: NA	
	WINDOW: 6 KTS	STORE MASS: 9.30 KG	T/FINISH: 41.73 S	

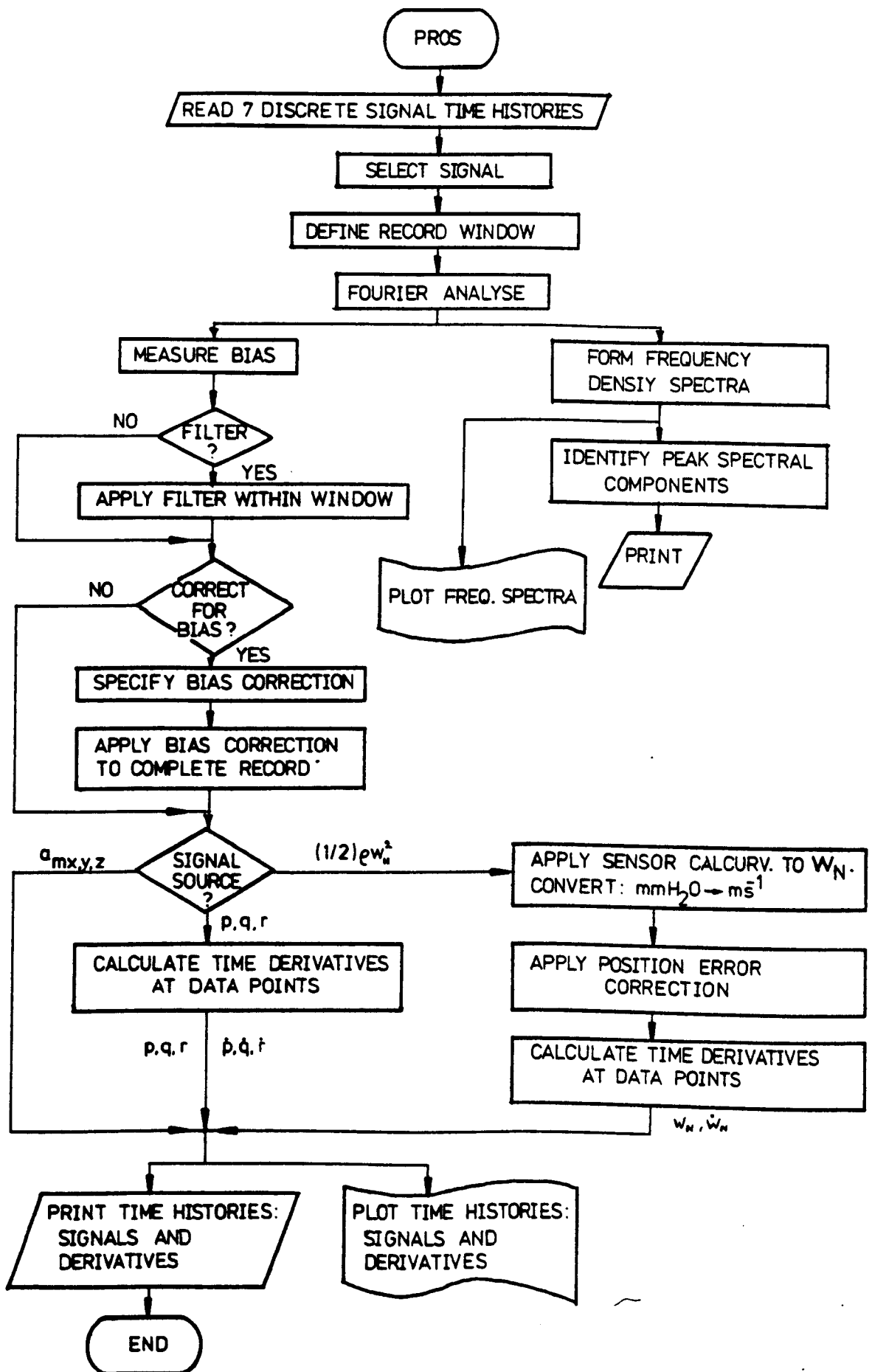


FIGURE 3.39 High-level flow diagram of programme PROS

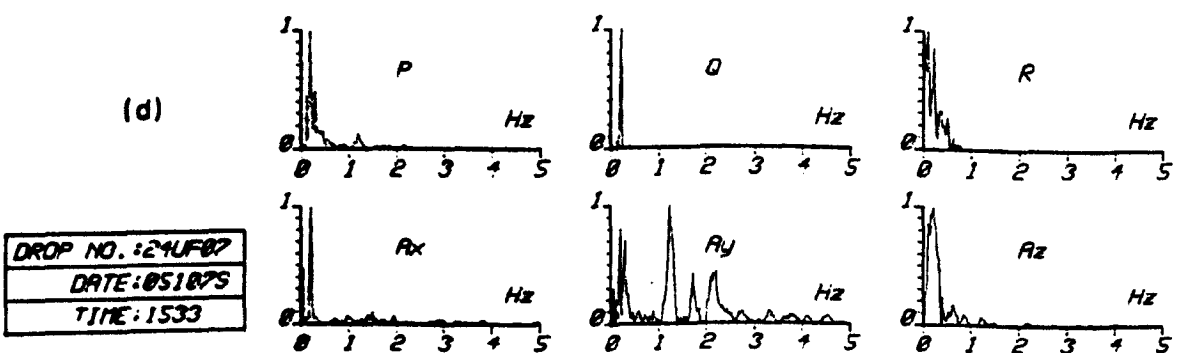
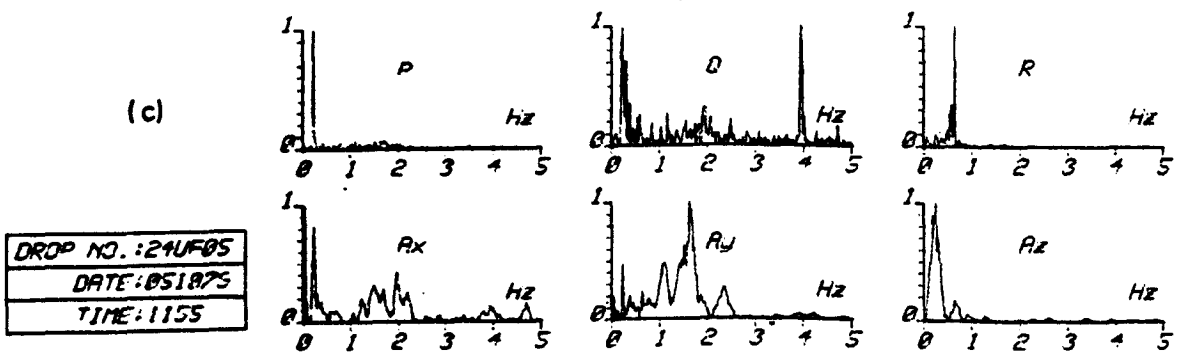
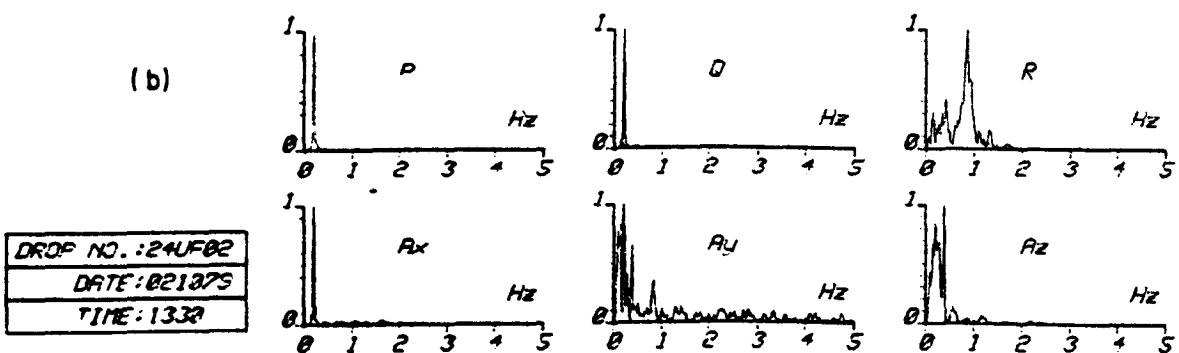
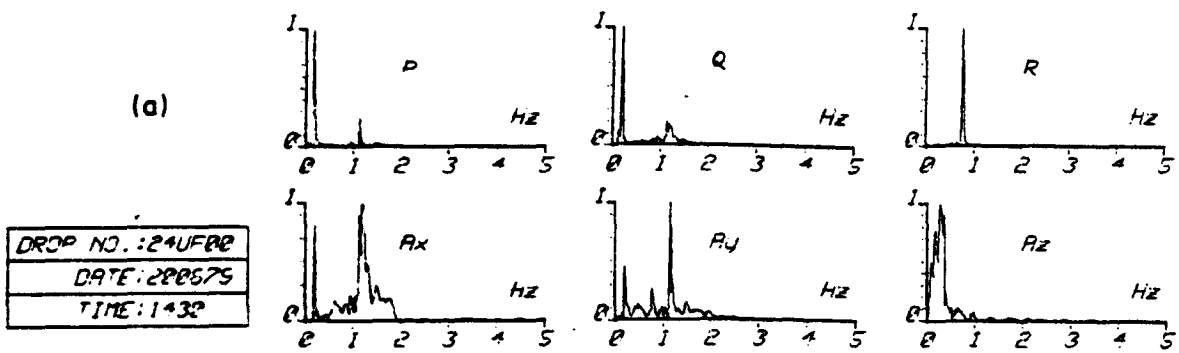


FIGURE 3.40

Amplitude spectra of inertial transducer signals for BB24-configuration drops

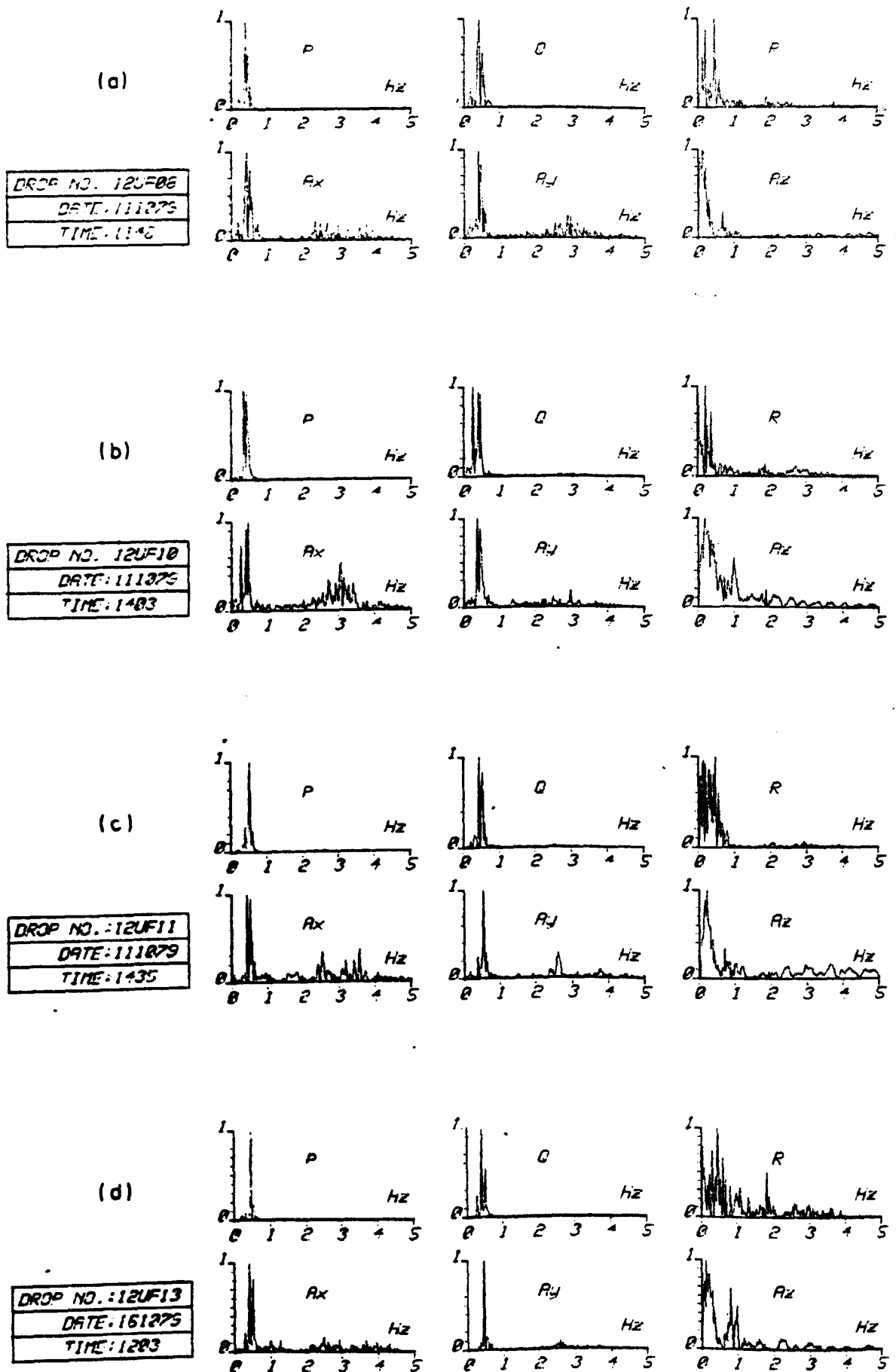


FIGURE 3.41 Amplitude spectra of inertial transducer signals for BB12-configuration drops

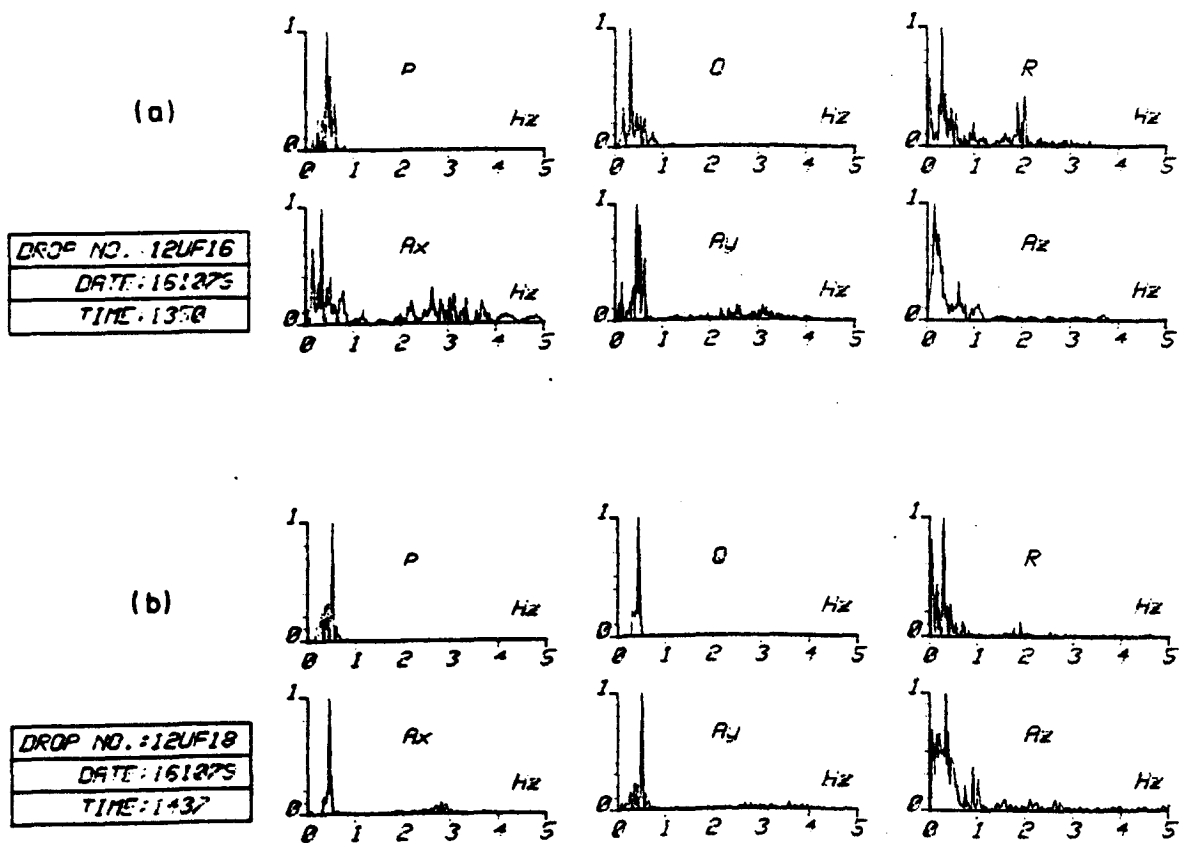


FIGURE 3.42 Amplitude spectra of inertial transducer signals for BB12-configuration drops

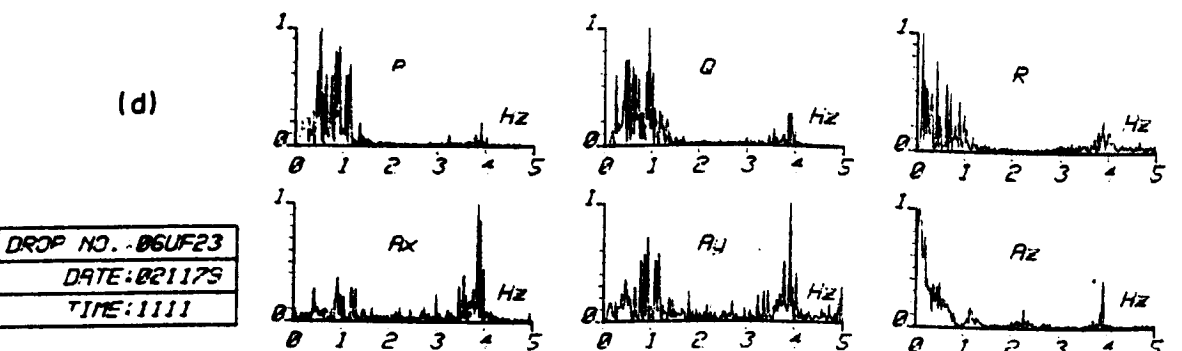
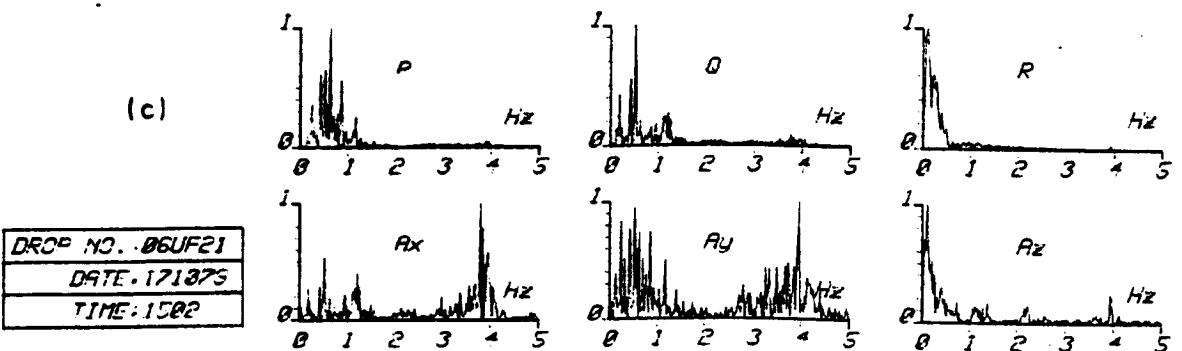
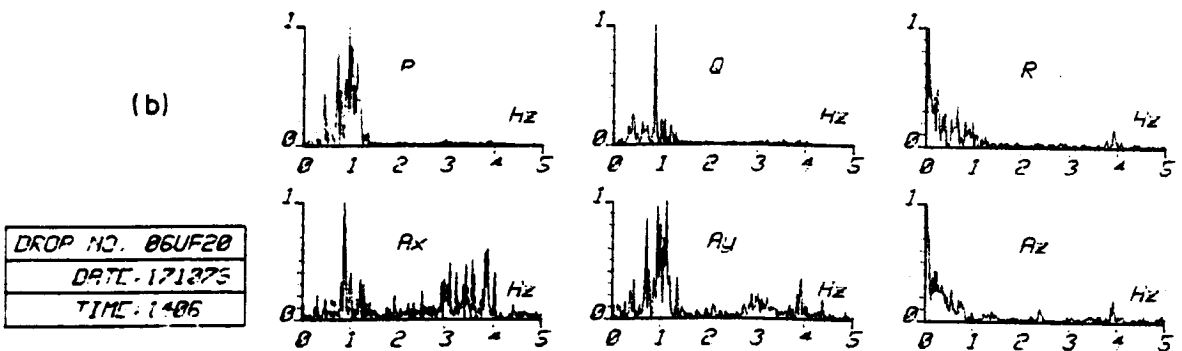
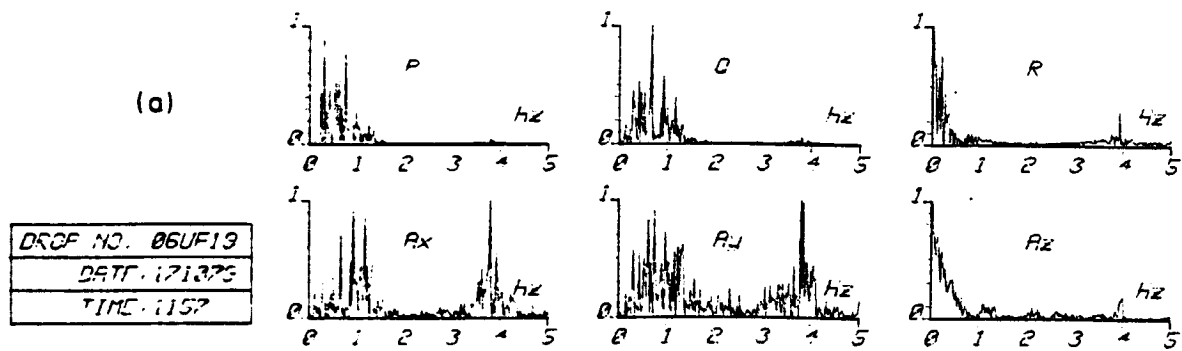


FIGURE 3.43 Amplitude spectra of inertial transducer signals for SB06-configuration drops

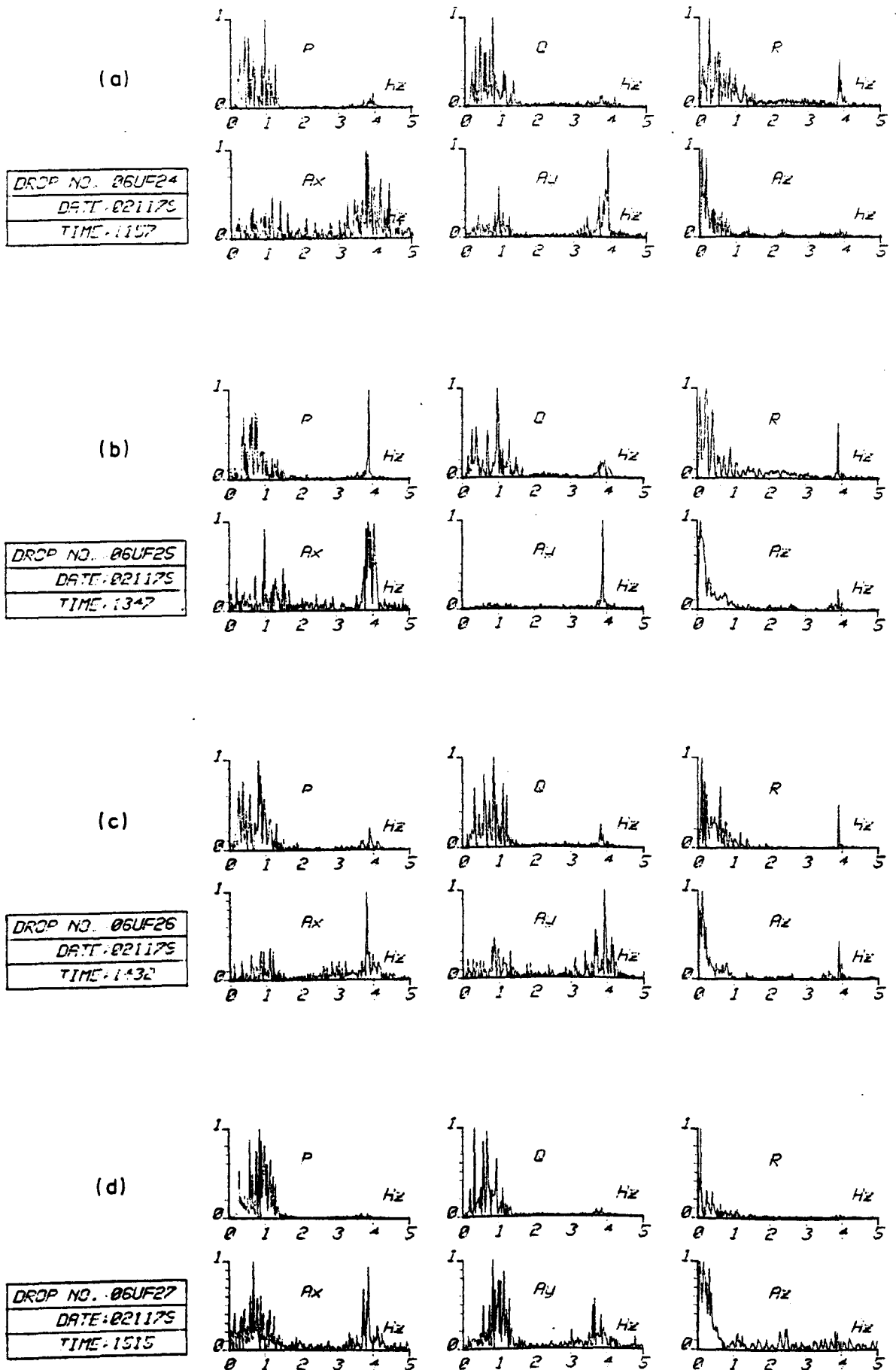


FIGURE 3.44 Amplitude spectra of inertial transducer signals for SB06-configuration drops

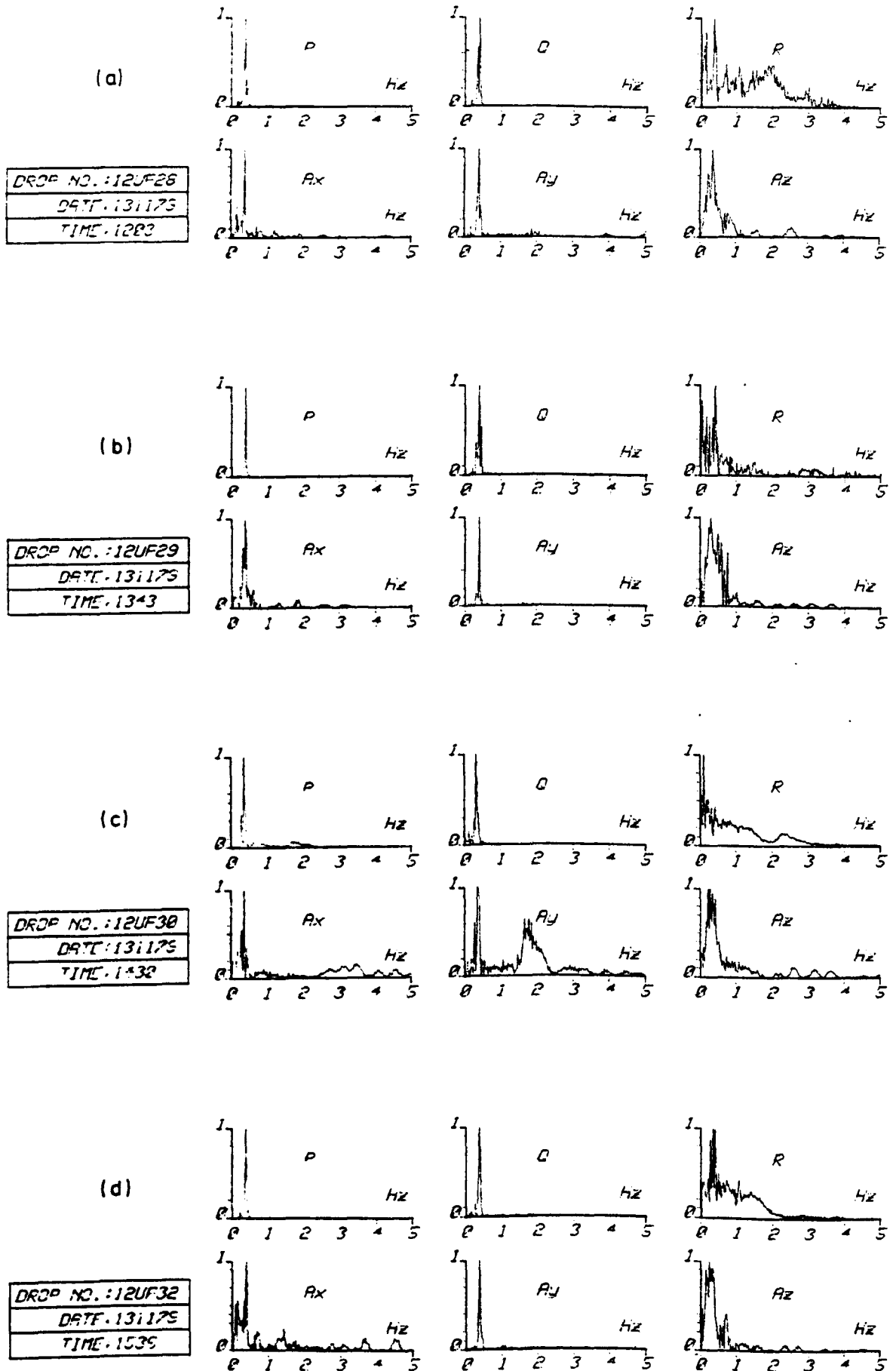
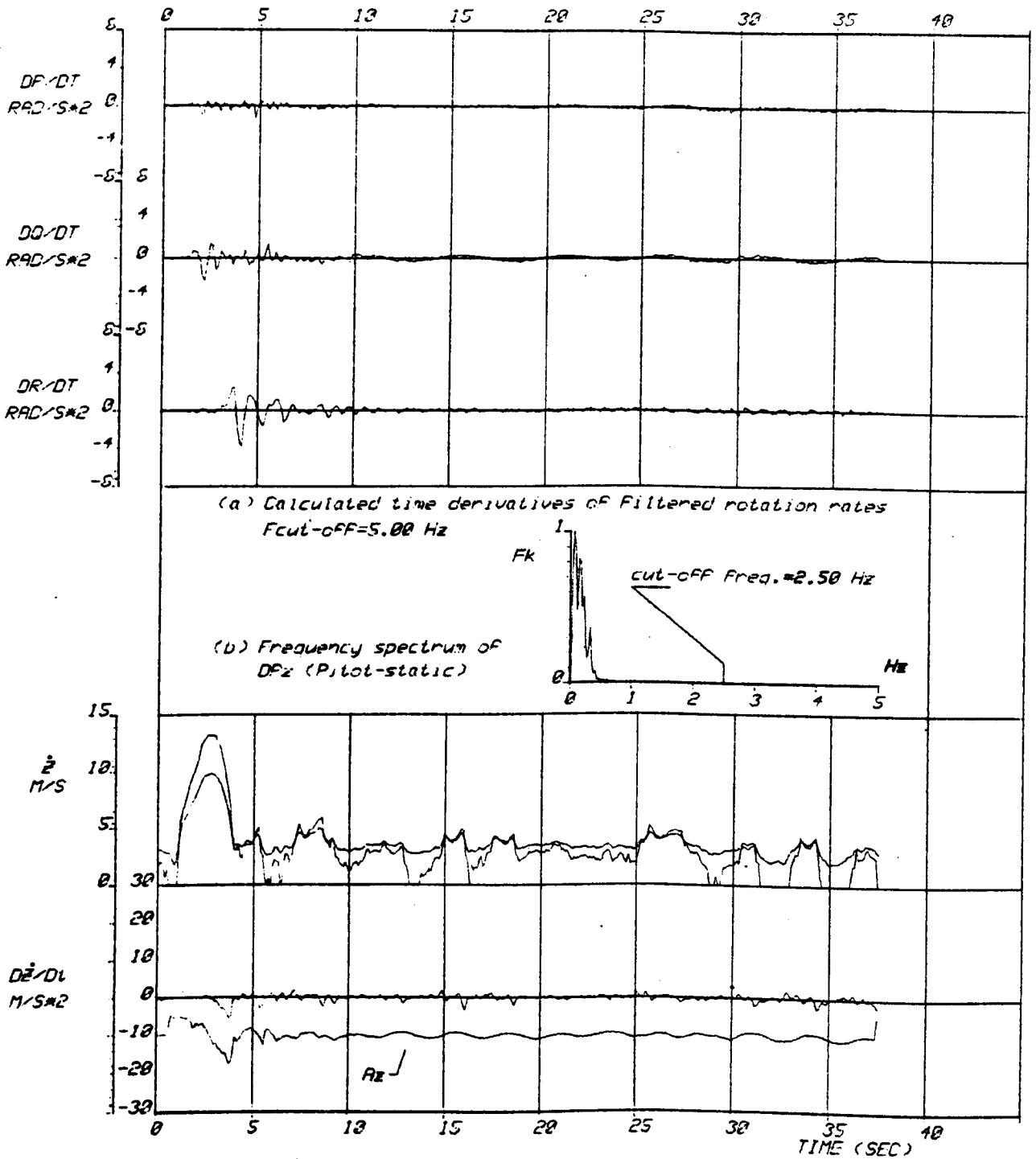


FIGURE 3.45

Amplitude spectra of inertial transducer signals for SB12-configuration drops

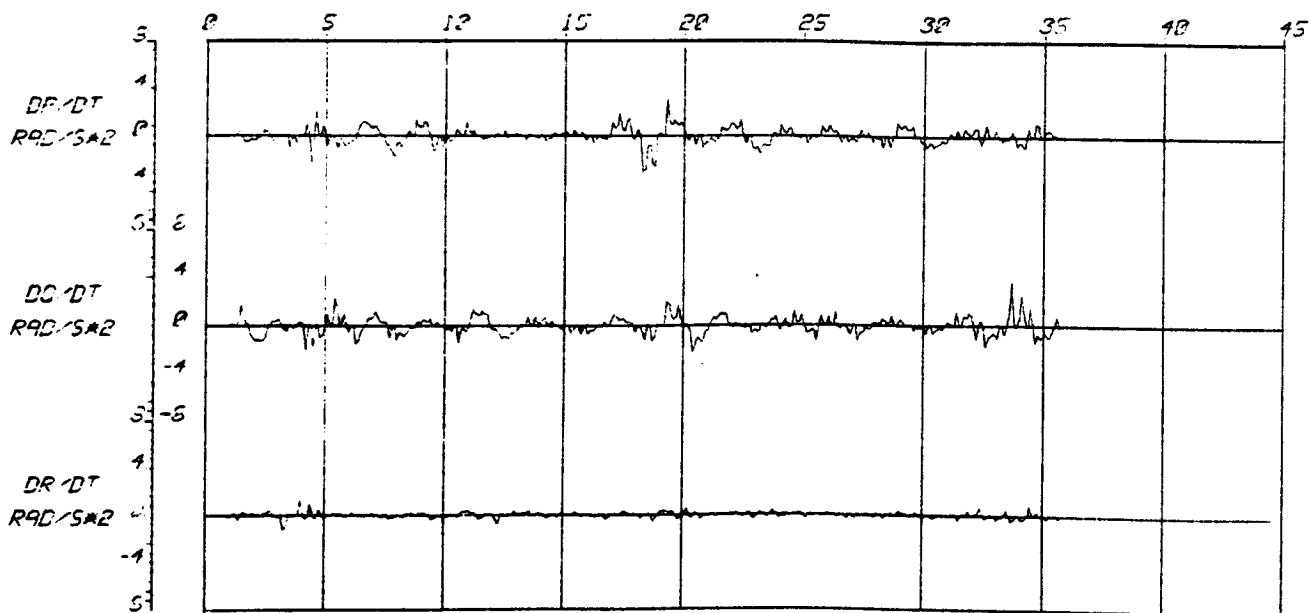


(a) Calculated time derivatives of Filtered rotation rates
 $F_{\text{cut-off}} = 5.00 \text{ Hz}$

(b) Frequency spectrum of DPz (Pilot-static)

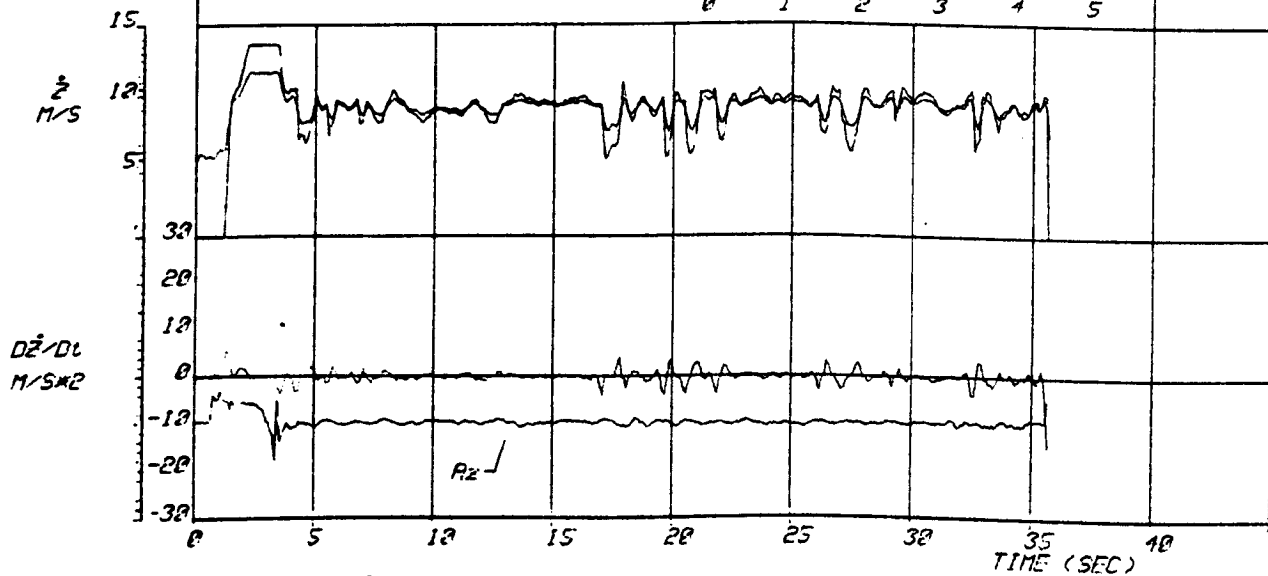
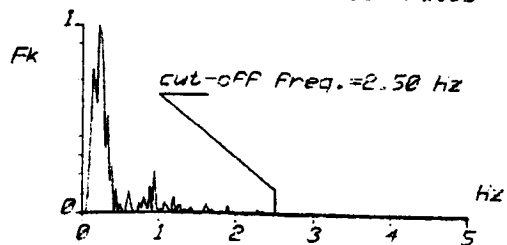
(c) \dot{z} From digitally Filtered DPz ; calculated $D\dot{z}/Dt$

FIG. 3.46	DROP NO. : 24UF02
	DATE : 02/07/75
	TIME : 1330



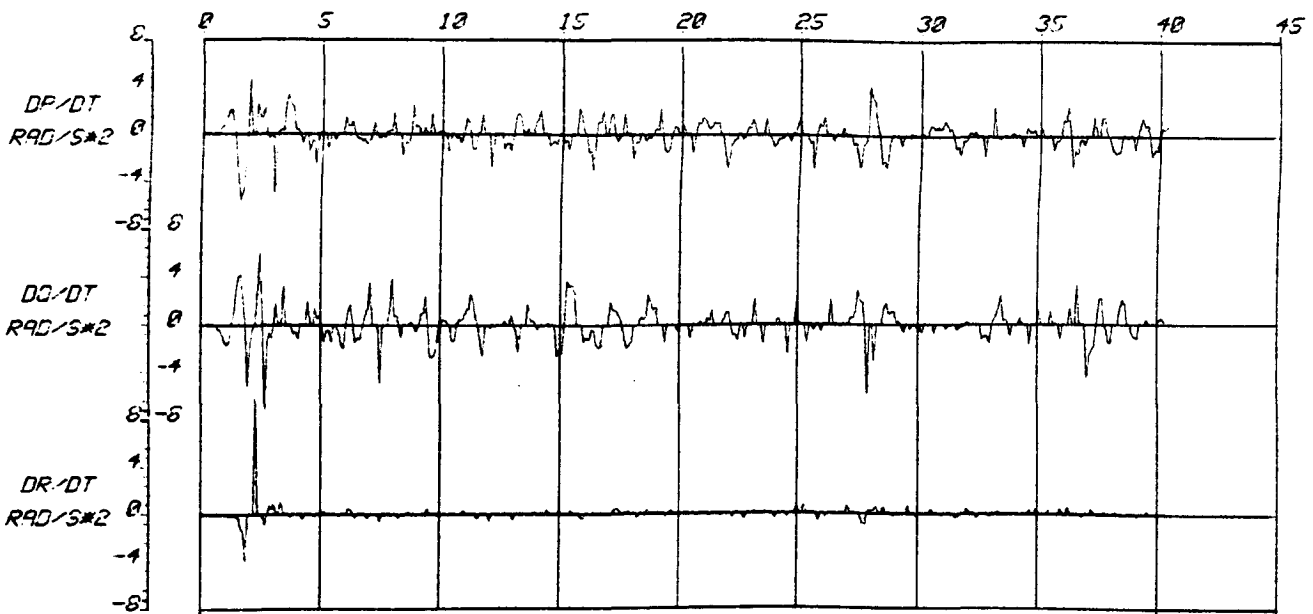
(a) Calculated time derivatives of Filtered rotation rates
 $F_{cut-off} = 5.00$ hz

(b) Frequency spectrum of DP_z (Pilot-static)

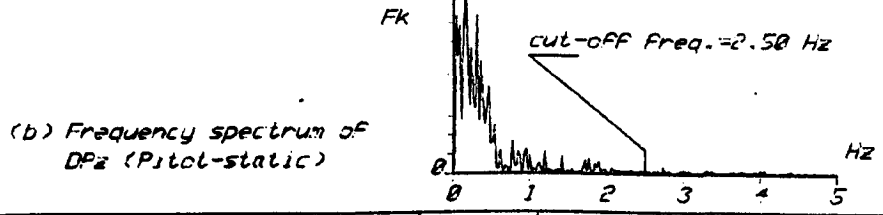


(c) \dot{z} from digitally Filtered DP_z ; calculated D^2z/Dt^2

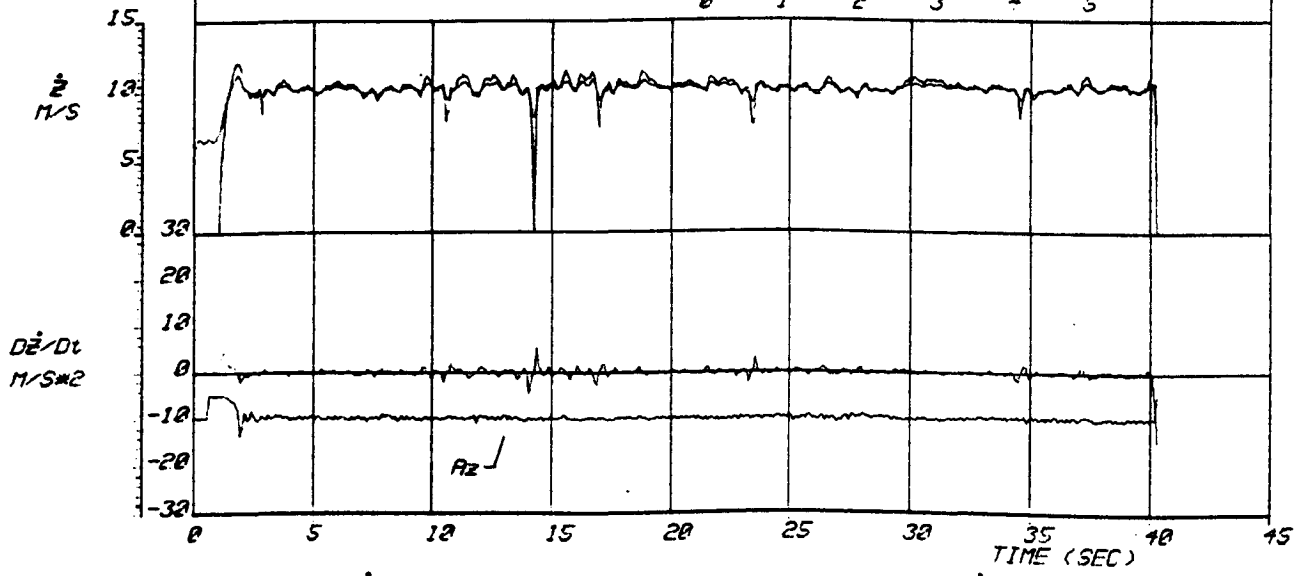
FIG. 3.47	DROP NO.: 12UF08
	DATE: 111075
	TIME: 1148



(a) Calculated time derivatives of Filtered rotation rates
 $F_{\text{cut-off}} = 5.00 \text{ Hz}$

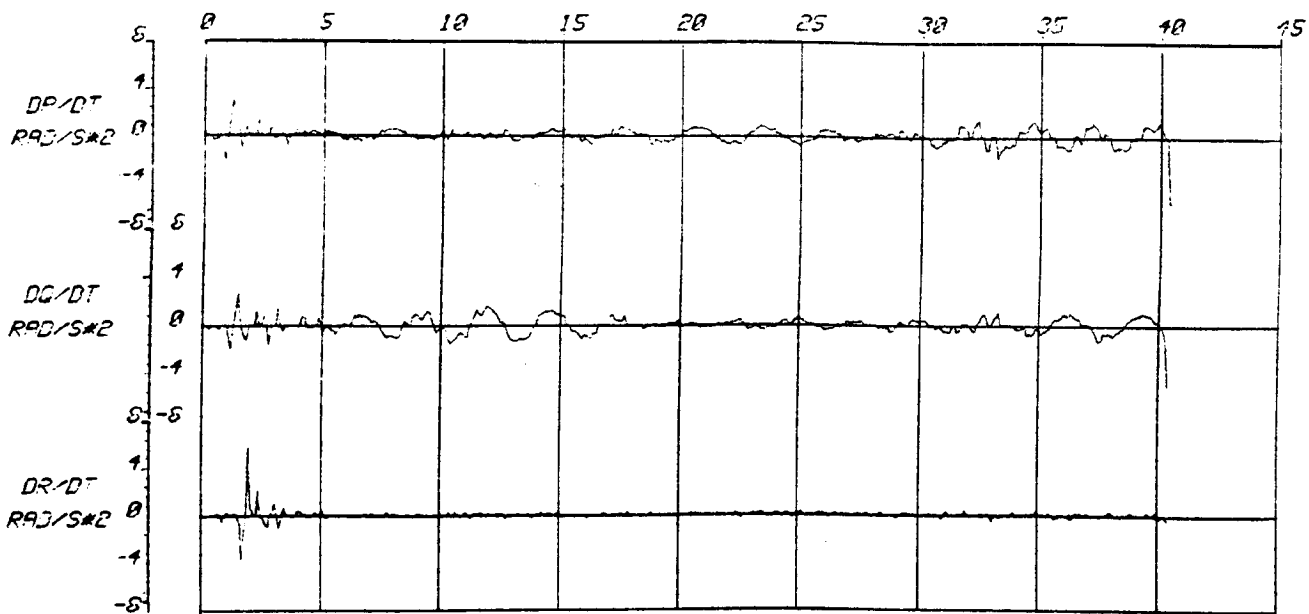


(b) Frequency spectrum of DP_z (Pistol-static)



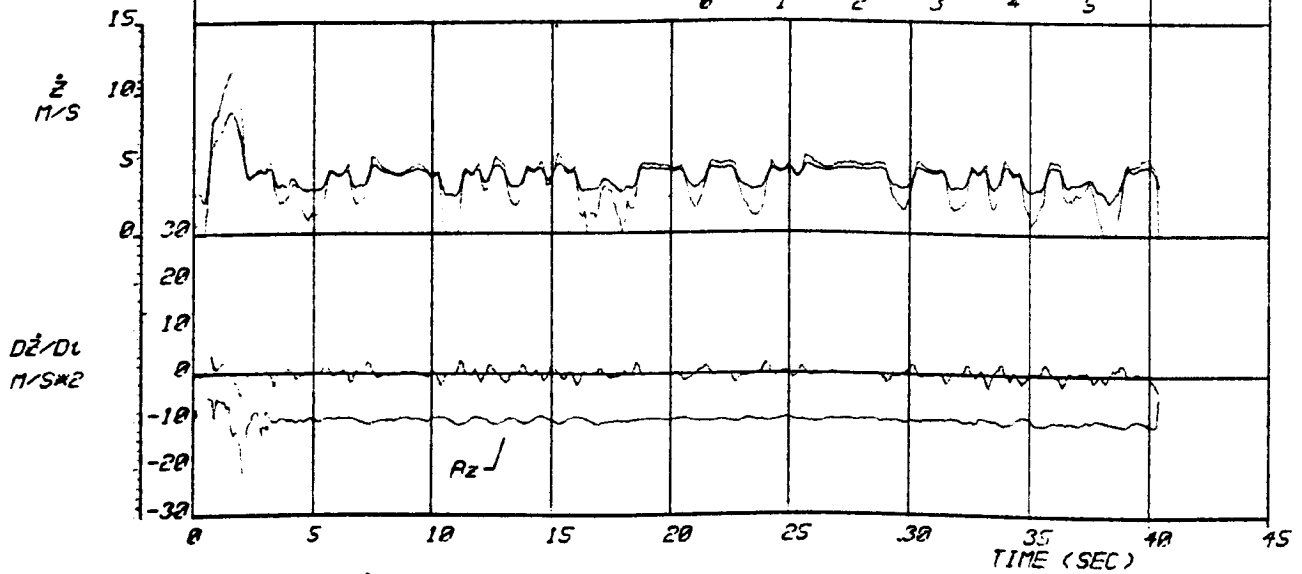
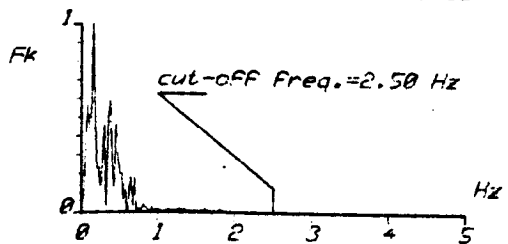
(c) \dot{z} From digitally Filtered DP_z ; calculated $D\dot{z}/Dt$

FIG. 3.48	DROP NO. 06UF19
	DATE: 171075
	TIME: 1157



(a) Calculated time derivatives of Filtered rotation rates
 $F_{\text{cut-off}} = 5.00 \text{ Hz}$

(b) Frequency spectrum of DP_z (Pilot-static)



(c) \dot{z} from digitally filtered DP_z ; calculated $D\dot{z}/Dt$

FIG. 3.49	DRO# NO. : 12UF20
	DATE: 131175
	TIME: 1203

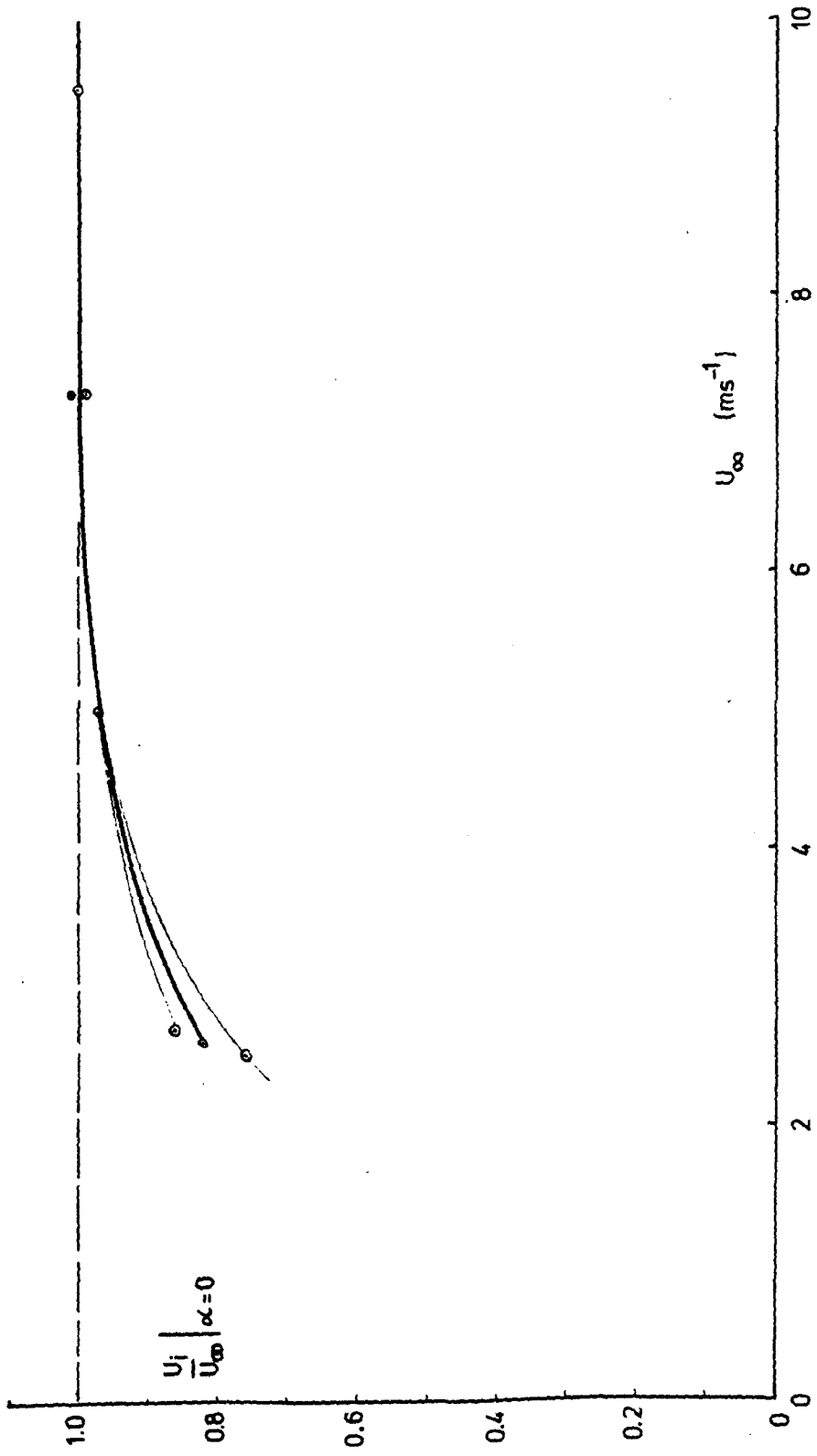


FIGURE 3.50 Calibration curve interpolation for Pitot-static sensor of BB

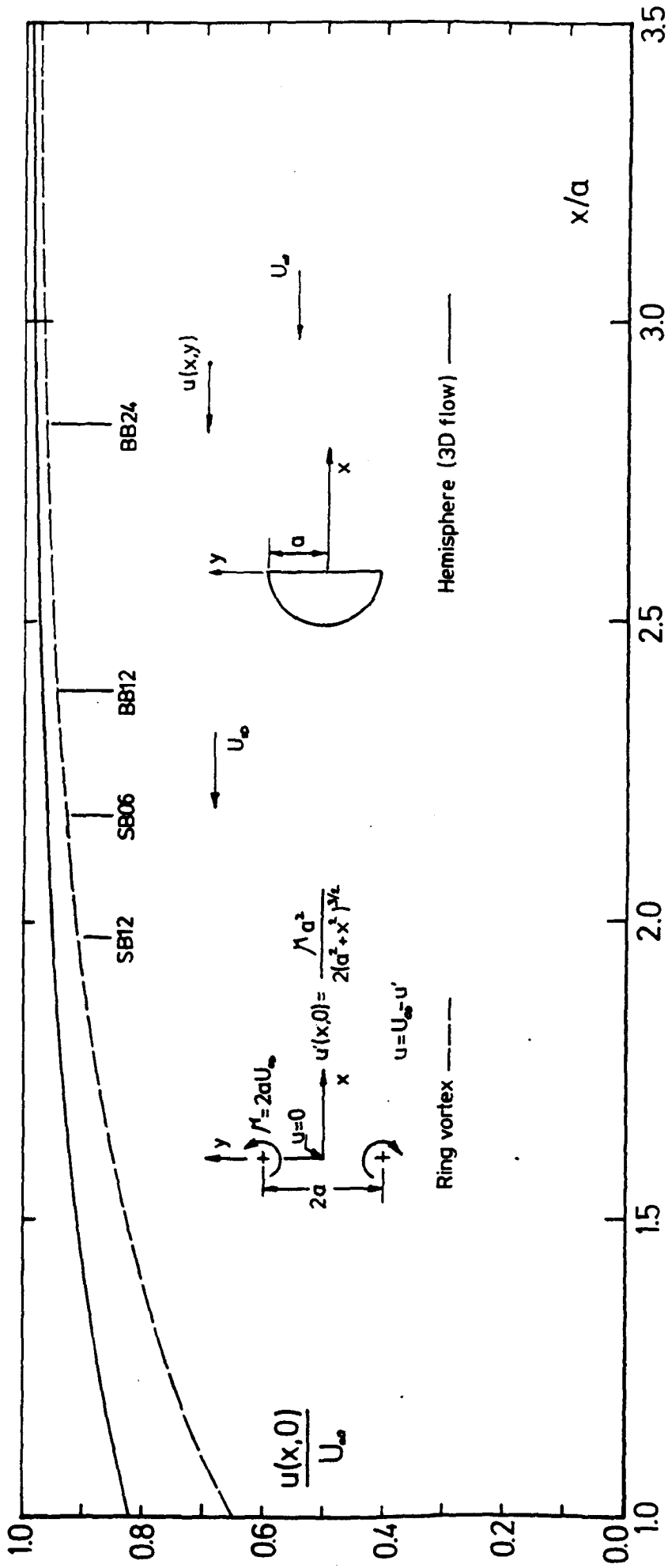


FIGURE 3.51 Position-error correction curves

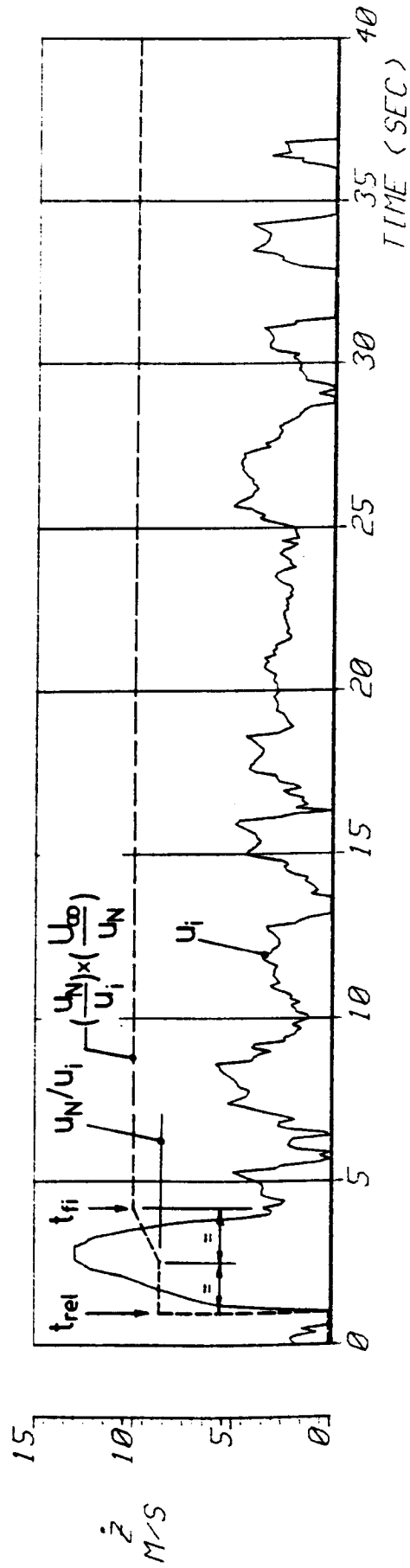


FIGURE 3.52 Implementation of the position-error correction factor

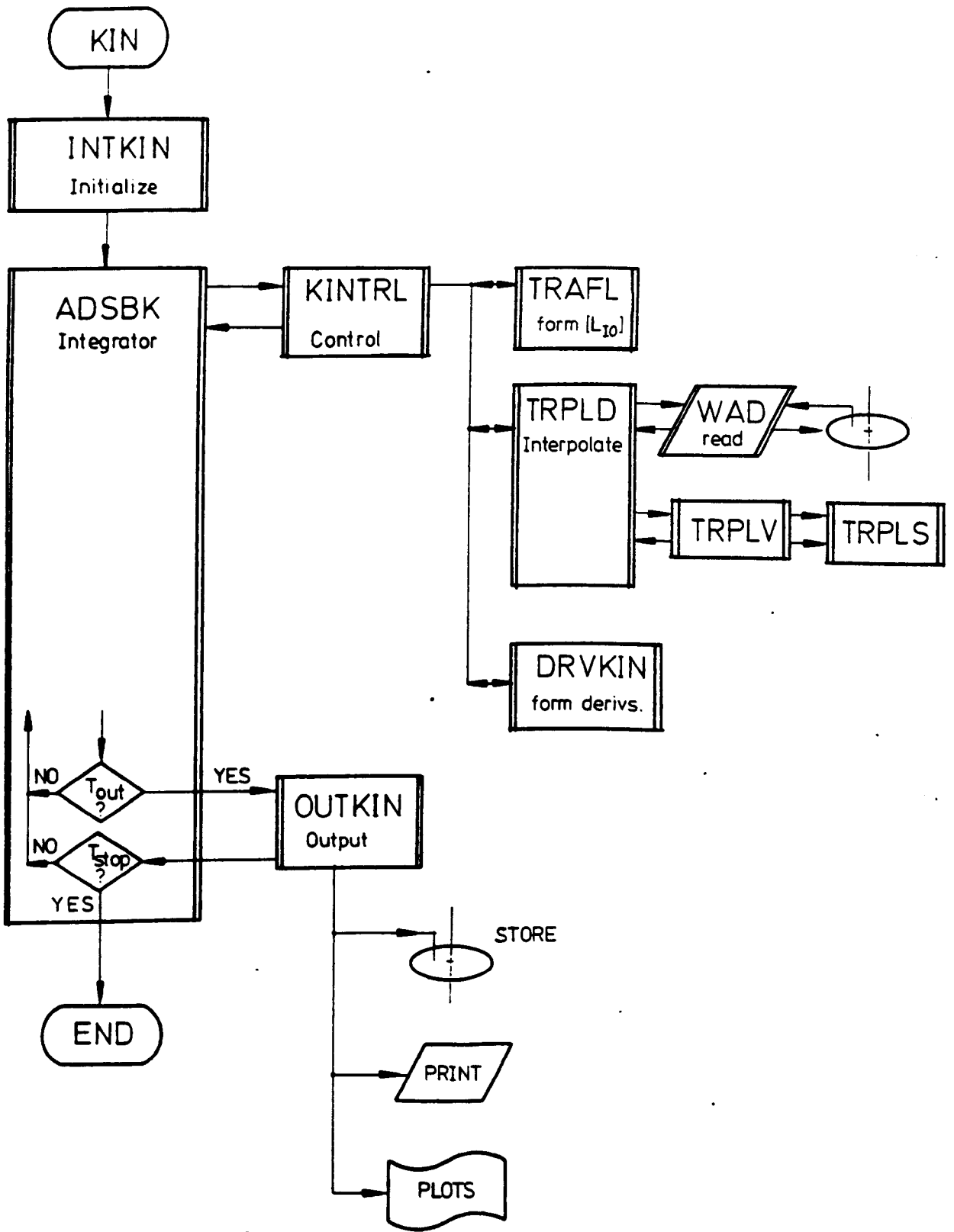
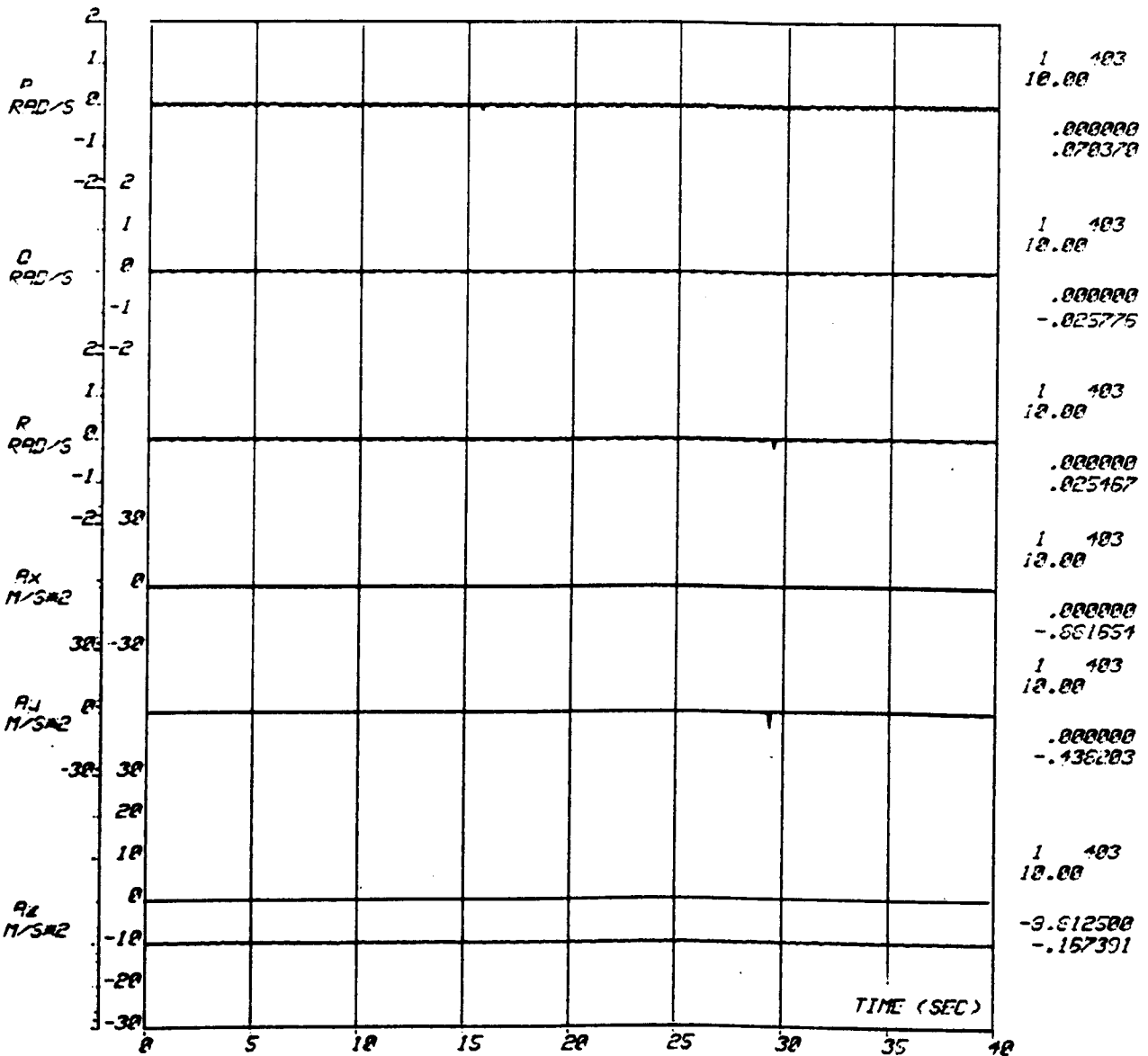
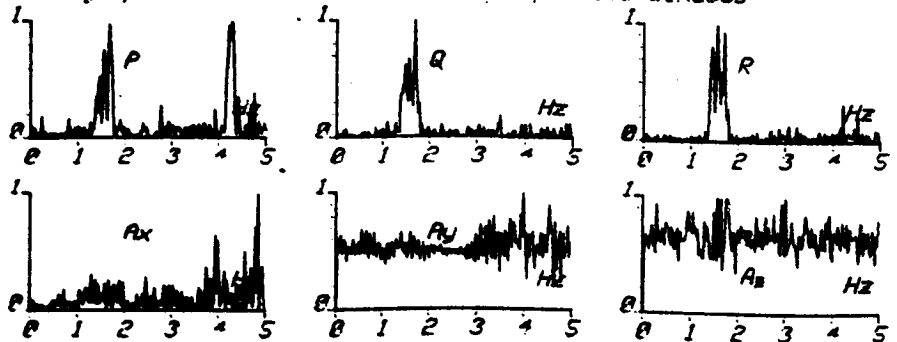


FIGURE 3.53

High-level flow diagram of programme KIN



(a) Signals after digital processing (window Filtering and bias correction options)
 (b) Normalised Frequency density spectra as measured within respective windows

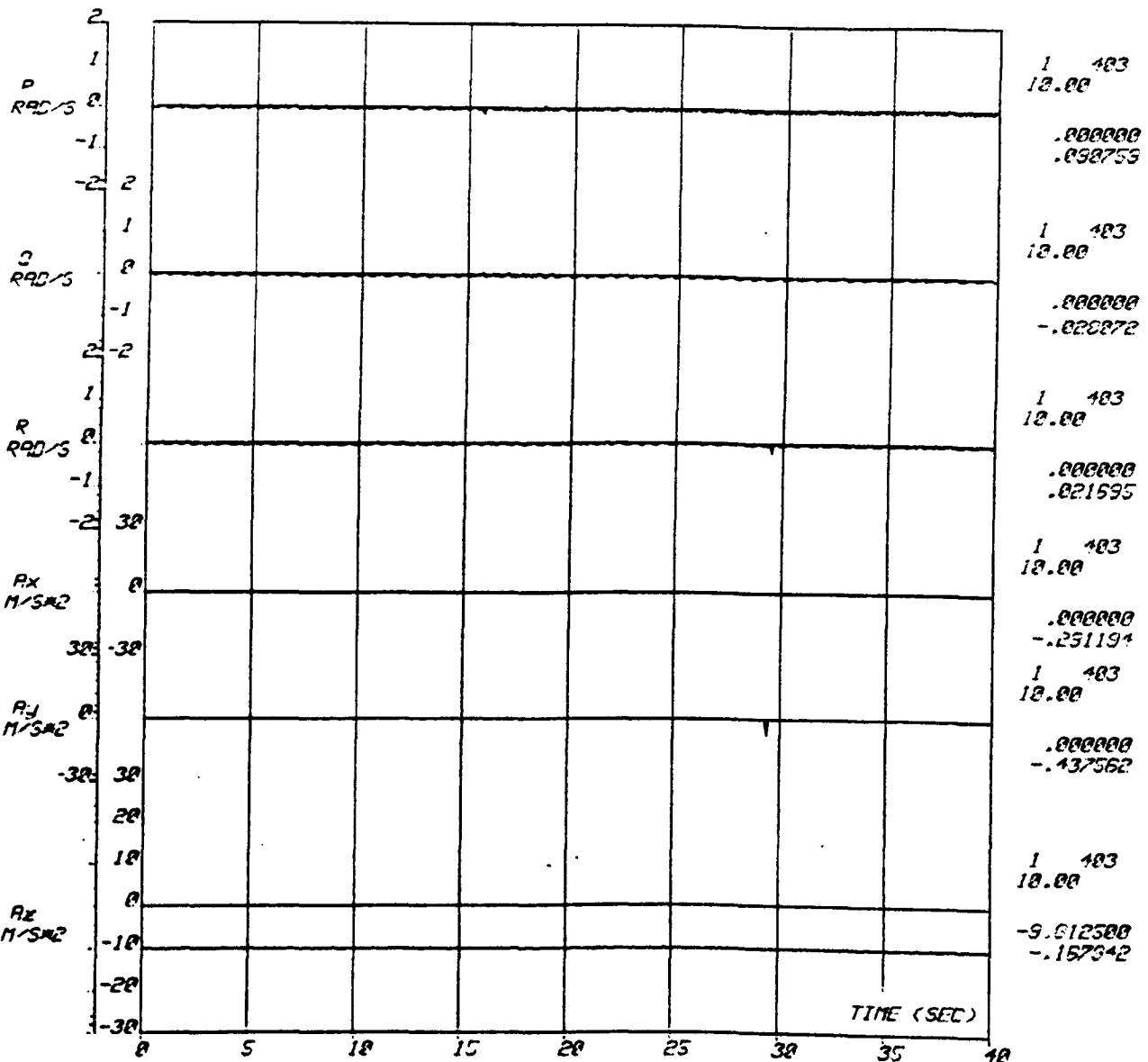


DROP NO.: 24UF 6
 DATE: 051879
 TIME: 1357

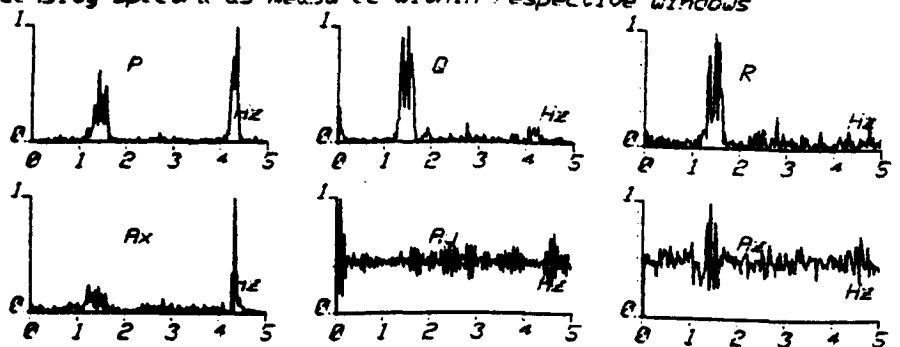
Signal	Peak (Normalising) Value $\hat{F}_k^2 (k \neq 0)$	(Units) ^{1/2}
P	4.35×10^{-2}	rad.s ⁻¹
Q	3.23×10^{-2}	rad.s ⁻¹
R	2.98×10^{-2}	rad.s ⁻¹
Ax	4.11×10^{-2}	m.s ⁻²
Ay	2.61×10^{-2}	m.s ⁻²
Az	2.97×10^{-2}	m.s ⁻²

FIGURE 3.54

Noise input signals from trial UF06



(a) Signals after digital processing (window filtering and bias correction options)
 (b) Normalised Frequency density spectra as measured within respective windows



DROP NO. MACH 1
 DAT: 878182
 TIME: XX

Signal	Peak (normalising) Value $F_n^2 (k \neq 0)$	(Units) ²
p	5.97×10^{-3}	rad. s ⁻¹
q	3.58×10^{-3}	rad. s ⁻¹
r	2.66×10^{-2}	rad. s ⁻¹
ax	6.12×10^{-3}	m. s ⁻²
ay	2.86×10^{-2}	m. s ⁻²
ay	3.40×10^{-2}	m. s ⁻²
az	7.23×10^{-3}	mm H ₂ O

FIGURE 3.55

Noise input signals from trial CH01

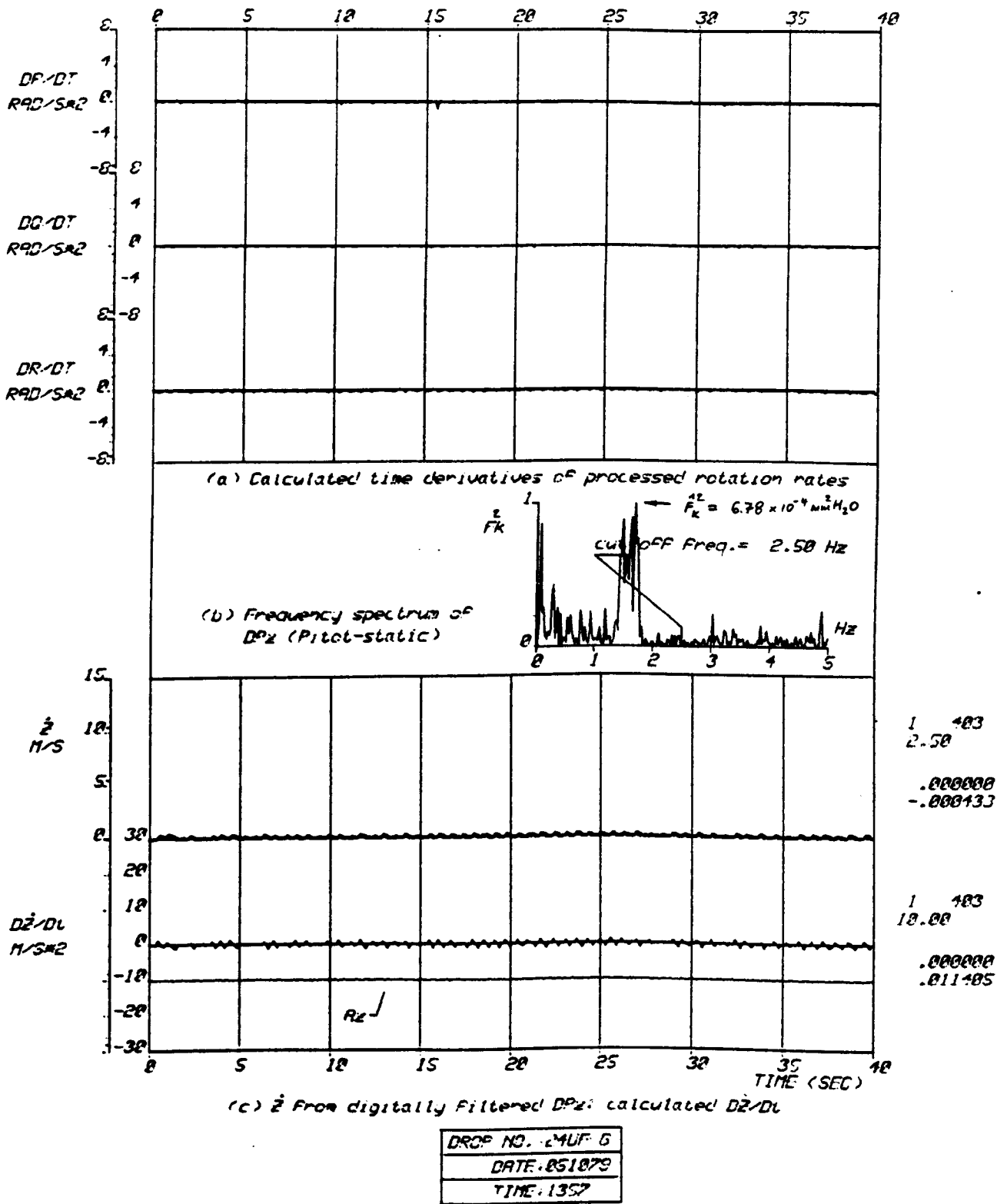


FIGURE 3.56

Time derivatives of noise input signals from trial UF06

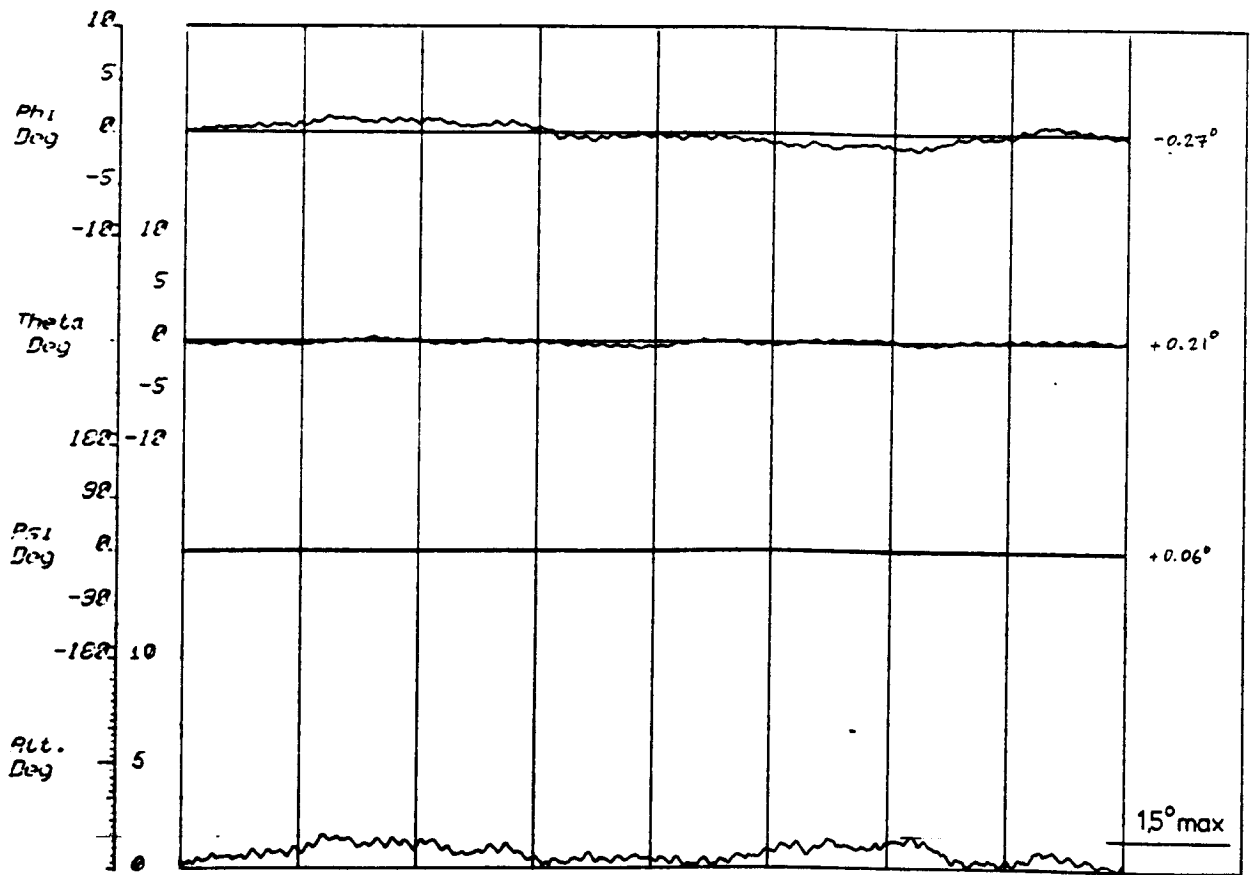


FIGURE 3.57 Euler angle and attitude errors: trial UF06

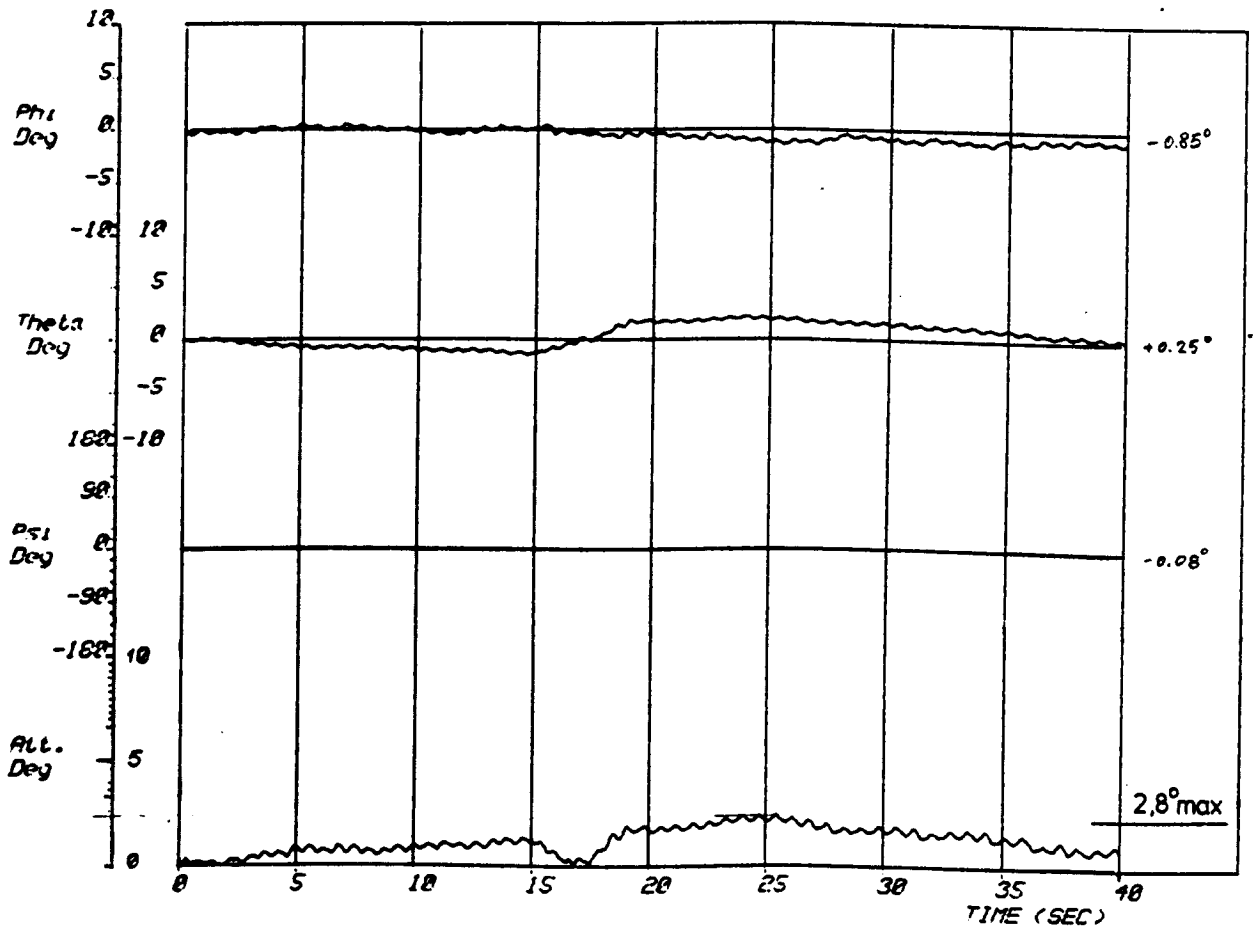
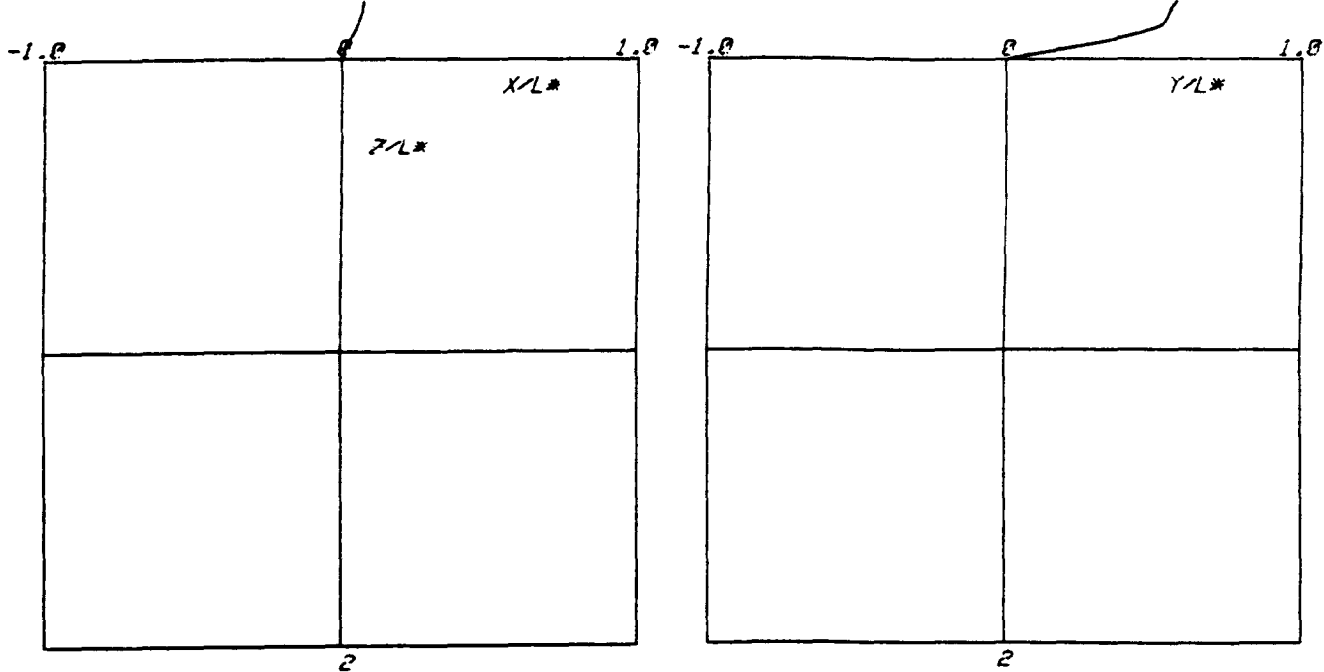
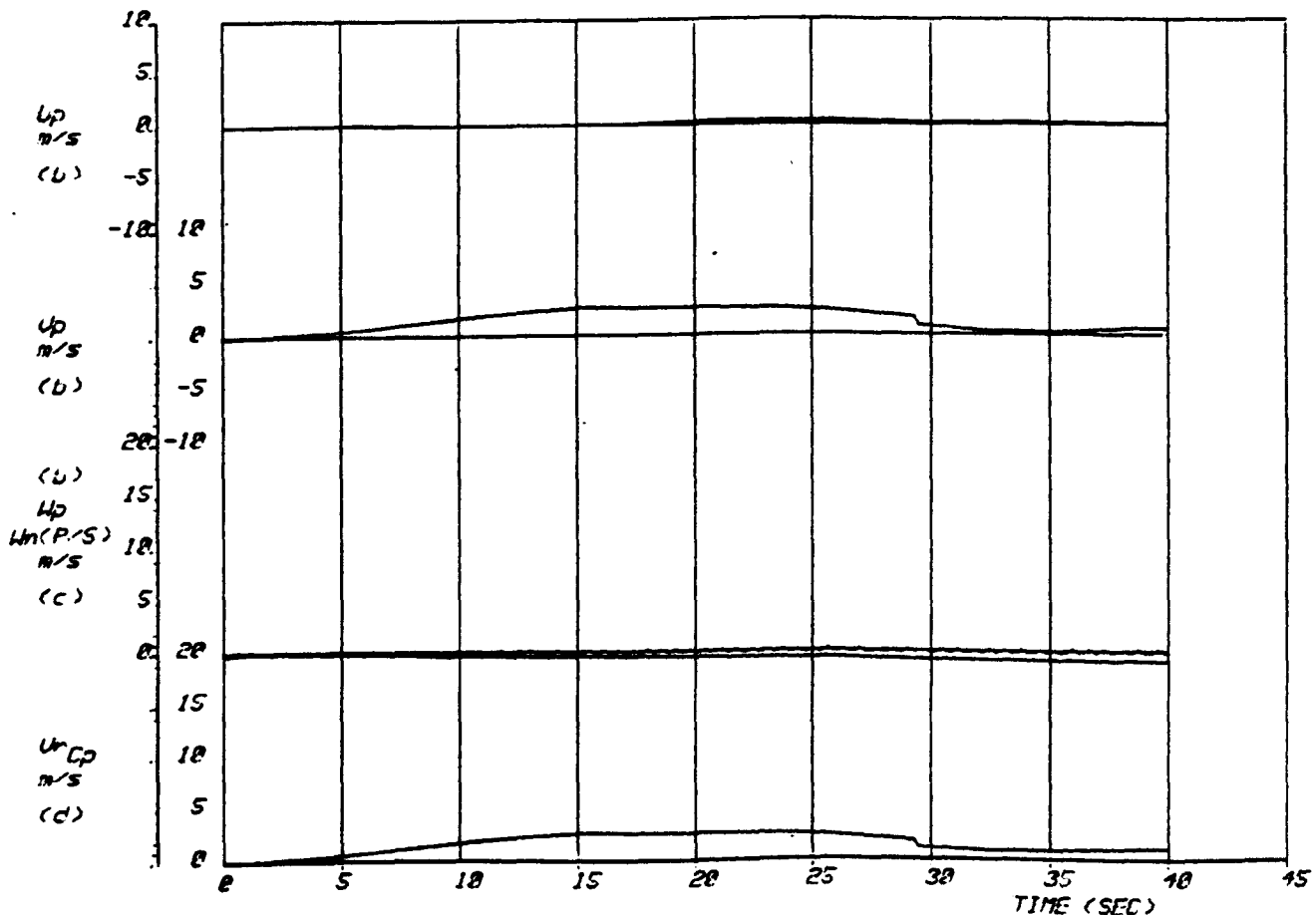


FIGURE 3.58 Euler angle and attitude errors: trial CH01



(a) Spatial trajectory of point P ($L^* = 120.0m$)

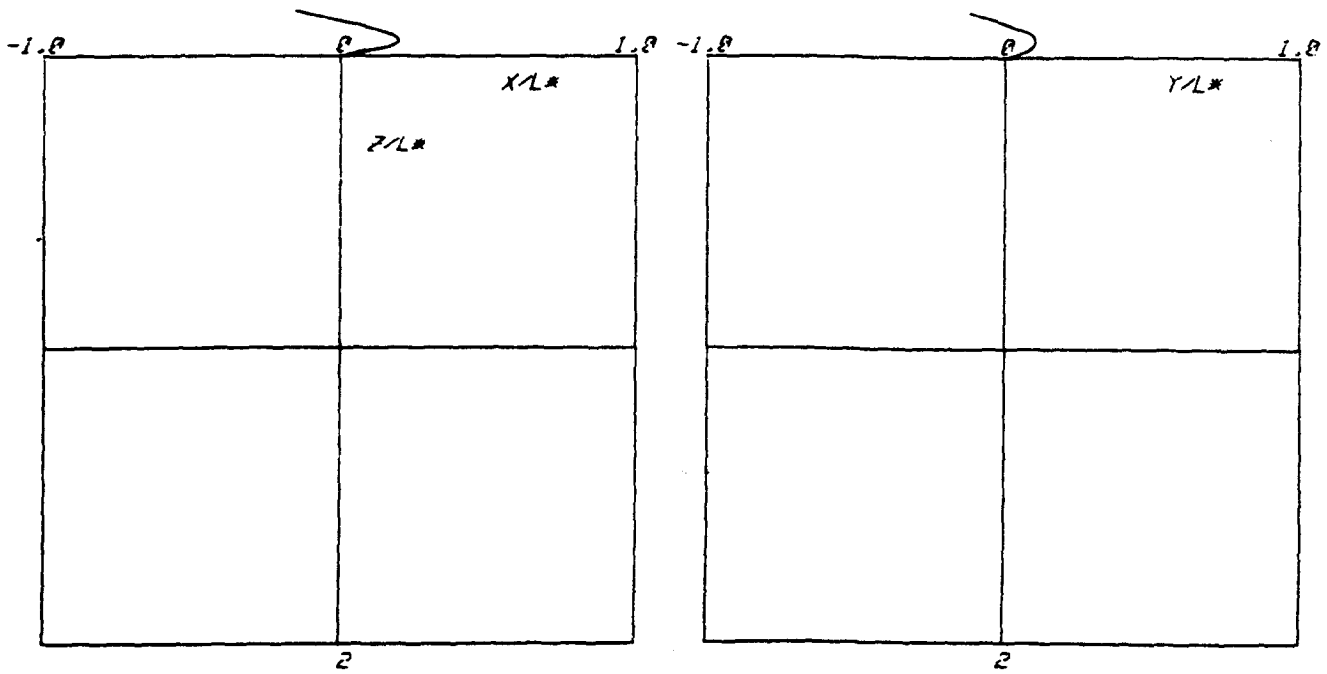


(a) Velocity components along body axes at P
 (c) airspeed along z at N
 (d) resultant airspeed at canopy Cp

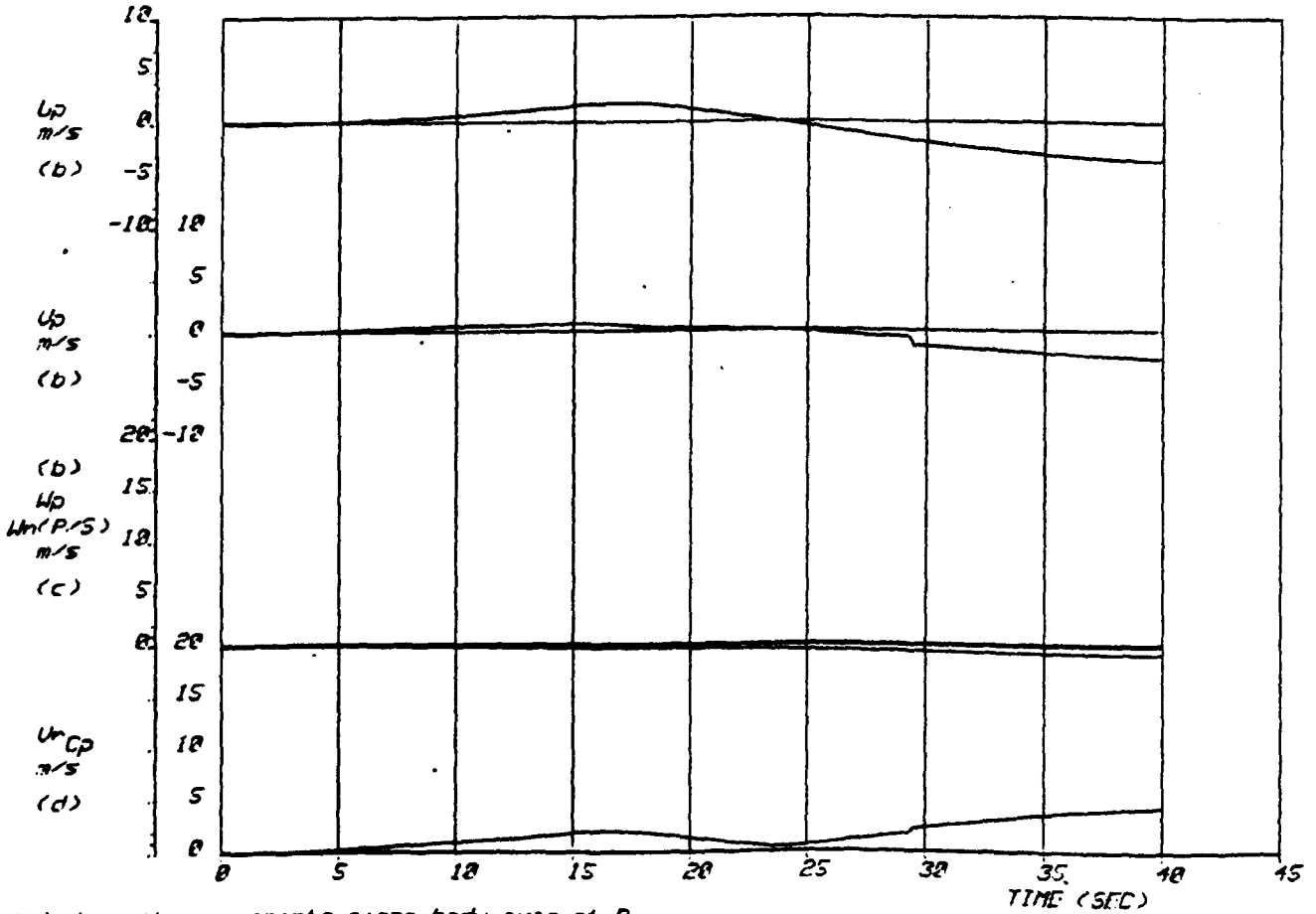
DROP NO.: 24UF 6
 DATE: 051079
 TIME: 1357

FIGURE 3.59

Position and speed errors: trial UF06



(a) Spatial trajectory of point P ($L_A=120.0m$)



(b) Velocity components along body axes at P
 (c) airspeed along x at N
 (d) resultant airspeed at canopy S_p

DROP NO.: MICH 1
DATE: 07/01/68
TIME: XX

FIGURE 3.60

Position and speed errors: trial CH01

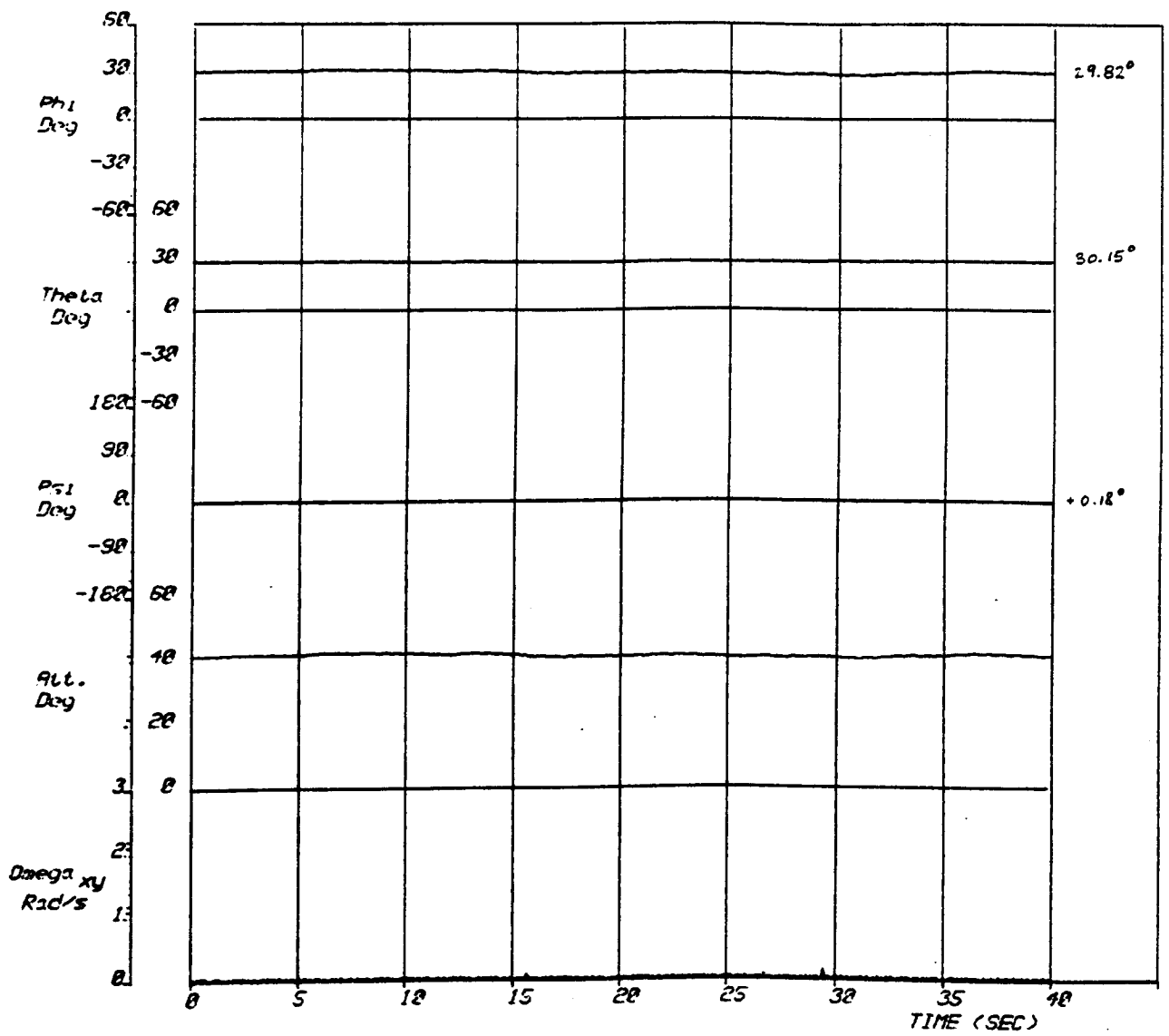


FIGURE 3.61 Euler angle plots: trial UF06 with $\phi_0 = \theta_0 = 30$ deg.

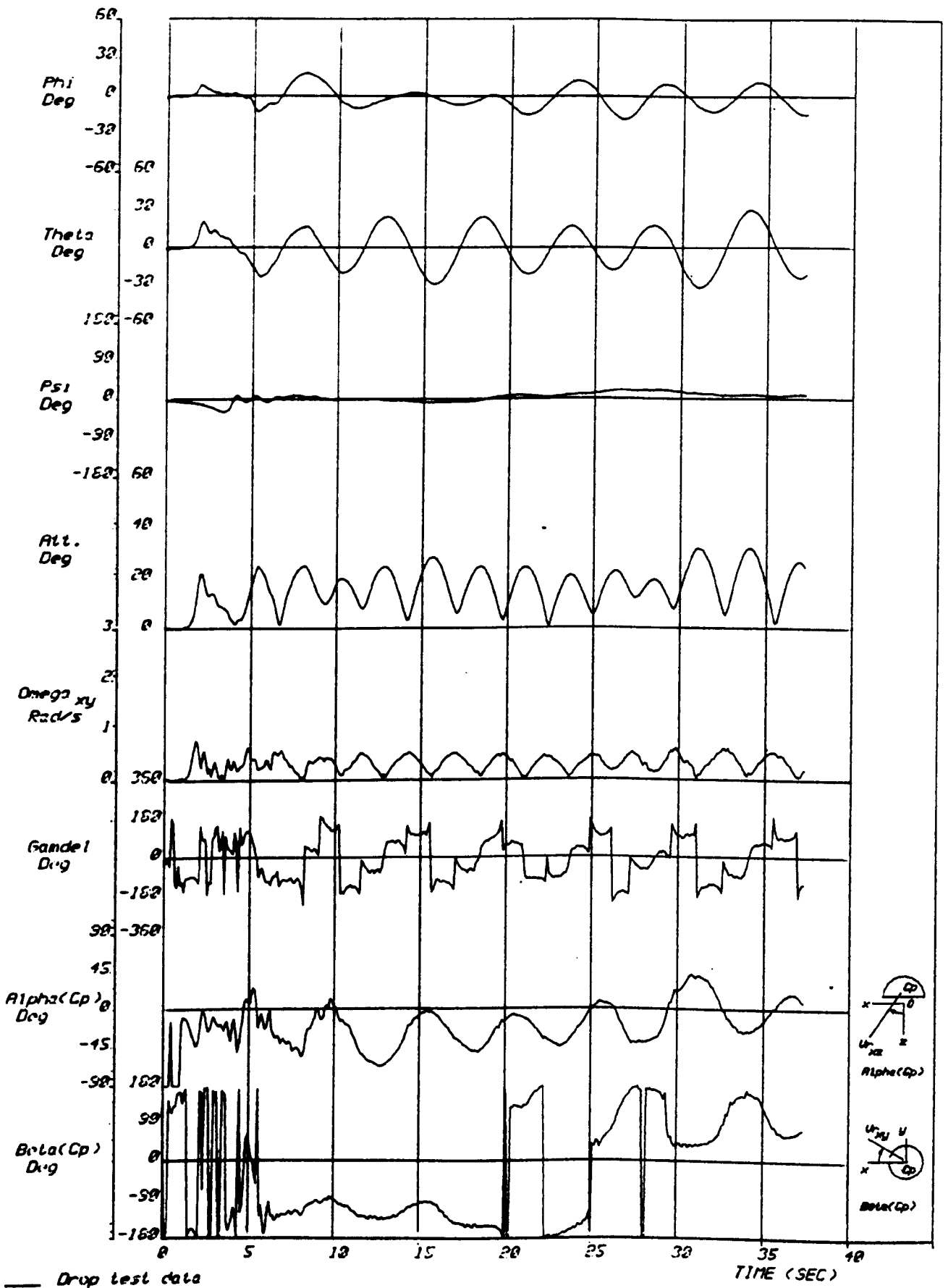
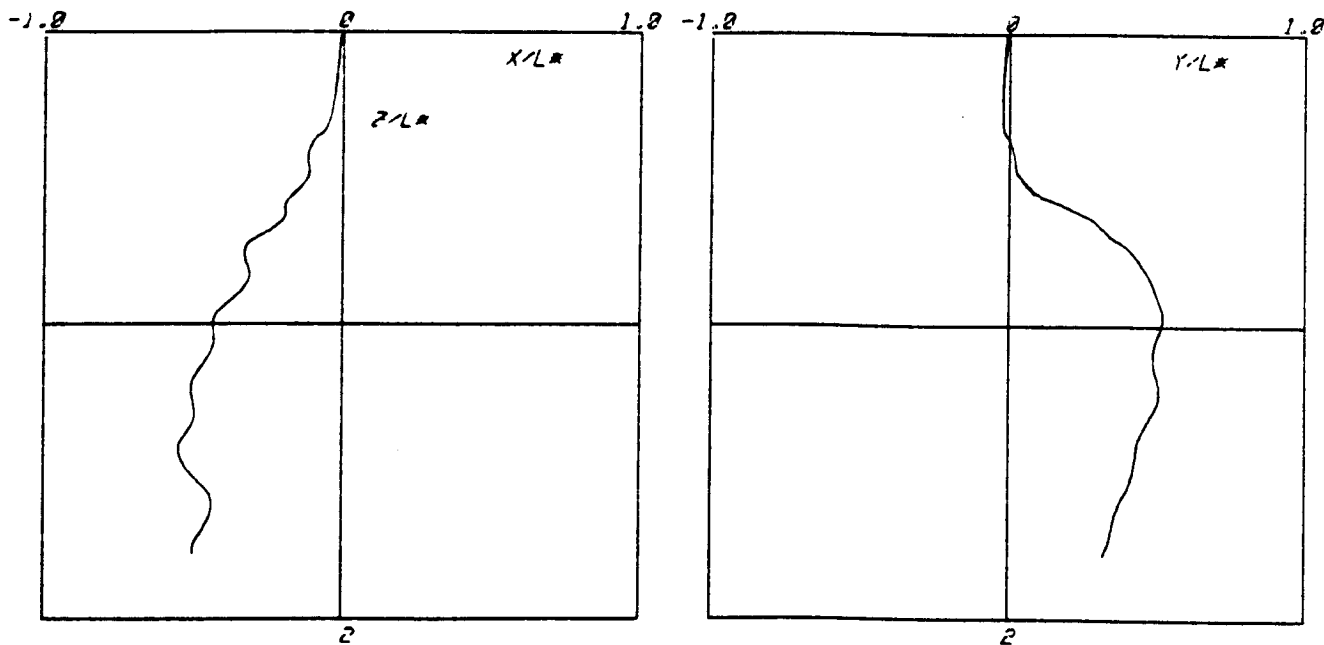
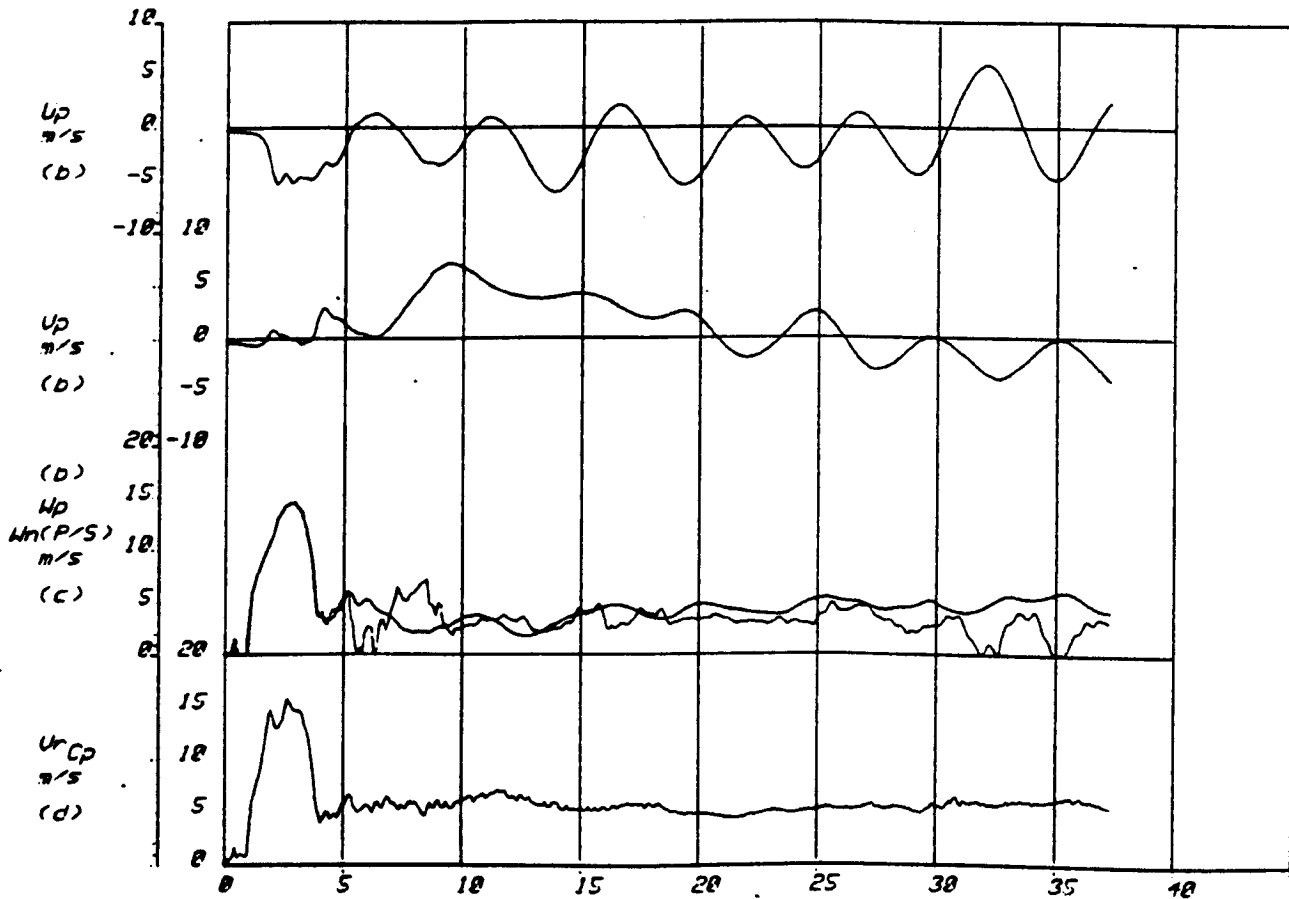


FIG.	DROP NO.: 24UF 2
3.62	DATE: 021079
1 OF 2	TIME: 1330
	WIND: 6 KTS

Calculated time histories of angles for Drop 2 (BB24)



(a) Spatial trajectory of point P ($L^* = 120.0m$)



(b) Velocity components along body axes at P

(c) airspeed along z at N

(d) resultant airspeed at canopy Cp

— Drop test data

FIG.	DROP NO. 24UF 2
3.63	DATE: 021079
2 of 2	TIME: 1330
	#WIND: 6 KTS

Calculated trajectory and speeds for Drop 2 (BB24)

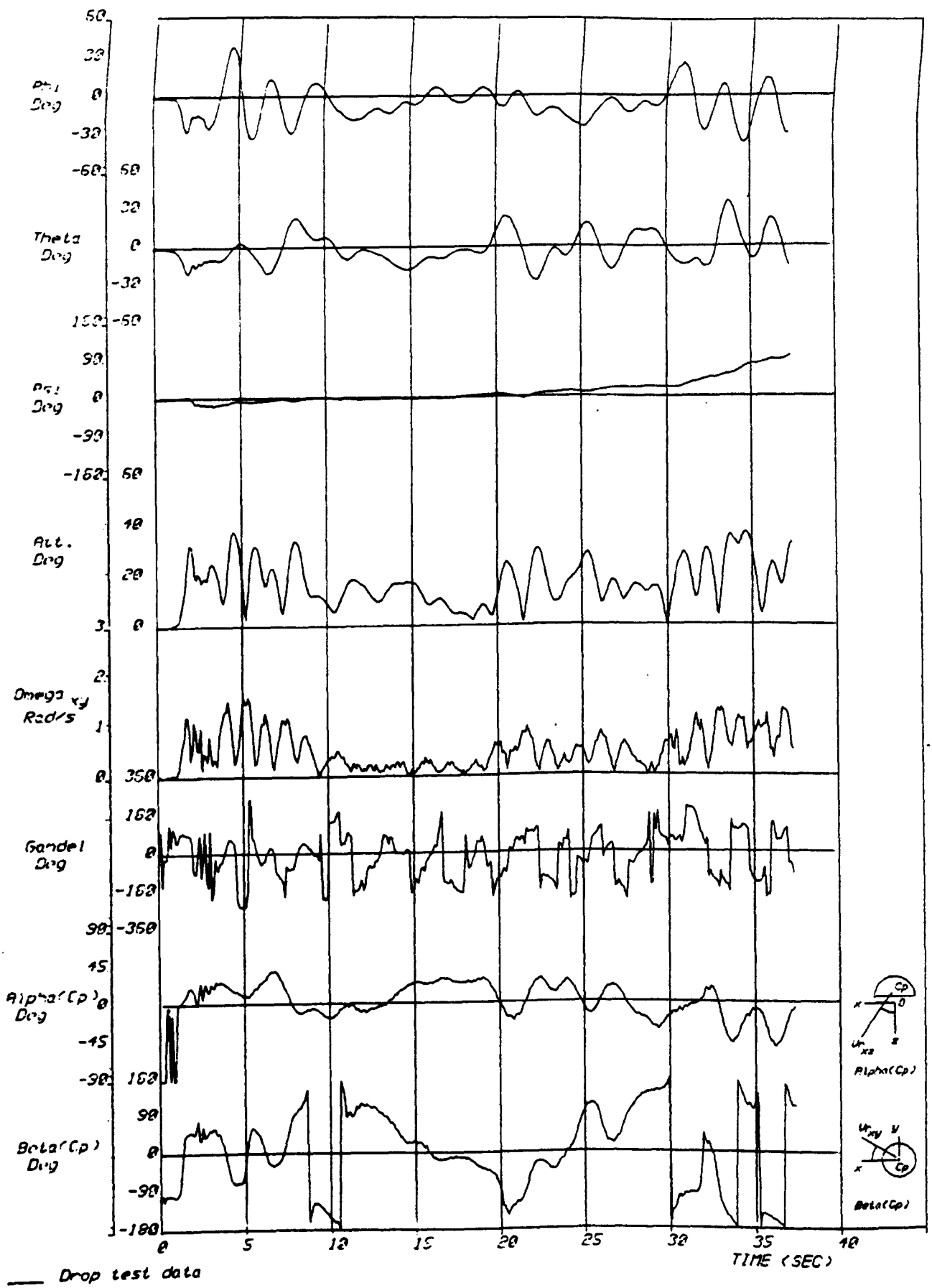
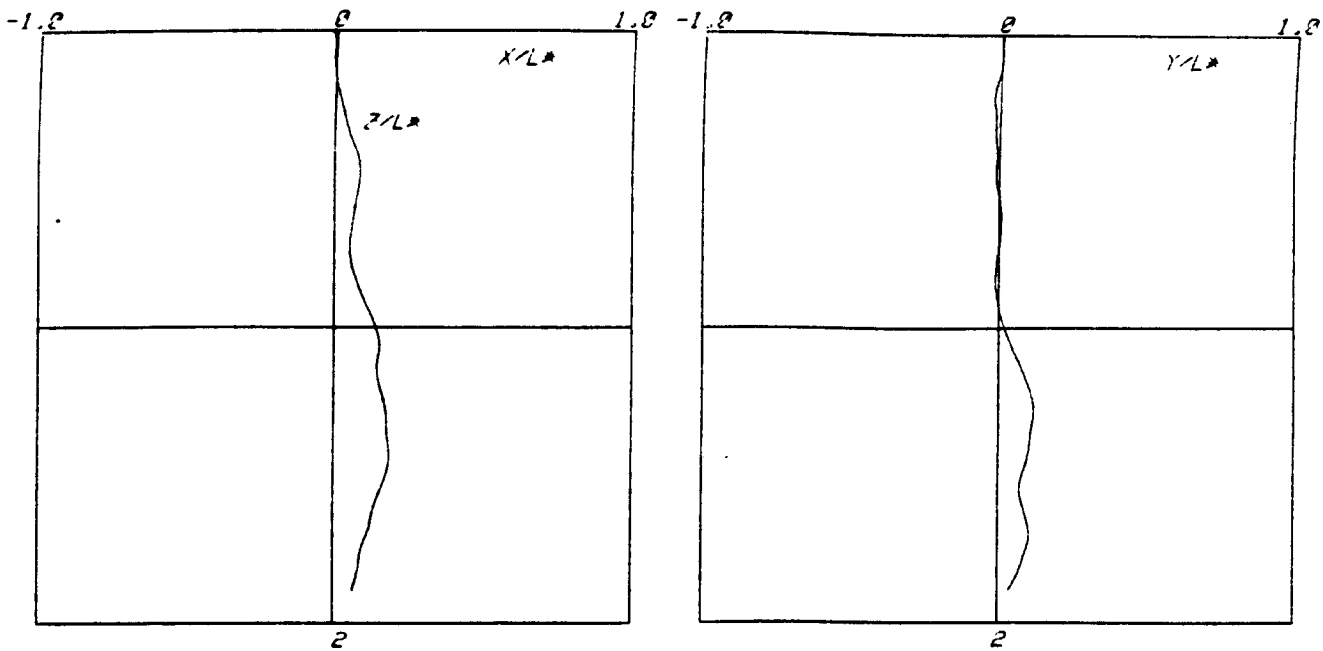
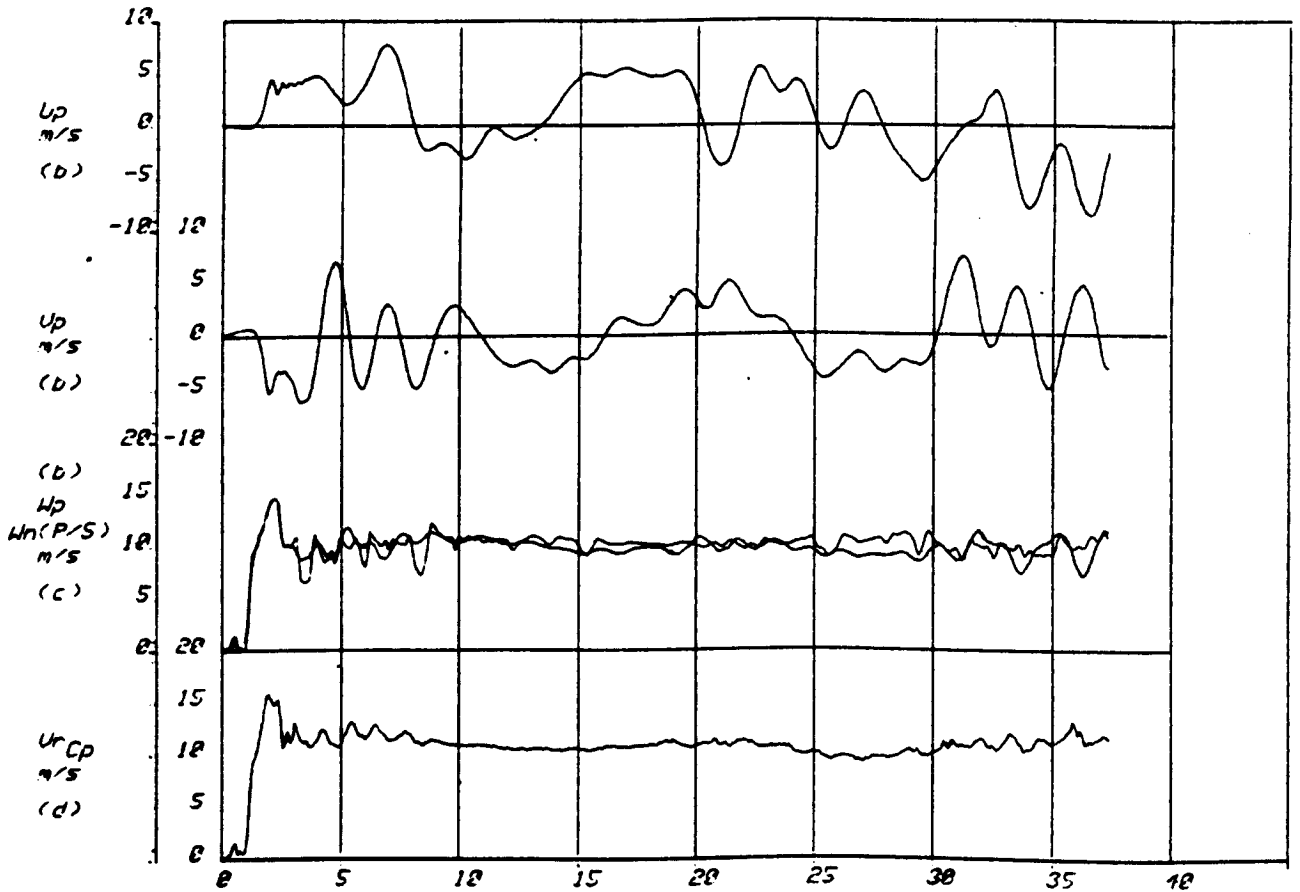


FIG. 3.64 1 of 3	DROP NO.: 12UF18
	DATE: 111079
	TIME: 1403
	WIND: 7 KTS

Calculated time histories of angles for Drop 10 (BB12)



(a) Spatial trajectory of point P ($L^* = 200.0m$)



(b) Velocity components along body axes at P

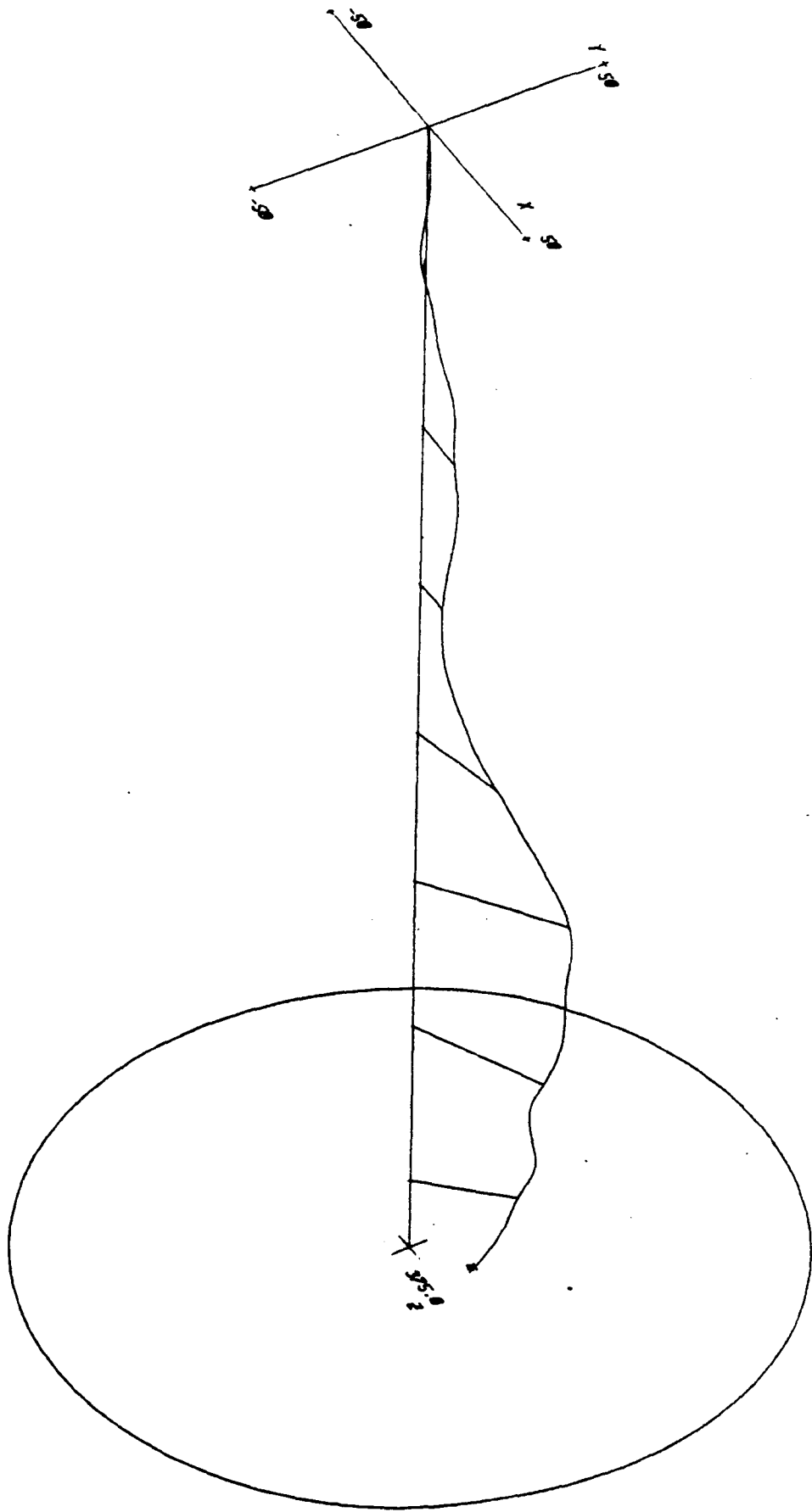
(c) airspeed along x at N

(d) resultant airspeed at canopy C_p

— Drop test data

FIG. 3.65	DROP NO.: 12UF10
	DATE: 111079
2 of 3	TIME: 1403
	WIND: 7 KTS

Calculated trajectory and speeds for Drop 10 (BB12)



Axonometric view of trajectory of point P.
 Dimensions in metres. Horizontal lines correspond to 5sec intervals.

FIG.	DROP NO.: 12UF10
3.66	DATE: 111079
	TIME: 1403
3 of 3	WIND: 7 KTS

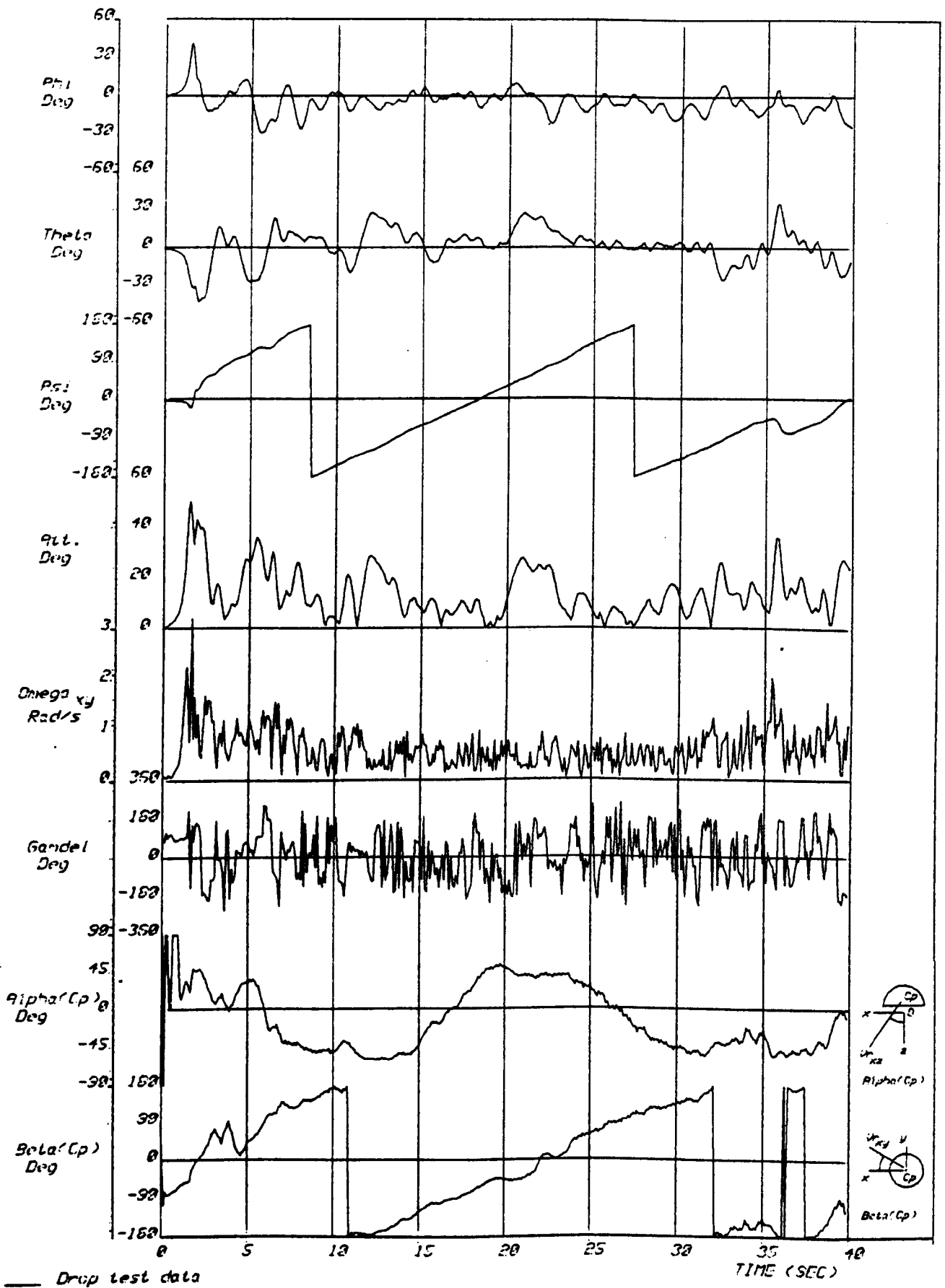
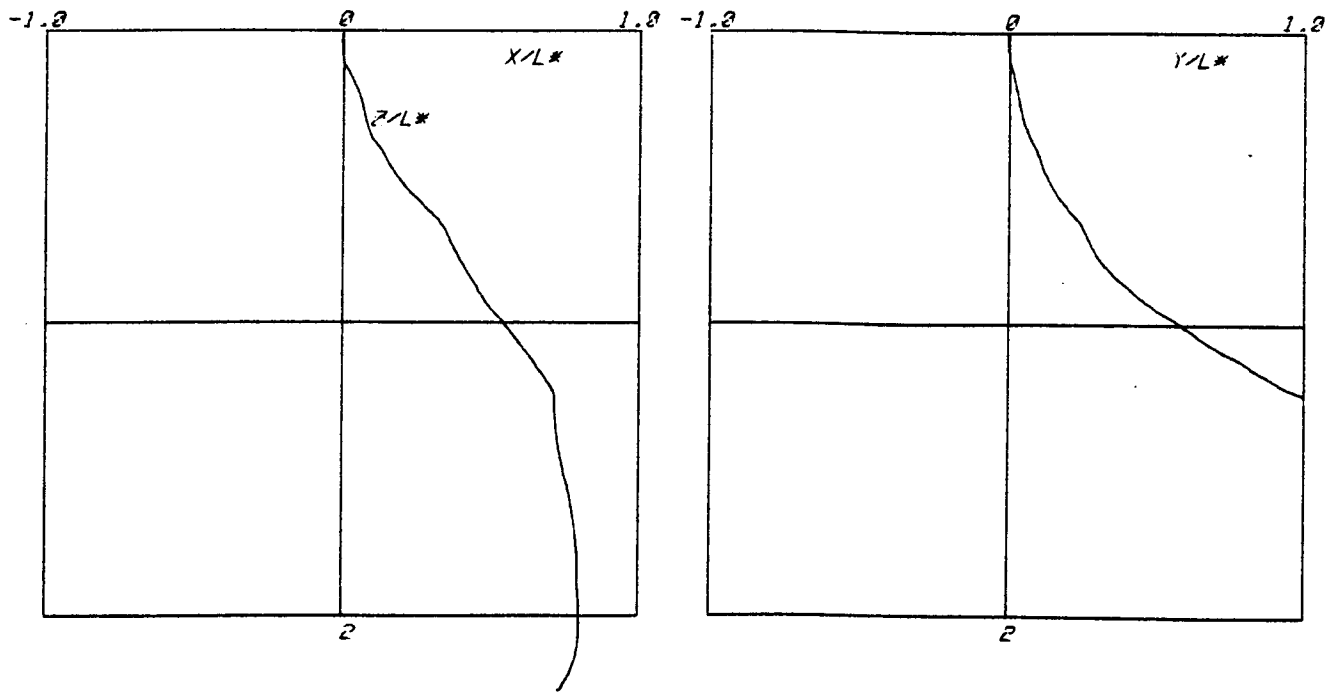
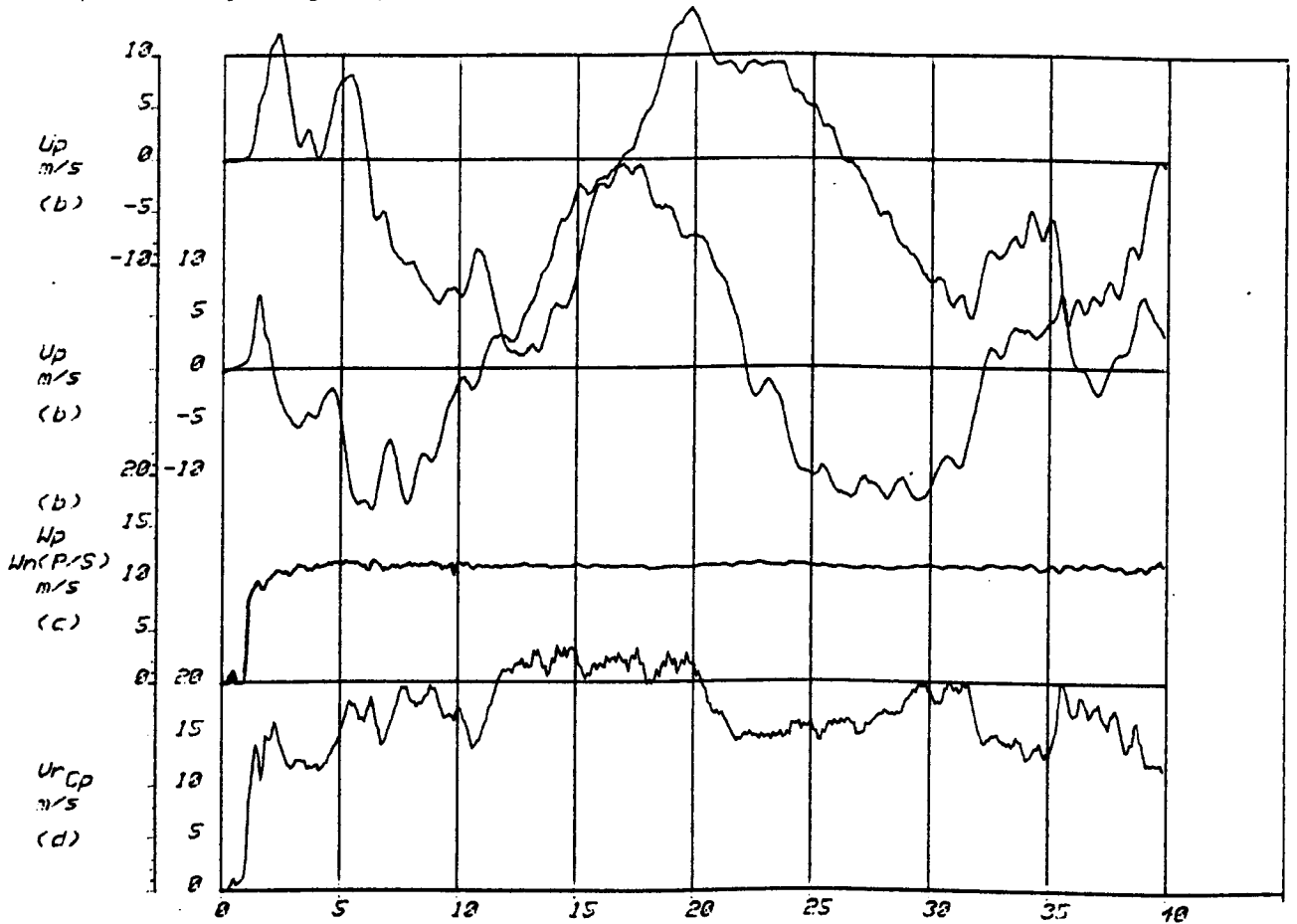


FIG.	DROP NO.: 06UF25
3.67	DATE: 021175
1 of 2	TIME: 1347
	#WIND: 6 KTS

Calculated time histories of angles for Drop 25 (SB06)



(a) Spatial trajectory of point P ($L^* = 200.0m$)



(b) Velocity components along body axes at P

(c) airspeed along z at N

(d) resultant airspeed at canopy C_p

— Drop test data

FIG.	DROP NO.: 06UF25
3.68	DATE: 021179
2 of 2	TIME: 1347
	#WIND#: 6 KTS

Calculated trajectory and speeds for Drop 25 (SB06)

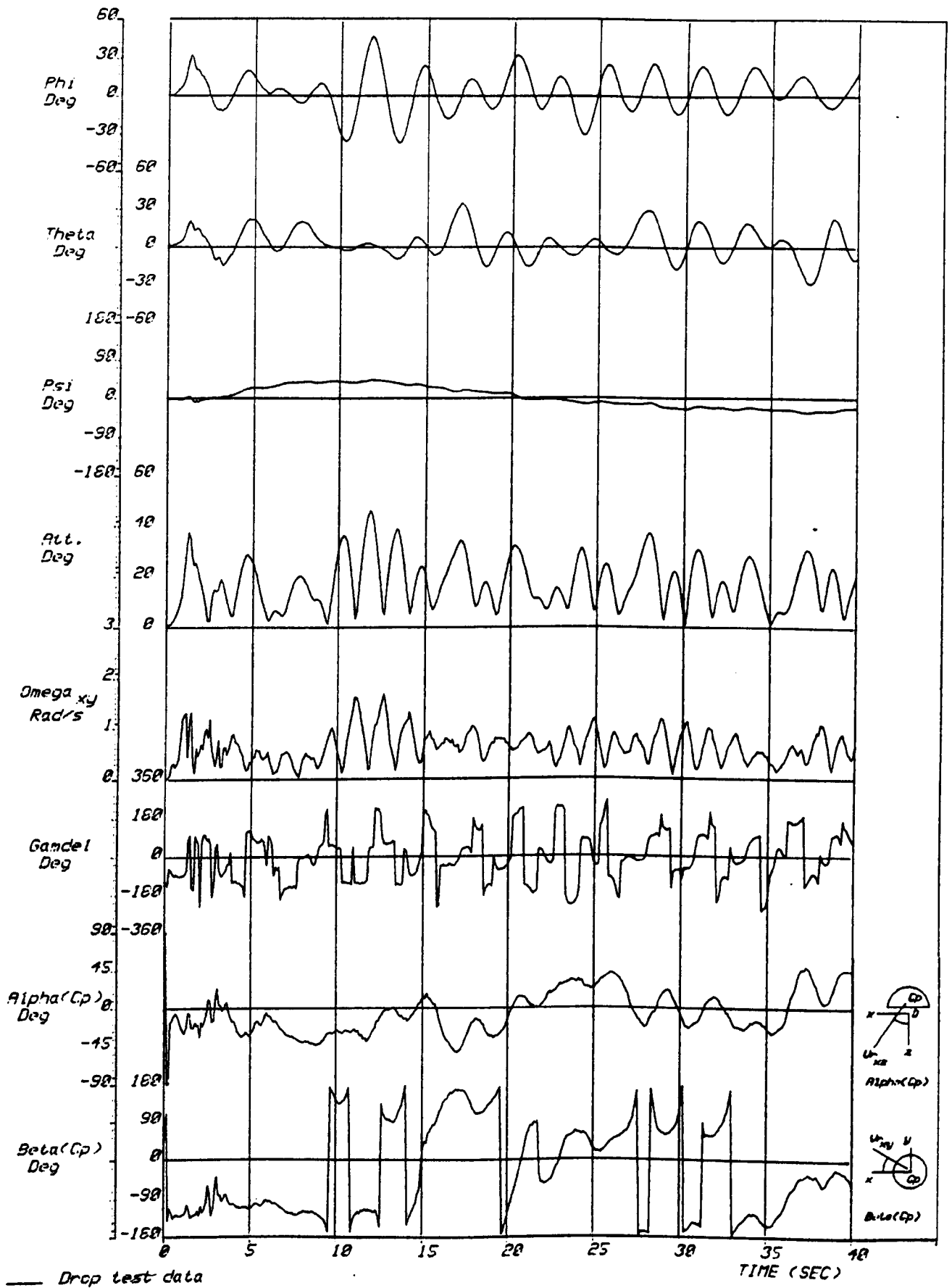
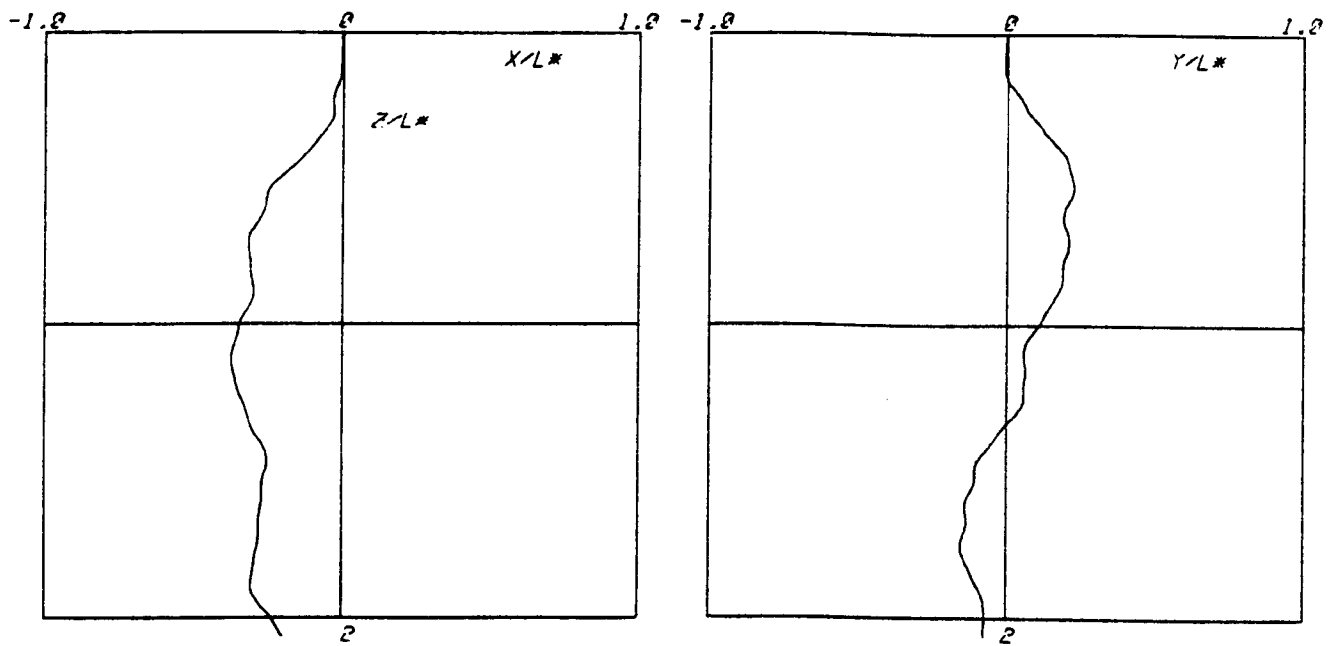
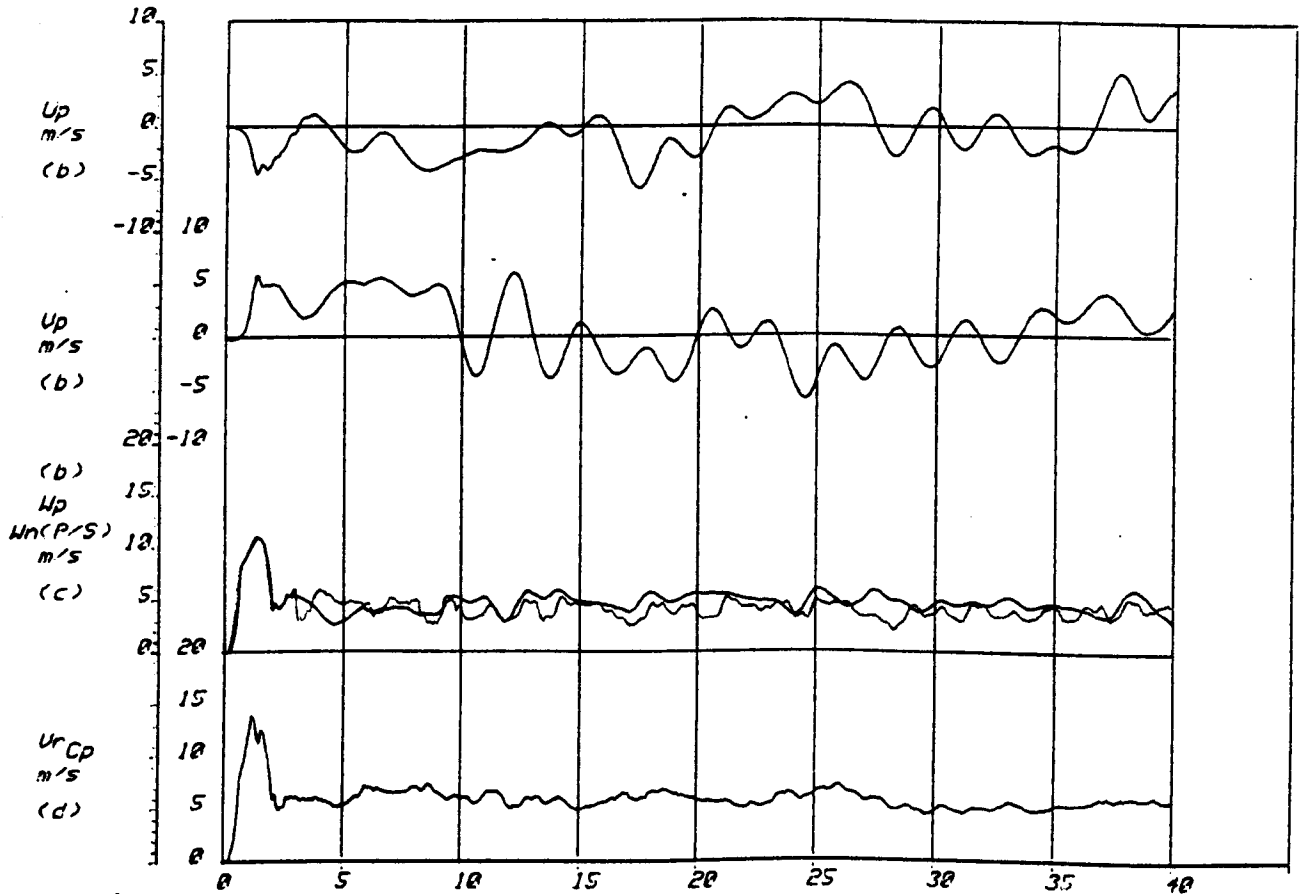


FIG.	DROP NO. - 12UF29
3.69	DATE: 131179
1 of 2	TIME: 1343
	WIND: 0? 7KT

Calculated time histories of angles for Drop 29 (SB12)



(a) Spatial trajectory of point P ($L^* = 100.0m$)



(b) Velocity components along body axes at P

(c) airspeed along z at N

(d) resultant airspeed at canopy Cp

— Drop test data

FIG.	DROP NO.: 12UF29
3.70	DATE: 131179
2 of 2	TIME: 1343
	WIND: 0? 7KT

Calculated trajectory and speeds for Drop 29 (SB12)

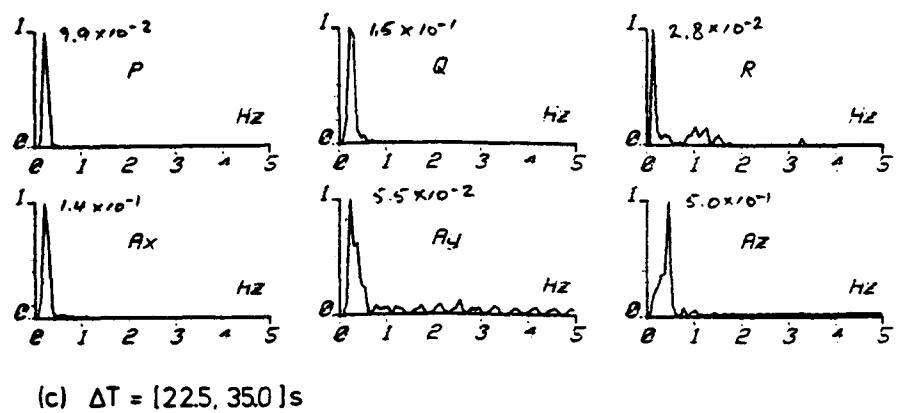
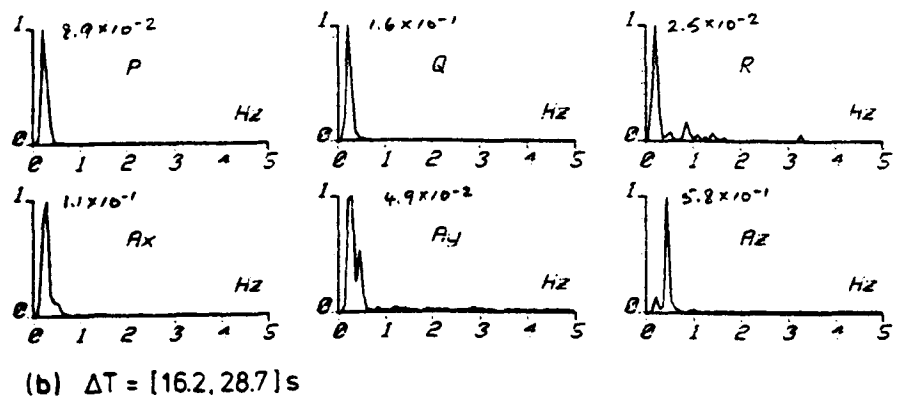
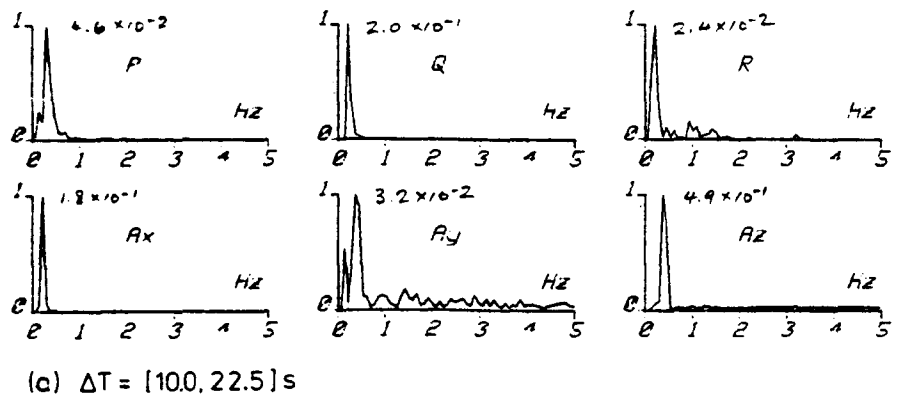
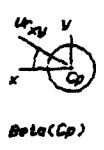
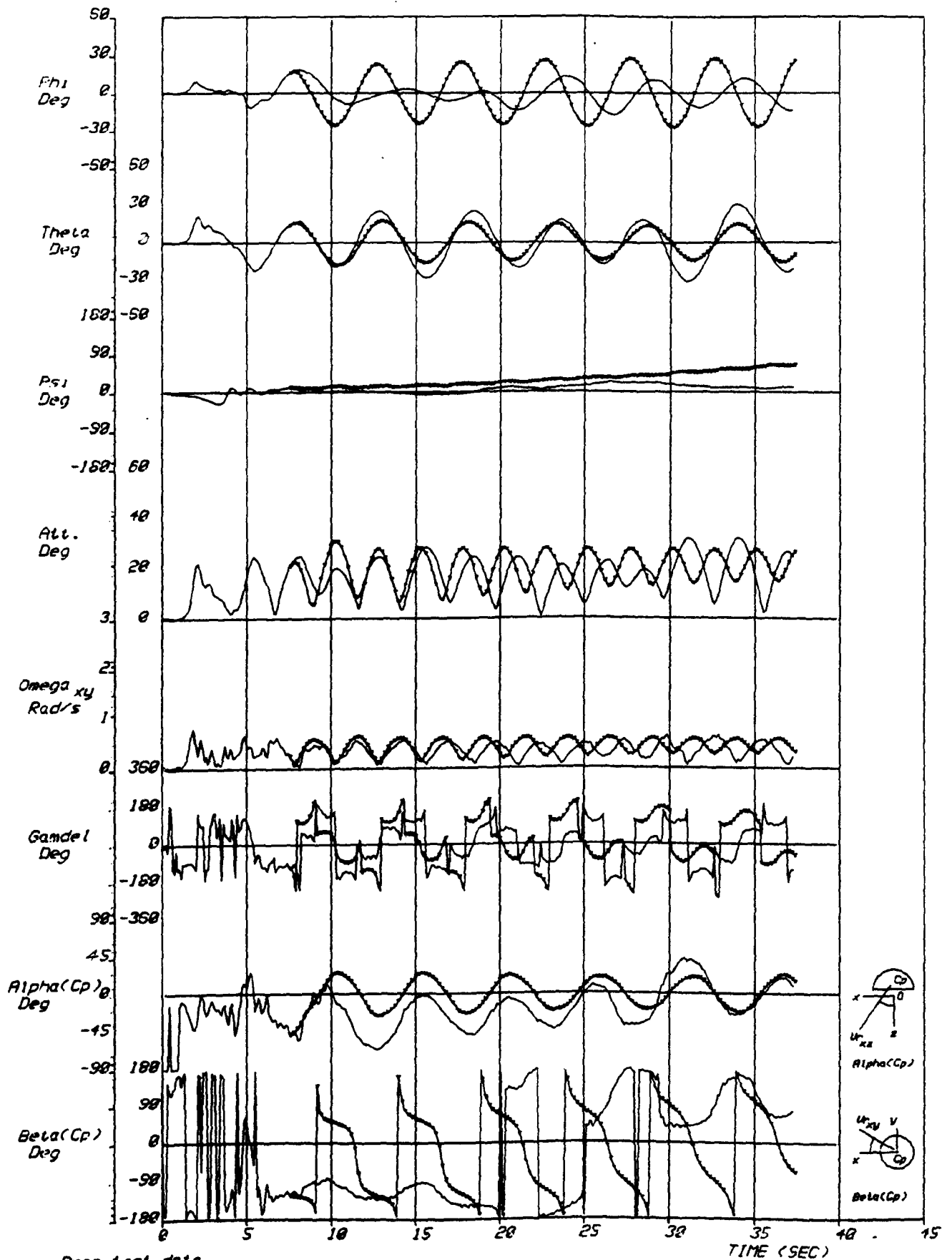


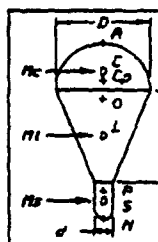
FIGURE 3.71

Power spectra for record partitions of Drop 2 (BB24)



— Drop test data
 - - - Simulation

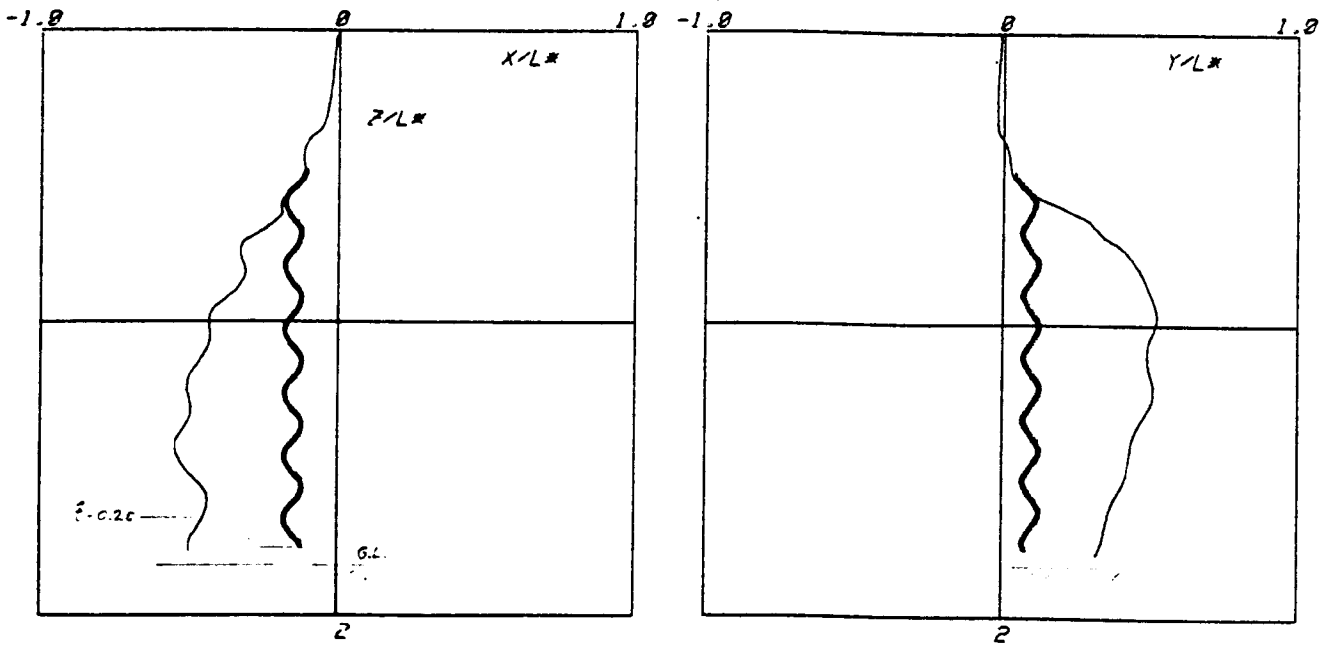
FIG. 4.1	DROP NO.: 21UF 2
	DATE: 021079
	TIME: 1330
	#WIND#: 6 KTS



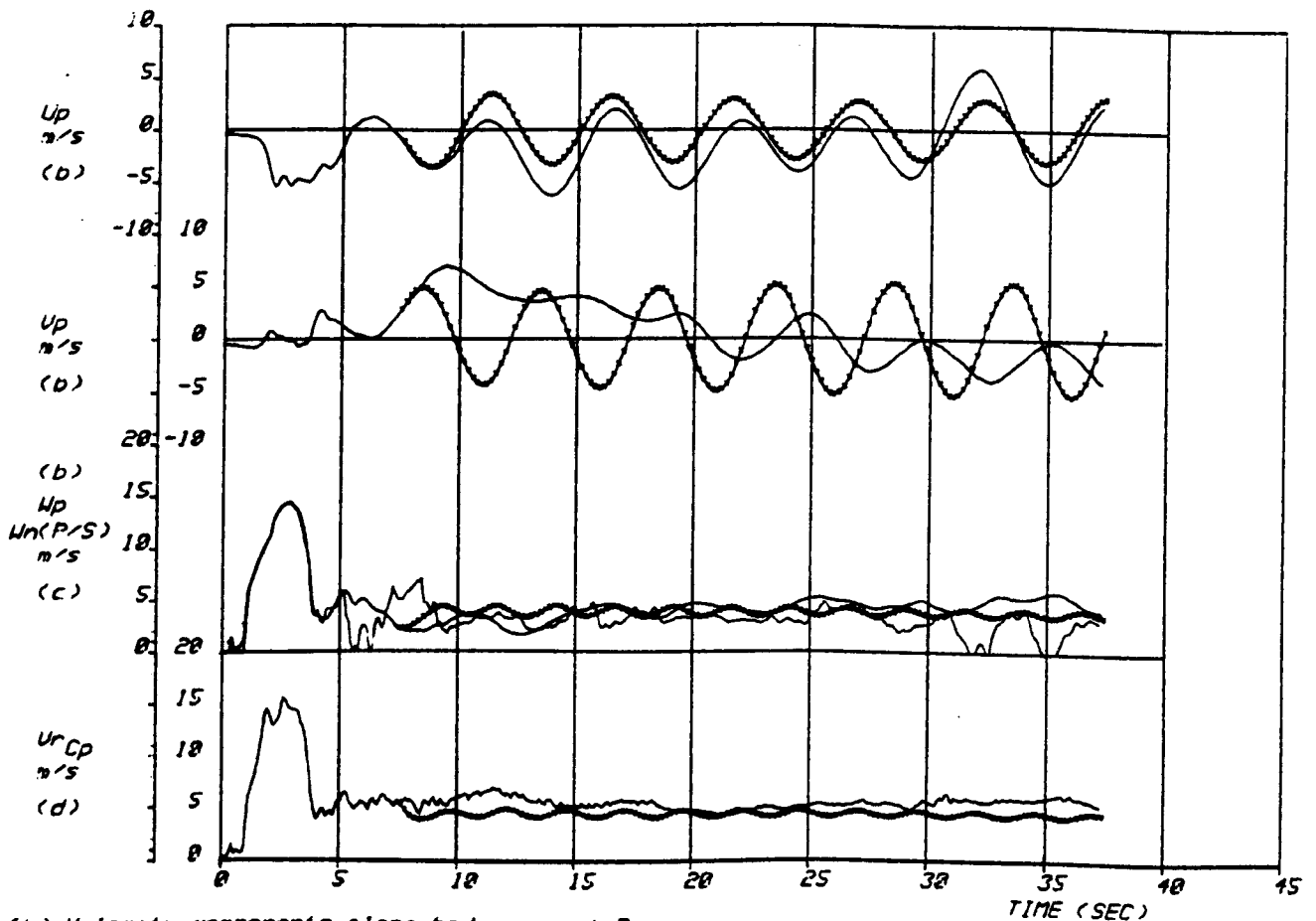
F. CIRCUMPLEX

D : 5.816 m	M_c : 2.30 Kg
d : .480	M_1 : 2.30
OC : -1.341	M_2 : 01.50
DC : -.717	K_{11} : .30
CCp : .000	K_{33} : .00
CL : 1.072	K_{55} : .27
CP : 7.521	K_{15} : .00
CS : 8.143	Lp : -.1000
OS : 8.657	M_3 : .0000
U : 7.690	ρ_{air} : 1.2132
	Kg/m^3

INPUT PARAMETERS



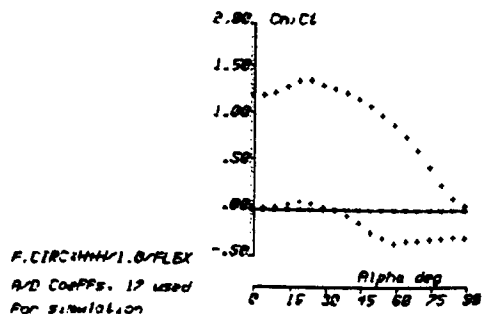
(a) Spatial trajectory of point P ($L^* = 100.0m$)

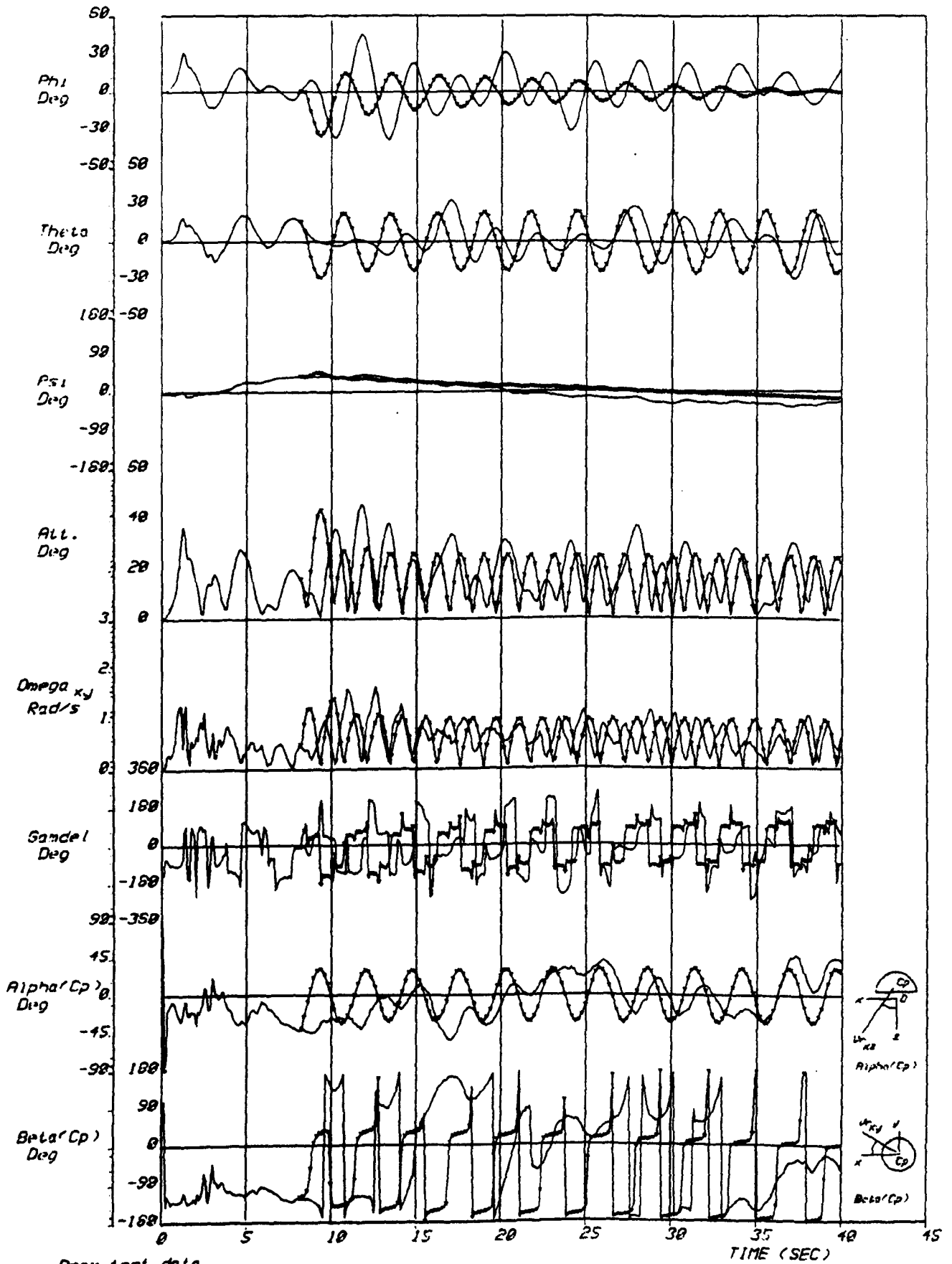


(b) Velocity components along body axes at P
 (c) airspeed along z at N
 (d) resultant airspeed at canopy Cp

— Drop test data
 - - - Simulation

FIG. 4.2	DROP NO. 24UF 2
	DATE: 021079
	TIME: 1330
	WIND: 6 KTS





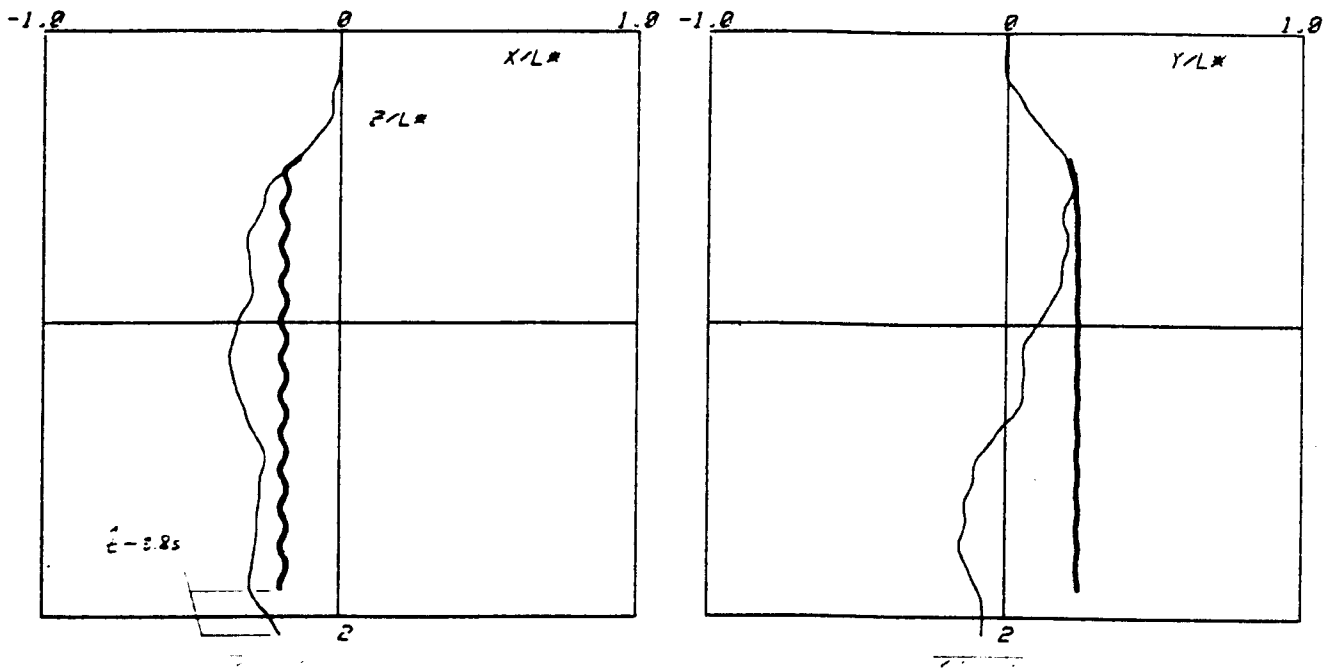
— Drop test data
 - - - Simulation

FIG. 4.3	DROP NO.: 12UF29
	DATE: 131129
	TIME: 1343
	WIND: 0? 7KT

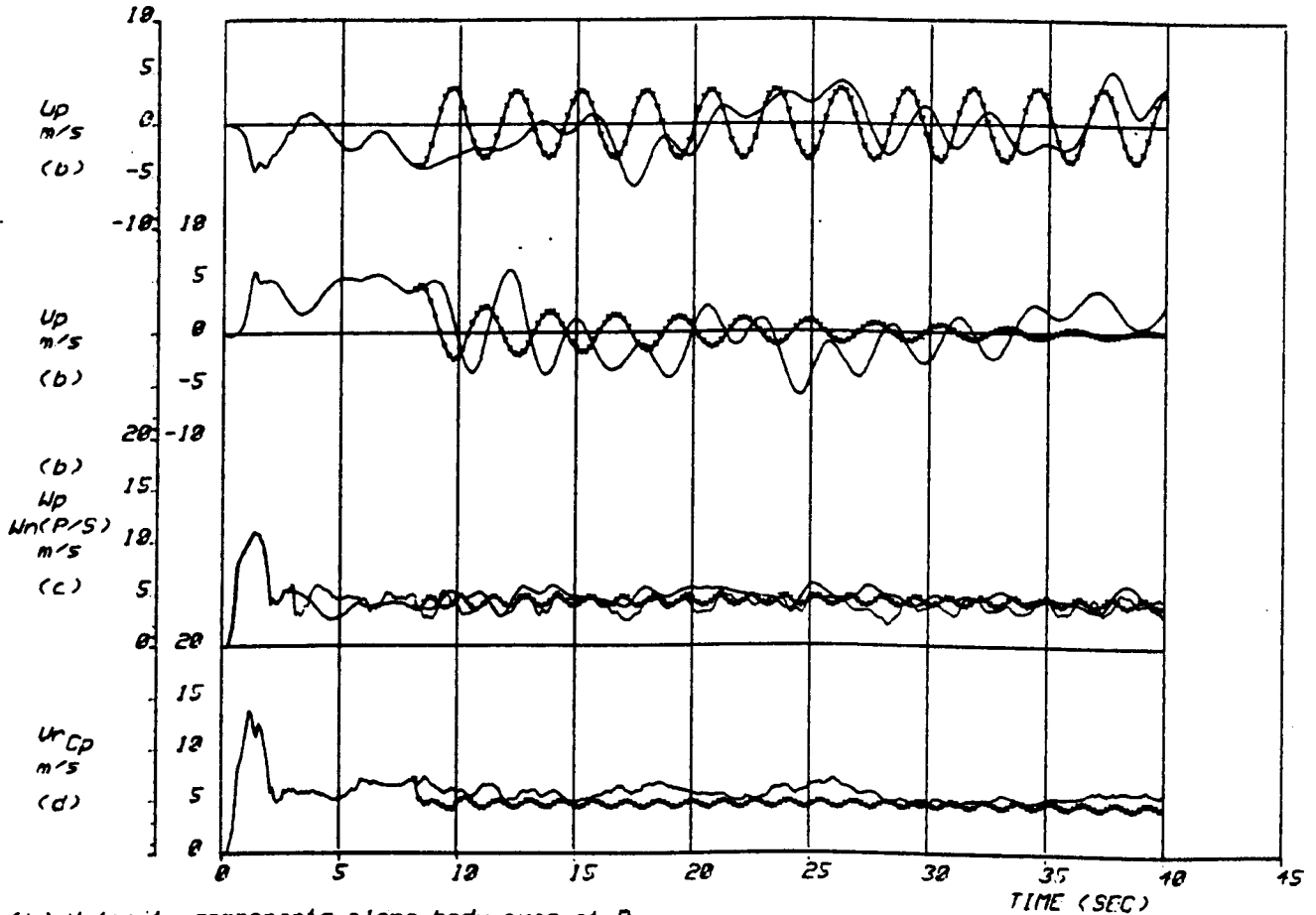
F. CIRCUMPLEX/1.0/ALEX

D: 2.918 m	rho_c: .98 Kg
d: .248	rho_l: .40
DA: -.245	rho_n: 18.02
DC: -.334	K11: .32
DCp: .008	K33: .61
DL: 1.445	K55: .27
OP: 2.245	K15: .00
OS: 2.658	LP: -.1000
ON: 3.122	NP: .0000
UI: 2.352	Rho: 1.2670
	Kg/m^3

INPUT PARAMETERS



(a) Spatial trajectory of point P ($L^* = 100.0m$)

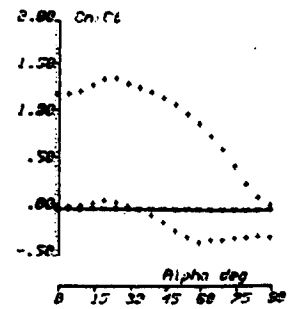


(b) Velocity components along body axes at P

(c) airspeed along z at N

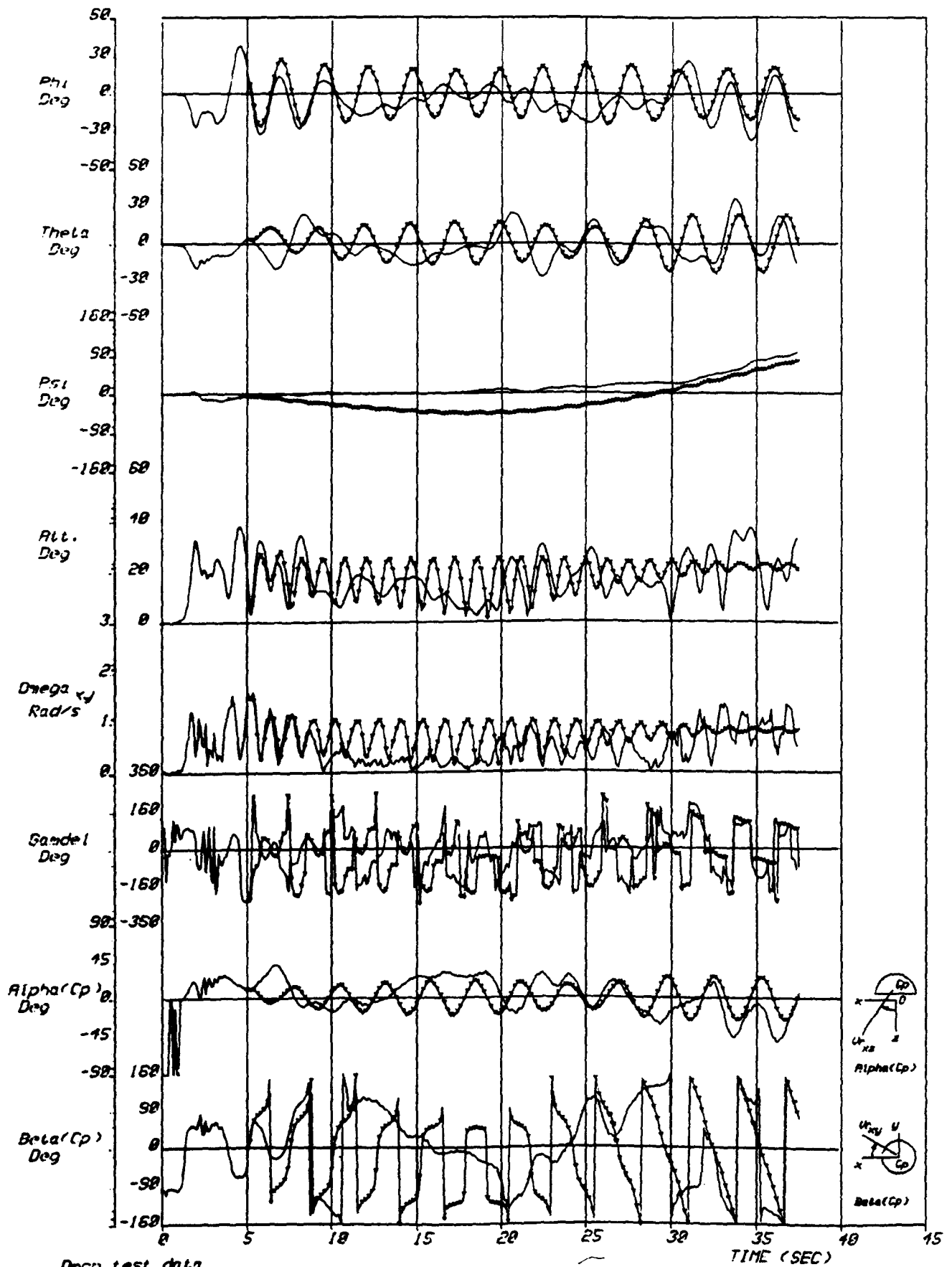
(d) resultant airspeed at canopy C_p

— Drop test data
 — Simulation



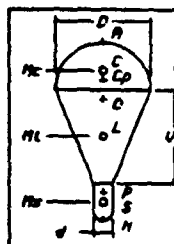
F.CIRC(ANN)1.B/FLEX
 A/D Coeffs. 17 used
 for simulation

FIG. 4.4	DROP NO.: 12UF29
	DATE: 131179
	TIME: 1343
	WIND: 0? 7KT



— Drop test data
 - - - Simulation

FIG. 4.6	DROP NO.: 12UF10
	DATE: 111079
	TIME: 1403
	WIND: 7 KTS

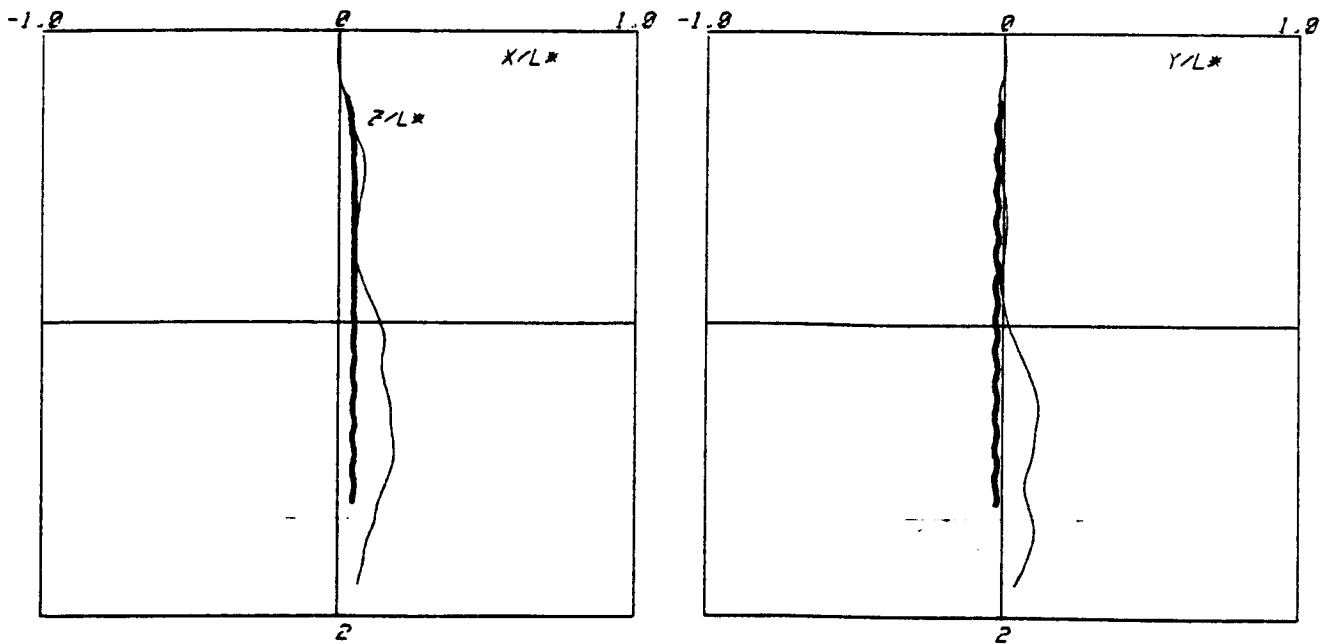


F. CIRC: 11111. B. FLEX

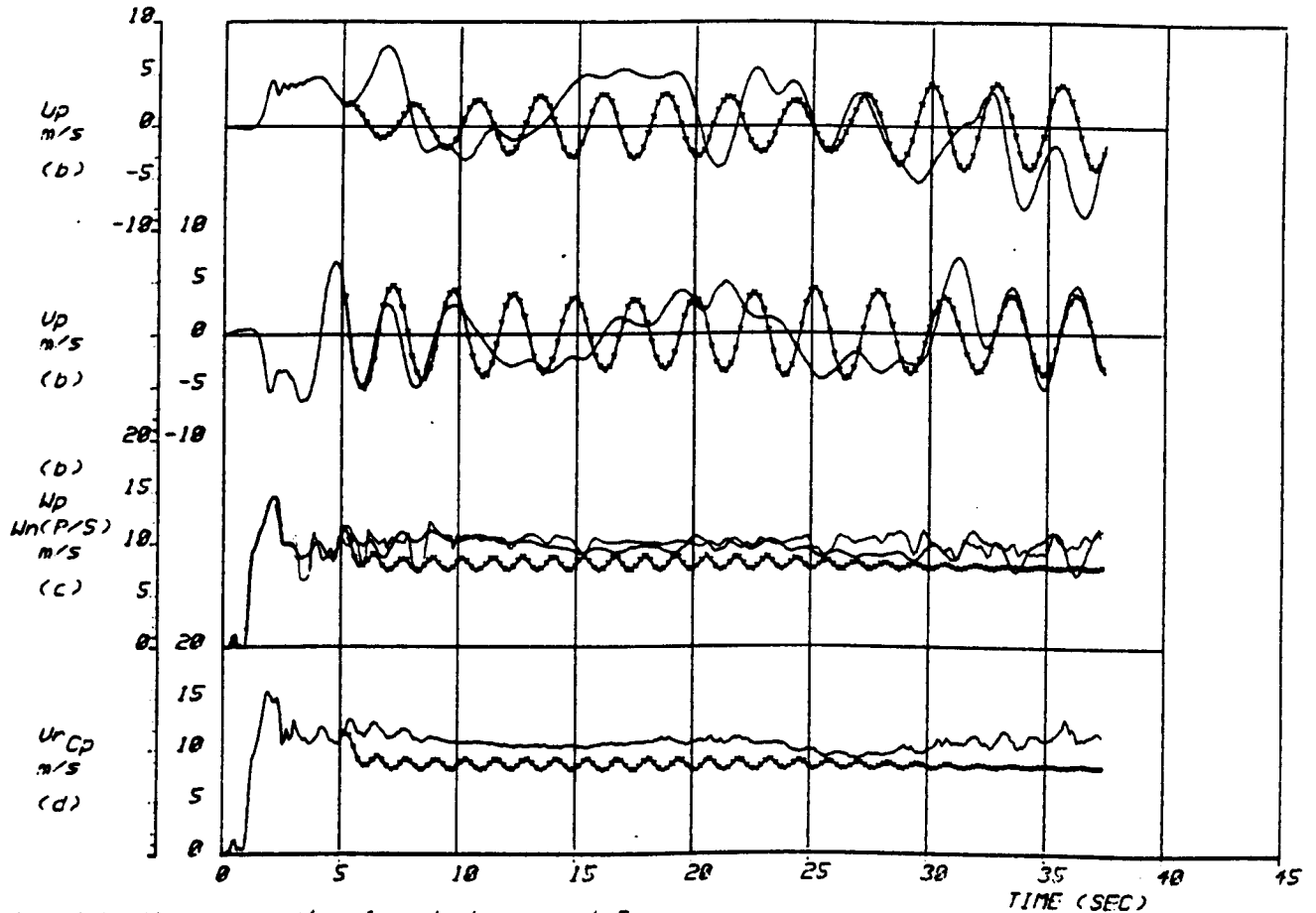
D: 2.811	Mc: .50	Kg
C: .480	M1: .40	
DA: -.725	M2: 31.98	
DC: -.326	K11: .30	
DCp: .869	K33: .51	
CL: 1.151	K55: .27	
DP: 2.824	K10: .00	
DS: 3.185	Lp: -.1400	
DY: 3.620	Np: .0000	
DI: 2.418	Rho: 1.2300	Kg/m ³

AND COEFFS. 17





(a) Spatial trajectory of point P ($L^* = 200.0m$)



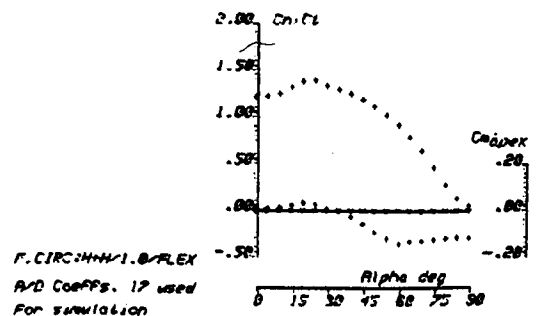
(b) Velocity components along body axes at P

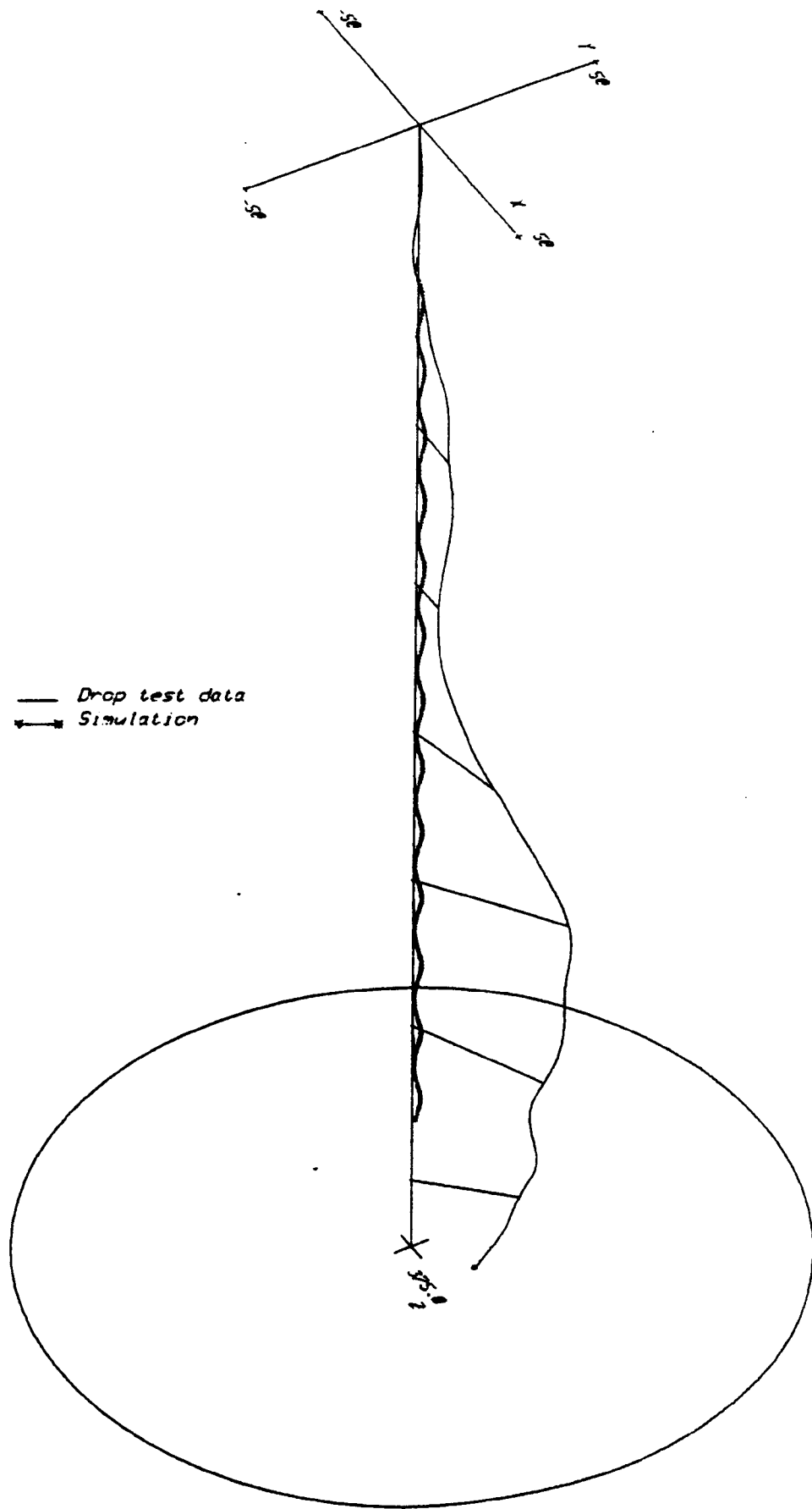
(c) airspeed along x at N

(d) resultant airspeed at canopy C_p

— Drop test data
 - - - * - - - Simulation

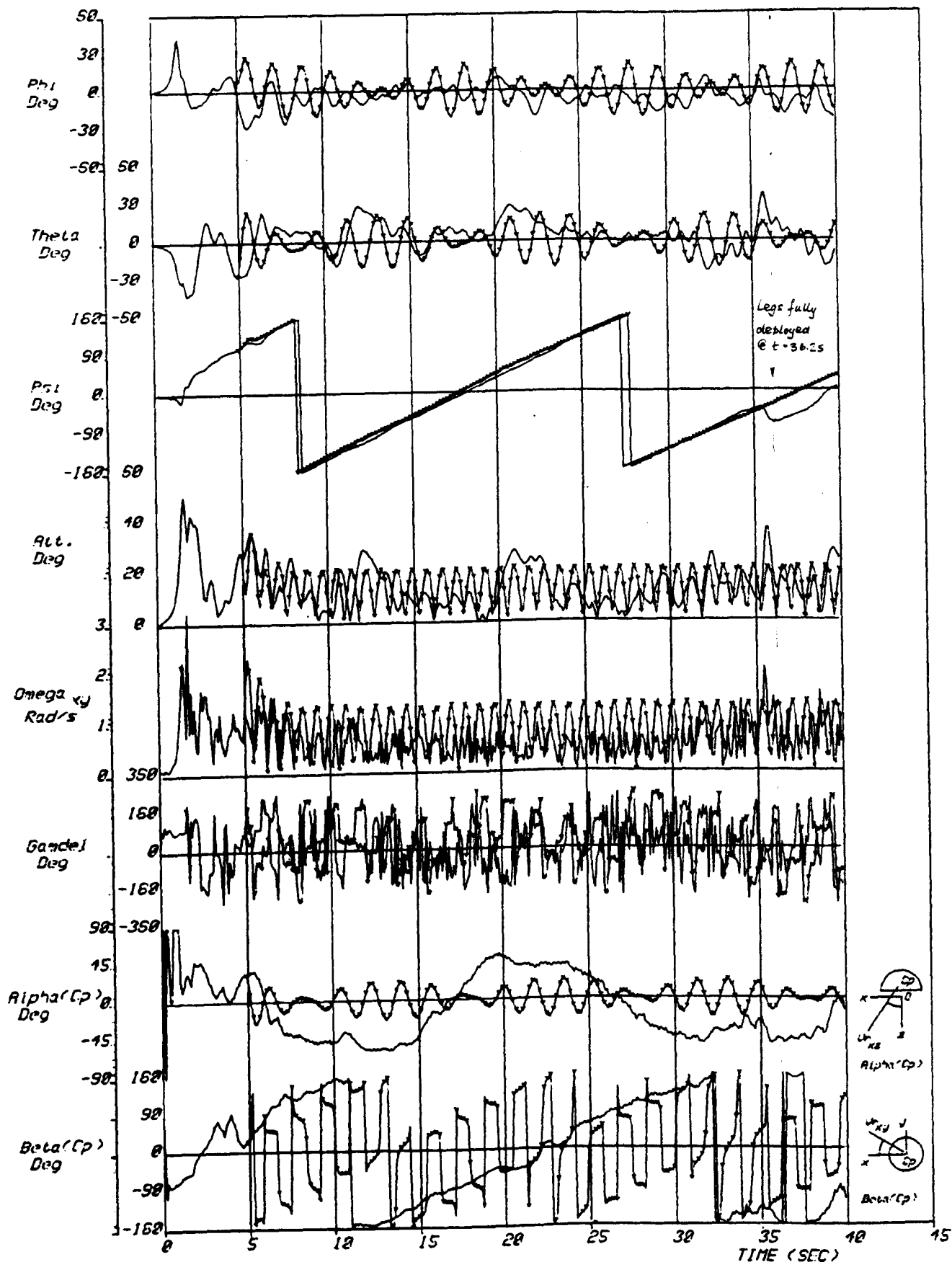
FIG. 4.7	DROP NO. 12UF10
	DATE: 111079
	TIME: 1103
	#WIND#: 7 KTS





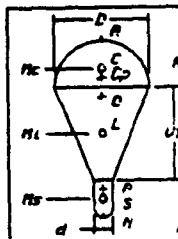
Axonometric view of trajectory of point P.
 Dimensions in metres. horizontal lines correspond to 5sec intervals.

FIG. 4.8	DROP NO.: 12UF10
	DATE: 111075
	TIME: 1403
	WIND: 7 KTS



— Drop test data
 - - - Simulation

FIG. 4.9	DROP NO.: 06UF25
	DATE: 021179
	TIME: 1347
	WIND: 6 KTS

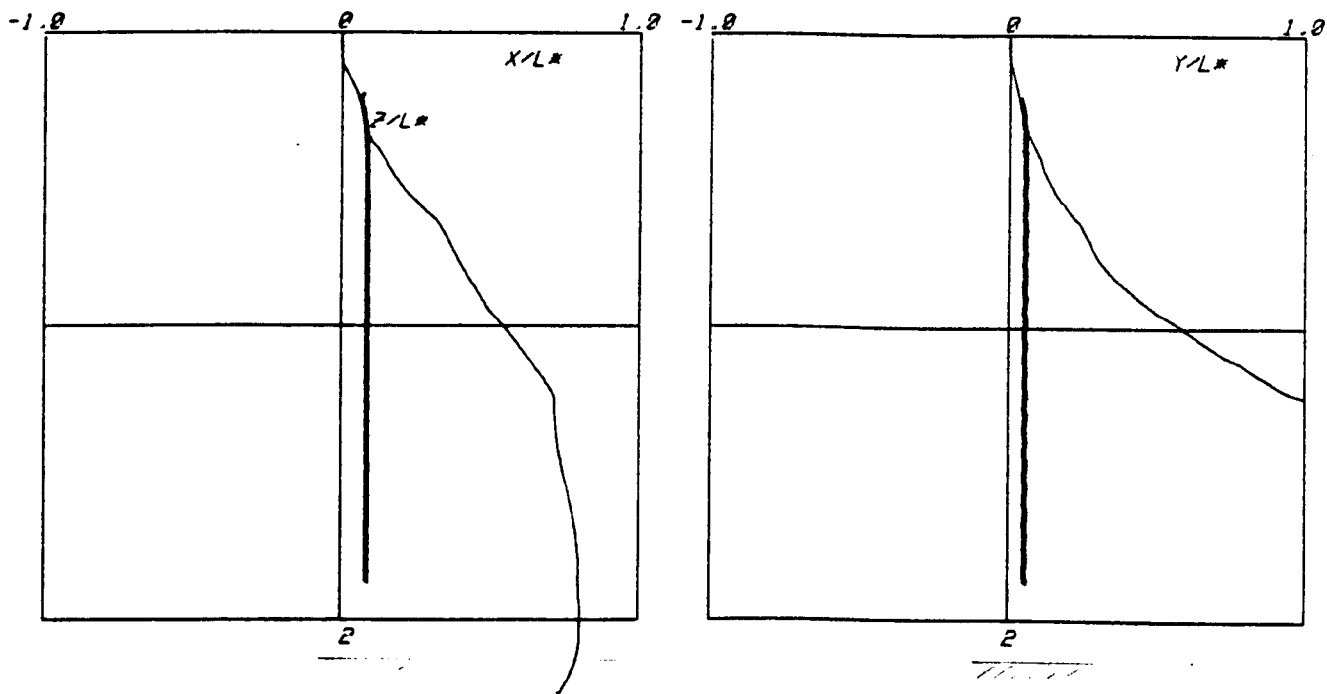


R/D Coeffs. 17

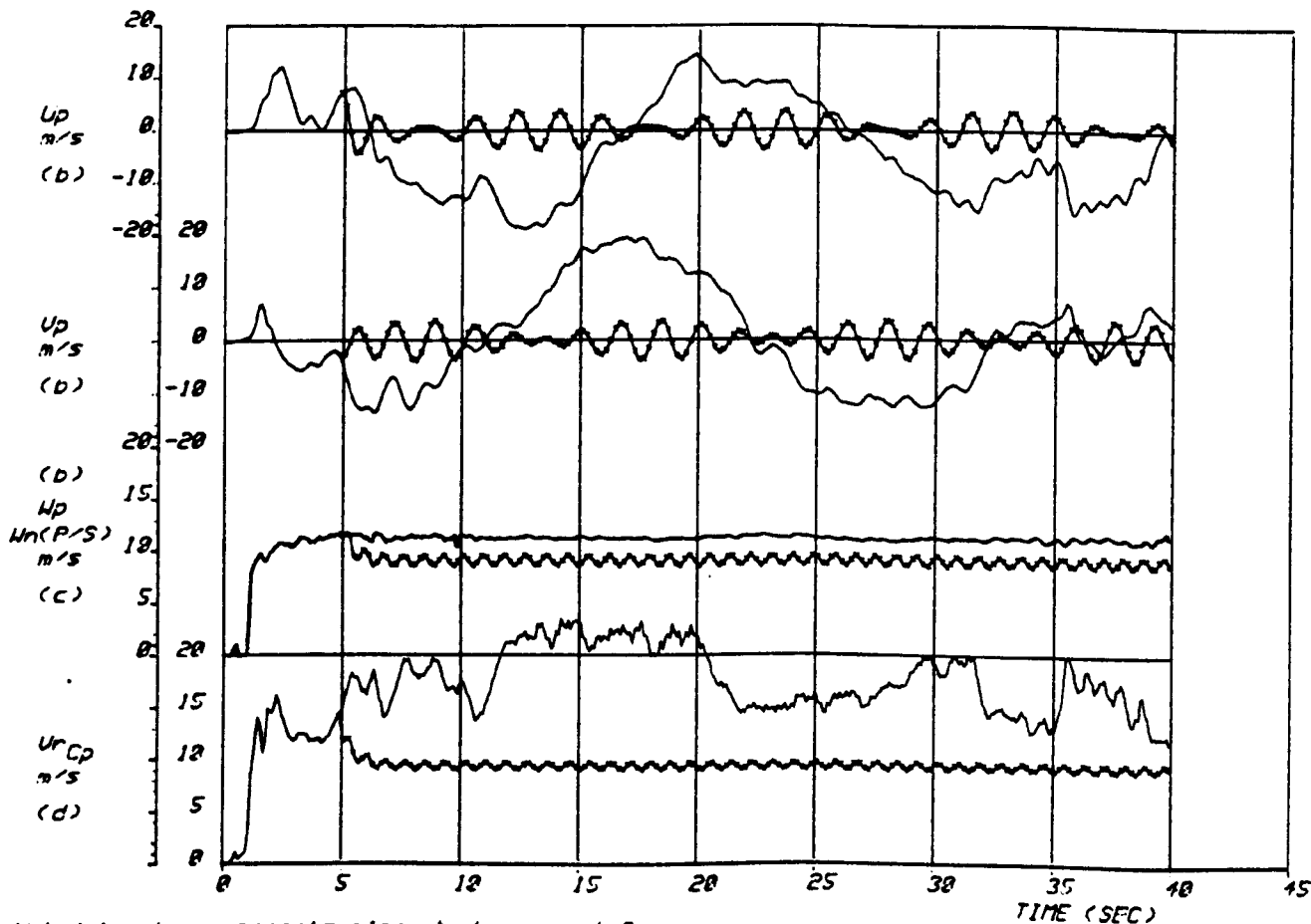
F. CIRCUMPLEX

D	1.412	m	M	.25	kg
C	.046		M	.12	
CP	-.332		M	10.72	
CC	-.152		M	.30	
CCP	.000		K	.60	
CL	.355		K	.27	
CP	1.267		K	.60	
CP	1.375		L	.1500	
CP	1.552		M	.0000	
U	1.152		M	1.2010	
				K	1.0000

INPUT PARAMETERS



(a) Spatial trajectory of point P ($L^* = 200.0m$)



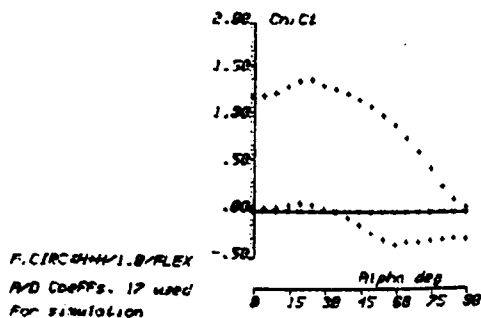
(b) Velocity components along body axes at P

(c) airspeed along z at N

(d) resultant airspeed at canopy Cp

— Drop test data
 - - - Simulation

FIG. 4.10	DROP NO.: 06UF25
	DATE: 021179
	TIME: 1347
	#WIND: 5 KTS



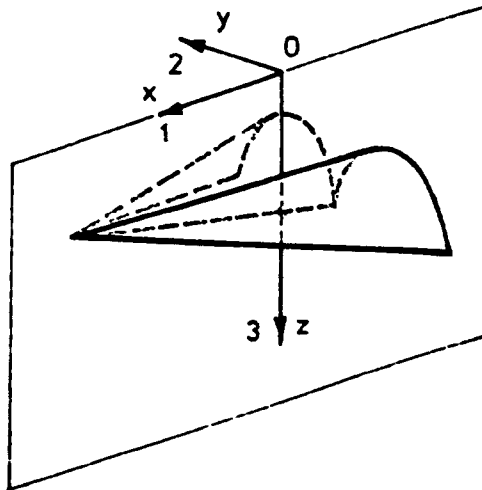


FIGURE B1.1 Plane-symmetric body: location of body coordinate frame to minimize the number of added mass components

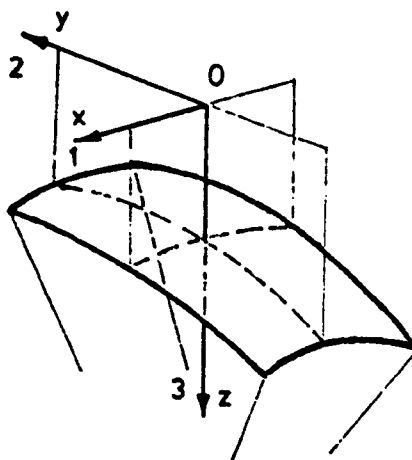


FIGURE B1.2 Two-fold-symmetric body: location of the body coordinate frame to minimize the number of added mass components

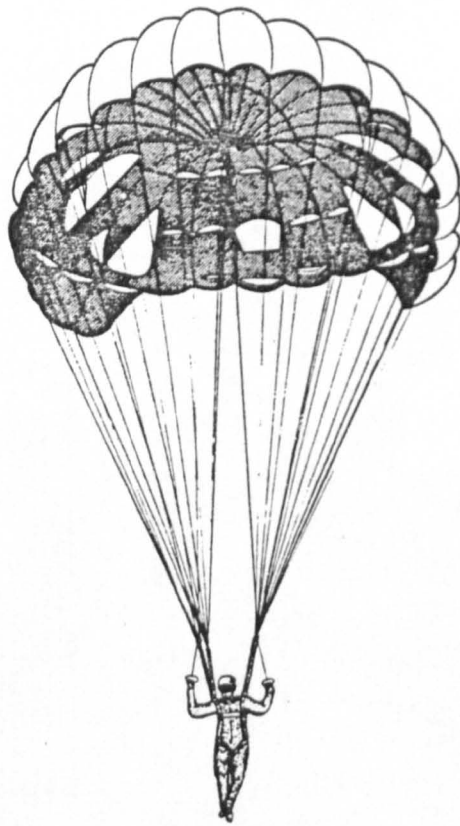


FIGURE C1.1 Conventional rigging, twin riser-pairs

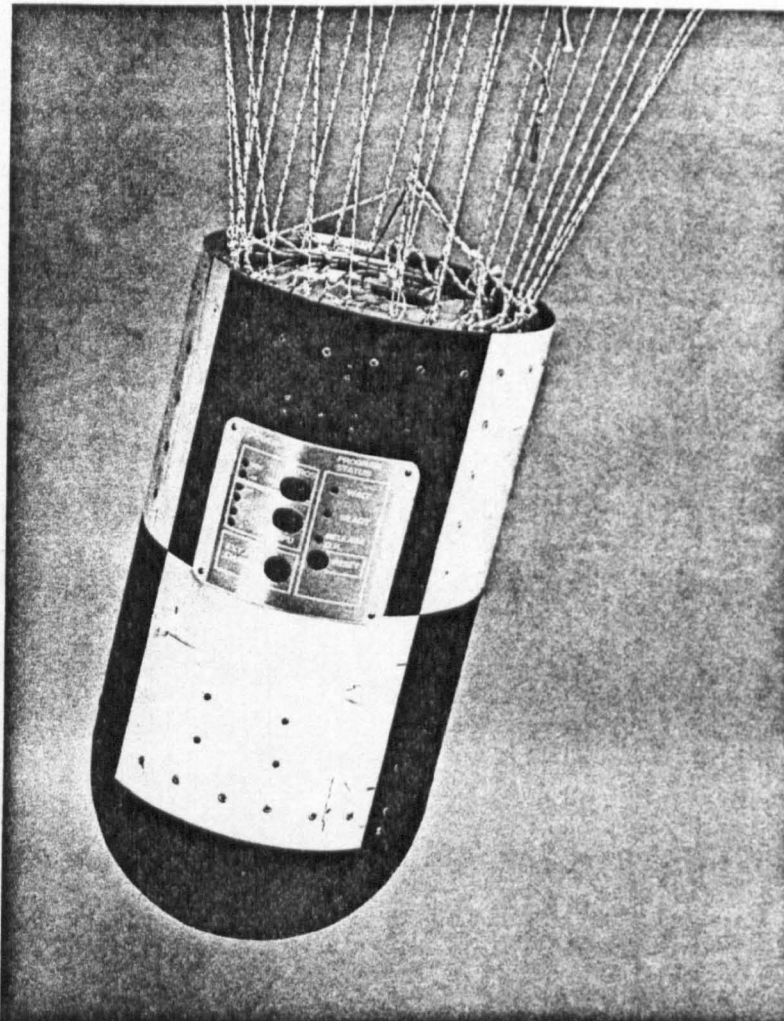


FIGURE C1.2 Peripheral, frustum rigging arrangement

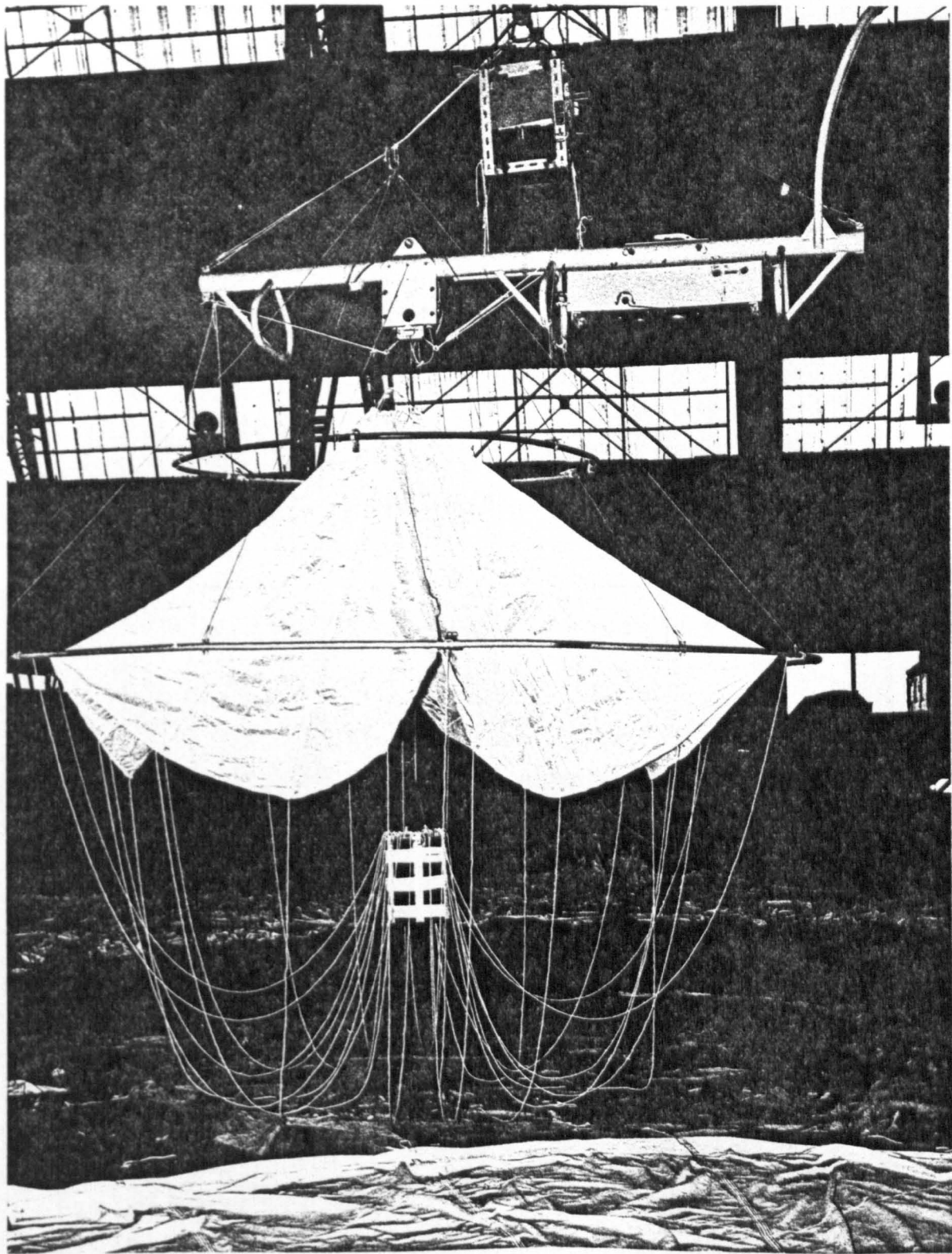


FIGURE C1.3 Drop test dummy body on hoisting rig in the airship hangar

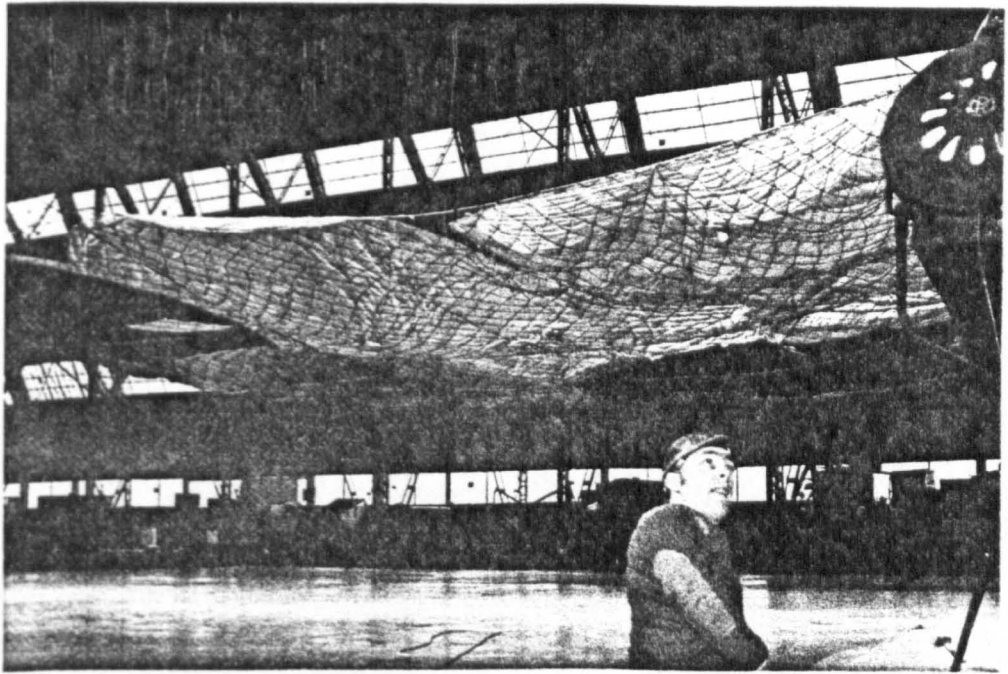


FIGURE C1.4 View of the catchnet arrangement

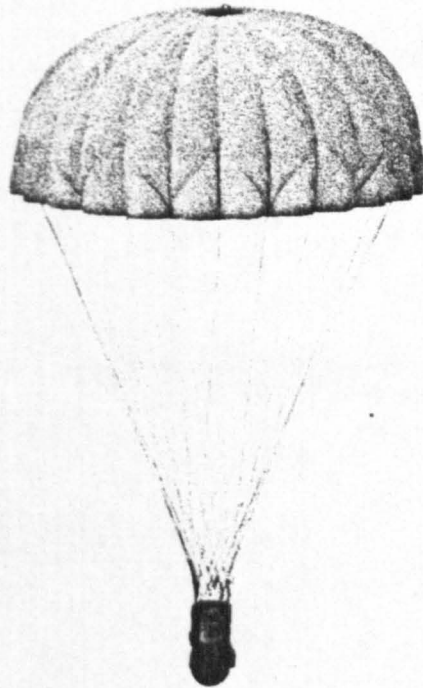


FIGURE C1.5 Final ('geodetic') rigging arrangement

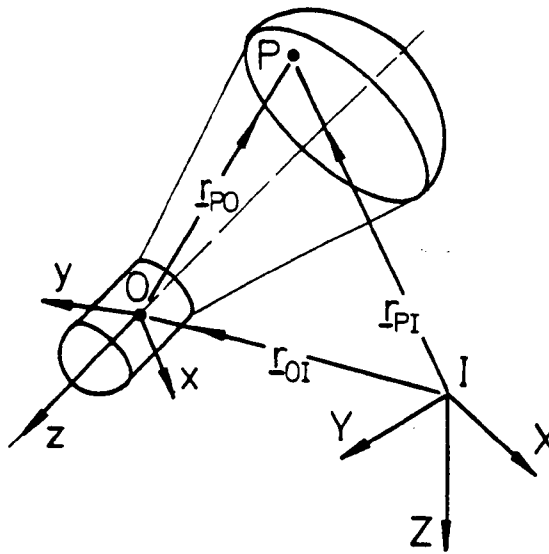


FIGURE C2.1 Coordinate frames for kinematic analysis

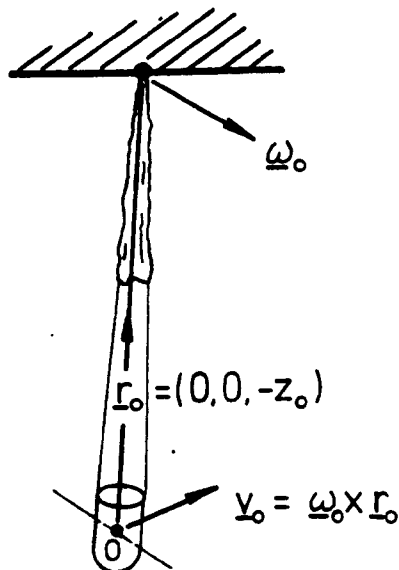


FIGURE C2.2 Assumed initial velocity conditions

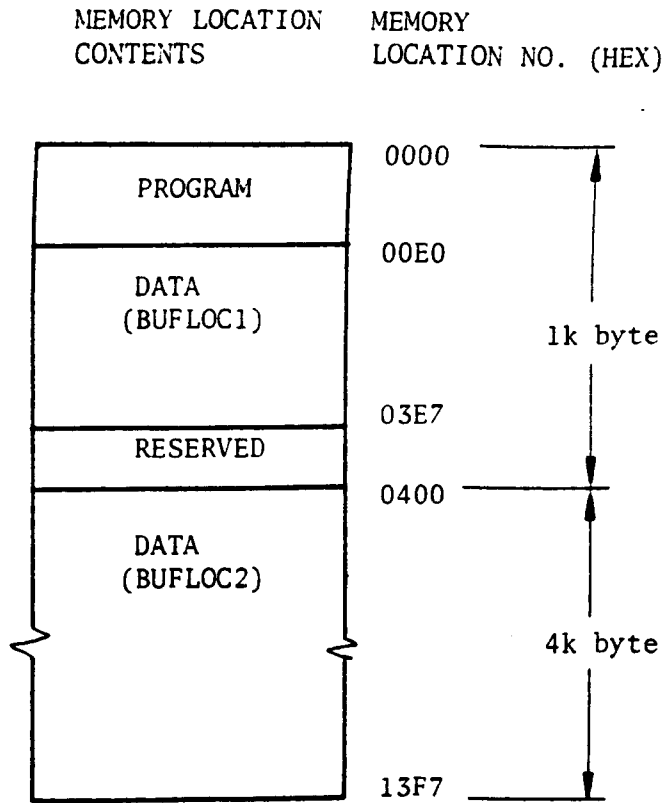


FIGURE C3.1 Memory map for the MPU data acquisition programme

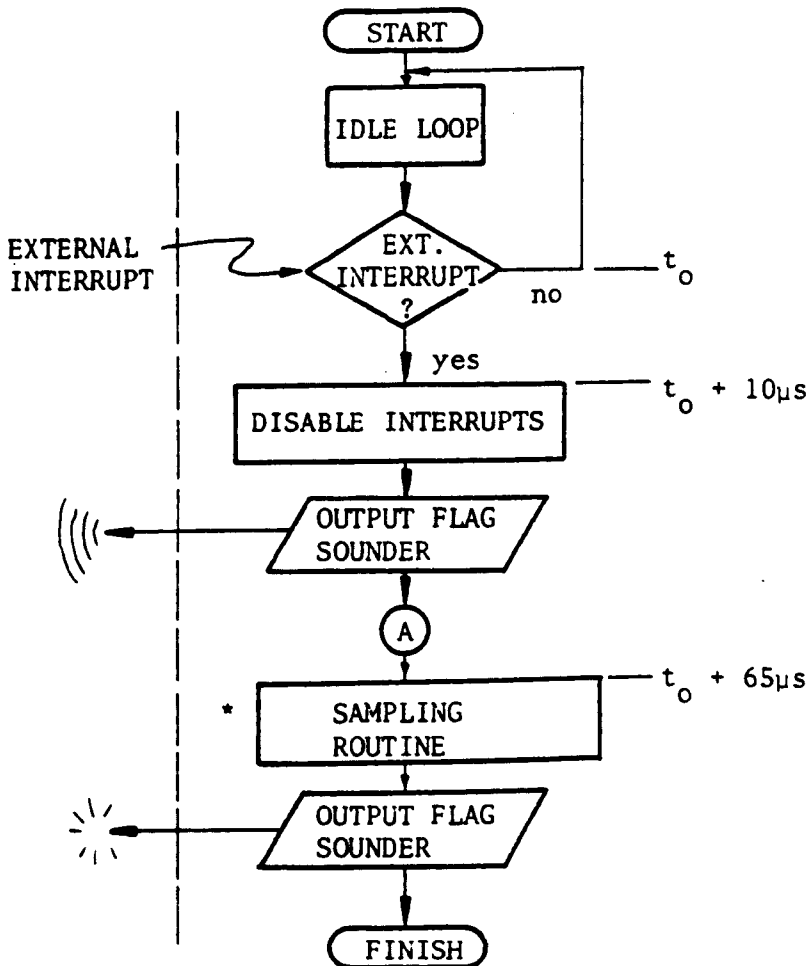


FIGURE C3.2 Flow diagram of the MPU data acquisition programme

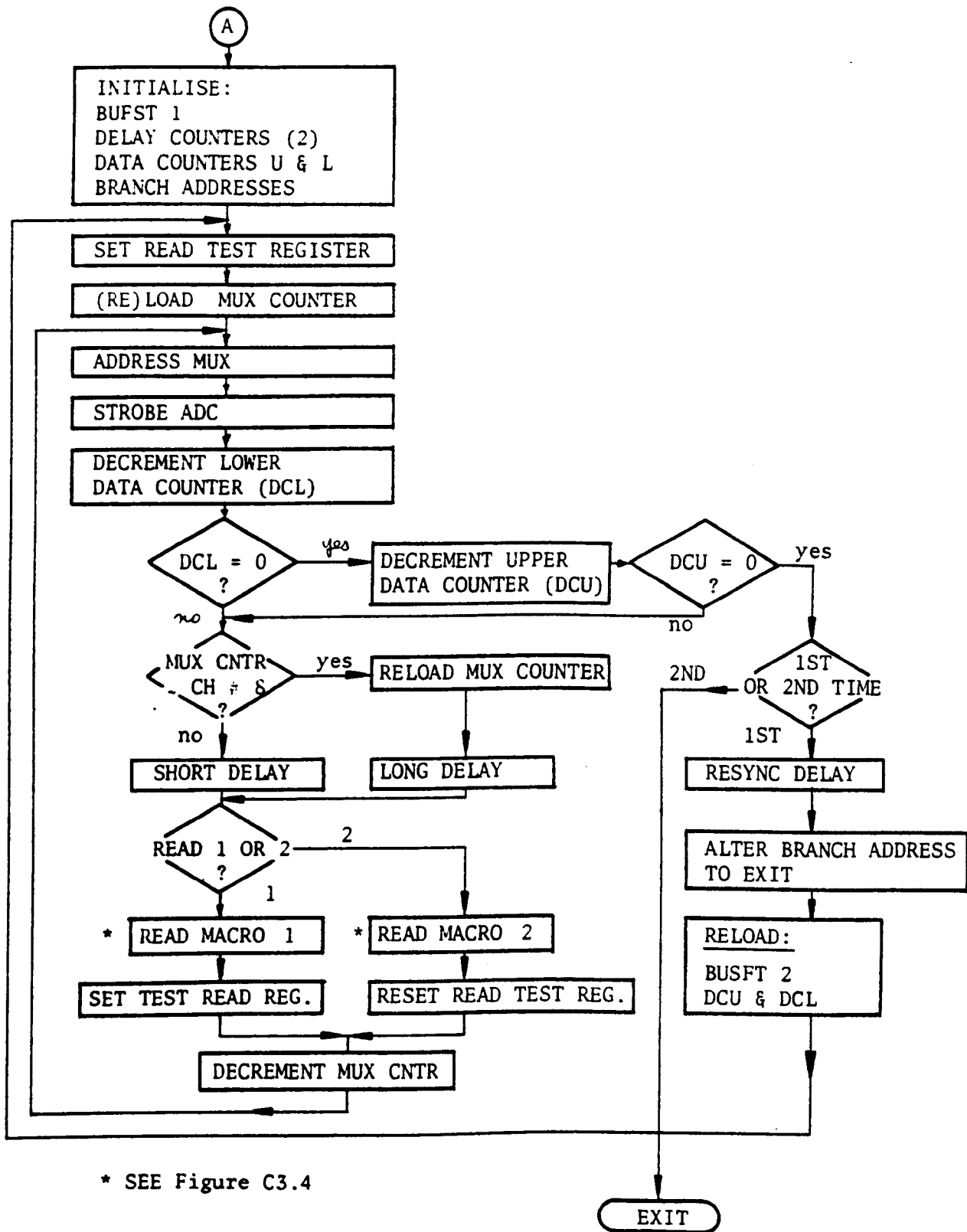


FIGURE C3.3

Flow diagram of the sampling routine

Read Macro 1						
Operation	Register/ Port	Contents		Register/ Port	Contents	
		7 - 4	3 - 0		7 - 4	3 - 0
Clear I/O 0	0	0	0			
Clear I/O 1	1	0	0			
Input from I/O 0	A	a1	a2	DCo	M1	M1
Store	M1	a1	a2	DCo	M2	M2
Input from I/O 1	A	0	a3			
Shift left 4	A	a3	0			
Store	M2	a3	0	DCo	M3	M3
Decrement DCo	DCo	M2	M2			
Set READ test bit	SR4	0	1			
Read Macro 2						
Clear I/O 0	0	0	0			
Clear I/O 1	1	0	0			
Input from I/O 0	A	b1	b2			
Store in scratchpad 1	SR1	b1	b2			
Shift right 4	A	0	b1			
OR with memory	A	a3	b1	DCo	M3	M3
Store in scratchpad 3	SR3	a3	b1			
Decrement DCo	DCo	M2	M2			
Load from scratchpad 3	A	a3	b1			
Store in memory	M2	a3	b1	DCo	M3	M3
Load from scratchpad 1	A	b1	b2			
Shift left 4	A	b2	0			
Store in memory	M3	b2	0	DCo	M4	M4
Decrement DCo	DCo	M3	M3			
Input from I/O 1	A	0	b3			
OR with memory	A	b2	b3	DCo	M4	M4
Store in scratchpad 3	SR3	b2	b3			
Decrement DCo	DCo	M3	M3			
Load from scratchpad 3	A	b2	b3			
Store in memory	M3	b2	b3	DCo	M4	M4
Reset READ test bit	SR4	0	0			

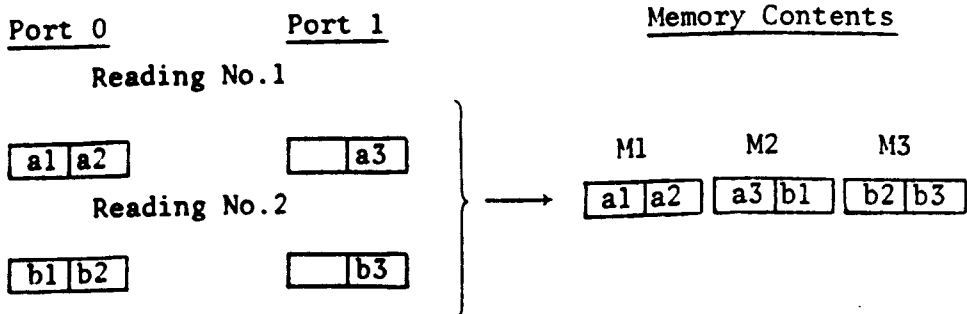
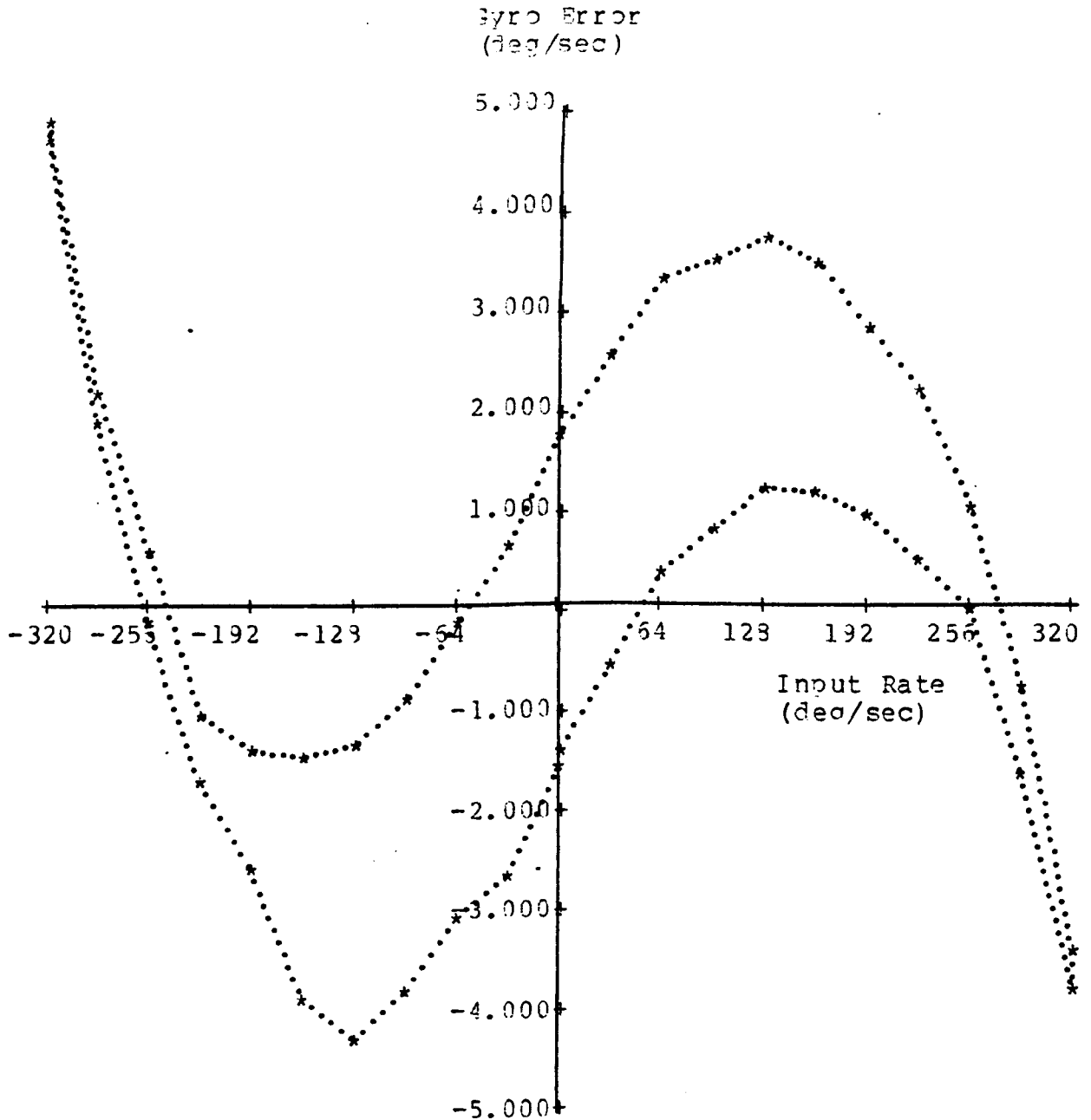


Figure C3.4 READ macros for packing 12-bit data into 8-bit memory bytes

RATE TRANSFER TEST NO. 2 TYPE 401 GYRO #024 11 Sept 79
 TABLE NO. 339 R.P.S.F 32.73 MV/DEG/SEC
 SWITCH ON 1255 HOURS SWITCH OFF 1317 HOURS
 RUN UP TIME 0.0 SECS RUN DOWN TIME 0.0 SECS
 MAX TEMP 24.57 DEG C MIN TEMP 24.31 DEG C



GYRO SCALE FACTOR (SLOPE)	-5.7343	MV/DEG/SEC	
S D OF NON LINEARITIES	2.4355	DEG/SEC	
MAXIMUM NON LINEARITY	4.7521	DEG/SEC	%AGE MAXIMUM RATE
INTERCEPT OF BEST ST LINE	0.3509	DEG/SEC	= 1.4850
ZERO OFFSET	0.4312	DEG/SEC	(with zero comp.)
ZERO HYSTERESIS	3.1993	DEG/SEC	
MAXIMUM HYSTERESIS	3.2741	DEG/SEC	TABLE RATE
			= -32.00 DEG/SEC

FIGURE C4.1 x-direction gyro, pre-trial calibration

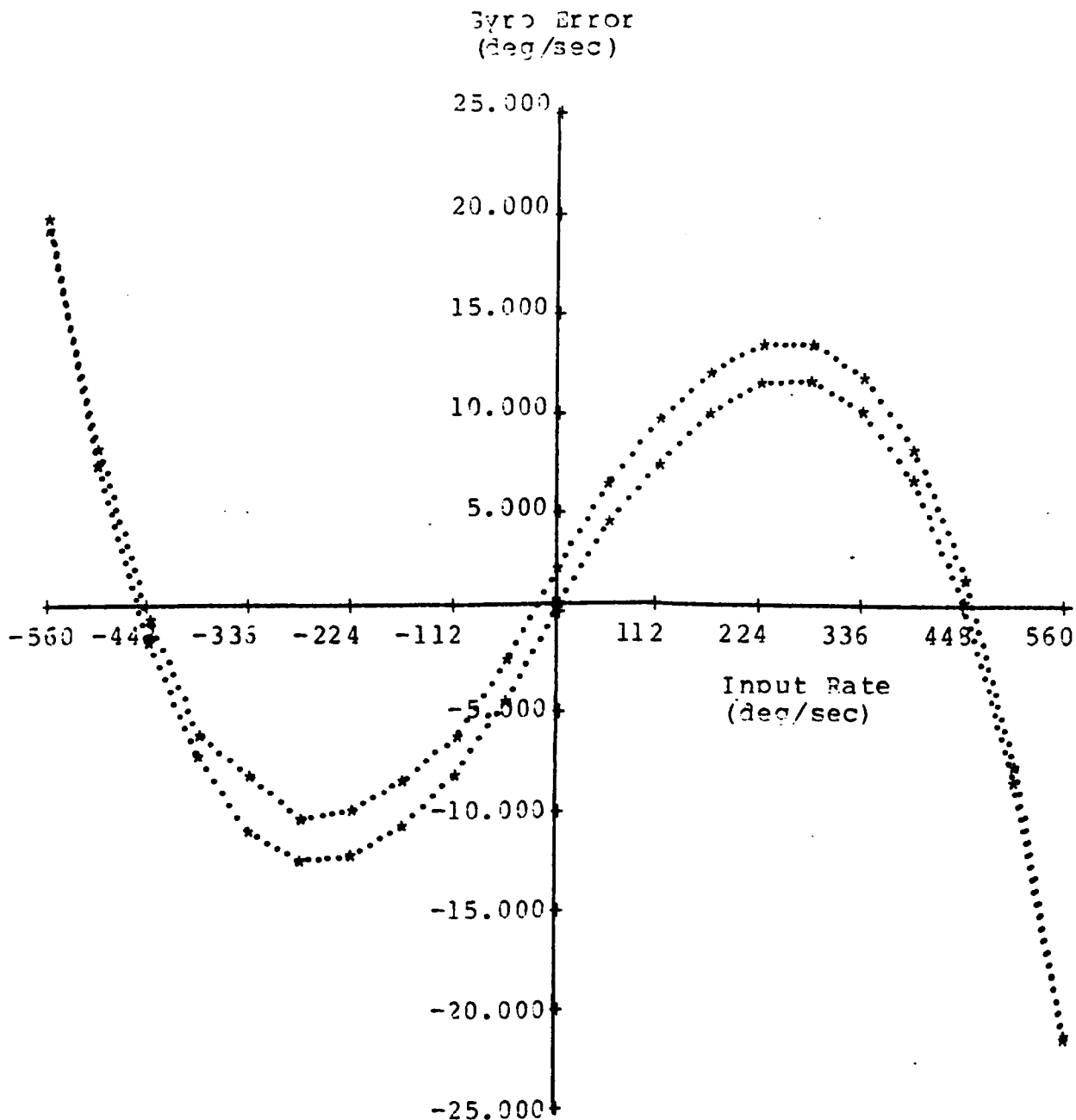
RATE TRANSFER TEST NO. 1 TYPE 406 GYRO #056 11 Sept 79

TABLE NO. 339 R.T.S.F 82.78 MV/DEG/SEC

SWITCH ON 1140 HOURS SWITCH OFF 1150 HOURS

RUN UP TIME 0.0 SECS RUN DOWN TIME 0.0 SECS

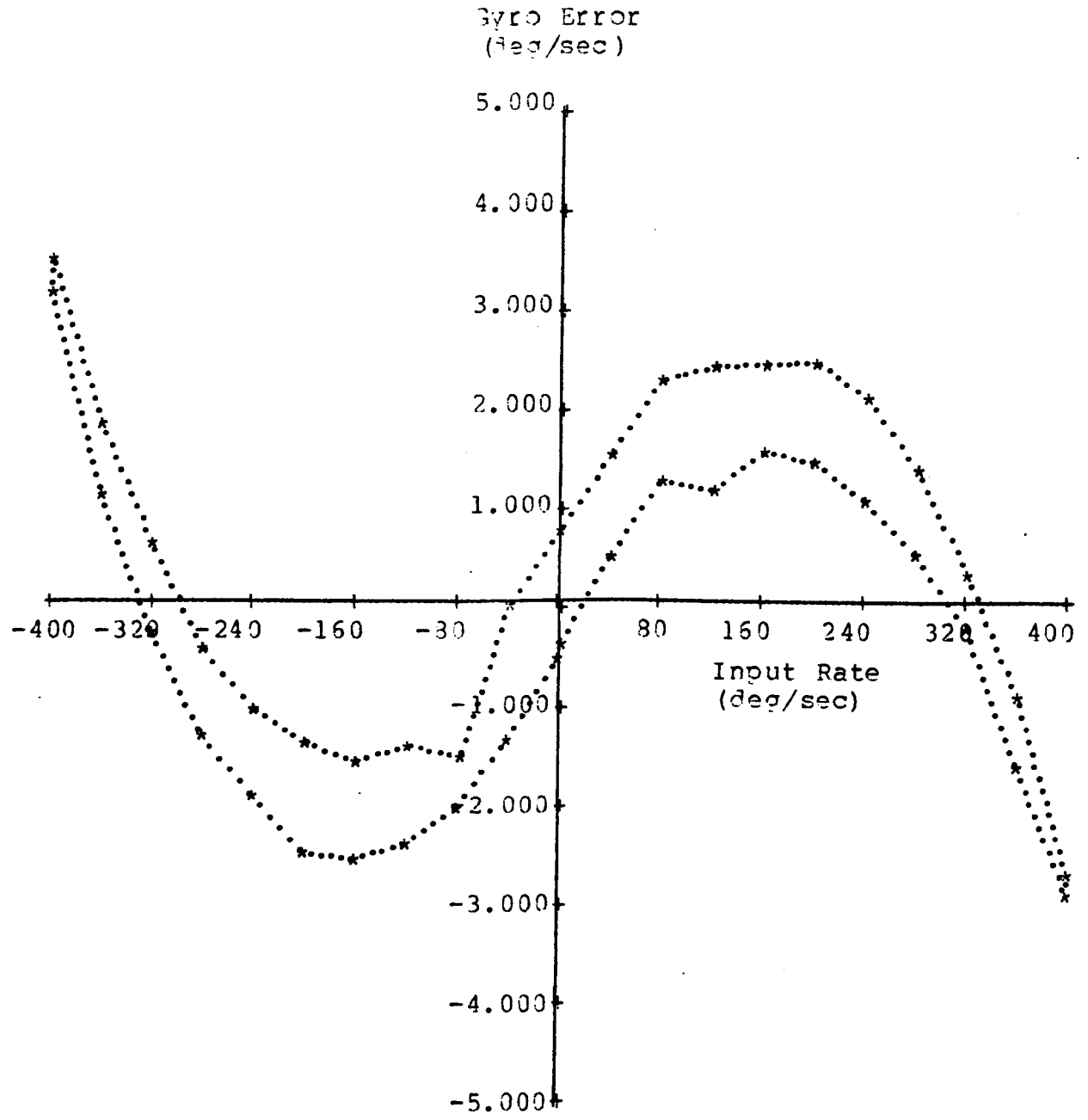
MAX TEMP 24.46 DEG C MIN TEMP 24.02 DEG C



GYRO SCALE FACTOR (SLOPE)	-7.7102	MV/DEG/SEC	
S D OF NON LINEARITIES	10.3304	DEG/SEC	
MAXIMUM NON LINEARITY	-21.6304	DEG/SEC	%AGE MAXIMUM RATE
INTERCEPT OF BEST ST LINE	-1.6790	DEG/SEC	= -3.8715
ZERO OFFSET	-0.9040	DEG/SEC	(with zero comp.)
ZERO HYSTERESIS	1.8283	DEG/SEC	
MAXIMUM HYSTERESIS	2.7741	DEG/SEC	TABLE RATE
			= -337.00 DEG/SEC

FIGURE C4.2 y-direction gyro, pre-trial calibration

RAPE TRANSFER TEST NO. 4 TYPE 401 GYRO #025 11 Sept 79
 TABLE NO. 339 R.T.S.F 32.73 MV/DEG/SEC
 SWITCH ON 1420 HOURS SWITCH OFF 1450 HOURS
 RUN UP TIME 0.0 SECS RUN DOWN TIME 0.0 SECS
 MAX TEMP 24.72 DEG C MIN TEMP 24.50 DEG C



GYRO SCALE FACTOR (SLOPE)	-3.5542 MV/DEG/SEC	
S D OF NON LINEARITIES	1.7475 DEG/SEC	
MAXIMUM NON LINEARITY	3.3940 DEG/SEC	%AGE MAXIMUM RATE
INTERCEPT OF BEST ST LINE	-2.6025 DEG/SEC	=0.8485
ZERO OFFSET	-2.5190 DEG/SEC	(with zero comp.)
ZERO HYSTERESIS	1.1957 DEG/SEC	
MAXIMUM HYSTERESIS	1.3427 DEG/SEC	TABLE RATE
		= -41.00 DEG/SEC

FIGURE C4.3 z-direction gyro, pre-trial calibration

A AXIS R.T. NO. 4 TYPE 401 GYRO #024 29 Jan 80

TABLE NO. 339

R.T.S.F 82.78 MV/DEG/SEC

SWITCH ON 1100 HOURS

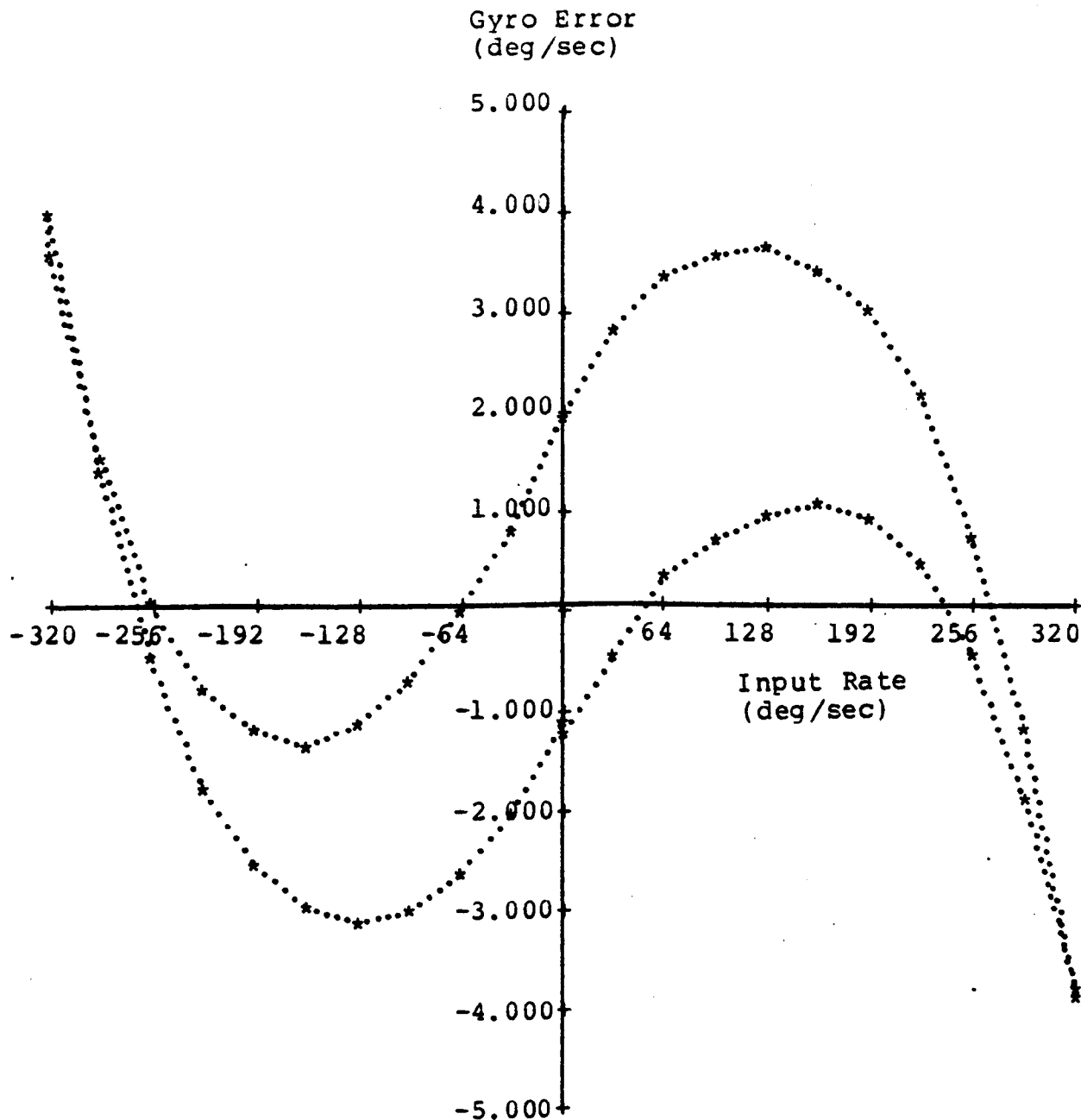
SWITCH OFF 1433 HOURS

RUN UP TIME 0.0 SECS

RUN DOWN TIME 0.0 SECS

MAX TEMP 24.56 DEG C

MIN TEMP 24.22 DEG C



GYRO SCALE FACTOR (SLOPE)	-5.9399 MV/DEG/SEC	
S D OF NON LINEARITIES	2.2052 DEG/SEC	
MAXIMUM NON LINEARITY	-3.9163 DEG/SEC	%AGE MAXIMUM RATE
INTERCEPT OF BEST ST LINE	-0.4958 DEG/SEC	= -1.2239
ZERO OFFSET	-0.1875 DEG/SEC	(with zero comp.)
ZERO HYSTERESIS	3.0772 DEG/SEC	
MAXIMUM HYSTERESIS	3.2587 DEG/SEC	TABLE RATE
		= 33.00 DEG/SEC

FIGURE C4.4 x-direction gyro, post-trial calibration

A AXIS R.T. NO. 4 TYPE 406 GYRO #066 29 Jan 80

TABLE NO. 339

R.T.S.F 82.78 MV/DEG/SEC

SWITCH ON 1715 HOURS

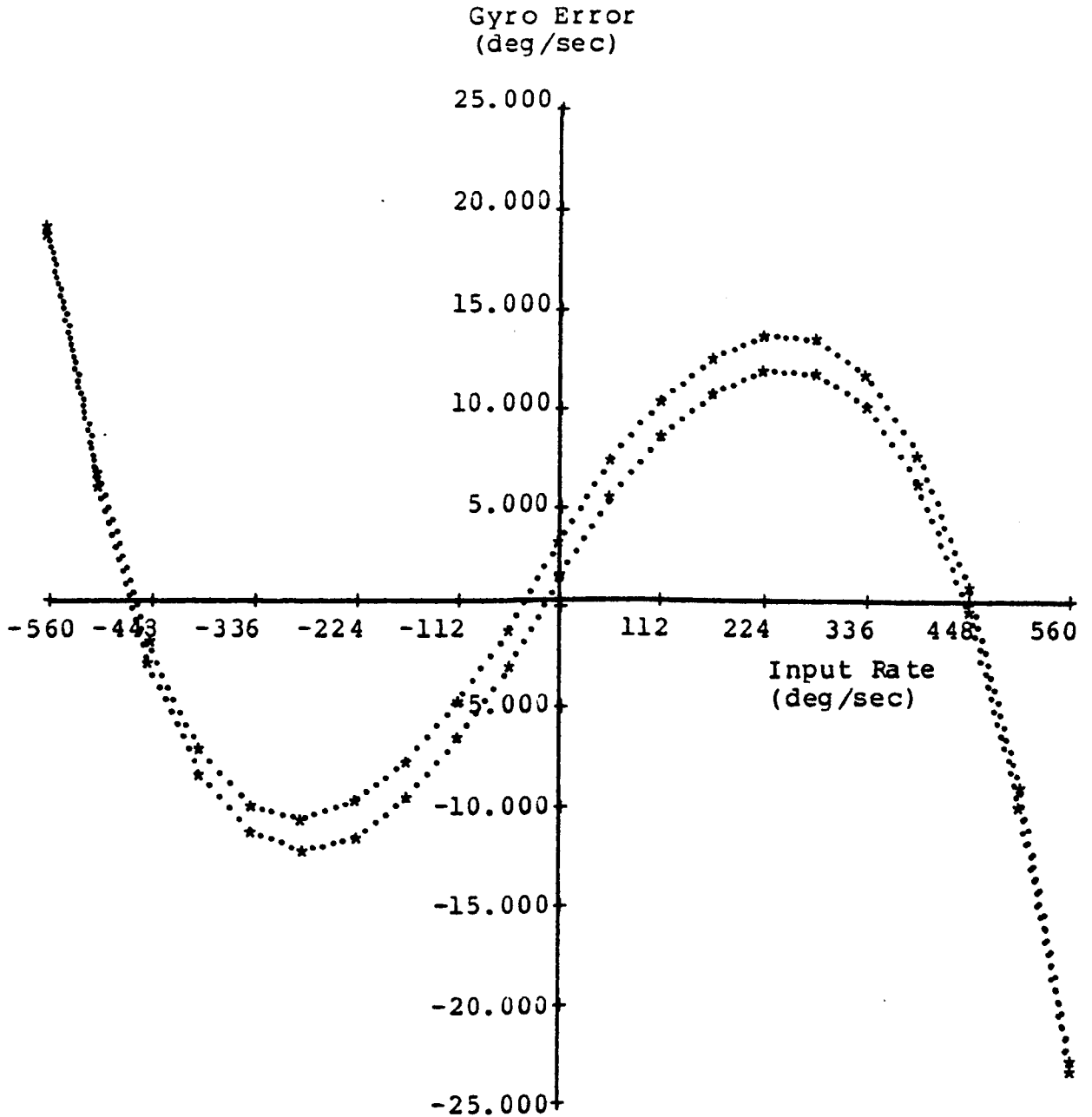
SWITCH OFF 1815 HOURS

RUN UP TIME 0.0 SECS

RUN DOWN TIME 0.0 SECS

MAX TEMP 24.50 DEG C

MIN TEMP 24.16 DEG C



GYRO SCALE FACTOR (SLOPE)	-7.9530 MV/DEG/SEC	
S D OF NON LINEARITIES	10.5386 DEG/SEC	
MAXIMUM NON LINEARITY	-23.4964 DEG/SEC	%AGE MAXIMUM RATE
INTERCEPT OF BEST ST LINE	-4.2201 DEG/SEC	= -4.1958
ZERO OFFSET	-2.2431 DEG/SEC	(with zero comp.)
ZERO HYSTERESIS	1.7067 DEG/SEC	
MAXIMUM HYSTERESIS	1.8222 DEG/SEC	TABLE RATE
		= -224.00 DEG/SEC

FIGURE C4.5 y-direction gyro, post-trial calibration

A AXIS R.T. NO. 5 TYPE 401 GYRO #025 29 Jan 80

TABLE NO. 339

R.T.S.F 82.78 MV/DEG/SEC

SWITCH ON 1550 HOURS

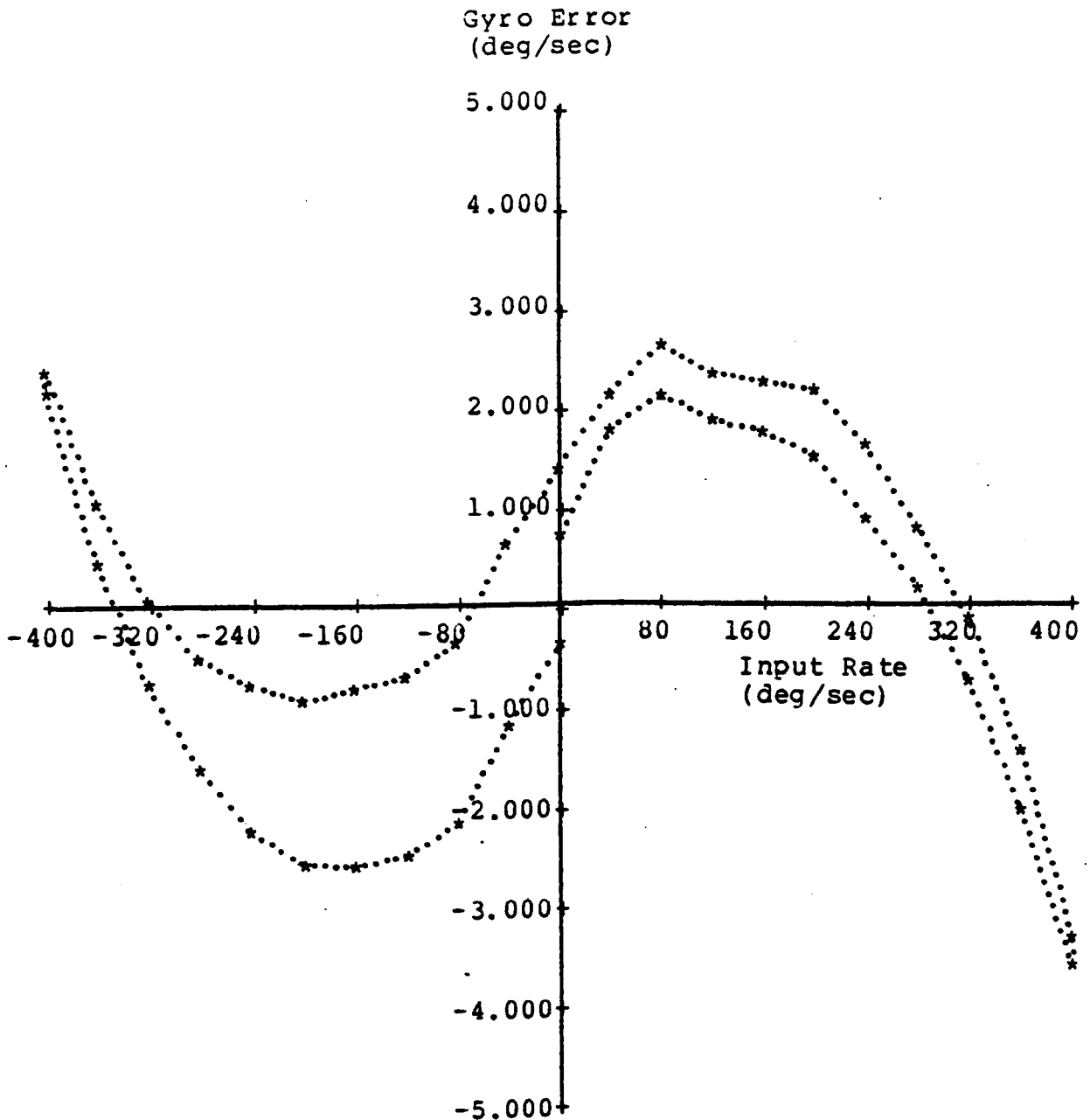
SWITCH OFF 1642 HOURS

RUN UP TIME 0.0 SECS

RUN DOWN TIME 0.0 SECS

MAX TEMP 24.29 DEG C

MIN TEMP 23.99 DEG C



GYRO SCALE FACTOR (SLOPE)
S D OF NON LINEARITIES
MAXIMUM NON LINEARITY
INTERCEPT OF BEST ST LINE
ZERO OFFSET
ZERO HYSTERESIS
MAXIMUM HYSTERESIS

-3.6445 MV/DEG/SEC
1.7554 DEG/SEC
-3.5946 DEG/SEC
-3.9224 DEG/SEC
-3.1956 DEG/SEC
1.1969 DEG/SEC
1.7802 DEG/SEC

%AGE MAXIMUM RATE
=-0.8987
(with zero comp.)
TABLE RATE
=-40.00 DEG/SEC

FIGURE C4.6 z-direction gyro, post-trial calibration

$I_n = 9.81 \times 10^9 \text{ m/s}^2$

TEST RECORD SHEET FOR ACCELERATION TRANSDUCER

CODE NO. 503 ADA/30
 SER. NO. AE 1705/75
 TYPE NO. AL-V-692
 RANGE -3g - +3g
 SPEC. NO. 56017 Issue 1. AL. 3
 ERROR (%FSO) = (ACTUAL OUTPUT - THEORETICAL OUTPUT) x 100 / FSO
 NON-LINEARITY 0.15 % FSO
 HYSTERESIS 0.1 % FSO
 ZERO g_n ERROR 0.40 % FSO
 SENSITIVITY 1.005 V/gn
 OUTPUT RESISTANCE 0.22 kOhms
 OUTPUT NOISE 9.0 mV
 AXIS ALIGNMENT 4.53 mV
 EXCITATION CURRENT 3.7 mA
 OVERLOAD OUTPUT + 4.028 - 4.068 Volts g/n
 TRANSVERSE SENSITIVITY Volts g/n
 STOPS UPPER LIMIT 22 % Span
 LOWER LIMIT 20 % Span
 EXCITATION VOLTAGE 6.0 Volts

PLOT OF OUTPUT DEVIATION FROM THEORETICAL CURVE • EXCITATION VOLTAGE

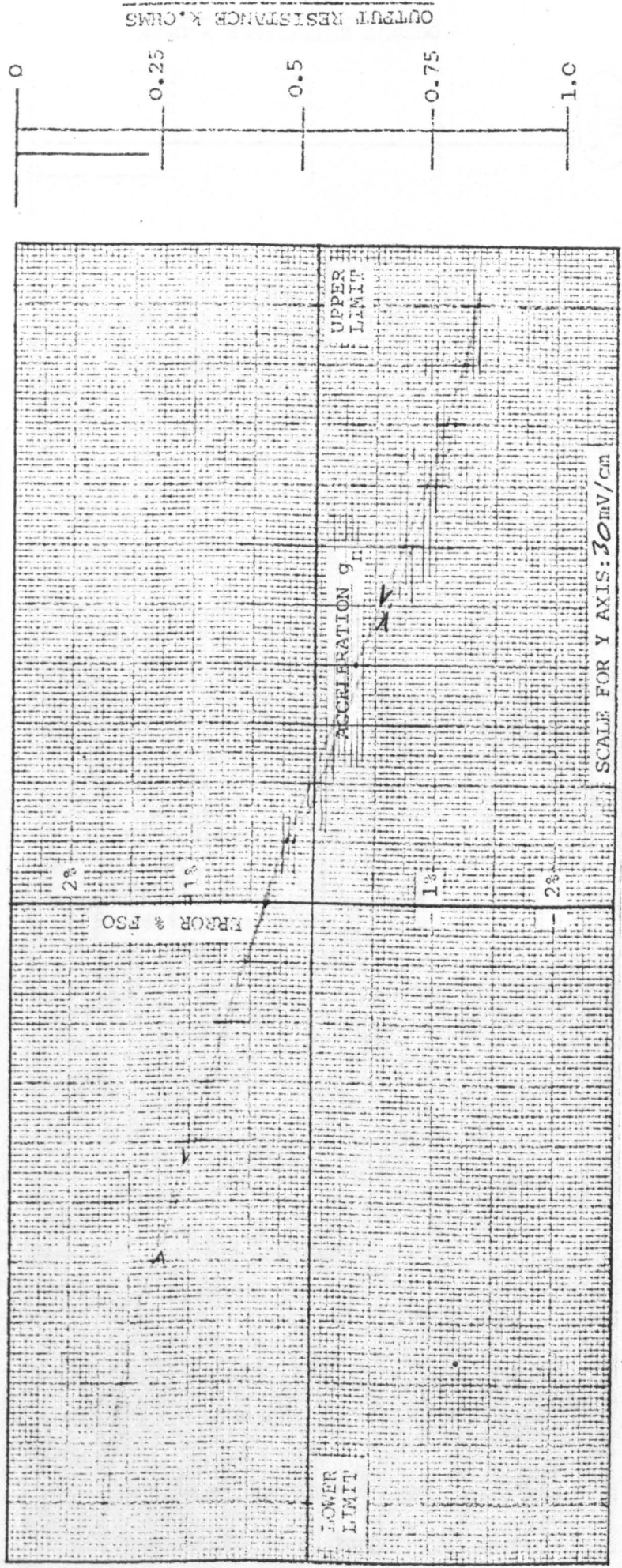


FIGURE C4.8 y-direction accelerometer, pre-trial calibration

TEST RECORD SHEET FOR ACCELERATION TRANSDUCER

CODE NO. *503 ADA/31.*
 SER. NO. *AE 2871/77*
 TYPE NO. *63-169*
 RANGE *50g Issue 1 AL 4*
 SPEC. NO. *56027*
 ERROR (%FSO) = (ACTUAL OUTPUT - THEORETICAL OUTPUT) x 100

NON-LINEARITY *0.20* % FSO
 HYSTERESIS *0.10* % FSO
 ZERO g_n ERROR *0.20* % FSO
 SENSITIVITY *0.4977* V/ g_n
 OUTPUT RESISTANCE *0.22* kohms

OUTPUT NOISE *9* mV
 AXIS ALIGNMENT *0.92* mV
 EXCITATION CURRENT *3.5* mA
 OVERLOAD OUTPUT *+ 4.416 - 4.797* Volts
 TRANSVERSE SENSITIVITY *6* g_n/g_n

STOPS UPPER LIMIT *+ 23* % Span
 LOWER LIMIT *- 27* % Span

PLOT OF OUTPUT DEVIATION FROM THEORETICAL CURVE. EXCITATION VOLTAGE.

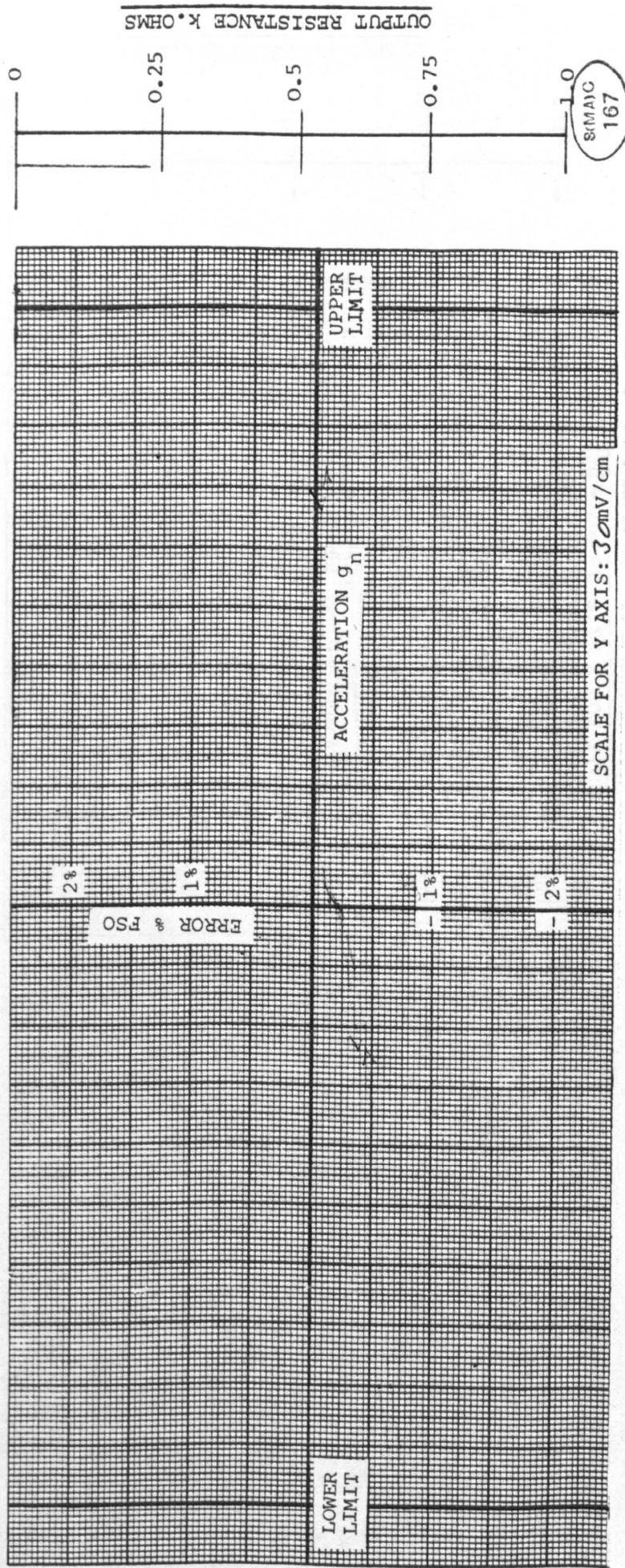


FIGURE C4.9 z-direction accelerometer, pre-trial calibration

TEST RECORD SHEET FOR ACCELERATION TRANSDUCER

503 ADA/30
AE 2435/176

CODE NO.
 SER. NO.
 TYPE NO.
 RANGE $\pm 3.0 \text{ gm}$
 SPEC. NO. Issue AL
 ERROR (%FSO) = $\frac{\text{ACTUAL OUTPUT} - \text{THEORETICAL OUTPUT}}{\text{FSO}} \times 100$
 NON-LINEARITY % FSO
 HYSTERESIS % FSO
 ZERO g_n ERROR % FSO
 SENSITIVITY V/g_n
 OUTPUT RESISTANCE kohms
 OUTPUT (%FSO) = $\frac{\text{ACTUAL OUTPUT} - \text{THEORETICAL OUTPUT}}{\text{FSO}} \times 100$
 STOPS UPPER LIMIT +
 LOWER LIMIT -
 EXCITATION VOLTAGE 6.0

PLOT OF OUTPUT DEVIATION FROM THEORETICAL CURVE. EXCITATION VOLTAGE.

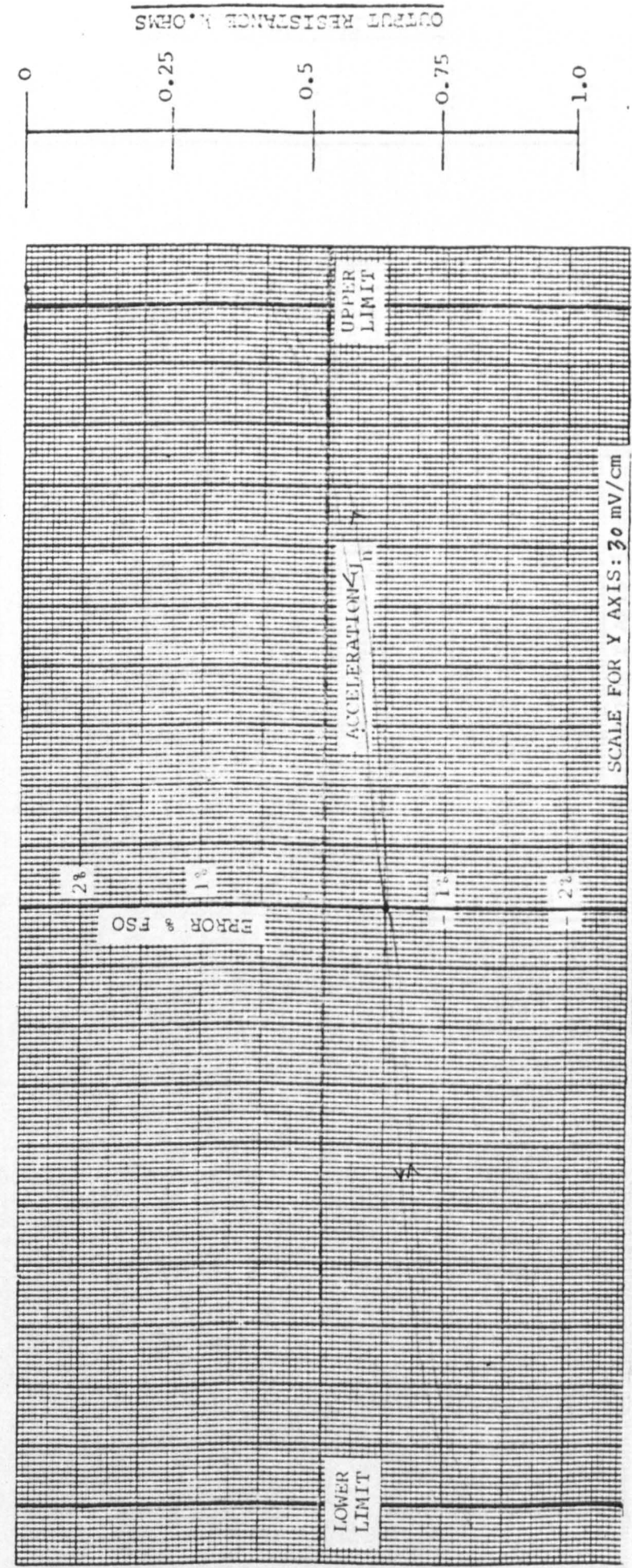


FIGURE C4.10 x-direction accelerometer, post-trial calibration

TEST RECORD SHEET FOR ACCELERATION TRANSDUCER

CODE NO. 503 ADA/31
 SER. NO. AE 2871/7
 TYPE NO. $\pm 6g_n$
 RANGE Issue
 SPEC. NO. AL
 ERROR (%FSO) = (ACTUAL OUTPUT - THEORETICAL OUTPUT) x 100
 FSO
 NON-LINEARITY % FSO
 HYSTERESIS % FSO
 ZERO g_n ERROR % FSO
 SENSITIVITY V/ g_n
 OUTPUT RESISTANCE kohms
 OUTPUT - THEORETICAL OUTPUT) x 100
 FSO
 OUTPUT NOISE mV
 AXIS ALIGNMENT Degrees
 EXCITATION CURRENT mA
 OVERLOAD OUTPUT Volts
 TRANSVERSE SENSITIVITY g_n/g_n
 STOPS UPPER LIMIT + % Span
 LOWER LIMIT - % Span
 EXCITATION VOLTAGE Volts
 C.A.Q.

PLOT OF OUTPUT DEVIATION FROM THEORETICAL CURVE • EXCITATION VOLTAGE

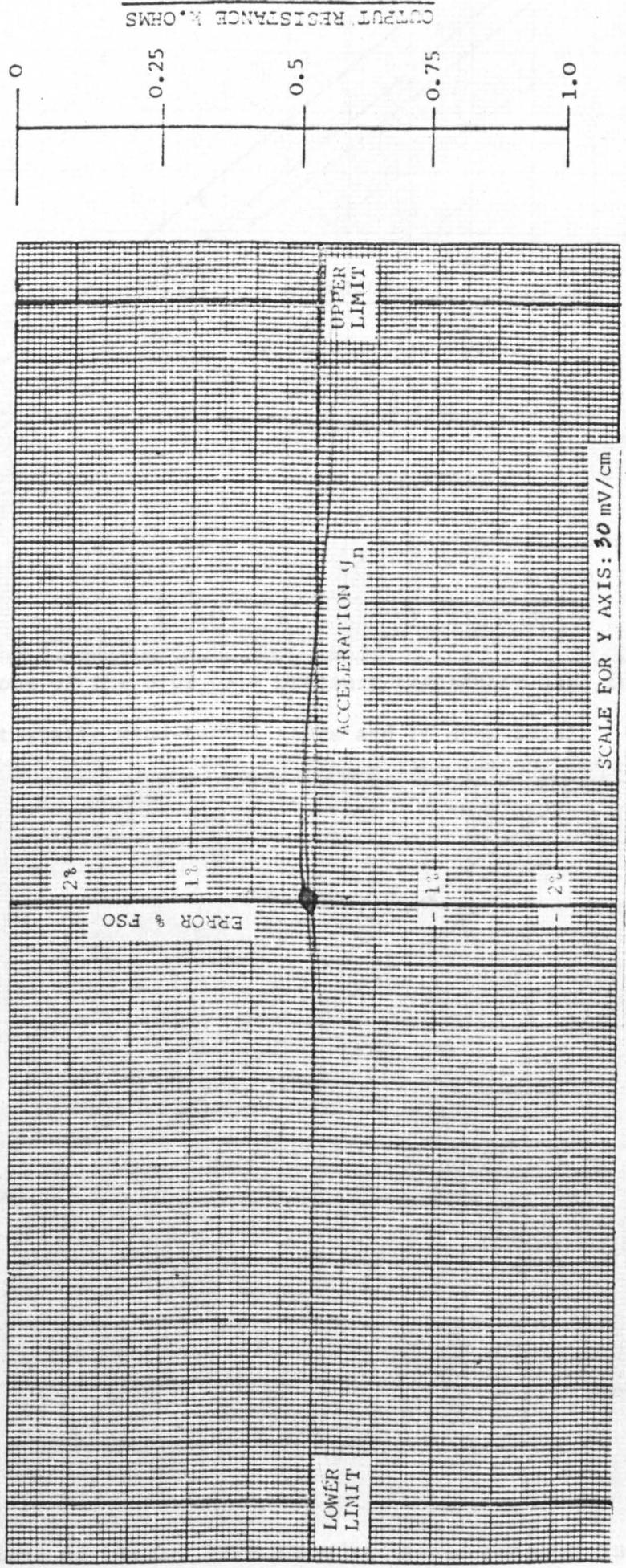


FIGURE C4.12 z-direction accelerometer, post-trial calibration

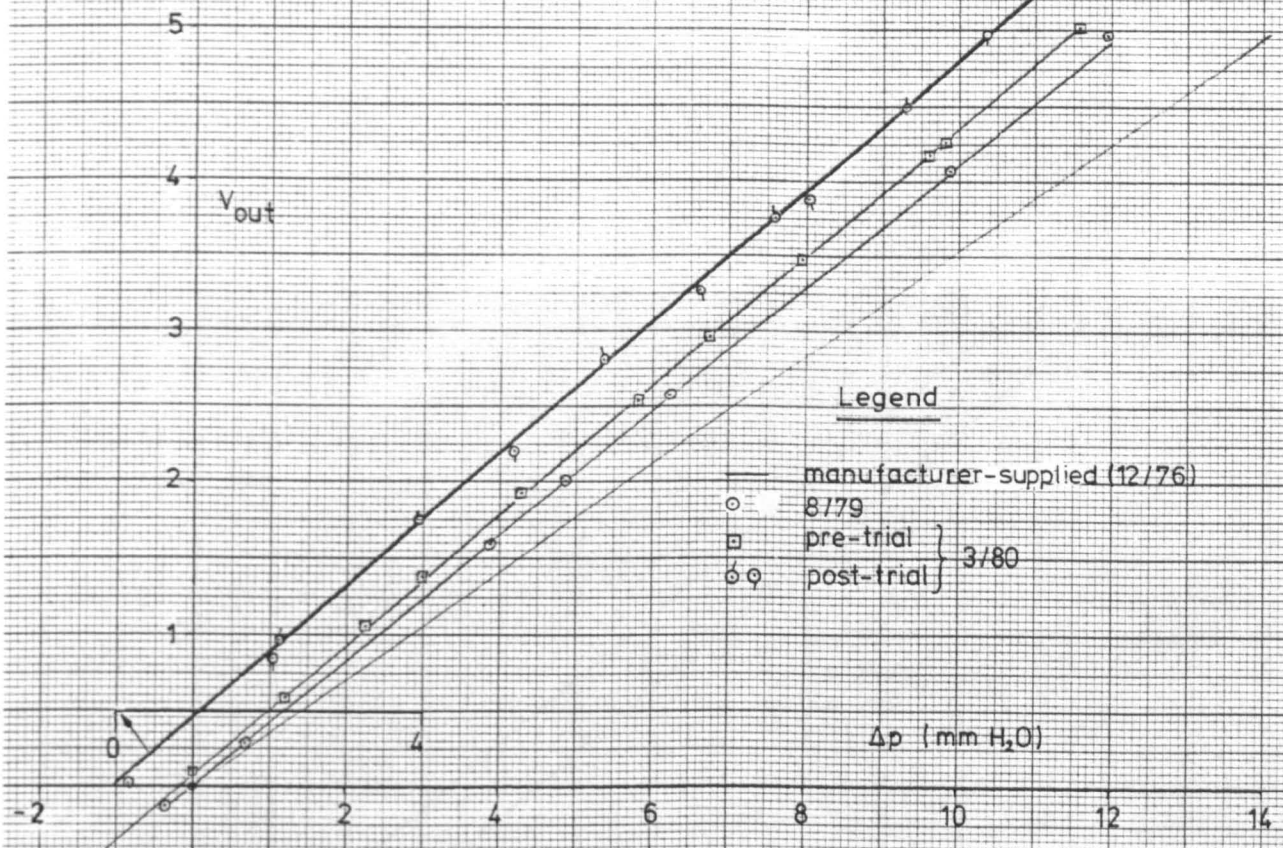


FIGURE C4.13 Calibrations of the 0.02 psid pressure transducer used in SB Pitot-static wind-tunnel tests and in drop trials

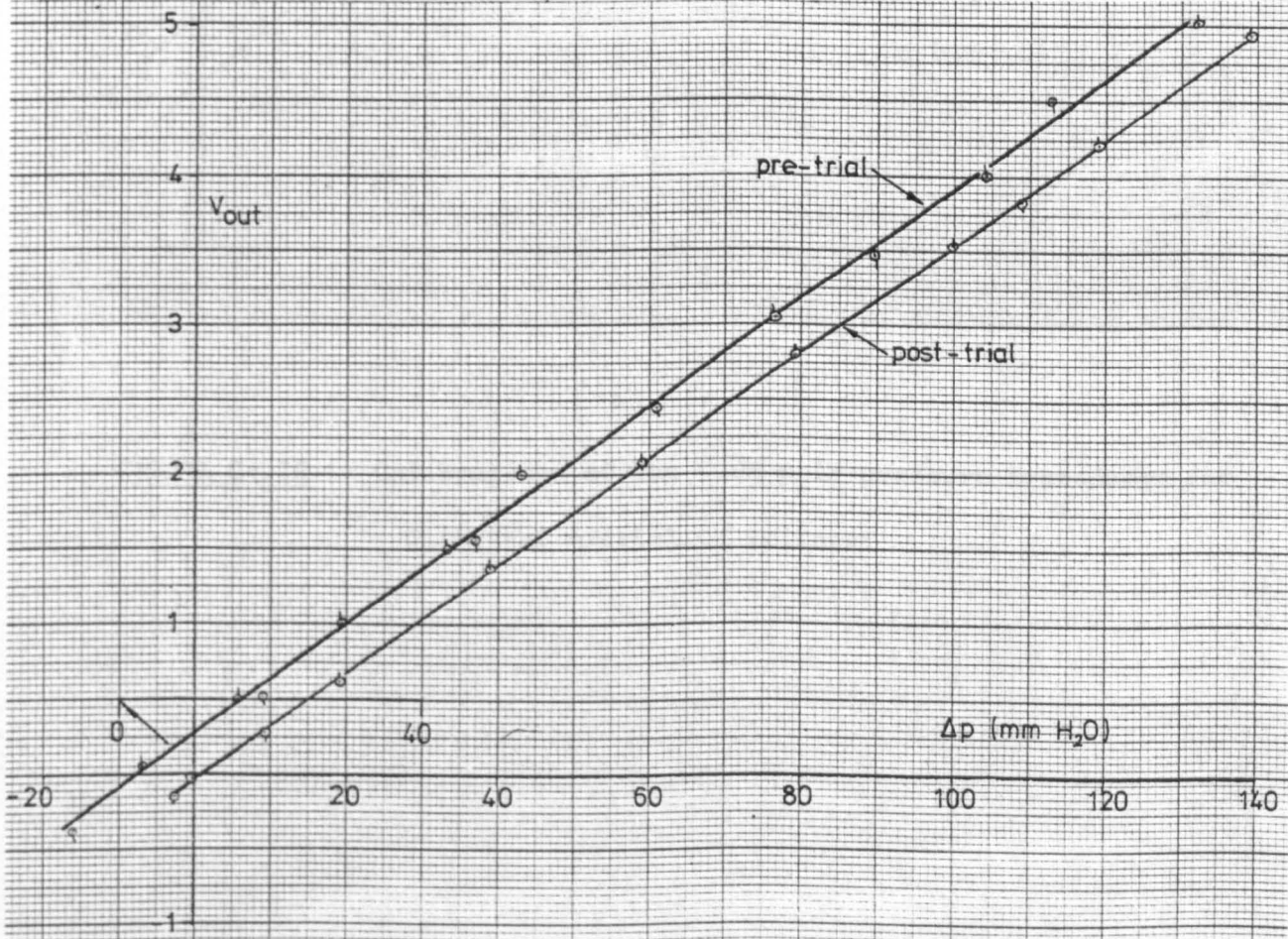


FIGURE C4.14 Calibrations of the 0.2 psid pressure transducer used in BB Pitot-static wind-tunnel tests

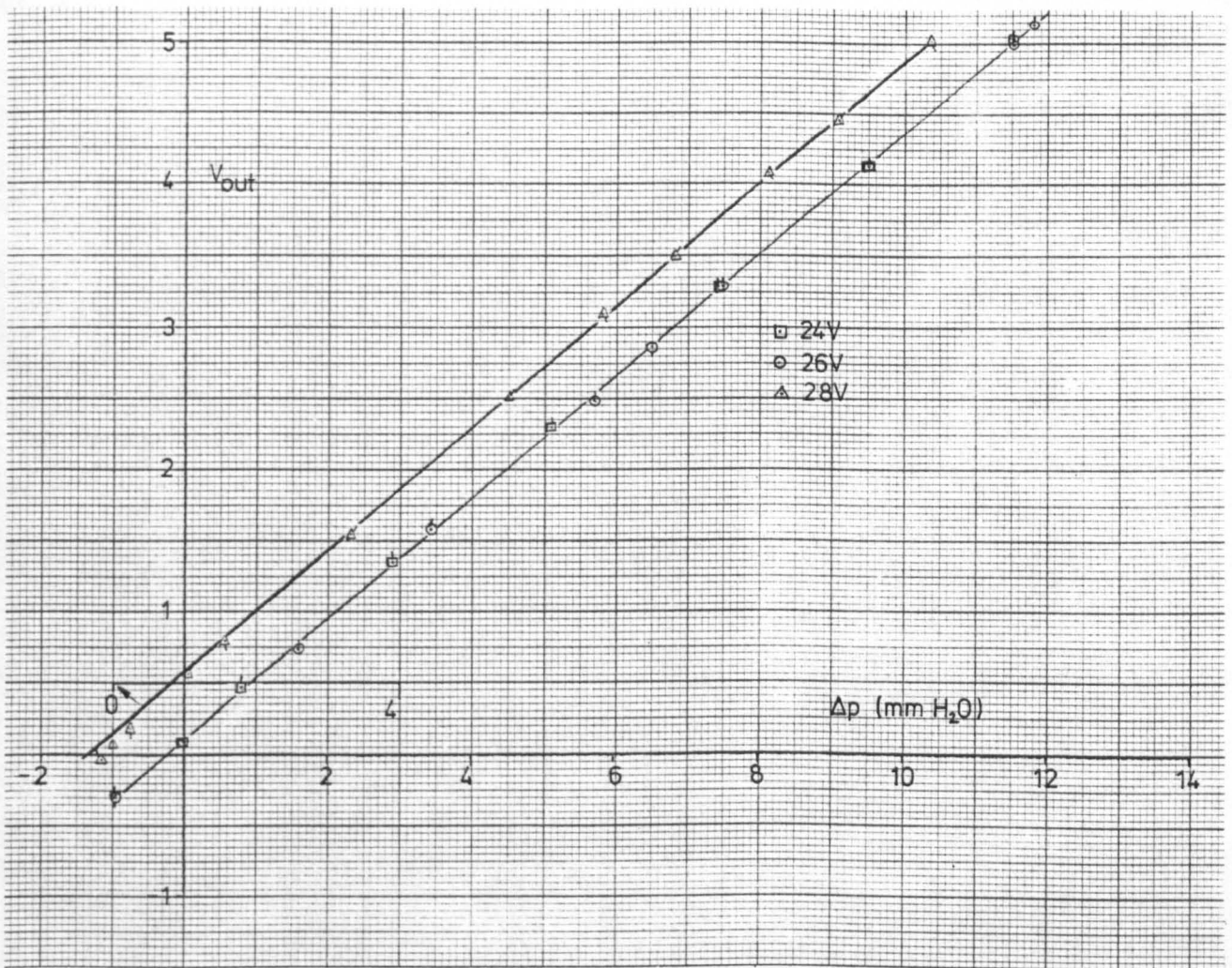


FIGURE C4.15 Calibrations of the 0.02 psid pressure transducer for different excitation voltages

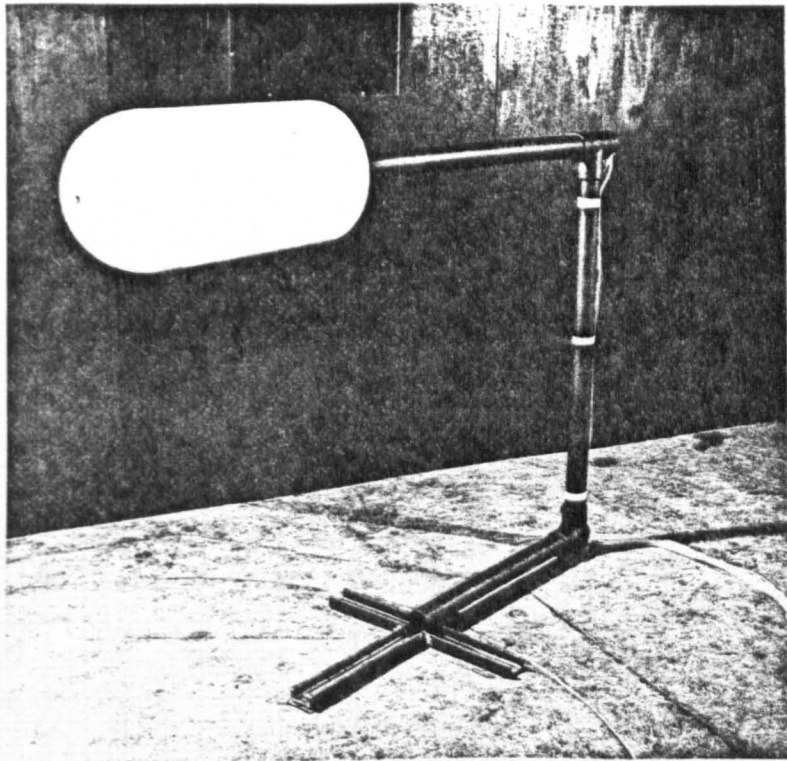


FIGURE C4.16 SB Pitot-static sensor test rig in the Leicester University 2.5 m x 1.8 m wind-tunnel



FIGURE C4.17 SB Pitot-static sensor calibration test rig in the Bristol University 7ft x 5ft wind-tunnel

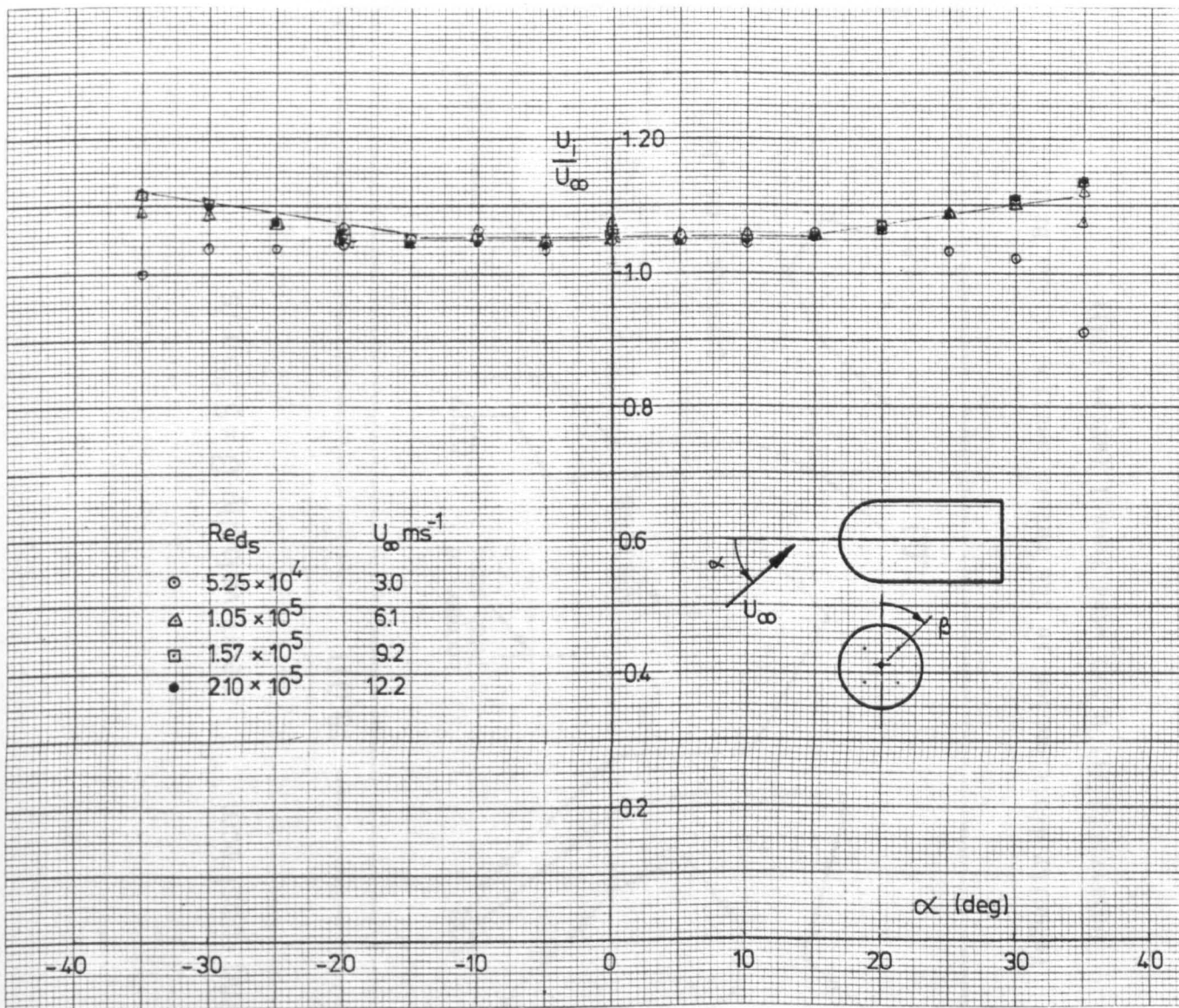


FIGURE C4.18 Calibration curves for the SB Pitot-static sensor

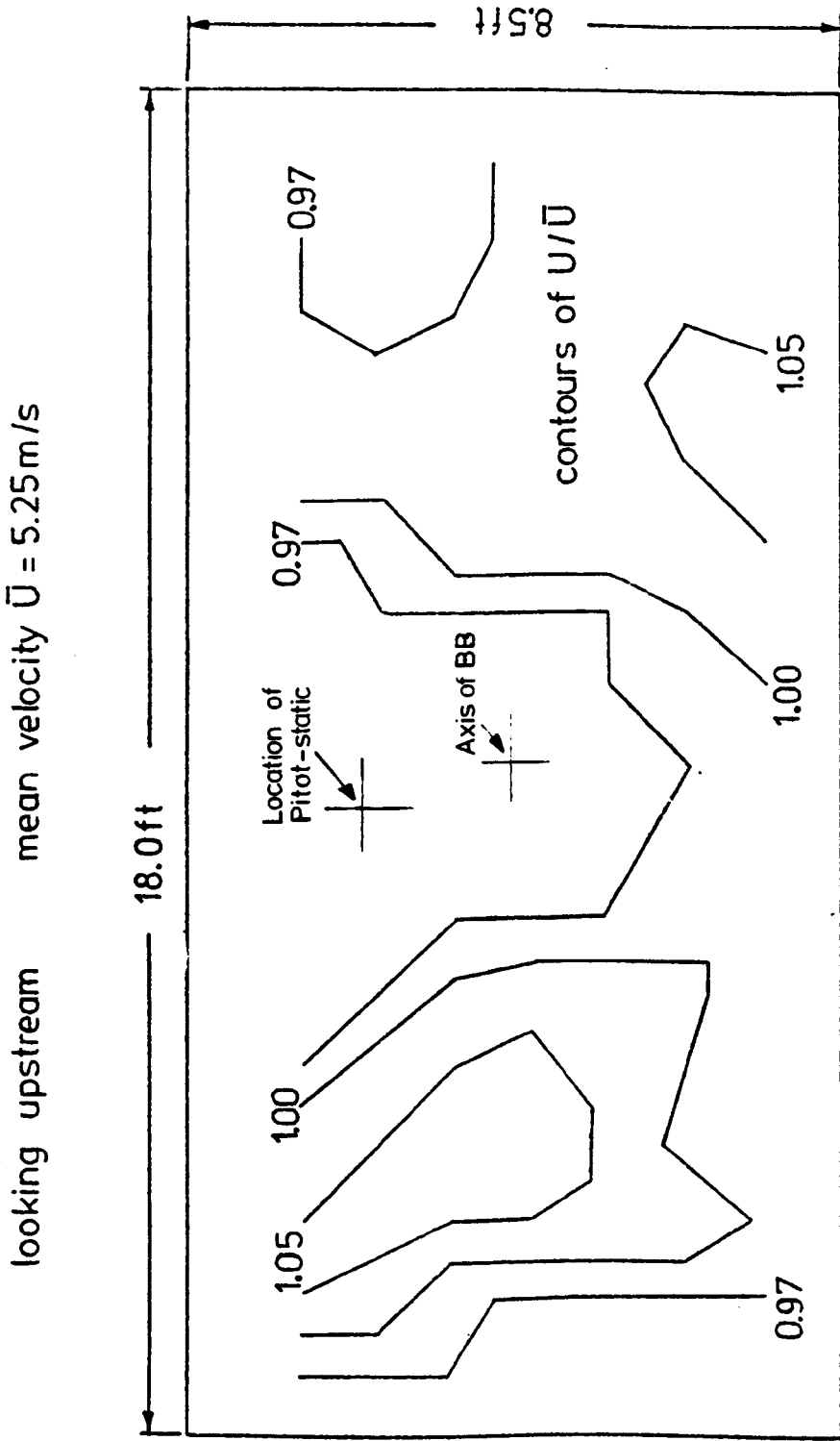


FIGURE C4.19 Velocity distribution in the return section of the Bristol University 7 ft x 5 ft wind tunnel (after [79])

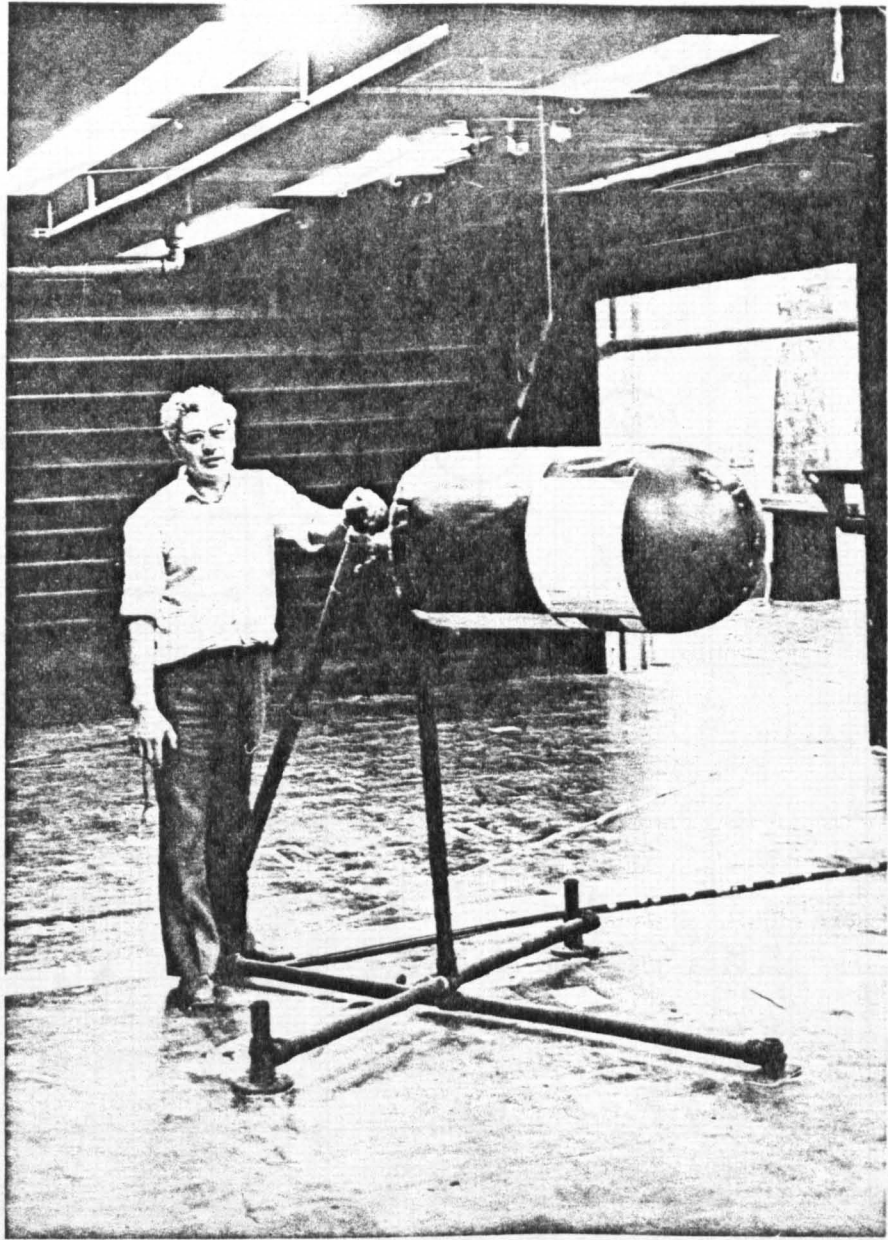


FIGURE C4.20 BB Pitot-static calibration in the return section of the Bristol University 7ft x 5ft wind-tunnel

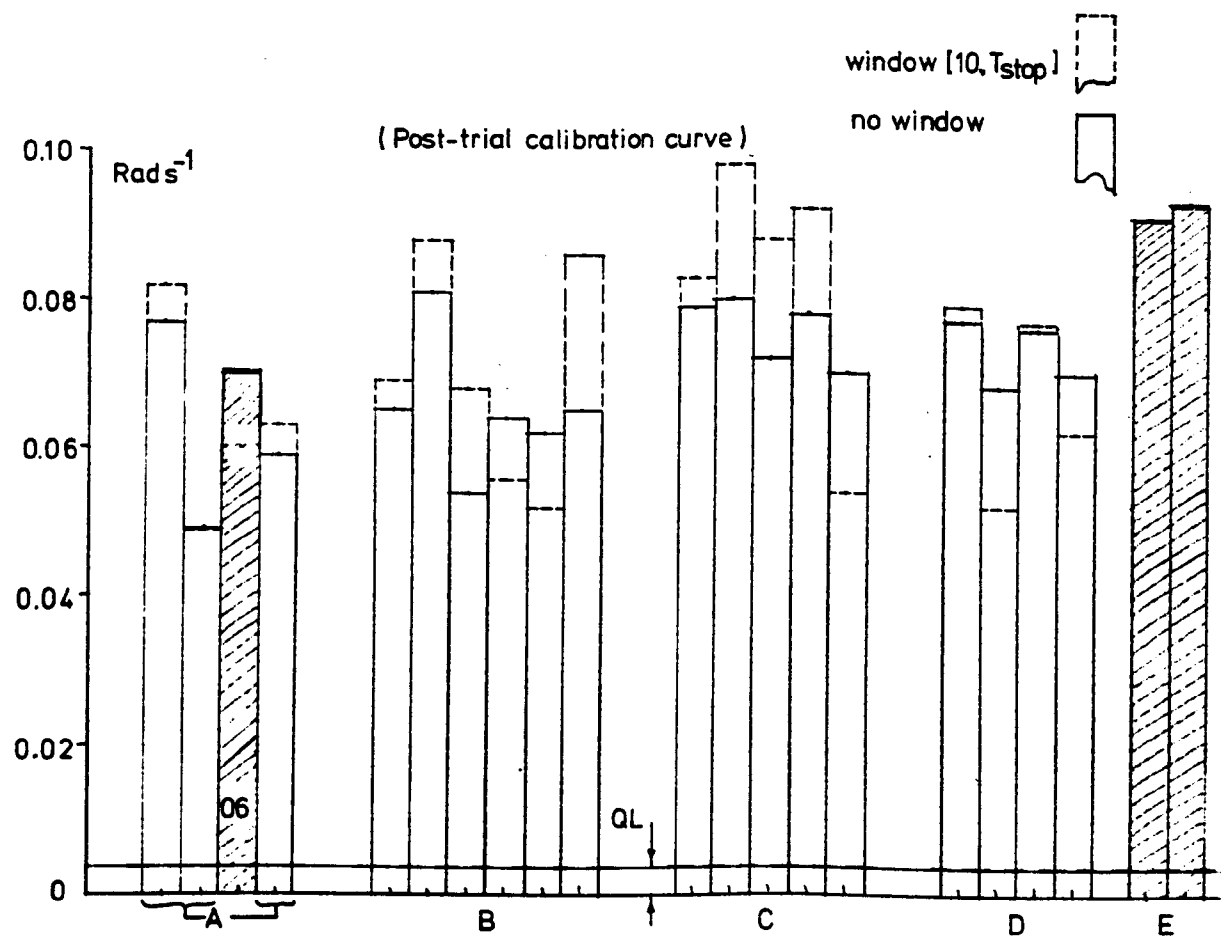
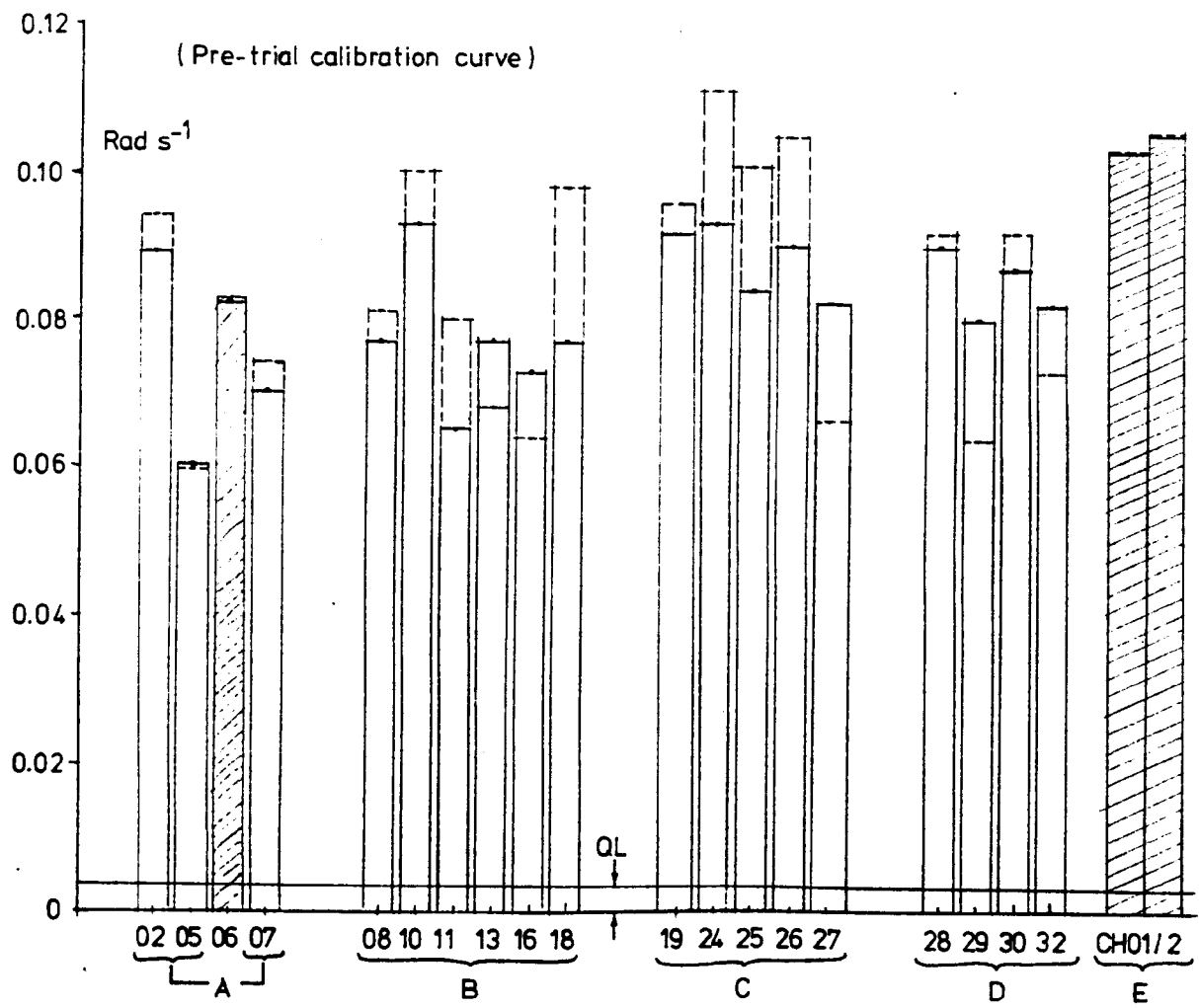


FIGURE C5.1 Measured bias, p-gyro

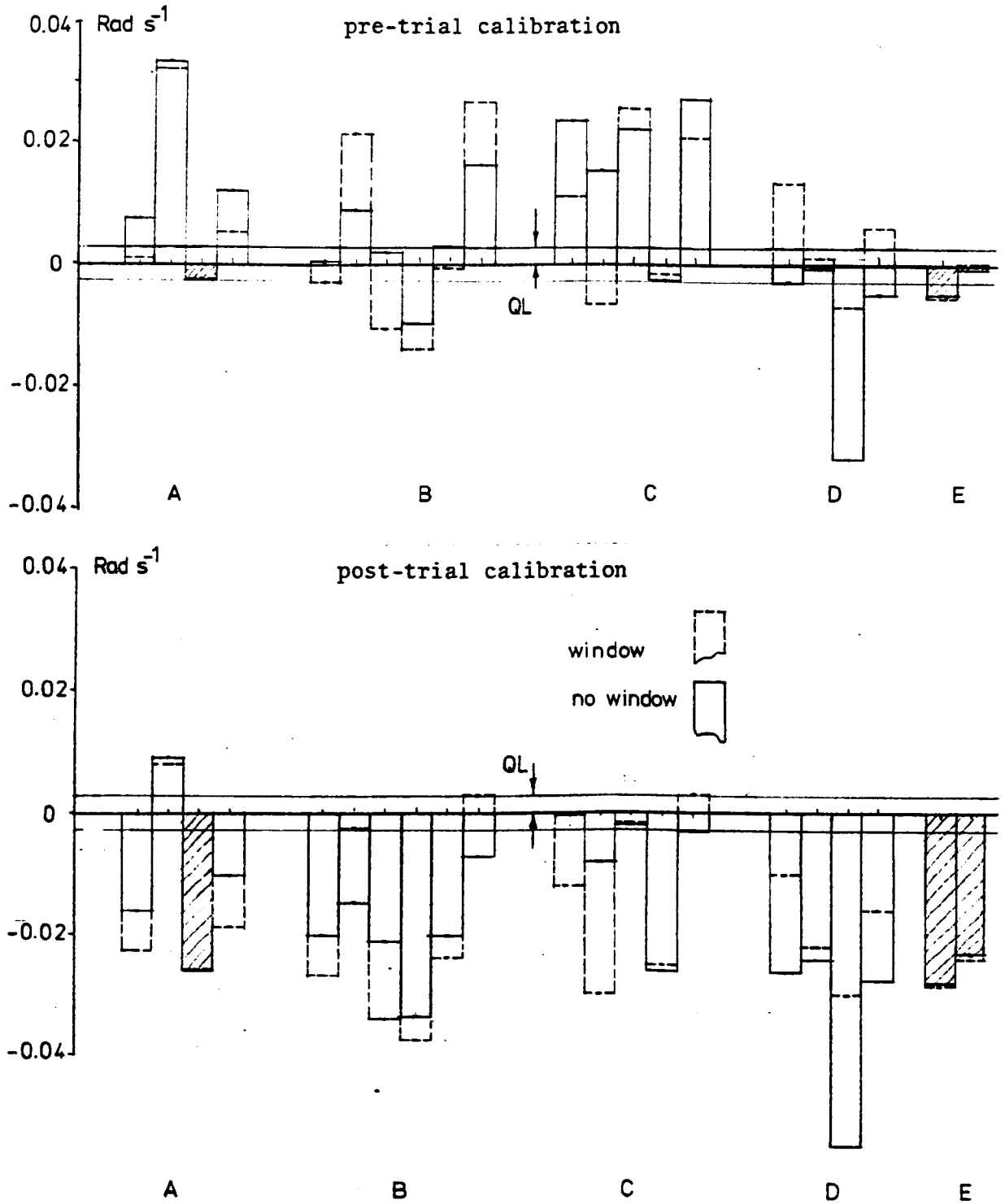


FIGURE C5.2 Measured bias, q-gyro

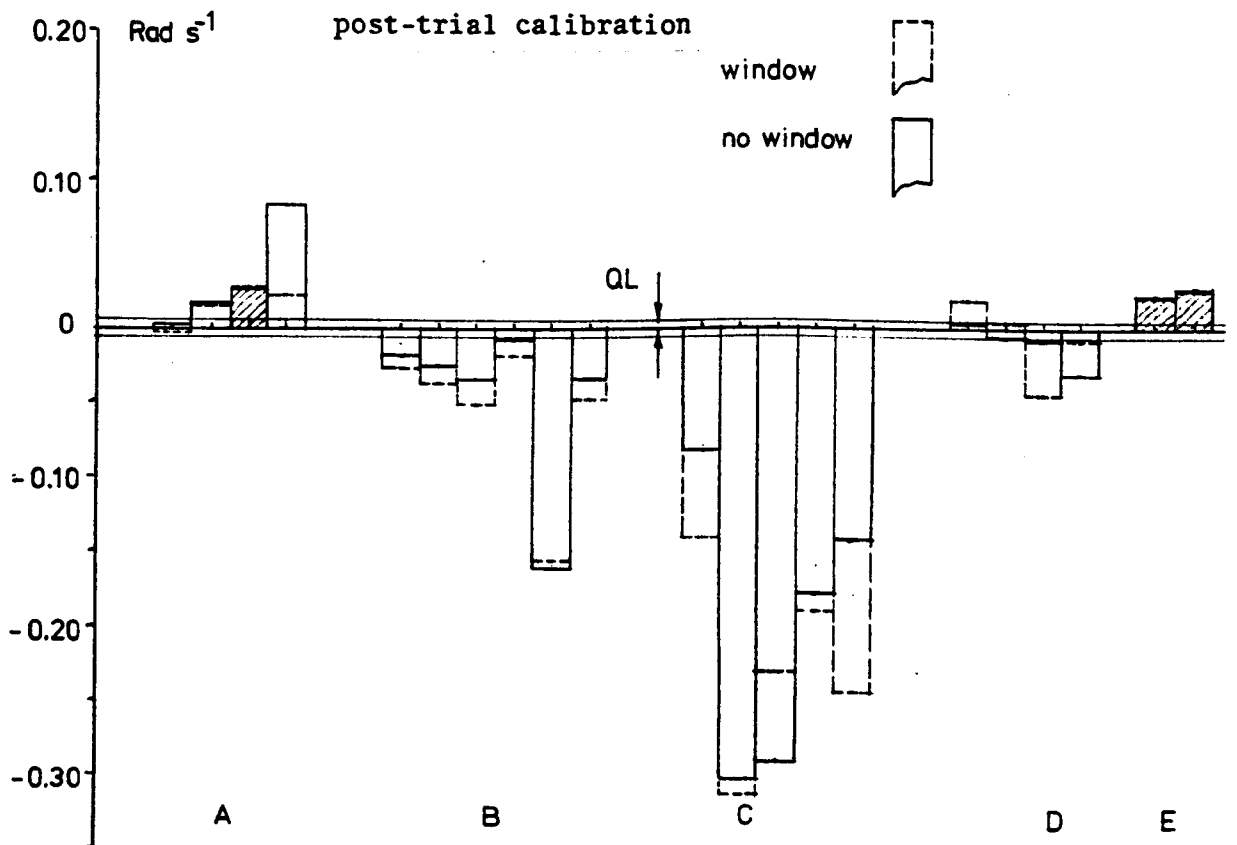
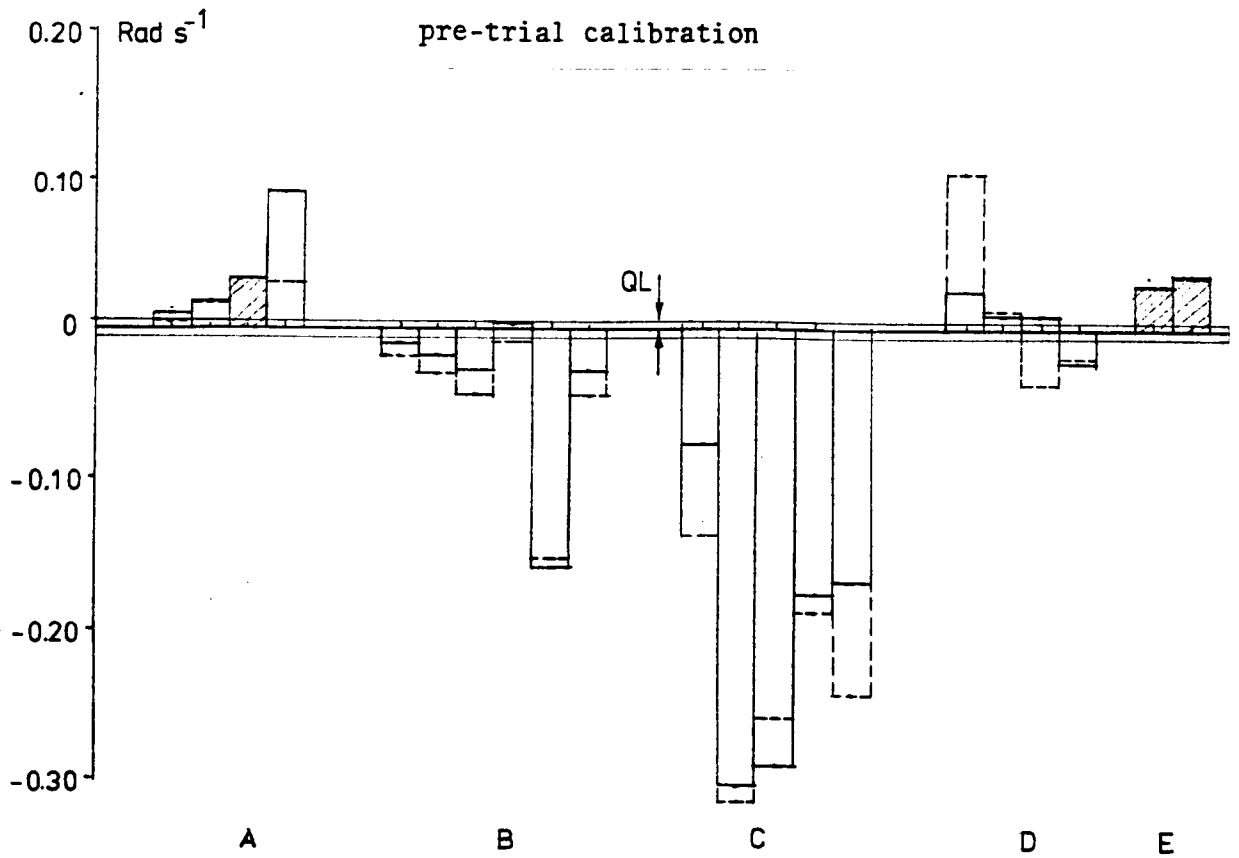


FIGURE C5.3 Measured bias, r-gyro

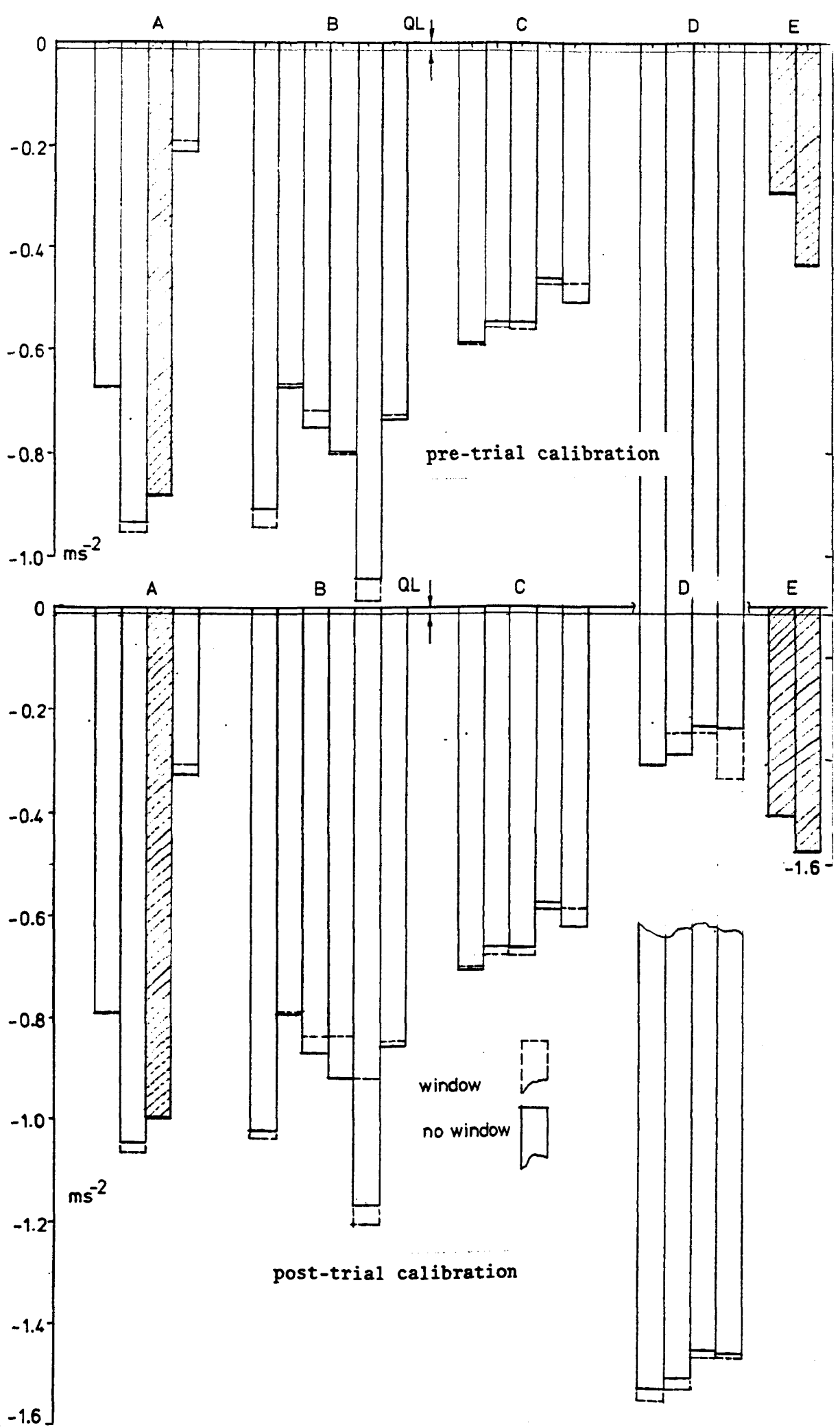


FIGURE C5.4

Measured bias, x-direction accelerometer

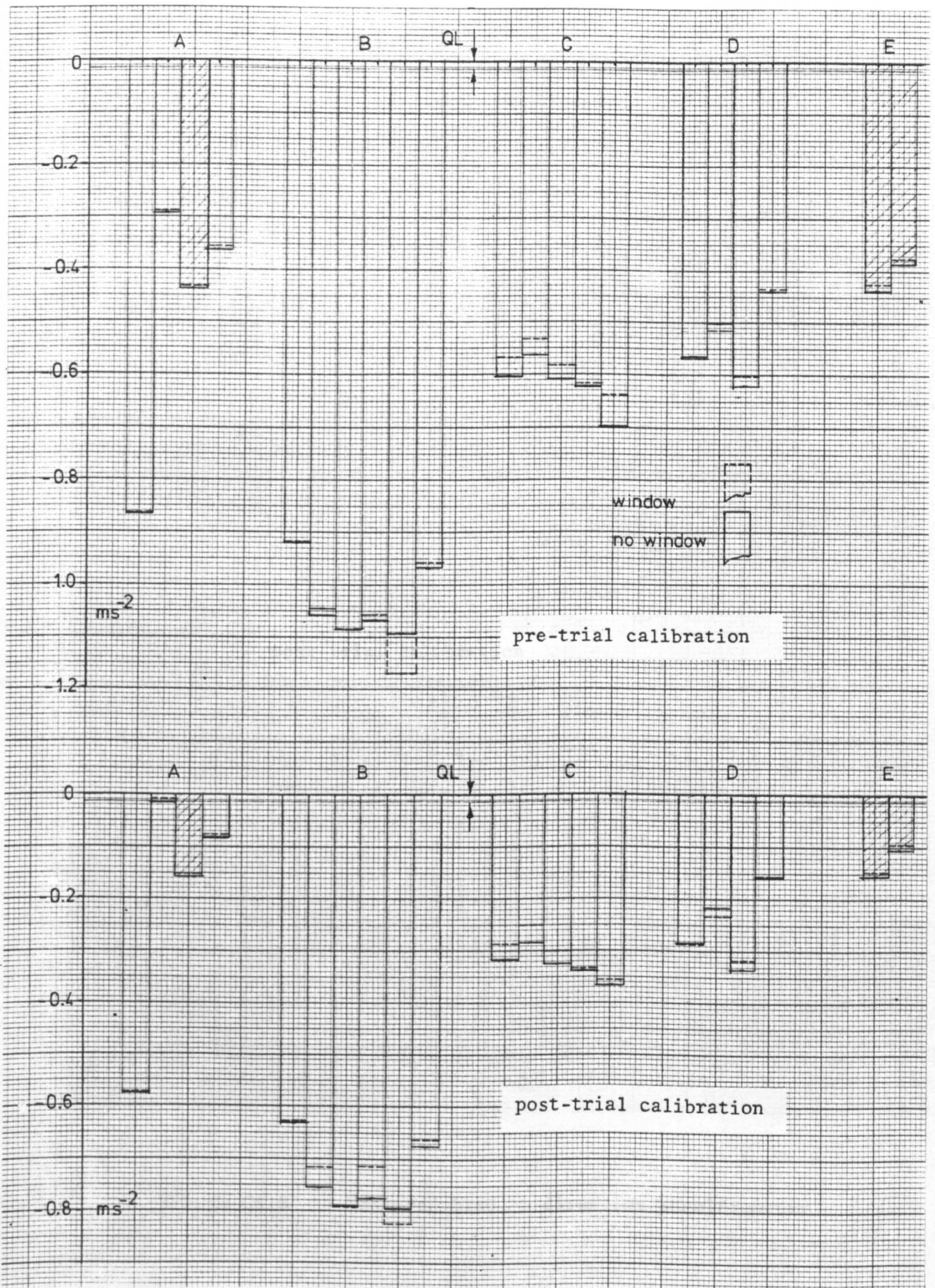


FIGURE C5.5

Measured bias, y-direction accelerometer

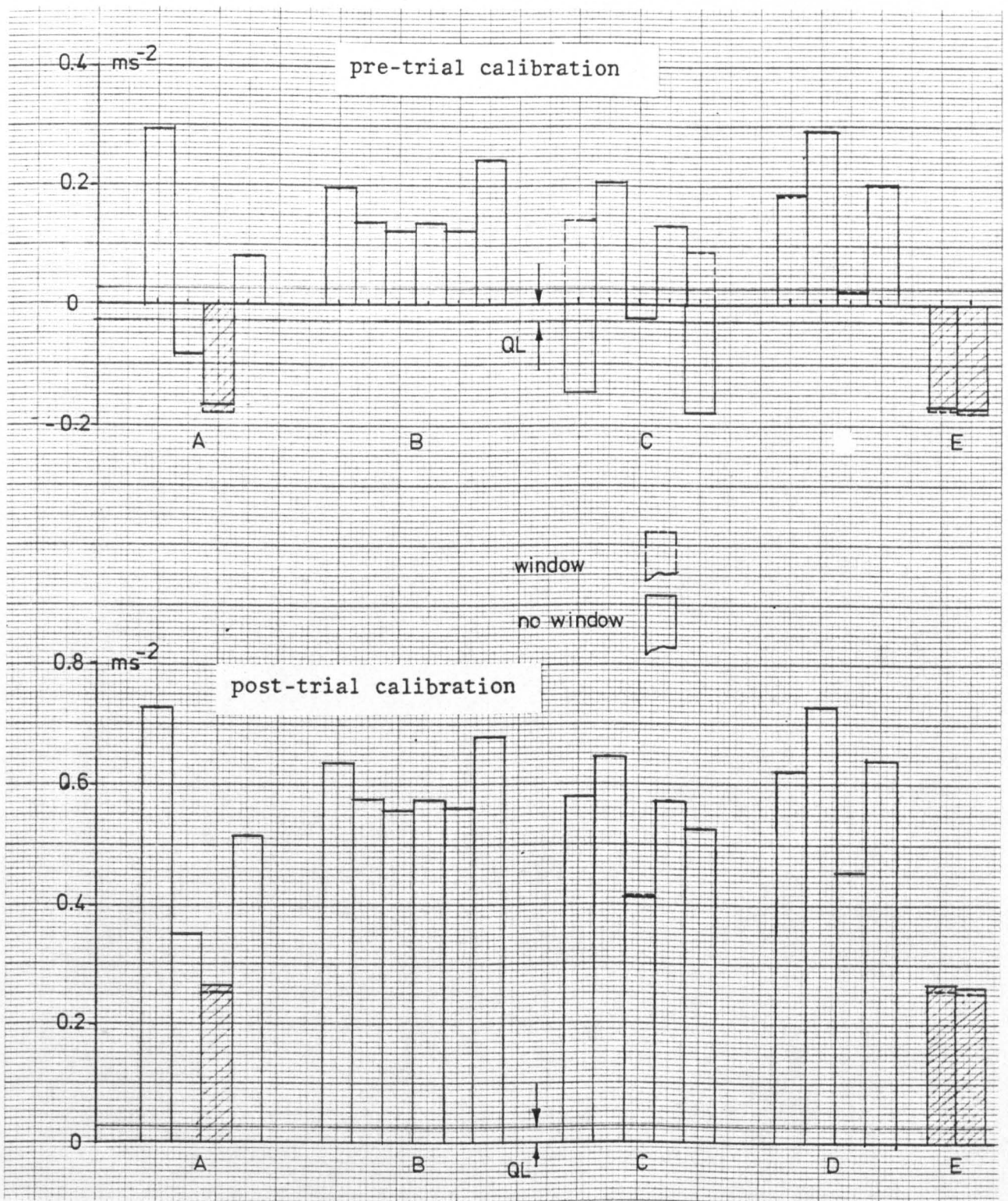


FIGURE C5.6

Measured bias, z-direction accelerometer